Deformation and Strain Concentrations in Coarse-Grained Alpha-Uranium



Philip David Earp

St Catherine's College

University of Oxford

A thesis submitted for the degree of

Doctor of Philosophy

Michaelmas 2015 - Trinity 2019

Ministry of Defence © British Crown Copyright 2020/AWE

Ministry of Defence © British Crown Copyright 2020/AWE

This thesis is dedicated to my late grandmother,

Betty McDonald

for inspiring me to achieve

Ministry of Defence © British Crown Copyright 2020/AWE

Ministry of Defence © British Crown Copyright 2020/AWE

Acknowledgements

I am eternally grateful for the support and assistance I have received throughout my four years in Oxford. I would like to thank the countless academic, industrial, and technical staff who have enabled this project – it couldn't have been done without your help!

I give sincere thanks to Professor James Marrow for sharing his time and expertise, and for providing invaluable guidance at all stages of this DPhil project. I am fortunate to have worked under such an excellent supervisor. I am also grateful for the supervision and logistical support from Dr John Askew at AWE plc, and would like to thank the company for their financial support.

The modelling aspects of this project have been expertly performed by Dr Nicolò Grilli, Dr Edmund Tarleton, and Professor Alan Cocks, and I thank them for their significant contributions towards the project.

I would like to thank those who have assisted with the logistical and safety aspects of working with uranium – Mark Bradley and Professor Chris Grovenor in Oxford, Dr Marek Jura at ISIS, and Dominick Hallett at AWE plc.

Much of this work involved complex neutron diffraction experiments, and I would like to thank all who have assisted in this area. From the Los Alamos Neutron Science Center, LANL, USA, I am grateful to Dr Bjørn Clausen, Dr Don Brown, Dr Rod McCabe, Dr Sven Vogel and from the ISIS Neutron Source, UK, I would like to thank Dr Saurabh Kabra, Dr Joe Kelleher and Dr Winfried Kockelmann. I extend these thanks to colleagues who assisted during these experiments; Dr Dong Liu, Thomas Zillhardt, Shixiang Zhao, and Talha Pirzada. I give special thanks to Tom Shaw from AWE plc. for providing assistance and good company during our experiment in the USA.

I am grateful to the staff and students at the Interface Analysis Centre, School of Physics, University of Bristol who provided invaluable assistance with the EBSD sample preparation and measurement – in particular, Dr Keith Hallam, Professor Tom Scott, Dr Chris Jones, Joseph Sutcliffe and Dr Xander Warren.

I would like to thank my colleagues in the Department of Materials, whom I now consider good friends. I'd like to thank Dr Selim Barhli for welcoming me into the group at the start of the project, for sharing his expertise in writing MATLAB code and for putting up with my constant questioning and interruption during my first year. I'd also like to thank Matthew Jordan for giving guidance and support inside and outside of work. In addition I'd like to thank all members of my research group for making my time in Oxford so enjoyable, particularly Dr Matt Molteno, Dr Ahmet Cinar, Liye Yan and Chloe Farrar.

Ministry of Defence © British Crown Copyright 2020/AWE

Outside of work, I have an excellent support network of family and friends. I'd like to thank Timothy Davies, Juliane Borchert, and all my housemates for our endless kitchen conversations and fun times living together. I'd like to thank all of my friends from King Henry VIII School in Coventry, Fitzwilliam College, Cambridge, Cambridge University Air Squadron, and St Catherine's College, Oxford for their irreplaceable friendship, and to the 43rd Oxford Scout Group and all those in Oxford Spires scouting, for providing a much-needed break from academic work.

Finally, I'd like to thank my family, and in particular my parents Jane and Peter, for their unconditional love and support throughout my life. I could not have succeeded without you.

Ministry of Defence © British Crown Copyright 2020/AWE

Abstract

This thesis presents an experimental characterisation of the deformation of coarse-grained cast alpha-uranium to assist the development of crystal plasticity finite element (CPFE) models.

Uranium exhibits elastic and plastic anisotropy and deforms heterogeneously via multiple slip and twinning modes. Strain concentrations that develop in the deforming grains may initiate fracture. There is an industrially-motivated drive to perform CPFE simulations that incorporate the unique properties of uranium to allow a better understanding of the conditions leading to fracture.

Experiments have been performed by the author to provide data for calibration and validation of a CPFE model for cast α-uranium.

Time-of flight neutron diffraction was used to measure internal lattice strain development and texture changes during in-situ tension and compression. The coarse microstructure raises experimental challenges – these are solved in a subsequent experiment. Deformation twinning causes a lattice reorientation that is detectable as a macroscopic texture change. A novel analysis was performed allowing active twinning modes to be identified from the texture changes. Twinning accounts for the observed tension-compression asymmetry in the material.

Digital image correlation (DIC) was used to measure the full-field surface strains during tensile deformation of cast uranium. The measured strains were highly heterogeneous – the locations of strain concentrations were related to the crystallographic orientations measured with electron backscatter diffraction (EBSD).

The data generated in this thesis are found to be suitable to calibrate and validate a crystal plasticity model of cast α-uranium.

Ministry of Defence © British Crown Copyright 2020/AWE

Ministry of Defence © British Crown Copyright 2020/AWE

Research Output

Literature Review

First-year literature review "Short Crack Propagation in Uranium, an Anisotropic Polycrystalline Metal – A Literature Review" incorporated as part of internal working document at AWE plc.

Publications

Conference paper [1] P. D. Earp, S. Kabra, J. Askew, and T. J. Marrow, "Lattice strain and texture development in coarse-grained uranium – a neutron diffraction study," *IOP Conf. Ser. J. Phys.*, vol. 1106, p. 012012, 2018.

Journal paper (Accepted Dec 2019) [2] E. Tarleton, N. Grilli, P. D. Earp, A. C. F. Cocks, and T. J. Marrow, "Characterisation of slip and twin activity using digital image correlation and crystal plasticity finite element simulation: Application to orthorhombic α-uranium," *J. Mech. Phys. Solids*, 2019.

Conference Presentations

Poster presentation at the AWE Materials and Analytical Science Student Conference, June 2019 and at the NuFor Nuclear Forensics 2019 Conference, July 2019.

Invited Presentation "Experimental characterisation of deformation in coarse-grained uranium to aid the development of crystal plasticity models" at the Integrated Computational Materials Engineering (ICME) 2018 Seminar, organised by the Institute of Physics in London, UK, in December 2018

Winner of the Three Minute Thesis (3MT) competition at the Defence Science Doctoral Symposium, Cranfield University, November 2018.

Poster "Characterisation of Stress Concentrating Features in Alpha-Uranium Using Electron Backscatter Diffraction" at the Defence Science Doctoral Symposium, Cranfield University, November 2017.

Oral Presentation "Characterisation of stress concentrations and fracture in alpha-uranium" at the International Conference on Fracture 14, Rhodes, Greece in June 2017.

Oral Presentation and Poster "Lattice strain development in coarse-grained uranium under tension and compression" at the UK Neutron and Muon Science User Meeting, University of Warwick, June 2017.

Ministry of Defence © British Crown Copyright 2020/AWE

Other Contributions

Novel analysis of EDXRD strain maps to study crack growth published in appendix of:

[3] T. Wigger *et al.*, "In situ mapping of normal strains in the field of a growing fatigue crack in a steel weld using digital image correlation and energy dispersive synchrotron X-ray diffraction," *Int. J. Fatigue*, vol. 115, no. May, pp. 11–19, 2018. https://doi.org/10.1016/j.ijfatigue.2018.05.016

Further work from above experiment. (awaiting review)

[4] A. Koko, P. D. Earp, T. Wigger, J. Tong, and T. J. Marrow, "J-Integral Analysis: An EDXD and DIC Comparative Study for a fatigue crack," *Int. J. Fatigue*, 2019.

Ministry of Defence © British Crown Copyright 2020/AWE

Table of Contents

Acknowledgements iii
Abstract v
Research Output vii
Table of Contents ix
Chapter 1 Introduction 1
1.1 Motivation 1
1.2 Outline of Thesis Contents 3
Chapter 2 Literature Review 8
2.1 Introduction 8
2.2 Properties of Uranium 9
2.2.1 Crystal Structure 9
2.2.2 Elastic Properties 12
2.2.3 Thermal Expansion Coefficients 16
2.2.4 Mechanical Properties 17
2.2.5 Microstructure 19
2.2.6 Texture 20
2.3 Deformation Mechanisms in Uranium 21
2.3.1 Slip 21
2.3.2 Twinning 28
2.3.3 Effect of Orientation 38
2.4 Fracture of Uranium 39
2.4.1 Twins as Stress Concentrators 46
2.5 Crystal Plasticity Modelling 49
2.6 Experimental Investigation of Deformation 51
2.6.1 Mechanical Testing 52
2.6.2 Diffraction 57
2.6.3 Microstructural Evaluation with EBSD 65
2.7 Summary 67
Chapter 3 Challenges of Neutron Diffraction in Coarse-Grained Uranium 68

Ministry of Defence © British Crown Copyright 2020/AWE

3.1 Introduction 68
3.2 Microstructural Characterisation 70
3.3 Experiment Overview 71
3.4 Key Results 73
3.4.1 Lattice Strains 73
3.4.2 Axial Texture Changes 75
3.5 A Method to Identify Twinning Modes from Texture Changes 76
3.5.1 Definition of Diffracting Parent Crystal 78
3.5.2 Application of Twinning Rotation 81
3.5.3 Calculation of (*hkl*) Parallel to LD in Twin 82
3.5.4 Filtering by Schmid Factor 84
3.5.5 Plotting Possible Twinning Reorientations 84
3.5.6 Experimental Observations 89
3.6 Issues with Specimen Movement 89
3.7 Discussion & Summary 93
3.7.1 Strengths 95
3.7.2 Limitations 95
3.7.3 Areas for Improvement in a Future Experiment 96
Chapter 4 An Improved Neutron Diffraction Experiment on Cast Uranium - Collecting Data Suitable for CPFE Modelling. 98
4.1 Introduction 98
4.2 Experimental Procedure and Data Analysis Methodology 99
4.2.1 Specimen Design 101
4.2.2 Experimental Set-up 104
4.2.3 Experimental Testing Procedure 113
4.2.4 Single-Peak Fitting 118
4.2.5 Rietveld Refinement 119
4.2.6 DIC Strain & Displacement Measurement 121
4.2.7 Correction of Specimen Movement 124
4.3 Results 126
4.3.1 Texture in the Gauge Region 126
4.3.2 Macroscopic Behaviour 128

Ministry of Defence © British Crown Copyright 2020/AWE

4.3.3 Texture Changes 137
4.3.4 Lattice Strain Development 151
4.3.5 Fracture and Fractography 161
4.4 Discussion 162
4.4.1 Macroscopic deformation 163
4.4.2 Texture Development 164
4.4.3 Lattice Strains 173
4.4.4 Comparison with fine-grained uranium 181
4.4.5 Summary of Experimental Discussion 183
4.5 CPFE Modelling of Neutron Diffraction Experiment 184
4.5.1 Results and Discussion 185
4.5.2 Suggestions for future model development 188
4.6 Chapter Summary 189
Chapter 5 Full-field Strain Measurement during Tensile Deformation of Cast Uranium 192
5.1 Introduction 192
5.2 Microstructural Characterisation 194
5.2.1 Specimen Preparation 195
5.2.2 EBSD Data Acquisition 198
5.2.3 EBSD Data Processing 203
5.3 Tensile Rig Development 212
5.3.1 Requirements 213
5.3.2 Design Development 213
5.3.3 Validation 216
5.4 Experimental Method 217
5.4.1 Copper Bar Deformation 217
5.4.2 Stereo DIC System Set-up 219
5.4.3 Tensile Testing Procedure 227
5.4.4 Data Processing 230
5.5 Results 239
5.5.1 Specimen Dimensions 239
5.5.2 Microstructure 240

Ministry of Defence © British Crown Copyright 2020/AWE

5.5.3 Grain Cluster Segmentation 245
5.5.4 Schmid Factor Maps 247
5.5.5 Overall Deformation 256
5.5.6 Deformation Maps 257
5.5.7 Stress-Strain Curves 270
5.6 Discussion 280
5.6.1 General Observations 281
5.6.2 Specimen Deformation 283
5.6.3 Demonstrating Data Validity 288
5.6.4 CPFE Modelling of Tensile Test 292
5.7 Chapter Summary 297
Chapter 6 General Discussion & Future Work 301
6.1 Behaviour of Cast Uranium 301
6.1.1 Tension-Compression Asymmetry 301
6.1.2 Deformation Modes 302
6.2 Experimental Summary 303
6.2.1 Experimental Challenges 303
6.2.2 Use of Complementary Techniques 304
6.2.3 Applicability of Results 305
6.2.4 Key Developments 305
6.3 Future Work 306
6.3.1 CPFE Simulation 306
6.3.2 Twin Growth 308
6.3.3 Fracture 309
Chapter 7 Conclusion 311
Literature Cited 313
Chapter 8 Appendices 341
A1 Glossary of Abbreviations 341
A2 Specimen List 342
A3 Material Characterisation 345
A3.1 Introduction 345

Ministry of Defence © British Crown Copyright 2020/AWE

A3.2 Microstructural Characterisation with EBSD 345
A3.2.1 Method 345
A3.2.2 Visualisation of the Microstructure 349
A3.2.3 Calculation of Grain Size 352
A3.2.4 Grain Boundaries 355
A3.2.5 Summary of Microstructure 361
A3.3 Chemical Composition 361
A3.4 Summary 362
A4 Systematic Absences in Diffraction 363
A5 Preliminary Neutron Diffraction Experiments on Cast Uranium 365
A5.1 Introduction 365
A5.2 Experimental Procedure and Data Analysis Methodology 366
A5.2.1 Neutron Diffraction on ENGIN-X 366
A5.2.2 Neutron Texture Measurement on GEM 405
A5.3 Results 416
A5.3.1 Neutron Spectra 416
A5.3.2 Texture in the Gauge Region 418
A5.3.3 Predicting Deformation using the Schmid Factor 424
A5.3.4 Lattice Strain Development 428
A5.3.5 Axial Texture Changes 437
A5.4 Discussion 444
A5.4.1 Initiation Stresses – comparison with prediction 445
A5.4.2 Identifying Twinning Mode from Texture Changes 448
A5.4.3 Texture Movement Artefacts 450
A5.5 Summary 454
A6 Deformation and Fracture in Chapter 4 459
A6.1 Heterogeneity of Deformation 459
A6.1.1 Specimen ND-T3 461
A6.1.2 Specimen ND-T4 463
A6.1.3 Specimen ND-C3 466
A6.1.4 Specimen ND-C4 469

Ministry of Defence © British Crown Copyright 2020/AWE

A6.2 Fracture and Fractography 471
A6.2.1 Specimen ND-T3 472
A6.2.2 Specimen ND-T4 476
A7 CPFE Modelling of Uranium 483
A7.1 Method 483
A8 Calculations 487
A8.1 Schmid Factor Calculations 487
A8.2 Extensometer Calculations for Chapter 4 498
A8.2.1 Offsetting the extensometer 498
A8.2.2 In-situ exchange of extensometers 500
A8.3 Texture Change Correction Errors for Chapter 4 502
A8.4 Estimation of stress-error in tensile tests in Chapter 5 505
A8.5 Estimation of Compressive Buckling Stress on SMARTS 508
A9 Additional Data - Chapter 5 511
A9.1 Tensile Rig Initial Design 511
A9.2 Loading Curves 513

Ministry of Defence © British Crown Copyright 2020/AWE

Chapter 1 Introduction

1.1 Motivation

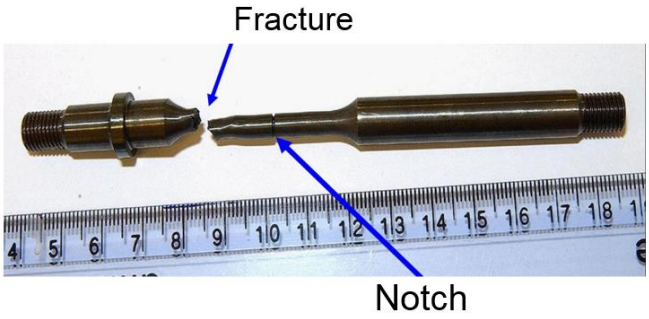
Most engineering structures fail due to cracks forming. If the development of such cracks could be predicted in advance, vast sums of money could be saved, and safety of engineering structures could be improved. Unfortunately, the physics and mechanics of crack formation are extremely complex, and the most problematic cracks typically occur deep inside a material where it is difficult to observe until it is too late.

There is a desire to develop predictive modelling of crack formation in engineering components, and this requires a complete understanding of the physics, chemistry and materials properties, both at the time of manufacture and throughout the design life of the product. The desire to operate parts beyond their original design life makes the understanding of crack formation increasingly relevant.

Whilst their motivations are sensitive, the project sponsor, AWE plc., has a scientific interest in understanding the behaviour of complex metals such as uranium. Whilst many materials properties can be predicted with accuracy, it has been demonstrated that the fracture behaviour of cast uranium is irregular. Figure 1.1 shows some of the challenges in determining the mechanical properties of cast uranium using conventional mechanical tests.

Ministry of Defence © British Crown Copyright 2020/AWE

(a)



(b)

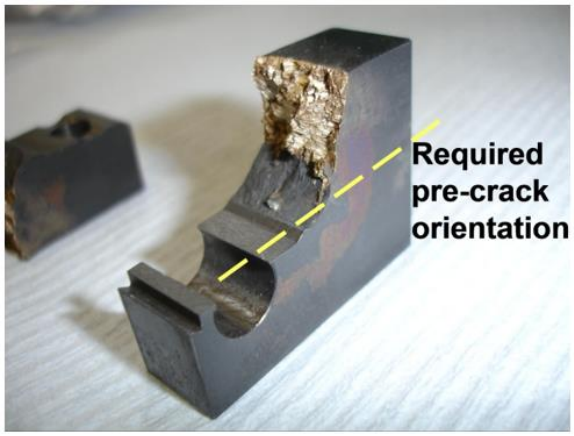


Figure 1.1. (a) Notched cast uranium tensile specimen with the location of fracture away from the notch. (b) Cast uranium compact test specimen where the fatigue pre-crack has deviated from the plane of the notch, rendering the specimen useless. Images courtesy of John Askew, AWE plc.

In the notched cast uranium tensile specimen, fracture has occurred away from the location of assumed maximum stress (the notch). Compact test specimens are used to measure fracture toughness, and require a small planar fatigue pre-crack to be produced ahead of the notch. In the cast uranium specimen, the fatigue pre-crack deviated from the plane of the notch, rendering it useless.

With the development of modern materials modelling techniques, alongside the rapid increase in computer processing capability in the 21st Century, it is now possible to create computer models of a component including an accurate description of the microstructure which can be used to predict crack initiation and propagation.

Ministry of Defence © British Crown Copyright 2020/AWE

There is a move in industry to adopt Integrated Computational Materials Engineering principles [5]. This simulates a material throughout its whole life cycle, using multi-scale experimentally validated modelling and interdisciplinary collaboration [6] (for example between the chemists designing an alloy, the metallurgists casting it, and the machinists manufacturing the part ready for use in the engineering application).

This DPhil project is part of an AWE-sponsored research programme at the University of Oxford, with the aim of developing crystal plasticity finite element (CPFE) models for cast uranium.

The aim of this DPhil project is to provide the experimental data needed to develop and validate these CPFE models. Specifically, there is a need to characterise the deformation response of cast uranium under applied external loading, and measure the distribution and magnitude of stress concentrations that are likely to initiate fracture.

1.2 Outline of Thesis Contents

This thesis presents experimental work performed between 2015 and 2018, and describes a dataset which will be used by colleagues in the University of Oxford, at AWE plc, and by collaborating partners worldwide, to develop and validate the aforementioned CPFE models.

Compared to many engineering materials, uranium is relatively understudied. Chapter 2 comprises a literature review which places the research in context with the status quo

Ministry of Defence © British Crown Copyright 2020/AWE

and presents the necessary background knowledge on the metallurgy of uranium, a complex and unusual metal.

In order to simulate and predict the mechanical response of cast uranium, we must identify the underlying mechanisms that are obscured in the macroscopic mechanical data. To achieve this, we must probe the microscopic deformation mechanisms whilst sampling a large enough volume of material to average out any extreme local inhomogeneities. Diffraction methods such as neutron diffraction can accurately measure the changes in internal elastic strain as bulk samples are deformed. Chapter 3 summarises two preliminary neutron diffraction experiments in which the internal lattice strain and texture development were measured during external tensile and compressive loading. A novel method is presented to relate observed texture changes to the formation of deformation twins. This work highlights the challenges of neutron diffraction measurements in coarse-grained microstructures, in particular the texture artefact due to specimen movement which prevented the identification of deformation twins from measured texture changes.

Chapter 4 presents an improved neutron diffraction experiment where the aforementioned issues were eliminated. Deformation twinning was successfully identified from the lattice strains and texture changes, and accounts for the observed tension-compression asymmetry. The Schmid factor is seen to be a good predictor for twin formation. The results of CPFE models developed by Dr Nicolò Grilli in the Department

Ministry of Defence © British Crown Copyright 2020/AWE

of Engineering Science, University of Oxford, are presented to demonstrate how neutron diffraction data can be used to optimise the deformation parameters required in the model.

A well-designed and well-calibrated CPFE model should be able to correctly simulate both the elastic and plastic strain responses when a real heterogeneous cast microstructure is loaded. Neutron diffraction cannot resolve the local micro-scale heterogeneity in strains, nor is it well suited to measuring the magnitude and direction of plastic strain. There is therefore a need to experimentally measure the micro-scale development of plastic strains during deformation of cast uranium.

Chapter 5 describes an experiment which investigates the effect of microstructure on the heterogeneity of deformation in cast uranium. Digital image correlation (DIC) measured the strain distribution during tensile deformation of cast uranium. The strains were related to the crystallographic orientations, measured with electron backscatter diffraction (EBSD). Again, this experiment directly contributed towards the development of the CPFE models.

Chapter 6 provides a general discussion of the work. The experiments successfully measures the elastic and plastic behaviours of cast uranium, allowing CPFE models to be calibrated by our collaborators. Texture changes observed by neutron diffraction are related to the activation of particular twinning modes. The experiments were challenging and an assessment of the applicability of the results is given. This is followed by

Ministry of Defence © British Crown Copyright 2020/AWE

suggestions for a range of future computational and experimental work, before the thesis concludes in Chapter 7.

Ministry of Defence © British Crown Copyright 2020/AWE

Ministry of Defence © British Crown Copyright 2020/AWE

Chapter 2 Literature Review

2.1 Introduction

Uranium is a complex metal, and is often unfamiliar to even those with a metallurgical background as its applications are specific and limited to legacy civil nuclear and modern defence applications, such as armour piercing kinetic energy penetrators for main battle tanks and as a constituent of nuclear warheads. Details regarding the latter applications are often classified and not in the public domain.

The majority of open research was performed from the 1950s to the 1970s since metallic uranium was also used as the fuel-rod material in Magnox power reactors. Research interest faded however, when subsequent reactor designs were fuelled by uranium oxide rather than uranium metal.

Since the turn of the century there has been an increase in publications, many coming out of national laboratories in the USA, where self-consistent crystal plasticity models have been developed. Experimental data has also been published, mostly on wrought uranium, which provides a good comparison with the cast uranium studied in this work.

The literature review will:

- Provide the reader with an understanding of the complexities of uranium,
- Detail relevant research upon which the work of the thesis is based,

Ministry of Defence © British Crown Copyright 2020/AWE

- Provide a summary of relevant crystallographic data and deformation systems, which will be referred back to in the subsequent chapters.

2.2 Properties of Uranium

Uranium is a metallic element in the actinide series of the periodic table with atomic number 92. It exists a solid with a very high density of $19.040\ \mathrm{g\ cm^3}$ at room temperature [7]. Naturally occurring uranium is weakly radioactive due to containing mostly U-238 (>99 %) and some of the more highly radioactive (U-235). Depleted uranium (DU), containing a much smaller amount of U-235 (defined by the United States Nuclear Regulatory Commission as having less than 0.711 wt.% U-235 [8], but typically about 0.2 wt.% [9]), is produced as a by-product of uranium enrichment for nuclear energy or military uses and is the only type of uranium considered in this review. U-238 has a long half-life of 4.468×10^9 years [10] and the half-life for U-235 is 7.1×10^8 years giving DU a specific activity of $15\ \mathrm{kBq\ g^{-1}}$ [9].

There are three crystalline phases of pure uranium. The alpha (α) phase is stable below 668°C, the beta (β) phase between 668°C and 775°C and the gamma (γ) phase is stable until the melting temperature of 1132°C [11]. α-uranium is the stable phase at room temperature, so we shall consider this phase only.

2.2.1 Crystal Structure

The crystal structure of α-uranium was first determined in 1937 by Jacob and Warren [12] using X-ray powder diffraction. Lukesh [13] verified this structure in 1949 using

Ministry of Defence © British Crown Copyright 2020/AWE

single crystal diffraction. The structure is base centred orthorhombic, space group *Cmcm*, with lattice parameters $a = 2.854$ Å, $b = 5.869$ Å and $c = 4.955$ Å (all ± 0.001Å) [14]. There exists a double lattice structure, with a motif of atoms placed at $[0, u, \frac{1}{4}]$ and $[0, -u, \frac{3}{4}]$ relative to the two Bravais lattice points in each unit cell [15]. The atomic position parameter has been determined as $u = 0.1025$ by Sturcken [14]. Due to the complexity of the structure, it was originally proposed by Wilson [16][1] to be monoclinic; however Lukesh [13] realised that the proposed cell was contained within the now accepted orthorhombic cell of Jacob and Warren [12].

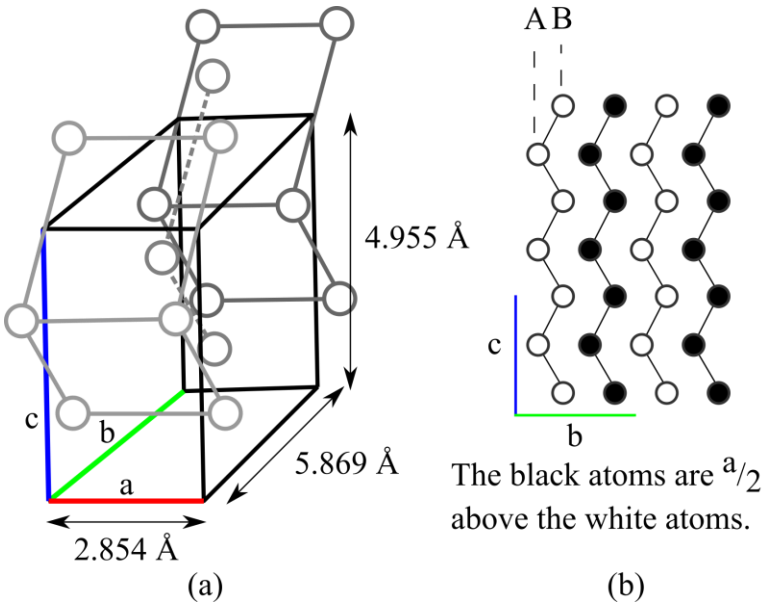


Figure 2.1. (a) Crystal structure of alpha-uranium. (b) Structure projection of (100) plane. Based on the original figure in Cahn [15] and updated for clarity.

Figure 2.1 [15] shows the crystal structure of α-uranium and a structure projection along the (100) plane. It is different to that of other metals, the closest being that of neptunium which is similar but with a hexagonal lattice [12]. α-uranium can be considered to have

[1] This citation [16] was provided in Lukesh's paper [13] but the original paper could not be retrieved.

Ministry of Defence © British Crown Copyright 2020/AWE

a distorted hexagonal lattice; the unit cell is also similar to hcp zinc, differing by an expansion along the b-axis [17].

A notable feature is the anisotropy of the bonding, which is partly covalent in nature. Sheets of atoms are corrugated about the (010) plane with covalent bonds between the atoms to form 'giant molecules'. These sheets are held together by metallic bonding forces between neighbouring sheets. Interestingly, this orthorhombic structure is much more common in polymers; the corrugated arrangement of the atoms in α-uranium is very similar to the arrangement of carbon atoms in crystalline polyethylene [18]. The anisotropy of bonding in α-uranium affects which deformation mechanisms can be active; this is discussed in section 2.3.

The orthorhombic crystal structure results in the (*hkl*) plane normal not generally being parallel with the [*hkl*] crystal direction, as shown in the stereographic projections in figure 2.2.

Ministry of Defence © British Crown Copyright 2020/AWE

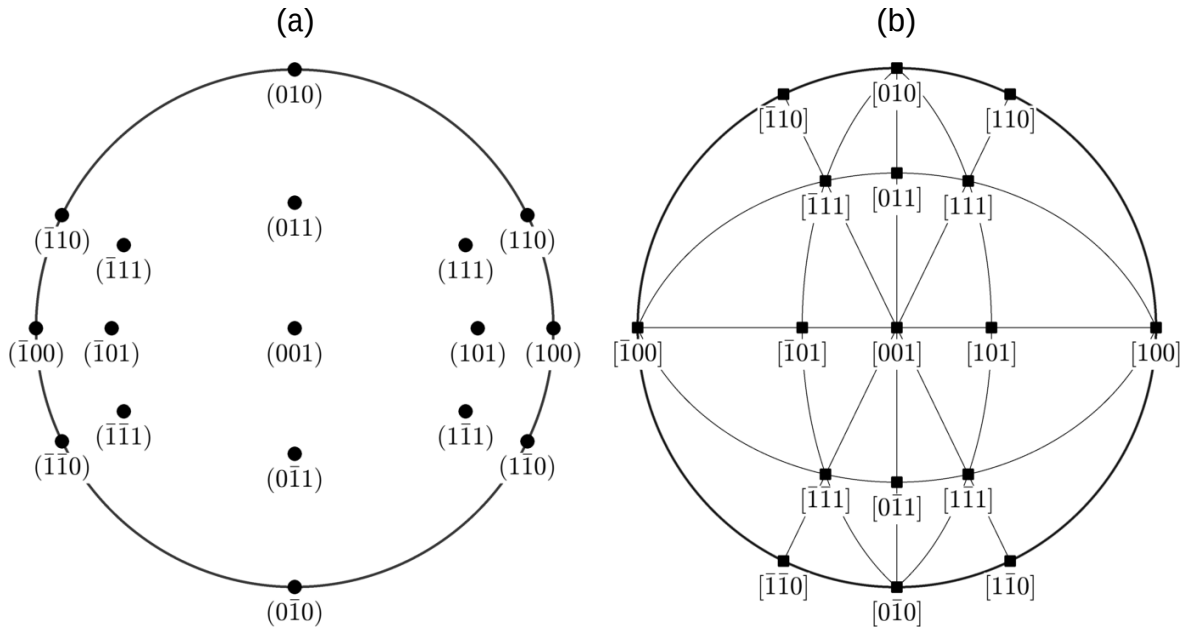


Figure 2.2. Stereographic projections along the crystal *c*-axis showing (a) poles (plane normal) and (b) crystal directions.

2.2.2 Elastic Properties

The anisotropy of bonding also results in anisotropic elastic properties. The elastic moduli of single crystal α-uranium were first measured using ultrasonic transducers by Fisher [19]. The temperature dependence of the elastic properties was also investigated [20], but since in this study we are focusing on room temperature phenomena this need not be discussed here. The room temperature *elastic stiffness moduli,* c_{ij}*, elastic compliance moduli,* s_{ij}*,* $Young's\ moduli$ and $Poisson's\ ratios$ as determined by Fisher, but converted into SI units, are presented overleaf, with zero values shown as blank:

Ministry of Defence © British Crown Copyright 2020/AWE

Anisotropic Stiffness Tensor

$$c_{ij} = \begin{bmatrix} 214.74 & 46.49 & 21.77 & & & \\ 46.49 & 198.57 & 107.91 & & & \\ 21.77 & 107.91 & 267.11 & & & \\ & & & 124.44 & & \\ & & & & 73.42 & \\ & & & & & 74.33 \end{bmatrix} \text{GPa} \quad [2.1]$$

Anisotropic Compliance Tensor

$$s_{ij} = \begin{bmatrix} 4.91 & -1.19 & 0.08 & & & \\ -1.19 & 6.73 & -2.61 & & & \\ 0.08 & -2.61 & 4.79 & & & \\ & & & 8.04 & & \\ & & & & 13.62 & \\ & & & & & 13.45 \end{bmatrix} \times 10^{-12} \text{ Pa}^{-1} \quad [2.2]$$

Young's Moduli

$$E_{100} = 204 \text{ GPa} \quad [2.3]$$

$$E_{010} = 149 \text{ GPa} \quad [2.4]$$

$$E_{001} = 209 \text{ GPa} \quad [2.5]$$

Poisson's Ratios

$$\nu_{ij} = \frac{\text{compressional strain in } j \text{ direction}}{\text{extensional strain in } i \text{ direction}} \text{ for extension in } i \text{ direction} \quad [2.6]$$

$$\nu_{12} = +0.24 \quad [2.7]$$

$$\nu_{21} = +0.17 \quad [2.8]$$

$$\nu_{13} = -0.02 \quad [2.9]$$

$$\nu_{13} = -0.02 \quad [2.10]$$

$$\nu_{23} = +0.39 \quad [2.11]$$

$$\nu_{32} = +0.55 \quad [2.12]$$

Ministry of Defence © British Crown Copyright 2020/AWE

The anisotropy of the elastic moduli can be related to the crystal structure. Figure 2.3, adapted from Fisher [19] shows structure projections of the α-uranium structure on the (100), (010) and (001) planes, alongside polar diagrams of the Young's moduli. In the corrugated structure, the interatomic distances between atoms within a layer is smaller than the distance to the nearest atom in a neighbouring layer. The nearest neighbour, covalent-like, bonds are angled 27° from $[001]$ in the (100) plane. These stiff bonds result in the maximum Young's modulus being observed $38.5°$ from $[001]$ in the (100) plane. The minimum Young's modulus is found to be along the $[010]$ direction, which corresponds to the pulling apart of the corrugated sheets; the metallic bonding between sheets is considerably weaker than the covalent-like bonding in the sheets. The anisotropy of bonding also results in a negative Poisson's ratio between the $[100]$ and $[001]$ directions.

Ministry of Defence © British Crown Copyright 2020/AWE

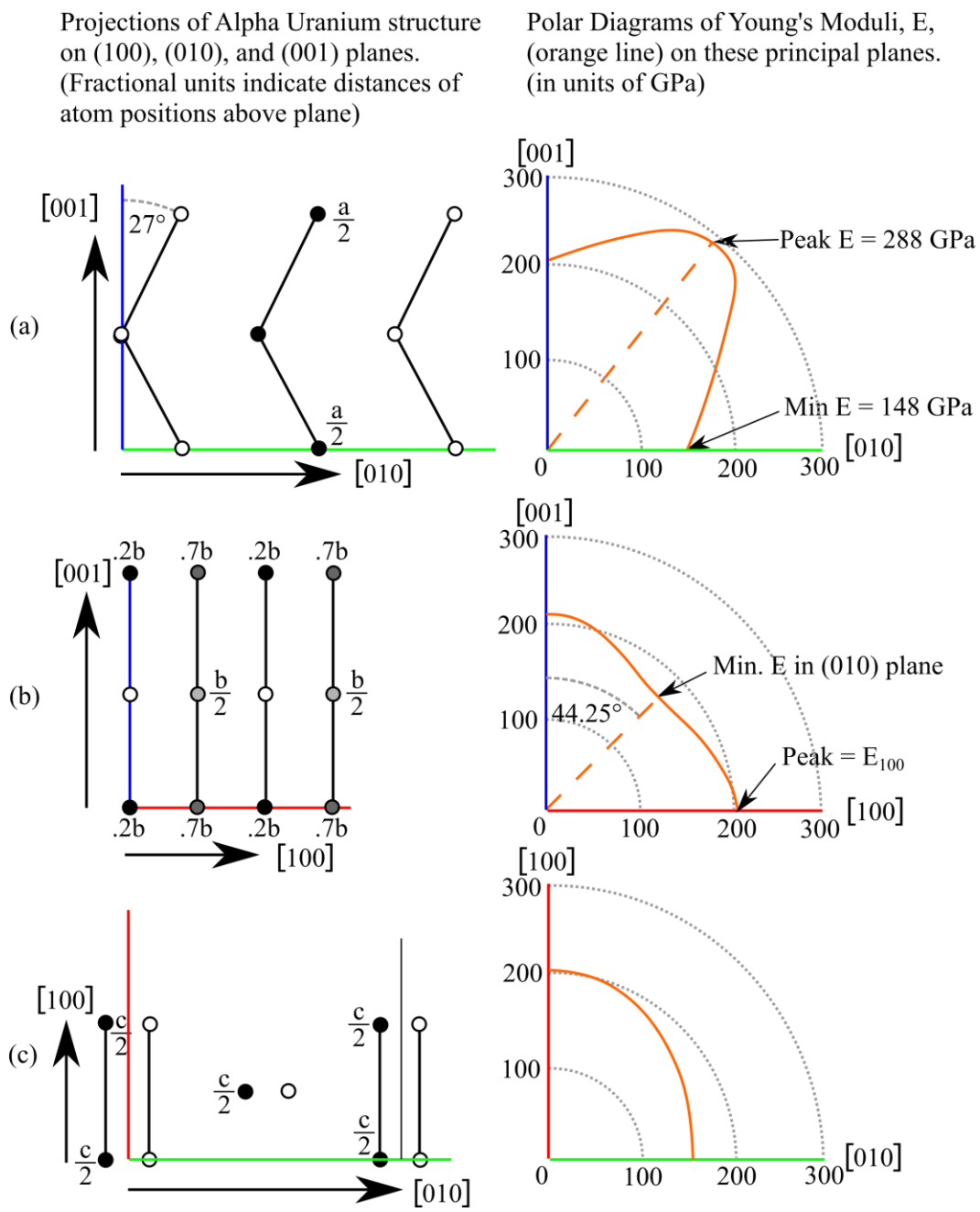


Figure 2.3. Structure projections of alpha-uranium onto the a) (100), b) (010), and c) (001) planes alongside polar diagrams of the Young's moduli. Based on the original figure from Fisher [19], with colour added and units converted to GPa.

Ministry of Defence © British Crown Copyright 2020/AWE

Values of these elastic constants for randomly oriented polycrystalline material of $E = 195.1\ \mathrm{GPa}$ and $\nu = 0.2087$ were calculated by Rothman [21][2] and presented by Chiswik et al. [22] in 1958.

It is important to note that in practice uranium can acquire significant texture during solidification and processing [23] – the bulk elastic properties will then be anisotropic and differ from the randomly oriented data presented here.

More recently, Wheeler et al. [24] measured the elastic modulus of a large-grained (grain size between $500\ \mu\mathrm{m}$ and $750\ \mu\mathrm{m}$) polycrystalline cast uranium sample using micro-indentation and tensile testing, giving $E = 226 \pm 108\ \mathrm{GPa}$ and $E = 215 \pm 41\ \mathrm{GPa}$ respectively. Both of these measurements are consistent with the value calculated above. The large standard deviation in the micromechanical measurement can be attributed to the fact that the volume of material sampled in each test contains few grains; the anisotropy of elastic properties results in grains lying in elastically stiff or compliant orientations.

2.2.3 Thermal Expansion Coefficients

The temperature dependence of the lattice parameter, modified from Frost [25], is shown in figure 2.4. At room temperature the thermal expansion coefficient along the *a* and *c* axes is positive, unlike along the *b* axis where it is negative. This means that in polycrystalline α-uranium, temperature change causes the neighbouring grains to exert

[2] A copy of Rothman's work [21] could not be found.

Ministry of Defence © British Crown Copyright 2020/AWE

stresses on each other [25]. This is relevant as residual stresses which build up during cooling after casting can be great enough to cause plastic deformation, evidenced by the presence of deformation twins in the as-cast microstructure [23], and the phenomenon of 'thermal cycling growth' in textured uranium rods [26].

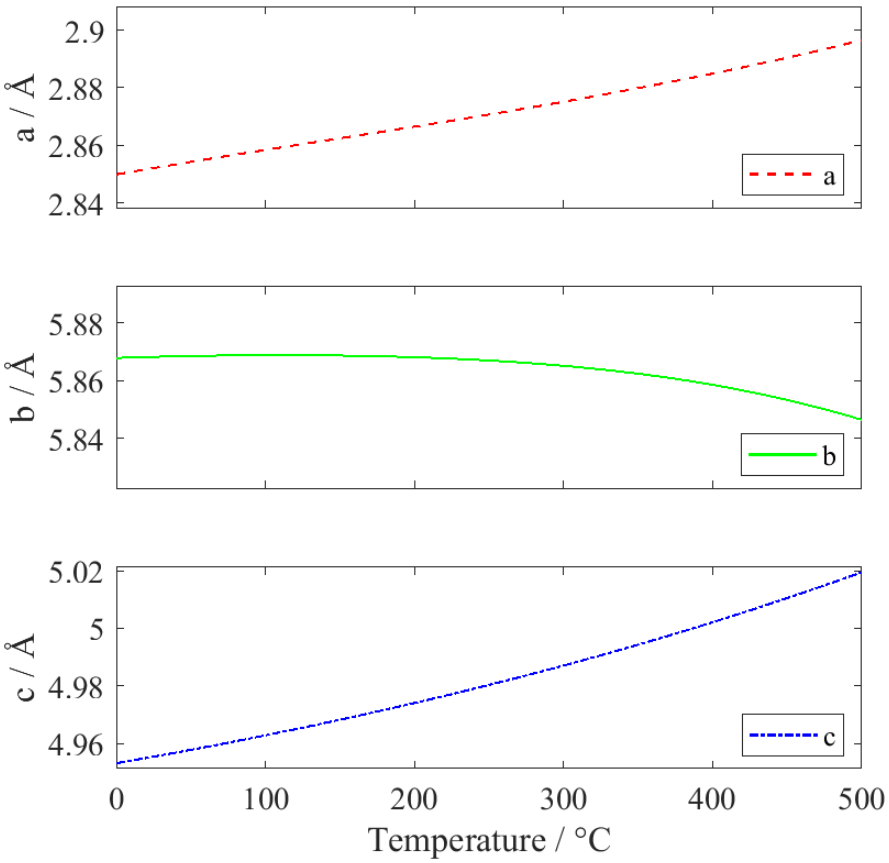


Figure 2.4. Temperature dependence of the lattice parameters for orthorhombic alpha-uranium. Data taken from the original figure from Frost [25].

2.2.4 Mechanical Properties

Garlea et al. [27] performed tension and compression experiments on cast uranium, measuring the flow curves shown in figure 2.5. Specimens loaded in compression yielded first but hardened rapidly. Significant variation was seen between the two specimens tested in each loading configuration as a result of the coarse microstructure.

Ministry of Defence © British Crown Copyright 2020/AWE

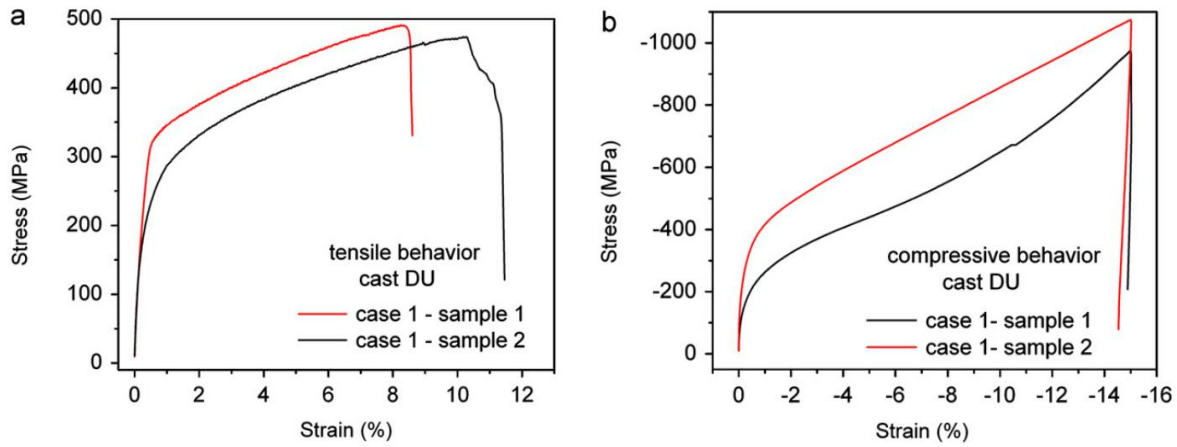


Figure 2.5. "Stress–strain curves for the as-cast uranium deformed in (a) tension and (b) compression showing large elastic and plastic anisotropy and inconsistent mechanical behavior results due to the inhomogeneous microstructure." Figure and caption reproduced from Garlea et al. [27]

Caskey Jr. [28] performed experiments on fine-grained hot-rolled uranium and found mechanical properties that strongly varied with orientation, and again had a very large variation in strength from one sample to the next. His results are summarised in table 2.1.

Table 2.1. Tensile properties of hot-rolled uranium. Data from Caskey Jr. [28] with conversion of values into SI units.

	Longitudinal (Rolling) Direction		Transverse Direction	
	Average	Range	Average	Range
Ultimate Tensile Strength (UTS) [MPa]	717	682 - 779	586	469 - 710
Yield stress (0.2 % offset) [MPa]	303	248 - 400	455	283 - 572
Elongation at failure [%]	10.2	5 - 20	3.4	Suspected error in data

The key point to note here is the large scatter in the results. For example, the elongation at failure of the least ductile sample was four times less than for the most ductile sample. There is also a variation of up to $\pm$ 20 % from the average value for the UTS and over

Ministry of Defence © British Crown Copyright 2020/AWE

$\pm 35\ \%$ for the yield stress. This variation in fracture strength is similar to what would be observed in a brittle ceramic, not a polycrystalline metal.

There are similar variations in microhardness values measured for polycrystalline uranium. Wheeler and Morris [24] report a hardness of $239 \pm 31\ \mathrm{H_v}$, and note the effect of mechanical anisotropy on their measurements.

2.2.5 Microstructure

2.2.5.1 Grain Size

Uranium is typically coarse grained, with as-cast uranium typically having a grain size in excess of $200\ \mu\mathrm{m}$ [23]. Mixed grain sizes are often seen, with some grains in excess of $500\,\mu\mathrm{m}$ in diameter [27]

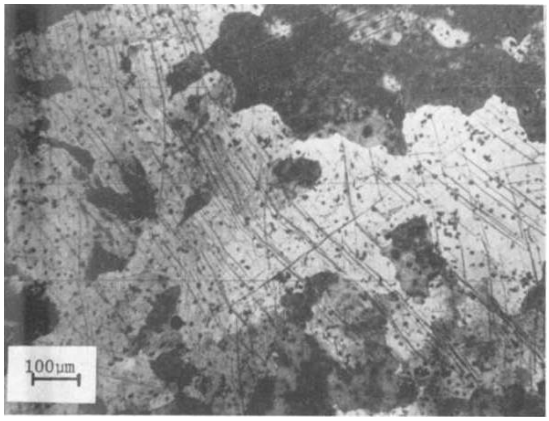


Figure 2.6. "As-cast adjusted uranium (electropolished); average grain size 0.3-0.5 mm". Reproduced from Sariel et al. [23]. Twins are visible as linear streaks.

In the early literature, microstructural characterisation is typically carried out by optical microscopy [23][29], with EBSD (section 2.6.3) used in more modern work [27][30][31]. Twins are often seen crossing entire grains (section 2.3.2).

Ministry of Defence © British Crown Copyright 2020/AWE

2.2.5.2 Carbides

Carbon is present in cast uranium due to casting in graphite moulds [32]. Multiple stoichiometries of carbide are possible [33], with uranium monocarbide (UC) the most prevalent, forming cuboidal carbides of edge length 10-20 μm [34]. Uranium monocarbide, UC, is a line compound in the U-C phase diagram [35], and Snow noted in his doctoral thesis [36] the presence of carbide inclusions at carbon contents as low as 0.007 wt. %, suggesting a room-temperature solubility of carbon in uranium metal close to zero. Consequently, all of the carbon is locked into the carbides and other carbon-containing inclusions.

2.2.6 Texture

Whilst there are a number of studies that look at the texture of rolled uranium [37][38][39], Sariel et al. [23][40] in 1986 investigated the texture of cast uranium. Surface X-ray diffraction was used to give pole figures of the preferred orientation in the sample. An inverse pole figure plots the density of occurrence of a particular real-space direction with respect to the crystal axes, in a standard stereographic quadrant for orthorhombic crystals (between (100), (010) and (001)). At the time there were not the available visualisation tools to display a complete inverse pole figure; instead pole densities were calculated for particular low-index crystallographic orientations. A large degree of preferred orientation was observed for as-cast samples when compared to α-phase annealed and quenched samples.

Ministry of Defence © British Crown Copyright 2020/AWE

2.3 Deformation Mechanisms in Uranium

Deformation beyond the elastic limit in crystalline metals is mediated by a number of deformation modes, the most common being dislocation slip and deformation twinning, discussed in the next sections.

2.3.1 Slip

Slip deformation, the macroscopic sliding of the crystal, is common to most metals and is mediated by the passage of microscopic line defects called 'dislocations' on a particular plane, the 'slip plane' (*hkl*), in a particular direction within the plane, the 'slip direction' [*uvw*].

In this thesis I make the distinction between slip systems or modes, and slip variants, the latter referring to a single plane/direction combination and the former including all symmetrically equivalent variants within the crystal.

Slip activates when a critical resolved shear stress (CRSS), on the slip plane and in the slip direction, is exceeded. This CRSS is the same for each variant in a mode, and differs between modes. The orientation dependence of the resolved shear stress on a slip system for a given loading direction is given by the Schmid factor (SF) [41]:

$$\mathrm{SF} = \cos\lambda\cos\phi \qquad [2.13]$$

where ϕ is the angle between the loading direction and the slip plane normal and λ is the angle between the loading direction and the slip direction, such that

Ministry of Defence © British Crown Copyright 2020/AWE

$$\tau = \sigma \cos\lambda \cos\phi \qquad [2.14]$$

where τ is the resolved shear stress and σ is the applied uniaxial tensile stress. For more complex stress states, the SF does not apply, but the resolved shear stress is still responsible for initiating deformation.

Loading in compression reverses the sign of the resolved shear stress causing dislocation motion in the opposite direction, therefore SFs for slip are symmetric in tension and compression.

The Schmid factors for slip are shown as inverse pole figures in figure 2.7, calculated using the analysis in Appendix A8.1. In cases where a mode has multiple variants, the SF of the variant with the highest SF for a particular direction is shown.

Ministry of Defence © British Crown Copyright 2020/AWE

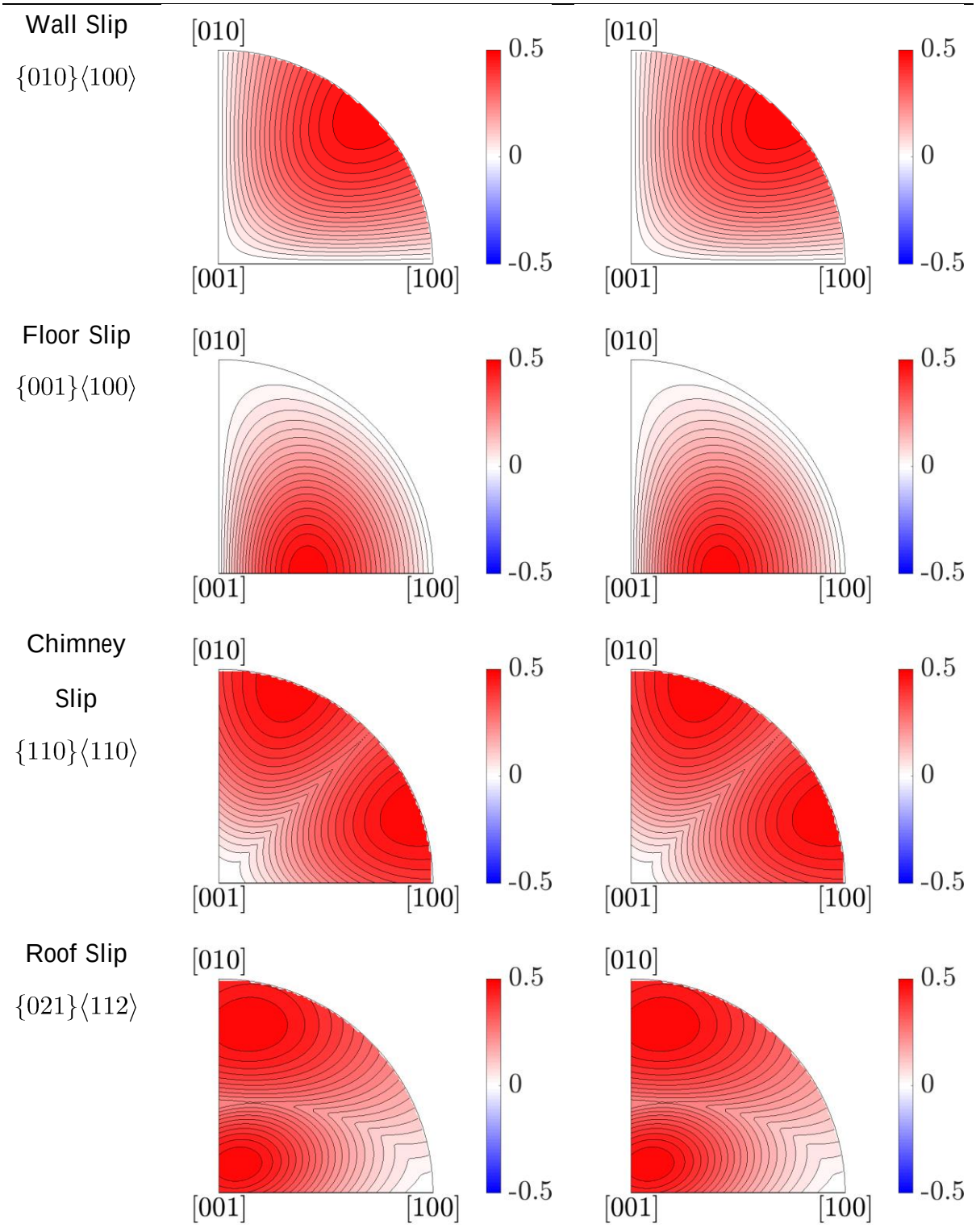


Figure 2.7. Orientation dependence of the Schmid factor for the most-stressed slip variant of Wall, Floor, Chimney and Roof slip in tension and compression. Here, the 'most-stressed' variant is the one with the highest Schmid factor in a particular direction. Calculation described in Appendix A8.1.

Ministry of Defence © British Crown Copyright 2020/AWE

2.3.1.1 Wall Slip

The most common slip mode in single crystal α-uranium at room temperature, $\{010\}\langle 100\rangle$ or 'Wall' slip, was first observed by Cahn [42] in 1951. After tensile deformation, the slip plane was determined by analysis of the trace of the plane on intersecting polished surfaces. The slip direction was found to be $[100]$ in subsequent work which used surface X-ray diffraction to identify the slip systems [15]. Slip lines were observed on the uranium surface; these were very fine at room temperature, and where there were multiple lines they were close together with a $\sim 1\ \mu\mathrm{m}$ spacing (figure 2.8).

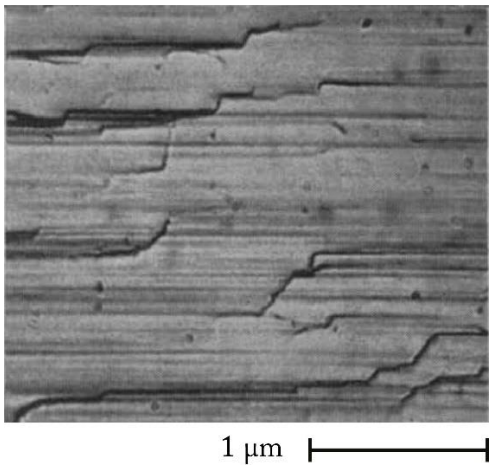


Figure 2.8. $\{010\}$ slip lines, with cross slips, on a stretched α-uranium specimen. Reproduced from Cahn [15] with scale bar added.

The fact that 010 is the most common slip plane is consistent with observations in other materials. Slip often occurs on the closest packed plane in a crystal; in α-uranium 010 is the plane around which the covalent-like atom sheets are corrugated, so it acts as the closest packed plane. The slip direction is often the closest packed direction within the slip plane, which in the case of α-uranium is $[100]$. Slip on this system does not

Ministry of Defence © British Crown Copyright 2020/AWE

require the breaking of any covalent-like bonds within the corrugated sheets – the sheets simply slide over one another along the line of corrugation. This is consistent with the observation that the critical resolved shear stress for slip on this system is largely temperature independent, as the thermally activated breaking of covalent-like bonds is not necessary [18].

Testing in compression was performed on single crystals by Lloyd and Chiswik [43], where again $010\ [100]$ was the most frequent mode. They noted that the slip preceded twinning as the load drops due to twinning occurred at a higher load than at the point where the stress-strain curve deviated from linearity. The authors measured the critical resolved shear stress for dislocation motion on this slip system as $0.34 \pm 0.02\ \mathrm{kgf\ mm^2}\ (3.3\ \mathrm{MPa})$. At room temperature this is significantly lower than the critical resolved shear stress for slip on any other mode [18]. Yoo [44] used anisotropic elasticity calculations to deduce that gliding is easier for a $010\ [100]$ dislocation of the edge-type than for one of the screw-type; consequently only edge dislocations are observed in practice.

The Schmid factor for Wall slip is maximised for tension or compression along the $\langle 110 \rangle$ directions.

2.3.1.2 Floor / Cross Slip

High magnification imaging of irregular slip traces by Lloyd and Chiswik [43] showed the traces to consist of mostly (010) with short segments of (001) cross-slip between

Ministry of Defence © British Crown Copyright 2020/AWE

them (see figure 2.8). Since cross-slip typically has the same slip direction as the major slip system, the cross slip was assigned to be of the $(001)[100]$ system. Daniel showed that at room temperature, this slip system has the second-smallest critical resolved shear stress at ~ 80 MPa [18]. The fact that this is an order of magnitude larger than the value for the dominant $(010)[100]$ slip explains why the $(001)[010]$ slip is limited to cross-slip.

2.3.1.3 Chimney Slip

Slip on the $\{110\}$ plane was observed by Cahn [42][15] and the slip direction was tentatively assigned to the $\langle 110 \rangle$ direction. At room temperature this slip mode is rarer as it involves disruption of the covalent 'giant molecules'. This slip mode is typically only distinguished experimentally at temperatures greater than $150°\mathrm{C}$ [18].

2.3.1.4 Roof Slip

This slip mode has a high critical resolved shear stress and has only been distinguished experimentally at temperatures greater than $400°\mathrm{C}$ [18]. However recent crystal plasticity modelling work [30][38][45] demonstrates this mode, and the aforementioned Chimney slip, activates alongside the other modes during deformation at room temperature.

2.3.1.5 {011}[100] Slip

This additional slip mode is only observed when the loading direction in compression is unfavourable for (010) slip [43]. Where observed, the slip traces were seen to originate at the tips of '$\{176\}$' twins (see section 2.3.2.4). Lloyd and Chiswik [43] postulated this

Ministry of Defence © British Crown Copyright 2020/AWE

slip mode requires a complex stress state to initiate. This mode will not be considered in this work.

2.3.1.6 Summary of Slip Modes

The active slip modes in α-uranium are summarised by Zecevic et al. [38], who give a name to each mode, as shown in table 2.2. These names, based on the orientation of the slip plane in the unit cell, are commonly used to describe the uranium slip systems and are used throughout the thesis.

Yoo [44] relates the slip systems in uranium to those of hcp metals. Slip systems which are equivalent in the hexagonal system become distinct when the symmetry is reduced to being orthorhombic.

Table 2.2. Slip modes in alpha-uranium

Slip Mode	$010\ [100]$ 'Wall'	$001\ [100]$ 'Floor'	$\{110\}\langle 110\rangle$ 'Chimney'	$\{021\}\langle 112\rangle$ 'Roof'	$\{011\}[100]$
Number of Slip Systems	1	1	2	4	2
Distinct slip systems	$010\ [100]$	$001\ [100]$	$(110)[110]$ $(\bar{1}10)[110]$	$021\ [\bar{1}12]$ $0\bar{2}1\ [112]$ $(02\bar{1})[112]$ $(0\bar{2}1)[\bar{1}12]$	$011\ [100]$ $(0\bar{1}1)[100]$
Experimentally-measured activity at RT	Active	Cross Slip only	Rare	Rare	Rare – only at "$\{176\}$" twins

Ministry of Defence © British Crown Copyright 2020/AWE

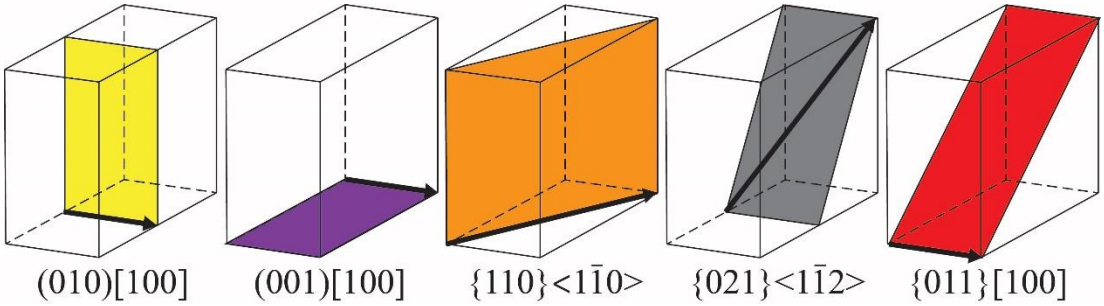


Figure 2.9. Slip modes in α-uranium. The slip plane is highlighted and the slip direction is indicated by the bold arrow.

2.3.2 Twinning

The von Mises criterion dictates that five independent slip systems are required for polycrystalline material to freely deform [46]. The slip systems operative in uranium at room temperature give only three independent modes, so other methods of deformation are required [18]. In particular, only Roof slip can accommodate deformation perpendicular to the (001) plane.

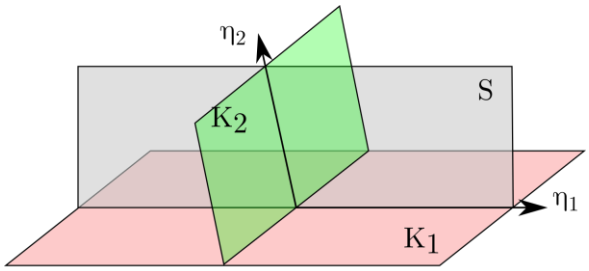
Many materials, especially those with limited slip systems, deform by a mechanism known as twinning in which regions of material shear to form deformation twins. Bilby and Crocker give a good definition:

> *"A deformation twin is a region of a crystalline body which has undergone a homogeneous shape deformation in such a way that the resulting product structure is identical with that of the parent, but oriented differently"* [47].

The twin crystal structure is deformed relative to the parent by a simple shear to give an invariant plane strain – the invariant plane is usually denoted as K_1 and the direction

Ministry of Defence © British Crown Copyright 2020/AWE

of shear by η_1. A second plane, K_2, is left undistorted but is rotated. These twinning elements are shown in figure 2.10.



K_1 - the twinning plane.
K_2 - the reciprocal twinning plane.
$\eta 1$ - the twinning direction
$\eta 2$ - the reciprocal twinning direction
S - the plane of shear

Figure 2.10. The twinning elements K_1, K_2, η_1, η_2 and S define a twinning system. Modified from original image by Crocker [48].

Twinning is prevalent in uranium at room temperature and the multiple twinning modes of α-uranium allow any arbitrary room temperature deformation to be accommodated.

Crystallographically, there exist multiple types of twin, defined by the orientation relationship between parent and twin and labelled Type I (K_1 & η_2 rational), Type II (η_1 & K_2 rational), or Compound twins (all elements rational).

The crystallographic orientation of the twin is related to its parent by a 180° rotation around the K_1 normal for Type I twins and the η_1 normal for Type II twins. This rotation axis is invariant and is shared between (i.e. is parallel in) both parent and twin [49].

For a more complete discussion of twinning the reader is pointed to the theoretical work of Bilby and Crocker [47].

Ministry of Defence © British Crown Copyright 2020/AWE

In addition to a homogeneous shear, atomic shuffles are sometimes required to reform the correct crystal structure in the twinned lattice [47]. For each twin variant, a reciprocal twin with swapped K_1 and K_2, η_1 and η_2 is possible, but one variant may appear more frequently in reality due to complexities with the required shuffles

The twins typically form very quickly, propagating at speeds near the speed of sound in the material [50]. This, coupled with the large shear, puts a large amount of strain in the material which leads to the development of lenticular-shaped twins. If a growing twin is blocked by microstructural features such as a grain boundary, high stresses can persist, and this may lead to crack nucleation if the stress cannot be relieved by slip. It is for this reason that deformation twinning must be understood to fully understand fracture in uranium.

In 1951, Cahn [42] observed that twins could be produced in α-uranium by thermal cycling or by applying small deformations. The author then showed [15] that deformation at room temperature always leads to twin formation. Twins in α-uranium are very thin, sometimes as narrow as $10\ \mathrm{nm}$ and rarely thicker than $10\ \mu\mathrm{m}$. They do not tend to coarsen with extended deformation; instead the number of twins increases. Twins often run across an entire grain, crossing low-angle grain boundaries [51], before being stopped by high-angle grain boundaries, other twins, or impurity particles [52][15] (figure 2.11).

Ministry of Defence © British Crown Copyright 2020/AWE

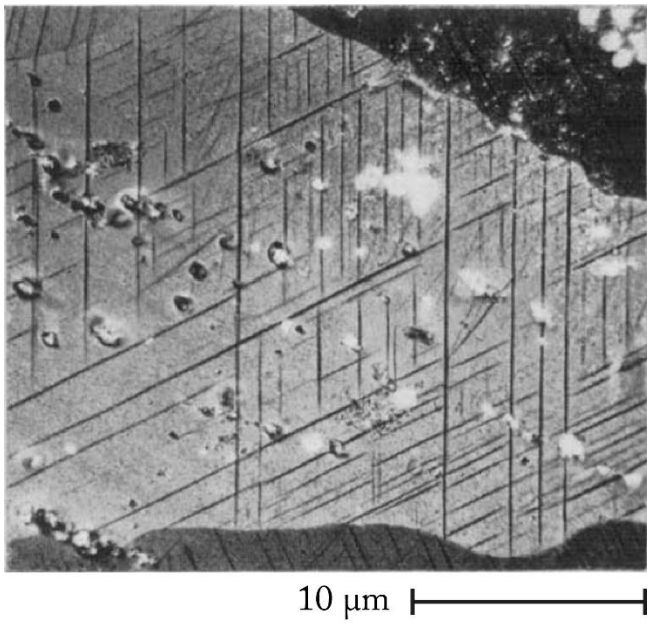


Figure 2.11. In α-uranium twins run across the entire grain before being stopped by grain boundaries or other twins. In this case, the twins were produced by stresses induced by cooling. Reproduced from Cahn [15] with scale bar added.

The two-surface method [42] and the pole-locus method [15] were used to determine the K_1 planes of operative twins in α-uranium; other parameters (K_2, η_1, η_2) being determined by analysis of twins which cross one another (see section 2.3.2.5). Twins on the {130}, {112} and irrational[3] '$\{176\}$' planes were determined, along with a tentative observation of {121} twins. In addition, Lloyd and Chiswik [43] observed '$\{176\}$' (also known as '$\{197\}$' [48]) twins. Kiho studied the crystallography of possible atomic movements during twinning and was in agreement with the previous authors, with the exception that the {121} twins were not observed.

Crocker performed a considerable theoretical analysis of the possible classical twinning modes in α-uranium, identifying 41 possible modes with twinning shears less than 1 and

[3] Miller indices for rational approximations to an irrational plane are indicated by surrounding the plane with quotation marks, e.g. '$\{hkl\}$' dictates that a plane is very similar to the rational $\{hkl\}$ plane.

Ministry of Defence © British Crown Copyright 2020/AWE

low shuffle complexities. The prevalence of each twin was rationalised in terms of the competition between shear magnitude and shuffle complexity. A similar analysis was performed by Bevis which also considered twins with a non-classical orientation relationship [53], however these twins had large shear magnitudes, and have not been observed in practice.

The observed twinning modes in α-uranium show similarity to those observed in hcp metals, due to their similar structures as discussed by Yoo [44], however Crocker suggests that the analogy is not sufficient to be useful in analysing twinning in α-uranium [48].

Twins can now be identified more easily using electron backscatter diffraction (EBSD – section 2.6.3) which measures the unique misorientation between the twinned and parent regions [54]. The relevant lattice misorientation for each twin was presented by Zhou et al [55] and is given in table 2.3.

Ministry of Defence © British Crown Copyright 2020/AWE

2.3.2.1 Summary of Twinning Modes

Table 2.3. Relevant twinning modes in alpha-uranium.

	$\{130\}$ twins	'$\{172\}$' twins	'$\{176\}$' twins	$\{112\}$ twins
Type	Compound Twin	Type I	Type II	Type I
K_1	$\{130\}$	'$\{172\}$'	'$\{176\}$'	$\{112\}$
η_1	$\langle 310 \rangle$	$\langle 312 \rangle$	$\langle 512 \rangle$	irrational
K_2	$\{110\}$	$\{112\}$	$\{111\}$	$\{172\}$
η_2	$\langle 110 \rangle$	irrational	irrational	$\langle 312 \rangle$
s	0.299 [43]	0.228 [15]	0.216 [43]	0.228 [55]
2ϕ	$81.5°$ [43]	$83.5°$ [15]	$83.8°$ [43]	
Lattice reorientation	$69.3°$ about $[001]$ [38]	$93°$ about $[\overline{1}0\ 7\ 0]$ [55]	$78°$ about $[0\ 10\ 7]$ [55]	$90°$ about $[110]$ [55]
Active near	$[100]_{\text{Tension}}$ $[010]_{\text{Compression}}$ [30]	$[001]_{\text{Tension}}$ [56]	$([100]_{\text{Tension}})$ $[001]_{\text{Compression}}$ [56]	$[001]_{\text{Tension}}$ [56]
Frequency of Occurrence:	Most Common	Common	Uncommon (especially rare in tension)	Rare

The Schmid factor can be used to calculate the resolved shear stress on a twin varient, just as for slip deformation. There is evidence, however, that the CRSS is not an accurate deformation criterion [57], suggesting that other factors, such as prior slip [58], affect the twinning stress. Christian and Magajan [57] note however that often the first twins that form are from the variant with the highest Schmid factor [59].

Unlike dislocation slip, which can proceed in the antiparallel slip direction in compression, twinning is polar and cannot activate if the resolved load is antiparallel to

Ministry of Defence © British Crown Copyright 2020/AWE

the twinning direction [57]. This is due to the microscopic shuffles not being able to reform the original crystal structure if the shear direction is reversed. Consequently, the Schmid factors for twinning are different in tension and compression.

McCabe et al. present the Schmid factors for $\{130\}$, '$\{172\}$' and $\{112\}$ twins in tension and compression as inverse pole figures [30]. For completeness I have re-plotted these in figure 2.12 along with the Schmid factors for the '$\{176\}$' twin. For a particular loading direction, the variant with the highest SF will be the most likely to operate. Therefore the overall SF for a deformation mode is calculated as the maximum (most positive) SF out of all the symmetrically equivalent variants (shown in Appendix A8.1).

Ministry of Defence © British Crown Copyright 2020/AWE

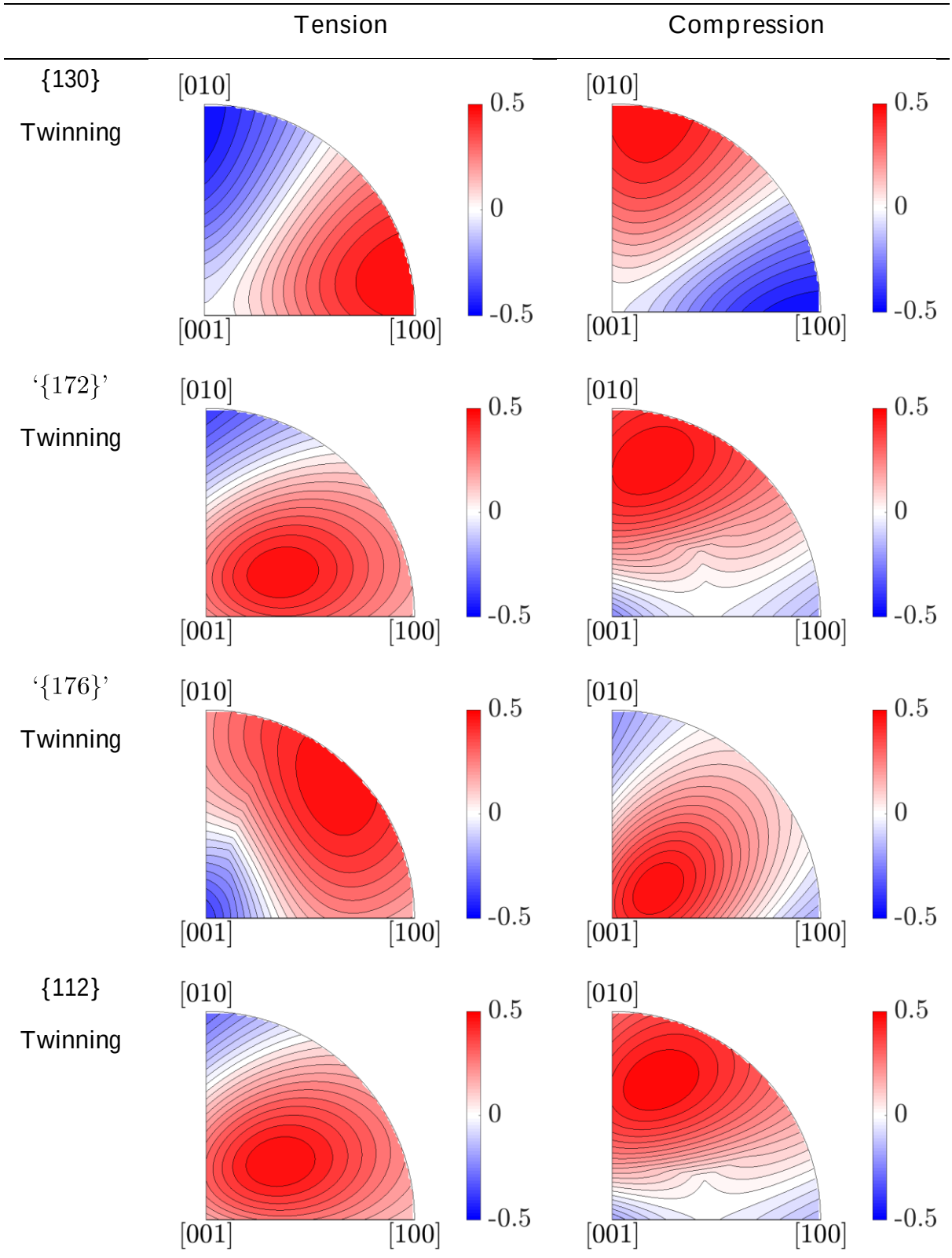


Figure 2.12. Orientation dependence of the Schmid factor for the most-stressed variant of the {130}, ‘{172}’, ‘{176}’ and {112} twin modes in tension and compression. Here, the ‘most-stressed’ variant is the one with the highest Schmid factor in a particular direction. The twin mode cannot operate for orientaions with a negative Schmid factor. Calculation described in Appendix A8.1.

Ministry of Defence © British Crown Copyright 2020/AWE

2.3.2.2 {130} Twins

Twins on the $\{130\}$ planes are the dominant deformation mode in wrought uranium, and depending on initial orientation, can be active in coarse-grained uranium [56]. Typically they have straight and parallel sides when the twins pass to a (stress-free) surface, and have a lenticular morphology when they terminate in the crystal [43]. $\{130\}$ twins are often thin, rarely thicker than $10\ \mu\mathrm{m}$ [15]. It has been shown that, after initiation, lateral growth of $\{130\}$ twins requires prior deformation on the Chimney slip system; with more prior strain leading to the formation of thicker twins [18].

$\{130\}$ twins are most active for grains in tension near $[100]$ or compression near $[010]$ [30]. (An earlier publication by the same author seems to suggest $[010]$ tension [56]). $\{130\}$ twins induced by tensile deformation cause a rotation of the grains such that those initially oriented with the tensile axis near $[100]$ end up with it near $[010]$. In compression, $\{130\}$ twinning rotates grains with their tensile axis near $[010]$ towards $[100]$ [56]. McCabe showed the degree of $\{130\}$ twinning correlates with the number of grains well-oriented for this deformation [30].

Crystallographically, $\{130\}$ twinning leads to a reorientation of the lattice of $69.3°$ about $[100]$ [38]. There are considerable stresses at the twin boundaries due to the atomic shuffles required to correctly reform the crystal structure [60].

Ministry of Defence © British Crown Copyright 2020/AWE

2.3.2.3 '{172}' Twins

The second most frequently observed mode of twinning occurs on a plane with irrational indices, however these can be approximated to '$\{172\}$' [15]. The twinning shear of '$\{172\}$' is less than for $\{130\}$, so these twins are predicted to be thicker than $\{130\}$ twins [60] (although this contradicts the early observations of Lloyd and Chiswik [43]). This is the reciprocal twinning mode of the rarely observed $\{112\}$ mode. In tension, this twin is most active when the tensile axis is near $[001]$ [56] and it leads to a reorientation of the lattice of $93°$ about $[\overline{10}\ 7\ 0]$ [55].

2.3.2.4 '{176}' Twins

Twins on the irrational '$\{176\}$' system have only been observed in compression when $\{130\}$, '$\{172\}$' twinning or (010) slip cannot occur due to the orientation of the crystal. This typically relates to compression near $[001]$, at angles slightly [43] towards $[100]$. Due to the asymmetry of twinning, this twin rarely forms in tension, since the orientation in tension which gives the highest resolved shear stress for '$\{176\}$' twinning also maximises the resolved shear stress for Wall slip, which instead dominates.

Daniel identified the same twin but gave it the indices '$\{197\}$' [18]. The author also suggested that the $\{121\}$ twin reported by Cahn [42][15] was actually a '$\{176\}$' twin. Since the shear for this system is the smallest out of all the observed twins, '$\{176\}$' twins tend to be thicker than those of other types. It has suggested that the formation of

Ministry of Defence © British Crown Copyright 2020/AWE

‘$\{176\}$’ twins requires prior dislocation motion on the Wall slip system, however the exact mechanism has not been verified [18].

‘$\{176\}$’ twinning can be identified by a reorientation of the lattice of $78°$ about $[0\ 10\ 7]$ [55].

2.3.2.5 {112} Twins

The $\{112\}$ twin is the reciprocal of the ‘$\{172\}$’ twin. It is only ever active in large grains oriented with their $[001]$ direction near to the tensile axis. The twinning leads to a reorientation of the lattice of $90°$ about $[110]$ [55].

2.3.3 Effect of Orientation

The effect of crystal orientation on the active deformation processes in compression at room temperature has been summarised by Holden [7] as a stereographic projection (figure 2.13). It shows which deformation modes (slip, twinning and kinking) are active depending on the orientation of the compression direction. Note that Roof and Chimney slip, and the rarely observed $\{112\}$ twinning are missing from this diagram. The $\{011\}\langle100\rangle$ slip is only observed alongside ‘$\{176\}$’ twins. The orientations where each mode activate correspond to regions of high SF for that mode in compression (figure 2.7 and figure 2.12).

A similar diagram could be drawn for deformation in tension. Slip would occur in the same orientations whilst twinning would change in response to the differing SFs..

Ministry of Defence © British Crown Copyright 2020/AWE

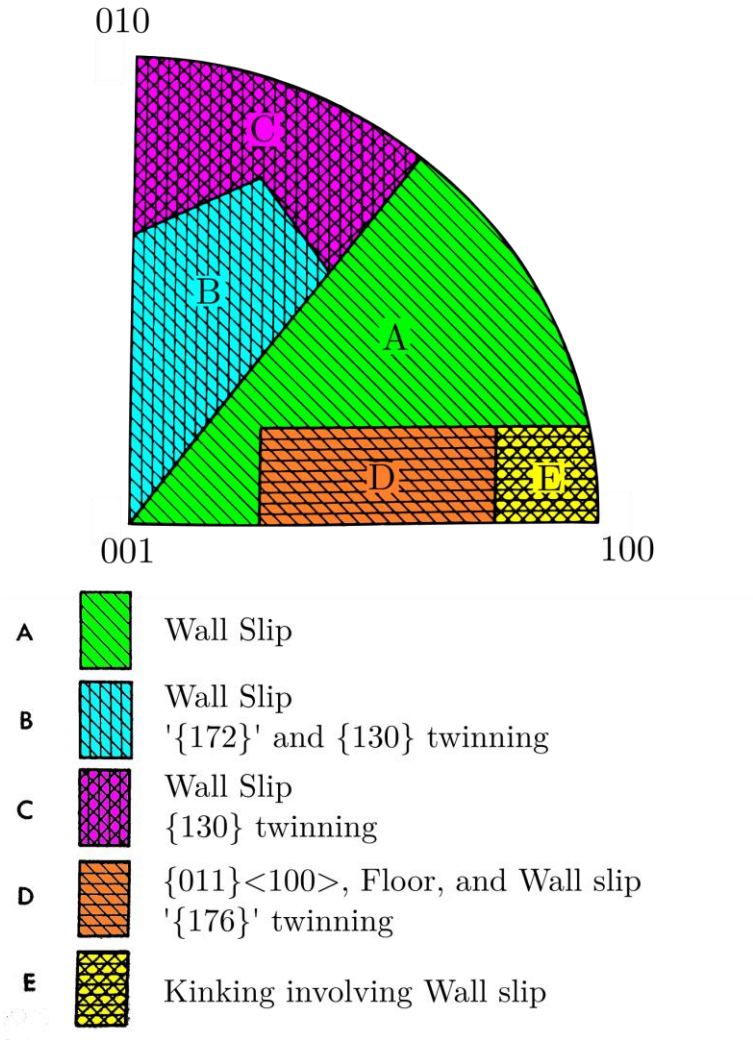


Figure 2.13. Compression of alpha uranium showing active modes of deformation as a function of the orientation of the compression direction. Note that Roof and Chimney slip, and $\{112\}$ twinning are missing from this diagram. Modified from Holden [7] with colour added and inverse pole figure rotated to be consistent with Schmid factor plots (figure 2.7 and figure 2.12).

2.4 Fracture of Uranium

Now that we have an understanding of the active deformation modes in uranium, we can discuss fracture in cast uranium. The observed fracture can then be related back to the deformation mechanisms that were active in the sample prior to failure. Fracture in uranium is complex, with a number of different observed fracture morphologies and associated initiation and propagation mechanisms.

Ministry of Defence © British Crown Copyright 2020/AWE

Fracture in α-uranium was first studied in 1953 by Cahn [15]. The author noted that the tensile fracture of coarse-grained specimens resulted in a dull, irregular fracture surface. Small 'cleavage' facets were observed, and Laue photograph analysis showed these facets were parallel to thick '$\{172\}$' twins. This suggests the local fracture mechanism was *twin parting*, a phenomenon common in some minerals, such as dolomite [61], where the fracture propagates along the boundary between parent and twinned material. This has been verified by more recent work by Field et al [62], who used EBSD to confirm twin parting along '$\{172\}$' twins (figure 2.14).

These observations suggest that twinning is closely related to fracture in α-uranium. The observed twin parting in uranium is parallel to the irrational '$\{172\}$' twin plane and is not therefore equivalent to crystallographic cleavage along close-packed atomic planes [15].

Ministry of Defence © British Crown Copyright 2020/AWE

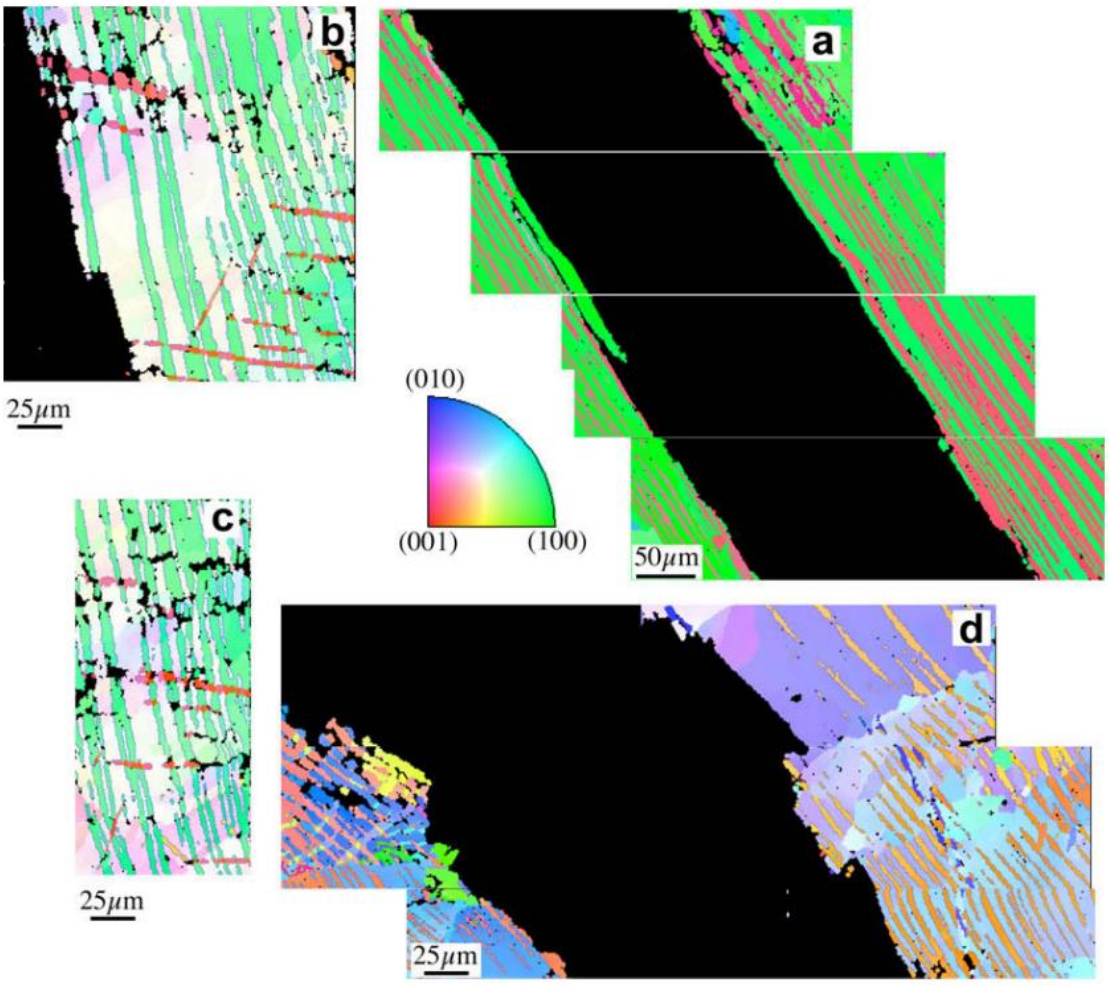


Figure 2.14. EBSD images of fracture parallel to '{172}' twins in uranium. Reproduced from Field et al. [62].

Uranium undergoes a transition from cleavage (specifically twin parting) at low temperatures, through a region of intergranular fracture (figure 2.16) near the ductile-brittle transition, to ductile fracture at high temperatures. The ductile-brittle transition has been shown to be related to the variation in temperature of the different fracture mechanisms, shown schematically in figure 2.15. Some research [63] suggests that for pure uranium samples, with no impurity segregation, there would not be an intercrystalline region, however there is substantial evidence to suggest that

Ministry of Defence © British Crown Copyright 2020/AWE

intercrystalline fracture occurs even in relatively pure material [64][65] (for example that containing 400 ppm C, 50 ppm S and 50 ppm Fe [66]).

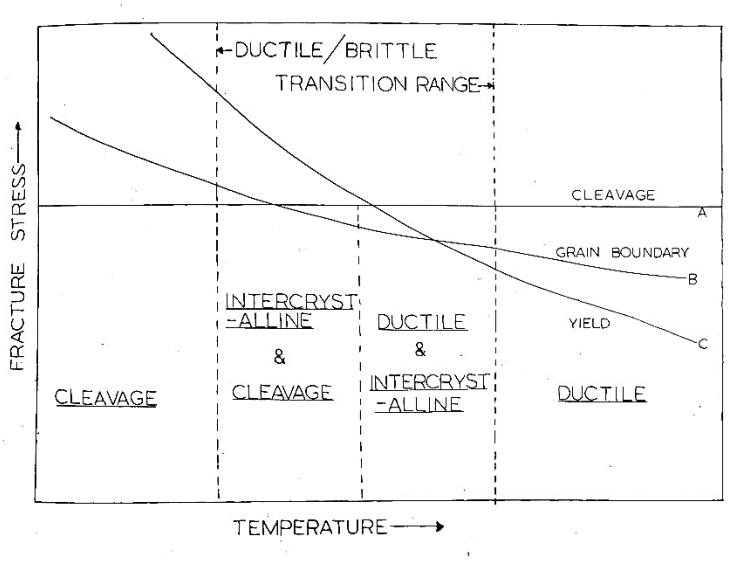


Figure 2.15. Schematic showing how changes in the cleavage strength (A), grain boundary strength (B) and yield strength (C) vary with temperature. Reproduced from Taplin's DPhil thesis, based on his experimental observations [60].

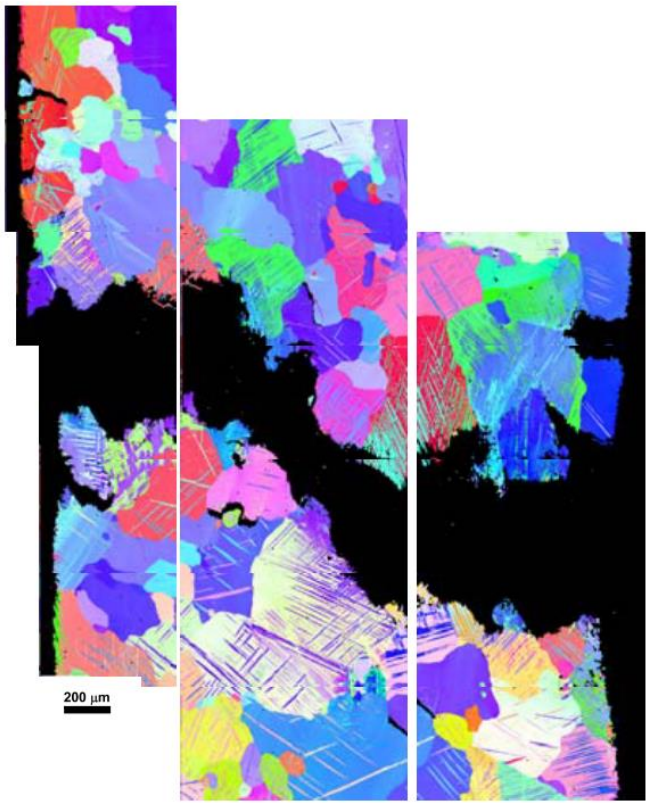


Figure 2.16. "Cross-section of mating fracture surfaces in an unalloyed uranium tensile specimen. Apparent is the prevalence of deformation twins and the intergranular fracture between grains of dissimilar orientation." Figure and caption reproduced from McCabe et al. [65].

Ministry of Defence © British Crown Copyright 2020/AWE

There have been a number of studies looking at the effect of impurities [67][63] (including hydrogen [68][69]), thermal cycling [70], annealing [71], strain rate [72][73], grain shape [74] and grain size [29][66][75][76] on the fracture of α-uranium, as well as a study of creep rupture [77]. Most of this work focused only on the effect the changes have on the ductile-brittle transition temperature, which typically exists around room temperature.

Observations of fracture on the micro-scale may give a clearer picture of the active mechanisms. In general, the fatal crack propagates either along a twin boundary, or a grain boundary. Figure 2.17 consists of metallographic images of typical room-temperature fracture in α-uranium. Figure 2.17(a) shows the path of a crack which has propagated between grains whilst figure 2.17(b) contains a crack which instead propagated parallel to a twin. The type of twin was not identified, but it is likely to be of the '$\{172\}$' type.

Interestingly, secondary microcracks (i.e. those other than the crack which caused failure) were commonly observed. This suggests that the critical step in the fracture of uranium is the propagation of the crack after it has formed, rather than its initial nucleation [60]. Most of the observed microcracks were associated with twins and either formed where a twin intersected a grain boundary (figure 2.17(d)), or near the point where a twin is blocked by another twin (figure 2.17(c)). These cracks were often arrested after a short distance of a few tens of microns, or where the grain boundary changes

Ministry of Defence © British Crown Copyright 2020/AWE

direction [60] (figure 2.18). At no point were cracks observed near twin crossings [60], - only where a twin intersection was blocked.

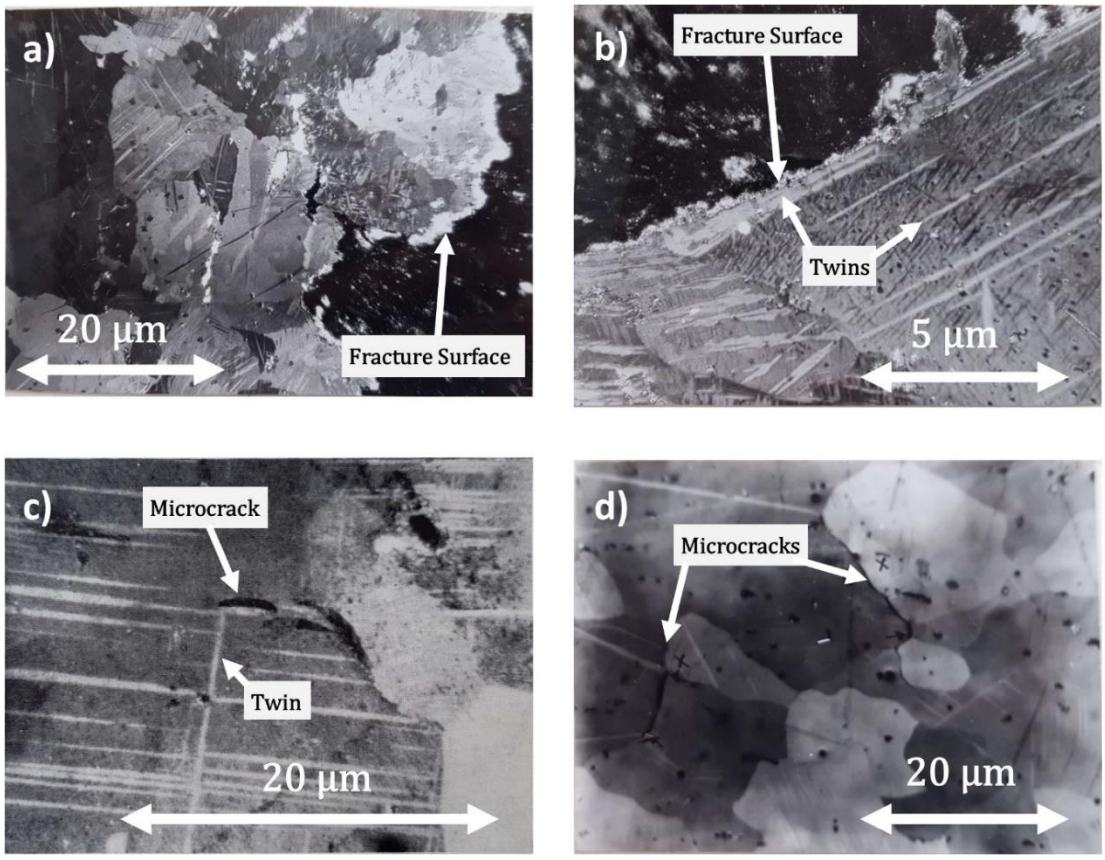
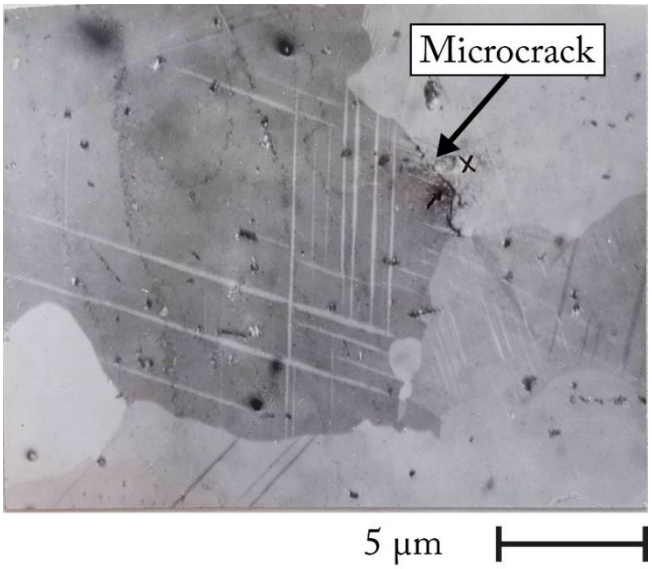


Figure 2.17. Metallographic observations of fracture in uranium. (a) Intercrystalline fracture in cross-section with the crack having propagated near to grain boundaries. In (b) 'twin parting' fracture is parallel to a twin boundary. c) shows a crack nucleated at a twin intersection alongside the blocking twin, opposite the tip of the blocked twin. Finally d) shows nucleation of an intergranular crack, apparently due to the impingement of a twin upon a grain boundary. a),b),d) from Taplin [60], c) from Taplin and Martin [70].

Ministry of Defence © British Crown Copyright 2020/AWE

(a)



(b)

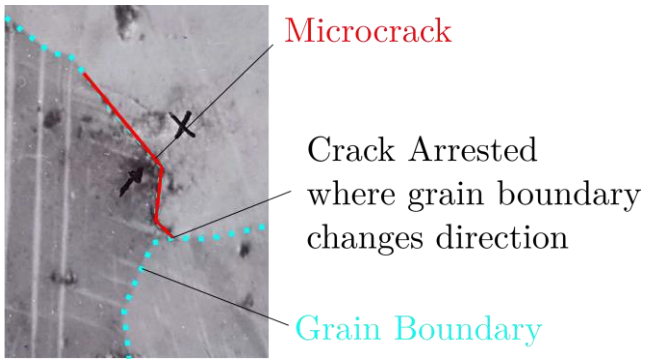


Figure 2.18. (a) Intercrystalline micro cracking in α-uranium. (b) Cropped image showing the crack has been arrested where the grain boundary changes direction. Images modified from Taplin [60]

A number of different nucleation mechanisms have been proposed in the literature to explain the observed features. Taplin [60] suggests that growing twins must have an elastic stress field ahead of the twin tip, and that this elastic strain energy could be relieved by the formation of a microcrack. The presence of an elastic stress field around a blocked twin in HCP Zircaloy-2 has been demonstrated by Abdolvand and Wilkinson [78] using HR-EBSD.

Ministry of Defence © British Crown Copyright 2020/AWE

An alternative mechanism was also proposed where slip dislocations are emitted from the twin apex and these subsequently pile up at obstacles, or interact with other dislocations, to form a microcrack. The formation of microcracks due to impinging dislocations has been predicted in the literature [79]. This mechanism could explain the prevalence of fracture along '{172}' twins, as these are often thick and therefore emit the largest number of dislocations [79], but no conclusive evidence is available.

A mechanism for grain boundary nucleation in the absence of twinning was proposed by Taplin and Martin [74] in which relative movement across a rough boundary results in stress concentrations and cavity formation. If correct, this would explain the prevalence of intercrystalline fracture at ambient temperature, where more slip systems are available to accommodate bulk deformation. There have been, however, no observations of fracture in uranium at a grain boundary where twins were not present.

In summary, it is generally agreed that blocked twins, or residual stresses at grain boundaries, could lead to crack initiation by providing sufficient strain energy to create new surfaces. Many of these cracks then arrest at a short length, as the strain energy is exhausted. There is limited knowledge of how these cracks then propagate to failure – this would require measurement of the work of fracture.

2.4.1 Twins as Stress Concentrators

It is well known that many materials that are brittle at low temperature deform by twinning, and that the twinning mechanism is linked to their fracture. In TWIP steels

Ministry of Defence © British Crown Copyright 2020/AWE

(bcc ferrite), the fracture mechanism is phenomenologically similar to that of uranium (figure 2.19); cracks are initiated at blocked twins and seen to propagate along both incoherent grain boundaries and deformation twin boundaries, depending on the twin orientation with respect to the tensile direction [80].

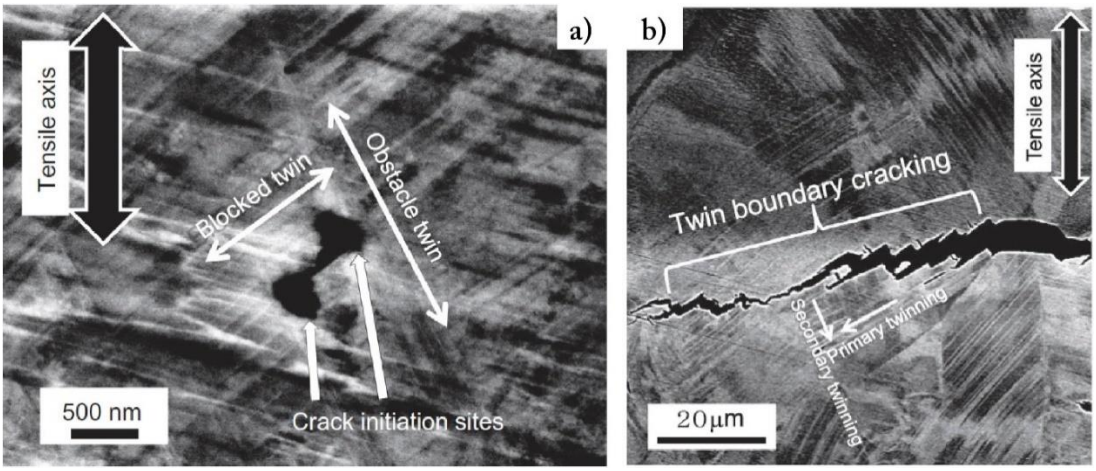


Figure 2.19. Electron channelling contrast images showing a) (transgranular) crack initiation associated with deformation twins and b) crack propagation along deformation twin boundaries, in a bcc ferritic TWIP steel. Figures reproduced from Koyama et al. [80].

Even though twins are formed to relieve stresses, the rapid formation and large shear means there is a large stress associated with the twin tip. Sleeswyk [81] proposed a mechanism by which this stress could be relaxed by *emissary dislocations* which slip ahead of the growing twin. This has been linked to the Stroh mechanism of fracture, where a pile up of slip dislocations at a grain boundary gives a tensile stress which nucleates a crack [82]. The presence of the emissary dislocations may make the interactions at a blocked twin tip similar to those at a blocked slip band.

Bieler et al. [83] propose a different mechanism which considers the effect of the twinning shear on a grain boundary. There is local tension where a parallel-sided twin meets a

Ministry of Defence © British Crown Copyright 2020/AWE

grain boundary, as shown in figure 2.20, and for the grain boundary to remain intact there must be sufficient elastic and plastic deformation of the grains on either side. This mechanism may be more appropriate for uranium, where often twins are seen to be fully developed and parallel-sided at their intersection with a grain boundary.

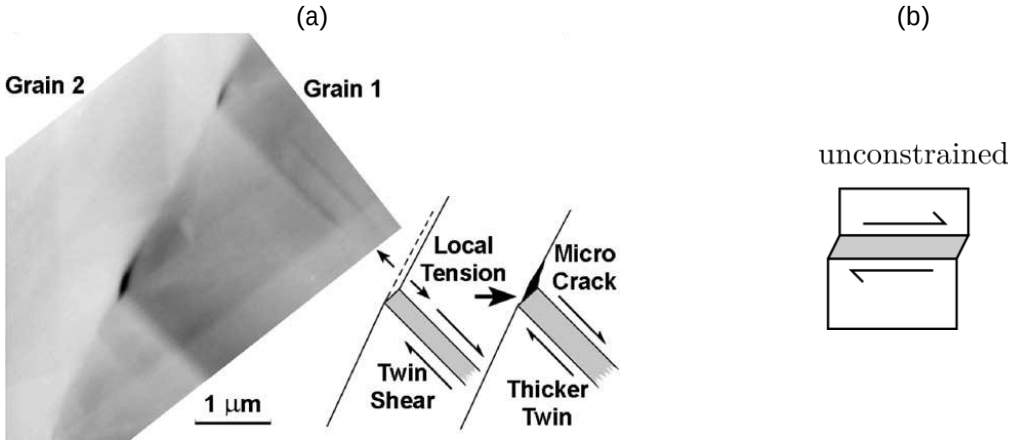


Figure 2.20. (a) The interaction between a twin and a grain boundary can produce local tensile stresses which can nucleate a crack in TiAl. Reproduced from Bieler et al. [83]. (b) Twin in an unconstrained grain.

In the brittle intermetallic TiAl, intergranular fracture was found to be insensitive to grain boundary orientation; it was observed that weak boundaries crack even if perpendicular to the tensile axis [83]. It instead was found to be related to the alignment of the dominant twinning system with the tensile axis, as well as the alignment of slip systems in the neighbouring grain. Similar observations have not been yet made for uranium.

The issue of twins nucleating fracture is not confined to uranium. As discussed by Mahajan and Williams [50], cracks are often found in areas of twin termination, with intergranular cracks being located near twin impingements in Cr, Mo and W [84][85]. It would appear as if the twins have caused failure, however the authors point to

Ministry of Defence © British Crown Copyright 2020/AWE

observations in Mo by Reid et al. [86] showing that whilst twin-induced microcracks are observed, the actual failure is slip-induced. What is not clear is the chronological order; do twins nucleate cracks that then cause failure, or do propagating cracks nucleate twins in their wake? Due to the high propagation speed of twins, interrupted tests are not possible. High speed magnetic measurements allowed the question to be answered for an Fe-3 wt. % Si alloy, where for notched specimens twinning occurred approximately $20\ \mu s$ before crack nucleation, and the mechanism in this case is therefore twin-induced fracture [87].

2.5 Crystal Plasticity Modelling

This project aims to develop a crystal plasticity model to simulate the deformation and fracture of cast α-uranium. No modelling work has been performed by the author, however the results of modelling by our collaborators in the Department of Materials and Department of Engineering Science, Unviersity of Oxford, UK, will be presented to demonstrate the utility of the experimental data. To put this work in context, it is necessary to provide a brief overview of the crystal plasticity technique and its application to uranium.

Crystal plasticity (CP) modelling is a method for simulating deformation of materials, taking to account that a material is neither linear elastic nor perfectly plastic, but a complex mixture of deformation modes influenced by the microstructure and loading state.

Ministry of Defence © British Crown Copyright 2020/AWE

The deformation gradient is split into elastic and plastic parts [88]. The evolution of plastic deformation is controlled by the shear rate on each deformation system. Twinning is incorporated as a varying volume fraction of constant shear [89].

The first modelling approaches were self-consistent, elasto-plastic (EPSC) or visco-plastic (VPSC), where a grain is approximated as a spherical particle inside a homogeneous medium [88][90].

Embedding CP laws into a finite element (FE) model allows the constraint-induced variation of the strain field between neighbouring grains to be simulated [91][92]. This is known as Crystal Plasticity Finite Element (CPFE). It effectively runs a CP model at each node in an FE simulation – each node has its own crystal orientation, displacement, strain, stress, volume fraction of twinning, dislocation density, and dislocation shear rate.

The formation of discrete twins has been simulated in FE models [93] and more recently CPFE models [94]. This allows the interactions between twins and microstructural features such as grain boundaries to be investigated.

Fracture can be simulated by incorporating cohesive zones [95], where the material separation is governed by normal and shear traction laws [96].

A common use of CPFE models is to obtain a set of material parameters from experimental data. An observable (e.g. macroscopic stress-strain relation) is calculated,

Ministry of Defence © British Crown Copyright 2020/AWE

and the simulation parameters are refined to achieve the best match between the simulated observable and the experimentally measured values. The optimised parameters should be a good approximation to those in the material.

Self-consistent models of uranium have been applied to fine-grained rolled uranium. VPSC models have been used to measure texture change during tension [30], compression [30][39] and rolling [39]. An FE implementation of the VPSC model has recently been performed by Knezevic et al. [97]. In each case, the model was validated by comparison with EBSD-measured textures. EPSC models have been used to investigate the effects of temperature [49], hydrogen [98] and thermal residual stress [45] on deformation of wrought uranium. No literature exists of modelling on coarse-grained α-uranium.

To calibrate a CPFE model, the following experimental data are required:

- Microstructural information, either as a texture or spatial microstructure map.
- Observable relation for calibration. This could include (a) the stress-strain response, either macroscopic, in individual grains, or in families of grains with similar orientations, (b) the texture change, relating to plastic deformation, or (c) the displacement or distortion of the specimen.

2.6 Experimental Investigation of Deformation

In this section we will cover the experimental methods for acquiring the aforementioned calibration data.

Ministry of Defence © British Crown Copyright 2020/AWE

2.6.1 Mechanical Testing

The simplest way to obtain deformation data is via mechanical testing, typically in compression, tension or bending. Strain measurement is often [24][72] performed with an extensometer which spans the area of interest, from which the average strain in this region can be calculated – consequently this is not suitable for heterogeneous strain fields, such as those expected in cast uranium.

2.6.1.1 Full-field Strain Measurement - DIC

Digital image correlation (DIC) is an image-based technique commonly used to measure the displacement field on the surface of a specimen during mechanical testing. The technique originated in the 1980s [99] and is described nicely in a recent review by Pan et al. [100].

An overview of the DIC process is shown in figure 2.21. Typically, a reference image is taken of the undeformed sample, and a sequence of test images are acquired during deformation (figure 2.21(a)). The DIC algorithm splits the images into an array of (often overlapping) subsets (figure 2.21(b), also known as facets), and by calculating and maximising the cross-correlation coefficient between each subset in the reference and test images, the displacement field is found (figure 2.21(c)).

Ministry of Defence © British Crown Copyright 2020/AWE

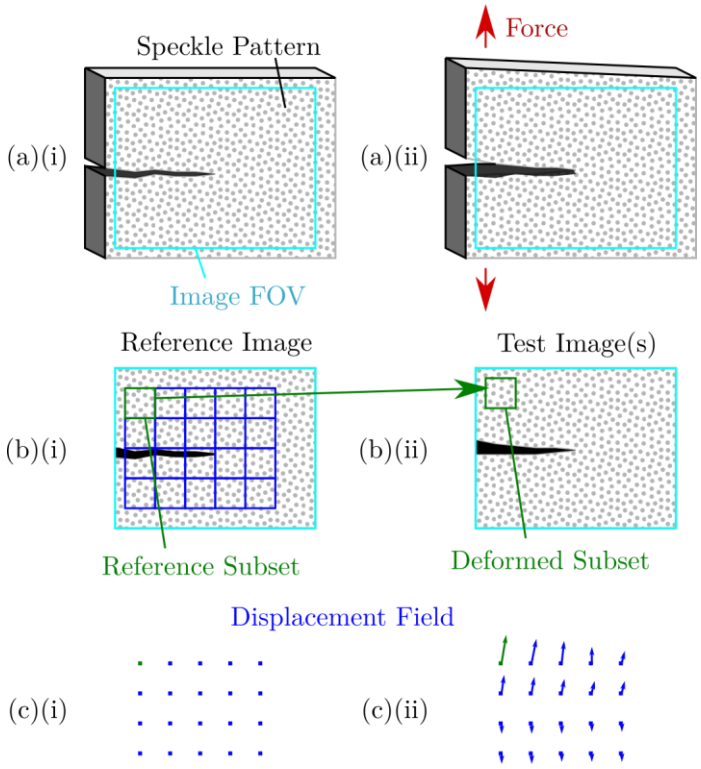


Figure 2.21. Schematic of the digital image correlation process. (a) Images are taken of the specimen surface (i) before and (ii) after deformation. These are known as reference and test images respectively. (b) The DIC algorithm splits the reference image into subsets and performs a cross-correlation to identify the position of each reference subset in the deformed image. (c) This results in a vector field of displacements for each test image, which can be differentiated to yield the strain field.

The different components of the strain field are obtained by differentiating the displacement field with respect to position:

$$\varepsilon_{xx}\ x,y\ = \frac{du_x\ x,y}{dx}, \qquad \varepsilon_{xy}\ x,y\ = \frac{du_x\ x,y}{dy} \qquad [2.15]$$

$$\varepsilon_{yx}(x,y) = \frac{du_y(x,y)}{dx}, \qquad \varepsilon_{yy}(x,y) = \frac{du_y(x,y)}{dy}$$

The correlation algorithm can achieve sub-pixel displacement accuracy, however it is not perfect, and uncertainties arise if the reference and deformed subsets cannot easily be matched. This could be due to random noise in the images from the camera sensor, or changes in lighting – variations in the external source, sample movement with respect to the illumination source, or changes in sample surface finish during deformation. These

Ministry of Defence © British Crown Copyright 2020/AWE

problems are exacerbated where there is less information available for correlation – for low bit depth images, low contrast images and for small subset sizes. Additional issues can arise where the speckle pattern is not 'random' enough, and multiple possible matches are found for each subset. An ideal speckle will be random with a good range of intensities such that the image histogram is broad, spanning dark and light grey-scale values.

The effect of subset size is significant as this is a parameter of the DIC algorithm, and can be varied to a suitable value for the given application. Typically it is seen that an increased subset size gives a better displacement resolution, quantified as the standard deviation of displacements for a rigid-body translation of the specimen where the ideal displacement field is uniform and single-valued (Haddadi et al. [101]).

This would lead us towards the use of large subsets, however there is a competing requirement that favours small subsets – spatial resolution. In the context of DIC, the phrase 'spatial resolution' is confusingly used to refer to a variety of different features of the deformation field. In the following paragraphs I will explain the difference and significance of these features, and provide a consistent definition for use in this work.

I define spatial resolution as *the smallest theoretically resolvable displacement feature*. The displacement vector associated with each subset is the 'average' displacement of the area inside the subset, so the spatial resolution is equal to the subset size – smaller subsets yield an improved (i.e. smaller) spatial resolution.

Ministry of Defence © British Crown Copyright 2020/AWE

Figure 2.22 shows a schematic of how the subset size may affect the measurement of a simplified 1D displacement field with a single discontinuity (a crack). The grey lines show the true displacement field – positive to the right of the crack and negative to the left. The orange lines show the theoretically best measurement of the displacement with (b) large and (c) small subsets. The displacement discontinuity is 'blurred' by a degree equal to the subset size – smaller subsets can give a better approximation of the true displacement field. A set of simulated displacement measurements are shown as square markers with vertical error bars showing the displacement uncertainty. There is a larger scatter in the displacements for the smaller subset.

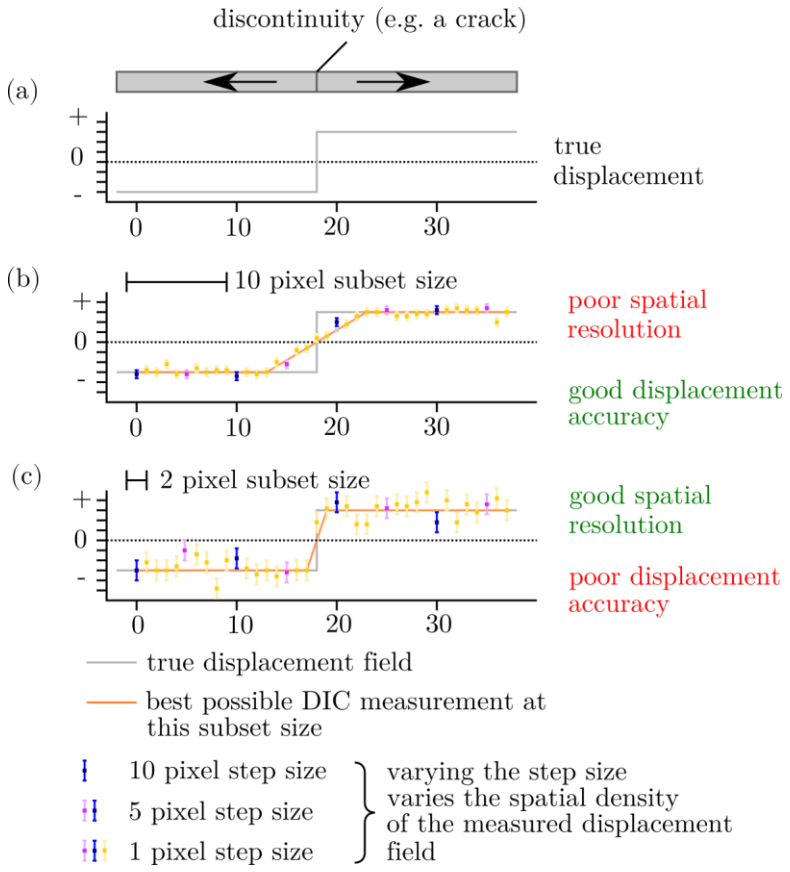


Figure 2.22. Influence of subset size on the spatial resolution and correlation accuracy of the DIC measurement. Increased subset sizes are associated with an improved displacement accuracy but a worsened spatial resolution.

Ministry of Defence © British Crown Copyright 2020/AWE

Note that decreasing the step spacing (increasing the subset overlap – blue → blue & pink → blue, pink & yellow markers in figure 2.22), which is sometimes erroneously referred to as improving the spatial resolution, decreases the spacing between points in the resulting vector field but does not allow smaller displacement features to be resolved.

Very small subsets, whilst theoretically able to resolve small displacement features, tend to have such large displacement uncertainties that they are worthless to aid the science in question. It is worth defining the effective spatial resolution as the *smallest resolvable displacement feature for a given required displacement accuracy, for a given set of images to be correlated*. This decreases with subset size but has a minimum where the displacement accuracy reaches the threshold value, as shown in figure 2.23.

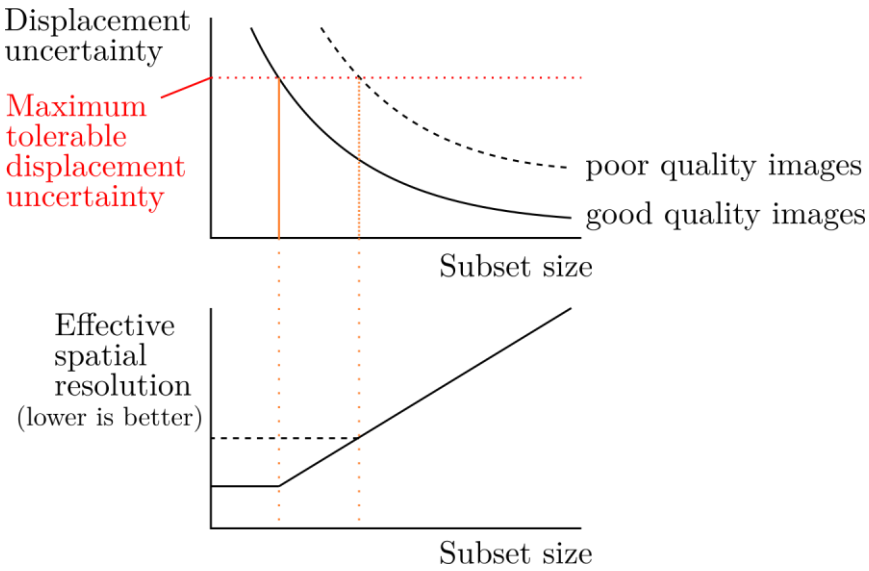


Figure 2.23. Influence of subset size on the effective spatial resolution for images well-optimised (continuous line) and less-optimised (dotted line) for DIC.

The effective spatial resolution therefore depends on the factors that influence the displacement accuracy, such as speckle pattern quality and lighting, and our choice of maximum tolerable displacement uncertainty. It can, to some extent, be improved by

Ministry of Defence © British Crown Copyright 2020/AWE

reducing the subset step size (tighter overlap) to oversample the displacement field, and applying a low-pass or median filter to reduce the subset-to-subset random noise.

A significant advantage of DIC is that it is non-contact, and can be performed on any material where a random 'speckle pattern' of intensity [101] is present. The technique is scale-independent and can use images from any source, from optical images of engineering structures [102] to secondary electron images in an SEM [103].

DIC has been used to investigate fracture, where the measured displacement fields were interpreted with field fitting [104] and J-integral [105] methods.

DIC is adversely affected by out-of-plane displacements of the specimen, towards or away from the camera, resulting in 'phantom' strains to be measured. Depending on the magnitude of the motion and the geometry of the DIC system, these strains can be significant compared to the actual in-plane strains [101].

3D-DIC or stereo DIC uses two (or more) cameras to image the specimen. A calibration procedure, first described by Helm et al. [106], allows accurate measurement of surface displacements in 3 dimensions. A variant of this algorithm is implemented in the commercial GOM ARAMIS software (GOM GmbH, Germany) used in this thesis.

2.6.2 Diffraction

Diffraction measurements measure the spacing between lattice planes inside a material with high sensitivity, according to Bragg's law,

Ministry of Defence © British Crown Copyright 2020/AWE

$$\lambda = 2d\sin(\theta) \quad [2.16]$$

where *d* is the interplanar spacing, λ is the wavelength of the diffracting wave or particle, and θ is the diffraction angle, half the angle between the incoming and outgoing beams.

The relative change in *d*-spacing is the lattice strain, and this is directly proportional to the normal stress on the diffracting plane. These lattice strains can be simulated in a CP model therefore diffraction data can be used to calibrate and validate such models.

2.6.2.1 Neutron Diffraction

Neutron diffraction is a common method for performing such experiments, and has been used extensively in the literature on uranium [45][49][107][108] and other materials [109]–[112] to provide data for CPFE or self-consistent models. In each case, the models were used to predict either a) flow curves indicative of the overall response, b) the lattice strain indicative of the intergranular stresses built up as a result of plastic deformation, and/or c) peak intensities related to the formation of deformation twins.

Neutrons have the advantage of a large penetration depth in high-Z materials, enabling testing of large specimens with gauge volumes of the order of 1 cm × 1 cm × 1 cm. Typically, this means averaging over hundreds or thousands of grains, and the specimen is assumed to have a consistent microstructure throughout.

Technique Overview

Neutron diffraction (ND) cannot be performed in a conventional laboratory, and is instead conducted at a number of large neutron sources around the world. Spallation

Ministry of Defence © British Crown Copyright 2020/AWE

sources generate pulses of neutrons by the collision of high-energy H^- ions into a dense target such as tungsten or mercury. Neutron energies within each pulse are distinguished according to their time of flight (TOF) from source to detector. TOF-ND experiments can measure spectra over a wide *d*-spacing range, making them suitable for low-symmetry materials such as uranium (with lattice parameters between 2.8 Å and 5.9 Å).

Engineering TOF-ND beamlines such as ENGIN-X at ISIS, UK and SMARTS at LANSCE, USA, typically have large sample environments, allowing the specimens to be exposed to stress, heat, or magnetic fields [113][114].

Analysis is performed using single-peak fitting or Rietveld refinement [115][116], the latter fitting the whole spectrum with a number of refinable parameters. The hkl peak is representative of the average behaviour of the hkl family of grains in the diffraction condition – i.e. those with hkl plane normals parallel to the diffraction vector. Changes in peak position relate to lattice strains, whilst changes in peak intensity relate to texture changes. By analysing the relative peak intensities in a spectrum, Rietveld refinement can measure texture [115][117]. This is implemented in the GSAS software package, commonly used by neutron beamlines [118]. Beamlines with many detector banks such as GEM, ISIS, UK, and HIPPO, LANSCE, USA, allow a complete measurement of texture in a specimen [117][119].

Certain peaks in the diffraction spectrum are missing due to destructive interference during scattering from the uranium crystal structure. These systematic absences result

Ministry of Defence © British Crown Copyright 2020/AWE

in the highest *d*-spacing reflection being the (002) at 2.935 Å (discussed in detail in Appendix A4).

Neutron Diffraction Investigation of Uranium

Neutron diffraction has been used to measure residual stresses in uranium after welding [120] and deformation [121], and used in conjunction with modelling to investigate the effect of these stresses on deformation [45], in addition to the effects of hydrogen [98] and temperature [49][107].

The significance of the thermal residual stresses on subsequence deformation was clearly demonstrated by Calhoun et al. [45], modelling being required to fully explain the neutron diffraction measurements.

Most neutron diffraction studies of deformation in uranium in the literature focus on fine-grained, wrought material. The only study of cast uranium to use neutron diffraction was by Garlea et al. [27], where the measurement was post-deformation rather than in-situ.

Plastically hard and soft orientations can be identified by inspection of plots of lattice strain as a function of stress. Saturation of lattice strain on a particular family of grains indicates the saturation of stress, corresponding to the initiation of plasticity in these grains. These grains are known as plastically soft. Reflections with large lattice strains must be carrying large stresses, suggesting a lack of plasticity – these are the plastically hard orientations. Figure 2.24 shows lattice strain development during tensile

Ministry of Defence © British Crown Copyright 2020/AWE

deformation of rolled uranium along the rolling and transverse directions. In both textures, (200)-oriented grains are plastically soft and (020) are plastically hard, consistent with the Schmid factors allowing and preventing {130} deformation in these orientations respectively (figure 2.12).

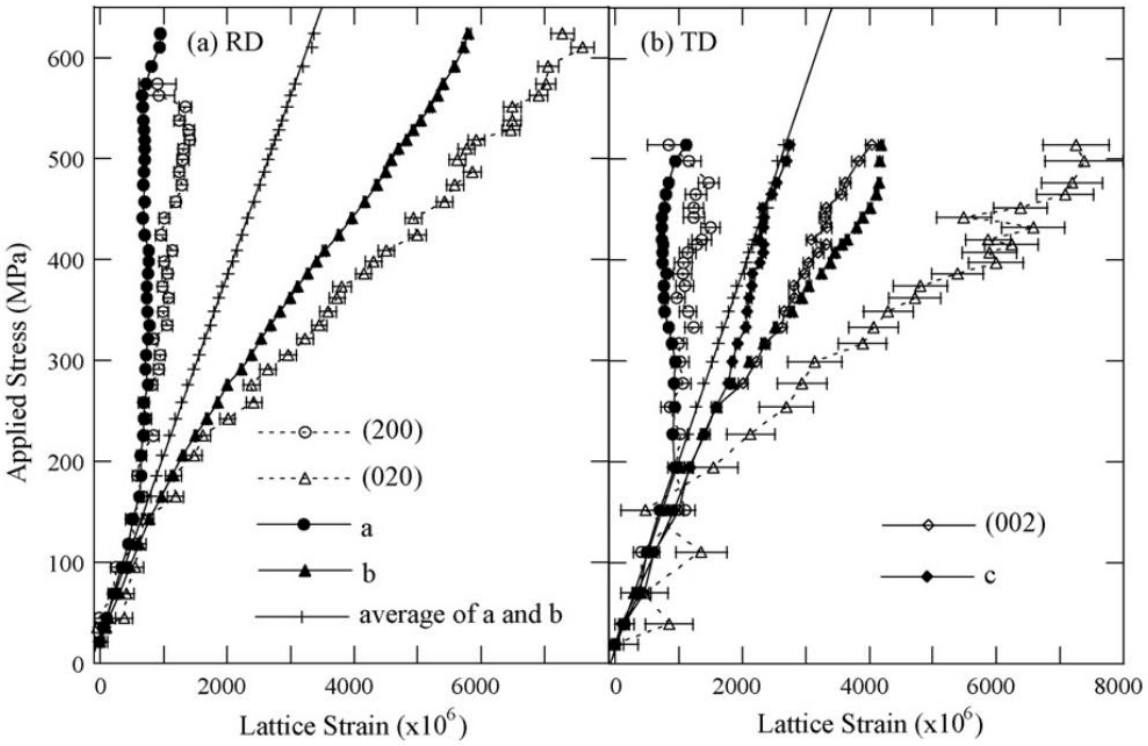


Figure 2.24. "Development of the elastic lattice strains in rolled uranium during tensile deformation in the (a) rolling (RD) and (b) transverse directions (TD). The filled and open symbols represent lattice parameter and single peak strains, respectively. The (+) signs represent the average of the a and b strain and the solid line a linear fit to that average.". Figure and caption reproduced from Brown et al. [107]

Twinning Texture Changes

The crystallographic reorientation during twinning can lead to a measurable texture change, often identified in diffraction experiments as a change in peak intensity – a reduction in peak intensity from planes oriented in the parent orientation and an increase in those in the twinned orientation – since the (*hkl*) peak intensity is proportional to the

Ministry of Defence © British Crown Copyright 2020/AWE

volume fraction of grains with their (*hkl*) plane normal parallel to the diffraction vector (which is typically parallel to the loading direction).

In hexagonal materials, where the dominant twinning mode is $\{1012\}\langle 1011\rangle$, the formation of these twins has been linked to changes in the {0002} peak intensity. Gharghouri et al. [122] studied a hcp Mg alloy, and during tensile deformation observed a decrease of {0002} peak intensity and related this to $\{1012\}\langle 1011\rangle$ twinning in grains oriented with their *c*-axes parallel to the loading direction. In compression, grains of this orientation cannot twin via these modes, however grains oriented with their *c*-axes perpendicular to the loading axis can twin, leading to an increase in {0002} peak intensity. Fitzner et al. [123] and Nervo et al. [124] used the increase in {0002} peak intensity measured with neutron diffraction to identify twin formation in hcp Ti alloys.

Figure 2.25 from Nervo et al. [124] shows the change in peak intensity is linear with applied strain. The authors verified the presence of $\{1012\}\langle 1011\rangle$ twins by performing X-ray Diffraction Contrast Tomography (DCT), which can measure the location and orientation of grains in a small 3D volume of material, and by matching the orientations of parent and twin grains. Figure 2.26 shows the orientations of parent and twin grains in the compressively strained specimen, plotted as an inverse pole figure (IPF) with respect to the loading direction. The increase in peak intensity near {0002} is due to twinning of grains oriented between $\langle 1010\rangle$ and $\langle 2110\rangle$.

Ministry of Defence © British Crown Copyright 2020/AWE

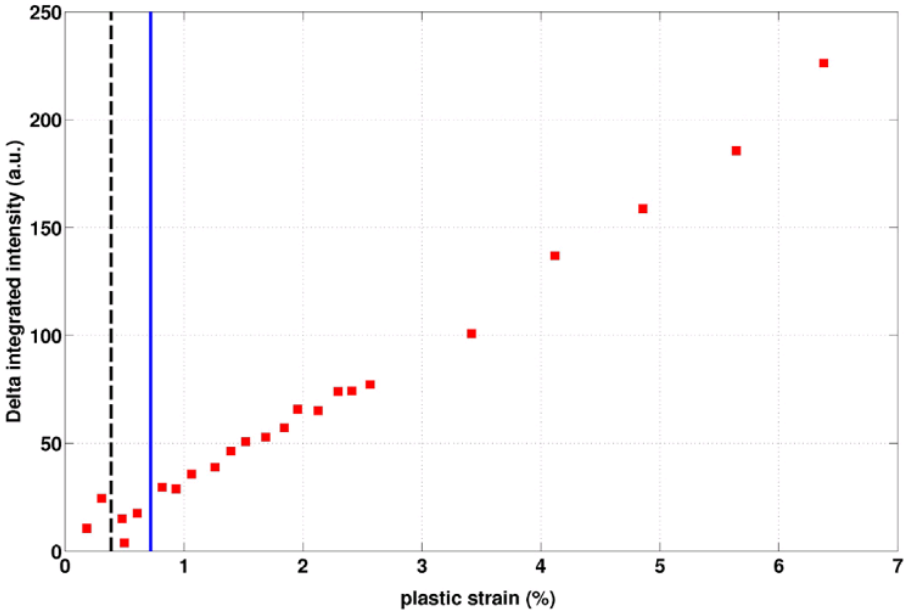


Figure 2.25. "Change of {0002} integrated intensity as a function of plastic strain recorded during in-situ loading on SALSA, at the ILL, Grenoble. Early signs of twinning by slight increase of intensity can be seen just below 1%." Figure and caption reproduced from Nervo et al. [124].

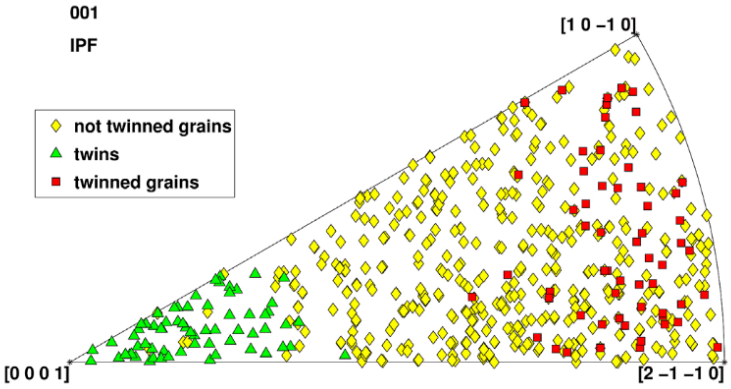


Figure 2.26. "Inverse Pole Figure (IPF) representation of the grain orientations with respect to the sample loading direction (001)" Figure and caption reproduced from Nervo et al. [124].

For uranium, with its multiple operative twin systems, the situation is more complex than just looking at the intensity of a single peak. Calhoun et al. [49] observed changes in peak intensity during straining of uranium. The authors presented a method for determining whether or not an intensity shift from one peak to another could be explained by twin formation, identifying '{172}' twin formation in their specimens. I

Ministry of Defence © British Crown Copyright 2020/AWE

shall describe their method here as it inspired an improved method in this thesis (section 3.5).

The rotation axis of twinning (K_1 normal for Type I, η_1 for type II) is parallel in the parent and twin (section 2.3.2). In order for intensity shift from peak (hkl) to peak $(h'k'l')$ to be a potential result of twin formation, the rotation axis must make the same angle with the diffraction vector in the parent, (hkl), and the twin, $(h'k'l')$. For each peak hkl in the spectrum that saw an intensity increase or decrease, the authors calculated the angle between the (hkl) plane normal and the relevant rotation axis K_1 (angle ψ) or η_1 (angle ϕ) in the twin (figure 2.27). This allowed certain peak pairs to be eliminated if they were at different angles to the rotation axis.

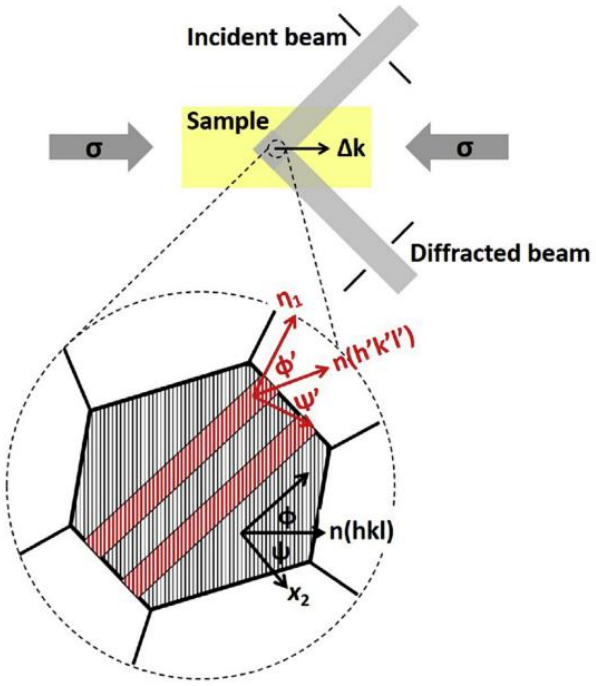


Figure 2.27. "Schematic illustration of the diffraction geometry and relationship to twinning elements.". Figure and caption reproduced from Calhoun et al. [49]

Ministry of Defence © British Crown Copyright 2020/AWE

This method has some limitations. The first was acknowledged by the authors, where the criterion of similar angles with respect to the rotation axis is necessary but not sufficient to relate texture increases and decreases to deformation twinning. There are multiple possible reflections $h'k'l'$ with plane normals at similar angles from the twinning rotation axis as (hkl). The twinning rotation is unique, and only one of these possible $(h'k'l')$ could be caused by the operation of a twinning mode. This method may falsely identify potential twinning modes by its inability to eliminate reflection pairs with similar angles from the rotation axis.

Secondly, this method does not consider the orientation dependence of twinning – i.e. whether the (hkl) orientation could ever twin by a particular mode given the loading conditions (tension/compression). If the (hkl) orientation had a low (or negative) Schmid factor for twins of a particular variant, this variant is unlikely (or impossible) to have caused the observed texture decrease along (hkl)

2.6.3 Microstructural Evaluation with EBSD

Optical microscopy has been commonly used to determine the shape and size of grains in uranium [34][60]. Etching [34] provided contrast between different grain orientations, however the individual orientations could not easily be determined.

Electron backscatter diffraction (EBSD) in the SEM is now routinely used in materials science to measure microstructures in crystalline materials [125].

Ministry of Defence © British Crown Copyright 2020/AWE

The method of electron backscatter diffraction (EBSD) is summarised by Wilkinson and Britton [126]. When an electron beam in an SEM vacuum chamber strikes the surface of a sample, some of these electrons are backscattered. If the sample is crystalline, the atomic planes at the sample surface can diffract these backscattered electrons to form a Kikuchi pattern which can be detected by a photosensitive detector, typically a charged coupled device (CCD). The sample is tilted to a large angle ($\sim 70°$) to maximise the yield of backscattered electrons. A schematic of the experimental set-up is shown in figure 2.28.

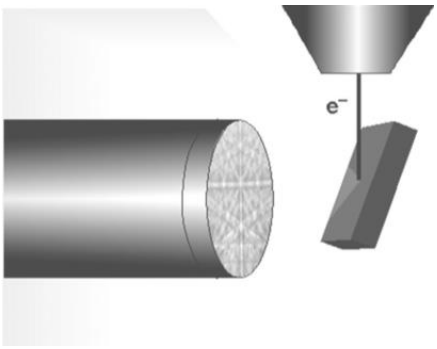


Figure 2.28. "Schematic of direct projection of EBSD pattern onto an imaging phosphor screen. The image is transferred to a computer by viewing the screen using a CCD video camera." Figure and caption reproduced from Dingley et al. [127].

Each band visible on the Kikuchi pattern corresponds to a set of crystal planes in the sample at the point where the electron beam impinges on it. Assuming the crystal structure of the sample is known, the Hough transform is commonly used to index each band (i.e. assign a particular crystal plane to it), allowing measurement of the orientation of the crystal at the location of beam impingement.

Scanning the beam over the sample and repeating the process allows the spatial variation of orientation to be measured. The data is often presented as an orientation map, where

Ministry of Defence © British Crown Copyright 2020/AWE

the colour of each pixel is related to the orientation of the crystal with respect to a standard stereographic projection. This technique is commonly used for microstructural characterisation and texture measurement.

EBSD requires a flat, stress-free surface, so electropolishing is often needed to prepare the sample. EBSD has been successfully applied to uranium to study texture [128][30][129] and recrystallization [130][131] phenomena, where surface preparation involved a $1\ \mu\mathrm{m}$ diamond polish followed by two electropolishing steps, as detailed by McCabe et al. [131][132].

2.7 Summary

This literature review gives an overview of the crystallographic and microstructural features that contribute to the unique mechanical properties of α-uranium. To understand fracture in uranium, one must understand the prior deformation, as deformation twins are closely linked with crack initiation.

A number of experimental techniques including EBSD, DIC and neutron diffraction can contribute towards the calibration and validation of CPFE models.

Ministry of Defence © British Crown Copyright 2020/AWE

Chapter 3 Challenges of Neutron Diffraction in Coarse-Grained Uranium

3.1 Introduction

In order for a crystal plasticity simulation to correctly model the deformation in cast uranium, the correct deformation parameters must be found. Material parameters such as the critical resolved shear stresses (CRSS) are crucial in predicting the active deformation modes, and subsequent hardening rates are determined by a set of hardening parameters [88][130]. The values of some of these parameters could be directly determined via experiment, for example the determination of CRSS by deformation of single crystals [18], but this requires precise, well aligned experimental set-ups. The results may be too specific to the experiment and therefore not be suitable for extrapolation to polycrystals of differing grain sizes, or to different loading geometries.

An alternative method is to measure the overall response of the material to deformation (e.g. macroscopic stress-strain curve or similar) in a number of different microstructures or experimental geometries. Simulations of these experiments would then be run, the overall response calculated, and the parameters tuned to achieve the best fit between model and experiment. However, because of the large number of parameters and the complex interdependencies between them and the overall response, it can be challenging to find a reliable solution for the parameters from such a simple experiment. The resulting CPFE model may therefore not correctly capture the subtleties of deformation.

Ministry of Defence © British Crown Copyright 2020/AWE

It is therefore desirable to find the middle ground – perform an experiment that captures the overall response of the material whilst also capturing the local or crystalline responses that result from the activation of each deformation mode. This would then allow the effects of individual deformation modes to be experimentally distinguished. A reliable CPFE model would correctly capture both the overall and local deformation in a variety of microstructures and experimental geometries.

Neutron diffraction is suitable to obtain such measurements, due to its high strain sensitivity and large penetration depth in high-Z materials such as uranium.

The microstructure of the cast uranium specimens is unusual, and this causes complexity in the analysis of experimental data. From our literature review, we are aware that cast uranium typically is coarse-grained, with a strong texture (section 2.2.5), however no microstructural information existed for the cast plate used in this study. A characterisation of the microstructure was performed, on samples from the same batch as all material tested in this thesis. A summary of the microstructure is given in section 3.2.

In this project, two neutron diffraction experiments with in-situ loading were performed along with a neutron texture measurement. The first experiment highlighted the challenges of performing neutron diffraction measurements on a coarse-grained material such as cast uranium. This is described in full in Appendix A5, with the key results and methodological developments presented in this chapter.

Ministry of Defence © British Crown Copyright 2020/AWE

This work was presented as a conference paper "Lattice strain and texture development in coarse-grained uranium – a neutron diffraction study" by Earp et al. [1] at the Modern Practice in Stress and Vibration Analysis (MPSVA) conference in Cambridge, UK in July 2018.

3.2 Microstructural Characterisation

Microstructural characterisation was performed with EBSD at the Interface Analysis Centre, School of Physics, University of Bristol, UK, described in full in Appendix A3. To achieve a surface suitable for EBSD, electropolishing was performed, using a method in the literature [131][31]. Uranium oxidises rapidly and even 5 minutes exposure to air after polishing can prevent EBSD patterns from being acquired from the surface. The EBSD data were visualised in the MTEX [134] toolbox in MATLAB. Multiple EBSD maps were stitched together to form a large-area map, shown in figure 3.1.

The cast uranium tested in this project has a coarse grain size of approximately 200 μm, but more importantly the grains are grouped together into clusters of similar orientation which can be over 10 mm in diameter. Therefore, at the sample scale of a few centimetres, the material only contains a few grain clusters in the area of interest and does not behave homogeneously. The single crystal anisotropy is much more apparent than in a conventional fine-grained engineering material.

Ministry of Defence © British Crown Copyright 2020/AWE

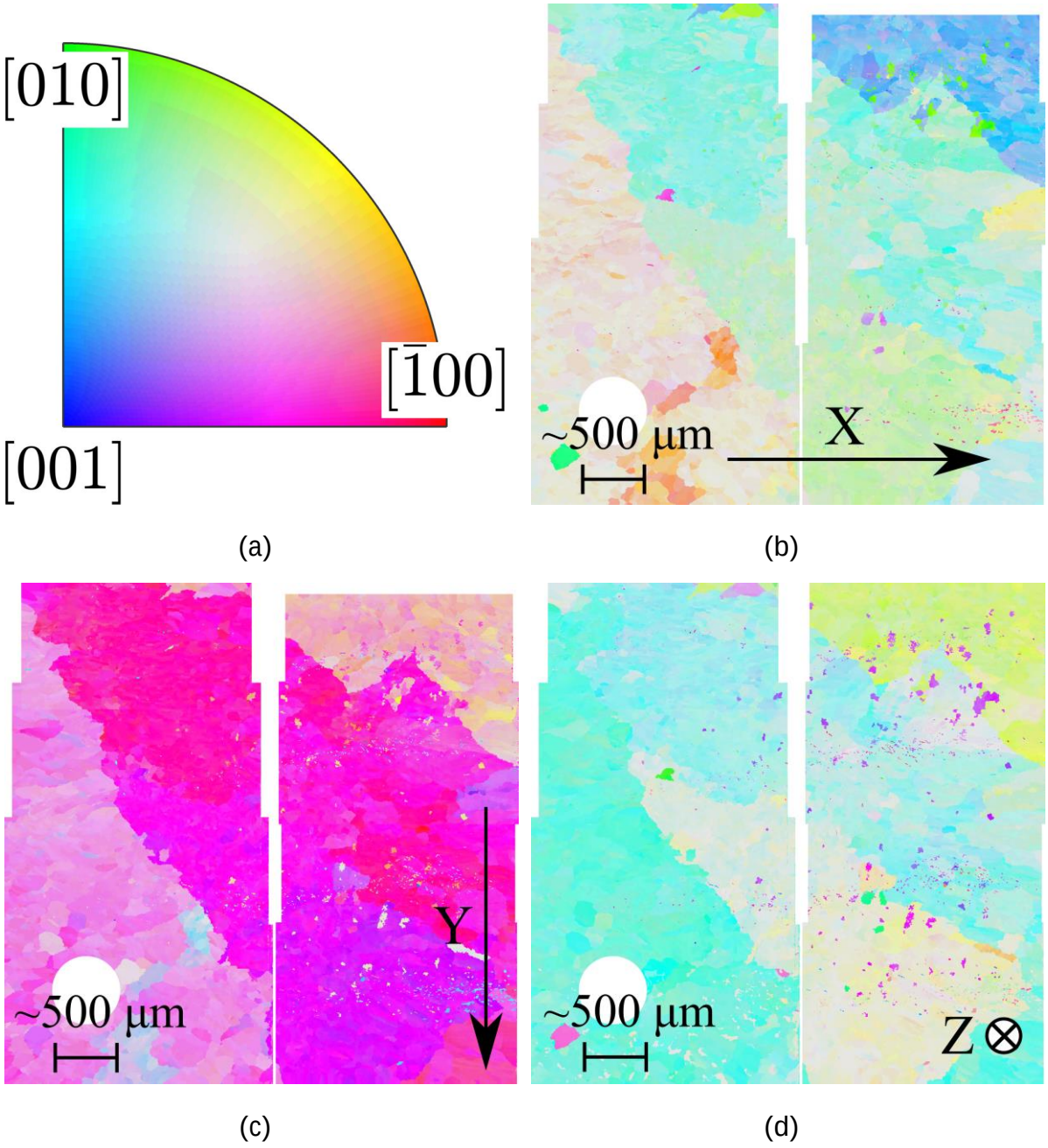


Figure 3.1. Composite orientation maps of the eight EBSD datasets showing grain orientation within specimen "831", with respect to the inverse pole figure colour key shown in sub-figure (a). Step size in each EBSD scan is 5 µm, with points arranged in a hexagonal grid. Sub-figures (b), (c), and (d) show grain orientation with respect to the X, Y and Z (into-plane) directions respectively.

3.3 Experiment Overview

The first neutron diffraction experiment took place on the ENGIN-X diffractometer at the ISIS Neutron and Muon Source, Rutherford Appleton Laboratory, Didcot, UK, under experiment number RB1710227. The experiment measured the evolution of lattice strain

Ministry of Defence © British Crown Copyright 2020/AWE

and texture with deformation, in tension and compression, during loading through the yield point, and is described in Appendix A5.

Tension and compression specimens were manufactured at AWE. Both specimen designs had a circular cross-section, with diameters of 8 mm and 14 mm respectively. The tensile specimens were denoted ND-T1 and ND-T2 whilst the compression specimen was denoted ND-C1.

The experimental geometry (figure 8.9 on page 368) limited the detected neutrons to those diffracting from planes with normals aligned with the loading direction.

Time-of-flight spectra were recorded at each increment of applied load. The position of each peak in the neutron spectrum relates to the interplanar spacing of a particular family of grains, denoted by their Miller indices (hkl), in the diffracting crystal. As well as being proportional to the multiplicity of the (*hkl*) planes, the (*hkl*) peak intensity is proportional to the volume fraction of material diffracting in the (*hkl*) orientation.

Peak fitting was performed by Rietveld refinement (Appendix A5.2.1.5), which fits parameters across the whole spectrum, and single-peak fitting (Appendix A5.2.1.4), which focuses on the position shifts in individual peaks. Axial textures were measured by fitting a spherical harmonic orientation correction factor in the Rietveld refinement. Inverse pole figures showing the texture along the loading axis were produced for each spectrum. Texture changes were identified as the difference in the inverse pole figures with respect to the initial texture. A method was developed to calculate the uncertainty

Ministry of Defence © British Crown Copyright 2020/AWE

in the measured texture changes from the uncertainties in the spherical harmonic parameters (section A5.2.1.6). The texture changes were found to be larger than the measurement uncertainty.

3.4 Key Results

3.4.1 Lattice Strains

The (hkl) lattice strain measures the average elastic strain on the (hkl)-planes of the family of grains with their (hkl)-plane normals parallel to the diffraction vector, (the loading direction). Lattice parameter strains are calculated from the Rietveld refinement (page 393) and show the relative distortion of the average unit cell due to the applied stress state. The 'a' lattice parameter strain contains contributions from all of the (hkl) lattice strains where $h \neq 0$, as noted by Brown et al.[107]. A large elastic strain corresponds to a high stress being supported through these grains. Grains which can support a high stress without this stress being relieved via deformation are plastically hard, whilst those whose elastic strains saturate (i.e. can no longer support any increase in stress) are plastically soft.

The development of lattice strains on the orthogonal (200), (020) and (002) families of grains is plotted in figure 3.2 along with the strains on lattice parameters *a*, *b*, and *c*. The uncertainties in the lattice strains are larger as they are calculated from a single-peak fit, rather than a Rietveld refinement which fits over all peaks in the spectrum. Data from the literature are shown for comparison, with Brown et al. performing tension

Ministry of Defence © British Crown Copyright 2020/AWE

along the rolling direction (RD) and transverse direction (TD) of rolled uranium plate [107] (figure 2.24). Calhoun et al. performed tension and compression along the RD and compression along the TD [45].

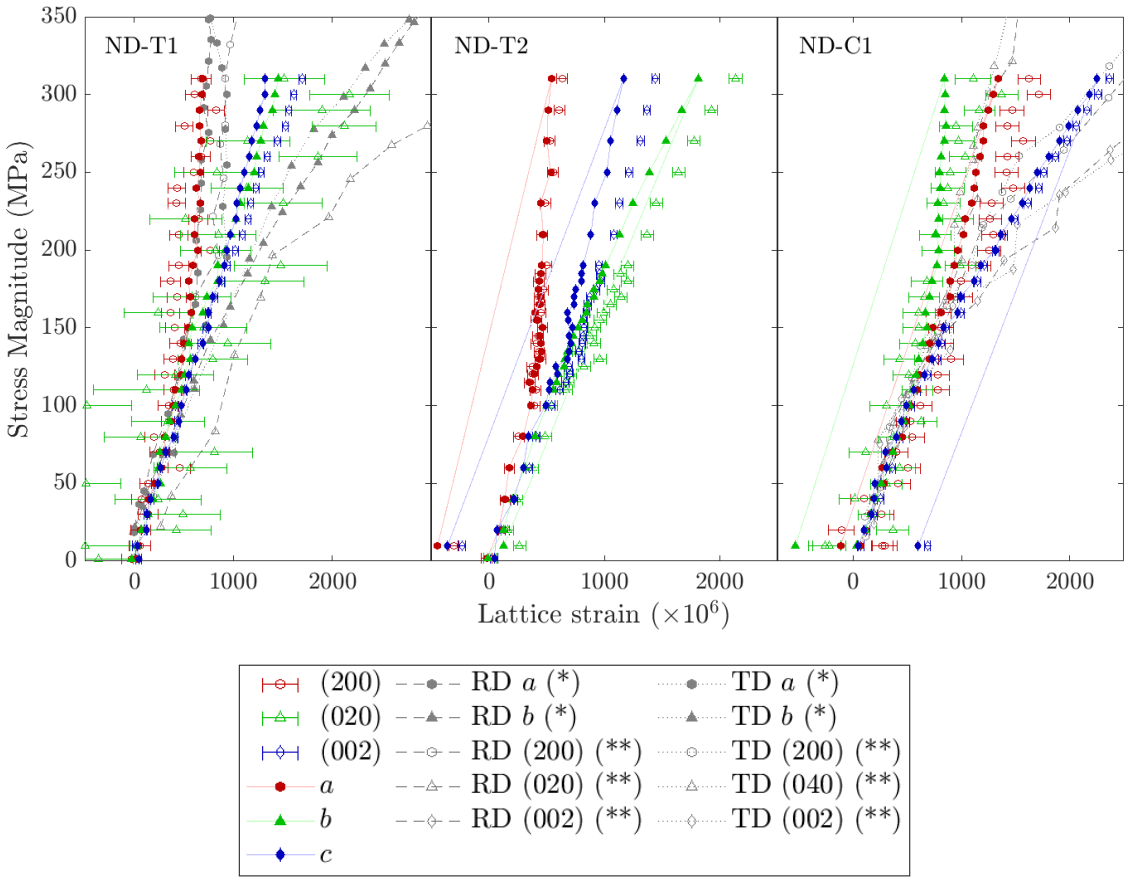


Figure 3.2. Development of lattice strain as a function of the magnitude of the applied stress for tensile specimens ND-T1, ND-T2 and compressive specimen ND-C1. Lattice strains for the (200), (020) and (002) reflections were measured from single-peak fitting. Lattice parameter strains for the *a*, *b* and *c* lattice parameters were calculated from the Rietveld refinement. Specimens ND-T2 and ND-C1 were unloaded to a stress magnitude of 10 MPa after reaching maximum load. Stress and lattice strain data from specimen ND-C1, tested in compression, were multiplied by -1 such that the data appears visually similar to the tensile data. Data from the literature are shown for comparison, with Brown et al. [107] (*) performing tension along the rolling direction (RD) and transverse direction (TD) of rolled uranium plate. Calhoun et al. [45] (**) performed tension and compression along the RD and compression along the TD.

These data were used in the crystal plasticity finite element (CPFE) modelling performed by our collaborator Nicolò Grilli, described in section 4.5.

Ministry of Defence © British Crown Copyright 2020/AWE

3.4.2 Axial Texture Changes

Plastic deformation will produce a reorientation of the crystal lattice that may be detectable in the measured textures. Slip would induce a steady rotation, seen as a 'peak' in the texture moving steadily from one location to another. Deformation twins have a fixed orientation relationship with respect to the parent grain, which would cause a decrease in intensity in the 'parent' orientation and an increase in texture in the 'twin' orientation. We cannot identify any twins present in the initial pre-load state, as contributions from twins and the parent grains cannot be separated. We can however aim to identify the twins induced via deformation from the changes in the measured texture.

All specimens tested had sharp textures, with peaks of up to 6 MRD (multiples of random distribution) with other orientations contributing < 0.5 MRD. As an example, the axial texture and texture difference at 310 MPa tensile load in specimen ND-T1 are shown in figure 3.3 (reproduced from figure 8.37 in Appendix A5.3.5).

Ministry of Defence © British Crown Copyright 2020/AWE

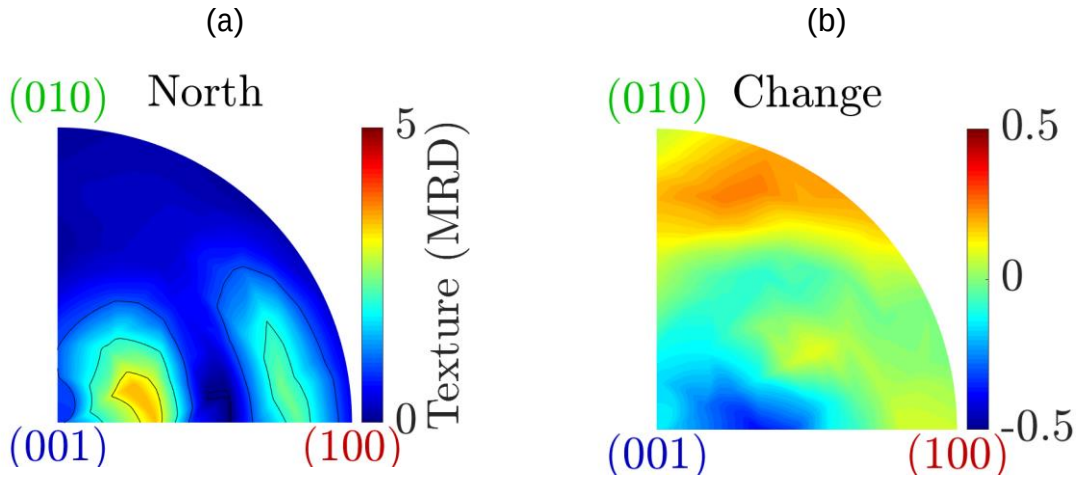


Figure 3.3. (a) Axial texture in specimen ND-T1 before loading. (b) axial texture change at maximum load of 310 MPa.

3.5 A Method to Identify Twinning Modes from Texture Changes

The twinning rotation that maps the parent orientation to the twin orientation is unique for each twin variant. It is possible to predict the effect that the formation of twins of a particular variant will have on the measured texture. For a parent crystal oriented with its (*hkl*) plane normal parallel to the loading direction (i.e. the (*hkl*) reflection appearing in the North bank on ENGIN-X), we can calculate the crystal axis in the twin crystal, (*hkl*)*, that lies parallel to the same loading direction. The formation of a twin would be identified as a decrease in (*hkl*) texture with a concomitant increase in the corresponding (*hkl*)* texture.

A method of calculating the possible texture changes associated with each twinning mode was implemented in MATLAB by the author, and formed a crucial part of the subsequent analysis. It produced an inverse pole figure for each twinning variant, with

Ministry of Defence © British Crown Copyright 2020/AWE

pairs of points plotted showing the possible parent and twinned orientations, as measured by diffraction along the loading axis.

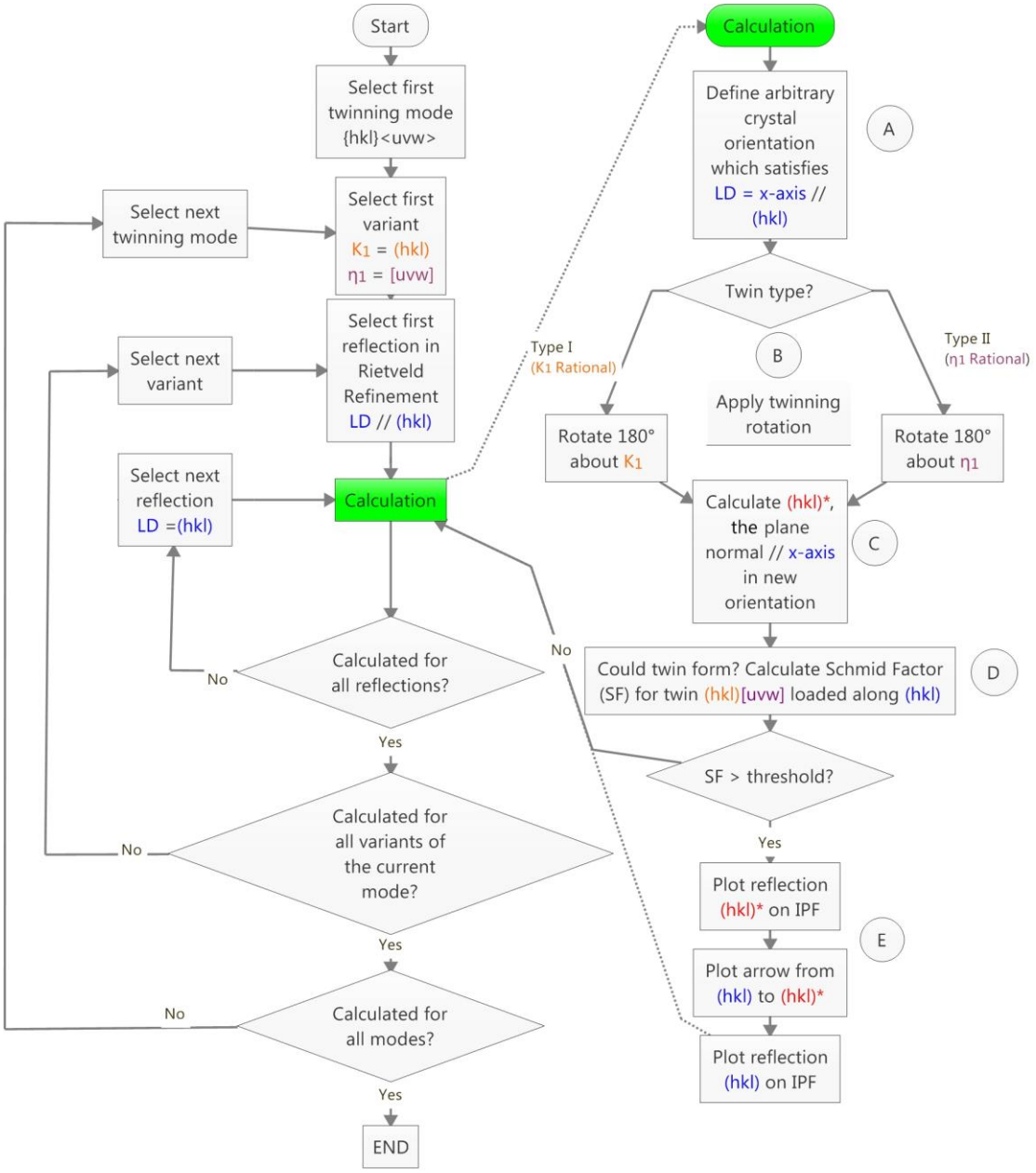


Figure 3.4. Flowchart of the MATLAB implementation of the calculation of possible twinning reorientations. LD = Loading Direction.

Ministry of Defence © British Crown Copyright 2020/AWE

A flowchart describing the method is shown in figure 3.4. For each twin variant, calculation of the twinned orientation was performed for the directions corresponding to the reflections fitted in the Rietveld refinement.

The calculation procedure is described here in brief, with the letters corresponding to those in the flowchart.

3.5.1 Definition of Diffracting Parent Crystal

Firstly, in step (A) of the flowchart, a right-handed orthogonal co-ordinate system (the specimen frame, *s*) was defined, and the x-axis (vector $\boldsymbol{x_s}$) was chosen to represent the loading direction, known hereafter as the LD.

$$\boldsymbol{x_s} = \begin{bmatrix} 1 \\ 0 \\ 0 \end{bmatrix} \qquad [3.1]$$

A crystal frame, denoted *c*, was defined with the unit cell vectors being defined with respect to this frame:

$$\boldsymbol{a_c} = \begin{bmatrix} 1 \\ 0 \\ 0 \end{bmatrix} \qquad \boldsymbol{b}_c = \begin{bmatrix} 0 \\ 1 \\ 0 \end{bmatrix} \qquad \boldsymbol{c}_c = \begin{bmatrix} 0 \\ 0 \\ 1 \end{bmatrix} \qquad [3.2]$$

To define the parent crystal in the specimen frame in a (*hkl*)-diffracting orientation, it was required to find unit cell vectors, $\boldsymbol{a}_s$, $\boldsymbol{b}_s$, and $\boldsymbol{c}_s$, such that the (*hkl*) plane normal is parallel to the LD ($= \boldsymbol{x}_s$). The (*hkl*) direction in the crystal frame was calculated from the reciprocal lattice vectors using equation [3.3], with the reciprocal lattice vectors defined in equation [3.4].

Ministry of Defence © British Crown Copyright 2020/AWE

$$(\boldsymbol{hkl})_c = ha_c^* + kb_c^* + lc_c^* \qquad [3.3]$$

$$\boldsymbol{a}_c^* = \frac{\boldsymbol{b}_c \times \boldsymbol{c}_c}{\boldsymbol{a}_c \bullet (\boldsymbol{b}_c \times \boldsymbol{c}_c)} \qquad \boldsymbol{b}_c^* = \frac{\boldsymbol{c}_c \times \boldsymbol{a}_c}{\boldsymbol{b}_c \bullet (\boldsymbol{c}_c \times \boldsymbol{a}_c)} \qquad \boldsymbol{c}_c^* = \frac{\boldsymbol{a}_c \times \boldsymbol{b}_c}{\boldsymbol{c}_c \bullet (\boldsymbol{a}_c \times \boldsymbol{b}_c)} \qquad [3.4]$$

The reciprocal lattice vectors can be simplified to the following in the orthorhombic system,

$$\boldsymbol{a}_c^* = \frac{1}{a}\boldsymbol{a}_c \qquad \boldsymbol{b}_c^* = \frac{1}{a}\boldsymbol{b}_c \qquad \boldsymbol{c}_c^* = \frac{1}{c}\boldsymbol{c}_c \qquad [3.5]$$

where a, b, and c are the α-uranium lattice parameters.

These frames are shown in figure 3.5.

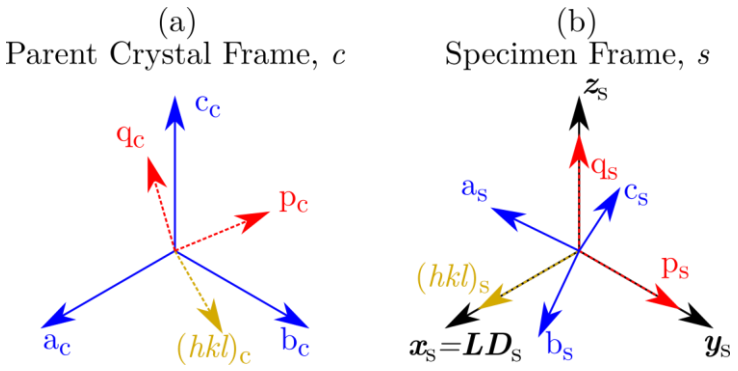


Figure 3.5. Parent crystal unit cell vectors (blue) defined in the specimen frame such that the loading direction (LD) is parallel to the desired (*hkl*) reflection. The vectors $\boldsymbol{p}_c$ and $\boldsymbol{q}_c$ (red) are defined in the calculation to ensure a mutually perpendicular set of vectors.

In the crystal frame, two vectors $\boldsymbol{p}_c$ and $\boldsymbol{q}_c$ were generated that form a right-handed set with $(hkl)_c$. To achieve this, a unit vector non-colinear with $(hkl)_c$ was defined as $\boldsymbol{\lambda}$. The vector product was then used to generate the vector $\boldsymbol{p}_c$, perpendicular to $(hkl)_c$ and $\boldsymbol{\lambda}$. Then, the vector product was used again to produce vector $\boldsymbol{q}_c$, perpendicular to $(hkl)_c$ and $\boldsymbol{p}_c$.

Ministry of Defence © British Crown Copyright 2020/AWE

The 3×3 rotation matrix $\boldsymbol{R}_{s2c}$, converting vector components from the specimen to the parent crystal frame was then defined as:

$$\boldsymbol{R}_{s2c} = [(\boldsymbol{hkl})_c \quad \boldsymbol{p}_c \quad \boldsymbol{q}_c] \qquad [3.6]$$

where $(\boldsymbol{hkl})_c$, $\boldsymbol{p}_c$, and $\boldsymbol{q}_c$ are all written as 3×1 column vectors.

The desired rotation matrix $\boldsymbol{R}_{c2s}$, which converts from the parent crystal frame to the specimen frame, was calculated as the inverse of $\boldsymbol{R}_{s2c}$:

$$\boldsymbol{R}_{c2s} = \boldsymbol{R}_{s2c}^{-1} \qquad [3.7]$$

Therefore the unit cell vectors in the specimen frame were found from:

$$\boldsymbol{a}_s = \boldsymbol{R}_{c2s}\boldsymbol{a}_c \qquad \boldsymbol{b}_s = \boldsymbol{R}_{c2s}\boldsymbol{b}_c \qquad \boldsymbol{c}_s = \boldsymbol{R}_{c2s}\boldsymbol{c}_c \qquad [3.8]$$

Using these vectors, the unit cell could then be plotted in the specimen frame. An example of this for a parent crystal oriented in the (111) reflection condition with its (111) plane normal parallel to the loading direction is shown in figure 3.6.

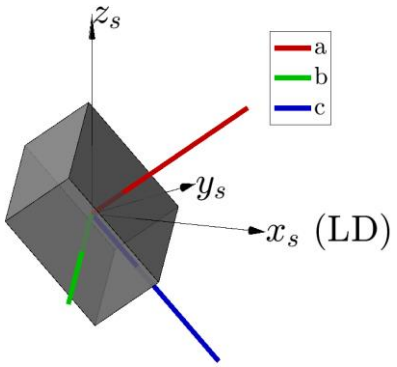


Figure 3.6. Definition of a possible parent crystal orientation that satisfies the condition for (111) diffraction into the north bank detector - LD // (111).

The next step was to apply the twinning rotation to the parent unit cell vectors $\boldsymbol{a}_s$, $\boldsymbol{b}_s$, and $\boldsymbol{c}_s$, and then to identify which crystal direction in this twinned unit cell is parallel

Ministry of Defence © British Crown Copyright 2020/AWE

to the LD ($= \boldsymbol{x_s}$). The orientation of the parent unit cell as defined here was somewhat arbitrary, as it depended on the choice of the vector $\boldsymbol{\lambda}$. One may be concerned that the choice of parent orientation may affect the subsequent calculation, however I will show here that it is unaffected.

The set of possible parent unit cell vectors ($\boldsymbol{a_s}$, $\boldsymbol{b_s}$, and $\boldsymbol{c_s}$) that satisfy the criterion that $(\boldsymbol{hkl})_s$ // LD are related by a rotation of an arbitrary angle θ about the LD axis. This means that the possible twinned crystals would all be related by the same rotation about the LD axis. Since a rotation of any angle about the LD does not change the crystal plane normal in the twin that is parallel to the LD, the calculation does not depend on the particular orientation of the parent grain as long as the criterion $(\boldsymbol{hkl})_s$ // LD is satisfied.

3.5.2 Application of Twinning Rotation

In section (B) of the flowchart, the twinning rotation is applied. From the definition of twins (section 2.3.2), the twinned unit cell is related to that of the parent via a rotation of 180° about either the K_1 or η_1 axis, whichever has rational indices. For Type I twins, this is the K_1 axis, and for Type II, the η_1. Compound twins have both K_1 and η_1 rational, so the rotations are equivalent and each give the same resultant unit cell.

The general rotation matrix for a rotation of angle θ about the unit vector $\hat{\boldsymbol{r}} = [r_x \quad r_y \quad r_z]$ is shown in equation [3.9], using the notation presented by Cole[135].

Ministry of Defence © British Crown Copyright 2020/AWE

$$\boldsymbol{R}(r_x, r_y, r_z, \theta) \qquad [3.9]$$

$$= \begin{bmatrix} \cos\theta + r_x^2(1-\cos\theta) & r_x r_y(1-\cos\theta) - r_z\sin\theta & r_x r_z(1-\cos\theta) + r_y\sin\theta \\ r_y r_x(1-\cos\theta) + r_z\sin\theta & \cos\theta + r_y^2(1-\cos\theta) & r_y r_z(1-\cos\theta) - r_x\sin\theta \\ r_z r_x(1-\cos\theta) - r_y\sin\theta & r_z r_y(1-\cos\theta) + r_x\sin\theta & \cos\theta + r_z^2(1-\cos\theta) \end{bmatrix}$$

In the case of twinning, where $\theta = 180°$, this simplifies to equation [3.11].

$$\boldsymbol{R}_{twin}(r_x, r_y, r_z) = \begin{bmatrix} -1 + r_x^2(1+1) & r_x r_y(1+1) - 0 & r_x r_z(1+1) + 0 \\ r_y r_x(1+1) + 0 & -1 + r_y^2(1+1) & r_y r_z(1+1) - 0 \\ r_z r_x(1+1) - 0 & r_z r_y(1+1) + 0 & -1 + r_z^2(1+1) \end{bmatrix} \qquad [3.10]$$

$$\boldsymbol{R}_{twin}(r_x, r_y, r_z) = \begin{bmatrix} 2r_x^2 - 1 & 2r_x r_y & 2r_x r_z \\ 2r_y r_x & 2r_y^2 - 1 & 2r_y r_z \\ 2r_z r_x & 2r_z r_y & 2r_z^2 - 1 \end{bmatrix} \qquad [3.11]$$

where r_x, r_y, and r_z are the components of the vector K_1 (Type I) or η_1 (Type II) about which the rotation is performed. The twinning rotation was applied to the parent unit cell vectors ($\boldsymbol{a}_s$, $\boldsymbol{b}_s$, and $\boldsymbol{c}_s$) via the equations below:

$$\boldsymbol{a}_s^{twin} = \boldsymbol{R}_{twin}\boldsymbol{a}_s \qquad \boldsymbol{b}_s^{twin} = \boldsymbol{R}_{twin}\boldsymbol{b}_s \qquad \boldsymbol{c}_s^{twin} = \boldsymbol{R}_{twin}\boldsymbol{c}_s \qquad [3.12]$$

3.5.3 Calculation of (*hkl*) Parallel to LD in Twin

The next step, labelled (C) in the flowchart, is to calculate the plane normal hkl^* parallel to the loading direction in the twinned crystal. Figure 3.7 shows the parent and twin unit cell vectors, with respect to the specimen frame, in blue and green respectively. It is necessary to find the Miller indices of the plane normal parallel to the LD in the twinned crystal frame, which therefore requires the transformation from the specimen to the twinned frame to be known.

Ministry of Defence © British Crown Copyright 2020/AWE

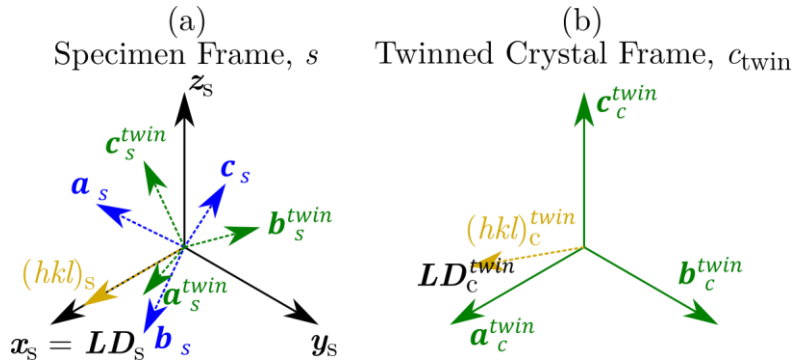


Figure 3.7. (a) Parent (blue) and twinned (green) unit cell vectors with respect to the specimen frame. (b) The aim is to calculate the (*hkl*) indices of the plane normal parallel to the LD in the twinned crystal frame.

The 3×3 rotation matrix $\boldsymbol{R}_{c2s}^{twin}$, converting vector components from the twinned crystal frame to the specimen frame can be written as:

$$\boldsymbol{R}_{c2s}^{twin} = [\boldsymbol{a}_s^{twin} \quad \boldsymbol{b}_s^{twin} \quad \boldsymbol{c}_s^{twin}] \qquad [3.13]$$

where $\boldsymbol{a}_s^{twin}$, $\boldsymbol{b}_s^{twin}$, and $\boldsymbol{c}_s^{twin}$ are written as column vectors.

The desired rotation matrix $\boldsymbol{R}_{s2c}^{twin}$, which converts from the specimen frame to the twinned crystal frame, was calculated as the inverse of $\boldsymbol{R}_{c2s}^{twin}$:

$$\boldsymbol{R}_{s2c}^{twin} = \boldsymbol{R}_{c2s}^{twin^{-1}} \qquad [3.14]$$

Therefore the loading direction can be calculated with respect to the twinned crystal:

$$\boldsymbol{LD}_c^{twin} = \boldsymbol{R}_{s2c}^{twin}\boldsymbol{x_s} \qquad [3.15]$$

3.5.3.1 Calculation of (hkl) Indices

The (hkl) indices of the LD in the twinned crystal are related to the vector components of $\boldsymbol{LD}_c^{twin}$ in equation [3.16]:

$$\boldsymbol{LD}_c^{twin} = h\boldsymbol{a}^* + k\boldsymbol{b}^* + l\boldsymbol{c}^* \qquad [3.16]$$

Ministry of Defence © British Crown Copyright 2020/AWE

Letting $\boldsymbol{LD}_c^{twin} = \begin{bmatrix} d_1 \\ d_2 \\ d_3 \end{bmatrix}$, and remembering the definition of the uranium reciprocal lattice vectors in equation [3.5], this can be rewritten as follows:

$$\begin{bmatrix} d_1 \\ d_2 \\ d_3 \end{bmatrix} = h \begin{bmatrix} 1/a \\ 0 \\ 0 \end{bmatrix} + k \begin{bmatrix} 0 \\ 1/b \\ 0 \end{bmatrix} + l \begin{bmatrix} 0 \\ 0 \\ 1/c \end{bmatrix} \quad [3.17]$$

Therefore the (*hkl*) indices can be found as:

$$h = d_1 a \qquad k = d_2 b \qquad l = d_3 c \quad [3.18]$$

3.5.4 Filtering by Schmid Factor

The formation of a particular twin variant cannot occur if the parent crystal is oriented such that its Schmid Factor (SF) is negative. Reflections where SF≤ 0 are removed from the subsequent analysis for that twin variant (step D in flowchart). The SFs are calculated for each variant using the method described in appendix A8.1.

3.5.5 Plotting Possible Twinning Reorientations

Finally, the possible twinning re-orientation for each reflection was plotted on an IPF along the loading direction. The parent orientations were drawn as circles, coloured in RGB according to their *h*, *k*, and *l* Miller indices. The resulting twin orientations were drawn as triangles, retaining the same colouring as their corresponding parent. Orientations in the lower hemisphere of the stereographic projection ($l < 0$) were plotted in faded colours. An example, is shown for the tensile formation of the '(172)'$[312]$ twin with a twinning rotation of 180° about $[312]$ in figure 3.8(a). Note that parent crystals

Ministry of Defence © British Crown Copyright 2020/AWE

oriented near (010) do not twin in tension due to their negative SF. By the symmetry of the orthorhombic crystal structure, and since diffraction cannot distinguish between (hkl) and (hkl) reflections [136], the twinned orientations can be 'reflected' into the upper-right quadrant to form the conventional IPF between (100), (010), and (001). The corresponding example for the $'(172)'[312]$ twin is shown in figure 3.8(b)

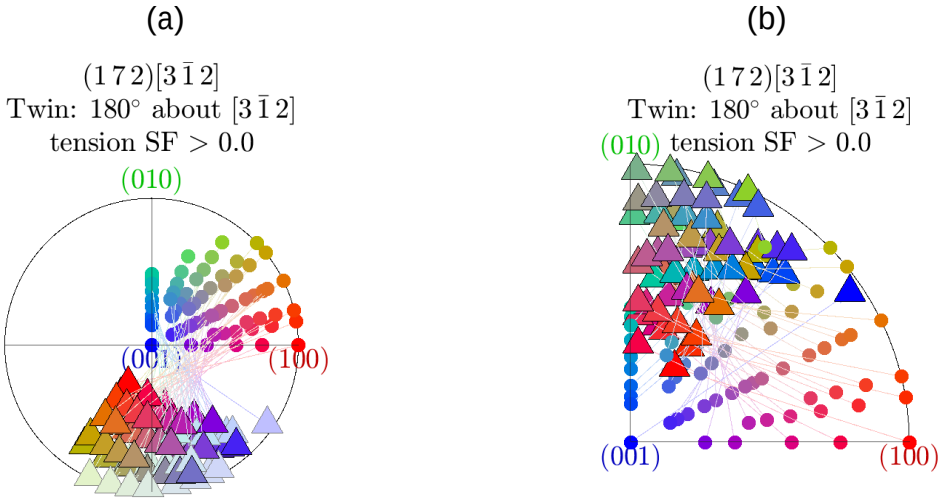


Figure 3.8. Plotting the possible twinning reorientation for the $'(172)'[312]$ twin, with a twinning rotation of 180° about $[312]$. (a) Calculated reorientation. (b) Twinned orientations reduced into orthorhombic quadrant of stereographic projection. The parent orientations are drawn as circles, coloured in RGB according to their *h*, *k*, and *l* Miller indices. The resulting twin orientations are drawn as triangles, retaining the same colouring as their corresponding parent. Orientations in the lower hemisphere of the stereographic projection ($l < 0$) were plotted in faded colours.

Plots similar to figure 3.8(b) were produced for each variant of the four twinning modes; $\{130\}$, $'\{172\}'$, $'\{176\}'$, and $\{112\}$. Separate figures were plotted for tension (figure 3.9) and compression (figure 3.10) since the SFs are different in each loading mode.

In summary, upon twinning, an increase in intensity would be observed in a direction (*hkl*)* defined by a) the operative twinning variant and b) the parent orientation (*hkl*) along which the corresponding decrease would be seen.

Ministry of Defence © British Crown Copyright 2020/AWE

By inspection of the reorientations shown in figure 3.8(b) It can be seen in that $\{130\}$ twinning in tension always reorients grains oriented near (100) to orientations near (010), whilst in compression, (010)-oriented grains are rotated to be aligned near (100). This is in agreement with what is reported in the literature [56].

For each of the '$\{172\}$' twin variants, there is a corresponding $\{112\}$ variant that produces a similar reorientation. This is presumed to be related to fact that the '$\{172\}$' and $\{112\}$ are reciprocal twinning modes with each other.

In this section we have developed a method to identify potentially active twinning modes from the inspection of axial texture changes parallel to the loading direction. The reorientations in figure 3.9 and figure 3.10 were used to interpret the neutron diffraction data.

This method is preferable to that of Calhoun et al.[49] (section 2.6.2.1) as it considers the specific twinning reorientation of each twin as well as the Schmid factor for deformation whilst correctly predicting the reorientations described in the literature [56].

Ministry of Defence © British Crown Copyright 2020/AWE

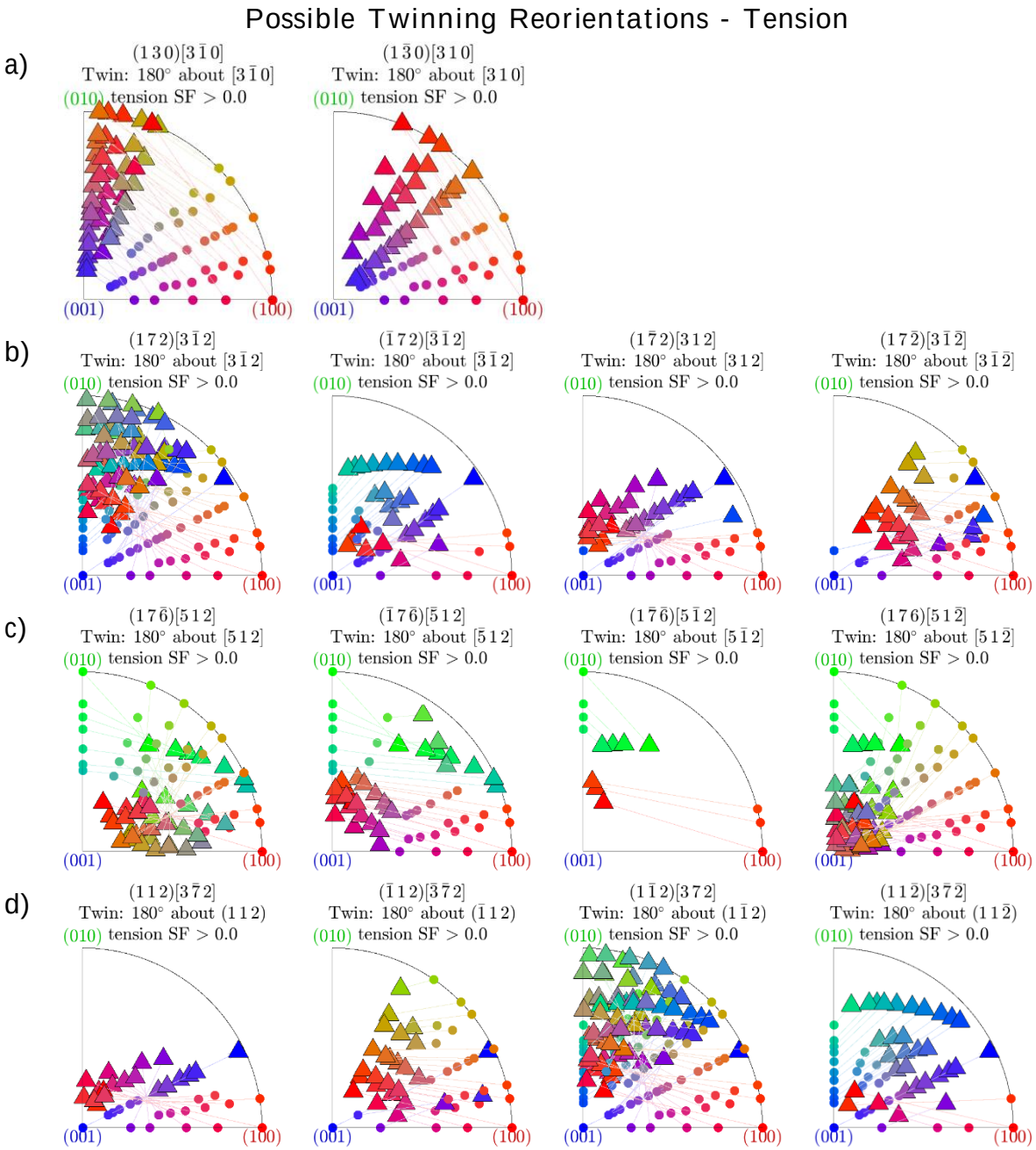


Figure 3.9. Possible twinning reorientations (circles → triangles) for loading in tension from a) {130}, b) '{172}', c) '{17$\bar{6}$}', and d) {112} twins. The crystal directions along which loading can induce twinning (SF > 0) are shown as circles, coloured according to their position in the IPF. The crystal directions parallel to the loading axis after twinning are shown as triangles, coloured according to the orientation of their corresponding parent.

Ministry of Defence © British Crown Copyright 2020/AWE

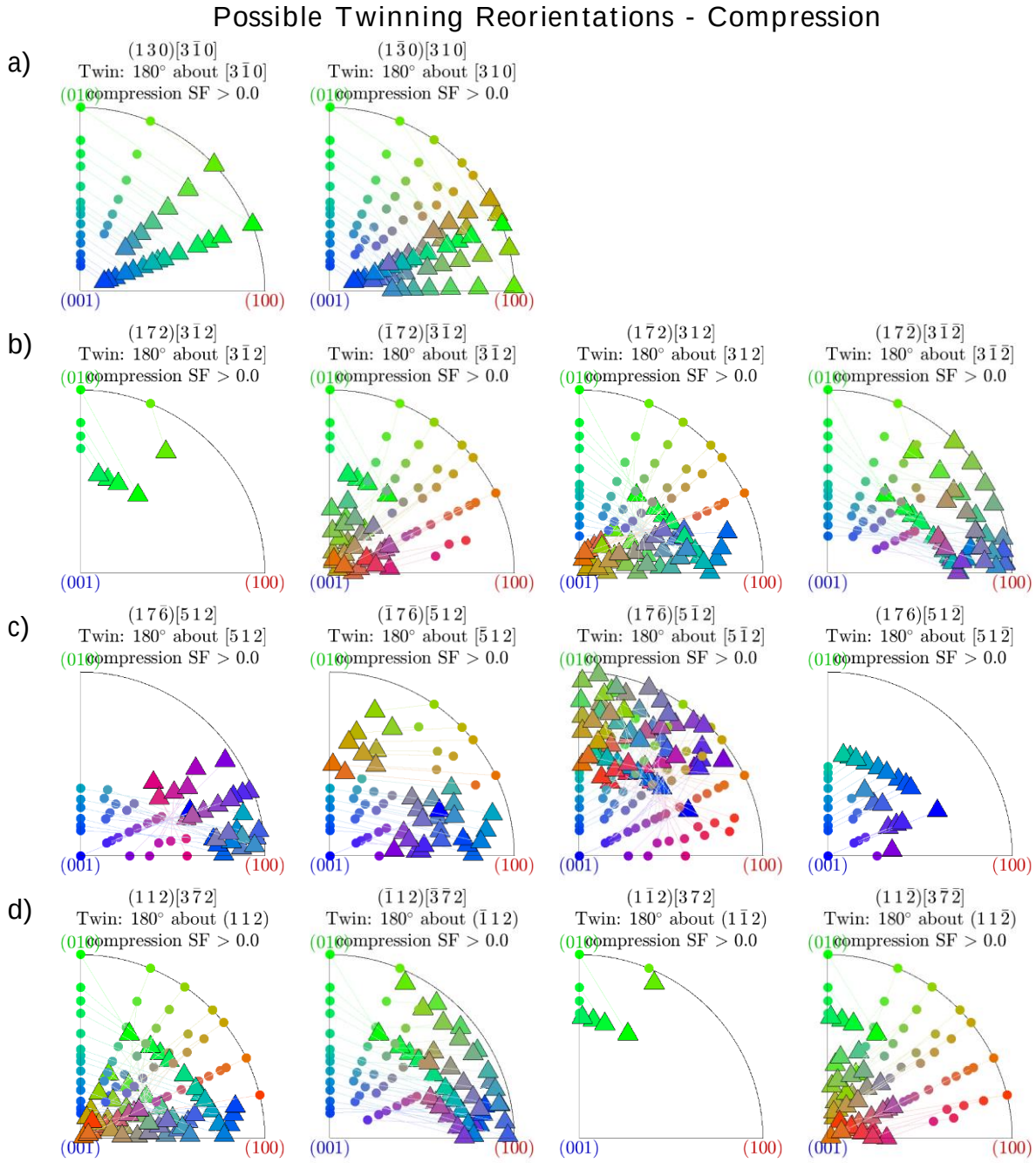


Figure 3.10. Possible twinning reorientations (circles → triangles) for loading in compression from a) {130}, b) '{172}', c) '{17$\bar{6}$}', and d) {112} twins. The crystal directions along which loading can induce twinning (SF > 0) are shown as circles, coloured according to their position in the IPF. The crystal directions parallel to the loading axis after twinning are shown as triangles, coloured according to the orientation of their corresponding parent.

Ministry of Defence © British Crown Copyright 2020/AWE

3.5.6 Experimental Observations

In general, the texture changes could not be explained by formation of a single twin mode. The texture changes were not very distinct and therefore do not provide strong evidence for the formation of the twins that were predicted by the Schmid factor analysis.

Factors which could contribute to the observations were identified:

1. Multiple twin modes were activating simultaneously in such a way that the texture changes from each mode add to give the observed texture change.
2. A significant part of the deformation was actually slip, and the deforming crystal was therefore slowly rotating. In the case of specimen ND-C1, the texture increases and decreases are adjacent to one another in the IPF (figure 8.37 on page 440), which could be evidence for slip in this specimen.
3. The observed texture change was partially or wholly an artefact of the movement of the specimen during the test. This effect was actually quite significant and is discussed in the following section.

3.6 Issues with Specimen Movement

The measured texture depends on the distribution of crystal orientations within the instrumental gauge volume (IGV) inside the specimen. During loading, it is possible that the specimen moves due to the compliance of the load frame.

If the gauge volume moves slightly into a region of the specimen with a different texture, then a texture change would be observed. A possible situation is depicted in figure 3.11,

Ministry of Defence © British Crown Copyright 2020/AWE

where the specimen moves with respect to a fixed gauge volume as the load is increased. This may be a combination of the specimen's deformation and rigid body movement. An increase in the orientations that are now inside the gauge volume, and a decrease in those orientations that have moved outside, would be observed.

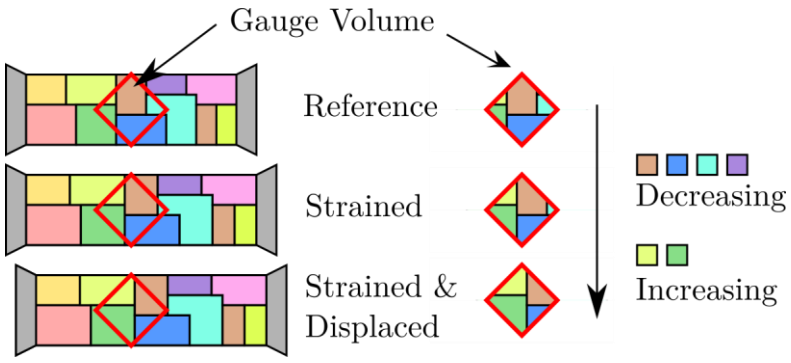


Figure 3.11. Movement of the specimen with respect to a fixed instrumental gauge volume (IGV) changes the distribution of grain orientations within the IGV, and therefore is seen as an apparent change in texture.

It is possible to calculate an approximation for the maximum percentage texture change that could be observed for a particular specimen movement, and that is presented in this section. Figure 3.12 shows a schematic of the specimen on ENGIN-X with the original gauge volume shown in red. For the purposes of this calculation it is assumed that when viewed from above, down the *z*-axis, the gauge volume has a square cross section with edge length l. Suppose that, upon applying load, the new gauge volume is displaced along the specimen's longitudinal axis by a distance Δx, where $\Delta x \geq 0$.

Ministry of Defence © British Crown Copyright 2020/AWE

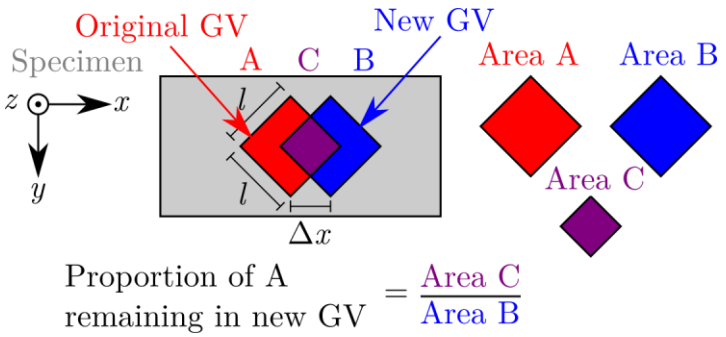


Figure 3.12. Calculation of texture change artefact due to specimen movement. A movement of Δx could produce a texture change if the texture in area B is different from that in area A.

The proportion of area A remaining inside the new gauge volume (GV) is given by:

$$\text{Proportion of old GV remaining in new GV} = \frac{\text{Area C}}{\text{Area B}} \qquad [3.19]$$

The fractional change from texture A is therefore:

$$\text{Fractional change in GV}, \frac{\Delta \text{GV}}{\text{GV}} = 1 - \frac{\text{Area C}}{\text{Area B}} \qquad [3.20]$$

The areas B and C can be found by simple geometry by consulting figure 3.12. Area A is equal to area B and is trivially seen to be l^2. The length of its diagonal is $\sqrt{2}l$, therefore the diagonal of area C is $\sqrt{2}l - \Delta x$.

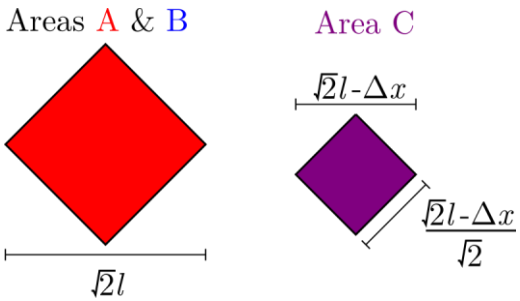


Figure 3.13. Calculation of areas A, B, and C as defined in figure 3.12.

Area C therefore has an edge length given by equation [3.21],

Ministry of Defence © British Crown Copyright 2020/AWE

$$\text{Edge length of C} = \frac{\sqrt{2}l - \Delta x}{\sqrt{2}} \quad [3.21]$$

and therefore an area given by equation [3.22]:

$$\text{Area C} = \frac{(\sqrt{2}l - \Delta x)^2}{2} \quad [3.22]$$

Therefore,

$$\frac{\Delta \text{GV}}{\text{GV}} = 1 - \frac{(\sqrt{2}l - \Delta x)^2}{2l^2} \quad [3.23]$$

Equation [3.23] behaves in a sensible manner as:

$$\frac{\Delta \text{GV}}{\text{GV}} \to 0 \text{ as } \Delta x \to 0 \quad [3.24]$$

i.e. a displacement of zero produces no texture change, and

$$\frac{\Delta \text{GV}}{\text{GV}} \to 1 \ (100\ \%) \text{ as } \Delta x \to \sqrt{2}l \quad [3.25]$$

i.e. a displacement equal to the diagonal of the gauge volume, such that the old and new gauge volumes cease to overlap, equals to a fractional gauge volume change of 1 as the entire gauge volume has been replaced. For larger displacements,

$$\frac{\Delta \text{GV}}{\text{GV}} = 1 \text{ for } \Delta x > \sqrt{2}l \quad [3.26]$$

A change in texture would only occur if the orientations in the new GV actually differ from those in the old GV, i.e. the new grain cluster is located just on the edge of the initial gauge volume. The effect may be smaller if the texture does not change so abruptly. The calculation therefore serves as an upper bound to the texture change artefact. Letting $\frac{\Delta T}{T}$ be the fractional change in texture,

Ministry of Defence © British Crown Copyright 2020/AWE

$$\frac{\Delta T}{T} \leq \frac{\Delta \mathrm{GV}}{\mathrm{GV}}. \qquad [3.27]$$

The issue is most prevalent where the microstructural features are of a similar size to the gauge volume, as depicted in figure 3.11, which is the case in the cast uranium tested. It would not be expected to be a problem for fine grained material with a homogeneous texture throughout the specimen, as on average the grains in the new and old GVs would have the same orientation distribution. It would also not be an issue for single crystal specimens, as the entire specimen has the same orientation.

By tracking the specimen position during the test with digital image correlation (DIC), the magnitude of the potential texture change artefact was evaluated. At maximum load, a texture change of up to 20% could be expected from this effect. This is of a similar magnitude to the observed texture changes.

3.7 Discussion & Summary

In this chapter, we have briefly described an experiment on the ENGIN-X instrument at ISIS which measured the deformation of coarse-grained uranium. Two specimens were tested in tension, and one in compression.

Single-peak fitting and Rietveld refinement were used to fit the measured diffraction spectra. Axial texture was measured using spherical harmonics in the Rietveld refinement. A novel implementation was used to quantify the error in the measured axial textures; this verified that any changes were not due to fitting error in the harmonic parameters, which may have been an issue for the sharp textures in our coarse-grained

Ministry of Defence © British Crown Copyright 2020/AWE

material. Between two and three grain clusters were present in the gauge volume of each specimen. Textures measured separately on the GEM diffractometer at ISIS match well with those measured on ENGIN-X, and provide a more complete orientation measurement for use in subsequent CPFE modelling.

In tension, (200)-oriented grains are plastically soft whilst (020)-oriented grains are seen to be plastically hard. The opposite is seen in compression. The initiation stresses for plastic deformation, calculated from the deviation from linearity in the lattice strain curves, did not match those predicted by critical resolved shear stress parameters from the literature, suggesting the CRSS parameters were not applicable for this microstructure. CPFE modelling work should identify an optimised set of deformation parameters.

Calculation and inspection of the 'texture differences' with respect to the texture measured at pre-load allowed small texture changes to be identified in the presence of strong textures. A novel method was developed to predict the axial texture changes upon activation of each variant of the $\{130\}$, '$\{172\}$', '$\{176\}$', and $\{112\}$ twinning modes. These were presented on inverse pole figures as pairs of parent and twin orientations. Different texture changes are expected in tension and compression due to the asymmetric Schmid factors for twinning.

It was not possible however to positively identify, from the observed texture changes, the operational twinning modes in any of the specimens. In materials with coarse or

Ministry of Defence © British Crown Copyright 2020/AWE

clustered grains, where the similarly-oriented regions are a similar size to the instrumental gauge volume, specimen movement can introduce significant artefacts into the measured texture changes. The magnitude of this artefact is large enough to have caused some or all of the observed gauge volume deformation.

3.7.1 Strengths

This experiment demonstrated the use of neutron diffraction to collect data that is suitable for use in the validation of crystal plasticity finite element (CPFE) simulations. The lattice strain response can be directly predicted with CPFE and can be used to refine the values of deformation system parameters. The use of full-texture measurement complemented the in-situ data and allows an accurate determination of the grain cluster orientation in the simulations.

The procedures and experimental modifications developed to test inherently radioactive specimens on ENGIN-X, such as the use of grip extensions (Appendix A5.2.1.1), could be used in any future experiments at a similar facility.

3.7.2 Limitations

This experiment revealed some of the many challenges of working with a coarse-grained radioactive material.

Whilst having only few clusters in the gauge volume allows them to be clearly identified, and their Schmid factors calculated, we don't know the spatial distribution of these clusters in the gauge volume, which introduces uncertainty into the modelling.

Ministry of Defence © British Crown Copyright 2020/AWE

We cannot separate the effects of deformation-induced texture change and specimen movement, which prevents unambiguous analysis.

Bulk strain measurement is required in order to fit the hardening rate in the CPFE simulations. It was not possible to use an extensometer, or to directly observe the specimen surface with DIC, due to the constraints of the risk assessment. Measurement of specimen extension from the DIC-measured displacement of the grips was unsuccessful since the grips moved with respect to the specimen in the early stages of the test. In any case, the clustered microstructure suggests the deformation would be highly heterogeneous, so the local strain near the gauge volume would have not been necessarily equal to the bulk strain across the whole specimen.

Only small twin volume fractions were expected at the maximum stress of 310 MPa. This made deformation-induced texture changes difficult to separate from any movement artefacts.

3.7.3 Areas for Improvement in a Future Experiment

A number of improvements were identified to be potentially implemented in future experiments. These include:

- Minimising the texture change artefact, to allow texture changes from deformation to be clearly identified.

Ministry of Defence © British Crown Copyright 2020/AWE

- Accurately measuring the total strain in the gauge volume, to allow the determination of flow curves, and therefore CPFE calculation of the hardening rates.
- Testing at higher loads, to induce greater levels of plastic deformation.
- Recording the orientation of specimens before loading.
- Extending the method of identifying twins from the texture changes by also incorporating data from the transverse neutron detector.

Some of these improvements were incorporated into the design of a subsequent experiment described in the next chapter.

Ministry of Defence © British Crown Copyright 2020/AWE

Chapter 4 An Improved Neutron Diffraction Experiment on Cast Uranium - Collecting Data Suitable for CPFE Modelling.

4.1 Introduction

In the previous chapter, we saw some of the challenges associated with neutron diffraction experiments on coarse-grained cast uranium. In this chapter, I will present an improved neutron diffraction experiment, incorporating many of the lessons learnt and different capabilities of the beamline at LANL (USA) compared to ENGIN-X (UK). Samples were tested to higher strains, allowing better measurement of hardening rates. In-situ DIC of the visible specimen surface allows a reliable measurement of the strain in the gauge volume, and enables the overall deformation of each specimen to be assessed. The texture change artefact from specimen movement is minimised by an evolved experimental design.

The observed texture changes will be related to $\{130\}$ and '$\{172\}$' twins using the twinning reorientations calculated in the previous chapter. These twins are responsible for the tension-compression asymmetry in uranium. Subtleties of deformation are visible in the single-peak strains that are not discernible in the Rietveld refinement. The deformation in the gauge volume was strongly influenced by texture – the first tensile specimen sees anomalous Rietveld *c*-parameter strains as a result of significant

Ministry of Defence © British Crown Copyright 2020/AWE

deformation in a texture component oriented with its tensile axis near to, but not parallel to, (001).

Crystal plasticity finite element (CPFE) modelling of the ENGIN-X experiment described in chapter Chapter 3 has been performed by Dr Nicolò Grilli, our collaborator in the Department of Engineering Science, University of Oxford. This has identified a set of activation stresses for deformation and has demonstrated that these cannot be determined from the experimental data without simulation. This justifies the use of neutron diffraction experiments to provide calibration data for a CPFE model for coarse-grained cast uranium. The results presented in this chapter will enable further development of this model.

4.2 Experimental Procedure and Data Analysis Methodology

A neutron diffraction experiment was performed at the Los Alamos Neutron Science Center (LANSCE) on the Spectrometer for Materials Research at Temperature and Stress (SMARTS) beamline. The experiment was granted 8 days of beamtime under proposal LC-2019-7889-A from 11th August 2018 to 20th August 2018 and was kindly supported by AWE and Los Alamos National Laboratory.

The SMARTS diffractometer at LANSCE is similar to ENGIN-X at ISIS – both are time-of-flight spectrometers with two detector banks located at $\pm 90^{\circ}$ to the incoming beam, and a load frame to perform in-situ loading of the specimen. The facility is

Ministry of Defence © British Crown Copyright 2020/AWE

described by Bourke et al. [137] and the key features are described here. The specimen was mounted at 45° to the beam such that detector bank 2 collects neutrons diffracted by planes with their normals parallel to the loading direction, and bank 1 collects those diffracted by perpendicular planes. A schematic is shown in figure 4.1.

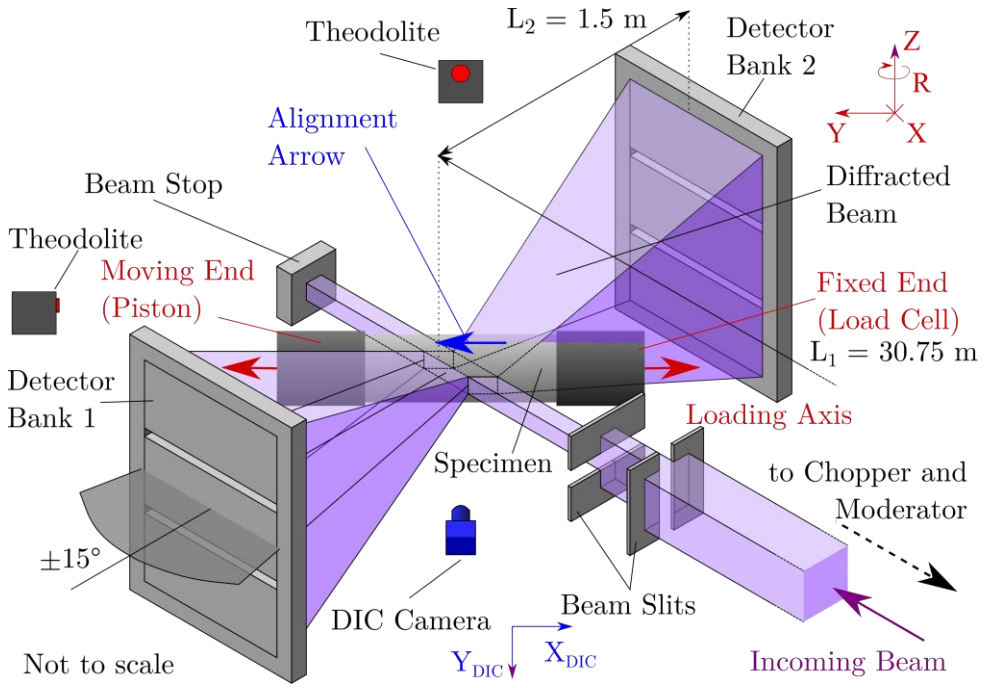


Figure 4.1. Schematic of the SMARTS instrument.

The beam passes through a chilled water moderator and along the 30.75 m primary flight path to the specimen. A T-zero chopper removes the fast neutrons from each neutron pulse. The incoming beam cross-section was defined via slits and unlike at ENGIN-X, no radial collimators were used. Each detector bank consists of 384 ^{3}He tubes located 1.5 m from the specimen centre.

The Instron servo-hydraulic rig has a maximum capacity of 250 kN and was mounted in an aluminium U-shaped frame. The load frame was mounted on a large positioning stage

Ministry of Defence © British Crown Copyright 2020/AWE

enabling X-Y-Z movement and rotation about the Z-axis. Two Leica theodolites allowed positioning of the specimen to an accuracy of 10 μm [137]. A recent addition to SMARTS was a single DIC camera (FLIR Grasshopper 3, 4096 × 3000, Mono, 30 FPS, Sony IMX253 sensor) with macro lens (Tamron SP 180 mm f3.5 Di). This was mounted on a tripod such that the camera was at the same height as the specimen and perpendicular to the specimen surface, as shown in figure 4.1.

4.2.1 Specimen Design

The specimen design was deliberately chosen to be similar to those tested on ENGIN-X. The compression specimens were identical; cylindrical with a 14 mm diameter and 28 mm gauge length. The tensile specimens had the same overall length of 82 mm and a longer gauge length of 50 mm was achieved by shortening the threaded grips at either end. Drawings of each specimen type are shown in figure 4.2. Two specimens of each type were machined at AWE via wire EDM; ND-T3 & ND-T4 (tensile), ND-C3 & ND-C4 (compression). Each specimen was marked with an axially-pointing arrow in the centre of the specimen, which was subsequently used to align the specimens.

Ministry of Defence © British Crown Copyright 2020/AWE

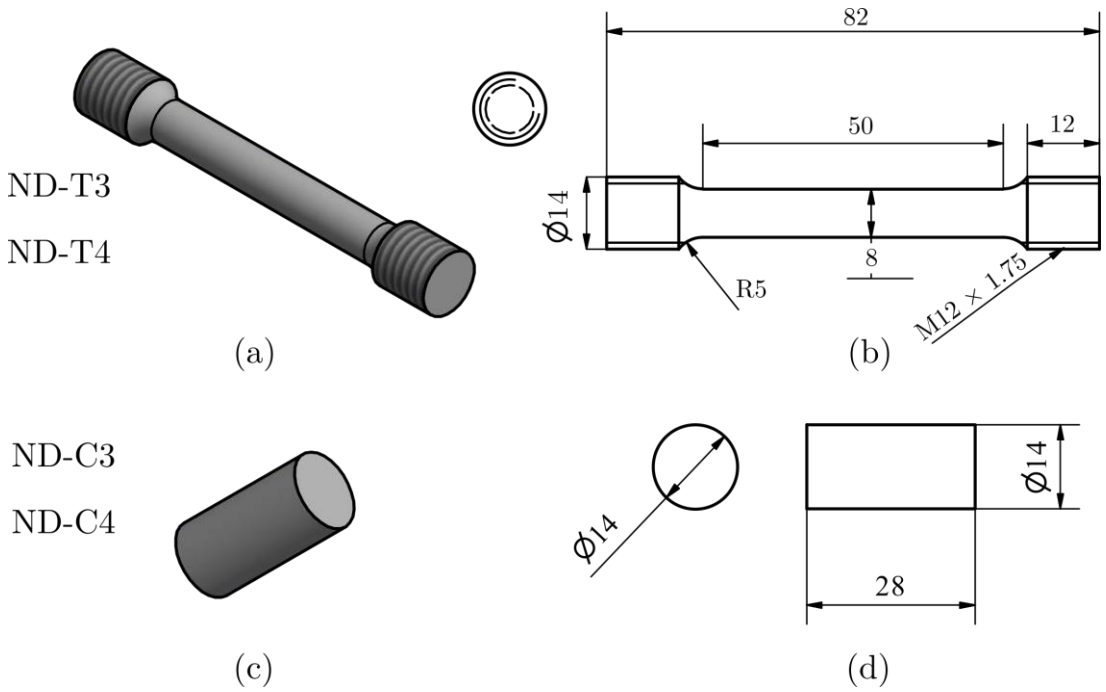


Figure 4.2. 3D rendering and engineering drawing of the tensile specimens, (a) and (b), and the compression specimens, (c) and (d), tested on SMARTS. All dimensions in mm.

The gauge diameter of each specimen was measured with digital calipers before the experiment, at three points along the specimen length, and the cross-sectional area was calculated from the mean diameter (table 4.1). The fractional error in the gauge cross-sectional area is shown as a percentage, and gives a lower bound to the error in the calculation of stress from the applied load.

Table 4.1. Cross-sectional area calculation from the mean gauge diameter. Fractional error in the gauge cross-sectional area is shown as a percentage.

Specimen	Mean gauge diameter (mm)	Gauge cross-sectional area (mm^2)
ND-T3	7.960 ± 0.003	49.76 ± 0.04 (0.08%)
ND-T4	7.960 ± 0.003	49.76 ± 0.04 (0.08%)
ND-C3	13.957 ± 0.007	152.99 ± 0.15 (0.10%)
ND-C4	13.940 ± 0.015	152.62 ± 0.33 (0.22%)

In a similar manner to the experiment on ENGIN-X, a set of grip extensions were produced to mount the specimens into the SMARTS load frame. Flat faces were

Ministry of Defence © British Crown Copyright 2020/AWE

machined and a black and white speckle pattern was applied with an airbrush to allow DIC tracking of the grips. The grip extensions were manufactured from C-350 maraging steel with a yield stress in excess of 2300 MPa. Drawings of the grip extensions are shown in figure 4.3.

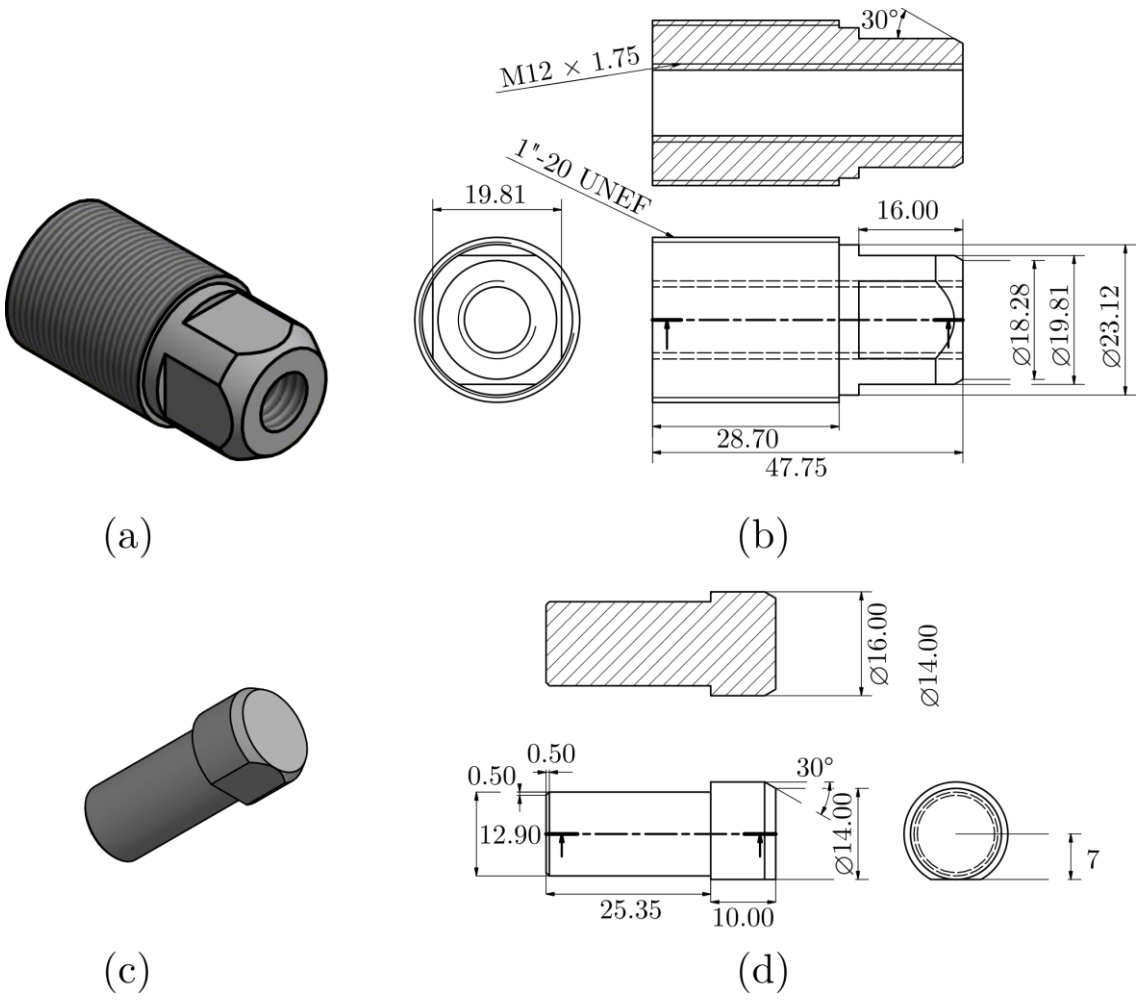


Figure 4.3. 3D rendering and engineering drawing of the tensile (a and b) and compressive (c and d) grip extensions manufactured for the experiment at ENGIN-X. All dimensions in mm.

Ministry of Defence © British Crown Copyright 2020/AWE

4.2.2 Experimental Set-up

4.2.2.1 Specimen Alignment

Each specimen and its associated grip extensions were mounted into the load frame with the alignment arrow facing upwards and pointing towards the piston (moving end). The tip of a steel pin mounted vertically above the load-frame centre was viewed through each of the two orthogonal theodolites, and the translation stage was moved to centre the pins in each theodolite's viewfinder, thus aligning the specimen in the X-Y plane. The stage was then raised to centre the specimen in the beam.

It was important to ensure good alignment of the specimens with the loading axis to ensure a uniaxial tensile/compression stress state. The tensile grip extensions were attached to the load frame via universal joints which naturally align the specimen. For the compression specimens, pressure-sensitive tape (Sensor Products, USA, 7100 – 18500 psi rating) was placed between the compression grip extensions and load was applied (figure 4.4(a)). The tape changes colour according to the maximum applied pressure, and the two ends of the load frame were aligned by adjusting the adjustment bolts on the piston and load cell until the grip extensions left a circular imprint with even intensity (figure 4.4(b)). The ends of each compression specimen were coated with molybdenum disulphide paste (MoS_2) which acts as a lubricant to reduce friction.

Ministry of Defence © British Crown Copyright 2020/AWE

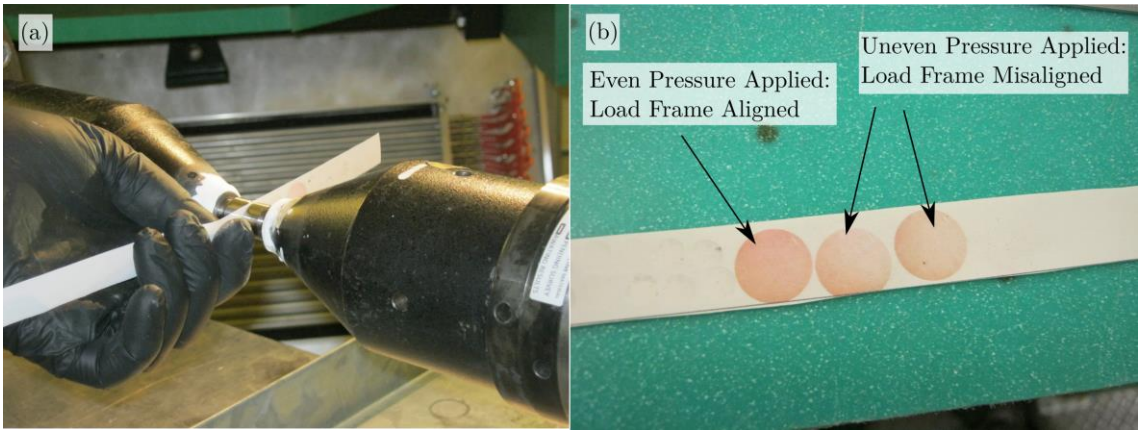


Figure 4.4. (a) Use of pressure-sensitive tape to align the compression grip extensions in the SMARTS load frame. (b) An even intensity indicates an even applied pressure and aligned grips.

4.2.2.2 Extensometer

For the tensile specimens, a clip-on extensometer (Instron 2620-601) with a nominal gauge length of 12.5 mm, was attached to the specimen with orthodontic bands (figure 4.5). Addition of a 15 mm extender was required to capture the strain across the majority of the specimen and to hopefully include the region in which fracture would occur. With an effective gauge length of 27.5 mm and a full-scale displacement range of $\pm$ 5 mm, strains of $\pm$ 18 % could be measured. The relevant gauge length was programmed into the Instron controller such that strain would be correctly calculated from the extensometer displacement.

Ministry of Defence © British Crown Copyright 2020/AWE

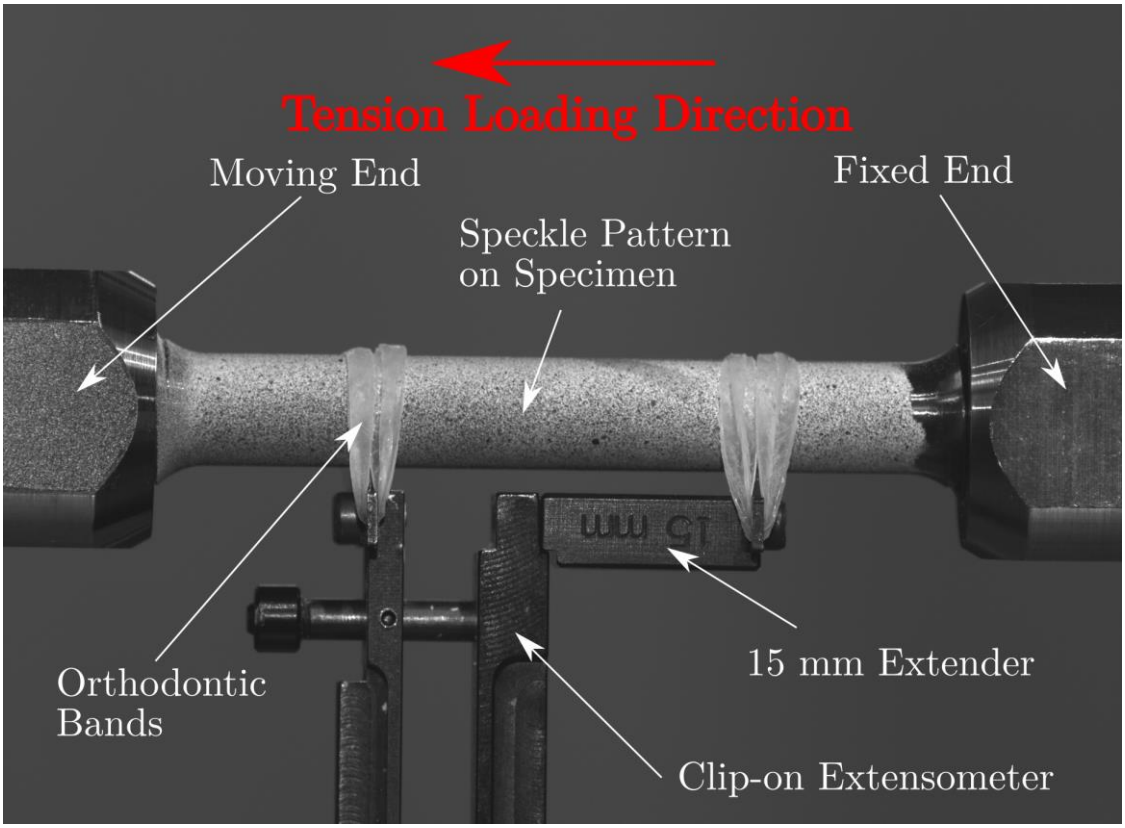


Figure 4.5. Tensile specimen ND-T4 with clip-on extensometer and 15 mm extender.

Typically, for compression specimens tested on SMARTS, a 10 mm extensometer is placed in the centre of the specimen and the strain is assumed to be homogenous throughout the specimen. The extensometer mounting bands would have restricted the DIC observation of the specimen surface, which was undesirable as our specimens were known to behave heterogeneously.

For compression specimen ND-C3, a 25 mm extensometer (Instron 2620-603 10 mm + 15 mm extender) was initially used and orthodontic bands were placed at the ends of the specimen. The full-scale range of this extensometer was only ± 1 mm corresponding to a strain range of ± 4 %. The desired compressive strain of approximately 7 % would therefore be outside the range of the extensometer when attached in the usual manner.

Ministry of Defence © British Crown Copyright 2020/AWE

The extensometer was therefore pre-strained with a positive strain of approximately 3.5 % before attaching it to the specimen. This allows a compressive strain of up to 7.5 % to be measured. The specimen strain, $\varepsilon_{\mathrm{sample}}$, was calculated from the displayed strain, $\varepsilon_{\mathrm{displayed}}$, and the offset pre-strain, $\varepsilon_{\mathrm{offset}}$, using equation [4.1], derived in Appendix A8.2.1.

$$\varepsilon_{\mathrm{sample}} = \frac{1 + \varepsilon_{\mathrm{displayed}}}{1 + \varepsilon_{\mathrm{offset}}} - 1 \qquad [4.1]$$

Unfortunately the orthodontic bands were observed to dissolve in the MoS_2 lubricant and the extensometer became detached during the experiment. At a nominal strain of 4.5 % it was decided to remove the 25 mm extensometer and attach the 10 mm extensometer with fluoroelastomer 'Viton' o-rings. This necessitated converting the recorded strain $\varepsilon_{\mathrm{displayed}}$ to the actual specimen strain $\varepsilon_{\mathrm{sample}}$. This is done via equation [4.2], derived in Appendix A8.2.2, where $\varepsilon_{\mathrm{exchange}}$ was the sample strain at which the extensometers were swapped.

$$\varepsilon_{\mathrm{sample}} = (1 + \varepsilon_{\mathrm{displayed}})(1 + \varepsilon_{\mathrm{exchange}}) - 1. \qquad [4.2]$$

For compression specimen ND-C4, the 25 mm extensometer was attached with the Viton o-rings and no issues were observed.

4.2.2.3 DIC Camera Setup

A speckle pattern was applied to the specimen surface facing the camera using Krylon ColorMaster Paint + Primer spray paint. A thin layer of white was applied, followed by a black speckle from a distance of ~50 cm until approximately 50 % of the specimen was

Ministry of Defence © British Crown Copyright 2020/AWE

painted black. With this method, a mix of black particles between $50\,\mu m - 300\,\mu m$ in diameter was achieved.

For tensile specimen ND-T3, the field of view was small and spanned ~20 mm along the specimen length, with the image centred on the middle of the gauge region. For the subsequent specimens, a larger field of view was used, where the grip extensions at each end were also visible. This change allowed the strain field to be measured across a larger region of the specimen.

Lighting was provided via high-intensity LEDs mounted on a tripod behind the camera. Images were acquired using Vic-Snap software by Correlated Solutions, Inc. The exposure time was increased as far as possible without overexposure – 50 ms for specimen ND-T3 and 25 ms for the remaining specimens.

Calibration images were taken after each specimen was removed from the load frame at the end of the test. A metal ruler was held up such that it was in the same *y-z* plane as the specimen surface facing the camera. The markings on the ruler were measured using the line tool in Fiji[138] and the pixel size was calculated. A single calibration image was taken for specimens ND-C3 and ND-C4 as the camera was not moved between these experiments. The calibrated pixel sizes were used in subsequent calculations and are shown in table 4.2.

Ministry of Defence © British Crown Copyright 2020/AWE

Table 4.2. Calibrated DIC pixel size

Specimen	Pixel Size (μm)
ND-T3	5.133
ND-T4	19.611
ND-C3	19.568
ND-C4	19.568

4.2.2.4 Thermocouple

The ambient air temperature in the LANSCE facility varied throughout the day, from 15 ℃ to 25°C. Since the ductile-brittle transition temperature of uranium is known to be around room temperature, variations in the specimen temperature could strongly affect the deformation modes. The hydraulic fluid in the load frame piston was warm (32°C), and heat could conduct into the specimen. K-type thermocouples were attached to each end of the gauge region of specimen ND-T4, and after an initial equilibration during pre-load, the specimen temperature was observed to be constant at $27^{\circ}\mathrm{C} \pm 2^{\circ}\mathrm{C}$.

4.2.2.5 Neutron Beam Gauge Volume

The beam axial cross-section was defined by the slits to be 12 mm × 12 mm (width × height) for the tensile specimens and 8 mm × 14 mm for the compression specimens. Beam widths were chosen to maximise the gauge volume whilst keeping the grip extensions out of the direct beam. A 2D plan-view schematic of the gauge volumes is shown in figure 4.6 – in the absence of collimators, the projection of the diffracting gauge volume onto the *x*-y plane is a parallelogram.

Ministry of Defence © British Crown Copyright 2020/AWE

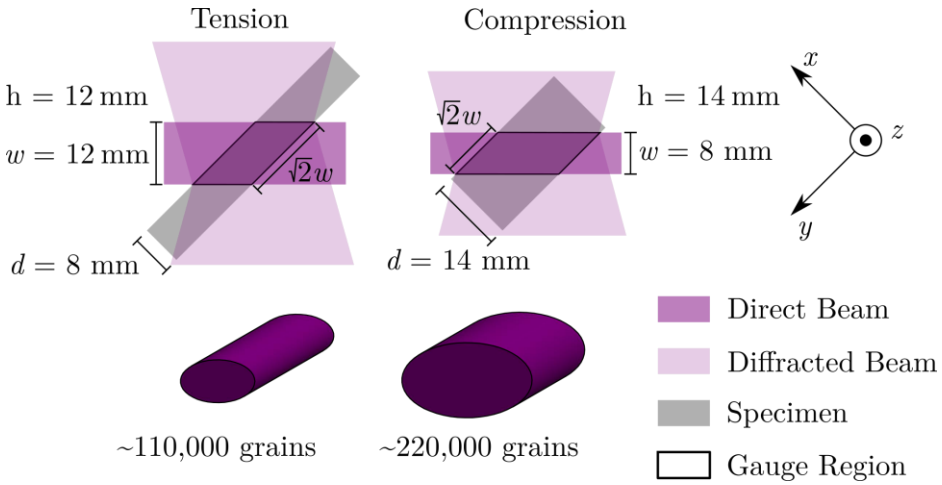


Figure 4.6. Plan view schematic of the gauge volumes defined on SMARTS. No radial collimators were used.

Since the beam height is greater than or equal to the specimen diameter, the volume of material inside the instrumental gauge region can be calculated by simple geometry using equation [4.3].

$$V = \frac{\pi d^2 w}{2\sqrt{2}} \qquad [4.3]$$

The tensile and compressive gauge regions have volumes of 850 mm^2 and 1740 mm^2, corresponding to approximately 1.1×10^5 and 2.2×10^5 grains respectively, assuming a nominal spherical grain diameter of 200 $\mu\mathrm{m}$. Assuming spherical clusters with diameter 6 mm, this would correspond to at least 4 and 8 clusters in the gauge volumes of the tensile and compression specimens respectively.

The load frame was made from strongly diffracting materials (steel, aluminium) so the diffracted beam may scatter from these materials and appear as unwanted peaks in the diffraction spectrum. Near-beam parts, such as the compressive grip extensions, were painted with gadolinium oxide (Gd_2O_3) paint, which absorbs these diffracted neutrons.

Ministry of Defence © British Crown Copyright 2020/AWE

The steel knife-edges of the extensometer were at the lower edge of the direct beam, so a neutron-absorbing cadmium (Cd) shield was positioned such that the neutron beam did not impinge on the extensometer. The initial spectra for each specimen were checked for Al or Fe peaks – none were observed.

4.2.2.6 Count time Optimisation

The neutron count time for each scan is a balance between spectrum quality and speed – longer count times give a better signal to noise ratio and consequently a better measurement of strain. SMARTS has a scripted procedure to optimise the count time; a continuously-integrated spectrum was saved at 1 minute intervals, giving spectra with count times of 1, 2, 3, etc. minutes. Single-peak fits to the dominant peak was performed for each spectrum and the optimal count time was found as the time required to achieve a single-peak-strain error smaller than 50 $\mu\varepsilon$.

For the tensile specimens, an integrated source current of 900,000 $\mu\mathrm{Ah}$ was required, corresponding to approximately 15 minutes per scan. The compression specimens, with their larger gauge volume, required an integrated source current of 600,000 $\mu\mathrm{Ah}$, corresponding to approximately 10 minutes per scan.

Ministry of Defence © British Crown Copyright 2020/AWE

4.2.2.7 Photograph of SMARTS set-up

An annotated photograph of the experimental set-up is shown in figure 4.7.

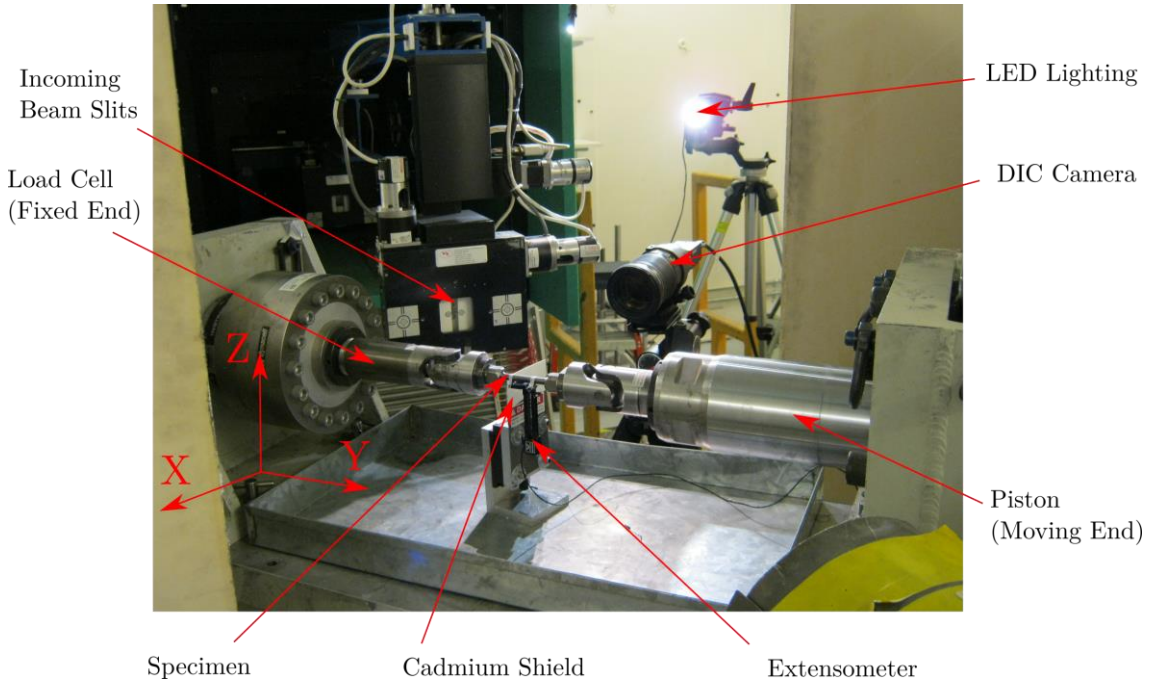


Figure 4.7. The SMARTS set-up before testing of specimen ND-T3.

Ministry of Defence © British Crown Copyright 2020/AWE

4.2.3 Experimental Testing Procedure

4.2.3.1 Pre-Load

Each specimen was held in load control at a pre-load of ~10 MPa for at least 20 minutes to allow the specimen to equilibrate in temperature with the load frame. Thermal expansion of the specimen was observed as an increase in the extensometer strain – the test began when further increase became indistinguishable from the noise in the strain data.

Slack in the tensile grips induced unexpected movement which was an issue in the previous ENGIN-X experiment. Each specimen was loaded to 30 MPa to remove slack in the grips before returning to the 10 MPa pre-load. The reference neutron measurement was then taken.

4.2.3.2 Texture Change Artefact Correction

The texture change artefact caused by specimen movement, observed in the ENGIN-X experiment (Chapter 3) needed to be minimised in order for deformation modes to be identified. From equations [3.23] and [3.27] on pages 92 and 93, we saw that:

$$\left(\frac{\Delta \mathrm{T}}{\mathrm{T}}\right)_{\max} = 1 - \frac{(\sqrt{2}l - \Delta x)^2}{2l^2} \qquad [4.4]$$

A number of methods were proposed to minimise the texture artefact $\frac{\Delta T}{T}$. The first involved reducing the effect of the specimen movement, whilst leaving the experiment largely the same. By sketching equation [4.4] as a function of gauge volume area

Ministry of Defence © British Crown Copyright 2020/AWE

(represented by l^2), figure 4.8, it can be seen that increasing the gauge volume size decreases the texture artefact for a given specimen displacement.

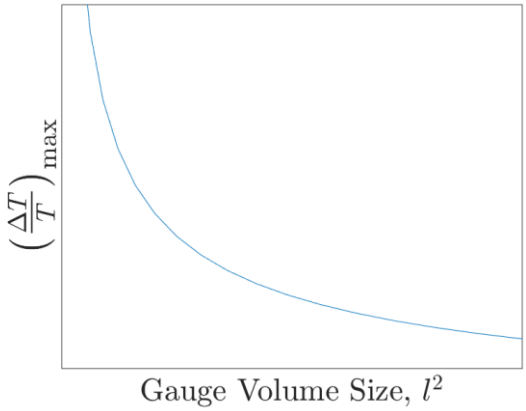


Figure 4.8. Increasing the gauge volume size decreases the texture artefact.

The removal of the collimators and the use of a larger incoming beam cross section resulted in an increase in gauge volume of 7× for the tensile specimens and 9× for the compression specimens compared to the ENGIN-X experiment.

The second method would involve reducing the actual specimen movement. A more rigid load frame could be used, or a smaller specimen could be tested, which would require smaller forces and therefore a smaller deflection of the load frame, minimising Δx. The load frame at SMARTS was made from aluminium instead of the steel at ENGIN-X, so may be more compliant. It was not desirable to reduce the specimen size as this would reduce the gauge volume, which was shown above to be undesirable.

The preferred method required the texture along the specimen axis to be known. If the specimen position was measured throughout the test, then the texture at load could be compared to the texture at unload at the same specimen position. This way, only the

Ministry of Defence © British Crown Copyright 2020/AWE

texture change due to deformation will be measured, and the texture change artefact can be eliminated. Since the specimen would move in the direction of the applied load, it was necessary to measure the texture in gauge volumes further away from the moving end of the load frame. This necessitated moving the positioning stage in the direction of load (figure 4.9).

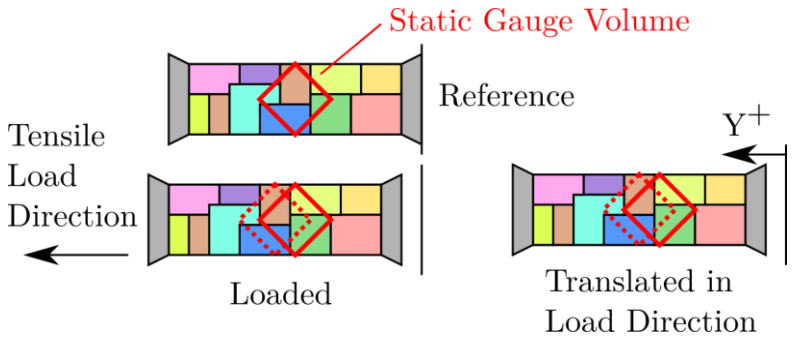


Figure 4.9. The unloaded specimen was translated in the load direction to measure the reference texture.

For specimen ND-T3, after the slack-removing pre-load, the positioning stage was moved from $Y = 0$ mm to $Y = 4$ mm in steps of 0.25 mm with a neutron measurement taken at each point. The observed movement of specimen ND-T3 during loading was less than 2 mm so specimen ND-T4 was only translated to $Y = 2$ mm, with the same step size.

Before testing of each compression specimen, neutron measurements were taken with the stage translated from $Y = 0$ mm to $Y = -3$ mm in steps of 0.2 mm.

4.2.3.3 Testing Methodology

The testing procedure for each specimen was similar to that shown in figure 4.10:

1. Firstly, load was applied in load control to take the specimen past the yield point. After each load increase, a neutron measurement was made.

Ministry of Defence © British Crown Copyright 2020/AWE

2. The specimen was then unloaded in load control to the pre-load of 10 MPa, followed by re-loading in load control up to a stress below the yield stress (to minimise creep), with neutron measurements at each step.
3. The specimen was then strained in position control to apply a predicted strain of approximately 1.5 %, with neutron measurements taken after increments of approximately 0.15 % strain.
4. After each straining period, a unload-load cycle was performed in load control.
5. For the tensile specimens, steps 3 & 4 were repeated until the specimen fractured. In compression, the test was stopped if the subsequent straining period would likely exceed a strain of 7 %.

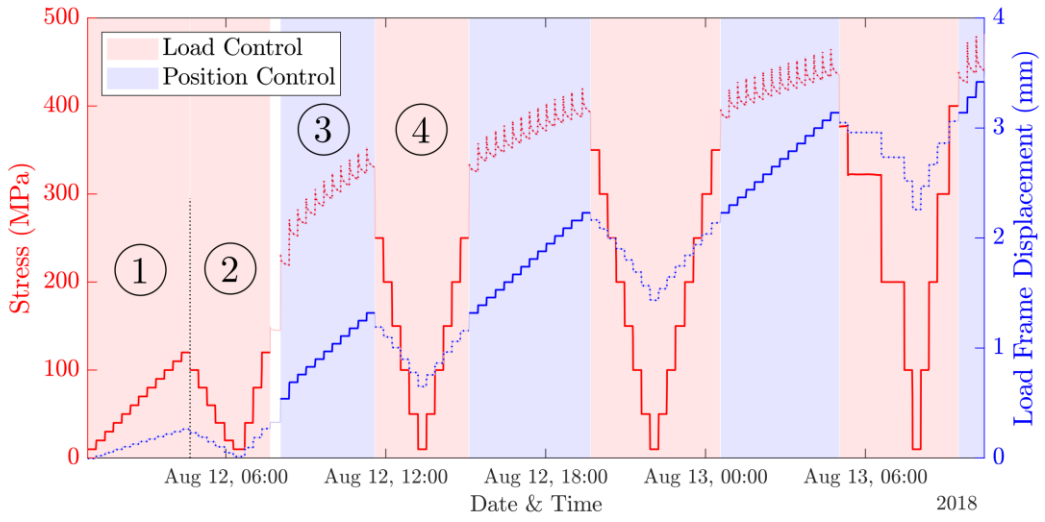


Figure 4.10. Testing procedure for specimen ND-T3. Stress (red line) and Load-frame displacement (blue line) are plotted as a function of time. Total time elapsed was 33 hours. Load frame control swapped between load control (pink) and position control (light blue). In general, loading was performed in load control below the yield stress and in position control above the yield stress.

DIC images were automatically acquired using the 'Timed Capture' feature in Vic-Snap (Correlated Solutions, Inc., USA) at a rate of 1 image per minute.

Ministry of Defence © British Crown Copyright 2020/AWE

4.2.3.4 Compression Specimens at High Strain

All experiments at LANSCE are risk assessed through a procedure that generates Integrated Work Documents (IWDs) dictating the approved procedure for each activity. The SMARTS IWD for compression testing of uranium dictates that specimens must be surrounded by a containment box, preventing the ballistic loss of the sample if it were to buckle. This would have prevented the observation of the specimen with DIC, as the camera could not see through the opaque aluminium containment box used on SMARTS.

Our specimen was expected to have a buckling stress almost 3× greater than the usual uranium specimens tested on SMARTS (Appendix A8.5). In the history of the beamline, no specimen had failed in such manner despite straining in excess of 7 %. A case was approved by the safety team at LANSCE that the increased buckling stress of our specimens should allow the removal of the box for strains up to 4.5 %. For higher strains, the box would be replaced.

A GdO-coated shield was positioned to prevent neutrons scattered from the beam-facing surface of the aluminium box from entering detector bank 1 (figure 4.11).

Ministry of Defence © British Crown Copyright 2020/AWE

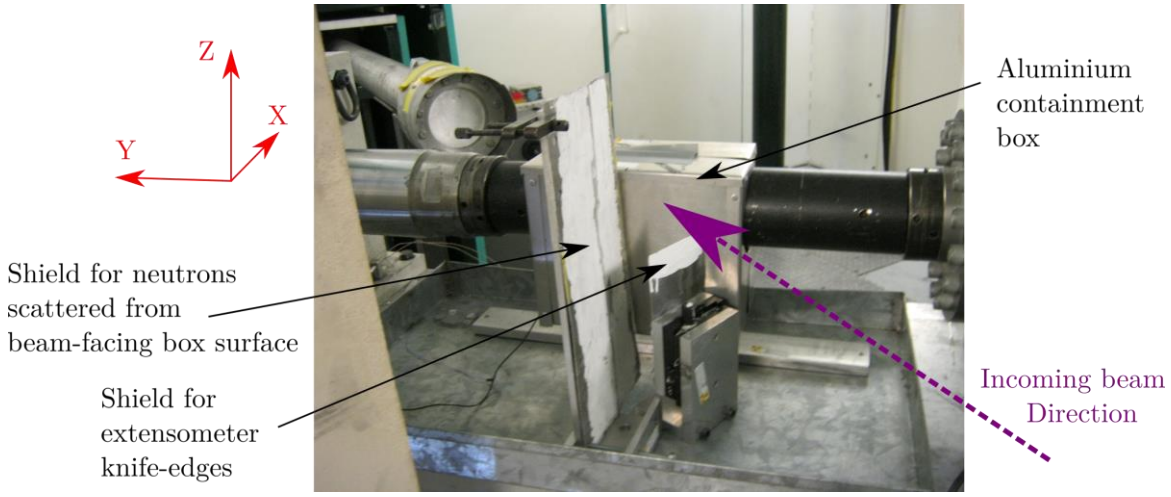


Figure 4.11. Compression set-up with containment box used at strains in excess of 4.5 %.

4.2.4 Single-Peak Fitting

Single-peak fitting was performed using the `SmartsSPF` function in SMARTSware [139]. This follows a similar procedure to the OpenGenie [140] fitting performed on the ENGIN-X data in section A5.2.1.4 on page 377. It however deals better with partially-overlapping peaks, fitting them in groups rather than individually. For example, the (110), (021) and (002) peaks are fitted as one group (figure 4.12).

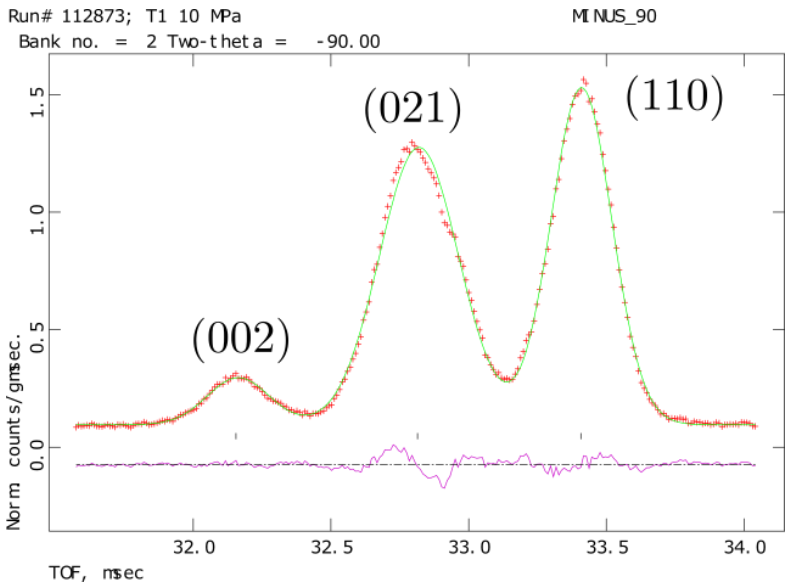


Figure 4.12. SmartsSPF fitting of groups of adjacent peaks. Data shown are the (110), (021) and (002) peaks from the pre-load scan of specimen ND-T3. The raw data are shown in red, with the best fit shown in green. The purple line shows the residual – the deviation of the raw data from the fit.

Ministry of Defence © British Crown Copyright 2020/AWE

The 14 peaks with the largest d-spacing were fitted – from the (020) peak at 2.933 Å to the (113) peak at 1.389 Å. These peaks span a wide area of the inverse pole figure – shown in figure 4.13, with each reflection coloured according to its orientation.

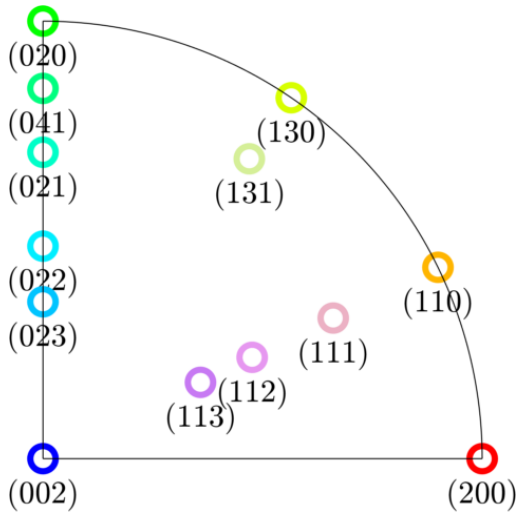


Figure 4.13. Reflections fitted using SmartsSPF, plotted on an inverse pole figure. The (040) reflection is not shown as it overlaps with the (020) reflection.

The full-width at half-maximum, FWHM, calculated by SmartsSPF is a combination of the Gaussian and Lorentzian widths. The Gaussian FWHM is related to the Gaussian width σ (equation [8.9] on page 378) by equation [4.5].

$$\mathrm{FWHM}_{\mathrm{Gaussian}} = 2\sqrt{2\ln 2}\,\sigma \qquad [4.5]$$

4.2.5 Rietveld Refinement

Rietveld refinement was performed in GSAS[118] following a similar routine to that used on the ENGIN-X data, described in Appendix A5.2.1.5. The SmartsRunRep command in SMARTSware was used to automate the process and sequentially refine all spectra for a given specimen. SmartsABC was used to extract the lattice parameters and strains from the output files. SmartsRefList was used to extract the Rietveld preferred orientation

Ministry of Defence © British Crown Copyright 2020/AWE

values for each reflection. `SmartsInvPol` calculated the inverse pole figures, and a MATLAB program was written to synthesise all of the data files into one dataset for each specimen.

Unlike on ENGIN-X, where TOF profile 3 was used, the usual peak profile used on SMARTS is TOF profile 1, described fully in the GSAS manual[118]. The peak profile is given in equation [4.6], where ΔT is the difference between a point on the profile and the relevant peak position and *N*, *u*, *y*, *v*, and *z* are functions of the 12 fitting parameters.

$$H\ \Delta T\ = N[e^{u}\mathrm{erfc}\ y\ + e^{v}\mathrm{erfc}\ z\ ] \qquad [4.6]$$

Equation [4.6] is the result of the convolution of a Gaussian function with two back-to-back exponentials:

$$H\ \Delta T\ = \int G\ \Delta T - \tau\ E\ \tau\ d\tau \qquad [4.7]$$

where τ is a dummy variable of integration, $E(\tau)$ is defined exactly as in equation [8.14] on page 380 and the Gaussian function is defined as

$$G\ \Delta T - \tau\ \frac{1}{\sqrt{2\pi\sigma^2}} = \exp\left(-\frac{(\Delta T - \tau)^2}{2\sigma^2}\right). \qquad [4.8]$$

N is the normalisation factor, defined in equation [8.15] on page 380. u, *y*, *v*, and *z* are functions of the Gaussian coefficient σ and the profile position ΔT.

The Gaussian coefficient comprises a constant term, σ_0, and terms linear and quadratic with *d*, σ_1 and σ_2, as well as orientation-dependent terms:

Ministry of Defence © British Crown Copyright 2020/AWE

$$\sigma^2 = \sigma_0^2 + \sigma_1^2 d^2 + \sigma_2^2 d^4 + f(\text{orientation}) \quad [4.9]$$

4.2.6 DIC Strain & Displacement Measurement

Digital Image Correlation (DIC) was performed on the image sequences of the specimen surface in LaVision DaVis 8.4.0.

4.2.6.1 DIC Mask Application

A mask was applied to each image to restrict the correlation to the central region of each specimen. This region would be in a similar location to surface of the diffracting gauge region, such that the measured surface strain would approximate the total strain in the gauge volume. The curvature of the specimen resulted in the images being out of focus at the top and bottom edges of the specimen; poor DIC data was seen here. The correlation area was chosen to be 10 mm in width, along the axis of the specimen, with vertical heights of 5 mm and 10 mm for tension and compression specimens respectively.

The mask was centred on the mid-point of each specimen. The vertical mid-point y_{mid} was determined as the average of the *y* co-ordinates of the top and bottom surfaces of the specimen. The horizontal mid-point x_{mid} was determined as the *x* co-ordinate mid-way between the grips. In specimen ND-T3 however, the grips were not visible, so x_{mid} was inferred from the part of extensometer that was aligned with the midpoint in specimen ND-T4, assuming that the extensometer was placed in the same place in both tensile specimens.

Ministry of Defence © British Crown Copyright 2020/AWE

From the pixel sizes listed in table 4.2, the desired mask area, and the relevant midpoint co-ordinates $(x_{\mathrm{mid}}, y_{\mathrm{mid}})$, the pixel co-ordinates of the vertices of each mask were calculated. Using these co-ordinates, a geometric mask in DaVis was applied to all of the images in the image sequence. The mask locations are displayed on images of each specimen at initial pre-load in figure 4.14.

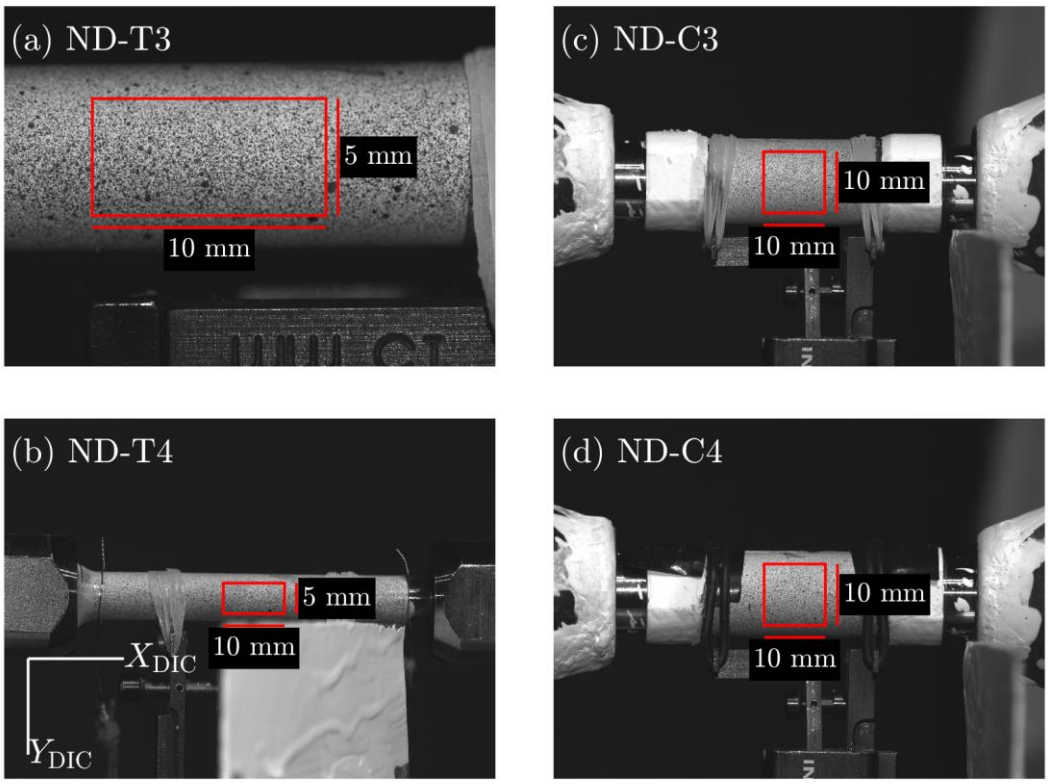


Figure 4.14. Locations of the geometric mask applied to each DIC image sequence for specimens (a) ND-T3, (b) ND-T4, (c) ND-C3, and (d) ND-C4 at pre-load.

Images where the speckle pattern was not visible, e.g. where the box was placed over the compression specimens, were removed from the correlation.

Ministry of Defence © British Crown Copyright 2020/AWE

4.2.6.2 DIC Calculation

Digital image correlation was performed on each image sequence using the parameters shown in table 4.3. 'Relative to first' correlation uses the first image of the sample under pre-load as the reference image. A seed point was defined in the unmasked region.

Table 4.3. DIC Parameters used in DaVis when processing images from the SMARTS experiment.

Specimen	ND-T3	ND-T4	ND-C3	ND-C4
Mask Centre (*x*, *y*) (pixels)	(1710, 1257)	(2083, 1498)	(2006, 1467)	(2011, 1467)
Mask Size (*x*, *y*) (mm)	(10, 5)	(10, 5)	(10, 10)	(10, 10)
Mask Size (*x*, *y*) (pixels)	(1948, 974)	(510, 255)	(511, 511)	(511, 511)
Correlation Mode	- - - - - - - - - - - - - - Relative to First - - - - - - - - - - - - - -			
Maximum Expected Displacement (pixels)	- 500 -			
Subset Size (pixels)	33	33	49	49
Step Size (pixels)	5	5	5	5
Correlation Mode	- - - - - - - - - - - - - - - - - Accurate - - - - - - - - - - - - - - - - -			

4.2.6.3 Results Export

The 'image-average' mean *x*-displacements, u_x^{Image}, and axial normal strain, $\varepsilon_{xx}^{\mathrm{Image}}$, were calculated as the mean of the u_x and ε_{xx} scalar fields for each image. These were exported from DaVis into MATLAB where the timestamps from the relevant DIC images were added. By comparison of the DIC image timestamp with the start and end times of each neutron measurement, the images taken during neutron measurement were identified and assigned to the correct neutron scan number. For each neutron measurement, the 'run-averages' u_x and ε_{xx} were calculated as the mean of the u_x^{Image} and $\varepsilon_{xx}^{\mathrm{Image}}$ values across the images acquired during the neutron measurement. The standard deviations in the image-averages, $\sigma(u_x^{\mathrm{Image}})$ and $\sigma(\varepsilon_{xx}^{\mathrm{Image}})$, relate to the heterogeneity of deformation in that single image. The standard deviations in the run-averages, $\sigma(u_x)$ and $\sigma(\varepsilon_{xx})$, relate to the variation in the sample displacement during a

Ministry of Defence © British Crown Copyright 2020/AWE

neutron measurement, e.g. stress relaxation when the sample was held under position control and creep when held under load control.

4.2.7 Correction of Specimen Movement

During each neutron measurement under load the specimen will therefore be at a position $y = -u_x$ along the *y*-axis relative to its original position (with the y^+ direction on SMARTS equivalent to the X^-_{DIC} direction). In order to calculate the texture change at load with no movement artefact, the correct reference texture for that particular *y*-position must be obtained. The reference texture was calculated from a), the measured position y and b), the sequence of pre-load textures captured at different *y*-positions (described on page 115), using the equations described below. This is shown pictorially in figure 4.15.

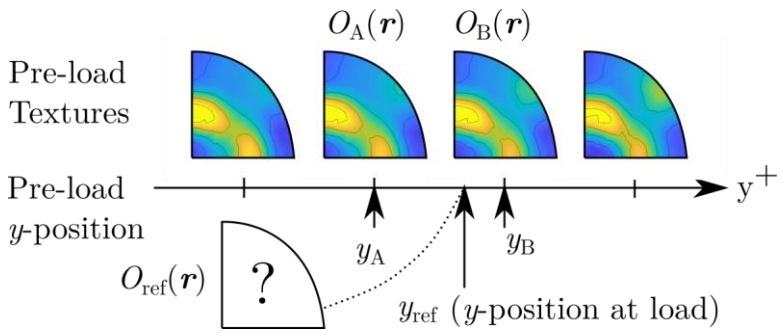


Figure 4.15. Calculation of the reference texture $O_{\mathrm{ref}}\ \boldsymbol{r}$ at loaded position y_{ref} from the pre-load textures $O_{\mathrm{A}}(\boldsymbol{r})$ and $O_{\mathrm{B}}(\boldsymbol{r})$. y_{A} and y_{B} are the pre-load positions closest to y_{ref}.

The reference texture, $O_{\mathrm{ref}}(\boldsymbol{r})$, was linearly interpolated from the two neighbouring pre-load textures $O_{\mathrm{A}}(\boldsymbol{r})$ and $O_{\mathrm{B}}(\boldsymbol{r})$ using equation [4.10],

$$O_{\mathrm{ref}}\ \boldsymbol{r}\ = f_{\mathrm{AB}} O_{\mathrm{B}}\ \boldsymbol{r}\ + (1 - f_{\mathrm{AB}}) O_{\mathrm{A}}\ \boldsymbol{r} \qquad [4.10]$$

Ministry of Defence © British Crown Copyright 2020/AWE

where $y_{\mathrm{A}} < y_{\mathrm{ref}} < y_{\mathrm{B}}$ and f_{AB} is the fractional displacement of the specimen between positions A and B:

$$f_{\mathrm{AB}} = \frac{y_{ref} - y_{\mathrm{A}}}{y_{\mathrm{B}} - y_{\mathrm{A}}} \qquad [4.11]$$

The uncertainty in each reference IPF, $\sigma(O_{\mathrm{ref}}(\boldsymbol{r}))$, can be estimated from the positions; y_{ref}, y_A, and y_B, the pre-load textures; $O_{\mathrm{A}}\ r$ and $O_{\mathrm{B}}\ r$, and their associated uncertainties. This is described in Appendix A8.3.

4.2.7.1 Movement-Corrected Texture Change

In this manner a reference texture was calculated for each neutron measurement. The texture change for the i^{th} measurement, $\Delta O\ \boldsymbol{r}\ _i$, was simply the difference between the texture at load, $O\ \boldsymbol{r}\ _i$, and the corresponding reference texture, $O_{ref}\ \boldsymbol{r}\ _i$:

$$\Delta O\ \boldsymbol{r}\ _i = O\ \boldsymbol{r}\ _i - O_{ref}\ \boldsymbol{r}\ _i. \qquad [4.12]$$

The uncertainty in the texture change is given by:

$$\sigma\left(\Delta \mathrm{O}\ \mathbf{r}\ \right)_i = \sqrt{\sigma\left(O\ \mathbf{r}\ \right)_i^{\ 2} + \sigma\left(\mathrm{O}_{ref}\ \mathbf{r}\ \right)_i^{\ 2}} \qquad [4.13]$$

Ministry of Defence © British Crown Copyright 2020/AWE

4.3 Results

In this section, the results of the experiment are presented. Firstly, the starting texture in the gauge volume is shown, as measured by the Rietveld refinement. The macroscopic deformation is then presented, with macroscopic flow curves and DIC-measured strain fields for each specimen. The two tensile specimens were loaded to fracture, and SEM micrographs of the fracture surface, acquired by Rod McCabe at LANL, are shown.

The texture changes observed during the test will be presented in a similar way to in the previous chapter. For each specimen, inverse pole figures are generated for a range of points during the test, showing the orientations for which the texture increased or decreased. The Rietveld preferred orientation parameter and single-peak intensities are plotted as a function of strain. It will be seen that the texture changes approximately linearly with the magnitude of applied strain.

Lattice strains and lattice parameter strains are plotted as a function of stress. The lattice strains on each family of grains behave differently depending on the orientation relative to the loading axis. Intergranular lattice parameter strains and strain broadening parameters are calculated from the Rietveld data.

4.3.1 Texture in the Gauge Region

Overall, the textures measured on SMARTS are weaker than those observed on ENGIN-X. This was expected due to the large gauge volume used on SMARTS smoothing the texture across more grain clusters. Figure 4.16 shows the bank 2 axial textures at pre-

Ministry of Defence © British Crown Copyright 2020/AWE

load in specimens (a) ND-T3, (b) ND-T4, (c) ND-C3, and (d) ND-T4. In each case orientations coloured yellow represent large numbers of grains oriented with this zone axis along the loading direction, and those coloured in blue are only present in small quantities. As expected from the coarse, clustered microstructure, the textures in each specimen are very different.

In specimen ND-T3, the strongest texture was near (023), at 2.1 MRD. Significant texture of 1.7 MRD was also present near (204), with a smaller 1.4 MRD cluster near (350). Very few grains are oriented with the loading axis along their (100), (010) and (001) directions.

Specimen ND-T4 has a maximum texture of 1.7 MRD at (351). Orientations approximately 70° from the (001) pole, between (151) and (402), are present at a frequency of nearly 1.5 MRD. The texture near (001) is low, at around 0.5 MRD.

In the first of the compression specimens, ND-C3, a strong peak of 1.7 MRD is seen between (202) and (204), alongside a broader texture peak near (151) of 1.5 MRD.

Specimen ND-C4 shows a strong texture, with components of 2.4 MRD and 1.7 MRD found along the (001) and (010) axes. A smaller contribution of 1.6 MRD is seen near (100). Orientations angled with the loading direction more than 20 degrees from the principal crystal axes occur much less frequently than would be expected in a random distribution.

Ministry of Defence © British Crown Copyright 2020/AWE

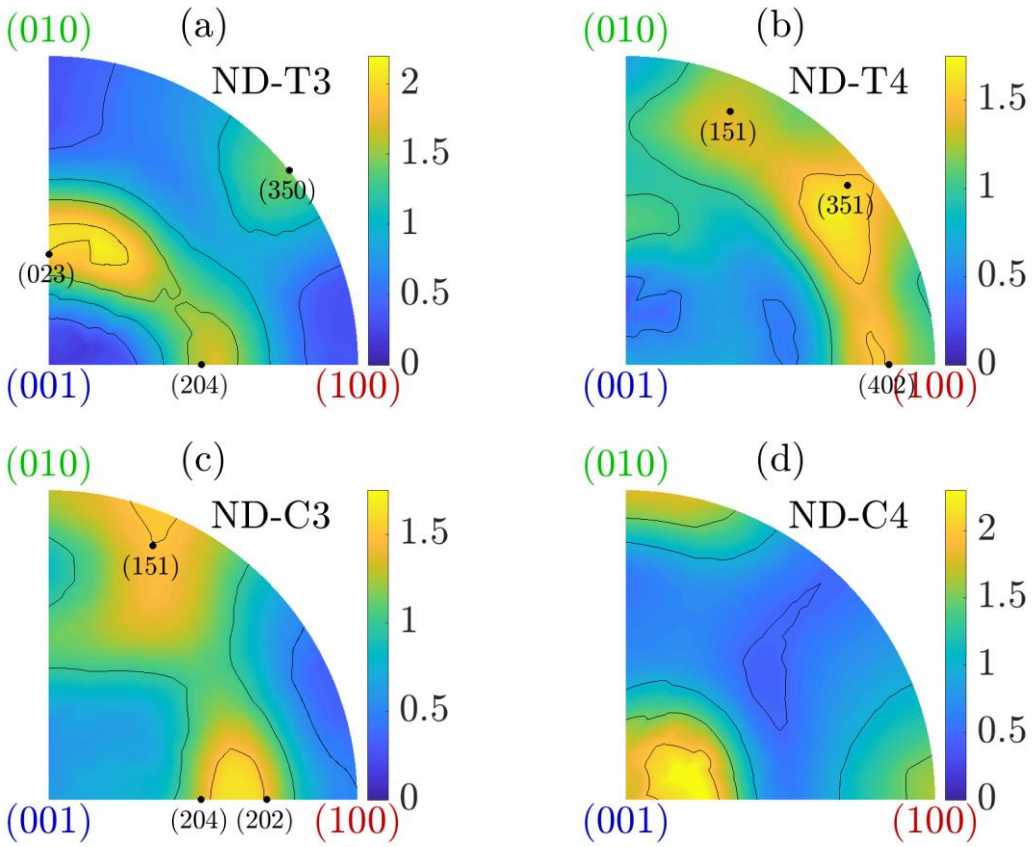


Figure 4.16. Inverse pole figures showing texture along the loading axis, for specimens (a) ND-T3, (b) ND-T4, (c) ND-C3, and (d) ND-C4. Colour scale is in multiples of random distribution (MRD), with a higher value (yellow) indicated a larger contribution of that orientation to the texture. Colour scale is different in each sub-figure to show the texture variation more clearly. Contour lines plotted at multiples of 0.5 MRD.

4.3.2 Macroscopic Behaviour

4.3.2.1 Flow Curves

Two strain measurements were performed during the test; with the extensometer and with DIC. The extensometer provided continuous measurement of the axial strain on the bottom surface of the specimen, averaged over the gauge length of 27.5 mm or 25 mm (section 4.2.2). DIC provided full-field measurement of axial (ε_{xx}), tangential (ε_{yy}), and shear (ε_{xy}) strains on the camera-facing surface, with a measurement taken every minute. Unlike the extensometer, the DIC data could be masked to restrict it to an area representative of the neutron gauge volume. In addition, since a grid of strain

Ministry of Defence © British Crown Copyright 2020/AWE

measurements is performed on each image, the spatial heterogeneity of deformation can be assessed. A more complete presentation of the strain fields is given in Appendix A6.1

A simple way to assess the deformation of a specimen is via its flow curve – the relationship between (engineering) stress and (engineering) strain during the test. Flow curves for the tensile and compressive specimens are plotted in figure 4.17 and figure 4.18 respectively. The extensometer strain is shown as a black line. Black dots depict the extensometer strain at the end of each neutron run, with blue circles showing the run-average DIC strain ($\varepsilon_{xx}^{\mathrm{DIC}}$), both plotted against the stress at the end of each run. Each unload is labelled with a letter, such that equivalent unloads can be identified despite having different DIC and extensometer strains.

Ministry of Defence © British Crown Copyright 2020/AWE

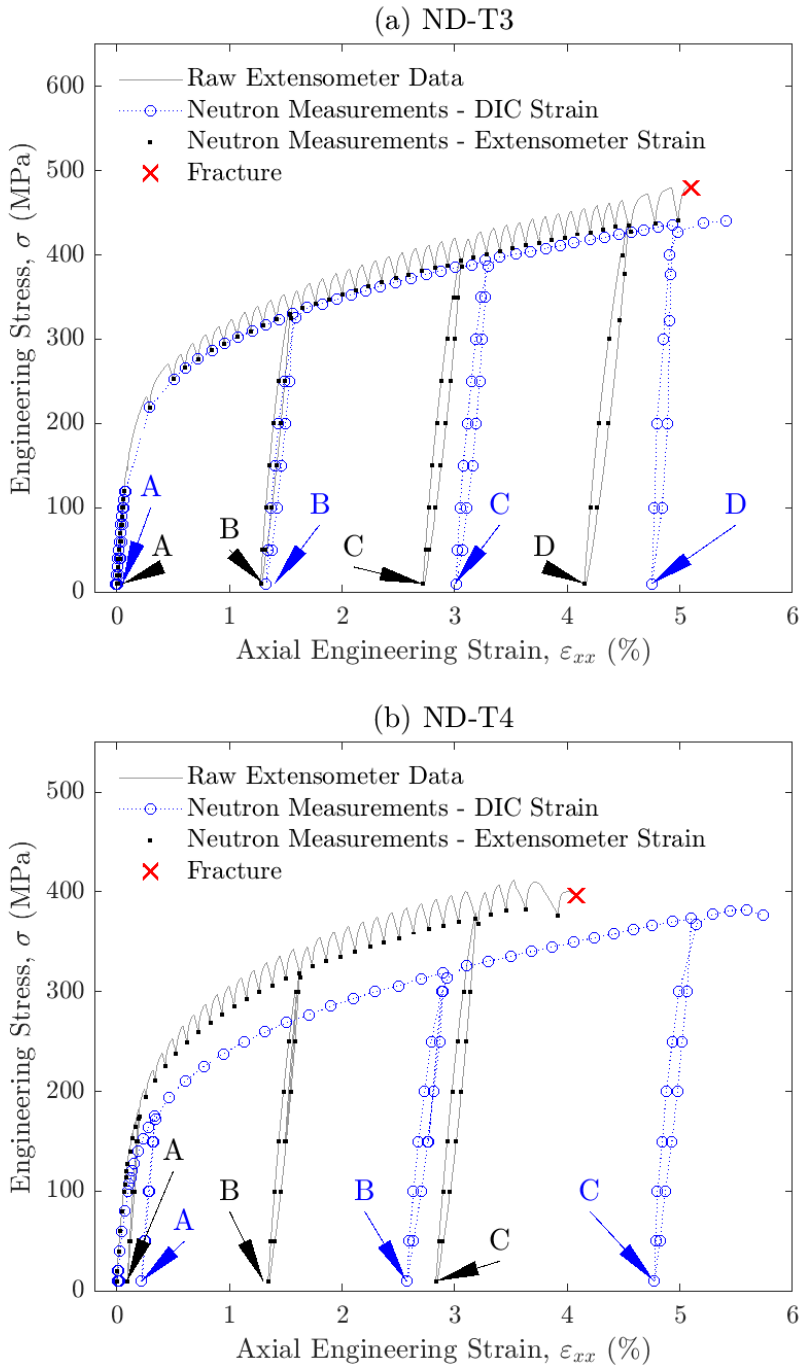


Figure 4.17. Flow curve for tensile specimens (a) ND-T3 and (b) ND-T4 tested on SMARTS. Engineering stress and extensometer strain at the end of each neutron measurement ('end-stress' & 'end-strain') is shown as black dots. The black solid line shows the continually-logged stress and extensometer strain. Stress relaxation can be observed during each scan as the saw-tooth profile. The fracture point is indicated by the red marker. The run-average axial strain measured by DIC is plotted against the end-stress as blue circles, with a blue dotted line added to guide the eye. The extensometer and DIC strains deviate from one another at high strains; equivalent data points at unload are labelled with letters ('A', 'B'… etc.).

Ministry of Defence © British Crown Copyright 2020/AWE

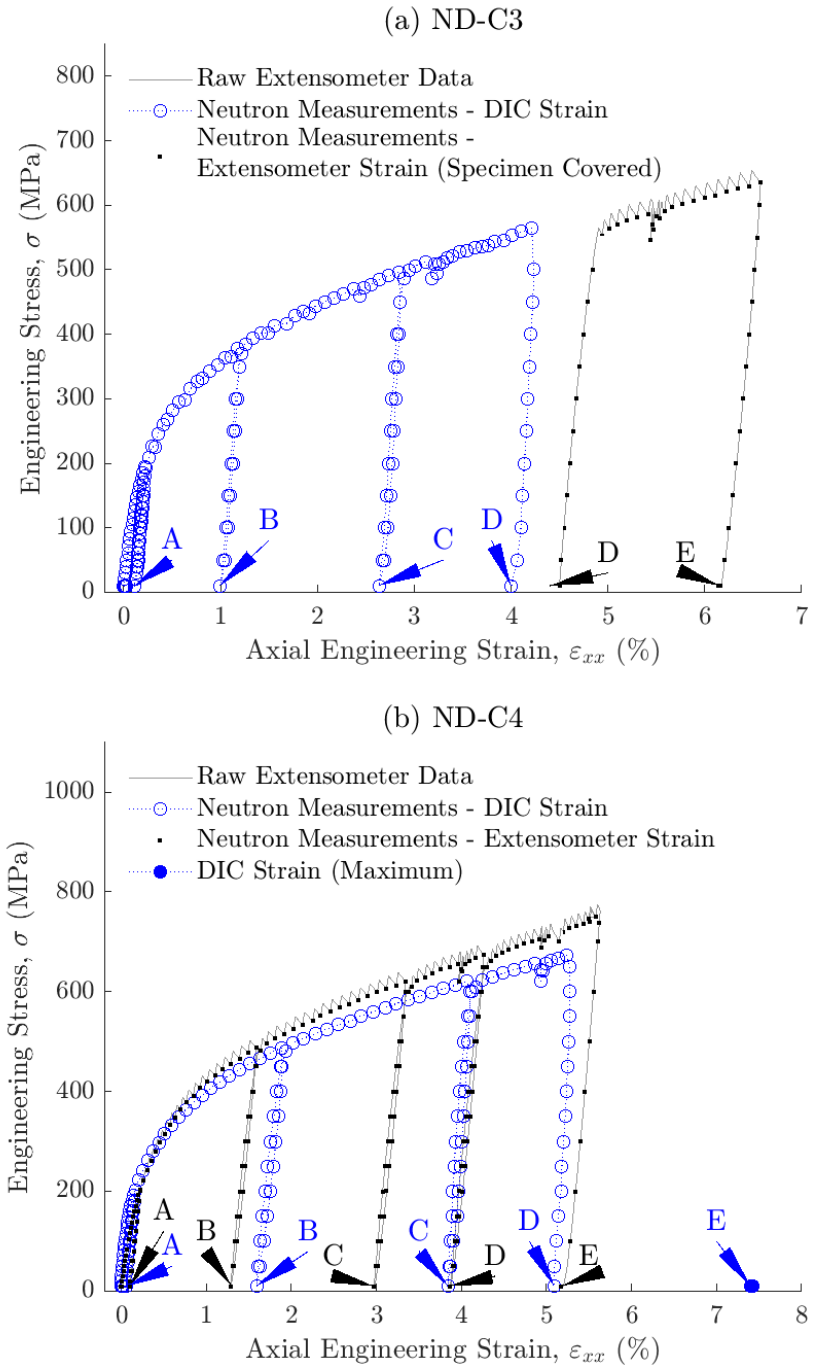


Figure 4.18. Flow curve for compression specimens (a) ND-C3 and (b) ND-C4 tested on SMARTS. Engineering stress and extensometer strain at the end of each neutron measurement ('end-stress' & 'end-strain') is shown as black dots. The black solid line shows the continually-logged stress and extensometer strain. Stress relaxation can be observed during each scan as the saw-tooth profile. The run-average axial strain measured by DIC is plotted against the end-stress as blue circles, with a blue dotted line added to guide the eye. The extensometer and DIC strains deviate from one another at high strains; equivalent data points at unload are labelled with letters ('A', 'B'… etc.). No DIC images were taken between unloads D and E as the aluminium box covered the specimen. Due to the repositioning of the extensometer, no DIC images were taken at unload E for specimen ND-C3.

Ministry of Defence © British Crown Copyright 2020/AWE

Specimen ND-T3

An incorrect position setpoint value was entered for the first measurement after the unload A - reload A cycle. This resulted in a large stress increase and the macroscopic yield point was passed so a neutron measurement could not be taken at the yield point. By inspection of the extensometer strain (figure 4.17(a)), yield occurs at approximately 170 MPa. During measurements after subsequent straining, whilst the specimen is at the yield surface, the specimen is held in position control. Stress relaxation can be seen as the saw-tooth profile in the continuously-logged extensometer strain.

Up to unload B, at approximately 1.5 % strain, the DIC and extensometer strains are in agreement. Subsequently, the DIC strain increases at a higher rate than the extensometer strain, such that the DIC strain is 15 % greater than the extensometer strain by unload D.

Fracture occurs at a stress of 480 MPa – the maximum stress obtained during the test – corresponding to a DIC strain of 5.4 %. Linear hardening is observed from 1.5 % strain to fracture.

Specimen ND-T4

In figure 4.17(b), the point of deviation from linearity is not distinct but occurs before 130 MPa. Strain concentrates at the centre of the gauge region (figure 4.19); by unload A the DIC strain is greater than the extensometer strain. A constant hardening rate is observed between 2 % and 5 % DIC strain. A slight reduction of stress from the maximum

Ministry of Defence © British Crown Copyright 2020/AWE

instantaneous stress of 412 MPa is seen before eventual fracture at 395 MPa. The DIC-measured strain at fracture (5.7 %) is 40 % larger than the extensometer strain at the same point (4.1 %)

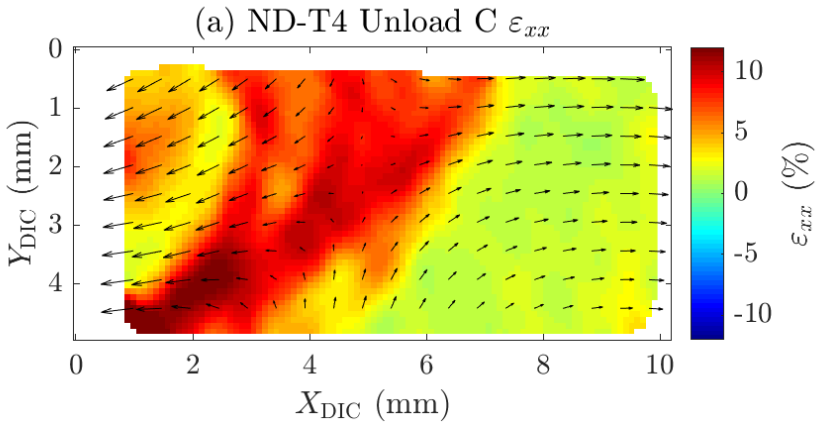


Figure 4.19. Axial strain field ε_{xx} on the surface at the centre of specimen ND-T4 at unload C, corresponding to a mean axial strain of 4.8 %. Positive strains are coloured in red, negative strains in blue. Arrows show the displacement of the specimen surface relative to the average motion (i.e. ignoring translational rigid body movement). Vector lengths are scaled to ensure visibility.

Specimen ND-C3

The extensometer data from the first compression specimen are not valid before unload D (figure 4.18) due to the attachment bands breaking (as described on page 107). DIC was not possible between unloads D and E due to the aluminium box being in place, so only the extensometer strain is available during this stage of the test. It is therefore not possible to compare DIC and extensometer strains.

The extensometer strain at unload D included disturbances from the breaking of the attachment bands and therefore its absolute value is not accurate. The extensometer strain between unloads D and E was used to estimate the corresponding DIC strain by assuming that hardening was linear throughout the test. The extensometer data (black)

Ministry of Defence © British Crown Copyright 2020/AWE

was scaled along the strain-axis such that its gradient during straining in position control was equal to the gradient of the DIC strain (blue) during straining between C and D. A constant strain offset was then applied to set the estimated strain at unload D equal to the DIC strain at the same point (4.0 %). This estimated DIC strain is shown in figure 4.20 and is used in all subsequent discussion of specimen ND-C3.

The specimen hardened until the final unload E was performed at a maximum stress of 653 MPa, at approximately 6.5 % strain.

Sudden reductions in stress of up to 40 MPa were observed at 3.2 % and 5.4 % strain. In each case, it took at least 3 subsequent straining steps before the stress recovered to the expected value. Inspection of the DIC-measured displacements and lattice strains (altered by changes in path length) yielded no evidence for the movement of the specimen at each of these points, and no subsequent explanation was found.

Specimen ND-C4

The final compression specimen yielded at approximately 100 MPa, and rapidly hardened to 500 MPa by 2 % DIC strain. The specimen hardened up to a maximum instantaneous stress of 771 MPa before unload E. Beyond unload A, the DIC strain was larger than that measured by the extensometer. Care was taken positioning the extensometer to enable a DIC measurement at unload E after removal of the containment box. This shows the final DIC strain of 7.4 % is 45 % larger in magnitude than the extensometer

Ministry of Defence © British Crown Copyright 2020/AWE

strain at end of the test. The aforementioned correction process was used to estimate the DIC strain between unloads D and E from the extensometer strains.

Comparison of Flow Curves

Figure 4.20 shows a comparison of the flow curves of the four specimens tested on SMARTS. Subfigure (a) shows the full range of strains and subfigure (b) focuses on the low-strain region. Differences in the responses of the tensile and compression specimens are apparent by 120 MPa. The tensile specimens are softer than the compression specimens and fracture between 5 % and 6 % strain. Both compression specimens harden faster than the tensile specimens. In every case, the elastic region is small, and an exact yield stress is difficult to determine from the flow curves. Specimen ND-T4 appears to yield first, by a low stress of 50 MPa.

Despite a large variation in texture between each sample, similarities can be seen between the macroscopic behaviour of the two compression specimens, and similarly between the two tensile specimens.

Figure 4.21 compares the DIC strain, averaged in the masked region at the centre of the specimen, and the extensometer strain, averaged along the 27.5 mm gauge length of the extensometer. In specimen ND-T3, where the strain concentration causing eventual fracture is outside the measurement region, the two measurements are approximately equal. Specimen ND-T4 has a strain concentration inside the DIC gauge volume, so the DIC strain is significantly larger than the extensometer strain.

Ministry of Defence © British Crown Copyright 2020/AWE

The similarity between the flow curves of ND-T3 and ND-T4 is therefore a result of heterogeneous strains in the DIC masked region, which biases the average.

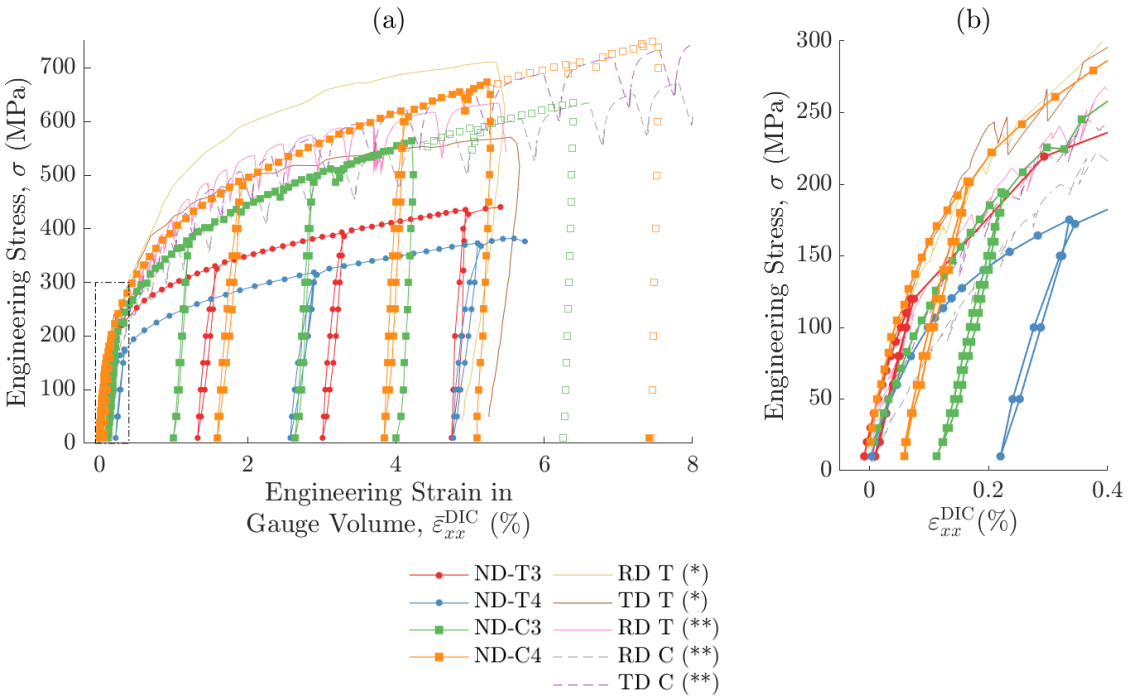


Figure 4.20. (a) Comparison of flow curves for the four specimens tested on SMARTS. Strains are the run-average gauge volume strains from DIC. Points marked by open circles are estimated from the extensometer strain whilst the aluminium containment box was in place (b) Close-up view of the elastic region showing the initial deviation from linearity. Data from the literature are shown for comparison, with Brown et al. [107] (*) performing tension along the rolling direction (RD) and transverse direction (TD) of rolled uranium plate. Calhoun et al. [45] (**) performed tension and compression along the RD and compression along the TD.

Ministry of Defence © British Crown Copyright 2020/AWE

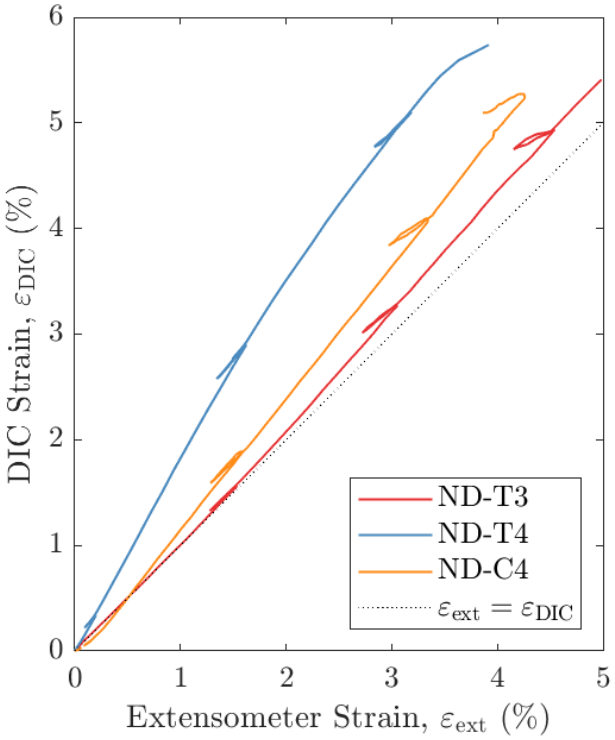


Figure 4.21. Comparison between DIC strain and the extensometer strain. Reliable extensometer data were not available for specimen ND-C3.

4.3.3 Texture Changes

As the specimen was deformed, the activation of plastic deformation modes led to changes in crystal orientation, detectable as a texture change within the neutron gauge volume. For each specimen, the texture change was calculated as the difference in texture from the reference IPF at the current specimen position, using the method described in section 4.2.7 on page 124.

In this section, texture change IPFs are plotted at a number of points during deformation; typically, at each of the unloads (B, C, D, etc.) and in the case of the tensile specimens, just before fracture. The texture change at unload shows just the effects of plastic deformation, and is not influenced by any elastic distortion or rotation

Ministry of Defence © British Crown Copyright 2020/AWE

that may occur under load. Each texture change IPF is coloured such that increases in texture are shown in red, decreases are shown in blue, and orientations with no change are in white.

The relative change in single-peak intensity is shown as a function of applied strain for each neutron measurement during loading at the yield surface (ignoring the intermediary unloads and re-loads). Data are presented for the 14 reflections on which single-peak fitting was performed (figure 4.13).

The value of the Rietveld preferred orientation parameter is also plotted as a function of strain, for the 13 unique crystal directions on which single-peak fitting was performed (the (020) and (040) reflections correspond to the same crystal direction). These are the same data as plotted on the IPFs, with a better strain resolution to allow trends to be identified.

Ministry of Defence © British Crown Copyright 2020/AWE

4.3.3.1 Specimen ND-T3

Rietveld Texture Changes

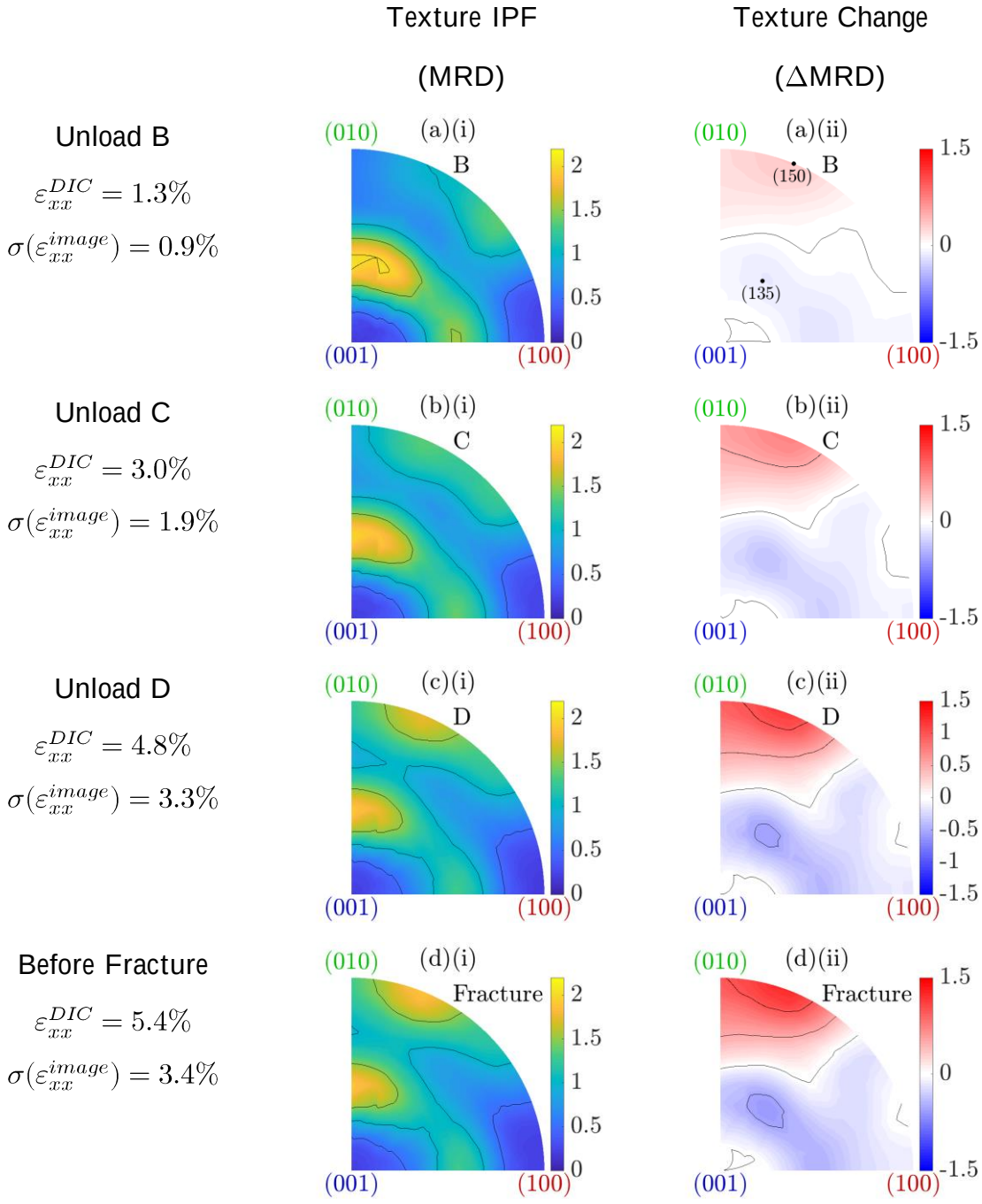


Figure 4.22. Texture changes in specimen ND-T3. (i) Axial texture along the loading axis (MRD). (ii) Changes in the axial texture at (a) unload B, (b) unload C, (c) unload D, and (d) at load before fracture. For each selected dataset, the run-average DIC axial strain is shown in the left hand column alongside the run-average image standard deviation (the mean value of the standard deviation of strain across each image, with the mean taken over all images acquired during that particular neutron measurement).

Ministry of Defence © British Crown Copyright 2020/AWE

Figure 4.22 shows a decrease in texture occurs near (135), the location of maximum initial texture, with a corresponding increases near (150). This is visible by the second unload, B, then strengthens in intensity as the plastic strain increases, with a maximum increase of 1.25 MRD just before fracture. The contour line between positive and negative texture change remains in the same location throughout the experiment.

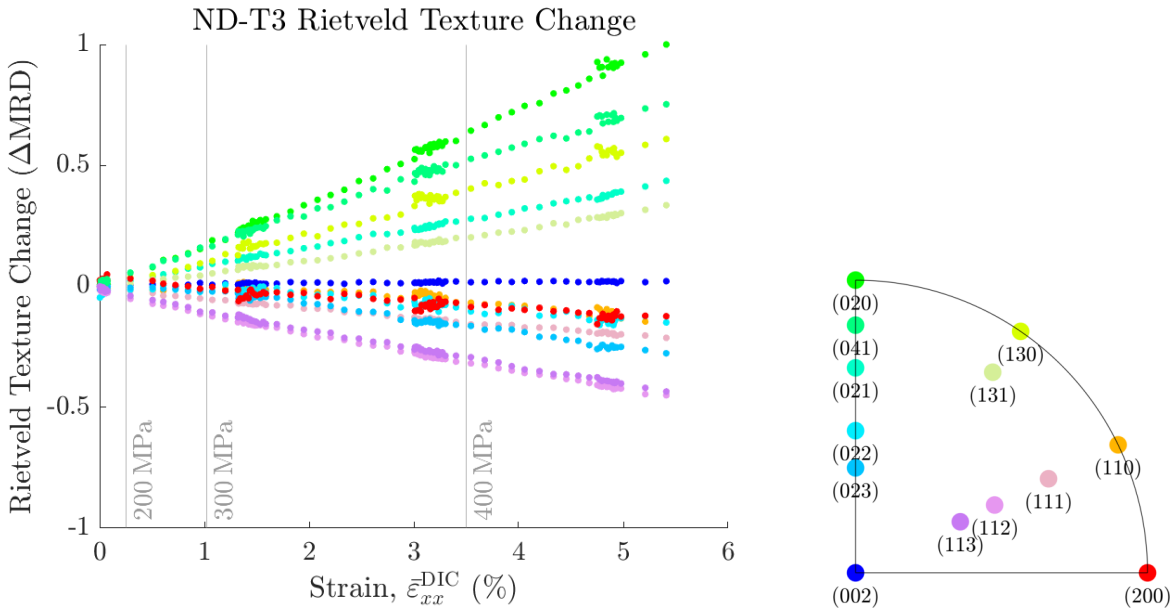


Figure 4.23. Absolute change in the Rietveld preferred orientation factor as a function of strain, for the 13 reflections from specimen ND-T3 shown in the inverse pole figure to the right of the figure. Each reflection is colour coded according to its crystal orientation.

Figure 4.23 shows a linear dependency of Rietveld texture change with applied strain. No texture change was observed along (002). Out of the 13 selected orientations, the largest increase was along (020), which increased by 1 MRD by fracture. The magnitude of the largest decrease, along (112), was smaller at 0.4 MRD.

Clusters of points at 1.4 %, 3.1% and 4.9% strain are those taken during the unload/reload cycle. In general the measured texture changes persist during unloading,

Ministry of Defence © British Crown Copyright 2020/AWE

with slight decreases in texture magnitude seen for all orientations, at a gradient identical to that during loading.

Single Peak Intensity Changes

There is a correlation between the single-peak intensity changes in figure 4.24 and the Rietveld texture changes in figure 4.23. The reflections plotted in green, near (020), increase whilst blue and purple decrease. The (002) reflection has a constant intensity throughout.

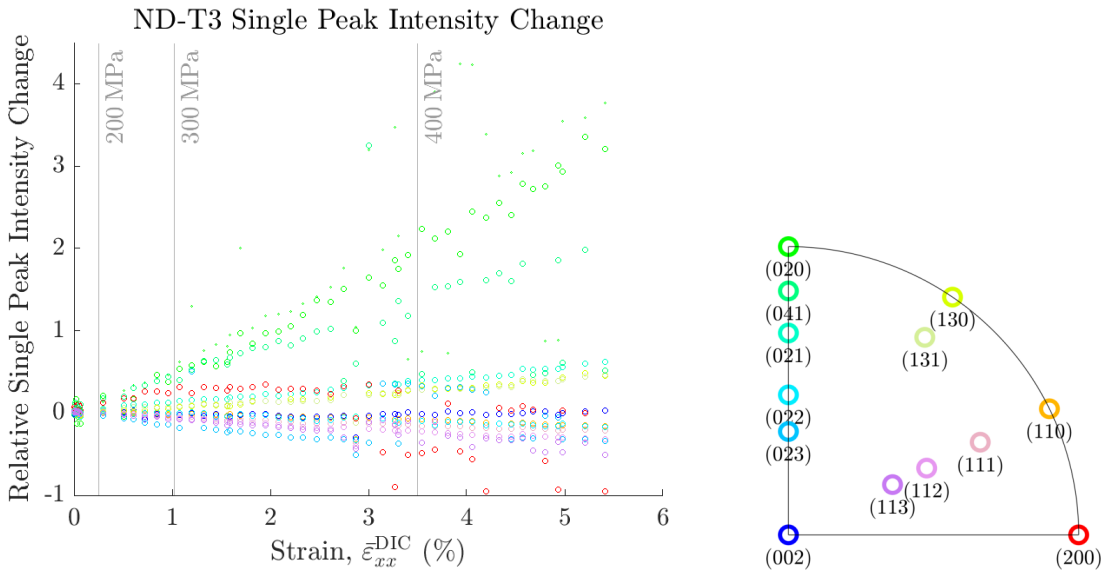


Figure 4.24. Relative change in the single-peak intensities as a function of strain, for the 14 reflections from specimen ND-T3 shown in the inverse pole figure to the right of the figure. Each reflection is colour coded according to its crystal orientation. (040) is shown with smaller markers. Only measurements during loading are shown.

The response of most reflections is linear, although the rate of (020) peak intensity gain slightly increases with strain. There is more scatter in the single-peak intensity changes than in the Rietveld texture changes.

Ministry of Defence © British Crown Copyright 2020/AWE

Compared to the response of the other reflections, the (020) peak intensity increases much faster than calculated from the Rietveld refinement – the (020) intensity increase is over 6 times the magnitude of the (112) decrease, compared to 2.3 times in the Rietveld textures.

4.3.3.2 Specimen ND-T4

Rietveld Texture Changes

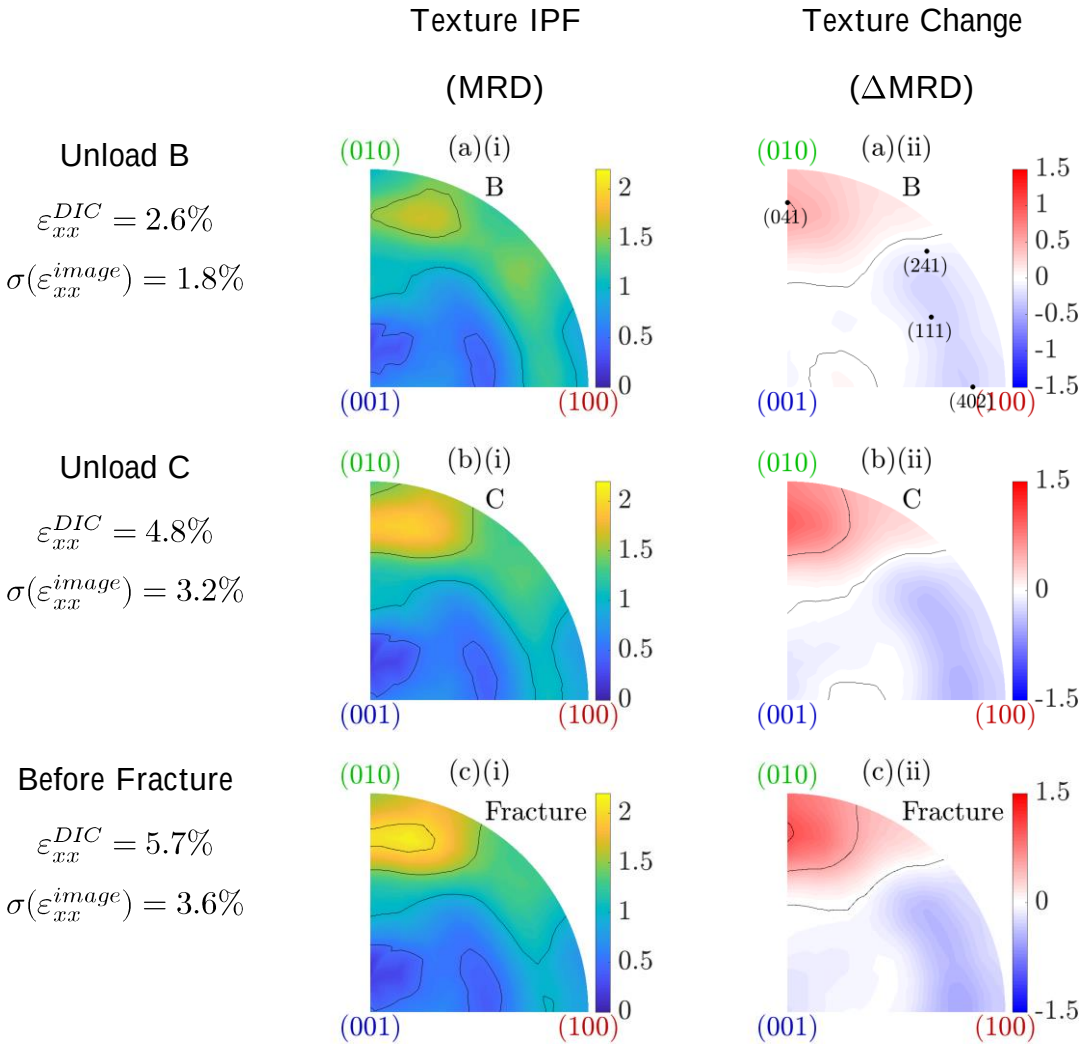


Figure 4.25. Texture changes in specimen ND-T4. (i) Axial texture along the loading axis (MRD). (ii) Changes in the axial texture at (a) unload B, (b) unload C, and (c) at load before fracture. For each selected dataset, the run-average DIC axial strain is shown in the left hand column alongside the run-average image standard deviation (the mean value of the standard deviation of strain across each image, with the mean taken over all images acquired during that particular neutron measurement).

Ministry of Defence © British Crown Copyright 2020/AWE

Figure 4.25 shows that the texture increase in specimen ND-T4 is concentrated in the region of highest starting texture, which increases by 1 MRD by the point of fracture. A corresponding decrease of 0.5 MRD is observed between (241) and (402). The shape of the contour between regions of texture increase and decrease is similar to the equivalent contour in specimen ND-T3.

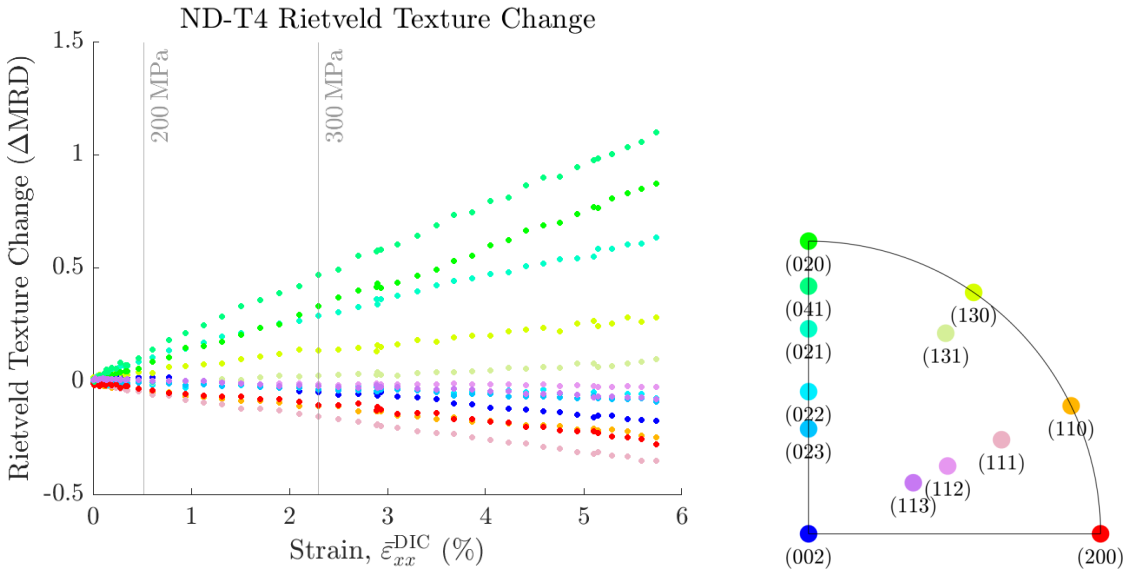


Figure 4.26. Absolute change in the Rietveld preferred orientation factor as a function of strain, for the 13 reflections from specimen ND-T4 shown in the inverse pole figure to the right of the figure. Each reflection is colour coded according to its crystal orientation. Only measurements during loading are shown.

Again, there is a linear change of texture with applied strain (figure 4.26). At the point of fracture, the largest increase is along (041), of 1.1 MRD, and the largest decrease is along (111). In this case, the (002) texture decreases throughout the test.

Ministry of Defence © British Crown Copyright 2020/AWE

Single Peak Intensity Changes

The relative single-peak intensity changes in figure 4.27 depend linearly on the strain, and have similar relative magnitudes to the Rietveld texture changes.

The (130) and (131) peak intensities decrease whilst their corresponding Rietveld textures increase. The largest relative single-peak intensity decrease was in the (200) reflection, which lost 40 % of its intensity by the point of fracture.

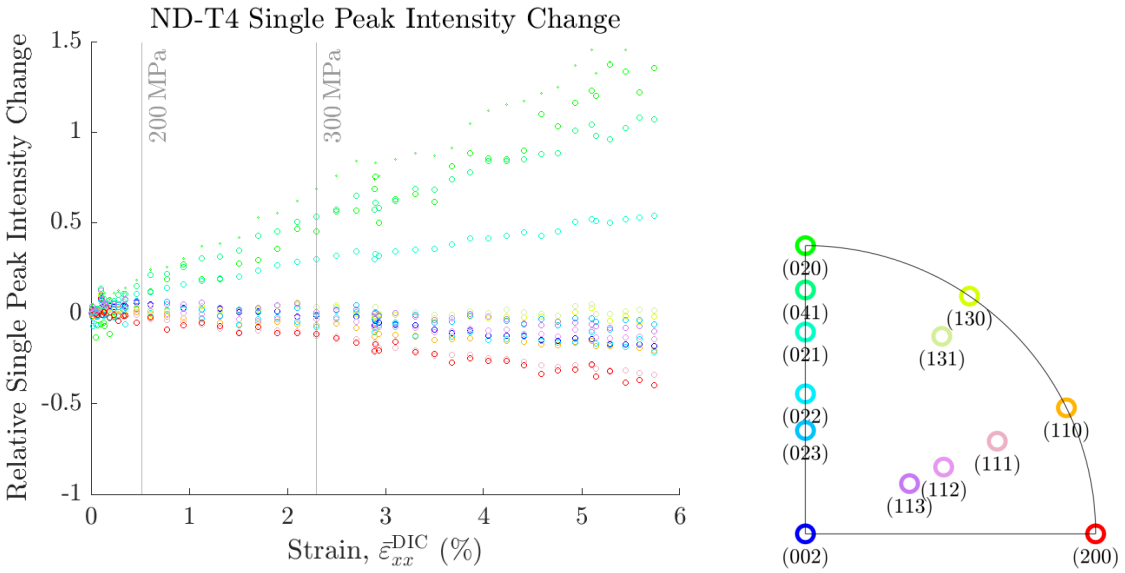


Figure 4.27. Relative change in the single-peak intensities as a function of strain, for the 14 reflections from specimen ND-T4 shown in the inverse pole figure to the right of the figure. Each reflection is colour coded according to its crystal orientation. (040) is shown with smaller markers. Only measurements during loading are shown.

Ministry of Defence © British Crown Copyright 2020/AWE

4.3.3.3 Specimen ND-C3

Rietveld Texture Changes

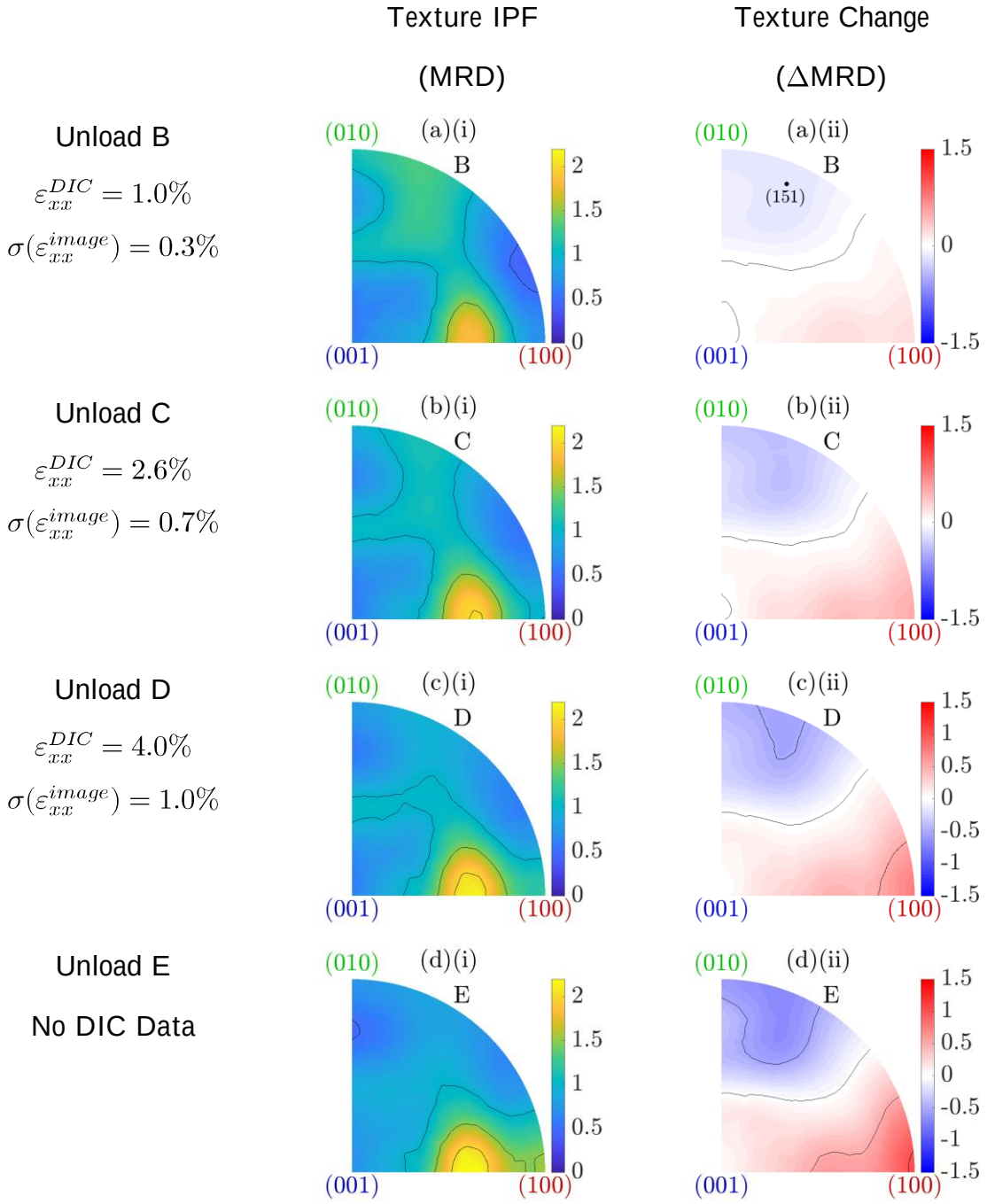


Figure 4.28. Texture changes in specimen ND-C3. (i) Axial texture along the loading axis (MRD). (ii) Changes in the axial texture at (a) unload B, (b) unload C, (c) unload D, and (d) unload E. For each selected dataset, the run-average DIC axial strain is shown in the left hand column alongside the run-average image standard deviation (the mean value of the standard deviation of strain across each image, with the mean taken over all images acquired during that particular neutron measurement).

Ministry of Defence © British Crown Copyright 2020/AWE

There is a significant difference between the texture changes in tension and compression. A decrease in texture is observed in figure 4.28 in the top region of the inverse pole figure, near (010). The maximum decrease was near (151), of 0.7 MRD, with the initial texture component in this direction nearly disappearing. Increases were seen between (001) and (100), with the largest increase of 1 MRD along (100).

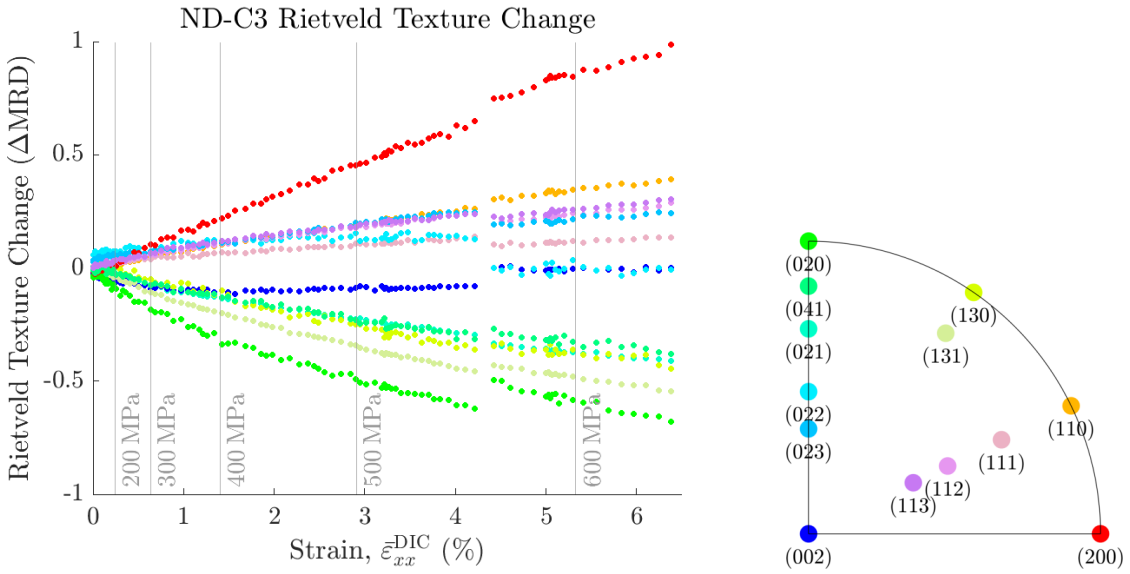


Figure 4.29. Absolute change in the Rietveld preferred orientation factor as a function of strain, for the 13 reflections from specimen ND-C3 shown in the inverse pole figure to the right of the figure. Each reflection is colour coded according to its crystal orientation. Only measurements during loading are shown.

A discontinuity in the Rietveld texture changes (figure 4.29) is visible at 4.2 % strain. This was seen to coincide with the addition of the aluminium containment box, and after its removal at unload E, the specimen was seen to have moved by approximately 1 mm in the *x*-direction. This would have moved the gauge volume in the specimen and the associated change in the diffracting orientations would change the peak intensities.

Ministry of Defence © British Crown Copyright 2020/AWE

The texture in the (200) orientation increases linearly with strain, gaining 1 MRD by 6 % strain. Orientations near (020), coloured green, decrease at a rate that reduces with strain.

Single Peak Intensity Changes

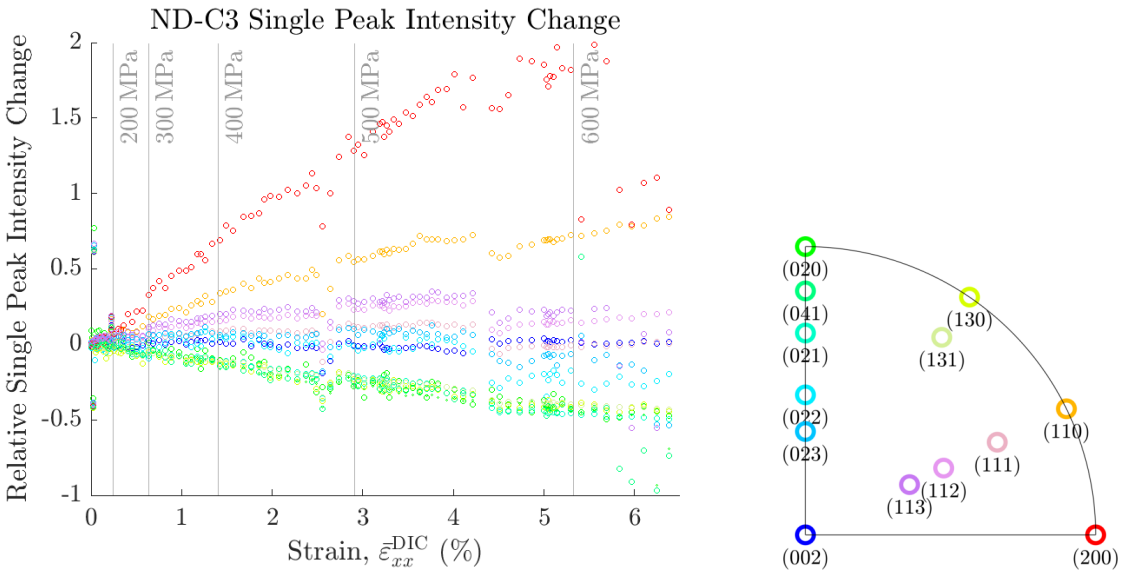


Figure 4.30. Relative change in the single-peak intensities as a function of strain, for the 14 reflections from specimen ND-C3 shown in the inverse pole figure to the right of the figure. Each reflection is colour coded according to its crystal orientation. (040) is shown with smaller markers. Only measurements during loading are shown.

The single-peak intensities change linearly with applied strain. Relative to the other reflections, the (200) intensity increases at a higher rate. The orange (110) reflection increases in intensity more than the light blue/purple reflections, unlike in the Rietveld refinement where the textures change by a similar amount.

Ministry of Defence © British Crown Copyright 2020/AWE

4.3.3.4 Specimen ND-C4

Rietveld Texture Changes

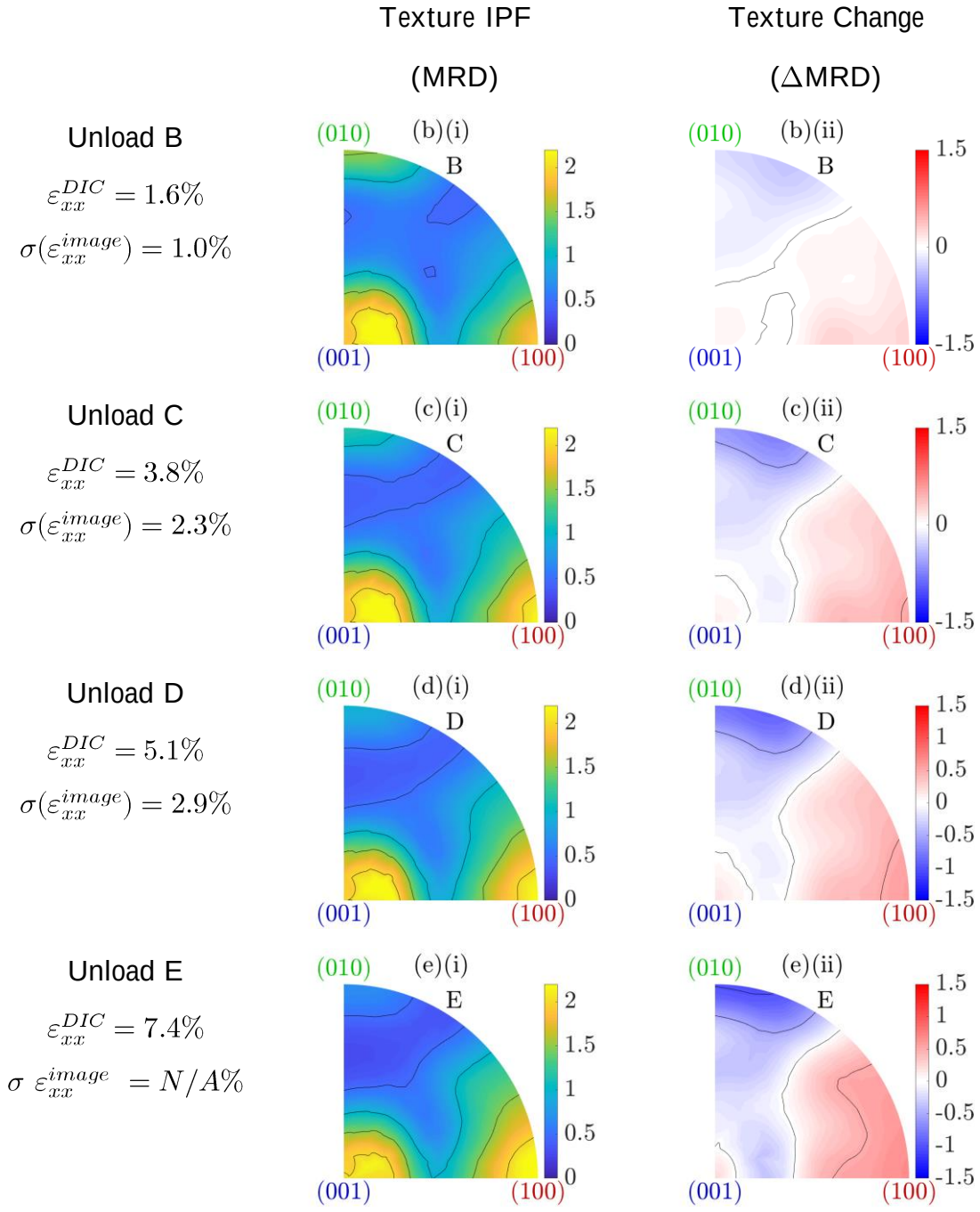


Figure 4.31. Texture changes in specimen ND-C4. (i) Axial texture along the loading axis (MRD). (ii) Changes in the axial texture at (a) unload B, (b) unload C, (c) unload D, and (d) unload E. For each selected dataset, the run-average DIC axial strain is shown in the left hand column alongside the run-average image standard deviation (the mean value of the standard deviation of strain across each image, with the mean taken over all images acquired during that particular neutron measurement).

Ministry of Defence © British Crown Copyright 2020/AWE

In a similar way to the first compression specimen, specimen ND-C4 (figure 4.31) exhibited decreases in texture near (010), and increases near (100). Whilst the (001) direction itself saw an increase in texture, orientations angled between 5° and 20° from (001) decreased in texture.

At the start of the test, the texture along (001) was greater than that along (100); by 7.4 % strain at the end of the test the latter had increased such that the orientations had equal contributions.

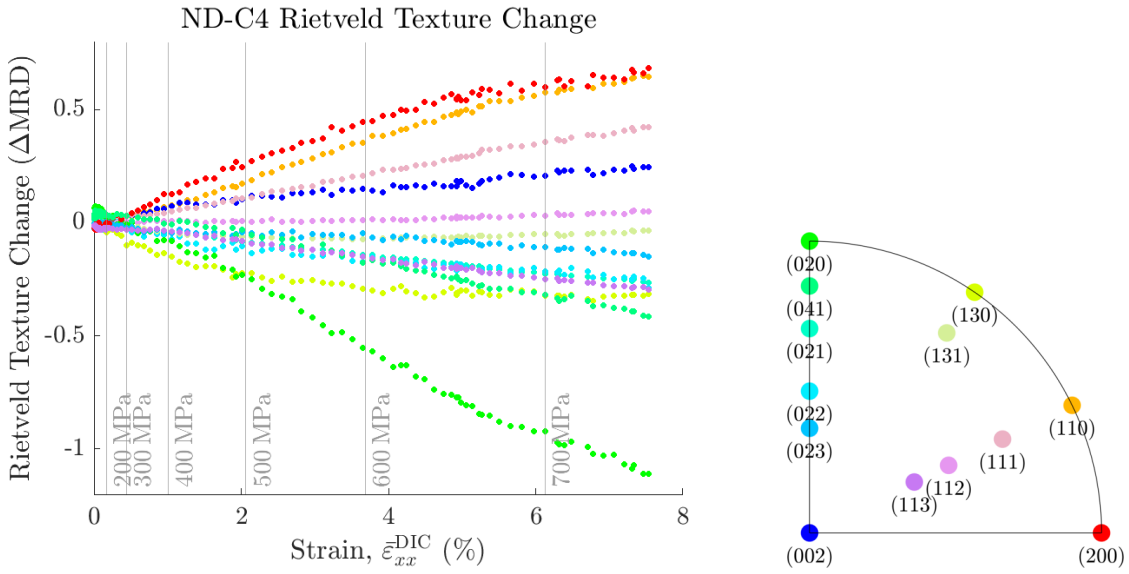


Figure 4.32. Absolute change in the Rietveld preferred orientation factor as a function of strain, for the 13 reflections from specimen ND-C4 shown in the inverse pole figure to the right of the figure. Each reflection is colour coded according to its crystal orientation.

(200) sees the largest increase, of 0.7 MRD, whilst (020) sees a considerably larger decrease of 1.1 MRD. Some of the increases, such as those along (110) and (111), are mostly linear with strain whilst along (200) and (002) the rate of increase decreases with strain.

Ministry of Defence © British Crown Copyright 2020/AWE

Most decreases are linear, with a couple of exceptions. After an initial decrease, the rate of decrease of the (130) and (131) textures reduces, and after 4 % strain no further change is observed. The (020) texture change is linear until 5 % strain and then continues to decrease with a shallower gradient until the end of the test. Since this change in gradient is clearly seen in other directions, such as (200) and (110), it is possible that this change in gradient is an artefact of the DIC strain estimation necessary due to the addition of the containment box.

Single Peak Intensity Changes

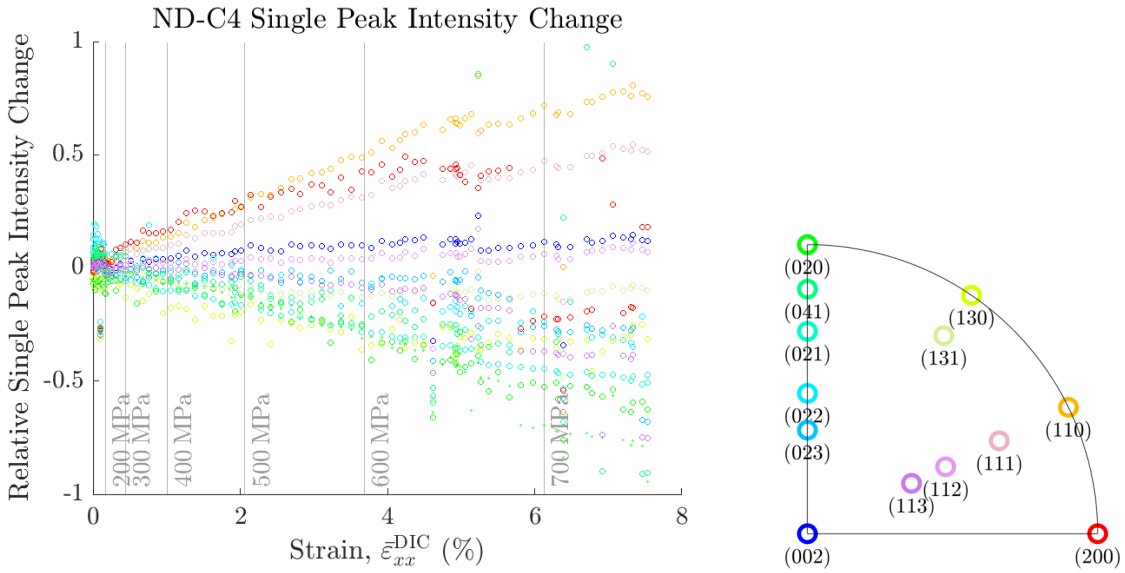


Figure 4.33. Relative change in the single-peak intensities as a function of strain, for the 14 reflections from specimen ND-C4 shown in the inverse pole figure to the right of the figure. Each reflection is colour coded according to its crystal orientation. (040) is shown with smaller markers.

The majority of the single peak intensities in specimen ND-C4 change linearly with strain. Similarly to the Rietveld texture changes, no change in (130) and (131) peak intensity is observed after 4 % strain. The sudden change in (200) peak intensity at the

Ministry of Defence © British Crown Copyright 2020/AWE

end of the test is attributable to poor fitting statistics – very large fitting errors were obtained for the (200) reflection for spectra taken above 4.5 % strain.

4.3.3.5 Summary of Texture Changes

The majority of orientations showed a linear change in texture with applied strain. Good correlation was seen between the changes in single-peak intensity and the texture change along the corresponding direction in the Rietveld refinement. For certain peaks, such as the (020) in ND-T3, and the (200) in ND-C3, the single-peak response was much stronger than seen in the Rietveld textures.

In general, the tensile specimens saw increases in texture near (010) and decreases near (100), whist the inverse was seen for specimens tested in compression. In all specimens, the texture along (001) either did not change or changed very weakly.

4.3.4 Lattice Strain Development

As load is applied to a specimen, the individual grains will deform elastically until the local stress exceeds the critical stress for the activation of a particular deformation mode. At this point, the elastic strain in this grain will cease to increase as further deformation is accommodated by plasticity. As deformation proceeds, the stress required for further deformation may increase (due to forest hardening of dislocations, for example), and since the elastic lattice strain is directly proportional to the local normal stress, the measured lattice strain would also increase.

Ministry of Defence © British Crown Copyright 2020/AWE

The measured (*hkl*) lattice strain is an average of the lattice strains in the (*hkl*) family of grains, therefore if only a subset of these grains actually yield, the measured saturation of strain will be less distinct.

The Rietveld refinement fits a single set of unit cell parameters - *a*, *b*, and *c* - to the entire spectrum. This represents the 'best-fit' unit cell dimensions across all the diffracting grains (those whose diffraction vector lies parallel to the loading direction).

4.3.4.1 Lattice Strain

In this section, the single-peak lattice strains and Rietveld lattice parameter strains are plotted as a function of applied stress, in a similar manner to the ENGIN-X data in figure 3.2 on page 74.

Ministry of Defence © British Crown Copyright 2020/AWE

Specimen ND-T3

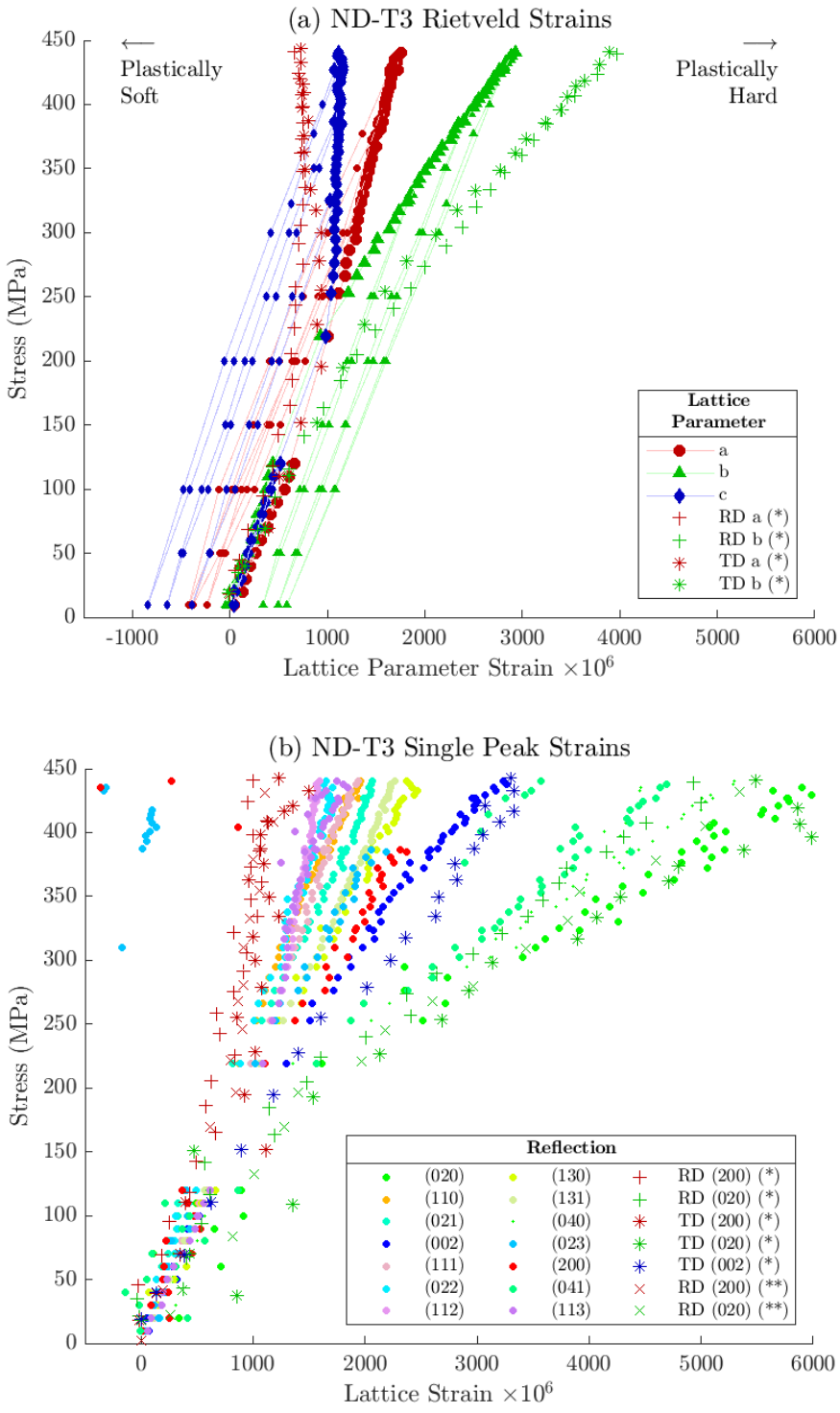


Figure 4.34. (a) Rietveld lattice parameter strains and (b) single-peak strains as a function of applied stress for specimen ND-T3. Measurements taken during unload-reload cycles are omitted from the single-peak data. Reflections are coloured according to their orientation. Data from the literature are shown for comparison, with Brown et al. [107] (*) performing tension along the rolling direction (RD) and transverse direction (TD) of rolled uranium plate. Calhoun et al. [45] (**) performed tension along the RD.

Ministry of Defence © British Crown Copyright 2020/AWE

The lattice parameter strains in specimen ND-T3 (figure 4.34(a)) are linear up to 120 MPa, indicative of elastic deformation. In this region, the *a*-parameter strains have a lower gradient than those of the other two parameters. Data were not collected between 120 MPa to 220 MPa. All 3 lattice parameter strains have the same value at 220 MPa.

From this point, the lattice parameter strains diverge linearly. The strain on the c-parameter saturates completely, the b-parameter takes up a higher strain, and the *a*-parameter sees a slight decrease in strain compared to what would be expected from extrapolation of the elastic region.

Figure 4.34(b) shows the lattice strains along the three principal crystal directions (200), (020) and (002) take up more strain after yield. The (020)-oriented grains see a large increase of strain, reaching 6000 microstrain at the maximum stress of 440 MPa. The reflections near (112), coloured light blue/purple, see partial saturation of strain, with the rate of strain accumulation with stress decreasing after yield.

Above 390 MPa, large scatter is seen in the (200) and (023) strains.

Ministry of Defence © British Crown Copyright 2020/AWE

Specimen ND-T4

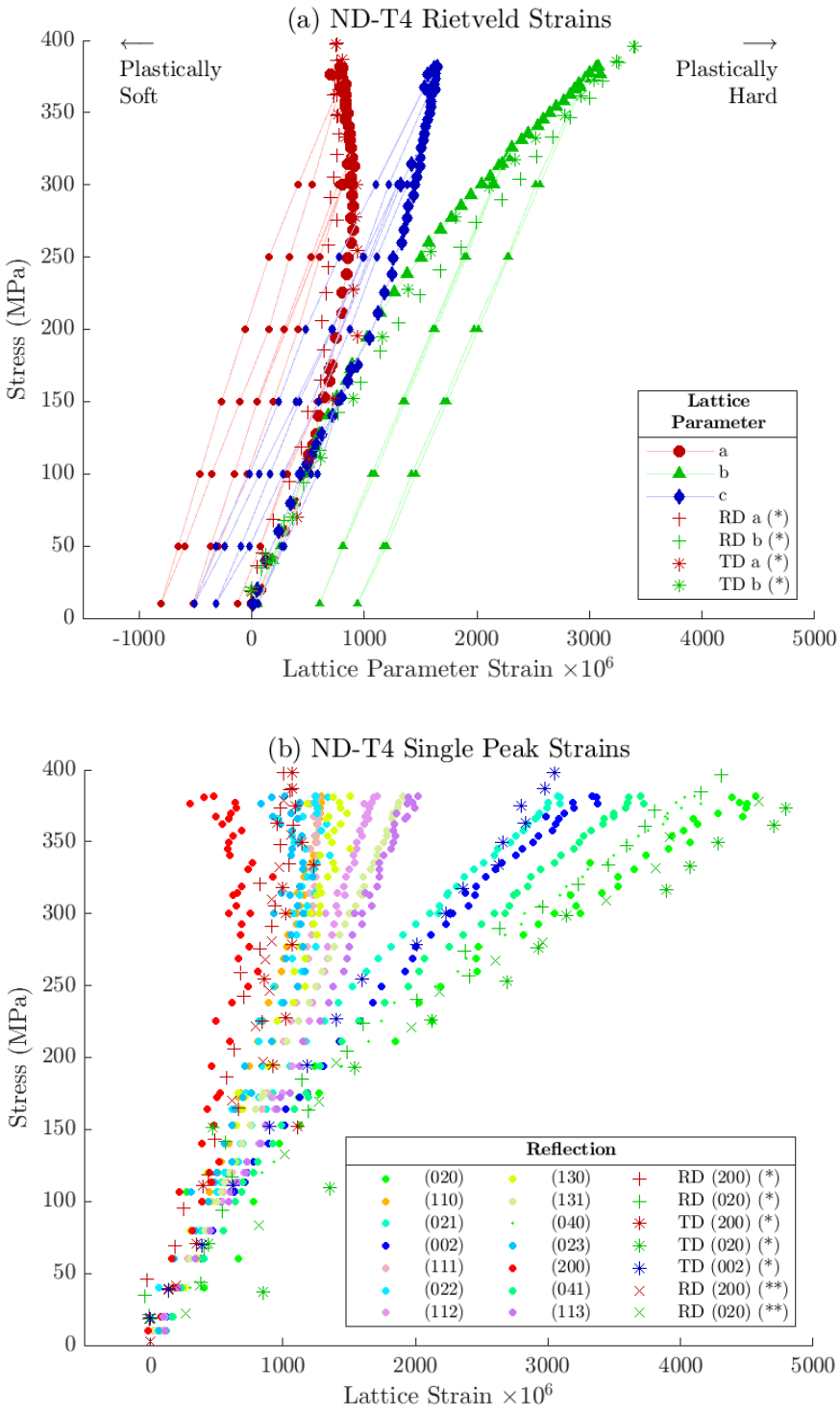


Figure 4.35. (a) Rietveld lattice parameter strains and (b) single-peak strains as a function of applied stress for specimen ND-T4. Measurements taken during unload-reload cycles are omitted from the single-peak data. Reflections are coloured according to their orientation. Data from the literature are shown for comparison, with Brown et al. [107] (*) performing tension along the rolling direction (RD) and transverse direction (TD) of rolled uranium plate. Calhoun et al. [45] (**) performed tension along the RD.

Ministry of Defence © British Crown Copyright 2020/AWE

Specimen ND-T4 behaves linear-elastically until 120 MPa (figure 4.35(a)), with all three lattice parameters showing a similar gradient. At higher stresses, the *a*-parameter steadily saturates until 250 MPa where the strain reaches a maximum value of 880 microstrain. As the stress is increased further, the *a*-parameter strain decreases. By the last measurement before fracture, a decrease of 100 microstrain was observed. The *b*-parameter is the most compliant, whilst the *c*-parameter follows the *b*-parameter until 200 MPa after which it steadily saturates.

The lattice strains in figure 4.35(b) show variability in their elastic gradients and begin to significantly diverge at 150 MPa. The smallest strain is carried by grains in the (200) orientation, and this strain reduces after 250 MPa in a similar manner to the *a*-parameter strains. The (020)- and (040)-oriented grains carry the highest strain, and therefore the highest stress. Unlike the *b* and *c*-parameters strains, which diverge considerably, the (020) and (002) reflections behave similarly across the whole stress range

Above 250 MPa there is clear separation between the grain families in which the elastic strains are saturating and those which are taking up a larger fraction of the stress.

Ministry of Defence © British Crown Copyright 2020/AWE

Specimen ND-C3

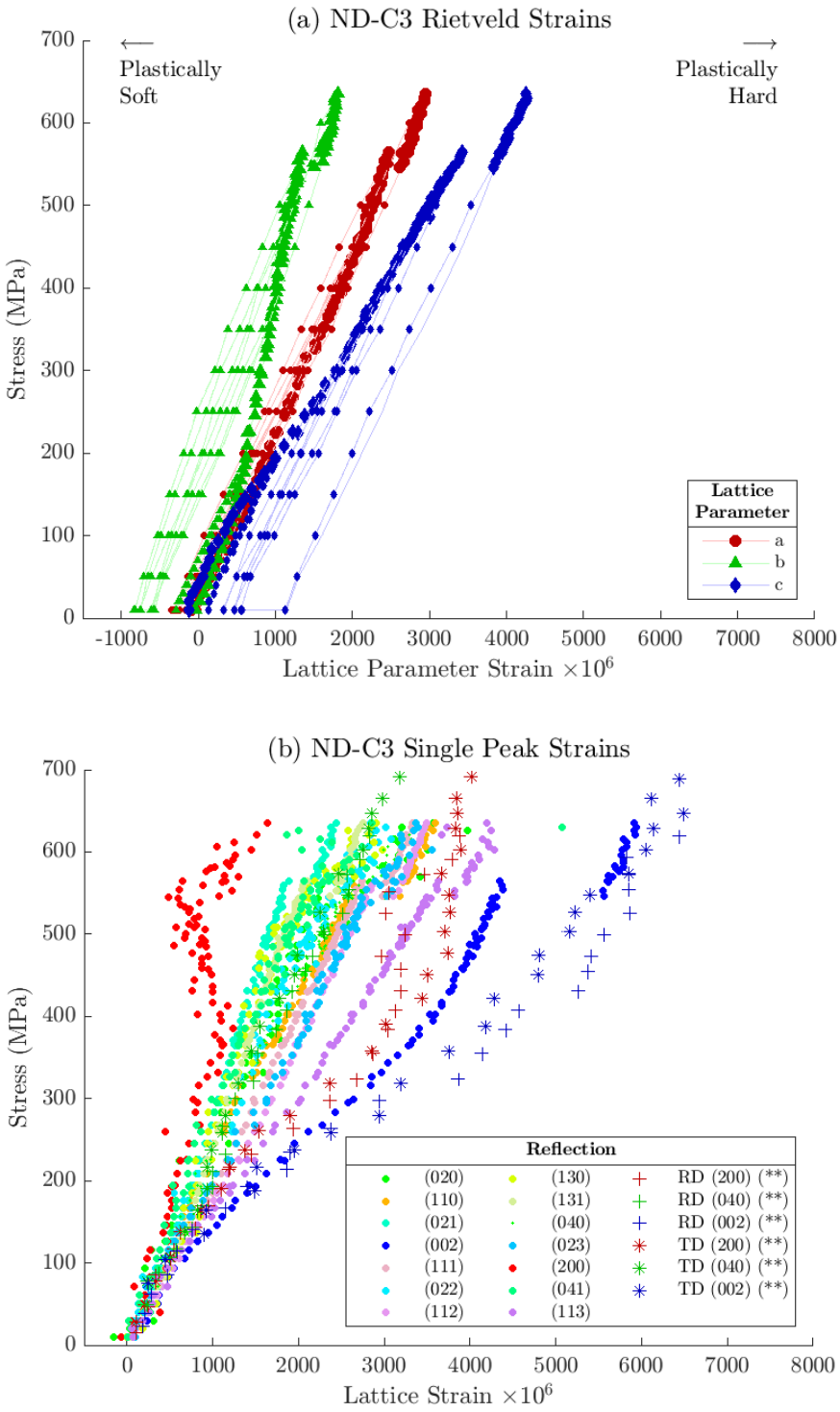


Figure 4.36. (a) Rietveld lattice parameter strains and (b) single-peak strains as a function of applied stress for specimen ND-C3. Compressive strains are plotted as positive for comparison with the tensile specimens. Measurements taken during unload-reload cycles are omitted from the single-peak data. Reflections are coloured according to their orientation. Data from the literature are shown for comparison; Calhoun et al. [45] (**) performed compression along the RD and TD.

Ministry of Defence © British Crown Copyright 2020/AWE

In the first compression specimen, the lattice parameter strains deviate from linearity at 120 MPa (figure 4.36(a)). The specimen movement as the box was added shifts the lattice strain for stresses above 550 MPa. The measured lattice parameter strains increased by approximately 350 microstrain. The increase in lattice parameter strain was caused by an increase in the measured d-spacings, which by inspection of the time-of-flight equation [8.6], must be due to a reduction in the neutron path length between source and detector. This would correspond to the specimen moving in the positive *x*-direction, towards the detector (see figure 4.1). After the test, specimen ND-C3 was translated in the *x*-direction and neutron spectra recorded at 0.2 mm intervals from $x = 0$ mm to $x = 1.4$ mm. The measured shift in the lattice parameter strains is shown in figure 4.37.

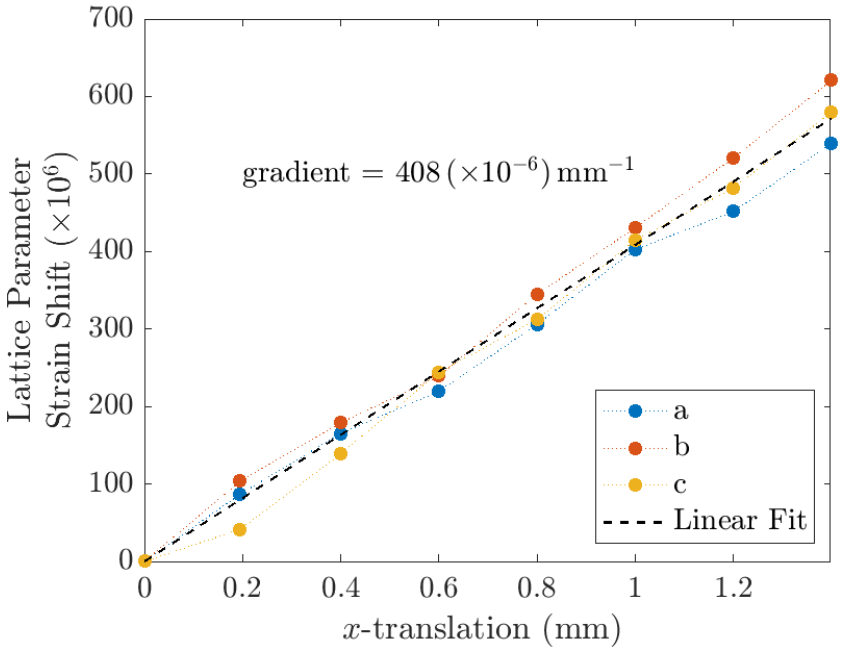


Figure 4.37. Shift in lattice parameter strain during translation of specimen ND-C3 in the x^+ direction.

Calculation of the linear best-fit line through the data allows us to estimate that a specimen displacement of 0.86 mm would have been necessary to cause the observed

Ministry of Defence © British Crown Copyright 2020/AWE

strain shifts. The specimen displacement was estimated by eye at approximately $x = +0.8$ mm during the experiment, consistent with the predictions.

Whist the lattice parameter strains appear to just be shifted by this movement, the single-peak strains appear to behave very differently after this point, likely due to the change in gauge volume strongly affecting the limited number of grains contributing to each reflection. As such, the single-peak strains at stresses above 550 MPa are ignored in the subsequent analysis.

As the stress is increased, the rate of accumulation of *a*-parameter strains decreases once at 120 MPa, and then decreases further at 450 MPa, with a linear response in between. After yield, the increase of *b*-parameter strain is linear with stress, at a rate lower than in the elastic region. The *c*-parameter strain accumulates more quickly between 120 MPa and 300 MPa, after which the curve runs parallel to the elastic region.

Above the yield stress, the (002) strains in figure 4.36(b) increase more quickly before a similar reduction in accumulation rate at 400 MPa. The (113) strains follow a similar, but less extreme path as the (002) strains. The (200) strains behave in an unusual manner, being completely linear until 370 MPa above which a sudden reduction in strain is observed, the strains almost reducing back to zero at the point of specimen movement at 550 MPa.

The other reflections have an approximately linear response, carrying between 2000 and 3000 microstrain by 550 MPa.

Ministry of Defence © British Crown Copyright 2020/AWE

Specimen ND-C4

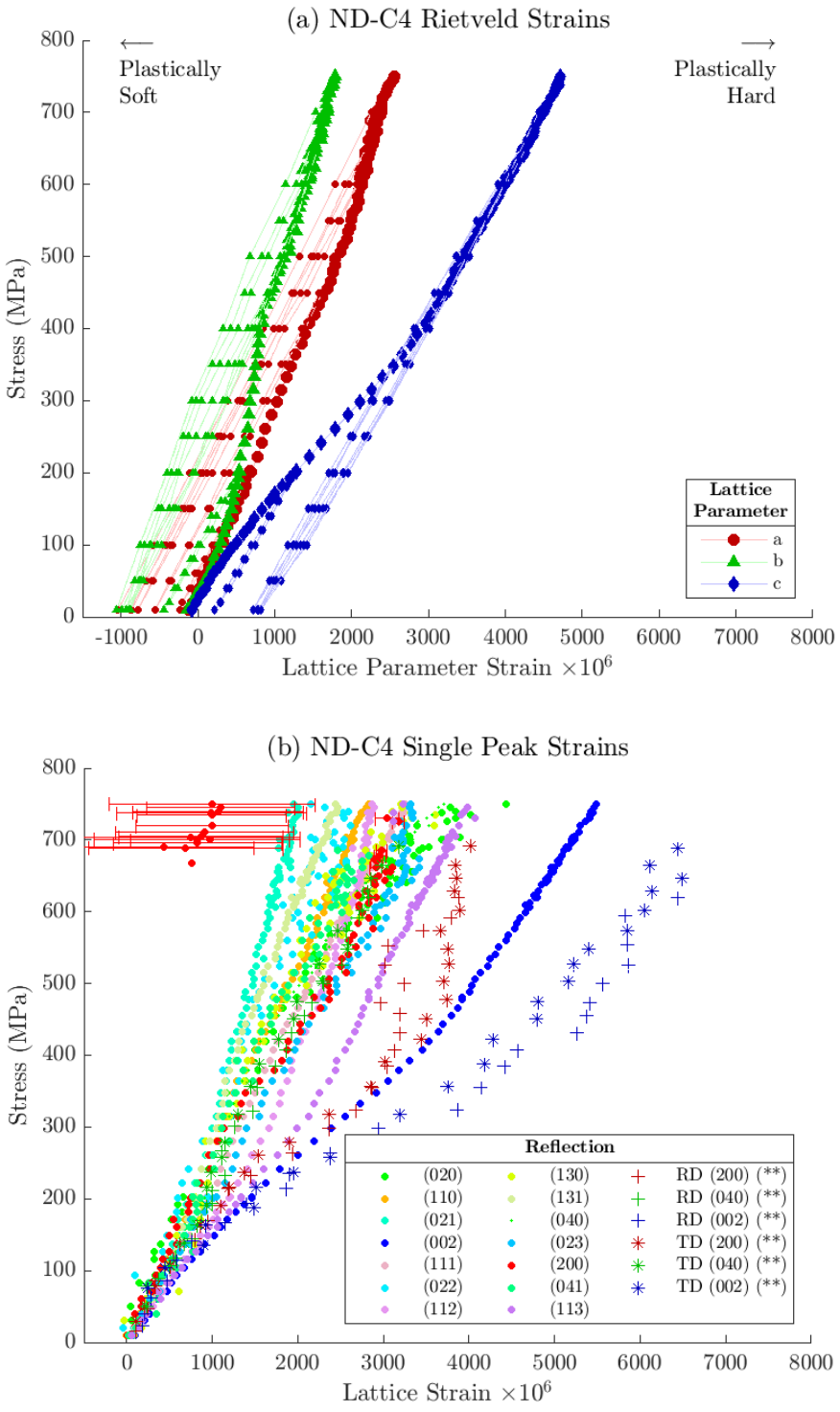


Figure 4.38. (a) Rietveld lattice parameter strains and (b) single-peak strains as a function of applied stress for specimen ND-C4. Compressive strains are plotted as positive for comparison with the tensile specimens. Measurements taken during unload-reload cycles are omitted from the single-peak data. Reflections are coloured according to their orientation. The lattice parameter strain errors are large for certain (200) reflections above 650 MPa. Data from the literature are shown for comparison; Calhoun et al. [45] (**) performed compression along the RD and TD.

Ministry of Defence © British Crown Copyright 2020/AWE

Specimen ND-C4 displayed divergence of the lattice parameter strains from 60 MPa (figure 4.38(a)). At stresses between 60 MPa and 400 MPa, the *b*-parameter strongly saturates and barely increases, the *c*-parameter rapidly accumulates strain, and the *a*-parameter slightly saturates. At 400 MPa, a distinct change in gradient is observed in the *b*- and *c*-parameter strains, which return to a gradient similar to in the elastic region. As the stress is increased towards the maximum compressive stress of 750 MPa, the *a*- and *b*-parameter strains steadily saturate.

Figure 4.38(b) shows the (002)-oriented grains hold the largest strain, in a similar manner to specimen ND-C3. The (113) strains are similar to the (002) strains until 200 MPa when they return to following the elastic gradient. The (020) and (040) strains accumulate more rapidly from 400-500 MPa such that are as large as the (113) strains when the maximum stress is reached. There is an anomalous reduction in the (200) strains above 650 MPa. As also seen in the peak intensities in section 4.3.3.4, the quality of fit on these (200) peaks was poor, with large associated uncertainties.

4.3.5 Fracture and Fractography

Both tensile specimens failed via fast fracture, with a crack propagating approximately perpendicular to the loading direction. SEM fractography, kindly performed by Rod McCabe at LANL, identified regions of ductile failure accompanied by large areas of cleavage, along thin planar features which appeared to be '{172}' twins (see Appendix A6.2).

Ministry of Defence © British Crown Copyright 2020/AWE

4.4 Discussion

In this section, we will discuss the results of this experiment, and identify any trends or key findings. Despite different starting textures, there are similarities in the macroscopic deformation responses of the tension specimens; these were seen to be a coincidence of the DIC gauge area selected. We will see that the compression specimens show a harder and more ductile response compared to those in tension.

Using the methodology developed in the previous chapter to calculate the possible texture changes due to twinning, we will relate the observed axial texture changes to the deformation modes in the material. We will compare this to the deformation modes predicted for each starting texture from the Schmid factors of each possible mode.

In certain specimens, discrepancies are seen between the lattice parameter strains calculated from the Rietveld refinement and the single-peak strains. In addition, the (200) strains behave anomalously in specimens ND-T4 and ND-C3. In each case, a potential explanation is proposed; it is clear that the clustered microstructure strongly affects the local deformation.

Finally, the behaviour of the cast uranium tested here is compared with that of the fine-grained, rolled material tested previously in the literature. Significant differences in both macroscopic and lattice deformation are seen.

Ministry of Defence © British Crown Copyright 2020/AWE

4.4.1 Macroscopic deformation

In their flow curves, all specimens showed a small elastic region with similar initial stiffness, and an indistinct yield point. The strain measured by DIC was, in all cases, larger than that measured by the extensometer, showing the effect of heterogeneous strains.

Failure occurred at a similar gauge-region strain in each tensile specimen, despite the fracture and associated strain concentration occurring inside the DIC region in specimen ND-T4 and well outside this region in ND-T3. This suggests that this similarity is just a coincidence of the size and location of the DIC region – chosen to be similar in size to the neutron gauge volume. Since we considered the average strain in the DIC region, if the region were smaller, the effect of the strain concentration in ND-T4 would be proportionately larger and a larger failure strain would be calculated.

Fracture occurred in very different regions of the tensile specimens, with significant rotation and distortion of the sample seen before failure. It appears that it is strongly affected by the misorientation between and constraint of neighbouring clusters. The fracture surface shows evidence for cleavage along large flat planes, thought to be '{172}' twin boundaries in the literature[62]. The thickness of the linear feature seen in the fractography (figure 8.54 in Appendix A6.2) is a similar to the thickness of '{172}' twins seen in figure 2.14. Sectioning and EBSD of specimen ND-T4 near the fracture surface would be needed to confirm this.

Ministry of Defence © British Crown Copyright 2020/AWE

The presence of ductile regions on the fracture surface shows that a) slip deformation is still significant, and b) there is heterogeneity in the fracture mode across different parts of the specimen, likely related to local grain orientation and the activation of '{172}' twins.

The specimens exhibit clearly different flow curves, with deviations from each other seen from 100 MPa or 0.1 % strain. The largest difference is seen between specimens tested in tension and compression. The latter do not fail via cleavage and consequently achieve larger strains, whilst also being harder and supporting higher stresses.

4.4.2 Texture Development

On average, the axial textures in the gauge volume are weaker than those observed at ENGIN-X as a result of the larger gauge volume used on SMARTS. Only ND-T3 and ND-C4 show texture components greater than 2 MRD; the texture in the latter is strong despite the gauge volume being very large at 1.7 cm^3. These textures are similar to those measured on GEM in the specimens tested on ENGIN-X (Appendix A5.3.2), although the GEM experiment used a smaller gauge volume of 1.1 cm^3. This suggests that the textures in specimens ND-T3 and ND-C4 are particularly strong, as larger gauge volumes would measure a weaker texture in similar microstructures.

As expected, there appears to be no correlation between the textures in different specimens due to the grain clusters being randomly oriented.

Ministry of Defence © British Crown Copyright 2020/AWE

On ENGIN-X, it was possible to consider the gauge volume as 2 or 3 clusters, and the GEM full texture analysis was used to identify their orientations, and subsequently to calculate the Schmid factors for deformation. In large regions of the IPF not corresponding to these clusters, the textures were low, below 0.5 MRD (figure 8.31, figure 8.32, and figure 8.33). Specimen ND-T1, for example, had large areas at around 0.15 MRD.

Here, many different orientations are present, and only small regions of the IPF have such weak texture. Therefore, to interpret the data from this experiment we cannot consider isolated clusters, and instead must consider the full distribution of grain orientations. We do not know how these grains are distributed spatially within the gauge volume; however we can assume several dominant clusters with small contributions from many others.

4.4.2.1 Prediction from Schmid Factors

The likelihood of a particular deformation mode activating and contributing to the overall texture change is related to both its Schmid factor and CRSS, but also to the starting texture – whether or not there is a significant number of grains well oriented for deformation by this mode.

We can qualitatively assess the likelihood of a particular mode contributing strongly to the overall deformation by generating Schmid factor-weighted texture IPFs – calculated by multiplying the textures in figure 4.16 by the orientation-dependent Schmid factors

Ministry of Defence © British Crown Copyright 2020/AWE

for slip, figure 2.7, and twinning, figure 2.12. These are shown for slip in figure 4.39 and for twinning in figure 4.40, plotted with a colour scale of 0 to 1 to allow comparison between modes and between specimens. Regions of negative Schmid factor for twinning are shown as zero-valued as twins cannot form in these orientations. IPFs containing higher values show a larger proportion of grains well-oriented for deformation, and indicate a greater ability of that mode to contribute to deformation if its CRSS is exceeded. As seen in the previous chapter, the CRSS values are not known for cast uranium (this is a goal of the subsequent CPFE modelling), so these scaled textures allow qualitative assessment only.

For example, specimen ND-C4 has a large texture component near (001), but it is poorly oriented for Wall slip so the texture-scaled IPF for Wall slip, figure 4.39(d)(i), is low-valued. Wall slip would not therefore be expected to contribute strongly to deformation in the gauge volume of specimen ND-C4.

By inspection of figure 4.39 and figure 4.40, we cannot determine if a mode will or will-not activate as this depends on the CRSS for that mode. However we can assess whether, at stresses well in excess of the yield stress, each mode can contribute significantly to the overall deformation.

Ministry of Defence © British Crown Copyright 2020/AWE

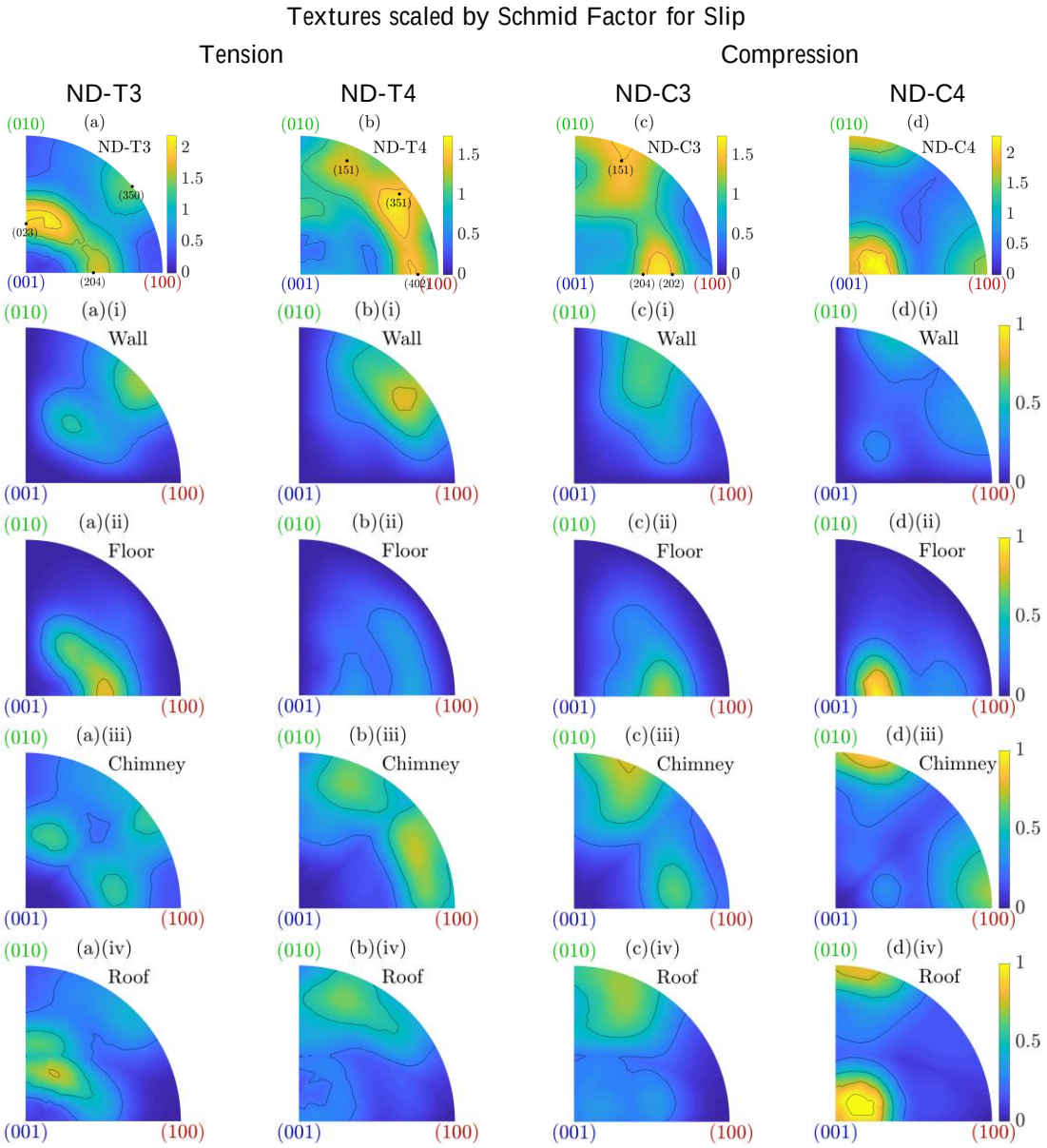


Figure 4.39. Schmid factor-weighted axial textures for tensile specimens (a) ND-T3, and (b) ND-T4, and compressive specimens (c) ND-C3, and (d) ND-T4, for (i) Wall, (ii) Floor, (iii) Chimney, and (iv) Roof slip. Orientations with high values contain large numbers of grains well-oriented for deformation by this mode. The top row shows the raw textures before weighting.

Ministry of Defence © British Crown Copyright 2020/AWE

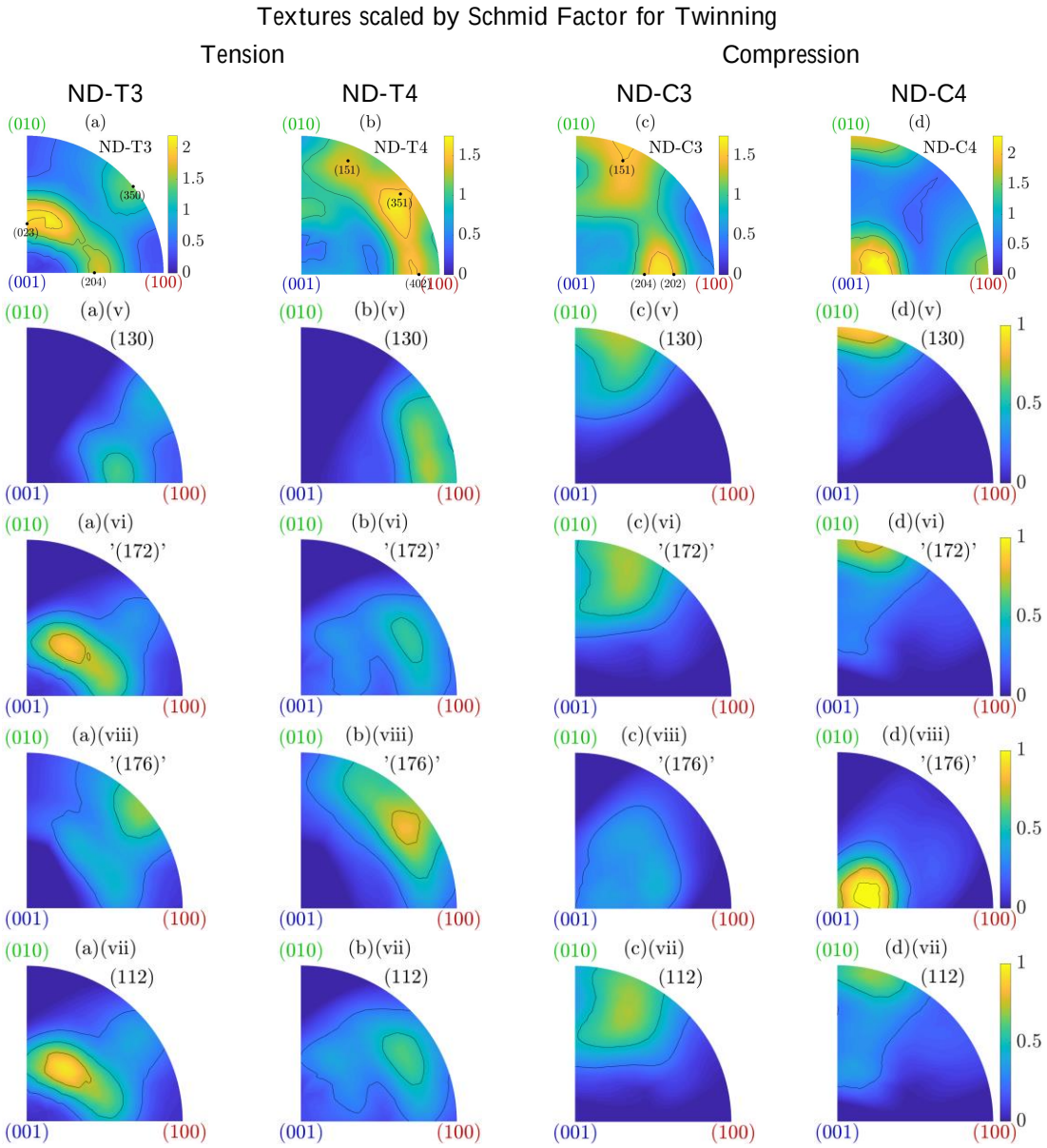


Figure 4.40. Schmid factor-weighted axial textures for tensile specimens (a) ND-T3, and (b) ND-T4, and compressive specimens (c) ND-C3, and (d) ND-T4, for (i) {130}, (ii) '{172}', (iii) '{176}', and (iv) {112} twinning. Orientations with high values contain large numbers of grains well-oriented for deformation by this mode. Regions of negative Schmid factor for twinning cannot deform by this mode are shown as zero-valued. The top row shows the raw textures before weighting.

Specimen ND-T3 is only well-oriented for Floor slip, and the majority of grains are poorly oriented for {130} and '{176}' twinning. We therefore expect it to deform by a mixture of Floor slip and '{172}'/{112} twinning, with small contributions from the easiest {130} mode. {112} twinning activates for very similar orientations to '{172}' twinning, due to its similar Schmid factor (figure 2.12), and results in similar lattice

Ministry of Defence © British Crown Copyright 2020/AWE

reorientations (figure 3.9), so it is challenging to separate the effects of these modes[30]. Only '{172}' twinning will be considered in the subsequent analysis.

The majority of grains in specimen ND-T4 are well-oriented for Wall slip. Deformation would be likely to proceed via this mode with additional contributions from the low-CRSS {130} twinning modes. It is well-oriented for '{176}' twinning, although the CRSS is thought to be high for this mode and therefore other modes may become active well before '{176}' twins contribute strongly to the overall deformation.

There are many grains in ND-C3 well-oriented for all slip modes, with orientations near (010) also being particularly well-oriented for {130} and '{172}' twinning. Interestingly, the strongest texture component, between (202) and (204), cannot deform via any twinning mode, and can only deform via Floor or Chimney slip.

As a result of grain clusters aligned with their (100), (010) and (001) axes parallel to the loading direction, Wall slip is highly unfavourable in specimen ND-C4. Instead, the cluster oriented near (001) is well-oriented for Floor and Roof slip, and '{176}' twinning. The texture component near (010) is well-oriented for {130} and '{172}' twinning.

The small component near (100) cannot deform by any twinning mode and only Chimney slip allows significant deformation of these grains.

4.4.2.2 Relating Texture Changes to Deformation Modes

The texture changes seen in this experiment are greater in magnitude than those seen on ENGIN-X, due to the applied strains being over 5 times larger. The movement

Ministry of Defence © British Crown Copyright 2020/AWE

correction successfully removed texture artefacts of magnitudes up to 0.15 MRD at the point of maximum specimen displacement. Whilst smaller in magnitude than the observed texture changes, the artefact could have had significantly affected the measured texture changes if it were present in regions of the IPF in which no deformation-induced texture change was seen.

In all specimens, the magnitude of texture change was linearly proportional to the magnitude of applied strain (e.g. figure 4.23). For twinning deformation, the volume fraction of twins is linearly proportional to the shear deformation accommodated by twinning [50], and is consequently proportional to the macroscopic sample strain. For slip, the lattice rotation is related to the plastic strain accommodated by dislocation glide, although the constraint of other grains means this dependence is not necessarily linear, and may vary between samples. This linear dependence is consistent with twinning being responsible for the majority of the observed texture change.

The magnitude of texture change decreased slightly during unload by an amount consistent to the decrease in elastic strain (the unload data follow the same gradient as the loading data in figure 4.23). Since these data have been corrected for specimen movement, this suggests that as the specimens are unloaded a small amount of reverse plasticity is occurring, either de-twinning or reverse slip.

In general, specimens deformed in tension saw a texture increase near (010), with concomitant decreases near (100) and (001), consistent with the activation of {130} and

Ministry of Defence © British Crown Copyright 2020/AWE

‘{172}’ twinning modes. In compression, increases near (100) were associated with decreases near (010), again consistent with the {130} and ‘{172}’ twinning modes. In both specimens ND-T3 and ND-C4, orientations near to (001) see a negative texture change, despite the change observed directly along (001) being close to zero.

By close inspection of the texture change IPFs (ND-T3: figure 4.22 p.139, ND-T4: figure 4.25 p.142, ND-C3: figure 4.28 p.145, ND-C4: figure 4.31 p.148), the Schmid factor-weighted textures (slip: figure 4.39 p.167, twinning: figure 4.40 p.168), and the twinning reorientations (tension: figure 3.9 p.87, compression: figure 3.10 p.88), active deformation modes can be identified.

Figure 4.41 shows the texture change after application of the maximum applied strain. To identify a twinning mode as active, one must see a texture decrease in the parent orientation as well as increase in the twin orientation. The deformation modes predicted in section 4.4.2.1 are marked on figure 4.41 with arrows going from the parent to twin orientations, marked in solid lines if the measured texture change is clearly consistent with that mode’s reorientation. Slip causes a rotation towards the slip direction, which is [100] in the case of Floor and Wall slip.

The twinning deformation predicted in specimen ND-T3 is consistent with the observed lattice reorientation. The increase in texture near (010) is the result of {130} and ‘(172)’[312] twinning. Although Wall slip is presumed to be active, no clear evidence is seen in the measured textures. This may be due to the lattice reorientation from slip

Ministry of Defence © British Crown Copyright 2020/AWE

being much smaller in magnitude than for twinning, and the effect is therefore indistinguishable from twinning-induced texture change.

The texture change in specimen ND-T4 can be explained as the {130} twinning of the texture component near (110). No evidence is seen for the predicted '{176}' mode.

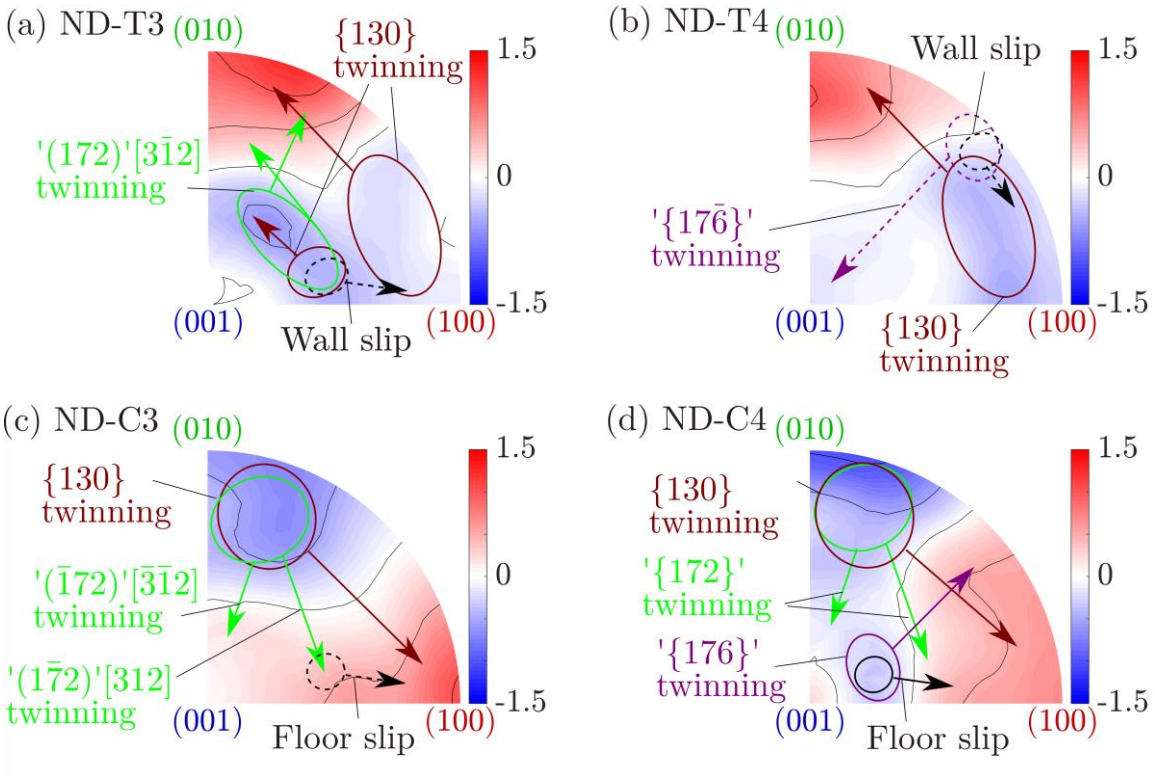


Figure 4.41. Identification of potentially-active twinning modes from the observed texture changes.

As predicted, deformation in the compression specimens is mediated by {130} and '{172}' twinning of grains oriented near (010). Specimen ND-C4, which has an additional texture component near (001), sees deformation in these grains consistent with '{176}' twinning and/or Floor slip.

In summary, there is good agreement between the twinning modes predicted and the resulting texture change. It is however not possible to identify the effects of slip

Ministry of Defence © British Crown Copyright 2020/AWE

deformation, nor the activation of other twinning modes with small volume fractions. From the texture changes alone, we cannot say whether the crystal in the orientations that increase in texture are deforming – we need to also look at the lattice strains, as these can identify deformation by the saturation of stresses on particular families of grains.

4.4.3 Lattice Strains

The lattice strain on the (*hkl*) family of grains is proportional to the stress on these grains. The stress on these grains increases with applied stress until the activation of a deformation mode limits further increases, and a saturation of the (*hkl*) lattice strains is seen. The stress is redistributed to non-deforming grains, and these see an associated increase in lattice strain.

4.4.3.1 Comparison with ENGIN-X Experiment

The lattice parameter strains for specimens strained in compression show a similar response to the compression specimen tested on ENGIN-X, ND-C1, and to fine-grained uranium tested in compression in the literature [45]. The *a*-parameter saturates whilst the *c*-parameter becomes the most compliant. Specimen ND-T4 exhibits lattice parameter strains comparable to specimens ND-T1 and ND-T2, and all fine-grained tensile specimens [45][107], with *a* saturating and *b* reaching the highest strains, and *c* showing intermediate behaviour. Specimen ND-T3, however, sees the response of the *a*- and *c*- parameters reverse, with the c-parameter completely saturating. This will be

Ministry of Defence © British Crown Copyright 2020/AWE

discussed in more detail in section 4.4.3.3 on page 180. In addition, in ND-T3 the lattice parameter strains deviate from their initial elastic gradient at a much higher stress (250 MPa) than in all other specimens tested (100 MPa – 150 MPa).

4.4.3.2 Correlation with Peak Intensity Change

An increase in texture in a particular orientation (*hkl*) does not necessarily mean that that orientation is not deforming – the original grains may still deform even if the newly-formed twins do not. A texture decrease along (*hkl*), however, is very strong evidence for the (*hkl*)-oriented grains deforming, and would be expected to be associated with smaller lattice strains.

We would therefore expect deforming grain families to have negative texture changes and low lattice strains, and non-deforming families to have high lattice strains and a positive or zero texture change, depending on whether or not the orientation is aligned with any resulting twins (figure 4.42). Slip would manifest itself as a decrease in lattice strain without the corresponding large decrease in texture.

To identify any correlation, in figure 4.43 the gradient of the single-peak intensity (texture) changes with strain were plotted against the lattice strain near maximum stress. For each specimen, the stress value chosen was the highest stress at which good peak fitting statistics were observed for all peaks. Since the texture changes were linear with strain, using the gradient reduces the error compared to looking at the values at a particular stress.

Ministry of Defence © British Crown Copyright 2020/AWE

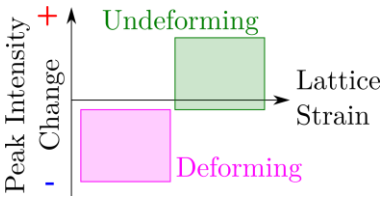


Figure 4.42. Predicted deformation-dependent correlation between texture change and lattice strain.

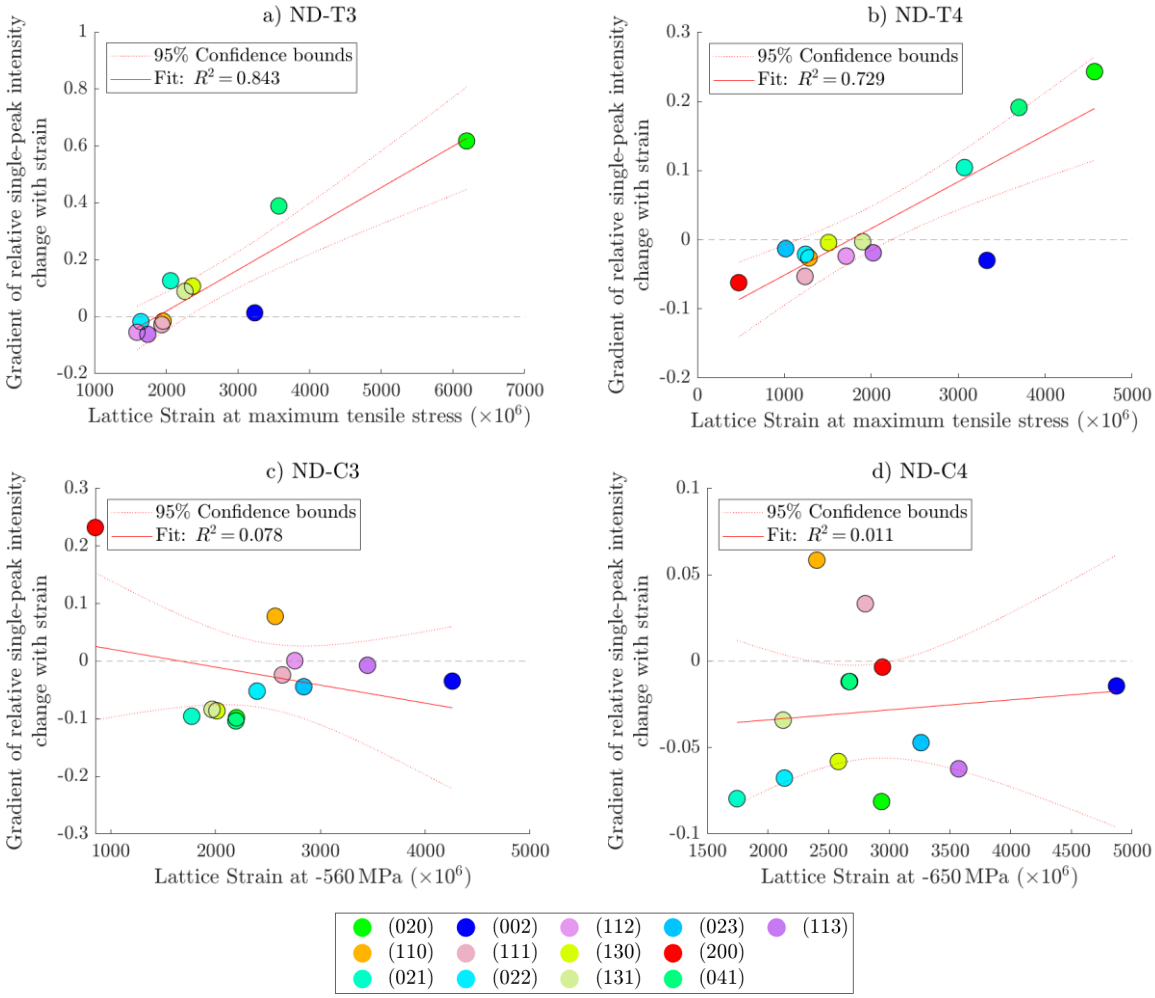


Figure 4.43. Assessment of the correlation between lattice strains and texture changes in specimens (a) ND-T3, (b) ND-T4, (c) ND-C3, and (d) ND-C4. The gradient of the single-peak intensity change with strain is plotted against the lattice strain at the highest stress for which good peak-fitting statistics were observed for all peaks. A linear line of best-fit is shown in red with 95 % confidence bounds in the fitting line shown as red dotted lines, along with the R^2 value in the legend of each subfigure.

Both tensile specimens show a correlation between lattice strain and texture change as expected. This suggests that the deformation is restricted to the orientations where a negative texture change is seen, and that the majority of deformation is mediated by the slip and twinning modes identified in figure 4.41(a) and (b). In both cases, the (002)

Ministry of Defence © British Crown Copyright 2020/AWE

peak is a clear outlier, with no texture change but an increase in strain; the few (002)-oriented grains in each tensile specimen do not deform easily and few of the resulting twins are aligned with (002).

In compression, however, no correlation is seen. The texture changes were as predicted from the Schmid factors, so it is the lattice strains that are not behaving in the simple manner seen in tension.

A possible explanation is that in compression there is greater constraint from neighbouring grains, and this affects the development of strain in particular families of grains. The tensile specimens have a diameter similar to the cluster size, so the individual clusters are free to rotate, whilst the compression specimens contain multiple grain clusters across the diameter, and therefore clusters near the central axis would have their deformation constrained by the surrounding clusters.

Grains outside of the neutron gauge volume would not contribute to the measured strains. If these grains were plastically hard and were loaded in parallel to the grains in the gauge volume, they would carry a high amount of stress, leaving the stress on the diffracting grains small compared to the applied stress. This would lead to smaller lattice strains in the gauge volume at a particular stress level. The converse would apply for plastically soft grains. The gauge volume of the specimens tested on SMARTS covered the whole width of the specimens (figure 4.6), so this effect is likely to be small.

Ministry of Defence © British Crown Copyright 2020/AWE

Within the gauge volume, there would be a similar stress redistribution effect causing a difference between clusters loaded in series and the same clusters loaded in parallel.

4.4.3.3 Discussion of Lattice Strains

Deformation of (200)-oriented grains in specimen ND-C3

The lattice strains on the (200)-oriented grains in specimen ND-C3 are small even though this orientation sees a large positive texture change. The (200)-orientation has a weak starting texture (<0.5 MRD).

Inspection of figure 4.36 shows a sudden decrease in (200) lattice strain at 370 MPa. This is not reflected in the *a*-parameter strains, which continue to increase at the same gradient. The *a*-parameter strains are intermediate in magnitude to the *b*- and *c*-parameter strains however throughout the test the (200) strains are smaller than their (020) and (002) counterparts.

One hypothesis for the small (200) lattice strain is that the newly-formed twins in the (200) orientations carry a low stress, therefore reducing the average strain on the (200) family of grains. However, twins are known to potentially contain large internal stresses[141] and these would likely increase via elastic deformation as the applied stress increases. Such an increase is not seen – in fact the (200) strains actually decrease with stress increases above 370 MPa.

Another possibility is that the few (200)-oriented grains present at pre-load are deforming. This cannot be via twinning as compressive loading along (200) has a negative

Ministry of Defence © British Crown Copyright 2020/AWE

Schmid factor for all twinning modes, and the only slip mode with non-zero Schmid factor is Chimney slip. I therefore propose that the reduction in (200) strain at 370 MPa is due to the activation of Chimney slip in the (200)-oriented grains. No sudden change in peak intensity is seen at 370 MPa (figure 4.30), consistent with the small lattice rotations associated with slip.

The Schmid factor for the most-stressed Chimney slip mode under compressive loading along (200) is 0.393 (figure 2.7). A simple calculation yields an estimate of the critical resolved shear stress (CRSS), $\tau_{\mathrm{crit}}^{\mathrm{Chimney}}$, for Chimney slip in these grains as:

$$\begin{aligned} \tau_{\mathrm{crit}}^{\mathrm{Chimney}} &= \sigma_{\mathrm{crit}}^{\mathrm{Chimney}} \times SF \\ &= 370\,\mathrm{MPa} \times 0.393 \\ &= 145\,\mathrm{MPa} \end{aligned} \qquad [4.14]$$

This is over 4 times the value of 35 MPa found for fine-grained uranium by Calhoun et al. [108].

The (200) texture is weak, suggesting that the (200)-oriented grains are scattered sparsely throughout the gauge volume – experimentally a few grains of differing orientation are seen to exist within the main clusters (figure 8.3, figure 8.8, figure 8.5). The (200)-oriented grains may therefore be exposed to extreme constraints from the surrounding clusters, both in the form of residual stresses in the as-cast material and in Poisson's ratio strains during deformation. As such the local stress state is probably

Ministry of Defence © British Crown Copyright 2020/AWE

considerably different from the applied stress, so the CRSS of 145 MPa calculated from the experimental data are unlikely to be valid.

Saturation of Strain After Yield

Saturation of elastic lattice strain is seen as yield occurs. Since the measured (*hkl*) strain is the average of the normal strains on the (*hkl*)-oriented grains, the proportion of (*hkl*)-oriented grains that yield will affect the degree of saturation. Since the Schmid factor for a particular mode is the same for all grains within the (*hkl*) family, it would be expected that all grains in the family will yield at the same time, however the effects of residual stress and constraint can affect each grain differently.

As deformation proceeds, the deformation modes typically harden, with a higher stress required to support further deformation. In the case of slip, this would be due to forest hardening associated with dislocation multiplication, interaction and pinning, and in the case of twinning, the reduced effective grain size caused by the formation of twins of one mode can increase the activation stress for twinning in another mode (non-coplanar interaction). In addition, the strain fields between parallel twins may increase the stress required to form another twin of the same type in the material between them (coplanar interaction).

On account of incomplete yielding and deformation hardening, we would expect the lattice strain to increase on all of the yielding (*hkl*) planes above the yield point, giving a (large) positive gradient to the stress vs. lattice strain plots.

Ministry of Defence © British Crown Copyright 2020/AWE

This is seen in all specimens except ND-T4, where the (200) and (023) strains actually begin to decrease above 300 MPa, and in ND-C3, with the aforementioned reduction in (200) strains. Either the deformation systems are softening, which would be unusual, or the constraint from nearby grains is imposing a compressive stress along the axis parallel to the loading direction in these grains.

Anomalous Lattice Parameter Strains in ND-T3

As mentioned in section 4.4.3.1, the lattice parameter strains behave anomalously in specimen ND-T3; the *c*-parameter saturating completely instead of the *a*-parameter as in all other tensile specimens tested. The (002) single-peak strains, parallel to the *c*-axis, are similar between specimens ND-T3 and ND-T4 and do not saturate, so an explanation is needed for the different response of the *c*-parameter strains. The fact that the (002)-oriented grains do not plastically deform is not surprising – there is a zero Schmid factor for the easy slip modes, Wall and Floor, and the easiest twinning mode, {130}.

The *c*-parameter behaviour can be explained if we recall that its value is calculated from the Rietveld refinement over the entire spectrum, and contains contributions from all (*hkl*) reflections with $l \neq 0$, with presumably a stronger contribution from planes aligned more closely to (002).

ND-T3 contains a large texture component located approximately 30° from the (002) axis that is not present in ND-T4. It is also not seen in the ENGIN-X specimen ND-T2, and is only present in ND-T1 to a smaller angular extent. In ND-T3, these grains undergo

Ministry of Defence © British Crown Copyright 2020/AWE

a large amount of {130} and '{172}' twinning, labelled in figure 4.41(a), leading to a saturation of the lattice strains on (111), (112), and (113) that is not seen in ND-T4. Because of their strong texture, these peaks are large and contribute strongly to Rietveld fitting and therefore to the saturation of *c*-parameter strains in ND-T3.

4.4.4 Comparison with fine-grained uranium

We can compare the behaviour of our coarse-grained (CG) cast uranium with fine-grained (FG) uranium tested in the literature. Brown et al. [107] tested rolled uranium plate in tension along the rolling direction (RD) and transverse direction (TD). Calhoun et al. [45] performed tension and compression along the RD and compression along the TD.

4.4.4.1 Flow Curves

In figure 4.20, all curves show an indistinct yield point in tension and compression. The response of FG material is similar in tension and compression, however the CG material is much softer in compression than in tension. In tension, the hardening rate for CG is greater than or equal to the rate for FG material. In compression, the yield point and hardening rates of CG and FG material are similar.

4.4.4.2 Lattice Strains

Despite significant differences in texture along the RD and TD of rolled FG uranium, only small differences between the lattice strains of the FG specimens are seen. CG specimen ND-T4 also shows a similar behaviour, with the *a*- and *b*-parameter strains

Ministry of Defence © British Crown Copyright 2020/AWE

and the (020) and (002) lattice strains agreeing well with the FG data. As discussed in section 4.4.3.3, the lattice parameter strains in CG specimen ND-T3 are anomalous. There is however good agreement between the (020)/(040) and (002) strains in ND-T3 and in the FG material.

Lattice-parameter strains during the deformation of FG uranium in compression are scarce in the literature, so comparisons will be made between the single-peak strains. The (002)-orientations hold less strain in CG material than in FG, suggesting that these grains start to yield at an earlier stage in coarse microstructures. This orientation can only deform in compression by Roof slip (which is thought to have a very high CRSS) or by '$\{176\}$' twinning. The softening of this twinning mode in the CG material is probably a grain-size effect in which twinning is easier in large grains[69].

There is a clear separation between the (200) and (020) strains in FG uranium, with $\varepsilon_{(002)} > \varepsilon_{(200)} > \varepsilon_{(020)}$. In specimen ND-C4, however, $\varepsilon_{(200)}$ follows the same path as $\varepsilon_{(020)}$, whilst in ND-C3, the situation is reversed with $\varepsilon_{(200)} < \varepsilon_{(020)}$.

Many of the subtle differences between specimens are hidden in the (*hkl*) lattice strains where $h \neq 0$, $k \neq 0$ and $l \neq 0$. These are not commonly published in the literature so a more detailed comparison between the neutron diffraction response of CG and FG material cannot be made without access to the raw data from the FG experiments.

Ministry of Defence © British Crown Copyright 2020/AWE

4.4.5 Summary of Experimental Discussion

In this section, we saw strong evidence for the twinning-induced texture change, and could identify potential twinning modes by reference to their Schmid factors and lattice reorientations, using the method developed in Chapter 3.

The difference between tensile and compressive deformation is mainly due to the asymmetry of activation of $\{130\}$ and '$\{172\}$' twins.

A correlation was seen between lattice strain and texture change in specimens loaded in tension, with deforming regions being associated with a negative texture change and low, saturated, strains. No correlation was observed in specimens tested in compression. This was rationalised as an effect of constraint in the larger compression specimens.

Despite having very different textures, the lattice-parameter strains calculated by Rietveld refinement are similar between specimens loaded in the same manner and match those seen in fine-grained material. The single-peak strains show more marked differences however, especially for reflections intermediate to (200), (020), and (002).

The effect of texture on the lattice strains is pronounced, with the strong texture component close to but not aligned with (002) in ND-T3 undergoing deformation and strain relaxation causing anomalous *c*-parameter strains. Rietveld refinement, whilst very useful to measure the axial texture changes, cannot capture the subtleties of deformation in this coarse-grained, clustered material with strong textures. Instead, it is the single-peak strains and intensities which yield the most information.

Ministry of Defence © British Crown Copyright 2020/AWE

Fine-grained uranium showed a similar macroscopic response in tension and compression, whilst our cast material was considerably softer in tension. There is some evidence for a lower $\mathrm{CRSS\ for\ `\{176\}'\ twinning}$ in the cast material – the lower (002) strains in compression – however the value for the CRSS of Chimney slip was estimated to be much higher than in the literature.

It is challenging to identify the activation of slip in the presence of the strain and texture changes associated with twinning. The overall response of the material is a complex mixture of deformation modes that can only be fully understood in conjunction with modelling.

4.5 CPFE Modelling of Neutron Diffraction Experiment

Crystal Plasticity Finite Element (CPFE) modelling of the deformation of the cast uranium investigated in this thesis is being performed at the University of Oxford by our team of collaborators in the Department of Engineering Science. Since the CPFE model is the desired outcome of the research project to which this thesis contributes, it is relevant to give a brief overview of the progress made in the modelling, as it demonstrates the utility of the experimental data presented here. All figures and modelling data were generated by Dr Nicolò Grilli, who kindly provided them for inclusion in this thesis. This work has resulted in two publications by Grilli et al. [88][130].

Ministry of Defence © British Crown Copyright 2020/AWE

A summary of the method is found in Appendix A7.

4.5.1 Results and Discussion

The optimised simulated deformation parameters are shown in table 4.4, along with parameters optimised for fine-grained (McCabe et al. [30]) and single-crystal (Daniel et al. [18]) uranium.

Table 4.4. Optimised constant friction stress parameters for slip, and critical resolved shear stress (CRSS) for twinning, for the cast uranium specimens tested on ENGIN-X, modelled by Grilli et al. [88]. Parameters for fine-grained (McCabe et al. [30]) and single-crystal (Daniel et al. [18]) uranium are shown for comparison.

		Constant Friction Stress τ_α^0 (MPa)				CRSS (MPa)
Material	Grain Size	Wall	Floor	Chimney	Roof	{130} twin
Fine-grained (McCabe et al.[30])	20 μm	60	270	295	270	300
Single crystal (Daniel et al.[18])	>2.5 mm	4	80	168	N/A	25
Coarse-grained (Grilli et al.[88])	>200 μm	7	10	35	235	25

Good agreement between simulation and experiment was seen for the flow curves (figure 4.44) and (100) and (010) lattice strains (figure 4.45(a) and (b)). The (001) lattice strains in figure 4.45(c) only qualitatively agreed with the experiment; more saturation seen in specimen ND-T1 than in ND-C1.

Ministry of Defence © British Crown Copyright 2020/AWE

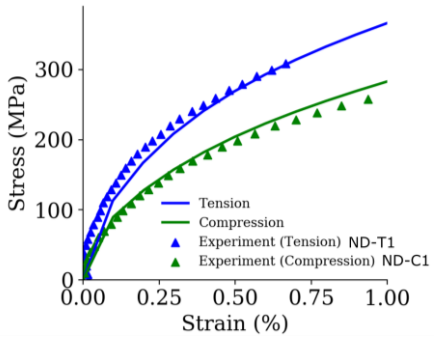


Figure 4.44. Simulated and experimental flow curves from simulations of ENGIN-X specimens ND-T1 and ND-C1. Reproduced from Grilli et al. [133].

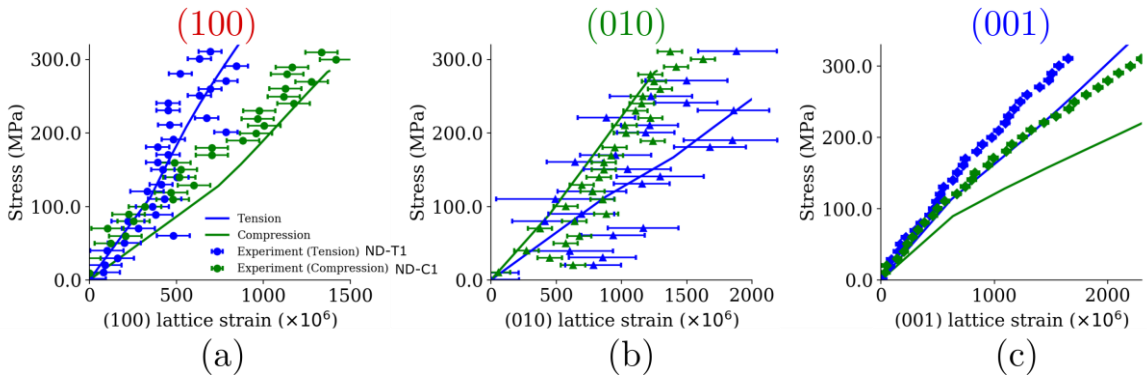


Figure 4.45. Lattice strains on (200), (020) and (002) reflections in specimens ND-T1 and ND-C1 compared with simulated (100), (010) and (001) strains on grains identified to be in the diffraction condition. Modified from Grilli et al. [133].

The strong tension-compression asymmetry was reproduced and seen to be a result of the asymmetric activation of {130} twins. Clustering of the grains into a bicrystal was seen to affect the simulated flow curves and lattice strains, and produced a better fit to the ND-T1 experimental data. A similar clustering performed for ND-C1, however, did not yield an improved fit.

The distribution of {130} twins after quenching is highly heterogeneous. The most-twinned grains have a twin volume fraction of between 5 % and 6 %, comparable with the experimentally characterised microstructure (figure 8.8 on page 358). The twin

Ministry of Defence © British Crown Copyright 2020/AWE

volume fraction is strongly influenced by the CRSS for twin activation; this agreement suggests the optimised CRSS of 25 MPa is sensible.

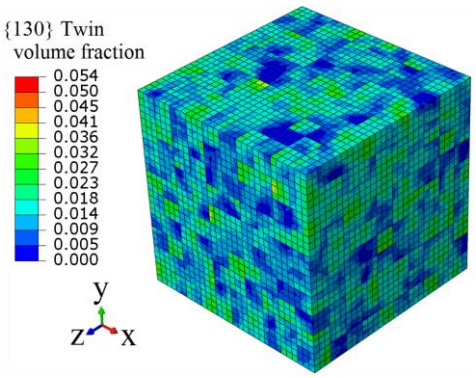


Figure 4.46. Volume fraction of {130} twins after quenching from 400 ℃ to 20 ℃. The volume fraction of twins is strongly affected by the CRSS for twinning, so can be used to calibrate the model. Reproduced from Grilli et al. [133].

For coarse-grained uranium, the constant friction stress for slip is typically less than that found in single crystals and significantly less than in fine-grained uranium. The CRSS for twinning was found to be equal to that in single crystals.

Grilli et al. [88] note that it is not possible to estimate the CRSS values directly from the experimental data without simulation. For example, in ND-T1, the yield at 115 MPa in (100)-oriented grains is attributed to the initiation of {130} twinning. With a Schmid factor of 0.47, this corresponds to a CRSS of 54 MPa, which is much greater than the CRSS of 25 MPa required in the model to fit the observed deformation.

In section 4.4.3.3, we estimated the CRSS for Chimney slip to be 145 MPa. The optimised constant friction stress of 35 MPa corresponds to a CRSS in the model at 20 ℃ of 43 MPa. Again, the experimental observation leads to an overestimation of CRSS as it ignores the constraint effects.

Ministry of Defence © British Crown Copyright 2020/AWE

The effect of grain clustering on the simulated strains highlights a drawback of neutron diffraction experiments – whilst the orientation distribution can be measured, the spatial distribution of grains is not. Whilst it is in principle possible to use a small gauge volume and translate the specimen during testing to measure regions of different orientation, the associated increase in neutron count time would make this unfeasible.

4.5.2 Suggestions for future model development

The modelling performed by Grilli et al. has so far only analysed the data from the experiment on ENGIN-X presented in Chapter 3. The data presented in this chapter will allow further development of this model. Data are available to much higher strains (4% - 6% rather than 1%), and the in-situ DIC of the specimen surface significantly reduces the strain error compared to the poorly-measured gauge volume strain on ENGIN-X. This allows better calibration of the hardening rates of the deformation modes.

Future iterations of this model should include '{172}' and '{176}' twinning, which were seen to strongly contribute to the difference in response of specimens ND-T3 and ND-T4. It should also predict the observed texture changes, which are now reliable due to the improvements in experimental design of the SMARTS experiment.

Many of the subtleties of deformation between specimens were captured in the lattice strains for (*hkl*) reflections not aligned along the crystal axes (i.e. not (100), (010), or (001)). It would therefore be sensible to also perform a comparison between these lattice

Ministry of Defence © British Crown Copyright 2020/AWE

strains in simulation and experiment in order to accurately optimise the deformation parameters.

4.6 Chapter Summary

In this chapter we have seen how an improved neutron diffraction experiment, conducted on the SMARTS beamline at LANL, USA, provided reliable data suitable for simulation via CPFE modelling. With a series of neutron spectra, one can measure the response of grains in multiple orientations, in terms of their lattice strain and texture change. The sample movement texture change artefact, prevalent in the ENGIN-X experiment, was minimised by careful experimental design and a pre-load texture measurement at different locations along the specimen axis to calculate the correct reference texture for texture change calculation. Higher strains were achieved in this experiment, and the gauge volume in specimen ND-T4 was centred on the region of strain localisation before fracture.

Whilst the Rietveld refinement allowed measurement of axial texture, the fact that it averages over the entire spectrum caused some issues with strain measurement in these highly textured specimens. The difference in yield stresses between FG and CG material seen with the SPF strains was not seen so clearly in the Rietveld refinement, and the anomalous behaviour of the ND-T3 Rietveld strains was attributed to the strong texture. The single-peak strains, whilst noisier than the Rietveld data, correctly capture the deformation.

Ministry of Defence © British Crown Copyright 2020/AWE

The tension-compression asymmetry was seen to be the result of the asymmetric Schmid factors for twinning. With reference to the twinning reorientations calculated in chapter Chapter 3, the texture changes were seen to be the result of the activation of {130} and '$\{172\}$' twinning modes in the dominant texture components of each specimen.

Neutron diffraction experiments like the one presented in this chapter can be simulated via CPFE modelling. The ENGIN-X experiment has been simulated by Grilli et al, and a set of optimised deformation parameters were calculated which best match the simulation to the experimental data. It was not possible to estimate these parameters directly from the experimental data without simulation. The texture changes measured in this chapter will allow the twin volume fraction to be calibrated in future simulations.

There are, however, limitations to diffraction experiments. Grain clustering is seen to have an effect in the modelling on the development of strain, but the spatial distribution of grains is not easily measured with diffraction. The large neutron gauge volume allows no measurement of the interactions between grains, such as along boundaries, nor does it allow the distribution of strain within a grain, and it is these locations which are likely initiation sites for fracture.

In the final experimental chapter, an experiment is presented where the distribution of strain within the grain clusters can be resolved.

Ministry of Defence © British Crown Copyright 2020/AWE

Ministry of Defence © British Crown Copyright 2020/AWE

Chapter 5 Full-field Strain Measurement during Tensile Deformation of Cast Uranium

5.1 Introduction

The work in the previous two chapters used time-of-flight neutron diffraction to measure texture changes and elastic strain development in bulk cast uranium specimens under tensile and compressive loading. This data has allowed the development and calibration of crystal plasticity models that could simulate such experiments with reasonable accuracy.

However, neutron diffraction experiments have some inherent limitations. In particular, the neutron gauge volume is large, sampling multiple grains. Since the spatial distribution of the grains inside the gauge volume is unknown, the misorientations between neighbouring grains are unknown, producing constraint effects which cannot be identified. In a typical gauge volume many deformation modes will be active, and it is challenging to separate the effects of each mode on the lattice strains. There is therefore some uncertainty around the CRSS values for the deformation modes, in particular of Wall and Floor slip, which are both predicted to activate at resolved shear stresses between 7 MPa and 10 MPa.

Whilst neutron diffraction is well suited to measuring changes in peak position (i.e. elastic strain), it cannot easily measure the plastic strain development in a grain. This

Ministry of Defence © British Crown Copyright 2020/AWE

makes the calibration of hardening parameters for each deformation system challenging as it can only be done by comparison with the macroscopic flow curve – which contains contributions from all active deformation modes, rather than for each grain individually.

In this chapter I will present an experiment which overcomes many of these limitations and will allows the calibration of CRSS parameters for each deformation system in subsequent CPFE models.

Flat dog-bone tensile specimens had the microstructure in their gauge volume characterised with EBSD. A tensile testing experiment with in-situ digital image correlation was then performed on each specimen, and the measured strain field in each grain was related to the underlying grain orientation. A bespoke tensile rig was designed and built to allow the testing of radioactive specimens within the University of Oxford. The observed strain field was highly heterogeneous and the localisation of strain was clearly correlated with grain orientation. The use of a stereo (2-camera) DIC system allowed the accurate measurement of strains in the presence of significant out-of-plane displacements.

Firstly, I will show the microstructural characterisation with EBSD. This was challenging, as it required the polishing of the entire gauge region to a standard suitable for EBSD, and then the stitching of multiple EBSD datasets together to produce a single orientation map for the gauge region of each specimen.

Ministry of Defence © British Crown Copyright 2020/AWE

I will then present the tensile testing experiment with in-situ stereo DIC, and the segmentation of the DIC-measured displacement and strain field according to grain orientation. In each specimen, strain is seen to localise in one or two locations; these strain concentrations and associated out-of-plane displacement are related to the activation of slip deformation. In the third specimen, Wall slip and Floor slip are each favoured respectively in two adjacent grain clusters loaded in series, with a similar magnitude Schmid factor in each case. The majority of the strain accumulates in the cluster favourable for Wall slip.

A brief section at the end of the chapter will show how the results from this test have allowed Nicolò and the CPFE modelling team to obtain a better calibration of the CRSS parameters and the interaction parameters between slip and twinning systems.

5.2 Microstructural Characterisation

In order for the observed deformation to be related to grain orientation and the corresponding Schmid factors for each deformation mode, a grain orientation map must be produced for the gauge region of each tensile specimen.

Three tensile specimens of identical design were produced by wire EDM at AWE plc. and shipped to the Interface Analysis Centre, University of Bristol, for EBSD analysis. Each specimen was a dog-bone shape (figure 5.1), 100.00 mm in length with a parallel gauge region with dimensions 32.00 mm $\times$ 6.00 mm. The grip regions at each end of the specimen had a width 3 times that of the gauge region. Each specimen had a thickness

Ministry of Defence © British Crown Copyright 2020/AWE

of 1.50 mm. Note that this thickness was reduced by the polishing process – the dimensions of each polished specimen were measured before testing.

The specimens were named DB-T1, DB-T2 and DB-T3 (Dog Bone-Tensile).

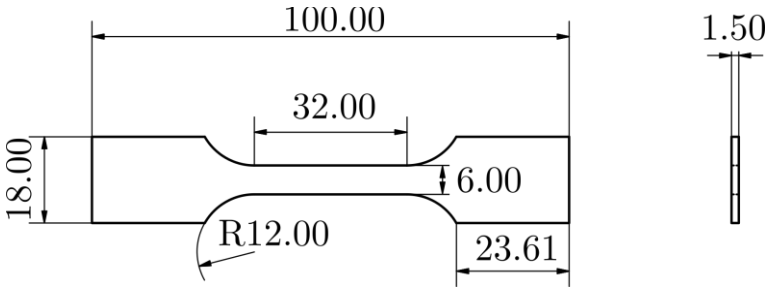


Figure 5.1. Drawing of the tensile bars used in this experiment. All dimensions in mm.

5.2.1 Specimen Preparation

Specimen preparation was performed in the radioactive lab at the Interface Analysis Centre, School of Physics, University of Bristol.

Each specimen was placed into the bottom of a plastic container and Struers ClaroCit clear acrylic cold mounting resin was added to a thickness of approximately 1 cm. After the resin had cured, the mounted specimen was removed from the container and a brass polishing handle was attached with cyanoacrylate glue on the top surface of the resin.

Ministry of Defence © British Crown Copyright 2020/AWE

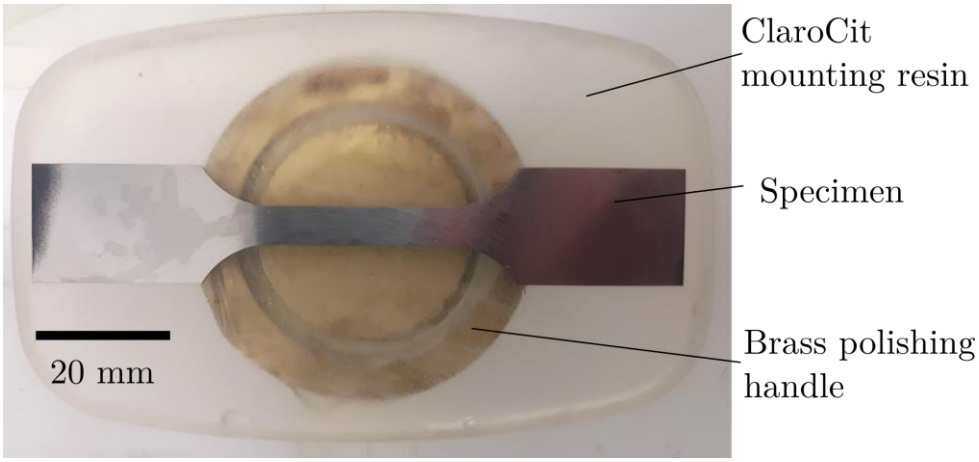


Figure 5.2. Uranium tensile specimen mounted in clear resin for grinding and mechanical polishing.

The specimen was ground on 180 grit paper to remove the oxide layer from the majority of the front specimen face, and then on progressively finer papers from 600 grit to 2500 grit until the surface in the gauge volume was flat. Figure 5.2 shows the specimen surface after grinding at 2500 grit. With downward pressure applied to the centre of the specimen from the polishing handle, the specimen bowed slightly and the polishing at each end of the specimen was not sufficient to completely remove the oxide layer, as shown towards the left hand side of figure 5.2. The specimen was then polished with 6 μm, 3 μm, and 1 μm diamond suspension until a scratch-free mirror finish was achieved.

The specimen was then removed from the mounting resin by immersion in acetone in an ultrasonic bath. The specimen was carefully removed from the resin by prising it out from each end. This was particularly challenging as care was required not to bend the specimen, and took in excess of 3 hours per specimen. The specimen was rotated by 180° about its longitudinal axis and re-mounted in resin. The rear face of the specimen was ground to remove the oxide layer and then sequentially ground to 2500 grit. Polishing

Ministry of Defence © British Crown Copyright 2020/AWE

was performed with 6 μm diamond suspension to remove any surface scratches which may act as stress concentrators during the subsequent testing. The specimen was then removed from the resin using the same procedure as described above, and was now ready for electropolishing.

The set-up for electropolishing is similar to that in Appendix A3.2.1 on page 345, with the specimen connected to the anode inside the same electrolyte of ethylene glycol, ethanol and phosphoric acid. The specimen was lowered into the electrolyte such that the majority of the gauge region was to be polished, as in figure 5.3(a). The specimen was polished for approximately 10 minutes at 12V with continuous stirring followed by rinsing in tap water. The polishing sequence of McCabe and Teter [131] was used, with a brief second electropolish in an electrolyte of 5 % phosphoric acid and 95 % water for 2 seconds. This second polish is believed to form a thin passivating oxide layer which slows the formation of a thicker oxide layer that would be detrimental to EBSD pattern quality [131]. The part of the specimen polished in the second electrolyte was seen to have a bright shiny surface compared to that just polished in the first. The specimen was again rinsed with tap water and acetone, and then dried with soft paper.

The specimen was then rotated 180° and then mounted in the inverse orientation for polishing of the other half of the specimen, as shown in figure 5.3(b). An identical two-step polish was then performed.

Ministry of Defence © British Crown Copyright 2020/AWE

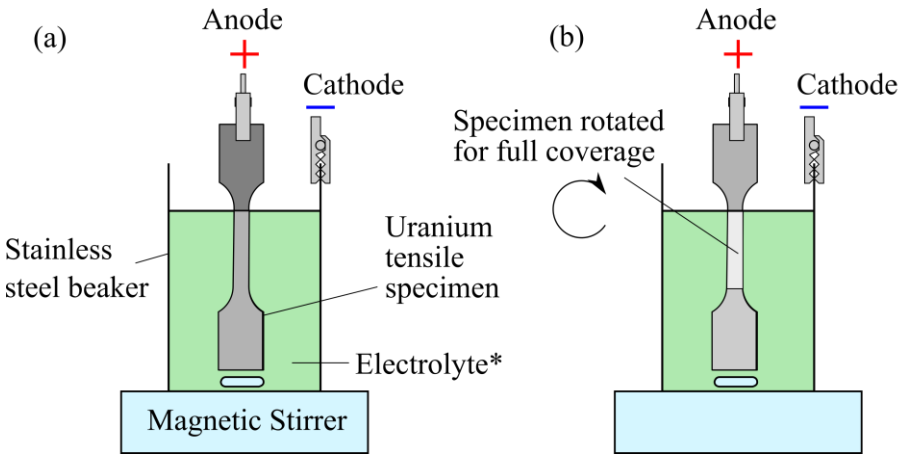


Figure 5.3. Electropolishing set-up for tensile specimens in the initial orientation (a) and inverted orientation (b), allowing polishing of the whole length of the specimen. (*) The beaker and electrolyte was exchanged between the first and second polishing stages in each orientation.

The specimen was then mounted onto two 18 mm diameter SEM pin stubs with adhesive carbon tape, and the specimen edges were covered with a layer of silver conductive paint to ensure good conductivity and prevent the heavy specimen from moving in the microscope when tilted. The specimen and stub were transferred rapidly to the SEM for EBSD analysis.

5.2.2 EBSD Data Acquisition

EBSD was performed in the same Zeiss Sigma HD VP Field Emission SEM used for the microstructural analysis in Chapter 3. The specimen was mounted such that when the stage was tilted, the specimen rotated about its longitudinal axis. Each specimen was labelled with the specimen name engraved on one surface of one grip region. This label was positioned towards the left of the SEM image, facing upwards, and would correspond to the uppermost camera-facing end of the specimen in the subsequent tensile testing. A tilt angle of 70° was then applied via the SEM stage. Figure 5.4 shows a schematic of the EBSD set-up viewed along the longitudinal axis of the specimen.

Ministry of Defence © British Crown Copyright 2020/AWE

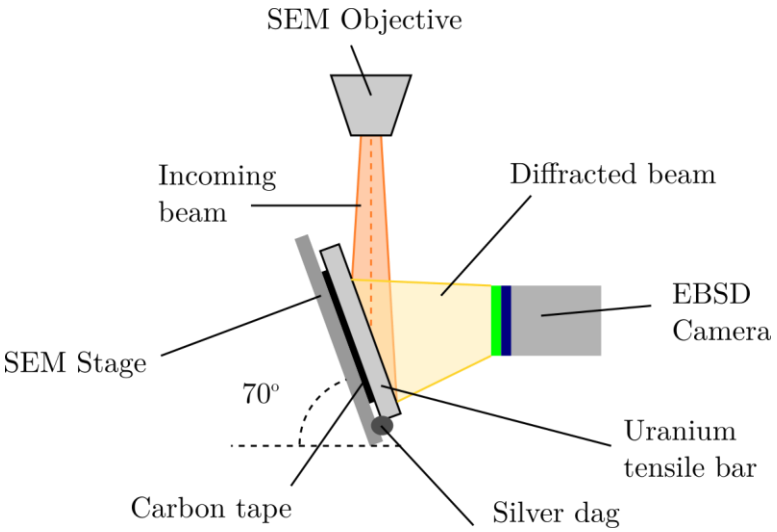


Figure 5.4. Schematic of the EBSD set-up for orientation mapping of the uranium tensile bars. Viewed along the specimen longitudinal axis (aligned with the stage tilt axis).

It was desired to characterise the microstructure across the entire tensile gauge section of 32 mm × 6 mm, a very large area for conventional EBSD. A series of smaller EBSD maps were acquired and stitched together to achieve full coverage. This was non-trivial and required a number of calibration and correction steps to achieve the final EBSD orientation maps. These steps are described in the following sections.

The microscope software was updated between the analysis of specimens DB-T2 and DB-T3 so the acquisition procedure is slightly different for the latter specimen.

5.2.2.1 Specimens DB-T1 & DB-T2

For specimens DB-T1 and DB-T2, at a working distance of 14 mm, the minimum magnification available was 32×. This allowed the entire width of the gauge section to be in the field of view of the microscope when tilted, as shown in figure 5.6.

Ministry of Defence © British Crown Copyright 2020/AWE

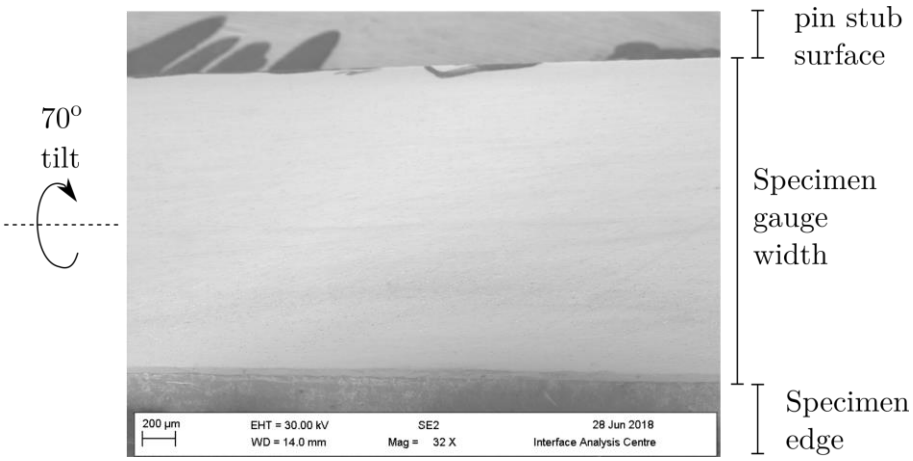


Figure 5.5. SEM image of a section of the gauge region of specimen DB-T2. Specimen was tilted by 70° about its longitudinal axis.

The EBSD scan is defined by rastering the beam in a grid whose bounds are defined by selecting a rectangle in the SEM image. The tilt of the specimen leads to the array of points on the specimen surface being distorted compared to the selected array. This is explained diagrammatically in figure 5.6. Since the specimen is tilted, the field of view is greater towards the lower part of the specimen (points B and C in figure 5.6) compared to the part closest to the SEM objective (points A and D). This means that the rectangular grid, defined on the SEM image (viewpoint 1 in figure 5.6), should correspond to a trapezium when viewed from a point normal to the specimen surface (viewpoint 2). The grid of EBSD points will therefore be distorted accordingly. In reality, the specimen axis may not be perfectly aligned with the horizontal axis in the SEM image, so the rectangle will distort to a more general quadrilateral.

Ministry of Defence © British Crown Copyright 2020/AWE

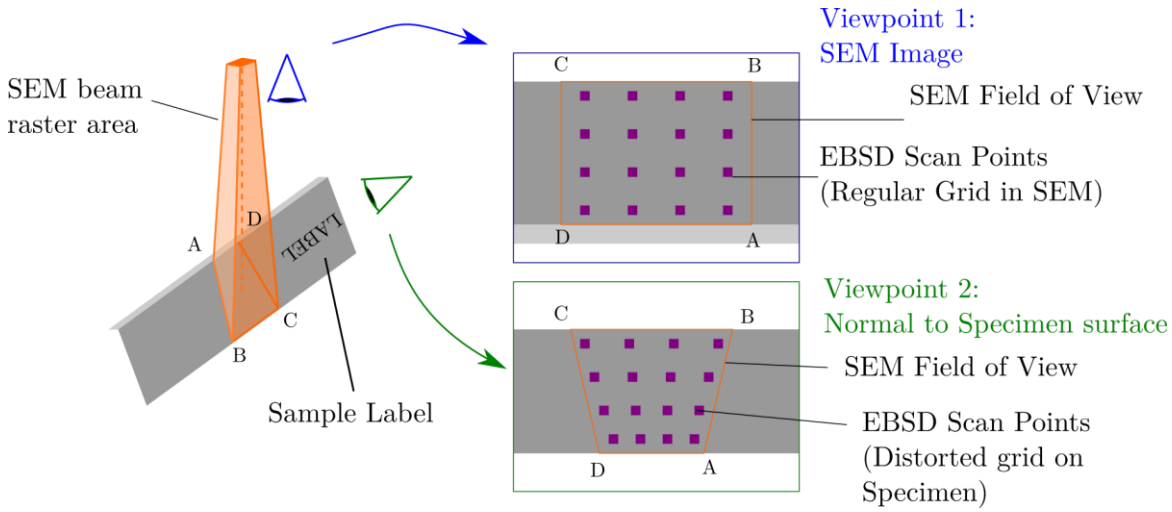


Figure 5.6. The tilt of the specimen results in the EBSD scan grid, defined in the SEM image, to be a distorted quadrilateral on the surface of the specimen.

To produce an orientation map of the entire gauge region, it is necessary to stich multiple EBSD maps together, with each constituent map having a translation along the specimen axis. The magnitude of translation was chosen such that neighbouring scans overlap such that the whole gauge region will be measured, as in figure 5.7(a). Each map had an approximate spatial resolution of 25 μm with around 60,000 points per scan. 14 scans were required to achieve full coverage of the gauge region. For specimen DB-T1, additional scans were taken covering approximately 5 mm of the curved region at each end of the gauge region.

The EBSD data was stored as a regular undistorted grid, and could not be directly stitched together. A distortion correction needed to be applied such that the EBSD data represented the correct points on the specimen surface (see figure 5.7(b)). The distortion-corrected EBSD orientation maps could then be stitched together to produce a map of grain orientations in the entire gauge region (figure 5.7(c)).

Ministry of Defence © British Crown Copyright 2020/AWE

The distortion correction method is described in section 5.2.3.

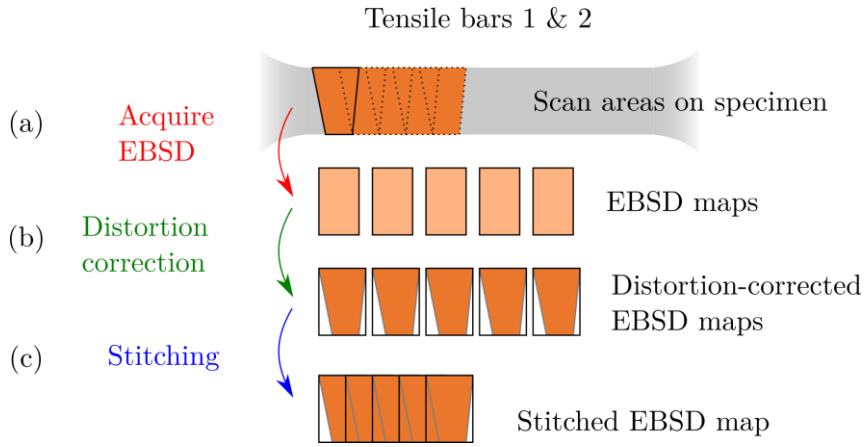
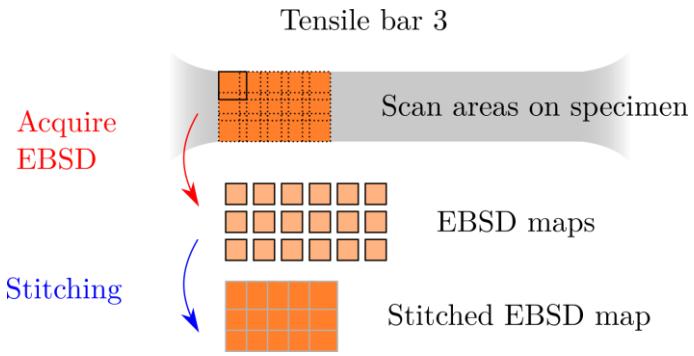


Figure 5.7. Workflow for obtaining EBDD orientation maps from specimens DB-T1 and DB-T2. (a) Acquisition of EBSD maps with overlapping scan regions. (b) Distortion correction to correct the EBSD data points to the distorted grid representative of the point locations on the specimen surface. (c) Stitching the EBSD maps together to produce a composite orientation map of the entire gauge region.

5.2.2.2 Specimen DB-T3

Before specimen DB-T3 was analysed, the microscope was recalibrated by the Zeiss engineer and the distortion correction was now automatically performed, at the expense of a smaller field-of-view at a minimum magnification of 84×. To achieve full coverage of the gauge region, three scans were made at different positions across the specimen width, as shown in figure 5.8. Stitching of the resulting EBSD scans to form the composite image was trivial as the distortion correction was already applied to the data.



Ministry of Defence © British Crown Copyright 2020/AWE

Figure 5.8. Workflow for obtaining EBSD orientation maps from specimen DB-T3, after the recalibration of the microscope. A smaller field-of-view required three scans to cover the specimen width. Distortion correction is automatically performed so stitching is trivial.

A total of 48 scans in a 3×16 array were required to cover the gauge region.

5.2.3 EBSD Data Processing

EBSD pattern indexing was performed in EDAX OIM Analysis™ software using the crystal information file for alpha-uranium [142] to identify the crystal orientation at each point. The EBSD data from each scan was saved in the `.ang` text format, with each file containing the positions (x, y) and the orientation Euler angles (ϕ_1, Φ, ϕ_2) of each point.

5.2.3.1 Orientation Map Generation

Subsequent processing was performed in MATLAB using the MTEX [134] toolbox. Some orientations in the raw data were noisy, with poorly indexed points being particularly prevalent towards the top and bottom of each EBSD map. Here, the beam was further from the nominal working distance of 14 mm, and was slightly out-of-focus, giving blurred patterns that are harder to index accurately. In addition, points towards the top and bottom of each image which were outside the specimen area could not be indexed correctly, and appear as regions with random orientations. A sequence of post-processing steps were applied to produce EBSD datasets with these poorly-indexed points removed. The steps are shown pictorially in figure 5.9.

Ministry of Defence © British Crown Copyright 2020/AWE

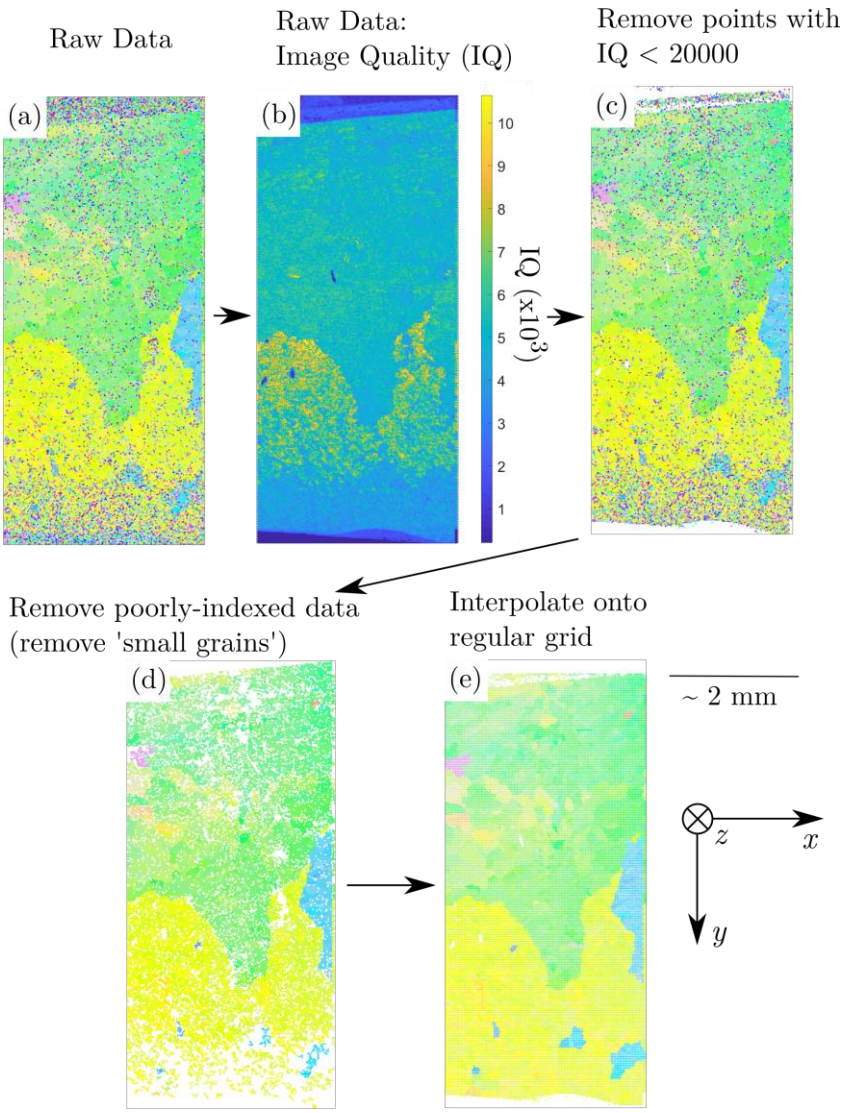


Figure 5.9. Pictorial representation of the processing steps taken to remove the poorly-indexed points and fill in resulting gaps in the EBSD data. Data points are coloured according to the crystal parallel to the out-of-plane direction. (a) Raw data from the microscope. (b) EBSD pattern Image Quality (IQ) at each data point. (c) Removal of data points from outside the specimen gauge region – those with an IQ less than 20000. (d) Removal of single poorly-indexed data points due to twinning, grain boundaries, carbides or EBSD patterns from out-of-focus parts of the specimen. (e). Filling in gaps in the dataset by interpolating the data onto a regular grid. Data points from outside the specimen gauge region remain absent. The EBSD co-ordinate system is shown.

The first step removes data points which are situated outside the specimen gauge region – those points either on the pin stub surface or on the specimen edge. Neither give good EBSD patterns therefore the 'pattern image quality' (IQ) parameter is low for these regions. The spatial variation of the IQ parameter is plotted in figure 5.9(b). It can be

Ministry of Defence © British Crown Copyright 2020/AWE

seen that the regions outside of the specimen have IQ values less than 20000. An IQ threshold is applied to identify and remove these points.

The resulting data, shown in figure 5.9(c), had a significant area fraction (up to 35 % in some scans) where the orientation varies randomly between neighbouring points. This is the result of poor EBSD indexing, to which a number of factors contribute. Firstly, if the electron interaction volume intersects a twin or grain boundary, the EBSD pattern will contain contributions from both orientations and will therefore be blurred. Secondly, if the beam impinges upon a carbide, the diffraction pattern will not match that of uranium metal, so the calculated orientation will be random. Finally, EBSD patterns from out-of-focus parts of the specimen (top and bottom of each map) may be blurred as the electron beam spot size on the specimen surface will be larger and may intersect regions of differing orientations.

In MTEX, each data point was assigned into grains according to a 10° misorientation threshold. The median grain area was the that of a single point, so those grains with an area less than 5 points were removed from the dataset. This left the properly-indexed EBSD data with gaps present where data were removed, as in figure 5.9(d).

Finally, the `fill` function in MTEX was used to perform a nearest-neighbour interpolation of the data onto a rectangular grid. In some cases, this resulted in data points being generated outside of the specimen area, so these were again removed using the mask generated by the IQ threshold. This produced an EBSD dataset in which

Ministry of Defence © British Crown Copyright 2020/AWE

orientations are known across the specimen width, and grain boundaries can be clearly seen.

Orientation maps were generated for each scan with each point coloured according to the crystal direction parallel to (i) the specimen axis (IPF-X), (ii) the vector normal to the specimen axis in the plane of the observed surface (IPF-Y), and (iii) the surface normal (IPF-Z).

5.2.3.2 Schmid Factor Map Generation

In order to assess the activation of deformation modes within the specimen it is useful to calculate the Schmid factors for tensile deformation at each point in the EBSD dataset. The Schmid factor is dependent on the angle of the crystal with the tensile axis (equivalent to the specimen axis or *x*-vector in the EBSD data).

From the Euler angles for each point, Schmid factor maps were generated for each scan, for Wall, Floor, Chimney and Roof slip, and for {130}, '{172}', '{176}, and {112} twinning. Each point was coloured according to its Schmid factor, with points with a negative Schmid factor coloured as if the Schmid factor was equal to zero.

5.2.3.3 Distortion Correction

As discussed previously, a distortion correction is required to convert the rectangular grid of EBSD data to a distorted grid representative of the data points on the specimen. If a transformation matrix can be found that distorts the rectangular EBSD grid to the quadrilateral on the specimen surface, then the transformation can be simply applied to

Ministry of Defence © British Crown Copyright 2020/AWE

all EBSD maps from a particular specimen. The required transformation is a 2D projective transformation, defined in MATLAB using the function `projective2d` [143] in the Image Processing Toolbox.

A calibration procedure was implemented as follows, shown diagrammatically in figure 5.10. A series of calibration images were taken of features that were known to be horizontal or vertical when viewed along the surface normal vector *z*. These features would appear distorted in the SEM image due to the oblique field of view. The correct transformation matrix, when applied to each of the calibration images, should result in the features being horizontal or vertical as required.

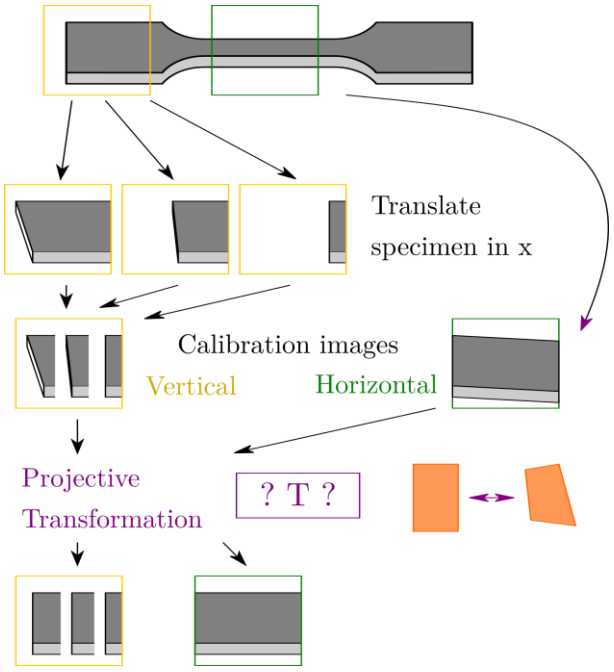


Figure 5.10. Overview of the procedure used to identify the projective transformation matrix T required to distortion-correct the EBSD datasets. The matrix T must be found such that the features in the calibration images are transformed to be vertical and horizontal in the images.

Ministry of Defence © British Crown Copyright 2020/AWE

The horizontal calibration image was a single image of the specimen gauge region, where the top and bottom edges of the specimen face should be horizontal in the EBSD dataset (figure 5.11(b)).

The distortion of features nominally vertical in the image varies with the horizontal position of the feature. A series of SEM images of the left-hand end of the specimen were acquired with the specimen at different *x*-positions. These were combined into a composite image, shown in figure 5.11(a).

The single transformation matrix T that corrects both the horizontal and vertical calibration images was manually identified. The transformed vertical and horizontal calibration images are shown in figure 5.11(c) and figure 5.11(d) respectively.

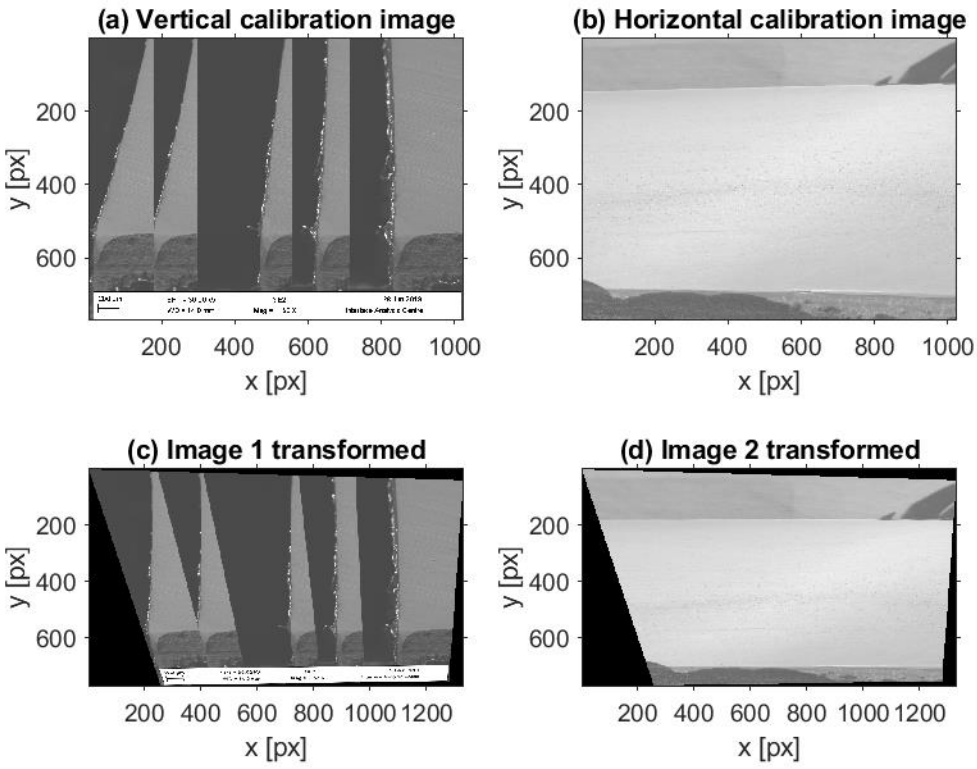


Figure 5.11. Distortion of the (a) vertical and (b) horizontal calibration images by the transformation matrix T to yield (c) vertical and (d) horizontal calibration features.

Ministry of Defence © British Crown Copyright 2020/AWE

A reduced co-ordinate system was defined where the corners of the calibration images were at $(0,0)$ – top left, $(1,0)$ – top right, $(1,1)$ – bottom right, and $(0,1)$ – bottom left. The required transformation was found to be one which mapped these co-ordinates to the following co-ordinates of a quadrilateral: $(-0.25,0)$ – top left, $(1.05,0.05)$ – top right, $(1,0.98)$ – bottom right, and $(0,1)$ – bottom left.

The associated transformation matrix was found from these 'control points' using the `fitgeotrans` function in MATLAB, and was found to be equal to:

$$T = \begin{bmatrix} 1.386 & 0.054 & 0.082 \\ 0.250 & 1.304 & 0.304 \\ -0.250 & 0 & 1 \end{bmatrix}$$

This transformation matrix was found to be suitable for distortion correction of EBSD data from both specimens DB-T1 and DB-T2.

The projective transformation describes the general transformation from co-ordinates in the SEM images to points on the specimen surface. The exact distortion that each EBSD scan should incur depends on the location of the EBSD scan outline rectangle in the SEM image.

The raw EBSD data were aligned with the scan outline rectangle in the SEM image, and the vertices of the rectangle were given reduced co-ordinates in the SEM image, as shown in figure 5.12(a). The transformation matrix *T* was applied to yield the distortion-corrected EBSD data in figure 5.12(b). It can be seen that the top and bottom edges of the specimen are now parallel, and that the field-of-view at the top of the image (the

Ministry of Defence © British Crown Copyright 2020/AWE

lower part of the specimen, as tilted) is greater than at the bottom, which is consistent with our expectations.

This distortion correction process was applied to each EBSD map from specimens DB-T1 and DB-T2.

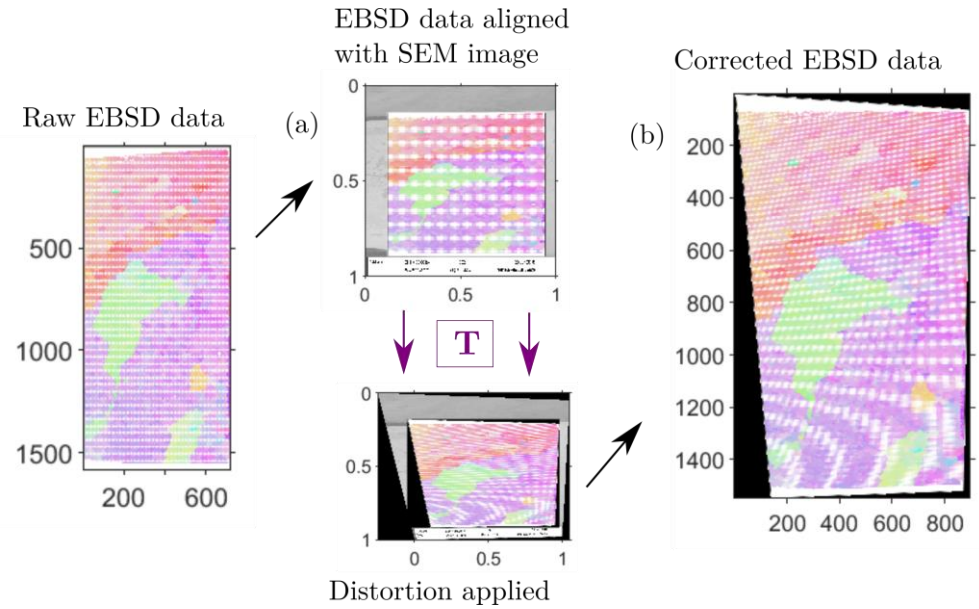


Figure 5.12. Distortion correction of the EBSD data by application of the transformation matrix *T*. The streaks are aliasing artefacts in the distorted image and are not features of the data.

5.2.3.4 Stitching Composite Maps

The series of distortion-corrected maps were manually stitched together in Inkscape v0.92 [144] based on the location of shared features in neighbouring scans. The resulting map was scaled such that the data with parallel specimen edges fill a rectangle of aspect ratio 32:6, representing the 32 mm $\times$ 6 mm dimensions of the specimen gauge region.

Ministry of Defence © British Crown Copyright 2020/AWE

This procedure was repeated to create composite maps for the three orientation colourings IPF-X, IPF-Y and IPF-Z, as well as the eight Schmid factor maps for each specimen.

Ministry of Defence © British Crown Copyright 2020/AWE

5.3 Tensile Rig Development

The tensile testing experiment was performed in the Mechanical Testing Laboratory in the Department of Materials, University of Oxford. This is not usually a radioactive lab, so a containment system was required to prevent contamination of the load frame during testing, as well as minimising the risk of the loss of uranium pieces in the event of the specimen fracturing.

The load frame selected for use was a Shimadzu Autograph AGS-X universal tensile tester with wedge grips. The associated tensile wedge grips apply a clamping force to flat specimens with small teeth which grip into the specimen surface. Directly gripping the uranium specimens would lead to contamination of the grips, so an alternative method of applying load to the specimen was required in which the specimen did not directly contact the grips.

The total strain applied to the specimen would be less than the failure strain seen in specimens ND-T3 and ND-T4. However, if the specimen were to fracture, a significant amount of the elastic strain energy contained in the load train would be released into the free specimen ends as kinetic energy. There were concerns that given the large grain size, it may be possible for such motion to release a grain or cluster of grains from the specimen, which would contaminate the laboratory and tensile tester. The tensile rig must dissipate this energy in the event of a specimen fracture.

Ministry of Defence © British Crown Copyright 2020/AWE

The specimens are large, with a mass of 35 g per specimen and an activity of 0.53 MBq. To minimise the external dose to the author when mounting the specimens and performing the test, the tensile rig must shield the specimen from the user. The alpha dose is not a hazard at the working distance of many tens of centimetres. Aluminium and Perspex are suitable materials for reducing the beta dose. The gamma dose is small and was considered insignificant. The specimen surface must, however, be observed with the DIC cameras, so it cannot be completely enclosed by the tensile rig.

5.3.1 Requirements

To summarise, the tensile rig must satisfy the following requirements:

A Shield majority of specimen from user

B Contain material in the event of a specimen fracture

C Dissipate energy in the event of a specimen fracture

D Prevent contact between the specimen and the tensile grips

E Allow viewing of the specimen surface with the DIC cameras.

5.3.2 Design Development

A bespoke tensile rig was designed by the author to satisfy all 5 of the above requirements. A validation 'dummy-run' was performed using a ductile steel specimen to ensure that the set-up was working as intended with no unwanted stress concentrations caused by the tensile rig.

Ministry of Defence © British Crown Copyright 2020/AWE

5.3.2.1 Tensile Rig Design

After consideration of a preliminary design (Appendix A9.1), a second, improved design was produced. The load was transferred to the specimen via two steel grips, with a replaceable ductile copper bar placed between them, in parallel with the specimen.

Ductile material loaded in parallel to the uranium specimen will absorb the released elastic strain energy in the event of specimen fracture. It will also bridge the gap between the two tensile grips and maintain the integrity of the grip-specimen-grip fixture, preventing rapid motion of the specimen.

The specimen would be mounted and then the whole rig surrounded by an aluminium cover. A small window was cut in the front aluminium plate, just large enough to view the gauge volume of the specimen with the DIC cameras (section 5.4.2). An external Perspex shield would be placed between the specimen and the operator, outside the field-of-view of the cameras. An exploded diagram of the tensile rig is shown in figure 5.13.

The copper sacrificial bar was to be attached to the upper and lower grips with 4 M4 screws, two per grip. Preliminary testing showed that if all four screws were tightened, the upper and lower grips would be pulled out of alignment. It was therefore decided to use just two screws – those closest to the specimen. The copper bar could therefore rotate with respect to the upper and lower grip and would interfere less with the loading force. It was necessary to narrow the gauge of the centre of the copper bar to prevent fracture occurring at the stress concentration around the screw mounting hole.

Ministry of Defence © British Crown Copyright 2020/AWE

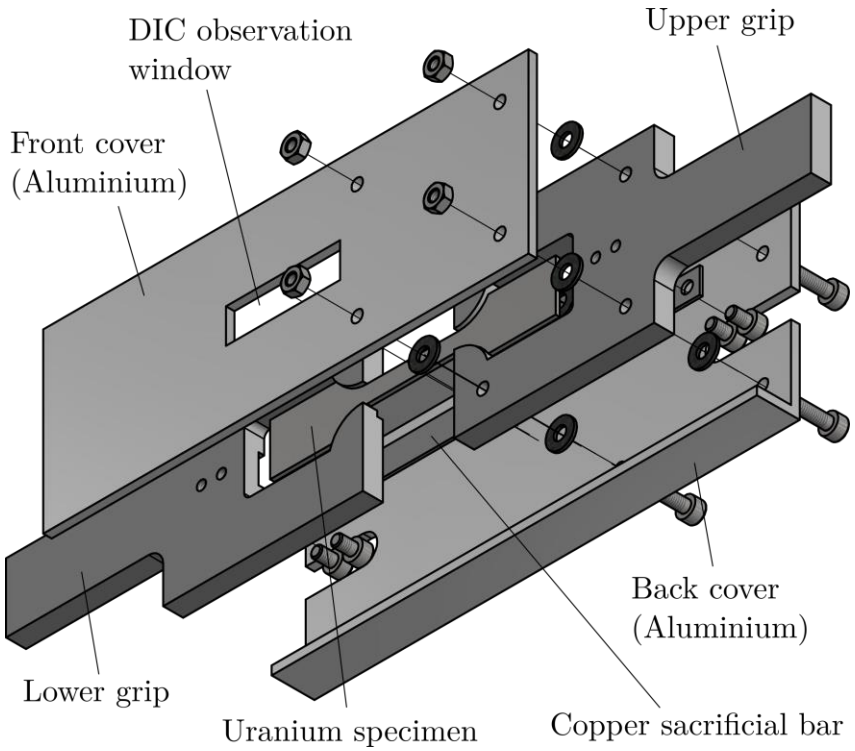


Figure 5.13. Final design of the uranium tensile rig. Exploded view showing the arrangement of the components.

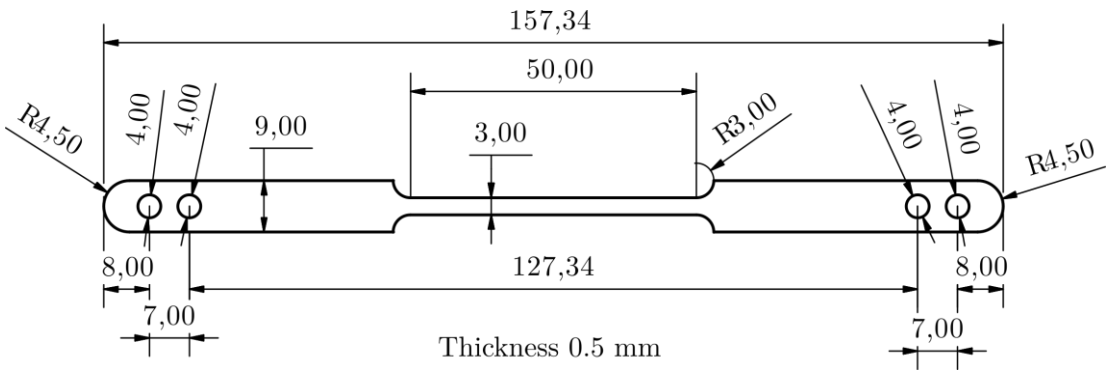


Figure 5.14. Drawing of the copper sacrificial bar used in the tensile test experiments.

The main tensile rig was manufactured by the workshop in the Department of Engineering Science, University of Oxford. The copper bars were laser-cut from a sheet of 0.5 mm copper by Charles Day (Steels) Ltd., Sheffield S4 8BT.

Ministry of Defence © British Crown Copyright 2020/AWE

5.3.3 Validation

It was necessary to ensure that the tensile rig performed correctly, applying a uniform axial force to the specimens without any undesired effects from the grips. A tensile test was performed on a dummy mild steel specimen with the stereo DIC system (described in section 5.4.2) used to measure the axial strain field on the specimen surface.

The specimen eventually failed due to necking in the gauge region. The measured strain field at the point just before neck formation is shown in figure 5.15. The strain is uniform in the gauge volume which demonstrates that the loading is axial, as required. No strain concentrations are seen at the contact points between the curved specimen edges and the tensile rig.

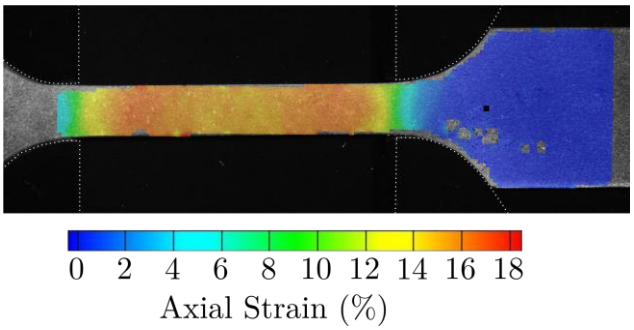


Figure 5.15. Axial strain field on steel specimen used to validate the tensile rig design.

Mild steel work hardens rapidly so any localised deformation at the contact point would be counteracted by a strengthening of the material preventing localised deformation at the contact point. We know from previous tests (e.g. ND-T3 and ND-T4 in figure 4.17 on page 130) that uranium also work hardens significantly, so in the uranium specimens strain is expected to also concentrate in the gauge region.

Ministry of Defence © British Crown Copyright 2020/AWE

5.4 Experimental Method

5.4.1 Copper Bar Deformation

The copper bar is loaded in parallel with the uranium specimen, so the load cell therefore measures the total force in both the copper bar and the uranium specimen. The force solely in the uranium is required to calculate the associated stress. If the force in the copper is known as a function of grip displacement, this can be subtracted from the total force to obtain the force carried by the uranium.

The copper bar is deliberately shorter than necessary to allow the specimen to be easily inserted into the gap between the upper and lower grips after the bar has been installed. The copper must therefore plastically deform for a displacement of approximately 5 mm before the uranium starts to take up load. It was therefore possible to extrapolate the load-displacement curve for copper from the region where solely copper is straining to the region at higher displacements where the uranium specimen is also under load.

A set of three tests were performed where copper bars were loaded without a specimen being in place. Plastic strain was visually seen to be uniform in the narrow 3 mm wide section of the bar. The load-displacement curve from one of these tests is plotted in blue in figure 5.16.

Ministry of Defence © British Crown Copyright 2020/AWE

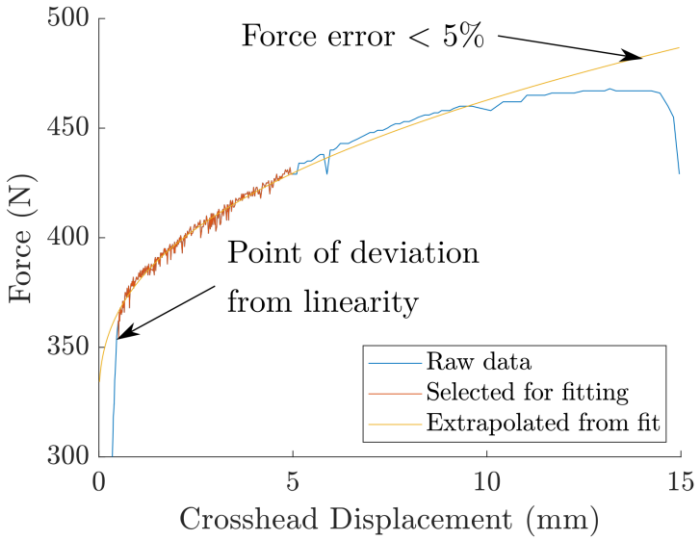


Figure 5.16. A power law curve was suitable to estimate the force in the copper specimens at displacements between 5 mm and 10 mm from the data at smaller displacements. When the copper is loaded in parallel with uranium this will allow the force in the copper to be separated from the total force in both specimens, allowing the force and therefore stress in the uranium to be calculated.

Data from the point of deviation from elastic linearity to a displacement of 5 mm (shown in orange in figure 5.16) was used to fit a power law curve of the form:

$$F = ax^b + c \qquad [5.1]$$

where x is the crosshead displacement, F is the force, and a, b, and c are the fitting parameters. The extrapolation of this curve to displacements greater than 5 mm is plotted in yellow in figure 5.16, and was compared with the raw data. This form of curve was chosen as it was seen to produce a good fit between the extrapolated force and the actual force for the expected displacements which are in the range $5 - 10$ mm.

Using the data at displacements less than 5 mm, a power law curve was found to be suitable to predict the force in all three copper specimens at displacements greater than 5 mm.

Ministry of Defence © British Crown Copyright 2020/AWE

5.4.2 Stereo DIC System Set-up

A GOM ARAMIS 5M Stereo DIC system was kindly provided by AWE plc. for the duration of the DPhil project. The expected displacement field is highly heterogeneous, with significant out-of-plane displacements as the specimen deforms. A multi-camera DIC system is therefore necessary to correctly measure the strains on the specimen surface, as discussed in the literature review (section 2.6.1.1)

5.4.2.1 Specifications

The specifications of the GOM ARAMIS 5M DIC system are shown in table 5.1.

Table 5.1 GOM ARAMIS 5M DIC system specifications

Component	Description
Sensor	2× ARAMIS 5M
Sensor Type	CCD
Sensor Resolution	2448 x 2050 pixels 8-bit mono
Lens	Titanar 75 mm
Specimen Lighting	2× High-power LED Arrays
Polarising Filter	Yes, on lights and lenses
Software	GOM Aramis v6.3.0-6
	S/N 2-2222160

With the components provided, two different calibrated measuring volumes could be achieved. The measuring volume is defined in figure 5.17, reproduced from the ARAMIS hardware manual [145]. The measuring volume length and width are determined by the positioning of the cameras and the lens set-up whilst the height is defined by the aperture-dependent depth-of-field.

Ministry of Defence © British Crown Copyright 2020/AWE

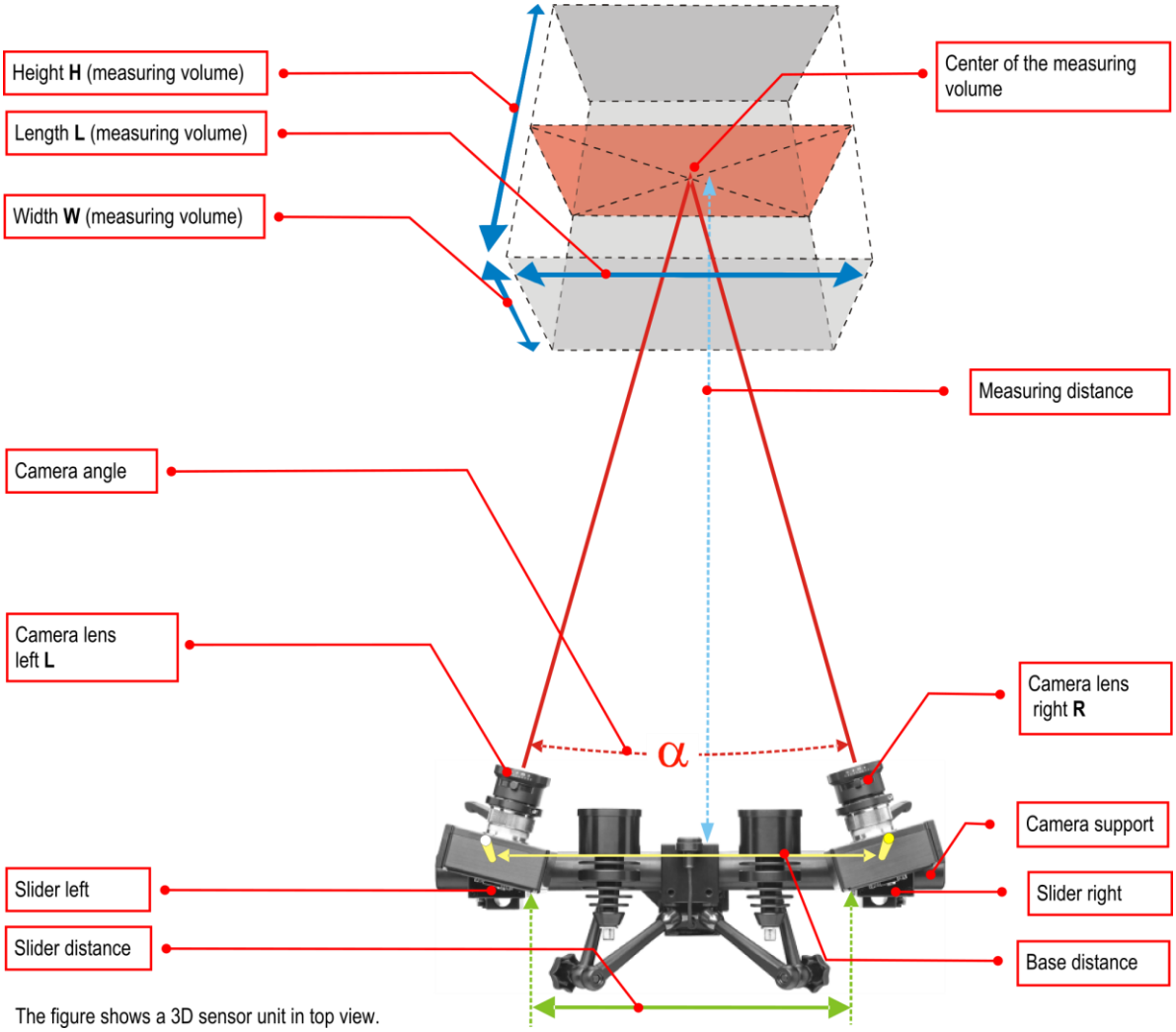


Figure 5.17. Definition of the measuring volume with respect to the camera system. Reproduced from the GOM ARAMIS hardware manual [145].

The possible measuring volumes are shown in table 5.2, with values taken from the ARAMIS Sensor Configuration Tables [146].

The camera angle of 25° was recommended by the manufacturer as a good compromise between the improved in-plane accuracy of smaller camera angles and the improved out-of-plane displacement accuracy of larger angles.

Ministry of Defence © British Crown Copyright 2020/AWE

Table 5.2. Potential measuring volumes for GOM ARAMIS 5M as configured.[146]

Parameter	Option A	Option B
Measuring volume length (mm)	15	50
Measuring volume width (mm)	13	44
Depth of field at minimum aperture (mm)	2.5	37
Approximate pixel size (μm)	6	20
Camera Angle (°)	25	25
Lens extension tubes (mm)	30	none
Measuring distance (mm)	310	595
Slider distance (mm)	98	224
Calibration object	CQ 15×12	CQ 55×44

The specimen surface must remain inside the DIC measuring volume during the entire test for the image correlation to be successful. The specimen gauge region has a length of 32 mm and will move approximately 5 mm as the copper is strained, followed by a further 1-2 mm in the subsequent deformation. We therefore selected option B, with a measuring volume length of 50 mm, rather than the 15 mm measuring volume length of option A, which would be too small.

5.4.2.2 Camera Alignment

The tensile rig was mounted vertically into the load frame and a dummy steel specimen was mounted. The cameras were positioned in front of the load frame as shown in figure 5.18.

Ministry of Defence © British Crown Copyright 2020/AWE

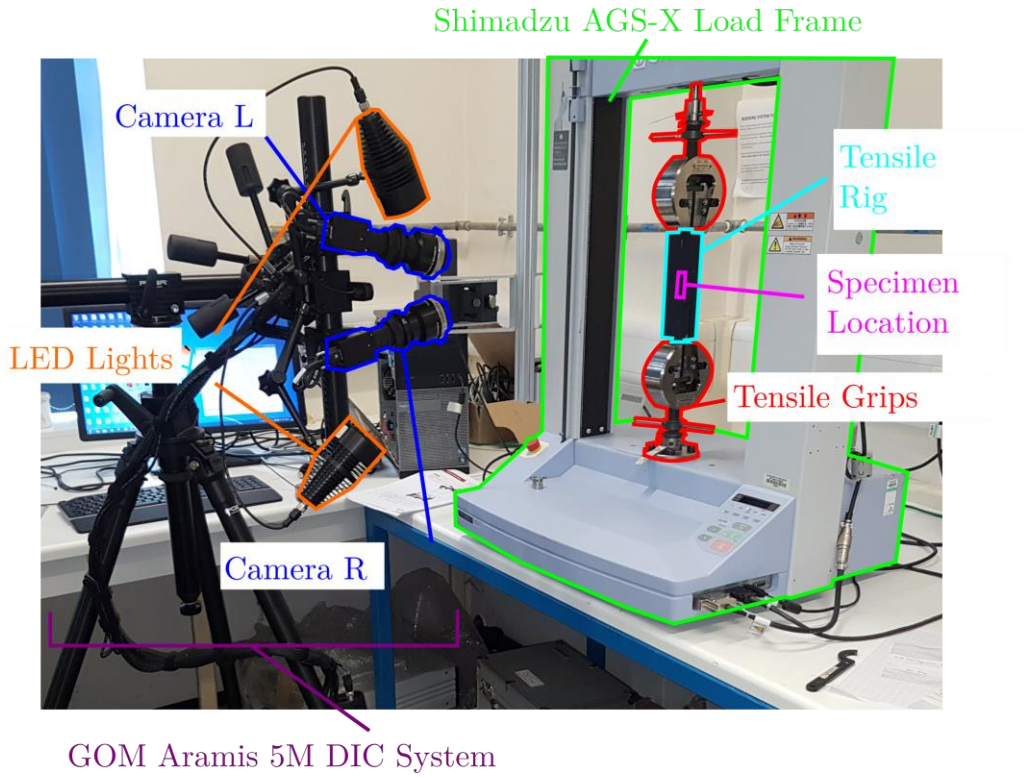


Figure 5.18. Annotated photograph of the DIC system positioned in front of the Shimadzu load frame. The specimen is mounted in the tensile rig which is clamped by the tensile grips. Note that in this photograph the cameras and lights have not been aligned and calibrated.

The slider was positioned on the included tripod such that the alignment laser beam was incident on the specimen surface. The tripod was moved such that the distance from the alignment laser to the specimen was approximately 595 mm. The slider was rotated 90° from horizontal to vertical such that the largest dimension of the measuring volume (length) was parallel to the specimen axis. The slider distance between the camera mounts was set to 224 mm using the scale marked on the slider. This ensures an inter-camera angle of 25° when aligned. With reference to a live feed from the cameras, both cameras were then rotated such that they pointed directly at the laser dot on the specimen surface.

Ministry of Defence © British Crown Copyright 2020/AWE

The focus on each camera was adjusted to bring the centre of the specimen into focus. This step was performed with the apertures opened as far as possible on each lens to achieve the most accurate focus. The apertures were then closed as far as possible to give the greatest depth of field during the tensile test.

The LED lights were angled towards the specimen surface and the polarising filters on the lights and lenses were adjusted in sequence as detailed in the ARAMIS Hardware Manual [145]. This minimises the effect of external lighting (e.g. from the laboratory) and minimises the number of overexposed points in the images that would interfere with the image correlation.

Figure 5.19 shows a schematic of the cameras after alignment. The DIC co-ordinate system is aligned with the measuring volume and, once calibrated, is therefore fixed with respect to the cameras. This is shown to the right of the image. The positive *x*-direction is nominally parallel to the specimen axis, pointing downwards towards the fixed end of the specimen. The z-vector is nominally perpendicular to the specimen surface, pointing along the alignment laser towards the camera system. The *y*-vector points across the specimen width, with the *x*, *y* and *z* vectors forming a right-handed set.

Ministry of Defence © British Crown Copyright 2020/AWE

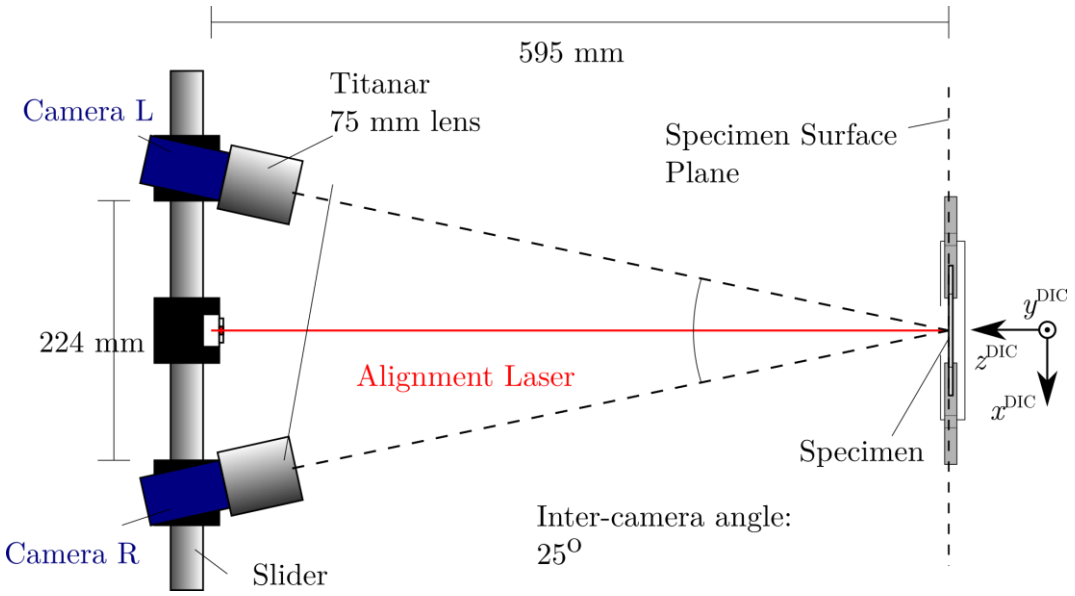


Figure 5.19. Schematic of the camera system after alignment. The co-ordinates of the DIC system are fixed relative to the cameras – the exact position is determined by the calibration procedure.

5.4.2.3 Calibration

The exact relationship between the pixel locations of a feature in each camera and the actual position of the object in 3D space is defined in ARAMIS by a calibration procedure. The calibration depends on the exact alignment of the cameras and therefore a recalibration must be performed if any part of the camera geometry is changed.

The calibration involved acquiring images of a special calibration object (GOM CQ20 55$\times$ 44) with a precisely-marked array of white points on a non-reflective surface. A pair of images was taken with the calibration cube in 13 distinct positions. Using a proprietary algorithm, the software identifies the location of each point in each image and solves a set of overdetermined simultaneous equations to relate points in 3D space to the corresponding pixel locations in each camera.

Ministry of Defence © British Crown Copyright 2020/AWE

The cube was held in each position with a clamp stand and supported by a metal bar attached to the lower grip (see figure 5.20). This was necessary as holding the cube by hand resulted in blurred images from which the individual white points could not be identified.

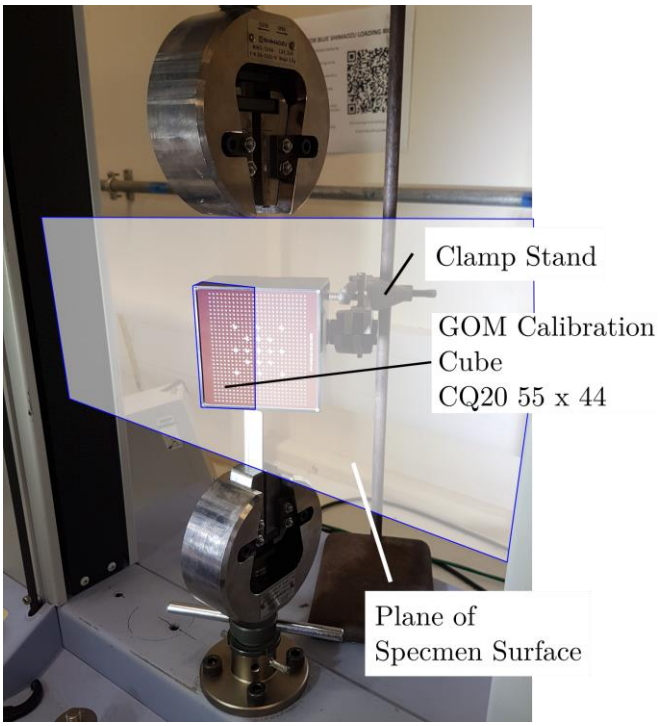


Figure 5.20. The calibration cube was held still by the clamp stand whilst each calibration image was acquired.

A successful calibration was achieved, with the calibration deviation (the uncertainty between a point in the left camera and the equivalent point in the right camera) being 0.031 pixels, which is in the range 0.01 – 0.04 pixels recommended by the manufacturer.

5.4.2.4 Speckle Pattern Application

Conventionally, a speckle pattern would be applied to the specimen surface with black and white spray paint. In the laboratory, we did not want to use flammable spray paint near the radioactive material, and the ideal speckle size was finer than that which could

Ministry of Defence © British Crown Copyright 2020/AWE

easily be achieved with spray paint. In addition, we did not have a simple way to remove paint if a mistake was made.

It was decided to use an airbrush, which sprays paint through a small nozzle using compressed air. A retractable needle controls the flow rate of the paint through the nozzle. Black and white artists' inks were found to be suitable for airbrush application (Daler – Rowney FW Acrylic Inks) through a 0.5 mm nozzle. A thin layer of white paint was first applied to cover the whole surface, reducing reflections from the metallic surface which would hinder correlation. A fine black speckle was then added until the surface looked a medium grey by eye.

When viewed through the cameras under the polarised LED lights, the speckle pattern was clearly visible, with features between 3 and 10 pixels in diameter, as shown in figure 5.21. A shutter time of 114 ms was selected as this gave the brightest image without overexposed pixels.

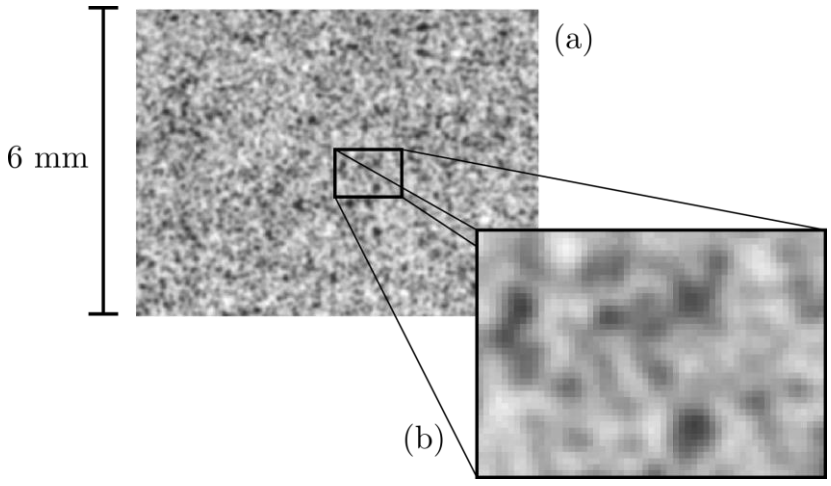


Figure 5.21. Sample of the speckle pattern on specimen DB-T1 as viewed in the left camera with illumination from the LED lights. (a) the pattern across the 6 mm width of the specimen. (b) magnified area showing the individual pixels.

Ministry of Defence © British Crown Copyright 2020/AWE

Good contrast was seen between the light and dark regions, with pixel intensities between 38 and 255 in the 8-bit range of 0-255. The histogram of the image in figure 5.21(a) is shown in figure 5.22. The distribution of pixel intensities covers a large proportion of the available values, without over- or under-exposed pixels. This facilitates a good image correlation as larger ranges of pixel intensities within a feature allow for a more accurate matching of the same feature in subsequent images.

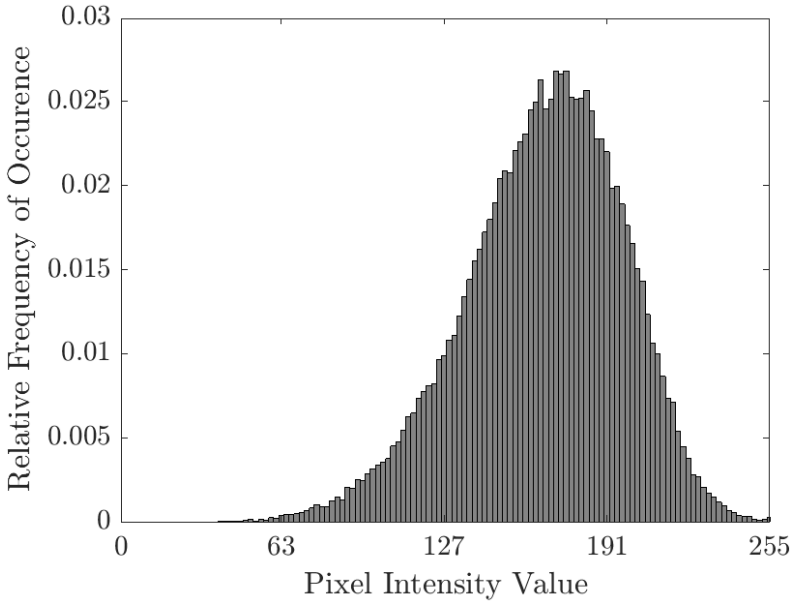


Figure 5.22. Histogram of pixel intensities in the image of the speckle pattern in figure 5.21(a).

5.4.3 Tensile Testing Procedure

The tests for each specimen were performed on subsequent days from 19th – 22nd November 2018. Two days were required for the first specimen DB-T1 due to the time consuming initial calibration – the test was therefore interrupted before plastic deformation was thought to occur in the uranium.

Ministry of Defence © British Crown Copyright 2020/AWE

The specimen dimensions in the gauge region were measured with digital calipers with an accuracy of ± 0.01 mm, in three separate locations evenly spaced along the gauge length. The average cross-sectional area was used in the stress calculation.

After calibration of the DIC system, the specimen was inserted into the tensile rig which was then clamped into the tensile grips on the Shimadzu load frame. The specifications of the load frame are shown in table 5.3.

Table 5.3. Specifications of the Shimadzu load frame used in this experiment.

Part	Description	Identification Number(s)
Load Frame	Shimadzu AGS-X 10 N-10 kN	P/N 346-55900-01
Load Cell	5 kN Force Transducer	Model SSM-DAK-5000N S/N 663196
Load Cell Calibration Device	Shimadzu 5 kN Load Cell Calibration Device	P/N 348-31180-01 S/N 663196
Tensile Grips	Shimadzu 5 kN Tensile Wedge Grips $\times 2$	P/N 346-52653-01

The test was controlled in Shimadzu's TrapeziumX software, with load applied in displacement control at a set displacement rate. The load cell force was polled every 10 ms and the time, displacement and force were saved into a text file. The test proceeded in three phases. Firstly, the copper bar was plastically deformed at a rate of 0.5 mm min^{-1} until the uranium started to take up load, identified as the point at which the gradient of the force with time suddenly increased. Secondly, the copper and uranium were deformed in parallel at a rate of 0.025 mm min^{-1} in the uranium elastic region followed by a rate of 0.05 mm min^{-1} for subsequent plastic deformation. Finally, the specimen was unloaded at a rate of 0.025 mm min^{-1}.

Ministry of Defence © British Crown Copyright 2020/AWE

DIC images were automatically acquired throughout the test. The delay between images varied between 2 s and 5 s to achieve approximately 2000 image pairs for each test.

The test was interrupted at various points during each phase and the DIC acquisition was paused to allow preliminary image correlation to be performed. The data verified that the specimen remained in the measuring volume and that the system had not gone out of calibration – such issues would have prevented the correlation of subsequent images. This correlation was performed with a facet size of 30 pixels $\times 30$ pixels and a 15 pixel $\times 15$ pixel facet overlap, chosen for the fast speed of correlation compared to smaller facets whilst allowing strain measurement with a spatial resolution of approximately 0.6 mm, small enough to resolve strained regions which may initiate fracture.

At each interruption of the test, the mean strain in the gauge region in the x-direction, ε_{xx}, (nominally parallel to the specimen axis) was calculated. It was strongly desired not the fracture the specimen. From the calculated strain values, a decision was made as to whether further tensile load would be applied, or if the final unload would be performed. Unloading was performed if the mean strain ε_{xx} exceeded 2.5 % (defined as part of the risk assessment) or the local strain exceeded 10 % (local strains in excess of 12 % were seen in neutron diffraction specimen ND-T4 before fracture).

Ministry of Defence © British Crown Copyright 2020/AWE

5.4.4 Data Processing

A number of processing steps were required to convert the raw data into a dataset suitable for analysis. Firstly, the stress in the uranium was calculated from the load-displacement curves and the specimen cross-section measurements. Secondly, the image correlation was performed using an optimised set of parameters, and an error analysis was performed. The DIC data and stress measurements were performed on separate computers, so the data were merged together to produce one coherent dataset for each specimen. Finally, the DIC strain data were segmented into the constituent grain clusters using the microstructure maps generated with EBSD.

These processing steps are now explained in detail.

5.4.4.1 Calculation of Stress in Uranium

Following the method detailed in section 5.4.1, a power-law curve was fitted to the load-displacement data from displacements of approximately 1.5 mm, where the copper begins to continuously strain, to 5 mm, where the uranium begins to take up load. This is shown for the case of DB-T1 in figure 5.23.

Ministry of Defence © British Crown Copyright 2020/AWE

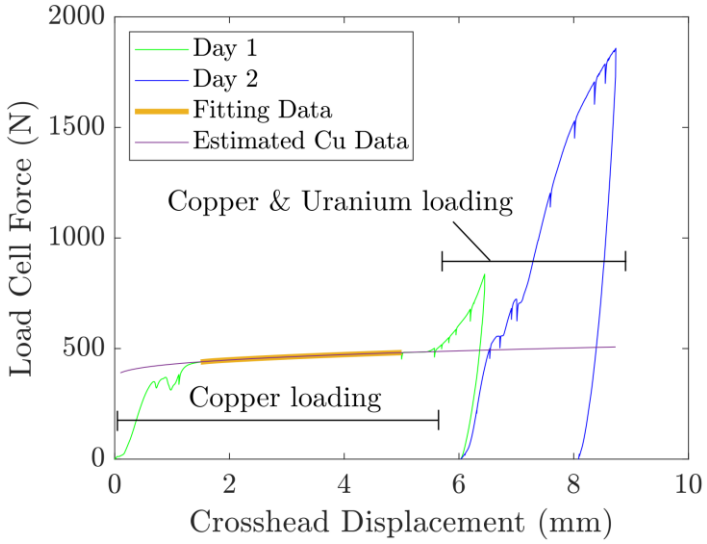


Figure 5.23. Load-displacement curve for specimen DB-T1 (green & blue) showing the estimation of the force in the copper (purple) from extrapolation of a power-law fit in the copper-loading region (orange).

The stress in the uranium, σ_{U}, as a function of the displacement, *x*, was calculated via equation [5.2], where F_{tot} is the force in the load cell, F_{Cu} is the estimated force in the copper, and A_{U} is the measured gauge cross-sectional area of the specimen. The uncertainty in the stress in the uranium was estimated to be less than $\pm$ 3% (see appendix A8.4).

$$\sigma_{\mathrm{U}}(x) = \frac{F_{\mathrm{tot}}(x) - F_{\mathrm{Cu}}(x)}{A_{\mathrm{U}}} \qquad [5.2]$$

An example stress-displacement curve, for specimen ND-T1, is shown in figure 5.24. Negative stresses during loading correspond to the initial loading of the copper, and were ignored in the subsequent analysis. During the final unload, the copper and uranium unload simultaneously with different elastic moduli. It is not trivial to calculate the distribution of force between the uranium and the copper during unload, so these data were also not analysed further.

Ministry of Defence © British Crown Copyright 2020/AWE

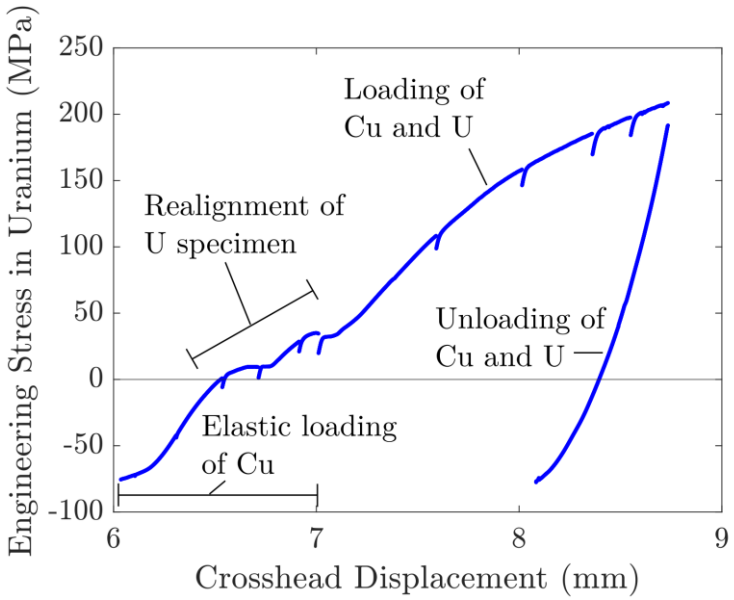


Figure 5.24. Stress-displacement curve for specimen DB-T1.

5.4.4.2 DIC Analysis

Digital image correlation (DIC) was performed in GOM Aramis v6.3.0. A mask was applied to restrict the correlation to parts of the specimen where the speckle pattern was visible in both cameras.

The correlation parameters 'facet size' and 'facet overlap' are a compromise between improved spatial resolution at small facet sizes and reduced uncertainty at larger facet sizes. The correlation was performed with an optimum facet size of 20 pixels $\times$ 20 pixels and a 50 % overlap in each direction (10 pixels $\times$ 10 pixels). Each facet is therefore approximately 0.4 mm $\times$ 0.4 mm in size, with the DIC deformation field grid having a step size of 0.2 mm.

The optimisation procedure is detailed in the next section along with a quantification of the DIC strain and displacement uncertainty.

Ministry of Defence © British Crown Copyright 2020/AWE

Identification of optimum facet size

Before testing of specimen DB-T1 commenced, images were captured before and after a rigid-body movement of the specimen; the specimen was moved upwards with a small manual 'jog' of the crosshead whilst no stress was being carried in the uranium. DIC processing was performed for square facets of edge length 10, 15, 20, 25, 30, 40, and 50 pixels, with a 50 % overlap in each direction, rounding up to the nearest pixel. The rigid body movement was small, with mean translations of $u_x = -5\,\mu\text{m}$, $u_y = 3\,\mu\text{m}$, and $u_z = -9\,\mu\text{m}$. No significant rotation of the specimen was observed.

Since for a rigid-body translation all displacement vectors should be equal, the displacement uncertainty for each component *x*, *y*, and *z* was calculated as the standard deviation of the magnitudes of each displacement component across all facets,

$$\sigma(u_j) = \sqrt{\frac{1}{N-1}\sum_{i=1}^{N}(u_{j,i} - u_j)} \qquad [5.3]$$

for $j = x, y, z$ where *i* identifies each of the *N* facets.

For a rigid-body translation the strain should be zero across the entire facet field. The correlation uncertainty in the axial strain was calculated as the mean of the absolute strains, as described by Haddadi et al.[101]

$$\sigma(\varepsilon_j) = \frac{1}{N}\sum_{i=1}^{N}\varepsilon_{j,i} \qquad [5.4]$$

for $j = xx$ (axial) or yy (transverse) where *i* identifies each of the *N* facets.

Ministry of Defence © British Crown Copyright 2020/AWE

The displacement uncertainty in microns and strain uncertainty in percent are plotted as a function of the facet size in figure 5.25.

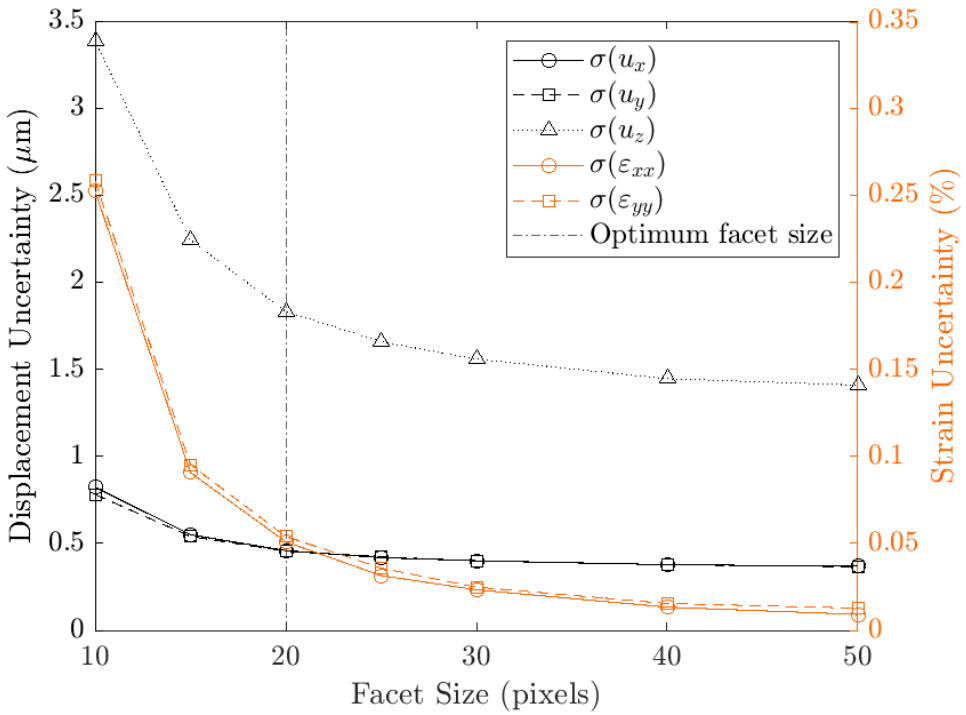


Figure 5.25. Displacement uncertainty (black) and strain uncertainty (orange) for the DIC measurement performed on a small rigid body movement on specimen DB-T1.

The in-plane displacement components u_x and u_y have similar uncertainties of around 0.5 μm. The out-of-plane uncertainty is larger; between 1.5 μm and 3.5 μm depending on the facet size. The strain uncertainty is similar for both components of normal strain and decreases rapidly between facet sizes of 10 and 20 pixels. At a facet size of 50 pixels, the strain uncertainty reaches 0.01 %, consistent with the manufacturer's claim.

A facet size of 20 pixels was chosen for the DIC calculation as sizes larger than this see diminishing returns in terms of reduced uncertainty for a linear worsening of spatial resolution. Each facet is 400 μm in diameter therefore this is the minimum feature size

Ministry of Defence © British Crown Copyright 2020/AWE

that can be distinguished in the displacement or strain fields. At least 10 points would be expected across grain clusters with diameters in excess of 4 mm. This is sufficient to see the shape of the strain field, and to calculate statistics within each grain cluster.

The speckle pattern was seen to be uniform across all three specimens, so the same facet size was used for the DIC computation of DB-T1, DB-T2, and DB-T3. The displacement uncertainty was assumed to be 0.5 μm (in-plane) and 1.8 μm (out-of-plane) and the uncertainty in normal strain 0.05 %, taken from figure 5.25.

Data export from ARAMIS

A co-ordinate transformation was performed in ARAMIS using the `3-2-1 Transformation` tool to align the DIC co-ordinate system with the specimen at the start of its elastic loading. Three non-colinear points on the specimen surface defined the *z*-plane, two points at opposite ends of one edge of the parallel gauge region defined the *x*-axis and a single point on the parallel edge defined the direction of the *y*-axis.

The displacement and strain fields were exported from ARAMIS as text files, and imported into MATLAB for further processing. The image timestamps for each DIC stage were used to identify the nearest data point from the load frame dataset – allowing the stress in the uranium to be related directly to the strain. The load frame data had a temporal resolution of 0.01 s compared to between 2 s and 5 s for the DIC stages, so the error introduced by this nearest-neighbour interpolation step is minimal.

Ministry of Defence © British Crown Copyright 2020/AWE

5.4.4.3 Segmentation of DIC data by grain cluster

To investigate the effect of grain orientation on deformation it was necessary to segment the DIC strain field according to the microstructure. This allowed the plotting of flow curves for each grain cluster from which the yield stress and hardening rate can be obtained. A grid of dimensions 32 mm $\times$6 mm, equal to the gauge region, was overlaid onto the EBSD orientation map, as shown in figure 5.26. Each grain cluster was defined as a polygon with vertex co-ordinates defined with respect to the grid.

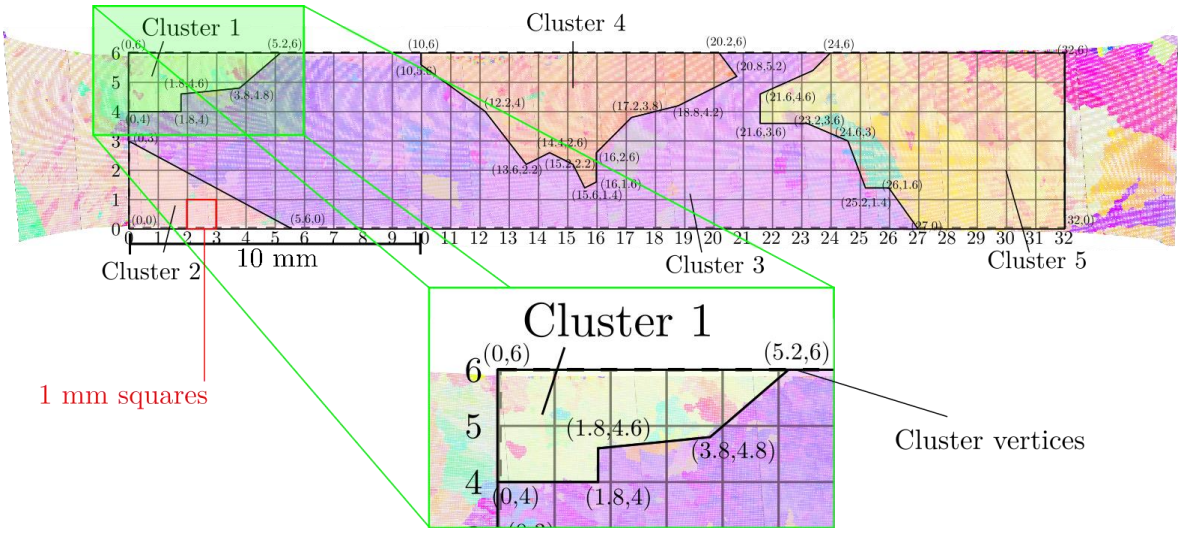


Figure 5.26. Each grain cluster was defined as a polygon with vertex co-ordinates with respect to a 32 mm $\times$6 mm grid overlaid onto the EBSD orientation map.

The EBSD grid was then aligned to the DIC data. The centreline of the specimen was found by fitting a straight line through the DIC data points in the gauge section, where $0 < x_{DIC} < 25$, as shown in figure 5.27. A perpendicular line was defined to represent the left-hand end of the parallel-sided gauge region.

The 32 mm $\times$6 mm grid was then aligned to these two lines, as shown in figure 5.28.

Ministry of Defence © British Crown Copyright 2020/AWE

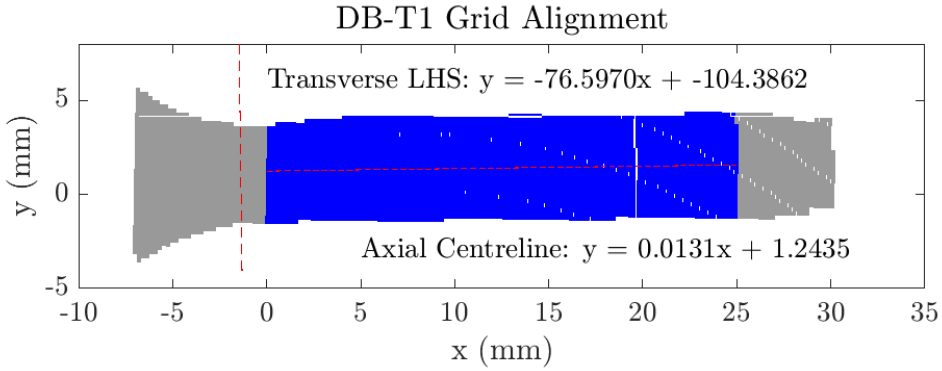


Figure 5.27. Calculation of the specimen centreline and gauge region location in the EBSD data. Blue data points were used to fit the axial centreline of the specimen. The perpendicular (~vertical) line represents the left-hand side of the parallel gauge region.

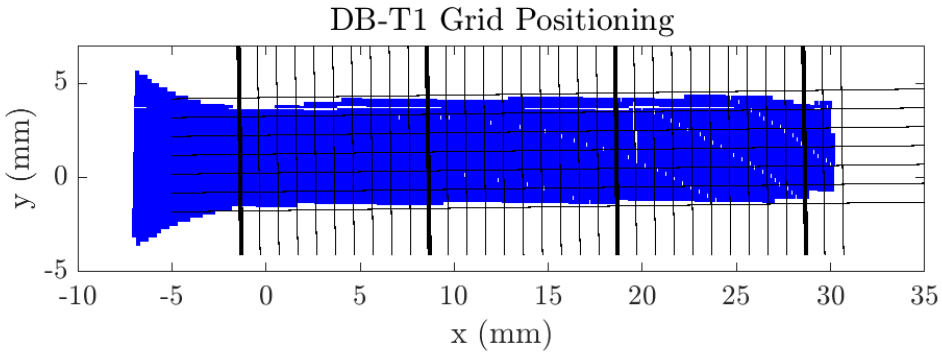


Figure 5.28. Alignment of the 32 mm × 6 mm EBSD grid onto the gauge region in the DIC data.

The vertices of each grain cluster were converted from the grid co-ordinate system to the DIC co-ordinate system and the DIC data were partitioned by selecting all data points within each cluster, as shown in figure 5.29.

Statistics were calculated for each grain, and for the whole gauge region – the mean, standard deviation and maximum and minimum values were calculated for each displacement and strain component in each cluster.

Ministry of Defence © British Crown Copyright 2020/AWE

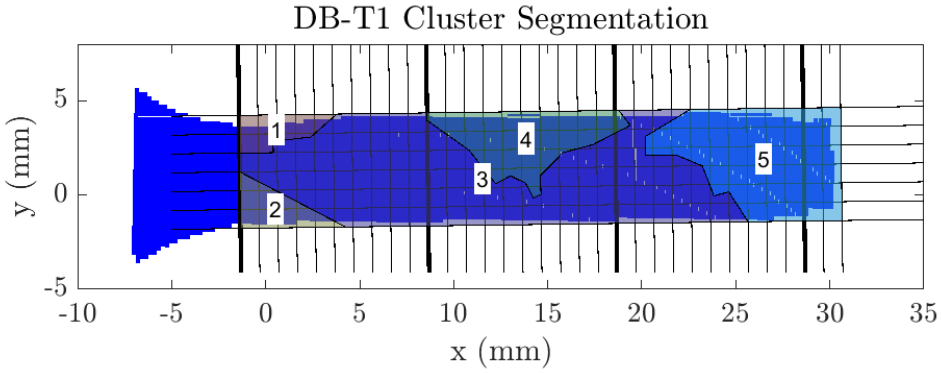


Figure 5.29. Segmentation of the DIC data according to the grain cluster polygons defined in the EBSD data.

5.4.4.4 Calculation of Elastic Stiffness and Yield Point

For each grain cluster, the flow curve was plotted as the applied stress as a function of the mean strain within the cluster. A smoothing spline was fitted in MATLAB through the strain data to minimise the effect of noise in the strain measurements. As detailed in the MATLAB documentation [147] the smoothing spline $s(\varepsilon)$ is constructed from the strains ε_i such that the quantity in equation [5.5] is minimised.

$$p\sum_i y_i - s(\varepsilon_i)^2 + (1-p)\int \left(\frac{d^2 s}{d\varepsilon^2}\right)^2 d\varepsilon \qquad [5.5]$$

The smoothing parameter p was chosen to be 0.9999 to achieve a smoothing of the data whilst maintaining the local shape of the flow curves.

First order polynomial (linear) fits were performed to the elastic region of each plot of stress against the smoothed strain data. The apparent elastic stiffness E was calculated as the gradient of this line.

Ministry of Defence © British Crown Copyright 2020/AWE

The yield stress was defined as the point of deviation from linearity - where the difference in stress between the extrapolation of the elastic fit line and the smoothed flow curve in first exceeds 5 MPa. The uncertainty in the yield stress was estimated by eye.

The yield point was indistinct in many clusters, so the 0.2 % offset stress was chosen as a more comparable measure of the relative yield strength of each grain cluster. This was defined as the stress at which a plastic strain of 0.2 % will have developed in the grain cluster compared to its strain state at zero stress. It was calculated by translating the elastic fit line by 0.2 % along the ε-axis and finding the stress at which this line intersects the spline curve.

5.5 Results

5.5.1 Specimen Dimensions

The dimensions of the three specimens tested are shown in table 5.4. In specimens DB-T1 and DB-T2, the gauge width does not vary along the specimen length. As a result of the electropolishing, the cross-sectional areas are much thinner than the $9\,\mathrm{mm}^2$ specified. Specimen DB-T3 was thicker due to a faster electropolish. Overall there is approximately a 0.6 % uncertainty in cross-sectional areas. The paint speckle pattern was thin enough to not change the dimensions within the precision of the measurement.

Ministry of Defence © British Crown Copyright 2020/AWE

Table 5.4. Table showing the measured specimen dimensions after EBSD, before application of the paint speckle pattern. The width and thickness were measured in three locations along the specimen length. At each position, the cross-sectional area was calculated. The mean area was used for the stress calculation.

Specimen	Gauge Width (mm)	Gauge Thickness (mm)	Cross-Sectional Area ($\mathbf{mm^2}$)
DB-T1	5.98 ± 0.01	1.10 ± 0.01	6.57 ± 0.06
	5.98 ± 0.01	1.07 ± 0.01	6.40 ± 0.06
	5.98 ± 0.01	1.08 ± 0.01	6.45 ± 0.06
		Average	$\mathbf{6.48 \pm 0.04}$
DB-T2	6.05 ± 0.01	1.06 ± 0.01	6.41 ± 0.06
	6.05 ± 0.01	1.03 ± 0.01	6.23 ± 0.06
	6.05 ± 0.01	1.01 ± 0.01	6.11 ± 0.06
		Average	$\mathbf{6.25 \pm 0.04}$
DB-T3	6.02 ± 0.01	1.30 ± 0.01	7.83 ± 0.06
	6.03 ± 0.01	1.27 ± 0.01	7.65 ± 0.06
	6.08 ± 0.01	1.30 ± 0.01	7.90 ± 0.06
		Average	$\mathbf{7.79 \pm 0.04}$

5.5.2 Microstructure

In this section the microstructure is shown in the form of EBSD orientation maps. Three maps are shown for each specimen, with the points coloured according to which crystal direction is parallel to (a) the specimen longitudinal axis (EBSD *x*-axis), (b) the specimen transverse axis (EBSD *y*-axis), and (c) specimen surface normal (EBSD *z*-axis). On each map, the gauge region is outlined with a dotted black line.

5.5.2.1 Specimen DB-T1

Specimen DB-T1 (figure 5.30) contains a large grain cluster which makes a triangular shape on the specimen surface, orientated with its [211] axis in tension. This cluster measures 10 mm on the upper edge and protrudes 5 mm into the specimen width. The large region surrounding the triangular grain is oriented closer to [001]. The right hand 10 mm of the specimen is complex with small regions in differing orientations. Within

Ministry of Defence © British Crown Copyright 2020/AWE

each cluster, the constituent grains are small (<1 mm diameter) with misorientations of a few degrees between each grain.

5.5.2.2 Specimen DB-T2

Specimen DB-T2 (figure 5.31) is dominated by the large cluster to the right-hand side, oriented close to [001], slightly towards [100]. This cluster is over 25 mm in length in the gauge region. To the left of this cluster is a complex mix of smaller clusters (<10 mm in diameter) in at least 6 distinct orientations. Between 8 mm and 15 mm from the left-hand end of the gauge region, small regions of approximately 1-2 mm diameter are seen in the large cluster, coloured orange in figure 5.31(a). These regions have similar orientations to one another so it is presumed they are from a separate cluster penetrating into the specimen from above or below the specimen plane. The lower of the two small clusters on the right-hand side of the gauge region is also in this orientation.

5.5.2.3 Specimen DB-T3

Specimen DB-T3 (figure 5.32) contains three main clusters. One occupies the right-hand half of the specimen, aligned between [001] and [100]. The central cluster intersects the specimen surface as a trapezium, 15 mm on the upper edge and 10 mm on the lower edge, crossing the whole gauge width and being oriented near (111). The final occupies the remaining space on the left-hand side, aligned nearer to [010]. The central cluster, whilst being fairly uniform in orientation, has a heterogeneous grain structure within it. The

Ministry of Defence © British Crown Copyright 2020/AWE

grains in the left-hand side of the cluster intersect the surface as long elongated streaks, with the right-hand side showing shorter streaks aligned in a different direction.

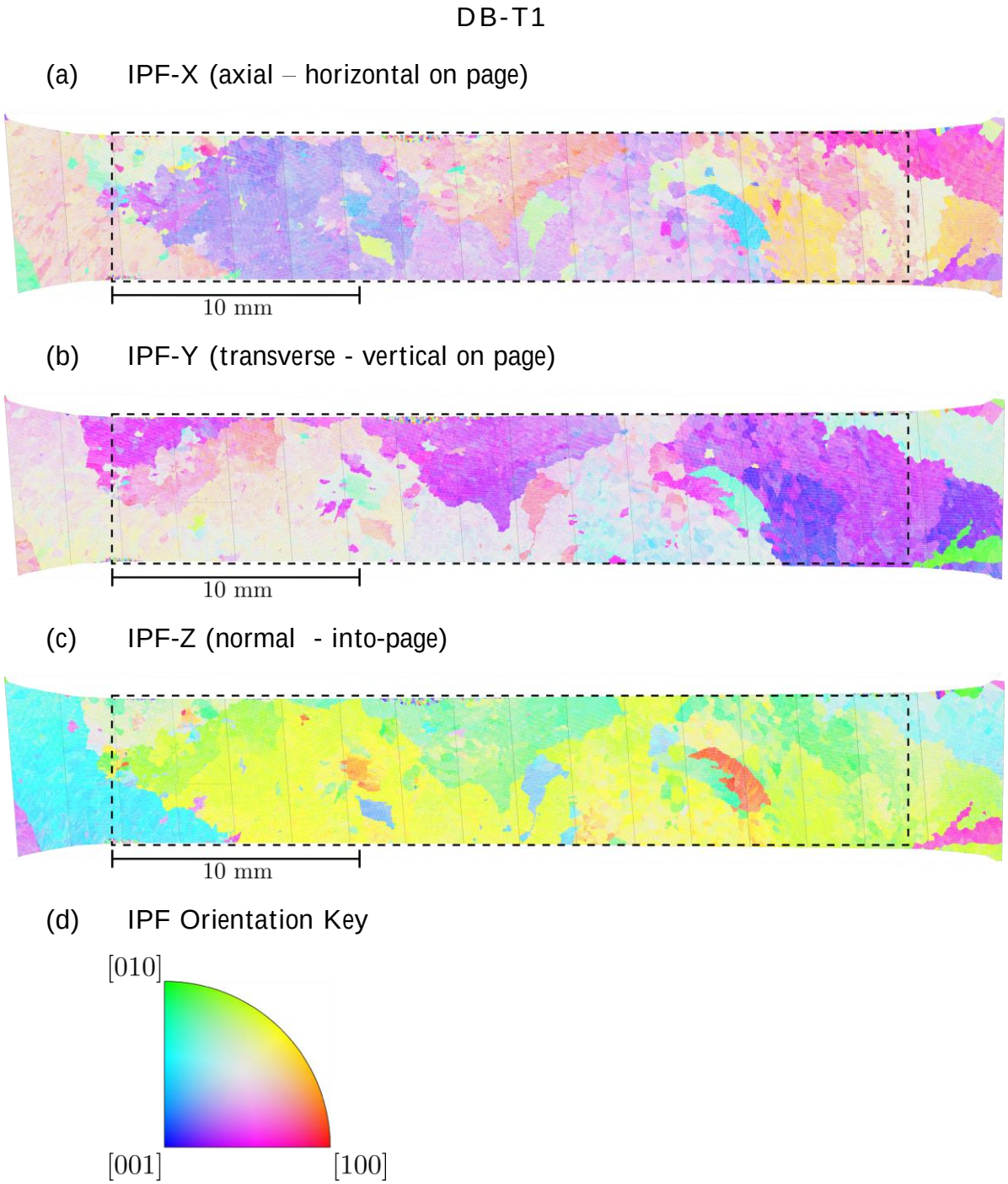
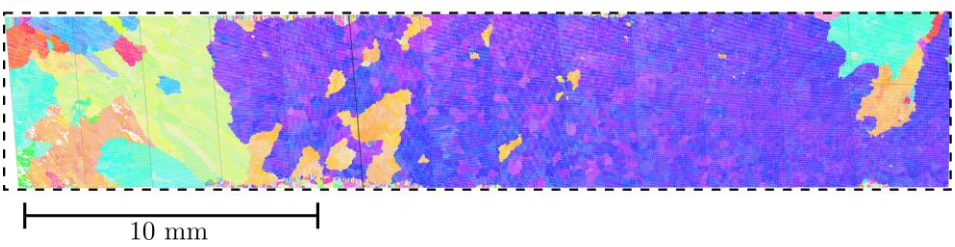


Figure 5.30. EBSD orientation maps for specimen DB-T1. Each map is coloured according to which crystal direction [*uvw*] is parallel to (a) the specimen longitudinal axis – horizontal on page – denoted IPF-X, (b) the specimen transverse axis – vertical on page – denoted IPF-Y, and (c) the specimen surface normal – in to page – denoted IPF-Z. Each crystal direction is uniquely coloured according to the inverse pole figure key (d). The gauge region is shown as a dotted black line.

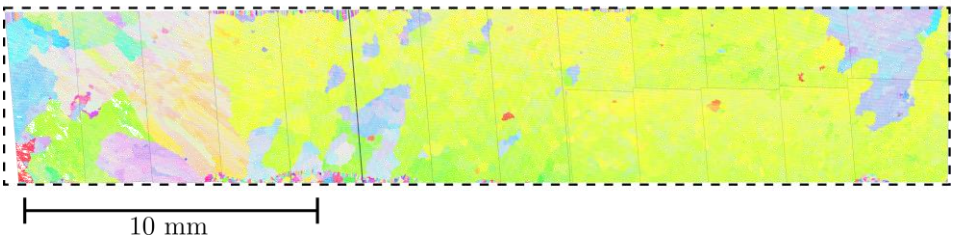
Ministry of Defence © British Crown Copyright 2020/AWE

DB-T2

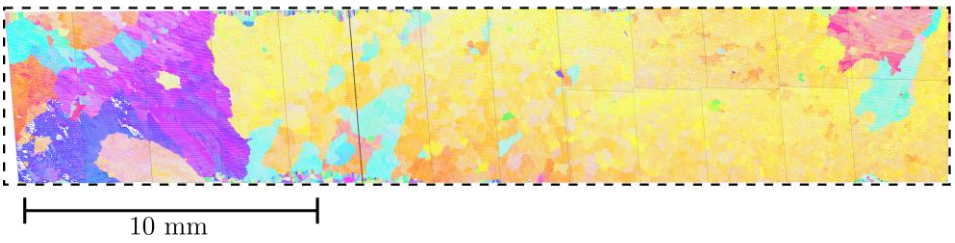
(a) IPF-X (axial – horizontal on page)



(b) IPF-Y (transverse - vertical on page)



(c) IPF-Z (normal - into-page)



(d) IPF Orientation Key

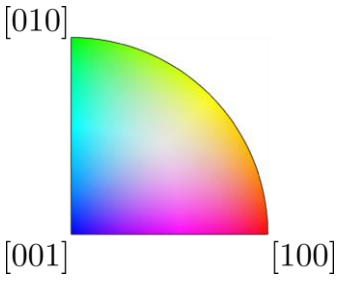
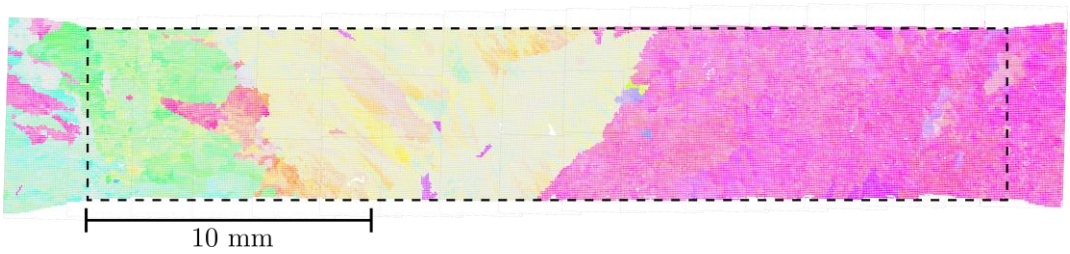


Figure 5.31. EBSD orientation maps for specimen DB-T2. Each map is coloured according to which crystal direction [*uvw*] is parallel to (a) the specimen longitudinal axis – horizontal on page – denoted IPF-X, (b) the specimen transverse axis – vertical on page – denoted IPF-Y, and (c) the specimen surface normal – in to page – denoted IPF-Z. Each crystal direction is uniquely coloured according to the inverse pole figure key (d). The gauge region is shown as a dotted black line.

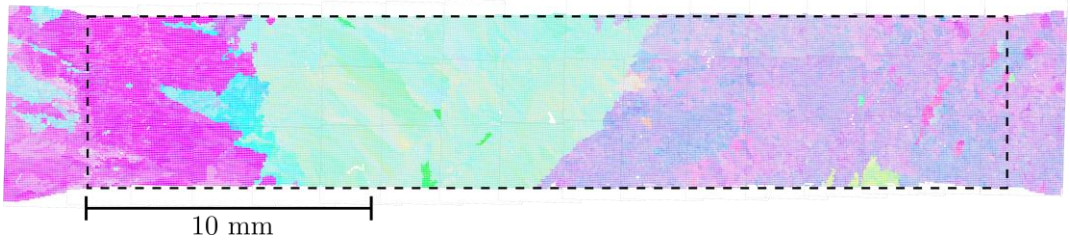
Ministry of Defence © British Crown Copyright 2020/AWE

DB-T3

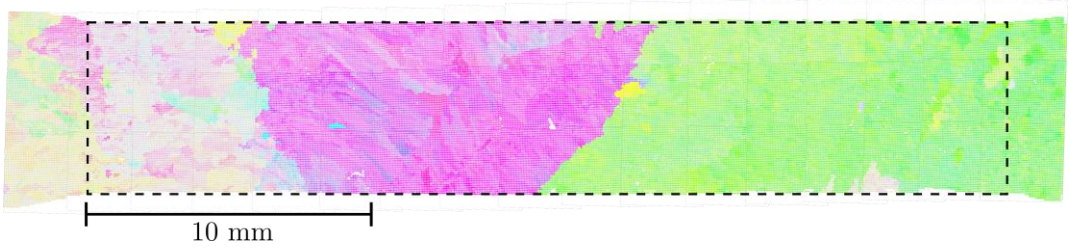
(a) IPF-X (axial – horizontal on page)



(b) IPF-Y (transverse - vertical on page)



(c) IPF-Z (normal - into-page)



(d) IPF Orientation Key

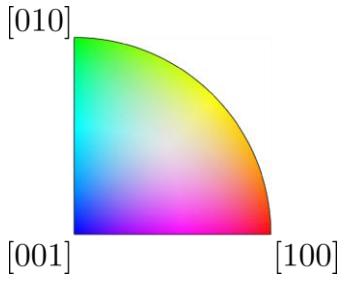


Figure 5.32. EBSD orientation maps for specimen DB-T3. Each map is coloured according to which crystal direction [*uvw*] is parallel to (a) the specimen longitudinal axis – horizontal on page – denoted IPF-X, (b) the specimen transverse axis – vertical on page – denoted IPF-Y, and (c) the specimen surface normal – in to page – denoted IPF-Z. Each crystal direction is uniquely coloured according to the inverse pole figure key (d). The gauge region is shown as a dotted black line.

Ministry of Defence © British Crown Copyright 2020/AWE

5.5.3 Grain Cluster Segmentation

In each specimen, the main grain clusters were defined as polygons to allow segmentation of the stress-strain data in the subsequent analysis. In this section, the polygons are overlaid on the IPF-X orientation maps for each specimen. Each cluster is identified by a unique colour[4] and number.

5.5.3.1 Specimen DB-T1

5 clusters were identified in specimen DB-T1. The central triangular grain is cluster 4, surrounded by cluster 3. Everything to the right of cluster 3 is grouped into a single cluster.

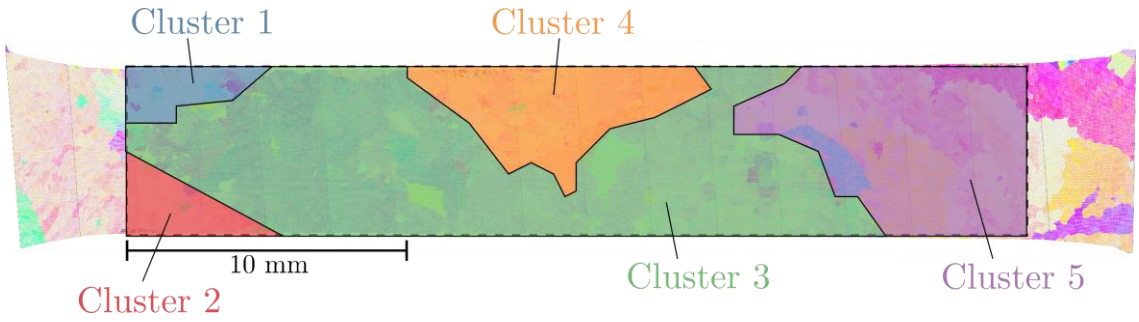


Figure 5.33. The main 5 grain clusters identified in the gauge region in specimen DB-T1.

5.5.3.2 Specimen DB-T2

The segmentation of specimen DB-T2 was more complex, with 10 clusters being defined. Due to their differing orientations, 6 separate clusters were assigned for the left-hand side. Cluster 8 is predominantly in one orientation and encompasses the majority of the

[4] Colours were assigned using linspecer function by Lansey[173] which uses colour maps developed by Brewer[174].

Ministry of Defence © British Crown Copyright 2020/AWE

large cluster seen to the right of the specimen. Cluster 7 encloses the region where this large cluster is intersected at the surface by the cluster from above/below the specimen.

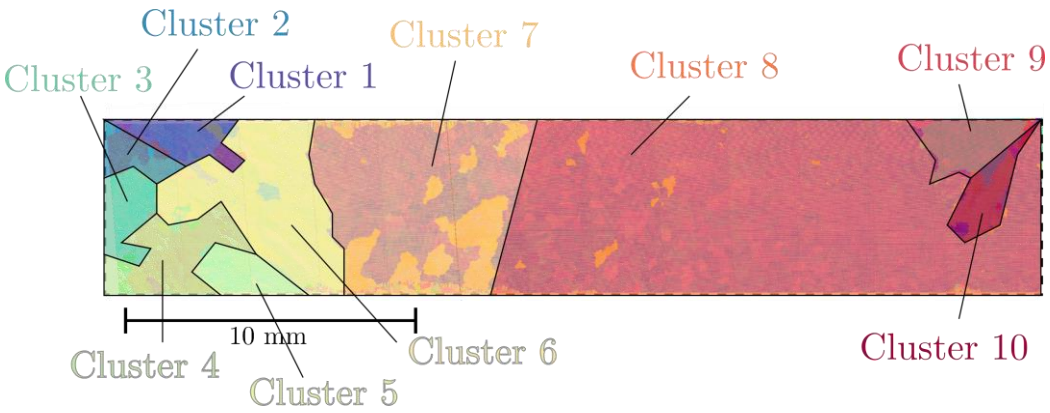


Figure 5.34. The 10 grain clusters identified in the gauge region in specimen DB-T2.

5.5.3.3 Specimen DB-T3

Specimen DB-T3 contains 4 clusters. From left to right, these are clusters 1, 3, and 4. Cluster 2 sits between 1 and 3 and protrudes approximately 4 mm into the gauge width.

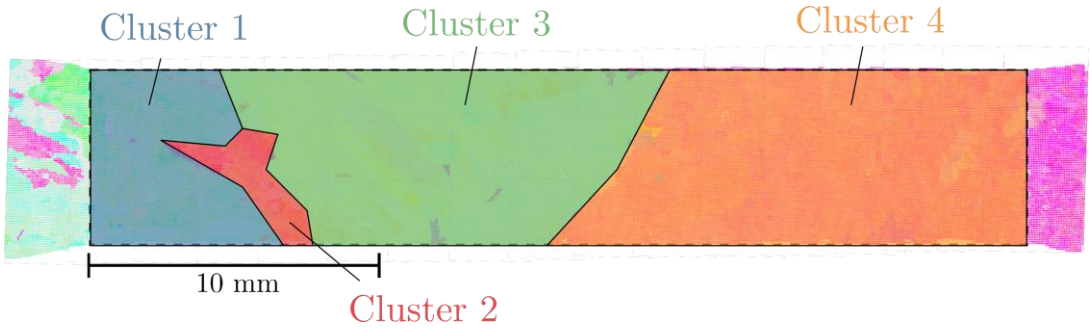


Figure 5.35. The main 4 grain clusters identified in the gauge region in specimen DB-T3.

Ministry of Defence © British Crown Copyright 2020/AWE

5.5.4 Schmid Factor Maps

5.5.4.1 Specimen DB-T1

Wall slip is favoured in cluster 5 to the right-hand side of specimen DB-T1 (figure 5.36), with a SF of approximately 0.5, and to a lesser extent across the whole specimen except for the cluster 3. Floor slip is possible everywhere apart from in a small section to the right-hand side, with SFs between 0.3 and 0.4. Chimney slip has a similar SF distribution to Wall slip. The map for Roof slip is approximately the inverse of that for Chimney slip, and Roof slip could be active in cluster 3.

{130} twinning is favoured towards the right-hand side of the triangular cluster 4 (figure 5.37), and is not likely in cluster 3, where it has a SF ≈ 0. The '$\{172\}$' twin, and its reciprocal {112}, is possible everywhere, with twinning of these types expected to be particularly strong in clusters 2, 3, and 4, where the SF ≈ 0.5. '$\{176\}$' twinning is possible in all clusters except cluster 3, where it is impossible with its SF < 0.

Ministry of Defence © British Crown Copyright 2020/AWE

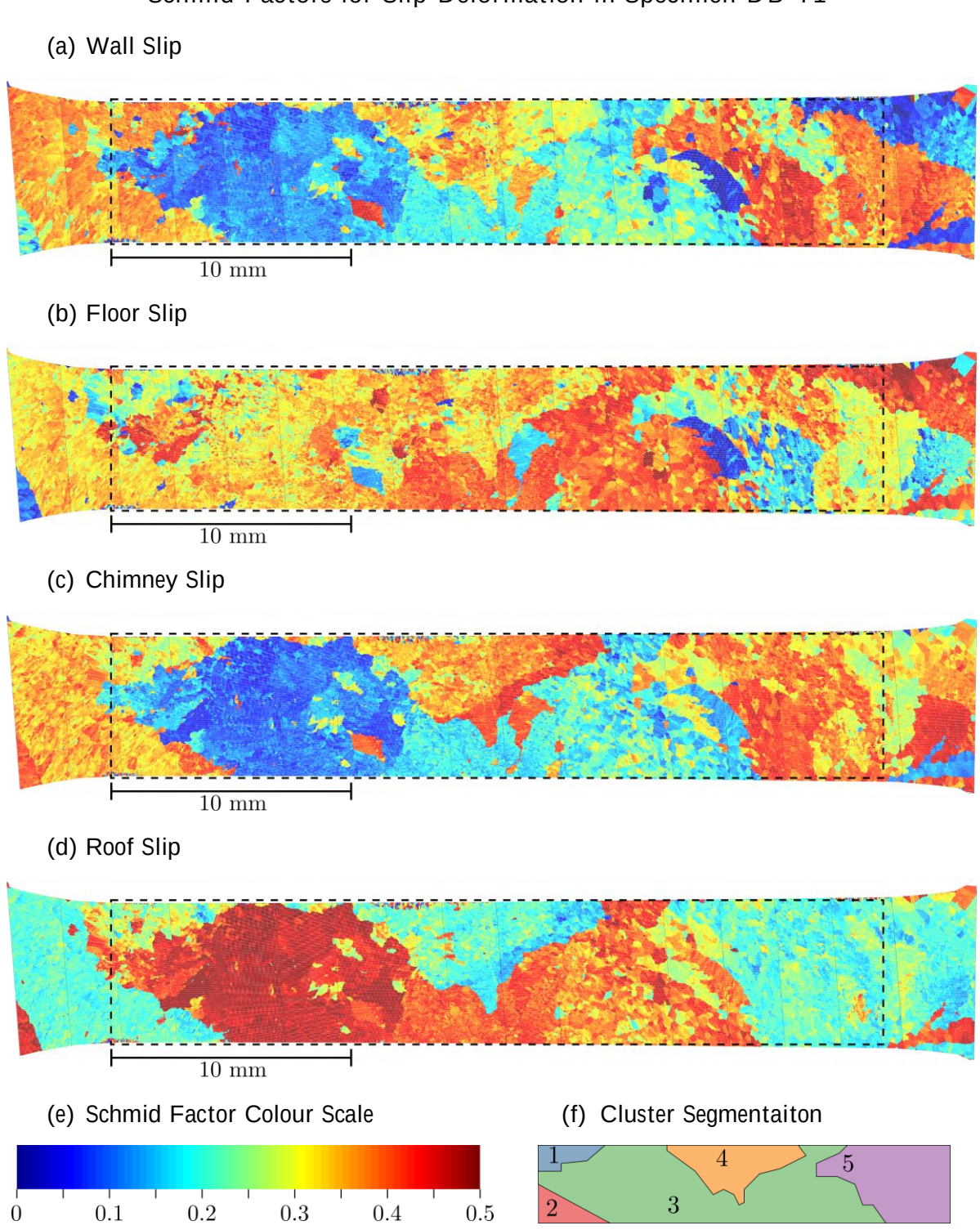


Figure 5.36. Maps of Schmid factors (SFs) for axial tensile loading of specimen DB-T1, for (a) Wall, (b) Floor, (c) Chimney and (d) Roof slip. SFs calculated from EBSD-measured orientations. High SFs coloured in red, low SFs in blue, according to key (e). (f) Cluster segmentation for specimen DB-T1.

Ministry of Defence © British Crown Copyright 2020/AWE

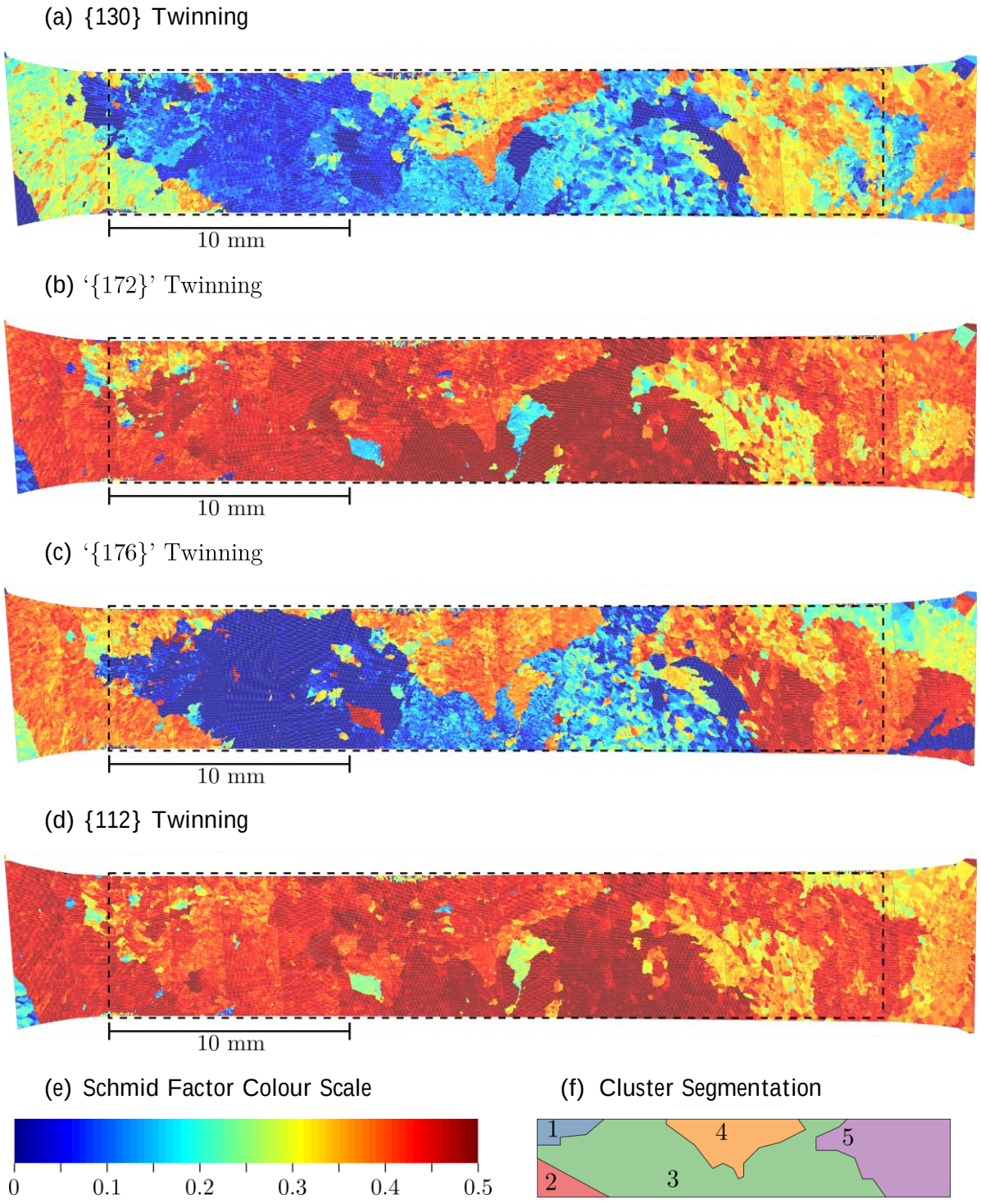


Figure 5.37. Maps of Schmid factors (SFs) for axial tensile loading of specimen DB-T1, for (a) {130}, (b) '{172}', (c) '{176}' and (d) {112} twinning. SFs calculated from EBSD-measured orientations. High SFs coloured in red, low SFs in blue, according to key (e). Negative SFs for twinning are displayed as zero for simplicity – these twins cannot form for tension in this orientation. (f) Cluster segmentation for specimen DB-T1.

Ministry of Defence © British Crown Copyright 2020/AWE

5.5.4.2 Specimen DB-T2

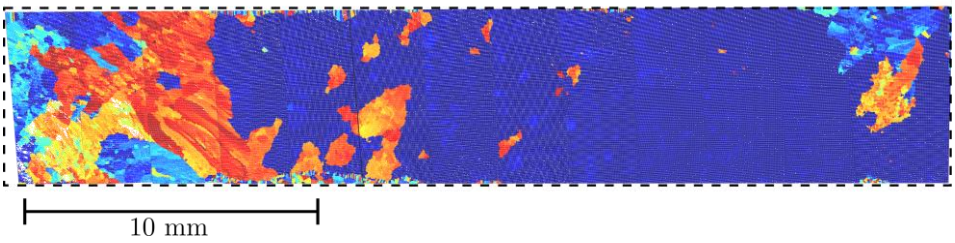
Wall and Chimney slip have similar SF distributions in specimen DB-T2 (figure 5.38), with SF $\approx$ 0 in the largest region comprising cluster 8 and the majority of cluster 7. It is possible however in the intersecting grains in cluster 7, and in cluster 6 adjacent to this. Floor slip is not favourable anywhere in the specimen. The SFs for Roof slip are similar to those for Wall/Chimney slip, but this mode is also strongly favoured in the largest cluster, 8.

The effect of the slight difference between the SFs for '{172}' and {112} twins is clear in this microstructure (figure 5.39), especially in cluster 9 to the top-right of the specimen surface. Overall, these twin modes have moderate SFs everywhere, with SFs between 0.2 and 0.4 in the largest cluster 8. For these modes, there is no difference in SFs between the main and intersecting grain orientations in cluster 7.

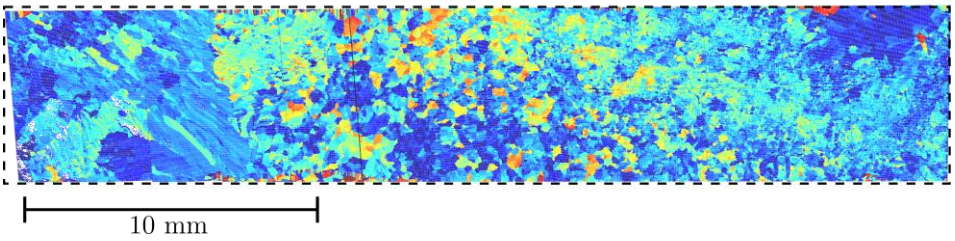
{130} and '{176}' twins have a negative SF in the largest cluster however the intersecting grains in cluster 7 can twin with a SF > 0.4.

Ministry of Defence © British Crown Copyright 2020/AWE

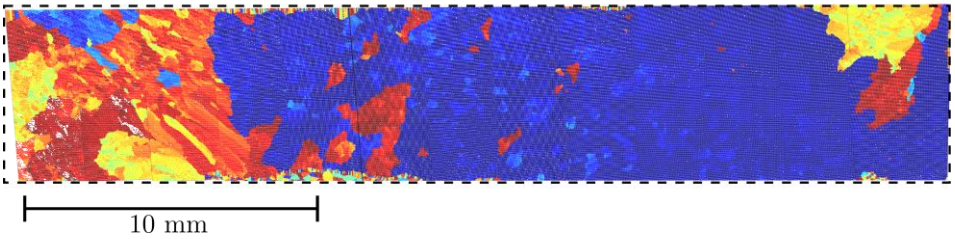
(a) Wall Slip



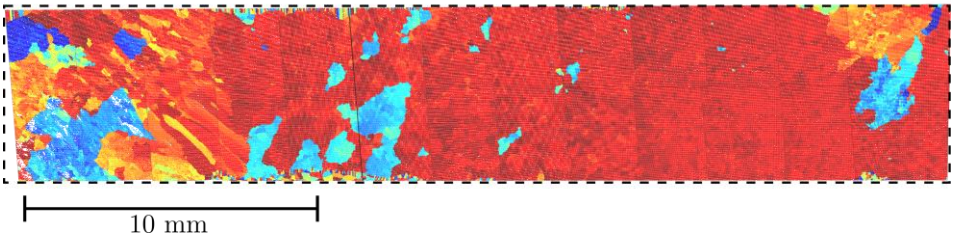
(b) Floor Slip



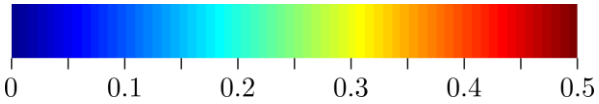
(c) Chimney Slip



(d) Roof Slip



(e) Schmid Factor Colour Scale



(f) Cluster Segmentation



Figure 5.38. Maps of Schmid factors (SFs) for axial tensile loading of specimen DB-T2, for (a) Wall, (b) Floor, (c) Chimney and (d) Roof slip. SFs calculated from EBSD-measured orientations. High SFs coloured in red, low SFs in blue, according to key (e). (f) Cluster segmentation for specimen DB-T2.

Ministry of Defence © British Crown Copyright 2020/AWE

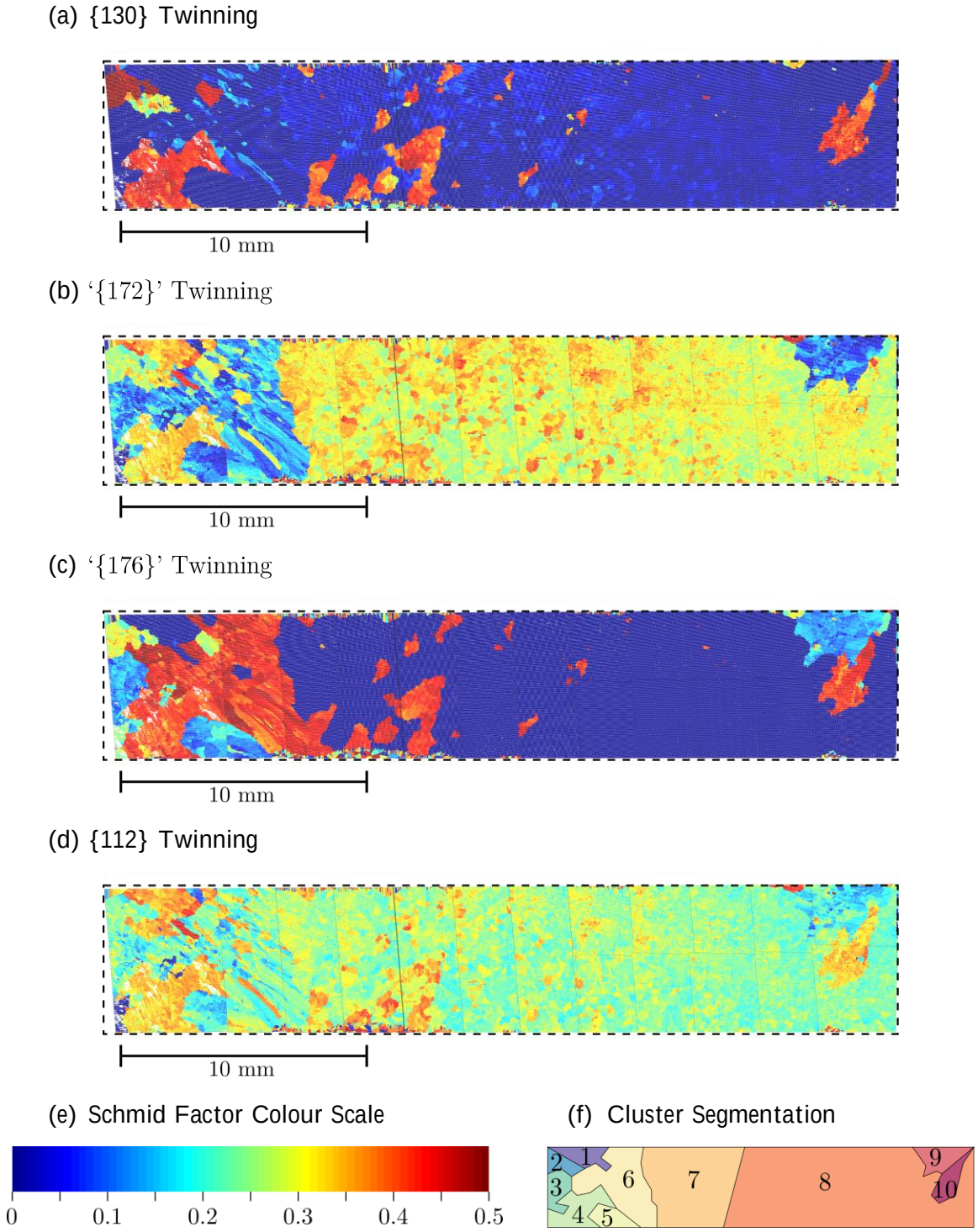


Figure 5.39. Maps of Schmid factors (SFs) for axial tensile loading of specimen DB-T2, for (a) {130}, (b) '{172}', (c) '{176}' and (d) {112} twinning. SFs calculated from EBSD-measured orientations. High SFs coloured in red, low SFs in blue, according to key (e). Negative SFs for twinning are displayed as zero for simplicity – these twins cannot form for tension in this orientation. (f) Cluster segmentation for specimen DB-T2.

Ministry of Defence © British Crown Copyright 2020/AWE

5.5.4.3 Specimen DB-T3

In the central cluster 3 of specimen DB-T3 (figure 5.40), only Wall slip is favourable with a SF > 0.4; all other slip modes have SFs < 0.3. In the neighbouring right-hand cluster, 4, only Floor slip is favourable. Chimney and Roof slip have similar SFs, and are favoured in the left-hand cluster 1, with SFs $\approx$ 0.5, and have moderate SFs in clusters 3 and 4 to the right-hand side.

{130} twinning is impossible in the left-hand cluster (figure 5.41), with its SF < 0. It is also not favourable in the trapezium cluster 3, however is possible in the small cluster 2 along the boundary between clusters 1 and 3. It is also possible in cluster 4 to the right-hand side, with a SF ≈ 0.4. '$\{172\}$' twinning is strongly favourable in the right-hand cluster 4, is possible in the central cluster 3 and not possible in the left-hand cluster 3. '$\{176\}$' and $\{112\}$ twinning are the most geometrically favourable twinning modes in the central trapezium-shaped cluster, 3.

Ministry of Defence © British Crown Copyright 2020/AWE

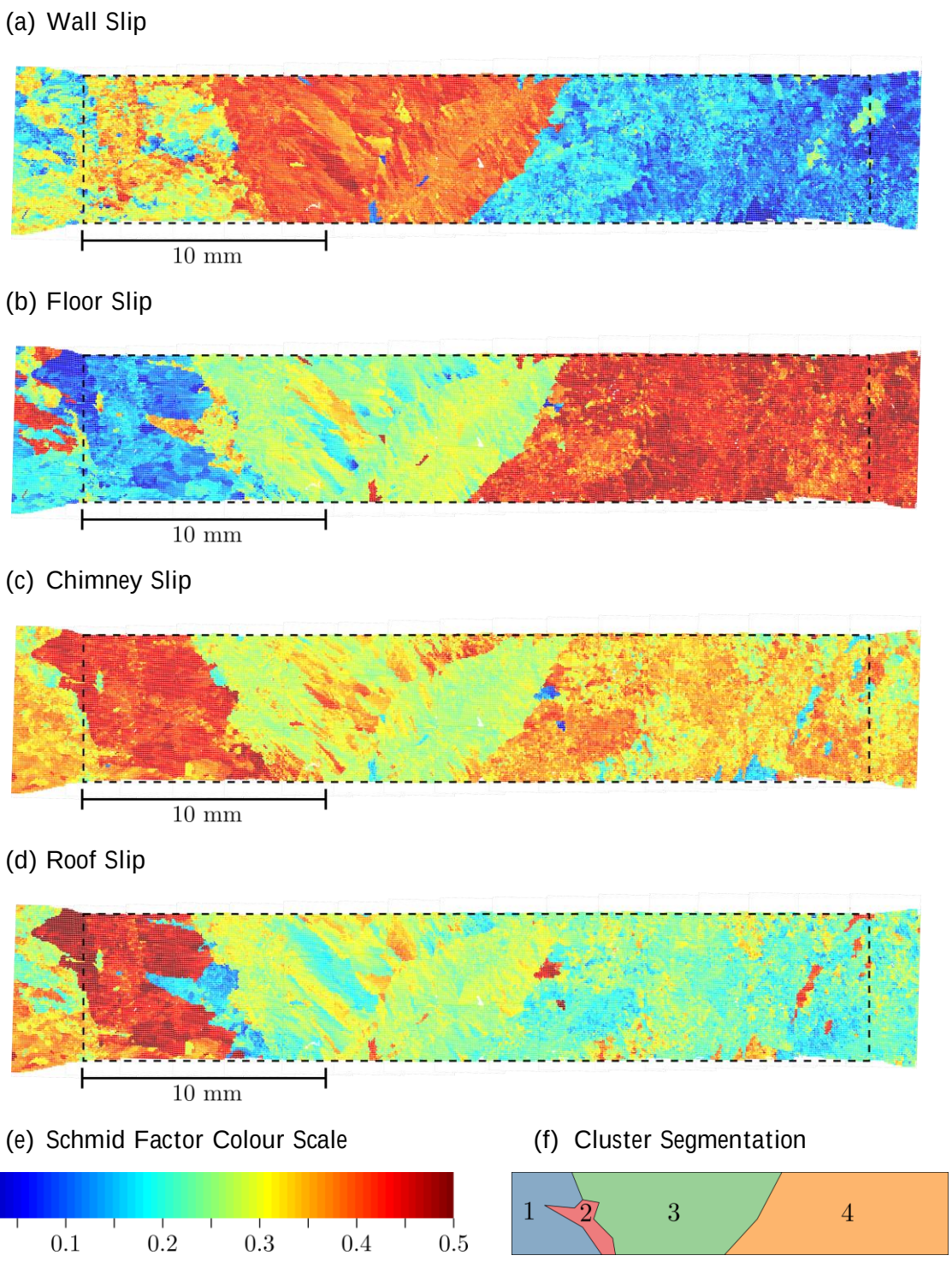


Figure 5.40. Maps of Schmid factors (SFs) for axial tensile loading of specimen DB-T3, for (a) Wall, (b) Floor, (c) Chimney and (d) Roof slip. SFs calculated from EBSD-measured orientations. High SFs coloured in red, low SFs in blue, according to key (e). (f) Cluster segmentation for specimen DB-T3.

Ministry of Defence © British Crown Copyright 2020/AWE

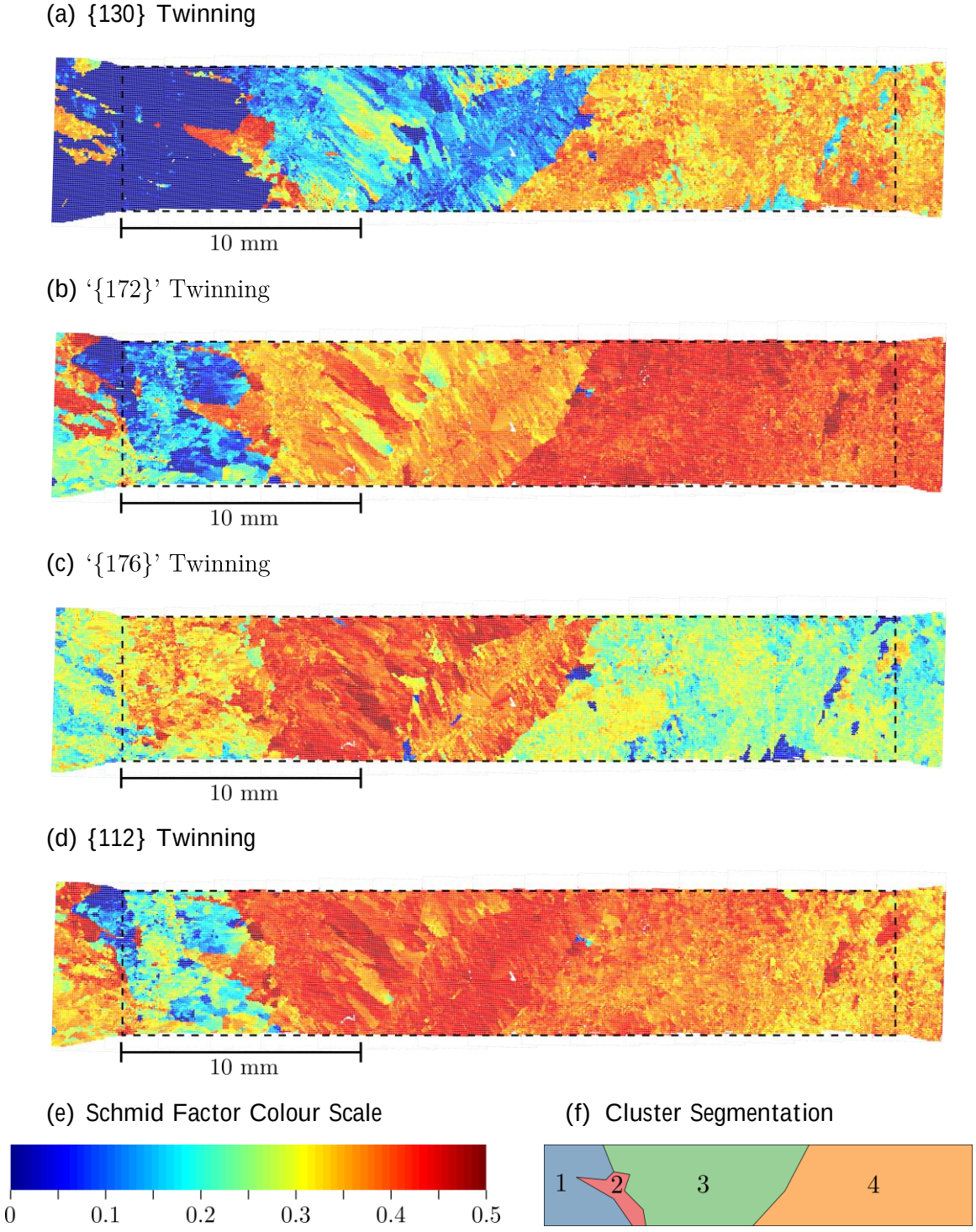


Figure 5.41. Maps of Schmid factors (SFs) for axial tensile loading of specimen DB-T3, for (a) {130}, (b) '{172}', (c) '{176}' and (d) {112} twinning. SFs calculated from EBSD-measured orientations. High SFs coloured in red, low SFs in blue, according to key (e). Negative SFs for twinning are displayed as zero for simplicity – these twins cannot form for tension in this orientation. (f) Cluster segmentation for specimen DB-T3.

Ministry of Defence © British Crown Copyright 2020/AWE

5.5.5 Overall Deformation

Flow curves for specimens DB-T1, DB-T2, and DB-T3 are plotted in blue, red and green respectively in figure 5.42 with the estimated uncertainty of $\pm$ 1 standard deviation in stress and strain shown as a shaded region. The estimated uncertainties are much smaller than the measured values, and are considered insignificant.

A linear region was seen at low strains, with each specimen having a different apparent stiffness – 207 GPa, 81 GPa, and 116 GPa for DB-T1, DB-T2 and DB-T3 respectively. Specimen DB-T2 yields first, at approximately 80 MPa, then work hardens rapidly, at a rate more than double that of the other specimens, reaching almost 200 MPa by an applied strain of 1.2 %. DB-T3 yields at around 90 MPa whilst DB-T1 yields at 100 MPa. Both then harden at similar rates, with DB-T1 being between 20 MPa and 30 MPa stronger throughout the stress range.

Ministry of Defence © British Crown Copyright 2020/AWE

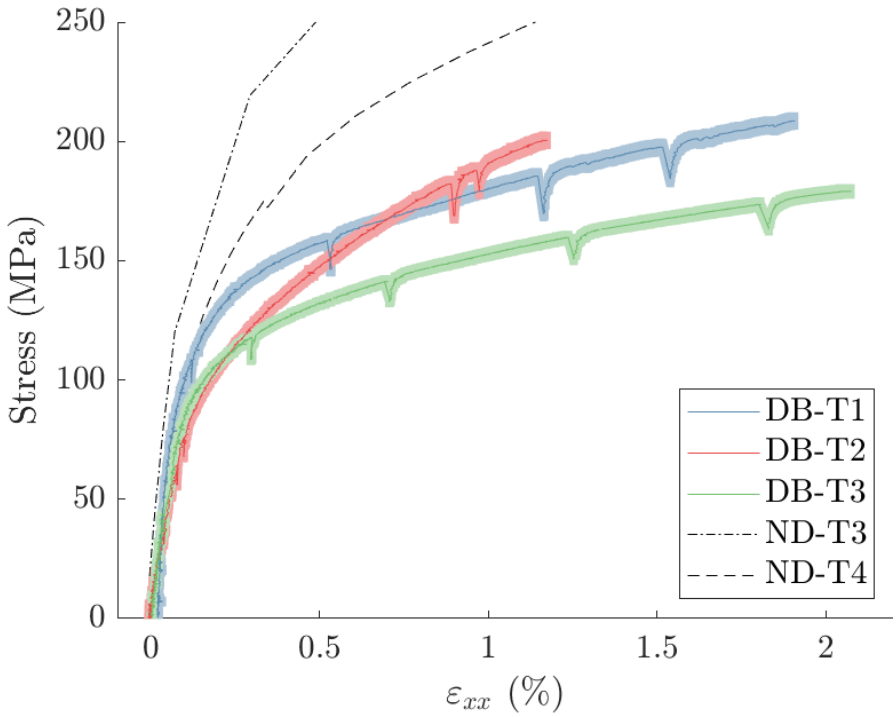


Figure 5.42. Flow curves for tensile specimens DB-T1 (blue), DB-T2 (red), and DB-T3 (green), with the uncertainty of $\pm$ 1 standard deviation in stress and strain shown as a shaded region. Sudden drops in stress were caused by creep relaxation as the specimen was held in position control whilst intermediate DIC calculations were performed. Also plotted are the flow curves from the two neutron diffraction specimens tested in tension on SMARTS at LANL – ND-T3 and ND-T4.

All three dog bone (DB) specimens were softer than the larger neutron diffraction (ND) specimens, with deviation from linearity for ND occurring at slightly higher stresses of 100 MPa – 120 MPa.

5.5.6 Deformation Maps

In this section, the full-field deformation of the specimen is visualised by plotting the spatial variation of each deformation component as a filled contour map. The normal axial strain $\varepsilon_{xx}(x_0, y_0)$ is the most relevant and is plotted for each specimen at three levels of applied strain (defined as the average axial strain in the gauge volume); (a) a point close to the macroscopic yield point, (b) an intermediate strain approximately half

Ministry of Defence © British Crown Copyright 2020/AWE

the maximum value, and (c) the strain at the maximum stress during the test. In addition, the normal transverse strain $\varepsilon_{yy}(x_0, y_0)$ and in-plane shear strain $\varepsilon_{xy}(x_0, y_0)$ at maximum stress is shown. In each case, the data were plotted at the reference co-ordinates (x_0, y_0) to allow comparison with the initial microstructure; the outline of each grain cluster identified in section 5.5.3 is shown as a dotted line. Each cluster is numbered and coloured consistent with those in figure 5.33, figure 5.34 and figure 5.35.

The out-of-plane displacement $u_z(x_0, y_0)$ at maximum stress is presented which includes the specimen deformation as well as any translation of the specimen. In some cases, the specimen rotated slightly from its initial orientation as the load was applied, and this made the out-of-plane distortion harder to discern. The out-of-plane distortion $u_z^{\text{relative}}(x_0, y_0)$ was calculated as the difference between the $u_z(x_0, y_0)$ values and $P(x_0, y_0)$, the plane of best-fit through $u_z(x_0, y_0)$. The in-plane distortions $u_x^{\text{relative}}(x_0, y_0)$ and $u_y^{\text{relative}}(x_0, y_0)$ were calculated by subtracting the mean in-plane displacement from the measured values. The out-of-plane distortion was plotted as a filled contour map, with the in-plane distortions overlaid as a quiver/velocity plot, with arrows pointing in the direction of the local distortion and lengths proportional to the magnitude of in-plane displacement.

5.5.6.1 Specimen DB-T1

In specimen DB-T1 (figure 5.43), axial strain localised in a vertical line in cluster 4; this was visible even at a small applied strain of 0.25 %. Strain also accumulated to a lesser

Ministry of Defence © British Crown Copyright 2020/AWE

extent in cluster 2. By an applied strain of 1.00 %, the concentration in cluster 4 was stronger, reaching 6 % in places, and was aligned with the tip of the triangular cluster. The strain in cluster 2 was only partially aligned with the grain cluster boundary. The region of cluster 3 loaded in parallel with cluster 4 also strained, reaching between 3 % and 4 % strain.

At the maximum strain of 1.90 % the magnitude of the strain concentration in cluster 4 had exceeded 10 % in places. The strained region in cluster 3 accumulated more strain, whilst the rest of the grain strained by a much smaller amount. The far left of cluster 3 did not significantly strain, barely reaching 1 % strain. Cluster 5, to the right-hand side, saw an increase of strain of approximately 2 % as the applied strain was increased from 1.00 % to 1.90 %.

The majority of specimen DB-T1 has small surface shear strains and transverse normal strains. The transverse strain ε_{yy} is positive near the axial concentration in cluster 3, reaching approximately 2 %, around 5 times smaller in magnitude than the axial strains in this location. The transverse strain is negative near the axial strain concentration in cluster 2, with a value of around -6 %.

The shear strains are much smaller, at around $+0.04$ % in cluster 4 and a similar magnitude but opposite sign in cluster 2.

Ministry of Defence © British Crown Copyright 2020/AWE

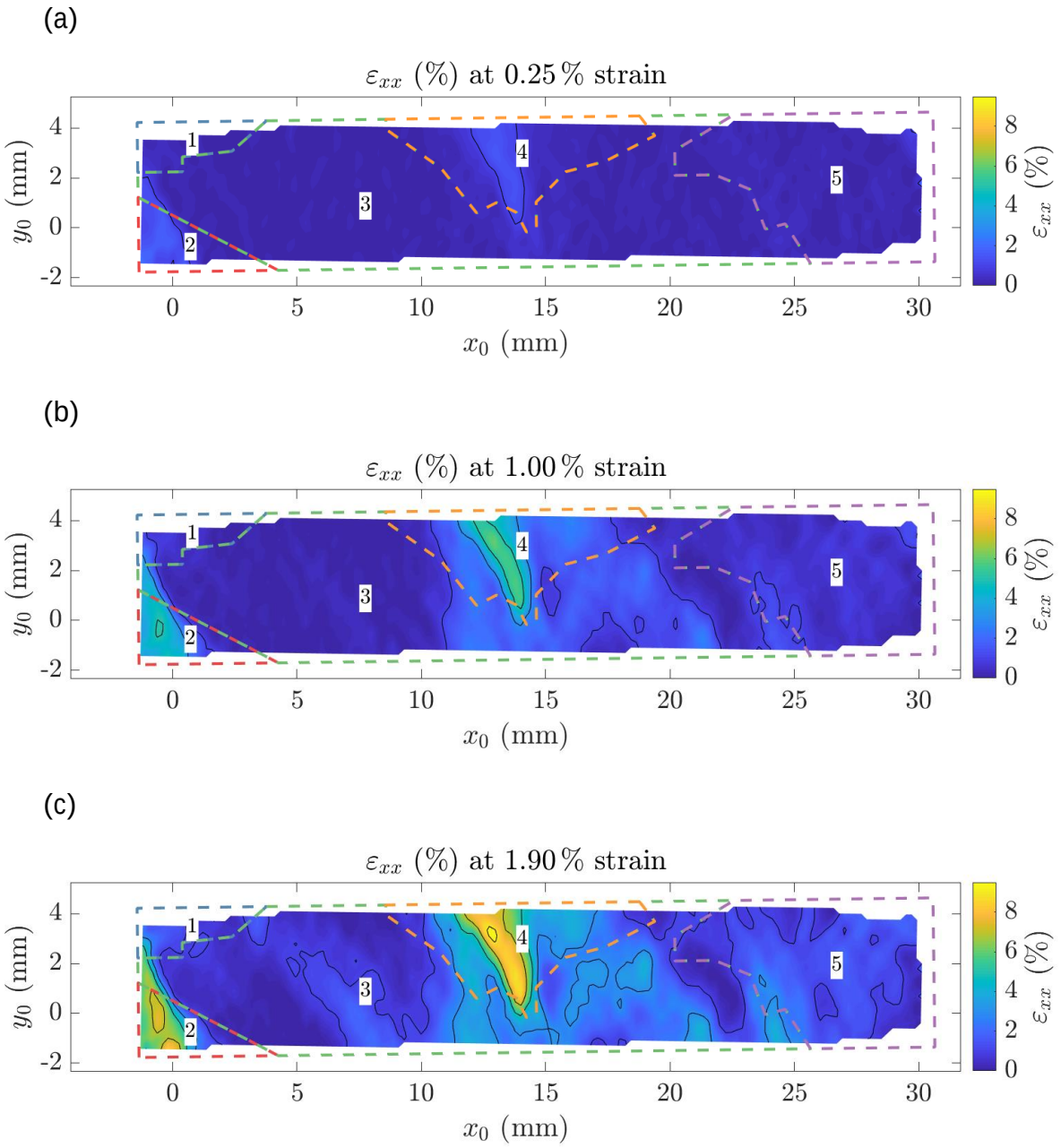
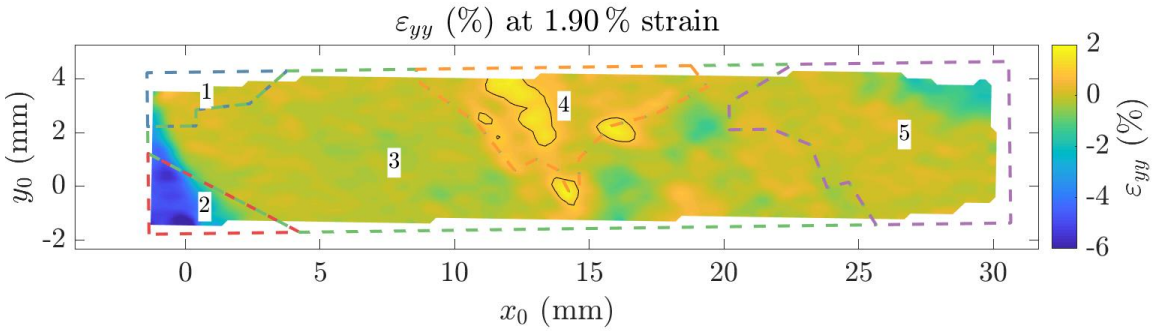


Figure 5.43. Development of axial normal strain ε_{xx} on the surface of specimen DB-T1 at (a) 0.25 %, (b) 1.00 %, and (c) 1.90 % applied strain. Strain contours are shown as black lines at 2 % intervals. The colour scale runs from 0.0 % to 9.5 % and is the same in each subfigure for ease of comparison. Data are plotted with respect to the reference co-ordinates (x_0, y_0) – the specimen position at the first DIC measurement at the start of the test. Grain cluster outlines are shown with dashed lines. Clusters are labelled with a number and with outlines coloured consistent with those in figure 5.33.

(a)

Ministry of Defence © British Crown Copyright 2020/AWE



(b)

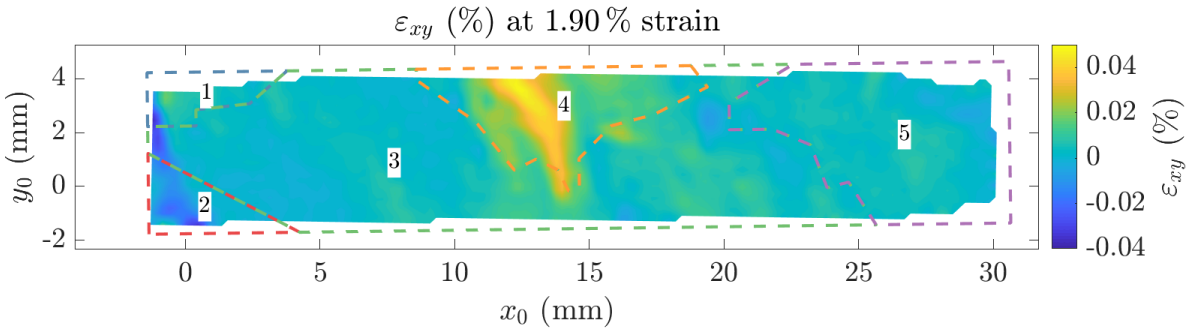


Figure 5.44. (a) Transverse normal strain ε_{yy} and (b) in-plane shear strain ε_{xy} on the surface of specimen DB-T1 at the maximum stress, corresponding to an applied strain of 1.90 %. Data are plotted with respect to the reference co-ordinates (x_0, y_0) – the specimen position at the first DIC measurement at the start of the test. Grain cluster outlines are shown with dashed lines. Clusters are labelled with a number and with outlines coloured consistent with those in figure 5.33.

The deformation of cluster 4 was larger than the deformation in the region of cluster 3 loaded in parallel with it. The specimen bent about its surface normal axis, with the central region being displaced by approximately 120 µm in the positive *y*-direction with respect to each end. This can be seen in the in-plane displacement arrows pointing slightly downwards in the region to the left and right of cluster 4.

(a)

Ministry of Defence © British Crown Copyright 2020/AWE

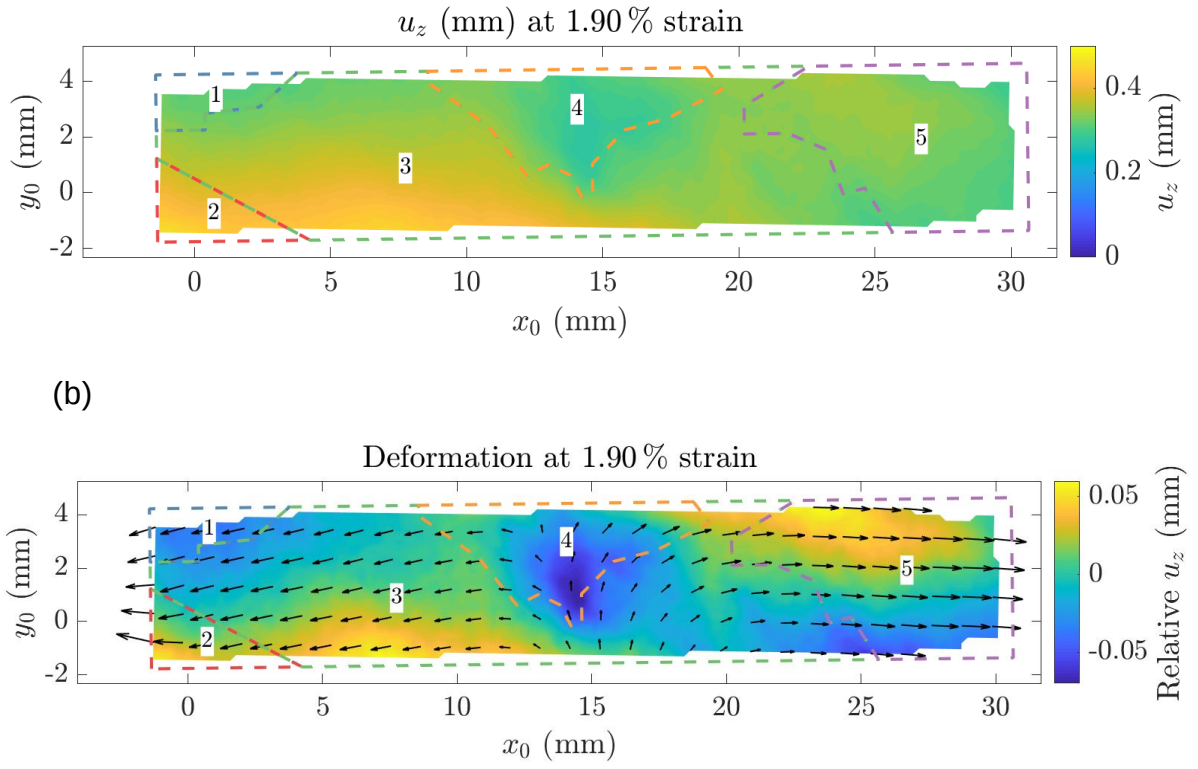


Figure 5.45. (a) Out-of-plane displacement of the specimen u_z and (b) out-of-plane distortion u_z^{relative} of surface of specimen DB-T1 at the maximum stress, corresponding to an applied strain of 1.90 %. The in-plane distortions are shown on subfigure (b) as black arrows pointing in the direction of the local distortion with lengths proportional to the magnitude of in-plane displacement. Data are plotted with respect to the reference co-ordinates (x_0, y_0) – the specimen position at the first DIC measurement at the start of the test. Grain cluster outlines are shown with dashed lines. Clusters are labelled with a number and with outlines coloured consistent with those in figure 5.33.

5.5.6.2 Specimen DB-T2

In specimen DB-T2, a strain concentration was detectable immediately after yield in a thin band approximately 2 mm thick located diagonally from cluster 5 to the top-left edge of cluster 7 (figure 5.46(a)). Throughout the test the majority of strain concentrated in this band – the local strain reached the test-end threshold of 12 % before the total strain exceeded 1.1 %. The rest of the specimen was largely undeformed except towards the end of the test where a perpendicular band, much weaker in magnitude than the first ($\varepsilon_{xx} < 4\%$), forms running from cluster 1 to the specimen edge in cluster 7.

Ministry of Defence © British Crown Copyright 2020/AWE

In figure 5.47 it can be seen that the band of strain concentration is associated with large positive shear strain and large negative transverse strain. A small region of shear is seen parallel to the boundary between cluster 7 and 8 – note that the exact location of this boundary was fairly arbitrary, being chosen to divide the homogeneous orientations in cluster 8 from the intersecting grains in cluster 7.

During deformation the specimen moved on average 0.6 mm away from the camera with the left-hand side (top of the specimen as tested in the load frame) moving 0.2 mm more than the opposite end. The actual deformation of the specimen surface was much smaller, with out-of-plane distortion accumulating near the shear band. The right-hand side moved towards the cameras, whilst the left-hand side moved away, resulting in a total distortion of around 100 microns over a distance of 2 mm – 3 mm on the specimen surface.

Ministry of Defence © British Crown Copyright 2020/AWE

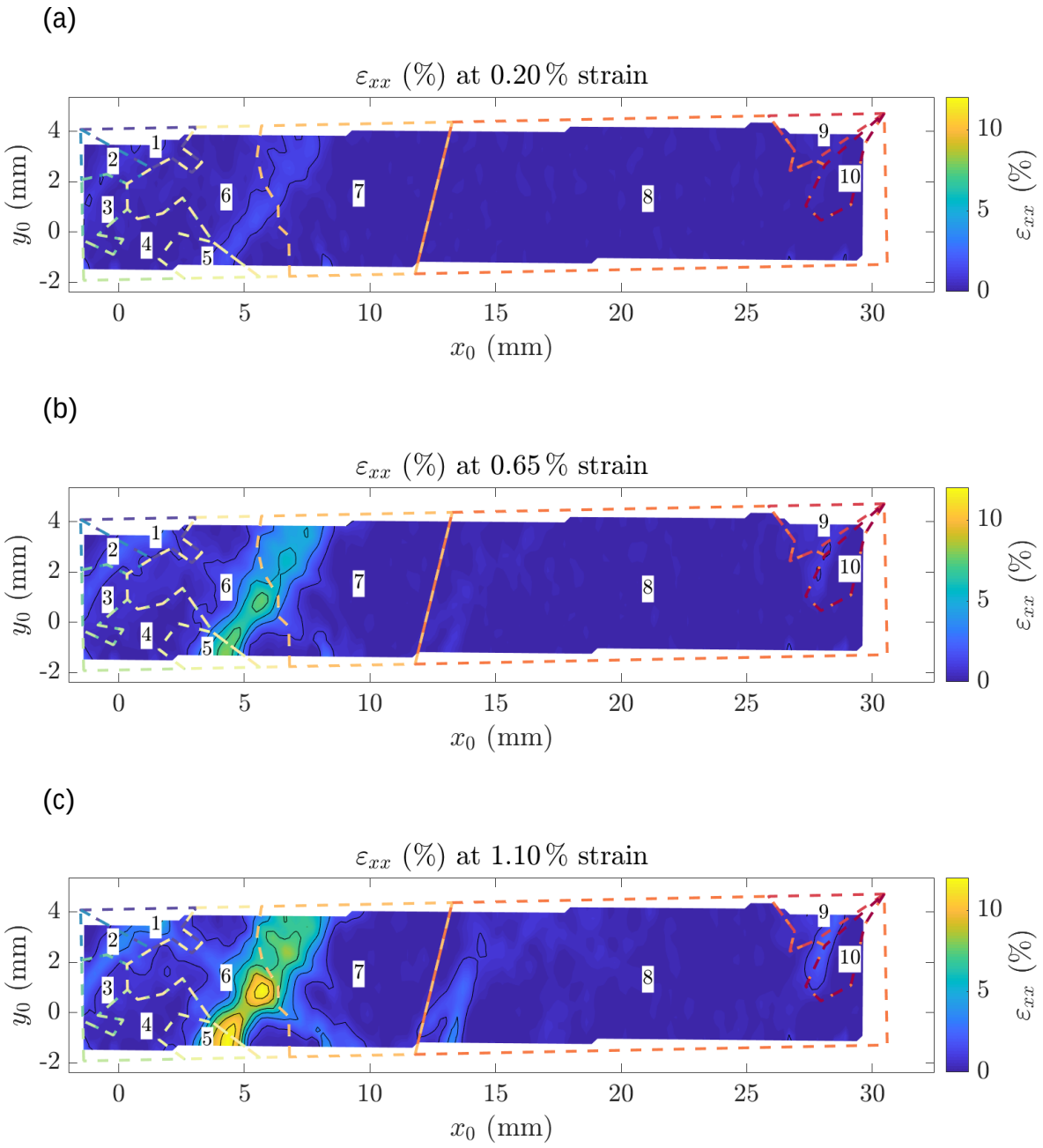


Figure 5.46. Development of axial normal strain ε_{xx} on the surface of specimen DB-T2 at (a) 0.20 %, (b) 0.65 %, and (c) 1.10 % applied strain. Strain contours are shown as black lines at 2 % intervals. The colour scale runs from 0.0 % to 12.0 % and is the same in each subfigure for ease of comparison. Data are plotted with respect to the reference co-ordinates (x_0, y_0) – the specimen position at the first DIC measurement at the start of the test. Grain cluster outlines are shown with dashed lines. Clusters are labelled with a number and with outlines coloured consistent with those in figure 5.34.

Ministry of Defence © British Crown Copyright 2020/AWE

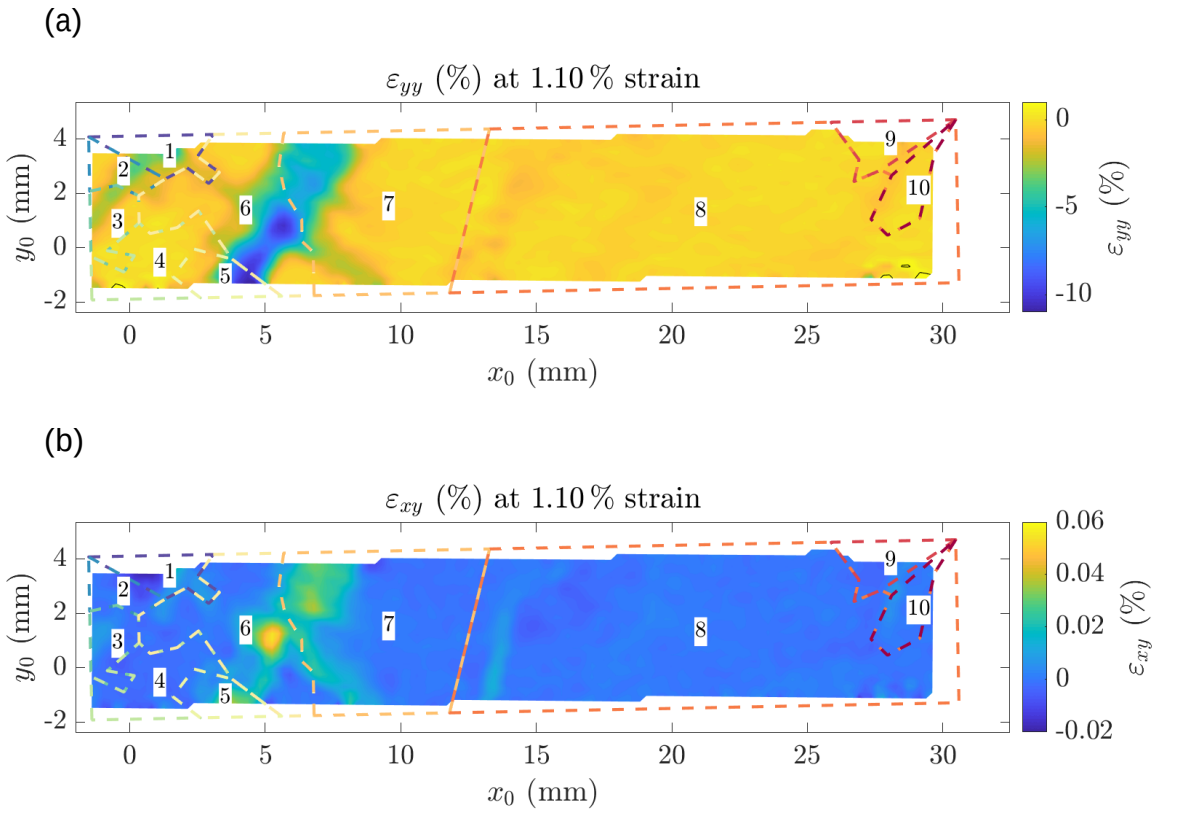
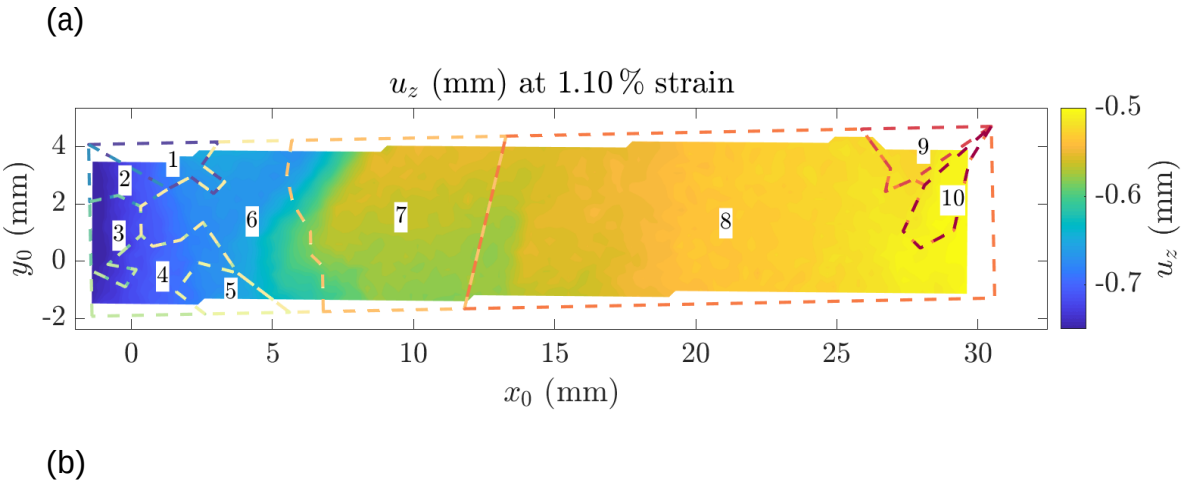


Figure 5.47. (a) Transverse normal strain ε_{yy} and (b) in-plane shear strain ε_{xy} on the surface of specimen DB-T2 at maximum stress, corresponding to an applied strain of 1.10 %. Data are plotted with respect to the reference co-ordinates (x_0, y_0) – the specimen position at the first DIC measurement at the start of the test. Grain cluster outlines are shown with dashed lines. Clusters are labelled with a number and with outlines coloured consistent with those in figure 5.34.



Ministry of Defence © British Crown Copyright 2020/AWE

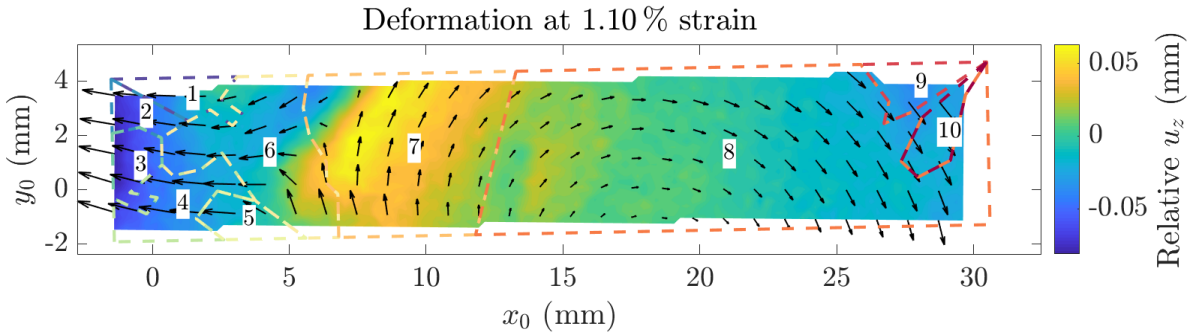


Figure 5.48. (a) Out-of-plane displacement of the specimen u_z and (b) out-of-plane distortion u_z^{relative} of surface of specimen DB-T2 at the maximum stress, corresponding to an applied strain of 1.10 %. The in-plane distortions are shown on subfigure (b) as black arrows pointing in the direction of the local distortion with lengths proportional to the magnitude of in-plane displacement. Data are plotted with respect to the reference co-ordinates (x_0, y_0) – the specimen position at the first DIC measurement at the start of the test. Grain cluster outlines are shown with dashed lines. Clusters are labelled with a number and with outlines coloured consistent with those in figure 5.34.

Ministry of Defence © British Crown Copyright 2020/AWE

5.5.6.3 Specimen DB-T3

In specimen DB-T3 a strain concentration initiates at the bottom-left of the trapezium –shaped cluster 3 near the border with cluster 2 (figure 5.49). Plastic deformation occurs in the majority of cluster 3, with the largest strains in the location of the original strain concentration. The right-hand edge of the deforming region in cluster 3 is parallel to the border between clusters 3 and 4 but offset by 2 mm into cluster 3.

At an applied strain of 1.00 %, the axial strain in the surrounding clusters, 1 and 4, was less than 2 %. By an applied strain of 2.00 %, the strain concentration in cluster 3 reached 10 % in magnitude, and a region of 2 % strain had developed in the centre of cluster 4.

A strong concentration of compressive transverse strain is seen in a similar spatial distribution to the axial strain, but with approximately two-thirds the magnitude. A slight build-up of tensile transverse strain is seen in cluster 4.

The shear strain is positive in cluster 4 but negative in cluster 3, in each case having a magnitude less than 0.02 %.

Ministry of Defence © British Crown Copyright 2020/AWE

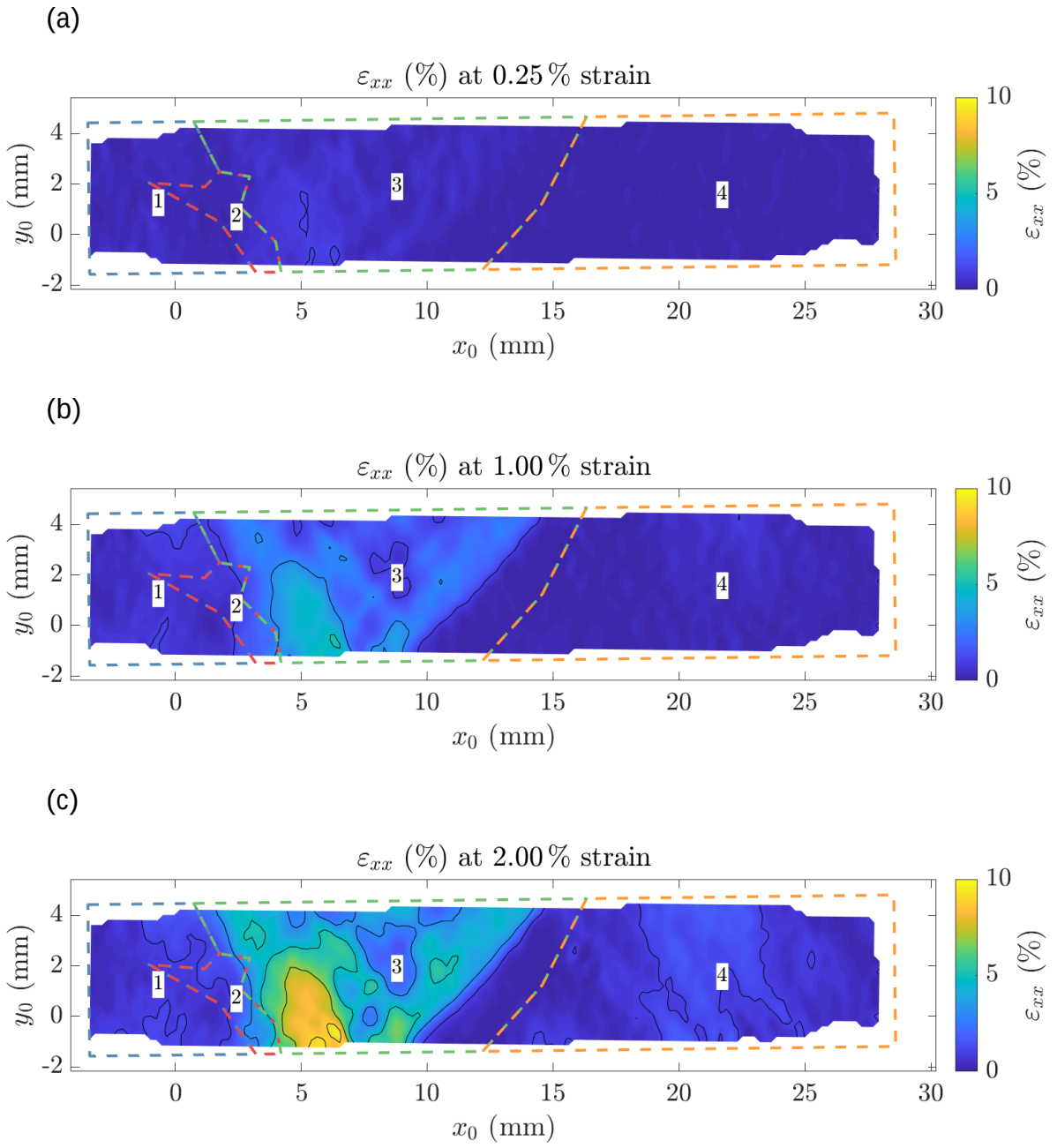
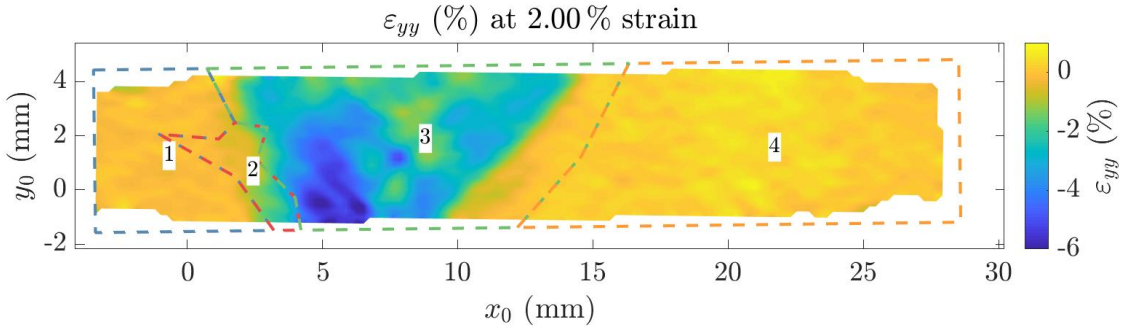


Figure 5.49. Development of axial normal strain ε_{xx} on the surface of specimen DB-T3 at (a) 0.25 %, (b) 1.00 %, and (c) 2.00 % applied strain. Strain contours are shown as black lines at 2 % intervals. The colour scale runs from 0.0 % to 10.0 % and is the same in each subfigure for ease of comparison. Data are plotted with respect to the reference co-ordinates (x_0, y_0) – the specimen position at the first DIC measurement at the start of the test. Grain cluster outlines are shown with dashed lines. Clusters are labelled with a number and with outlines coloured consistent with those in figure 5.35.

Ministry of Defence © British Crown Copyright 2020/AWE

(a)



(b)

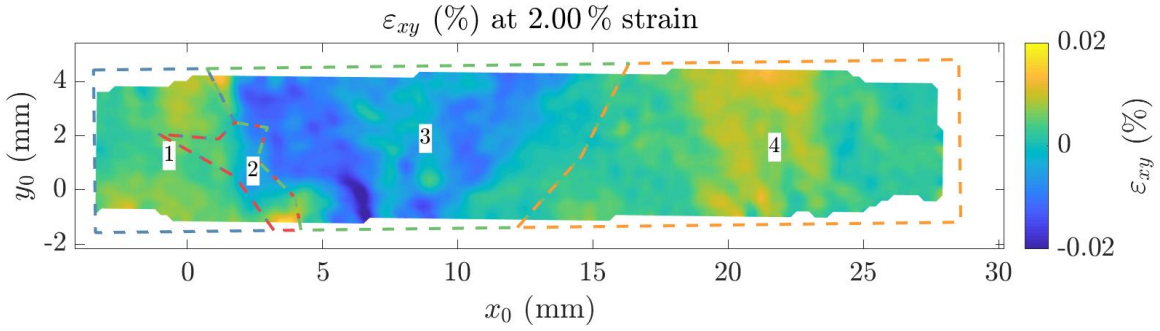


Figure 5.50. (a) Transverse normal strain ε_{yy} and (b) in-plane shear strain ε_{xy} on the surface of specimen DB-T3 at maximum stress, corresponding to an applied strain of 1.10 %. Data are plotted with respect to the reference co-ordinates (x_0, y_0) – the specimen position at the first DIC measurement at the start of the test. Grain cluster outlines are shown with dashed lines. Clusters are labelled with a number and with outlines coloured consistent with those in figure 5.35.

The specimen translated away from the camera by about 0.2 mm at maximum load (figure 5.51). The maximum out-of-plane distortion of 80 μm was found in cluster 3, along the right-hand edge of the straining region. The central part of the specimen twists about its longitudinal axis, with the top-left of cluster 3 moving 70 μm away from the camera in contrast to the aforementioned positive distortion in the same cluster.

The in-plane displacements lead to the specimen central axis being moved in the positive *y*-direction for $x < 5$ mm and in the opposite direction for $x > 15$ mm. By inspection of the displacement arrows in figure 5.51(b), it can be seen that this is not just a simple rotation of the specimen and that the central axis distorted during the test.

Ministry of Defence © British Crown Copyright 2020/AWE

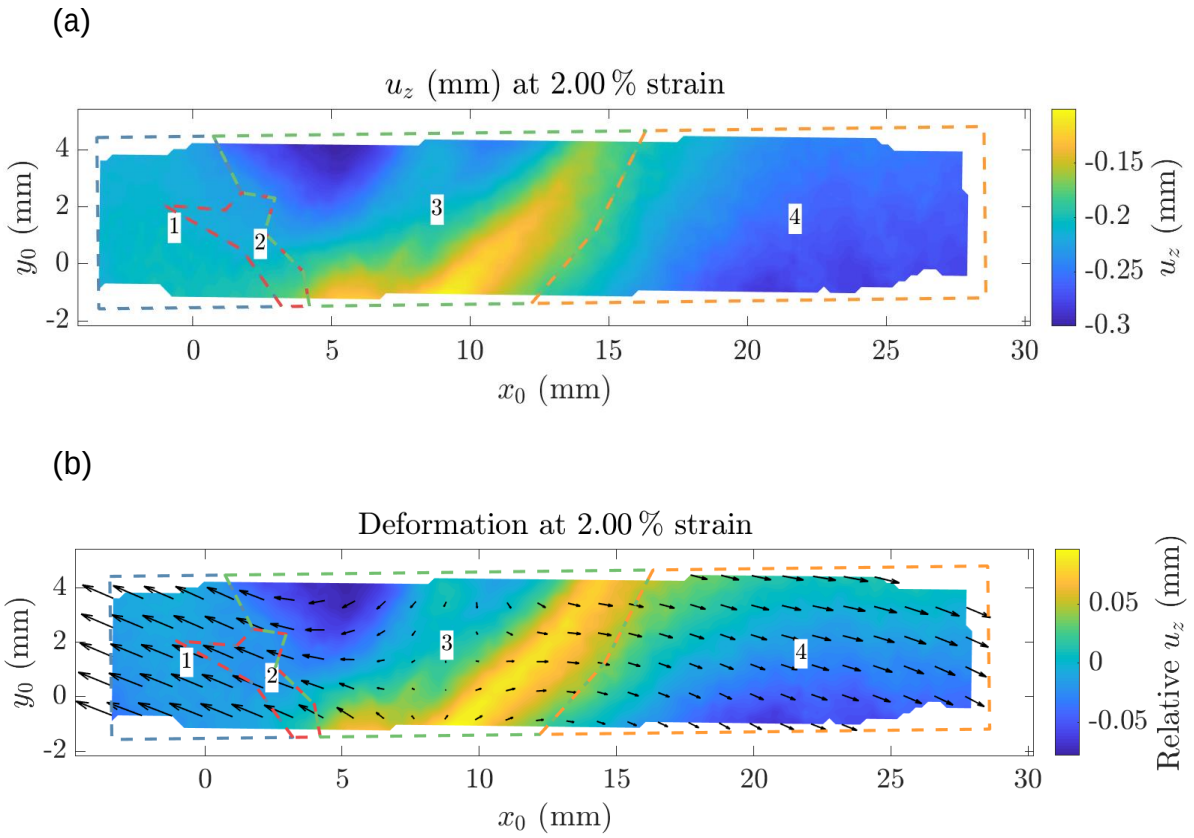


Figure 5.51. (a) Out-of-plane displacement of the specimen u_z and (b) out-of-plane distortion u_z^{relative} of surface of specimen DB-T3 at the maximum stress, corresponding to an applied strain of 2.00 %. The in-plane distortions are shown on subfigure (b) as black arrows pointing in the direction of the local distortion with lengths proportional to the magnitude of in-plane displacement. Data are plotted with respect to the reference co-ordinates (x_0, y_0) – the specimen position at the first DIC measurement at the start of the test. Grain cluster outlines are shown with dashed lines. Clusters are labelled with a number and with outlines coloured consistent with those in figure 5.35.

5.5.7 Stress-Strain Curves

The deformation maps in the previous section convey the heterogeneity of the strain field, but do not clearly show the rate at which each strain feature develops during the test. In this section, stress-strain curves are plotted for each grain cluster identified in section 5.5.3. To achieve this, the stress is assumed to be homogeneous throughout the specimen.

Ministry of Defence © British Crown Copyright 2020/AWE

A close-up view of the elastic region is also presented to show the differences in elastic response and yield point in each grain. For each specimen, a table contains the calculated stiffness, yield stress and 0.2 % offset stress for each cluster.

5.5.7.1 Specimen DB-T1

Figure 5.52 shows the flow curves for the 5 clusters identified in specimen DB-T1. As expected from the strain maps in figure 5.43, there are significant differences in deformation between each cluster.

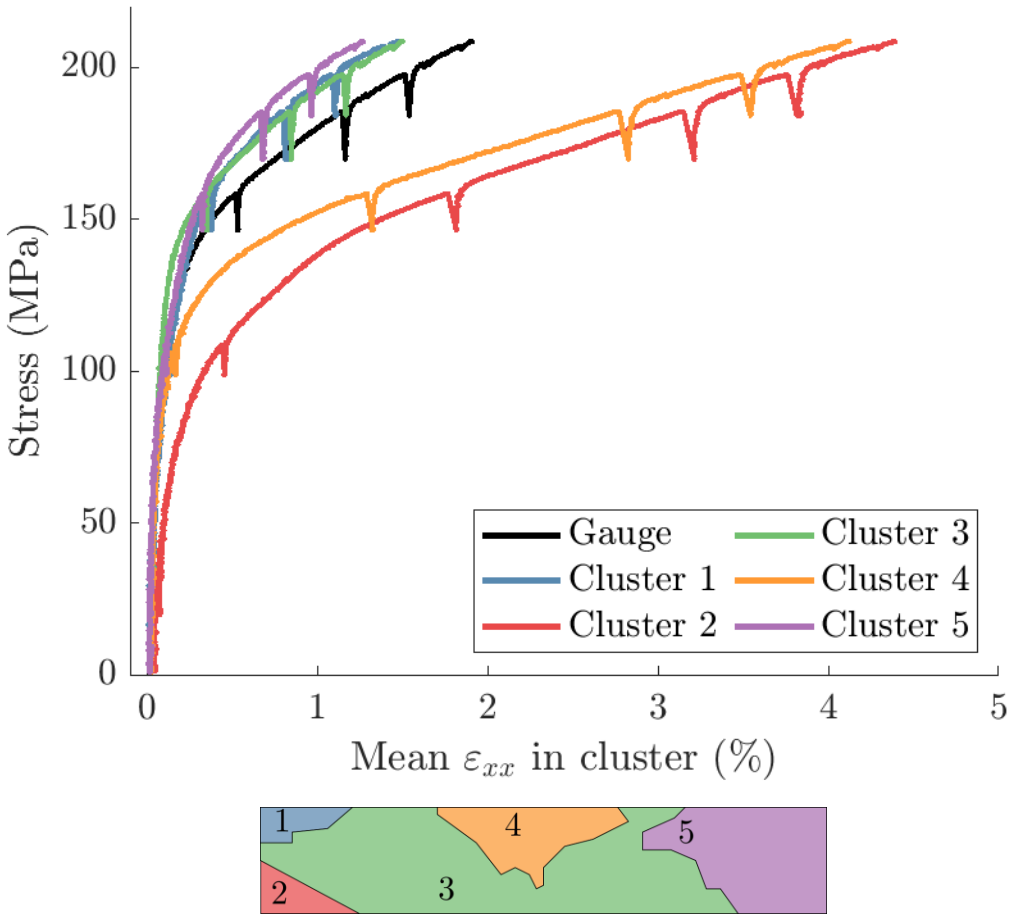


Figure 5.52. Flow curves for specimen DB-T1, showing the development of axial strain ε_{xx} as a function of stress. The strain in the gauge region is shown in black, the coloured curves show the segmented strain data for each of the 5 clusters identified in figure 5.33. The stress is implicitly assumed to be homogeneous throughout the specimen, and equal to the applied tensile stress.

Ministry of Defence © British Crown Copyright 2020/AWE

Clusters 2, to the bottom-left of the specimen, and 4, in the centre, are soft and accumulate more strain than the gauge region average, whilst clusters 1, 3, and 5 are much harder. Despite being the most compliant, with a stiffness of just 80 GPa, and yielding at a low stress of 50 MPa, cluster 2 hardens rapidly such that by the end of the test it carries a similar strain to cluster 4. At the maximum applied stress, clusters 2 and 4 are holding over double the strain seen in the whole gauge region (~4.2 % compared to 1.9 %), whilst the mean strain in the other clusters does not reach 1.5 %.

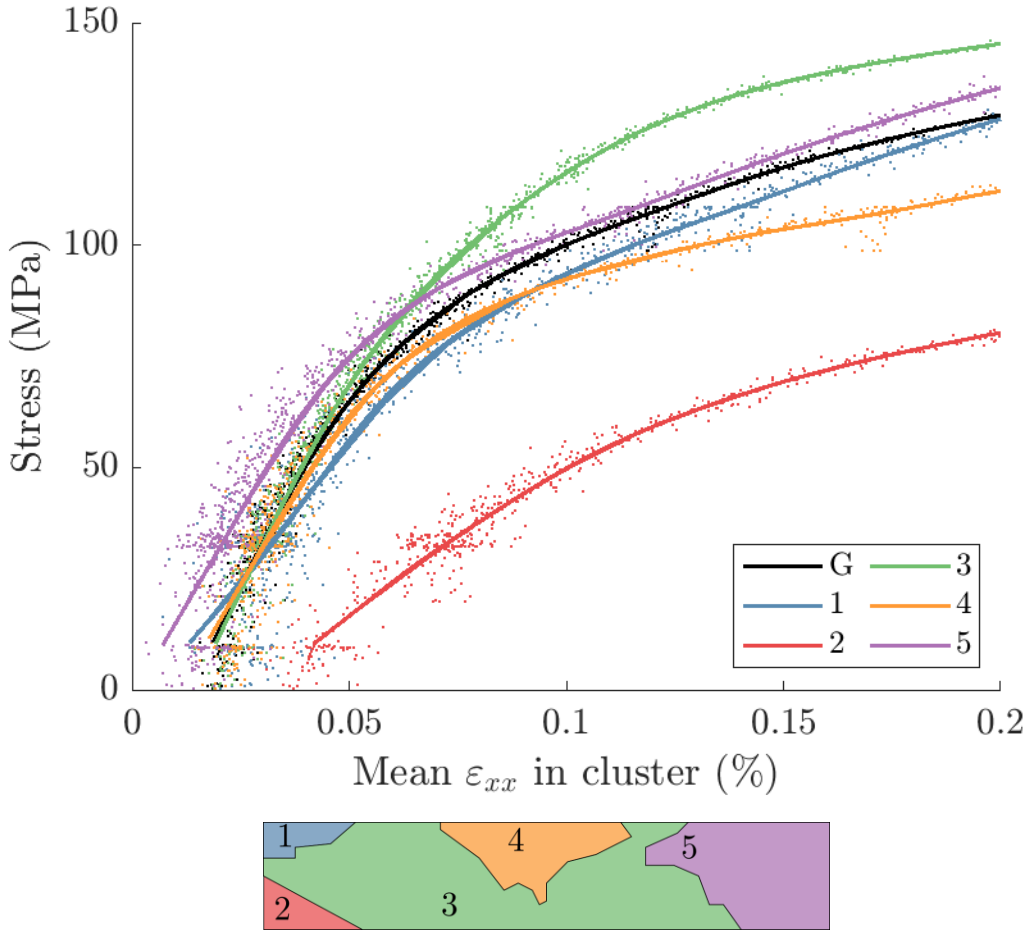


Figure 5.53. Elastic region of the flow curves for specimen DB-T1 showing the deviation from linearity at yield. For some clusters, in particular 2, the yield point is indistinct. The data from figure 5.52 are shown as dots with a smoothing spline added to aid comparison.

Ministry of Defence © British Crown Copyright 2020/AWE

Figure 5.53 shows the elastic region of the stress-strain curve and the deviation from linearity at yield. The calculated stiffnesses, yield stresses and 0.2 % offset stresses for each cluster are given in table 5.5. For some clusters, the deviation from linearity is indistinct and there is considerable uncertainty in the yield point. The uncertainty in offset yield stress was estimated to be 5 MPa by considering the scatter in the stress values and the uncertainty in the elastic gradient (stiffness).

At zero stress, the strains are non-zero and positive, with a magnitude approximately 2 times larger than the scatter in ε_{xx} – this will be discussed later in section 5.6.3.2.

With the exception of cluster 2, all clusters exhibit a clear linear region at low stress, and deviate from linearity between 50 MPa and 80 MPa; cluster 4, containing the largest axial strain concentration in figure 5.43, yields first. Clusters 1 and 3 have similar elastic gradients, at around 200 MPa whilst clusters 4 and 5 are stiffer at ~250 MPa and ~300 MPa respectively.

In general those clusters with a higher yield stress have higher 0.2 % offset stresses however this generalisation hides some of the differences between each cluster. Cluster 3 has the highest yield stress at 80 MPa, 30 MPa higher than the next strongest cluster, but has the lowest overall hardening rate so by 0.2 % strain in this cluster it is only 5 MPa harder. In figure 5.52 it can be seen that cluster 3 softens such that by the end of the test it carries more strain than clusters 1 and 5.

Ministry of Defence © British Crown Copyright 2020/AWE

Table 5.5. Calculated elastic and yield parameters for specimen DB-T1. (a) Calculated elastic stiffness, in GPa, for each grain cluster. (b) Yield stress, in MPa, defined as the point where the deviation in stress between the extrapolation of the elastic fit line and the spline curve in figure 5.53 exceeds 5 MPa. *Uncertainty in the yield stress was estimated by eye and is large due to the indistinct yield points in some grains. (c) 0.2 % offset stress, in MPa, defined as the stress at which a plastic strain of 0.2 % will have developed in the grain cluster compared to its strain state at $\sigma = 0$. Calculated by translating the elastic fit line by 0.2 % along the ε-axis and finding the stress at which this line intersects the spline curve. **Uncertainty in offset yield stress was estimated by the author to be 5 MPa by considering the scatter in the stress values and the uncertainty in the elastic gradient (stiffness).

Region	Stiffness (GPa)	Yield Stress (MPa)	0.2 % Offset Stress (MPa)
Gauge	207 ± 5	65 ± 5*	141 ± 5
Cluster 1	202 ± 9	50 ± 20*	149 ± 5
Cluster 2	80 ± 2*	50 ± 10*	102 ± 5
Cluster 3	192 ± 4	80 ± 15*	155 ± 5
Cluster 4	246 ± 9	55 ± 10*	121 ± 5
Cluster 5	301 ± 15	60 ± 20*	149 ± 5

The triangular-shaped cluster 4, whilst having a similar yield stress to cluster 1, starts accumulating strain in the main stress concentration immediately after yield, and is 30 MPa softer than cluster 1 as the mean strain in each cluster reaches 0.2 %.

Cluster 2 hardens rapidly up to a mean strain of 1 %, then the hardening rate reduces and becomes similar to cluster 4.

5.5.7.2 Specimen DB-T2

Specimen DB-T2 saw a significant concentration of strain develop in clusters 5 and 6 (figure 5.46), and this is reflected in the flow curves in figure 5.54 where these clusters carry the highest strain. Clusters 8 and 10 are particularly hard, with less than 0.5 %

Ministry of Defence © British Crown Copyright 2020/AWE

strain at the maximum applied stress of 200 MPa. Cluster 8 is the strongest cluster and yields at ~130 MPa.

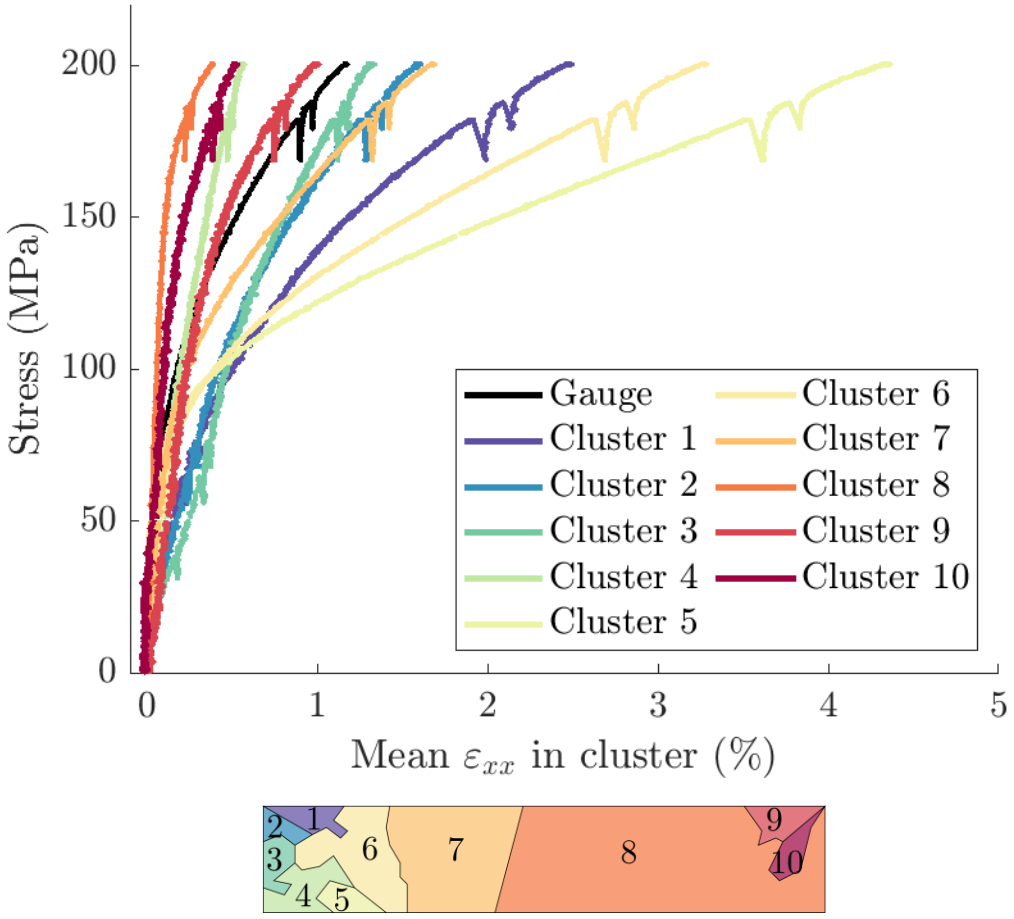


Figure 5.54. Flow curves for specimen DB-T2, showing the development of axial strain ε_{xx} as a function of stress. The strain in the gauge region is shown in black, the coloured curves show the segmented strain data for each of the 10 clusters identified in figure 5.34. The stress is implicitly assumed to be homogeneous throughout the specimen, and equal to the applied tensile stress.

The deformation of clusters 2 and 3 is abnormal and they appear to yield at low stresses of approximately 30 MPa. Then, at around 0.15 % strain, the gradient of the stress-strain curves increase and these clusters harden rapidly – by the end of the test only ~1.2 % has accumulated, much less than the 4.3 % seen in cluster 5 which yields at a much higher stress of 60 MPa.

Ministry of Defence © British Crown Copyright 2020/AWE

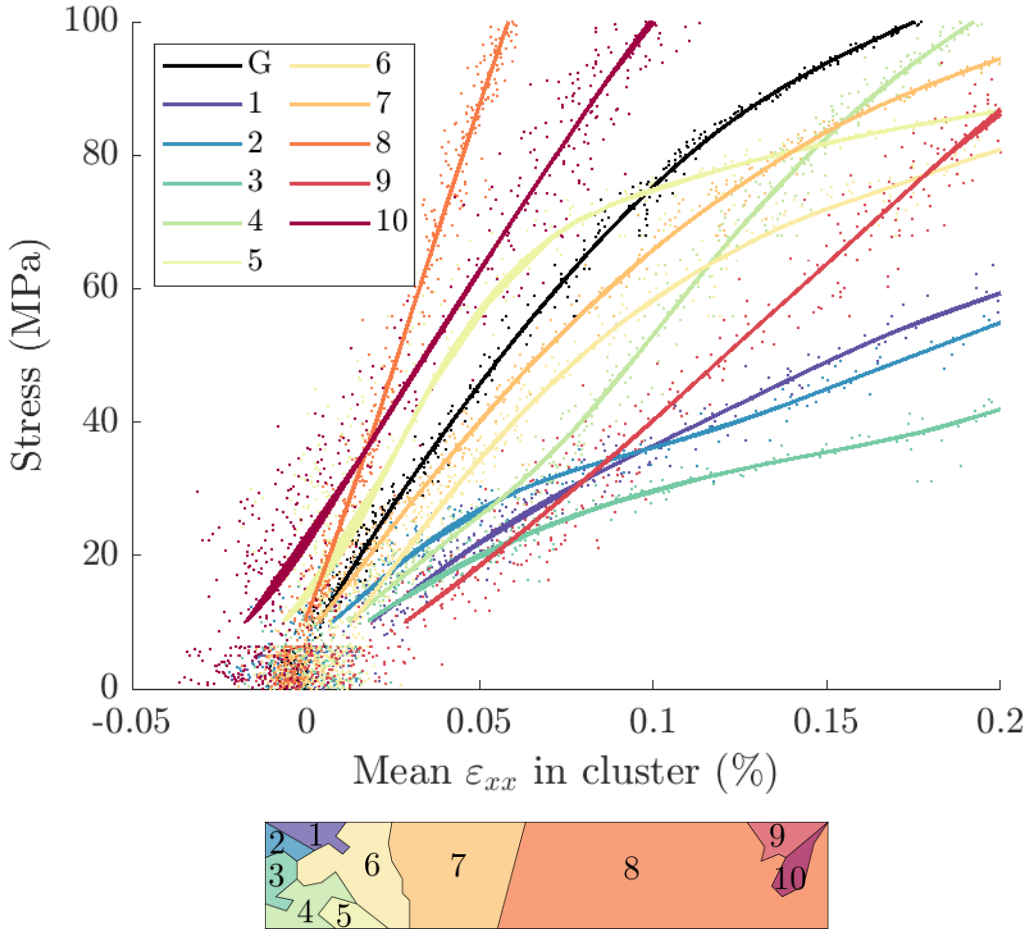


Figure 5.55. Elastic region of the flow curves for specimen DB-T2 showing the deviation from linearity at yield. For some clusters, the yield point is indistinct. The data from figure 5.55 are shown as dots with a smoothing spline added to aid comparison.

Cluster 1, which contains the secondary, perpendicular strain band (figure 5.46(b)) has a very low gradient of 30 GPa in its linear region. The mean axial strain then increases at a faster rate than in the overall gauge volume, with cluster 1 carrying 2.5 % strain at the maximum stress of 200 MPa.

The strongest cluster, 8, is also the stiffest, with an elastic gradient of 151 MPa. At maximum stress, this grain carries the least strain at 0.3 %. Clusters 2 and 3 deviate from linearity before any non-linearity is detectable in the gauge region as a whole. It was not possible to fit an elastic line to these data.

Ministry of Defence © British Crown Copyright 2020/AWE

In cluster 4, the stress-strain gradient after yield actually increases (figure 4.39). This is likely as a result of the stress redistribution and is discussed later in section 5.6.2.2.

At zero stress, the majority of clusters show close to zero strain, with the exception of the small cluster 10 which shows strains of $-0.03\,\%$

Table 5.6. Calculated elastic and yield parameters for specimen DB-T2. (a) Calculated elastic stiffness, in GPa, for each grain cluster. (b) Yield stress, in MPa, defined as the point where the deviation in stress between the extrapolation of the elastic fit line and the spline curve in figure 5.55 exceeds 5 MPa. *Uncertainty in the yield stress was estimated by eye and is large due to the indistinct yield points in some grains. (c) 0.2 % offset stress, in MPa, defined as the stress at which a plastic strain of 0.2 % will have developed in the grain cluster compared to its strain state at $\sigma = 0$. Calculated by translating the elastic fit line by 0.2 % along the ε-axis and finding the stress at which this line intersects the spline curve. **Uncertainty in offset yield stress was estimated by the author to be 5 MPa by considering the scatter in the stress values and the uncertainty in the elastic gradient (stiffness). *** Cluster 4 exhibited an anomalous stress-strain response and it was not possible to determine stiffness or yield parameters. **** Clusters 2 and 3 yield at a very low stress and the elastic gradient was difficult to measure.

Region	Stiffness (GPa)	Yield Stress (MPa)	0.2 % Offset Stress (MPa)
Gauge	81 ± 1	67 ± 5*	130 ± 5**
Cluster 1	32 ± 1	55 ± 10*	100 ± 5**
Cluster 2	N/A****	31 ± 5****	88 ± 5****
Cluster 3	N/A****	34 ± 10****	146 ± 5****
Cluster 4	N/A***	N/A***	N/A***
Cluster 5	134 ± 31	60 ± 10*	91 ± 5**
Cluster 6	71 ± 1	52 ± 5*	95 ± 5**
Cluster 7	66 ± 1	67 ± 5*	116 ± 5**
Cluster 8	151 ± 1	132 ± 5*	195 ± 5**
Cluster 9	42 ± 1	114 ± 5*	168 ± 5**
Cluster 10	138 ± 11	31 ± 5*	167 ± 5**

Ministry of Defence © British Crown Copyright 2020/AWE

5.5.7.3 Specimen DB-T3

The flow curve of each cluster in specimen DB-T3 is shown in figure 5.56. The main strain concentration in cluster 3 (figure 5.49) is clear; by the end of the test this region carries a strain double that of the gauge region average. The exact yield point of this cluster occurs in a region of missing data between 43 MPa and 60 MPa[5].

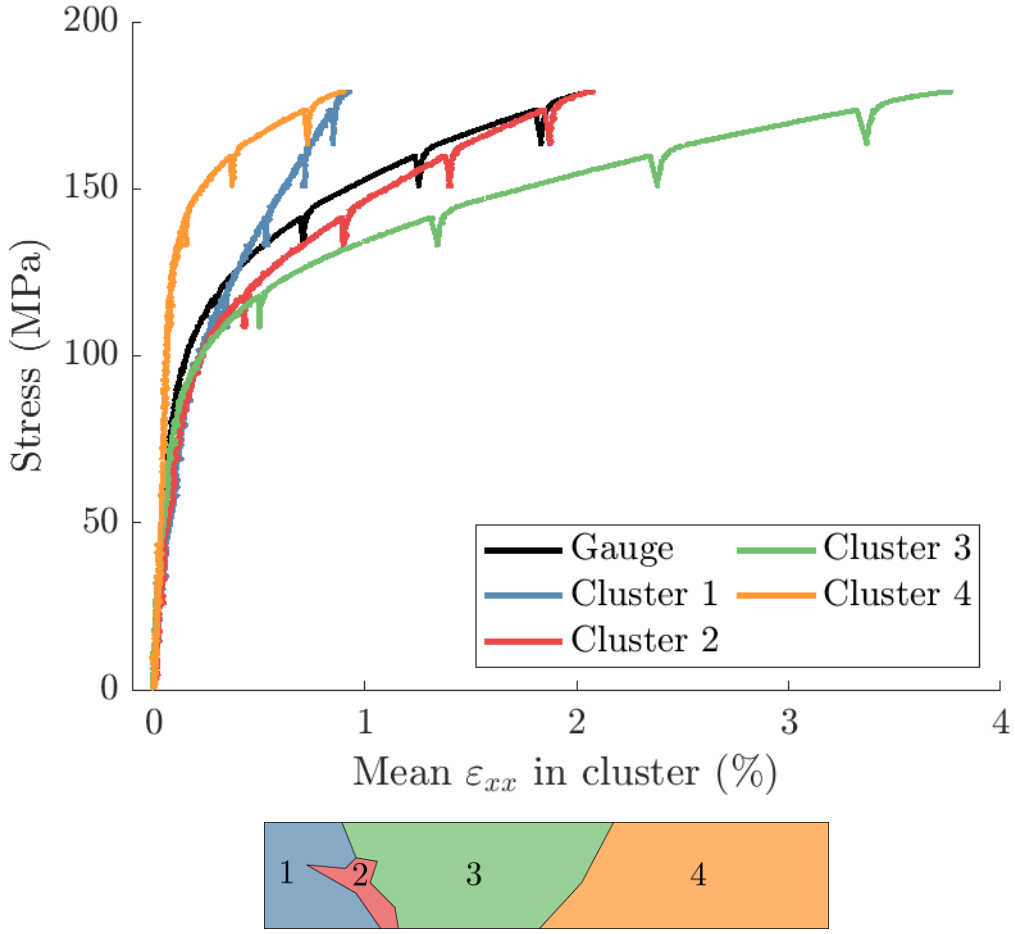


Figure 5.56. Flow curves for specimen DB-T3, showing the development of axial strain ε_{xx} as a function of stress. The strain in the gauge region is shown in black, the coloured curves show the segmented strain data for each of the 4 clusters identified in figure 5.35. The stress is implicitly assumed to be homogeneous throughout the specimen, and equal to the applied tensile stress. Data are missing for stresses between 43 MPa and 60 MPa due to an experimental issue with the DIC cameras.

[5] An experimental issue with the DIC cameras caused a series of images to exhibit poor image correlation statistics and as such no strain data were calculated for stresses between 43 MPa and 60 MPa.

Ministry of Defence © British Crown Copyright 2020/AWE

Cluster 4 is the hardest, yielding at 110 MPa and reaching 0.8 % strain at maximum load. Clusters 1 and 2 have similar yield points to cluster 3 but have very different hardening rates.

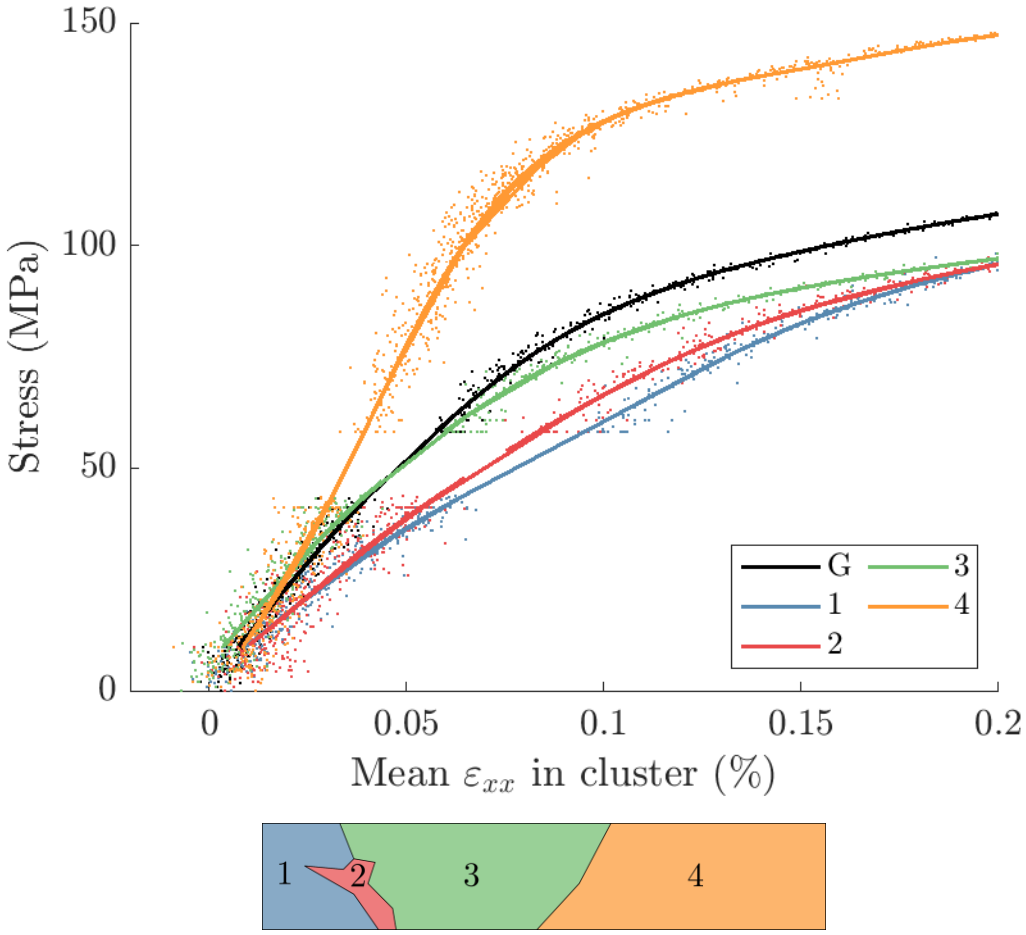


Figure 5.57. Elastic region of the flow curves for specimen DB-T3 showing the deviation from linearity at yield. For many clusters, the yield point is indistinct. The data from figure 5.56 are shown as dots with a smoothing spline added to aid comparison. Data are missing for stresses between 43 MPa and 60 MPa due to an experimental issue with the DIC cameras.

As well as carrying the least plastic strain, cluster 4 has the highest elastic stiffness at 171 GPa, and has an obvious linear elastic region until its yield point. Cluster 1 has the lowest measured stiffness at 70 GPa. Cluster 3 has a stiffness equal to that of the entire gauge region, at 116 GPa. The spline curves for each cluster pass through the origin.

Ministry of Defence © British Crown Copyright 2020/AWE

Cluster 1 yields first, at 40 MPa, but then hardens rapidly, achieving the second-highest 0.2 % offset stress of 122 MPa.

Table 5.7. Calculated elastic and yield parameters for specimen DB-T3. (a) Calculated elastic stiffness, in GPa, for each grain cluster. (b) Yield stress, in MPa, defined as the point where the deviation in stress between the extrapolation of the elastic fit line and the spline curve in figure 5.56 exceeds 5 MPa. *Uncertainty in the yield stress was estimated by eye and is large due to the indistinct yield points in some grains. (c) 0.2 % offset stress, in MPa, defined as the stress at which a plastic strain of 0.2 % will have developed in the grain cluster compared to its strain state at $\sigma = 0$. Calculated by translating the elastic fit line by 0.2 % along the ε-axis and finding the stress at which this line intersects the spline curve. **Uncertainty in offset yield stress was estimated by the author to be 5 MPa by considering the scatter in the stress values and the uncertainty in the elastic gradient (stiffness). ***For clusters 2 and 3 the yield point occurs in the region of missing data between 43 MPa and 60 MPa. The yield stress for these clusters is estimated to be 50 ± 10 MPa

Region	Stiffness (GPa)	Yield Stress (MPa)	0.2 % Offset Stress (MPa)
Gauge	116 ± 1	40 ± 5*	118 ± 5**
Cluster 1	70 ± 1	40 ± 10*	122 ± 5**
Cluster 2	87 ± 2	50 ± 10***	111 ± 5**
Cluster 3	116 ± 2	50 ± 10***	106 ± 5**
Cluster 4	171 ± 1	110 ± 5*	155 ± 5**

5.6 Discussion

In this section we will compare the deformation of the three specimens and identify any relationship between the location of strain concentration and the underlying microstructure. We will also discuss the validity of the measurements, and it will be seen that the numerical data are of good quality. Finally, the results of associated crystal plasticity modelling of these tests by our collaborators are presented; a set of improved CRSS parameters were found, allowing accurate simulation of these tests as well as an improved simulation of the ENGIN-X neutron diffraction experiment.

Ministry of Defence © British Crown Copyright 2020/AWE

5.6.1 General Observations

The microstructure in each specimen is very different, again with no correlation between the orientations in the specimens. The clusters are large, with each specimen having at least one cluster with a dimension in excess of 20 mm. The mechanical response of each specimen was unique and varied strongly within each specimen. In specimens DB-T1 and DB-T3 a clear correlation was seen between the microstructure and the observed strain field. In each specimen the maximum strain at maximum load was found in strain concentrations carrying over 5 times the mean gauge volume strain.

The macroscopic similarity of specimens DB-T1 and DB-T3 (figure 5.42) reflected the similarity in strain development - strain concentrations initiating near a grain boundary and then developing in a direction perpendicular to the applied load. Specimen DB-T2 showed an altogether different response, with the strain concentration crossing the entire gauge width. The majority of the strain was concentrated in this small region.

All three specimens deformed at lower stresses compared to the larger neutron diffraction (ND) specimens tested in Chapter 4. The dog-bone specimens have a smaller cross-sectional area and are therefore less constrained, with fewer clusters across the specimen width. In the dog-bone specimens, a soft cluster can freely deform and strain can localise in this region. In the ND specimens, however, it is likely that multiple clusters were deformed in parallel, so the deformation of a soft cluster will be limited by stress transfer to one of the harder adjacent clusters.

Ministry of Defence © British Crown Copyright 2020/AWE

It is seen in the CPFE modelling (table 4.4) that the CRSS for slip and twinning in this material are similar to those for single crystals (>2.5 mm) – i.e. the cluster size has a strong effect on the yield point rather than the low-angle grain boundaries between each ~200 μm grain in a cluster. Where a single cluster crosses the entire gauge width of a dog-bone specimen, the effective grain size is that of a single crystal, as slip can proceed to the free surface without dislocation pinning. This will also have contributed to the lower yield stress in the dog-bone specimens compared to the larger ND specimens.

The dog-bone specimens also have a lower hardening rate (figure 5.42) than the ND specimens. Hardening of slip systems is usually due to 'forest hardening', the formation of sessile jogs increasing the glide stress as dislocations on multiple independent slip systems interact. For twin systems, the equivalent effect is an effective reduction in grain size caused by crossing twins – the relative contribution of the high-strain-energy twin tip is larger for twins forming in smaller grains, so the twinning stress increases. If deformation localises onto fewer independent slip systems or twinning modes, due to strain concentrating in a single shear band (as seen in the dog-bone specimens), there will be fewer interactions with crossing slip/twin modes, and the hardening rate will be lower.

The point-to-point scatter in the DIC-measured strains is approximately 0.01 % (figure 5.53), the same as predicted by the rigid-body movement analysis (figure 5.25), and remains constant throughout the test and between specimens. This suggests the quality

Ministry of Defence © British Crown Copyright 2020/AWE

of DIC data is good, and consistent for each specimen. The stereo DIC system proved necessary as the out-of-plane translation of the specimens was large, with magnitudes of up to 0.5 mm, even though the distortions of the specimen surface were comparatively small. As will be seen in the next section, the accurate measurement of the out-of-plane distortion assists in the identification of the active deformation modes.

5.6.2 Specimen Deformation

5.6.2.1 Specimen DB-T1

In the centre of the gauge region of specimen DB-T1, clusters 3 and 4 are loaded in parallel. The boundary is not observed to slide so the clusters are initially loaded under equal-strain conditions. The stresses in each cluster will differ according to the stiffness and plastic deformation in each grain - the equal stress assumption used to plot the curves in figure 5.52 may not be strictly valid.

The largest strain concentration in the triangular-shaped cluster 4 is initially close to the lower vertex of the triangle. There is likely a stress concentration here due to the mismatch in mechanical properties between the softer cluster 4 and the harder cluster 3. Once established, the axial strain in this concentration increases near the top edge of the specimen, consistent with the observed bending of the specimen. As the specimen bends, the stress is misaligned with the specimen axis and the tensile rig prevents rotation of the specimen ends. The stress state at this point would have been complex,

Ministry of Defence © British Crown Copyright 2020/AWE

with the axial normal stress not equal to the applied stress, and varying across the specimen width.

Cluster 2, in the bottom-left corner of the gauge region, has positive axial and negative transverse strain, consistent with the extension of the specimen in this region (figure 5.44). Cluster 4, however has positive axial and transverse strains, indicative of the expansion or swelling of the surface. The conservation of volume would suggest that this was accompanied by the thinning of the specimen – we do see a depression on the surface in cluster 4 (figure 5.45), however since we did not observe the reverse side of the specimen, we cannot distinguish between out-of-plane bending and thinning.

Cluster 4 has a high Schmid factor for Chimney slip (SF > 0.4) at the location of initiation, and lower Schmid factors (SF < 0.25) for the other slip systems (figure 5.36). The low CRSS of Wall and Floor slip cause these modes to activate first despite having a lower Schmid factor. Whilst the Schmid factors for '$\{172\}$' and $\{112\}$ twinning are high at ~0.5 (figure 5.37), the CRSS for these modes is thought to be around 1.75$\times$ of that for {130} twinning[108] and the CPFE modelling has shown that the CRSS for {130} twinning in this material to be is 0.7$\times$ that of Chimney slip (table 4.4). Assuming therefore that the CRSS for these twin modes is ($0.7 \times 1.75 = 1.23$) times larger than that of Chimney slip, it is likely that Chimney slip initiates before twinning, despite having a smaller Schmid factor.

Ministry of Defence © British Crown Copyright 2020/AWE

In cluster 4, the Burgers vector for the Chimney slip variant with the highest Schmid Factor points into the plane of the paper, between the Z (in-to-plane) and X (specimen axis to right) axes defined in figure 5.9. Chimney slip could therefore account for the out-of-plane distortion that is seen in cluster 4 of specimen DB-T1.

5.6.2.2 Specimen DB-T2

The strain localisation in specimen DB-T2 does not clearly align with the microstructure. It is possible that the intersecting grains in cluster 7 form the majority of this cluster in the through-thickness direction, although we cannot verify this with single-surface EBSD. If this were the case, the deformation was likely mediated by Wall slip and {130} twinning, which both have Schmid factors in excess of 0.45 in these intersecting grains, despite having a very low Schmid factor in the grains which span clusters 7 and 8. Floor slip, with its low CRSS, is not expected to be active due to low Schmid factors.

The strain concentration has positive axial strain, negative transverse strain and a high magnitude of shear strain. This is therefore shear deformation, and is unconstrained by cluster boundaries as it spans the gauge width. This is consistent with the deformation field in figure 5.48.

For conventional tensile testing of fine-grained ductile metals, localisation of strain is usually a result of a low hardening rate – where the rate of hardening is not enough to counteract the local increase in stress due to the reduction of cross-sectional area. Localisation would occur at a length scale much larger than the grain size. In cast

Ministry of Defence © British Crown Copyright 2020/AWE

uranium, however, the localisation is within a cluster and the behaviour is similar to single-crystal deformation, where the shearing of the specimen reduces the local cross-sectional area and the strain concentration increases until failure.

The stress-strain curve for the lower-left cluster, 4, sees an unexpected increase in gradient after yield (figure 5.55). Since this cluster is in parallel with clusters 1, 2, and 3, this effect could be the result of stress redistribution between these grains. A decrease in the stress carried in cluster 4 would reduce its strain for a given applied load, increasing the gradient. Since we do not know the stress state in each location, only the total strain, we cannot validate this claim. In addition, the grain structure is complex in this part of specimen DB-T2, with many small clusters. The relative error from any misalignment of the DIC data with the EBSD orientations is larger for smaller clusters and may also be a contributing factor to the abnormal measurements.

5.6.2.3 Specimen DB-T3

In specimen DB-T3, the main clusters, 1, 3, and 4, are approximately loaded in series. The strain concentration in cluster 3 has positive axial and negative tangential strain, with a shear strain close to zero – this cluster is undergoing uniaxial tensile straining. The greatest strain is in cluster 3, near its boundary with cluster 2, at the lower edge of the specimen. Interestingly, strain develops in cluster 4 only in the region where it is not loaded in parallel with cluster 3 – the deformation of cluster 3 appears to shield this part of cluster 4 from deforming.

Ministry of Defence © British Crown Copyright 2020/AWE

Cluster 3 has a high SF for Wall slip and it is thought that this mode activated first. In this cluster the Burgers vector for Wall slip points into the specimen (–Z axis), angled towards the X-axis and slightly in the –Y direction. If the strain concentration were predominantly Wall slip, its right-hand side would be expected to move in the –Z direction, away from the cameras, and vice versa for its left-hand side. This is not apparent in the distortion field in figure 5.51(b). It is therefore likely that other deformation modes, including twinning, were responsible for the formation of the strain concentration, however these cannot be identified purely from the experimental measurements.

The CRSS values for Wall and Floor slip are similar, estimated to be 4 MPa and 7MPa respectively according to the CPFE simulation in section 4.5. There is uncertainty in these values due to the fact that both modes activate in the gauge region of the neutron diffraction specimens, and the effects of each mode are combined. Specimen DB-T3 is of particular interest as cluster 3 has a high SF for Wall slip, and a low SF for Floor slip, and vice-versa in cluster 4. This allows the initiation of each mode to be measured in the absence of the other mode – their contributions to deformation can be separated. To estimate the CRSS we cannot just look at the yield points presented in table 5.7. These were calculated from the mean strain in each cluster and the low-stress yield in a stress concentration would not be detected as a deviation from linearity until its magnitude was large. One could instead look at the maximum strain in a cluster, or segment the

Ministry of Defence © British Crown Copyright 2020/AWE

strain field to focus on the strain concentrations, however based on the aforementioned estimated CRSS values, and the SFs in figure 5.40, yield would be expected to occur between 10 MPa and 20 MPa in clusters 3 and 4. This is a very low stress and deviation from linearity would not be detectable directly from stress-strain curves.

The overall flow curve also depends on (a) the CRSS values of modes which initiate at higher stresses, (b) the self-hardening rates of each mode, and (c) the interdependencies of the slip and twinning modes on each other. These can only be understood with additional CPFE modelling.

5.6.3 Demonstrating Data Validity

Just as was seen for the neutron diffraction experiments, crystal plasticity modelling is required to extract the most information from the experimental data. In order for the calculated parameters to be trustworthy, we must be sure that the experimental data are good, and free from significant systematic error.

Close inspection of the experimental data identifies three potential issues, and in this section we will work through each issue in turn and demonstrate that the data are indeed valid.

5.6.3.1 Anomalous Measured Stiffnesses

The stiffness of each grain cluster would be expected to have a value between the maximum and minimum single-crystal values of 148 GPa to 288 GPa (figure 2.3). In many grain clusters the measured stiffness of the linear region of the stress vs. mean-

Ministry of Defence © British Crown Copyright 2020/AWE

axial-strain curves is much lower than expected (table 5.5, table 5.6, and table 5.7). This may indicate an systematic issue with either the stress or strain measurement.

We know that plastic deformation is likely to initiate at very low stresses – the CRSS values for Wall and Floor slip are <10 MPa. Also, some modes may be at their yield point at the start of the test due to thermal residual stresses present in the material (although the cutting of the specimen such that only one or two clusters are present across its width would somewhat relax these stresses). Plastic deformation at low stresses would increase the mean strain in a cluster, and if localised in a small relative area would not cause a significant deviation from linearity for that cluster's stress-strain curve, only a reduction in apparent gradient, and a consequently lower measured stiffness.

Some clusters have stiffnesses greater than expected, such as cluster 4 in DB-T3. This suggests the average stress in this cluster was lower than the applied stress, resulting in a lower mean strain than would be expected for a particular stress value. Indeed, the left part of cluster 4, where it is in parallel with cluster 3, must be carrying a lower stress as it does not strain. This reduces the mean strain in cluster 4 and gives a larger measured stiffness.

In general, if the mean stress in a cluster is higher than the applied stress, the strains would be higher and the measured modulus would be lower, and vice versa. This is known to happen in the dog-bone specimens, either due to grain clusters loaded in

Ministry of Defence © British Crown Copyright 2020/AWE

parallel or due to specimen bending during deformation, so this could satisfactorily account for the anomalous stiffnesses.

5.6.3.2 Non-Zero Strains at Zero Stress

The stress was calculated from the measured load in both the copper and uranium. In specimen DB-T1, and to a lesser extent DB-T2, non-zero strains were recorded at zero stress (figure 5.53 and figure 5.55). This could suggest that the uranium was loading at a lower load than calculated – that the load in the copper was overestimated and the stress in the uranium was underestimated.

From an extrapolation of the linear region of the flow curves in specimen DB-T1 (figure 5.53 on page 272) to the zero-strain (y) axis, the stress appears to be underestimated by 35 MPa. This would correspond to the force in the uranium being underestimated by 230 N; i.e. an equivalent overestimation of the force in the copper. This is ~40 % of the measured total load of 500 N at 4.5 mm cross-head displacement where the first load transfer to uranium was seen (figure 8.62(a) in Appendix A9.2). It was known from the geometry of the specimens and tensile rig that no load could be carried in the uranium for cross-head displacements less than 4.5 mm, so we know the copper must be carrying the full load up to this point. We also know the copper hardening can be modelled as a power-law curve so we cannot be conceivably overestimating its load by 230 N, so the measurement of applied stress appears valid.

Ministry of Defence © British Crown Copyright 2020/AWE

Testing of specimen DB-T1 was performed over 2 days, with the uranium being loaded to 300 N (~40 MPa) on day 1. On unload, it was noted that the uranium and rig were 'locked together', so the tensile stress in the uranium at unload was clearly non-zero. These stresses may have relaxed due to creep deformation overnight, which could give the copper/uranium an different strain state after subsequent loading compared to the before the unload, explaining the non-zero strains at zero stress.

In specimen DB-T2, a load drop was seen just after the uranium started to take up load (reaching ~10 MPa) (Figure 8.63(a) in Appendix A9.2). It is thought that this corresponded to a reorientation of the copper bar due to slippage near its screw mounts. Only data points after this artefact are included in the analysis, so the 'zero stress' data point contains any plastic strain accumulated during the initial loading.

Specimen DB-T3 loaded monotonically with no load drop and the measured flow curves pass through the origin.

In all specimens, the magnitude of these strains at zero stress is less than 0.03 % and since we are confident in the measured stresses, this does not significantly affect the overall flow curves, and they can still be used to calibrate CPFE models.

5.6.3.3 Alignment of DIC and EBSD Data

Any misalignment between the DIC data and the EBSD data used to define the grain clusters (described in section 5.4.4.3) would affect the mean strain in each cluster. This would be more significant for smaller clusters, such as those in specimen DB-T2, where

Ministry of Defence © British Crown Copyright 2020/AWE

the relative effect of the misalignment would be greater. The alignment perpendicular to the specimen axis is good, using the best-fit line through the DIC facets to determine the axis position in the DIC data (figure 5.27). The alignment along the axis was more subjective, performed by eye using the left edge of the parallel gauge region as a reference point; this was thought to be accurate to within ± 0.5 mm (figure 5.28).

In specimen DB-T1, the strain concentration is well aligned with the microstructure, initiating at a well-defined grain boundary. This validates the alignment between DIC and EBSD data in this specimen.

In specimen DB-T3, the right-hand side of the deforming region in cluster 3 is not aligned with the boundary between clusters 3 and 4, instead being parallel but offset by 2 mm. The left-hand side of the strain concentration is however aligned well with the cluster 2-3 boundary. This suggests the grain boundary between clusters 3 and 4 is not perpendicular to the specimen surface and instead penetrates into the region identified as cluster 3. In this overlap region, 2 mm thick, the stronger grain 4 is loaded in parallel and the grain identified as cluster 3 does not deform to the same extent as the rest of the cluster. This is a potential explanation for the observed deformation - EBSD on the rear surface of the specimen would be required to confirm the grain boundary orientation.

5.6.4 CPFE Modelling of Tensile Test

CPFE simulation is necessary to overcome the limitations of a purely experimental approach.

Ministry of Defence © British Crown Copyright 2020/AWE

CPFE modelling of the tensile testing experiments presented in this chapter were performed by Nicolò Grilli. This work, which I co-authored, has been recently submitted for publication in the Journal of the Mechanics and Physics of Solids [2] and is awaiting review at the time of writing.

There is significant evidence demonstrating that the stress in each grain is not necessarily the same as the applied stress. This makes interpretation of the data, such as calculation of the yield stress, challenging. This situation is however routine in a finite element implementation, as the stress field is calculated at each node in the simulation at each increment of applied strain.

Unlike in the neutron diffraction experiments, where the presence of twinning could be identified from the texture change, twinning deformation could not be distinguished from slip in this experiment. The CRSS values of the main modes are low compared to the overall applied stresses making them challenging to estimate from the yield stresses, which as previously discussed are unreliable if the stress state is not homogeneous. It is not just the CRSS, but also the relevant hardening rates, which produce the overall stress-strain curve. These interactions are simulated in the CPFE model.

The level of residual stress in the specimens can strongly affect the measured yield stress. Simulation of the entire specimen manufacturing process allows the residual stresses in the as-cast state to be determined.

Ministry of Defence © British Crown Copyright 2020/AWE

5.6.4.1 Method

Since the aforementioned paper has not yet been published, a brief description of the method is given here. It is similar to that presented in Appendix A7, so only the main differences will be described. All modelling work was performed by Nicolò Grilli and Ed Tarleton.

Specimen DB-T3 was initially simulated as there was a clear relationship between the microstructure and the deformation, and it had the unique property of having Wall and Floor slip occurring in different grains. A simplified microstructure was used, with clusters 1 and 2 being effectively merged together. For each cluster, the stress vs. mean axial strain curve was calculated, with the 'stress' being the applied stress to be consistent with the experiment.

A Nelder-Mead optimisation algorithm was used to minimise a residual function which characterised the goodness of fit between the experiment and model. Two optimisation steps were performed. In the first step, the yield stresses were optimised. In the second step, the stress-strain curves for each cluster were optimised. Three separate simulations were performed with different hardening models, representing (a) twin-slip interaction (twinning stress proportional to dislocation density), (b) the interaction between non-coplanar twins (e.g. (130) and (1̄30) twins), and (c) the interaction between coplanar twins (e.g. parallel (130) twins). By assessing the sensitivity of the simulation to each interaction type, the dominant interactions in the material could be assessed – e.g. if,

Ministry of Defence © British Crown Copyright 2020/AWE

despite optimisation, a particular hardening model could not produce a good fit to the experimental data, this hardening mode must not be relevant in the specimen.

Finally, an independent model validation was performed by simulating the deformation of specimen DB-T1 with the parameters calibrated on specimen DB-T3.

5.6.4.2 Results and Comments

After optimisation, a good fit was seen between the simulated and experimentally-measured strains (figure 5.58). The twin-noncoplanar models gave the worst fit, suggesting that only one twinning variant was significantly active in each cluster.

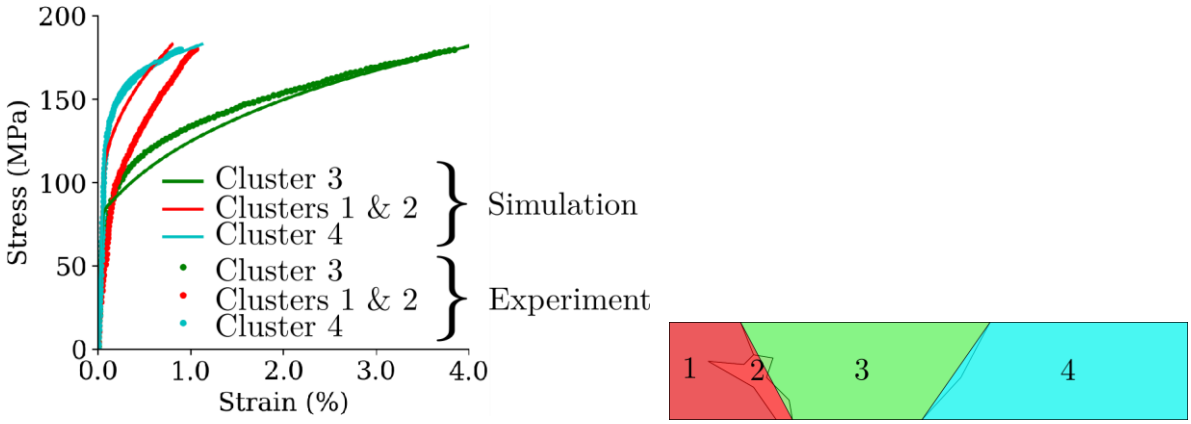


Figure 5.58. Experimental data (thin, dotted lines) compared with flow curves (thick lines) simulated using the twin-coplanar model for the three clusters in specimen DB-T3. Reproduced from Tarleton et al. [2] (awaiting review).

In the paper, the clusters were numbered differently so have been renumbered here to be consistent with the notation used in this chapter. Wall slip was seen to be responsible for the strain concentration in cluster 3, with a clear correlation between the spatial distribution of strain and wall slip dislocation density. The constant friction stress parameter for Wall slip was calculated to be 3.5× lower than for Floor slip. {130}

Ministry of Defence © British Crown Copyright 2020/AWE

twinning was most prevalent in cluster 4, as predicted by the Schmid factors, with a CRSS intermediate to Wall and Floor slip.

As well as a good match between the optimised flow curves, there is a semi-quantitative match between the spatial distribution of strains. Figure 5.59 compares the axial strain fields between the simulation and experiment. Note the experimental data have been plotted with the *y*-axis upwards.

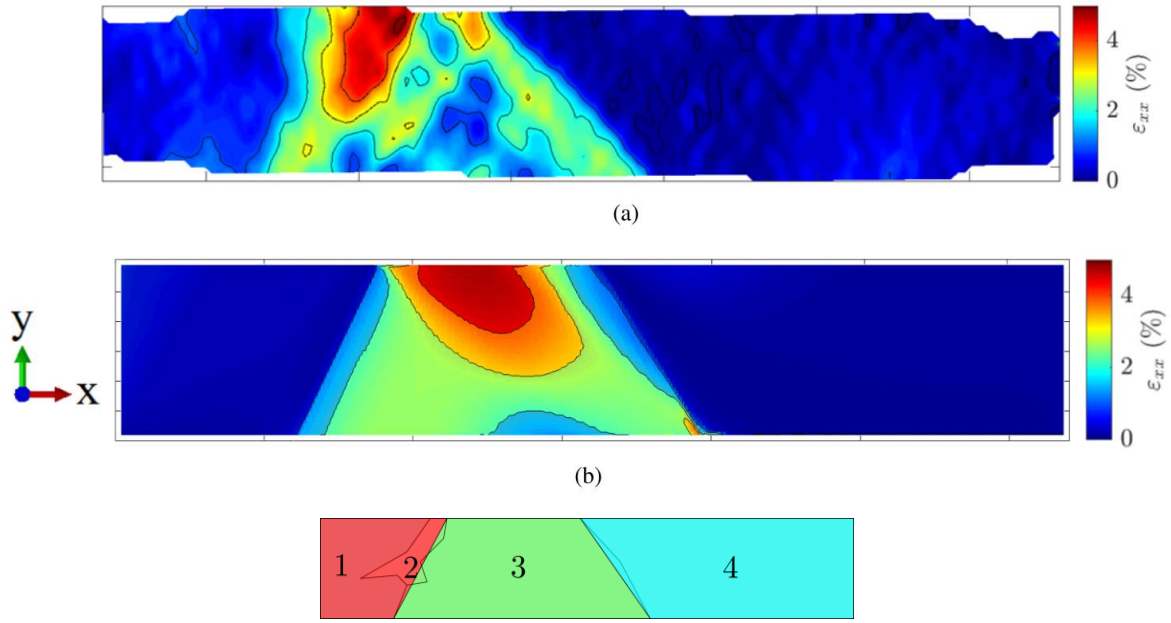


Figure 5.59. Axial strain ε_{xx} in specimen DB-T3 bar at 1% total strain: (a) DIC measurement, (b) simulation. Reproduced from Tarleton et al. [2] (awaiting review).

The strain concentration occurs in cluster 3, along the shorter edge of the trapezium-shape. The magnitude of the strains are similar, with the strains in excess of 4 % in this location, and strains of approximately 2.5 % in the rest of the cluster.

A similar quality of fit was seen between the shear strains, as well as the out-of-plane displacements (figure 5.60).

Ministry of Defence © British Crown Copyright 2020/AWE

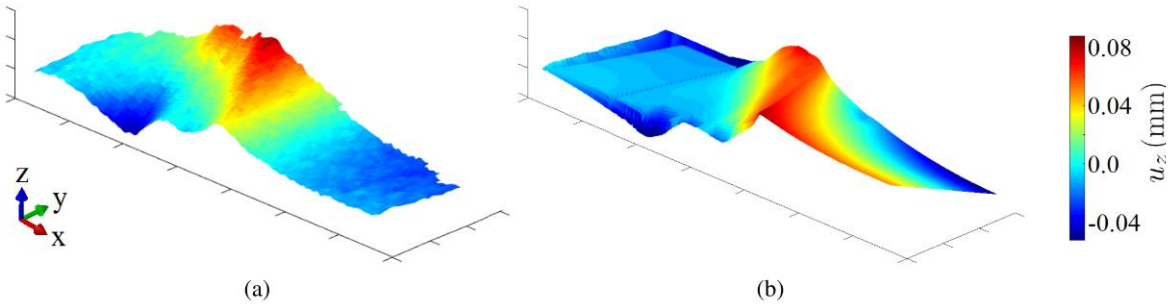


Figure 5.60. Out-of-plane distortion u_z^{relative} in specimen DB-T3 at 1% total strain: (a) DIC measurement, (b) simulation. Reproduced from Tarleton et al. [2] (awaiting review).

The independent simulation of specimen DB-T1 again sees good agreement with the experimental data (figure 5.61). This demonstrates the reliability of the CPFE modelling technique and that, once calibrated, the model can be used to predict deformation in an arbitrary microstructure.

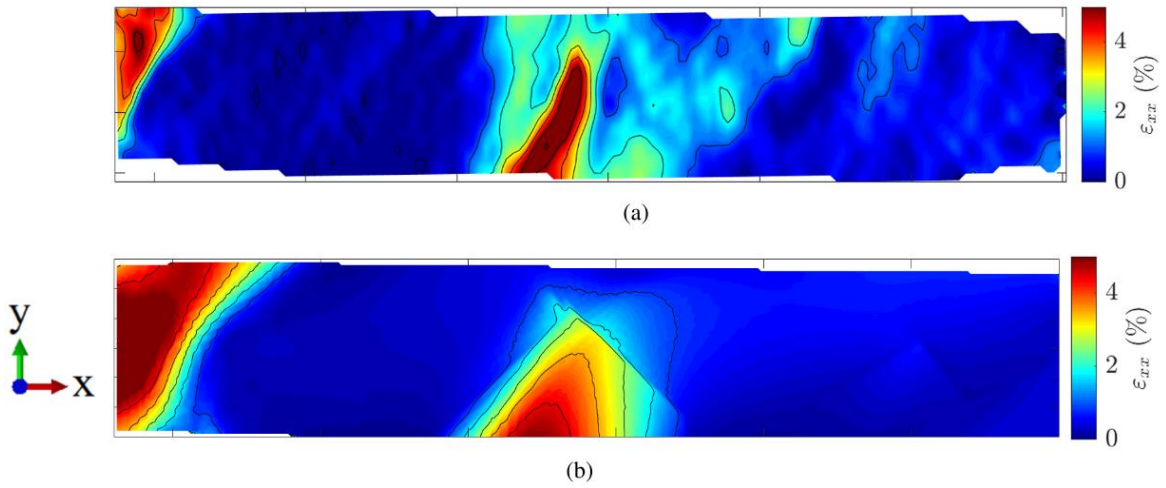


Figure 5.61. Axial strain ε_{xx} in specimen DB-T1 bar at 1% total strain: (a) DIC measurement, (b) simulation. Reproduced from Tarleton et al. [2] (awaiting review).

5.7 Chapter Summary

In this chapter we saw how the combination of stereo DIC and EBSD microstructure mapping allowed measurement of full-field surface strain and displacement in each grain cluster of cast uranium specimens. These data have then been used by our collaborators

Ministry of Defence © British Crown Copyright 2020/AWE

to improve the CPFE model of cast uranium, in particular assessing the hardening regimes and refining the CRSS parameters.

The bespoke tensile rig allowed the tests, on radioactive material, to be performed in the conventional laboratories at the University of Oxford. The significant time spent developing and testing the rig was well spent; the tests were performed safely with no contamination, all whilst the specimens were loaded according to the requirements of the test.

The stereo DIC system, whilst more time-consuming to set up and calibrate compared to single-camera DIC, allowed the measurement of the out-of-plane distortion and correctly determined the surface strain field in the presence of specimen translation and rotation. The correct optical set-up was chosen, giving the correct balance between the spatial resolution and field-of-view given the available hardware.

Performing orientation mapping on such a large area was challenging, and involved operating the SEM outside at low magnifications outside the typical working parameters for EBSD. The image calibration and distortion-correction scripts developed by the author successfully allowed images to be stitched together to create a composite map of the microstructure in each specimen. This allowed the DIC data to be segmented to evaluate the deformation in each grain cluster.

Some areas for improvement have been identified, were future experimentation to be performed. The use of fiducial reference markers to register the EBSD and DIC datasets

Ministry of Defence © British Crown Copyright 2020/AWE

could reduce the alignment uncertainty between these independently measured maps. This would allow a more accurate spatial orientation distribution size to be implemented in the simulations, with any local variations in orientation within a cluster being captured.

The analysis in this chapter assumed that the microstructure was quasi-2D, with the same orientations present through the thickness of the specimen. Whilst this assumption was on the whole valid, and allowed simulation of the data, certain cluster boundaries (e.g. the cluster 3-4 boundary in DB-T3) were thought to not be perpendicular to the specimen surface. Ideally, the microstructure would have been characterised on both sides of the specimen to verify these assumptions, or if not valid, produce a more accurate 3D microstructure for simulation.

High-magnification EBSD in selected locations before and after deformation would allow the change in twin volume fraction to be assessed. This would require either in-situ loading or the careful use of fiducial markers such as indents to re-centre the specimen between EBSD scans. These data would allow another variable of optimisation in the CPFE model.

Overall, the experiments succeeded in their aim to generate full-field strain data and orientation-dependent stress-strain curves suitable for the calibration and validation of CPFE models, produced by our collaborators. This work complemented the neutron

Ministry of Defence © British Crown Copyright 2020/AWE

diffraction work, allowing the separation of Wall and Floor slip modes, and measuring the spatial distribution of strain within a specimen.

Ministry of Defence © British Crown Copyright 2020/AWE

Chapter 6 General Discussion & Future Work

The aim of the overall project with AWE plc. is to develop CPFE models for use as part of an ICME framework, simulating materials from manufacture to their end of service life. In order to understand the mechanical behaviour of cast uranium, and to be able to predict its strength or deformation, we require an experimentally validated CPFE model.

On their own, mechanical tests on polycrystals with multiple deformation modes are of little use; multiple modes contribute towards the strain in a grain and these cannot easily be distinguished from each other unless the microstructure or loading conditions limit the available modes.

There are however some trends which have been identified from the experimental data.

6.1 Behaviour of Cast Uranium

6.1.1 Tension-Compression Asymmetry

By analysis of the lattice strains and texture changes measured with neutron diffraction, the tensile-compression asymmetry of cast uranium was related to the asymmetric Schmid factors of twins, in particular the dominant {130} and '{172}' modes.

A tensile-compression asymmetry was also seen in the macroscopic flow curves. In the neutron diffraction experiments, the tensile cast uranium specimens were softer than their fine-grained counterparts, whilst the compression specimens had similar behaviours for coarse and fine-grained material. The smaller dog-bone tensile specimens were even

Ministry of Defence © British Crown Copyright 2020/AWE

softer still – this was rationalised as an effect of reduced constraint allowing easier strain localisation without stress transfer to a parallel grain.

It was suggested that the constraint of neighbouring grain clusters also affected the correlation between lattice strain and texture change in the neutron diffraction data – the compression specimens were larger and had multiple clusters across the specimen width, increasing constraint. This suggests a specimen-size dependence of the hardness may be contributing to the observed specific tension-compression asymmetry. This could be investigated with modelling and does not necessarily require further experimentation.

6.1.2 Deformation Modes

The observed texture changes were consistent with twin formation, with reduction in texture typically observed in the strongest texture components and increases along the crystal direction predicted by applying the twinning misorientation of either {130} or '{172}' twins to the parent orientation. In some cases, evidence was seen for the rarer '{176}' mode. The Schmid factors for twinning were found to be suitable predictors of the observed texture changes.

In general, the Schmid factors appear to be good predictors of deformation for both slip and twinning, however once a mode has initiated the Schmid factor does not tell us how each mode hardens, nor how they interact with secondary modes.

From the CPFE modelling performed by Grilli et al. [88], we see that the twinning stress is much lower than in fine-grained material and is close to that of a single crystal, which

Ministry of Defence © British Crown Copyright 2020/AWE

makes sense as twins were seen in the EBSD data to pass through the grain boundaries within a cluster. The CRSS for Wall slip was found to be lower than for {130} twinning and Floor slip.

6.2 Experimental Summary

6.2.1 Experimental Challenges

Working with such a coarse-grained material presented some experimental challenges, particularly with the neutron diffraction. The texture change artefacts caused by specimen movement only occur when the cluster size (effective grain size) is similar to the gauge volume. Care was needed when interpreting the results, and it was easy to reach false conclusions. Initially it was thought that the texture changes on ENGIN-X that disappeared upon unloading were due to de-twinning, which would have been a new observation in uranium. We now know they are likely a result of the specimen movement texture change artefact.

In addition, the Rietveld refinement was unable to detect some subtleties in the deformation, for example strains affecting a small number of orientations only. In a material with a smoother texture, the Rietveld strains would more closely approximate the single-peak strains.

We used the coarse-grained microstructure to our advantage, using conventional macroscopic DIC to measure the orientation-dependent deformation in each cluster. This would not be possible in a fine-grained material.

Ministry of Defence © British Crown Copyright 2020/AWE

Uranium is radioactive, which limited the location and form of experiments that could be performed in a university laboratory. Fortunately, the universities of Oxford and Bristol were supportive in preparing and approving the risk assessments for the experiments, and for providing the necessary training. The delivery of specimens between sites was challenging, and in hindsight required more proactive management than I expected.

6.2.2 Use of Complementary Techniques

This project made good use of complementary techniques – the neutron diffraction and tensile testing with DIC each measured something the other could not. Neutron diffraction could measure the crystal reorientations due to twinning in the bulk of large specimens, without requiring high spatial resolution measurements, however it could not easily distinguish the contributions from each twinning mode, except in some special cases.

The measured elastic lattice strain is directly proportional to the average stress in a family of grains, which allowed the stress distribution between different families of grains to be optimised in the CPFE model.

The DIC measurements, on the other hand, measured the full-field strains in grains of a known orientation, allowing the strain distribution in the model to be optimised.

By optimising both the stress and strain distributions, the uncertainty in the optimised parameters can be reduced, improving the reliability of the model's predictions.

Ministry of Defence © British Crown Copyright 2020/AWE

6.2.3 Applicability of Results

The experiments in this thesis focused on a single type of microstructure – coarse-grained clustered cast uranium. Whilst the experimental data are only relevant to this material, the methods developed would be applicable to other uranium microstructures, or any coarse-grained material.

Many aspects of the modelling work by Grilli et al. [133][88] and Tarleton et al. [2] are applicable to any polycrystalline material. Recent work (in progress at the time of writing) shows that once calibrated with a single microstructure, the form of the grain-size dependence of the mechanical properties can be simulated without experiment.

Modelling could allow simulation of materials on which experiments cannot be performed - for example, the deformation of natural or enriched uranium could be simulated after calibration of the model on a depleted uranium specimen with a similar microstructure.

6.2.4 Key Developments

A number of techniques were developed or improved during this project to enable the measurement of deformation in coarse-grained materials.

We demonstrated the combined use of Rietveld and single-peak fitting to time-of-flight neutron spectra of coarse-grained materials. The Rietveld refinement measured texture whilst the single-peak fits were necessary to measure lattice strains, which differed significantly from the Rietveld lattice parameter strains.

Ministry of Defence © British Crown Copyright 2020/AWE

A method was developed to eliminate the texture change artefact caused by specimen movement in materials where the textured regions are a similar size to the neutron gauge volume.

A crystallographic method was developed to relate the texture changes measured in axial inverse pole figures to the activation of twinning modes. This allowed the Schmid factor to be verified as a key predictor for twin activation.

The tensile testing experiments represent the first published combined use of EBSD, DIC and mechanical testing on an active or coarse-grained material. A method was developed to acquire large-area EBSD maps from conventional laboratory SEMs not optimised for this purpose.

The tensile rig designed by the author enabled radioactive specimens to be mechanically tested in a university laboratory. The implementation of a ductile material deforming in parallel with the specimen reduced the risk of material loss in the event of a specimen fracture, and satisfied the necessary risk assessments.

6.3 Future Work

6.3.1 CPFE Simulation

The CPFE simulation performed by our collaborators has shown considerable promise for simulating deformation and fracture in cast uranium. It has demonstrated that despite the variance in macroscopic mechanical properties, it is possible to predict this

Ministry of Defence © British Crown Copyright 2020/AWE

deformation with a set of underlying parameters that correctly capture the microstructural dependencies of the deformation modes.

A future workflow would perform experiments on representative microstructures, and use the data to calibrate a CPFE model in which the material history (cooling, machining, deforming) is simulated. This model could then be used to answer the required engineering questions.

The initiation of fracture in cast uranium has not yet been measured experimentally. Since fracture is associated with twinning, and the formation of twins is related to prior deformation, it was decided to focus on understanding the deformation before investigating fracture.

Ongoing work by Nicolò Grilli is incorporating discrete twins into the CPFE model to investigate the strain concentrations around them. This requires an understanding of how the volume fraction of twins develops with applied strain – do the twins thicken, or do new twins form, and how does this depend on the twin type and local strain state? An experimental measurement of the strain field around twins in uranium was originally proposed as part of this project, using HR-EBSD [148] to measure the elastic strain fields around twins blocked by grain or twin boundaries. It was found to be prohibitively challenging to polish the material to the required standard for HR-EBSD, where the EBSD patterns must be of a higher quality than for conventional orientation-measuring EBSD.

Ministry of Defence © British Crown Copyright 2020/AWE

In any simulation, the microstructure is a required input, as the local grain orientations dictate the localisation of strain. One cannot predict the location of strain localisation and fracture in a generic cast uranium part without knowing the microstructure. It follows that there is a need to predict the solidification microstructures in cast uranium, and to understand why the grain clusters are so large. This would be an interesting area of future research.

The texture changes measured with neutron diffraction could provide another validation for the CPFE models. It would be simple to simulate the texture changes during deformation using a neutron detection criterion similar to that in Grilli et al.[88]. This would optimise in particular parameters affecting twin volume fractions.

6.3.2 Twin Growth

As previously mentioned, accurate simulation of the growth of twins is a prerequisite for the simulation of fracture. A number of methods have been proposed during the project to observe the growth of twins in-situ.

Cooling from near the α-β phase transition to room temperature would generate thermal stresses known to be above the yield stress. This could be performed on a neutron beamline, where twins could be detected by their associated texture change, with a similar CPFE model optimisation used to find the deformation parameters.

To distinguish between twin thickening and multiplication, mechanical or thermal straining could be performed inside a microscope. In-situ profilometry during cooling

Ministry of Defence © British Crown Copyright 2020/AWE

using high-speed atomic force microscopy (AFM) could detect the out-of-plane surface displacements [57] caused by twinning.

Alternatively, in-situ straining could be performed inside an SEM, with twins monitored with EBSD. A recent experiment was performed as a collaboration with Phil Edmondson at Oak Ridge National Laboratory, TN, USA. This used a high-speed EBSD system with an in-situ straining stage to deform small polished uranium specimens. Multiple discrete twins were seen to form, and the critical resolved shear stress for initiation can be calculated from the applied load and crystal orientation. Work is ongoing to simulate such experiments using a CPFE model.

6.3.3 Fracture

Understanding fracture requires knowledge of where a crack will initiate, and where it will eventually propagate. A cohesive-zone approach will be used to incorporate the material parting and stress redistribution during fracture into the CPFE models, but this will need experimental validation.

In-situ SEM experiments, with SEM-DIC to measure full-field strains [149][103][150], could be used to identify the location of fracture from the localisation of strain relative to microstructural features such as grain boundaries and twins. Post-test fractography with EBSD could identify the path of crack propagation once the initiation site is known.

An exciting development in neutron science is neutron imaging and tomography. On the IMAT beamline at ISIS it could be possible to use the carbides in our cast material as

Ministry of Defence © British Crown Copyright 2020/AWE

an internal 'speckle pattern' for Digital Volume Correlation (DVC), the 3D equivalent of DIC. This could identify crack growth and its interaction with microstructure at millimetre length scales. Energy-dispersive 'Bragg-edge' neutron imaging has the potential to detect twin formation in bulk single crystals [151] – this could potentially be used to measure the initiation of twins in coarse-grained uranium.

The work in this thesis has opened up avenues for future research at the micro and macro scales. It is hoped that the collaborations developed in this project can be developed to aid future research.

Ministry of Defence © British Crown Copyright 2020/AWE

Chapter 7 Conclusion

The mechanical behaviour of uranium is complex due to elastic and plastic anisotropy inherited from its unique crystal structure. The coarse microstructure of the cast uranium investigated in this project complicates conventional analysis, and leads to significant scatter in the mechanical properties measured with macroscopic measurements.

In order to achieve a better understanding of this material, we demonstrated the need for a combined experimental and modelling approach - this thesis presented the experimental part of the project.

Neutron diffraction measured the lattice strain and texture change during tensile and compressive deformation. Challenges of neutron diffraction in coarse microstructures were highlighted by preliminary experiments summarised in Chapter 3. An improved neutron diffraction experiment was presented in Chapter 4. A method was developed to prove the measured texture changes were larger than the measurement uncertainty. By considering the crystallographic reorientation during twinning, the texture changes were related to the twin formation. These data have demonstrable relevance for crystal plasticity finite element (CPFE) modelling.

In Chapter 5, digital image correlation measured the strain field during tensile testing in specimens with a prior microstructural characterisation with EBSD. The strain distribution was related to the underlying microstructure. A bespoke tensile rig was

Ministry of Defence © British Crown Copyright 2020/AWE

designed to allow mechanical testing of radioactive materials in a university laboratory. The strain in each grain cluster was used to calibrate the associated CPFE model, which was validated with data from a second specimen.

For AWE plc. this work represents a significant step forward towards the development of a CPFE model to understand the mechanical properties of cast uranium. From an academic viewpoint, this work demonstrates how model calibration data can be collected in coarse-grained or locally anisotropic materials. A clear research path ahead has been identified, and this thesis will provide the foundation for future work in this area.

Ministry of Defence © British Crown Copyright 2020/AWE

Literature Cited

[1] P. Earp, S. Kabra, J. Askew, and T. J. Marrow, "Lattice strain and texture development in coarse-grained uranium – a neutron diffraction study," *Journal of Physics: Conference Series*, vol. 1106, p. 012012, Oct. 2018. DOI: 10.1088/1742-6596/1106/1/012012.

[2] N. Grilli, P. Earp, A. C. F. Cocks, J. Marrow, and E. Tarleton, "Characterisation of slip and twin activity using digital image correlation and crystal plasticity finite element simulation: Application to orthorhombic α uranium," *Journal of the Mechanics and Physics of Solids*, vol. 135, p. 103800, Feb. 2020. DOI: 10.1016/j.jmps.2019.103800.

[3] T. Wigger *et al.*, "In situ mapping of normal strains in the field of a growing fatigue crack in a steel weld using digital image correlation and energy dispersive synchrotron X-ray diffraction," *International Journal of Fatigue*, vol. 115, no. May, pp. 11–19, 2018. DOI: 10.1016/j.ijfatigue.2018.05.016.

[4] A. Koko, P. D. Earp, T. Wigger, J. Tong, and T. J. Marrow, "J-Integral Analysis: An EDXD and DIC Comparative Study for a fatigue crack," *International Journal of Fatigue*, vol. Submitted.

[5] M. F. Horstemeyer, *Integrated Computational Materials Engineering (ICME) for Metals*. Hoboken, NJ, USA: John Wiley & Sons, Inc., 2012. DOI: 10.1002/9781118342664 ISBN: 9781118342664.

Ministry of Defence © British Crown Copyright 2020/AWE

[6] N. Chopra, "Integrated Computational Materials Engineering: A Multi-Scale Approach," *Jom*, vol. 67, no. 1, pp. 118–119, 2015. DOI: 10.1007/s11837-014-1260-0.

[7] A. N. Holden, "Physical metallurgy of uranium," in *(Atoms for Peace Conference, Geneva, 1958: United States of America presentation volumes)*, 1958.

[8] "NRC: 10 CFR 40.4 Definitions.," *United States Nuclear Reglatory Commission*. [Online]. Available: http://www.nrc.gov/reading-rm/doc-collections/cfr/part040/part040-0004.html. [Accessed: 30-Aug-2019].

[9] "Depleted uranium (DU): general information and toxicology," *Public Health England*, 2007. [Online]. Available: https://www.gov.uk/guidance/depleted-uranium-du-general-information-and-toxicology. [Accessed: 30-Aug-2019].

[10] IET, "The radioactive decay rate of uranium 238," 2008. [Online]. Available: https://www.theiet.org/impact-society/factfiles/energy-factfiles/nuclear-power/decay-rate/. [Accessed: 30-Aug-2019].

[11] W. W. Schulz, "Uranium processing," *Encyclopædia Britannica*, 2016. [Online]. Available: https://www.britannica.com/technology/uranium-processing#ref623654. [Accessed: 30-Aug-2019].

[12] C. W. Jacob and B. E. Warren, "The Crystalline Structure of Uranium," *Journal of the American Chemical Society*, vol. 59, no. 12, pp. 2588–2591, Dec. 1937. DOI: 10.1021/ja01291a035.

Ministry of Defence © British Crown Copyright 2020/AWE

[13] J. S. Lukesh, “Note on the structure of uranium,” *Acta Crystallographica*, vol. 2, no. 6, pp. 420–420, Dec. 1949. DOI: 10.1107/S0365110X49001107.

[14] E. F. Sturcken, “The atomic position parameter in alpha uranium,” *Acta Crystallographica*, vol. 13, no. 10, pp. 852–852, 1960. DOI: 10.1107/S0365110X60002077.

[15] R. . Cahn, “Plastic deformation of alpha-uranium; twinning and slip,” *Acta Metallurgica*, vol. 1, no. 1, pp. 49–70, Jan. 1953. DOI: 10.1016/0001-6160(53)90009-1.

[16] T. A. Wilson, “[Title Unknown - Orignal could not be found],” *Physics*, vol. 4, p. 148, 1933.

[17] F. . Frank, “A note on twinning in alpha-uranium,” *Acta Metallurgica*, vol. 1, no. 1, pp. 71–74, Jan. 1953. DOI: 10.1016/0001-6160(53)90010-8.

[18] J. . Daniel, B. Lesage, and P. Lacombe, “The influence of temperature on slip and twinning in uranium,” *Acta Metallurgica*, vol. 19, no. 2, pp. 163–173, Feb. 1971. DOI: 10.1016/0001-6160(71)90128-3.

[19] E. S. Fisher and H. J. McSkimin, “Adiabatic Elastic Moduli of Single Crystal Alpha-Uranium,” *Journal of Applied Physics*, vol. 29, no. 10, pp. 1473–1484, Oct. 1958. DOI: 10.1063/1.1722972.

[20] E. S. Fisher, “Temperature dependence of the elastic moduli in alpha uranium single crystals, part iv (298° to 923° K),” *Journal of Nuclear Materials*, vol. 18, no. 1, pp. 39–54, Jan. 1966. DOI: 10.1016/0022-3115(66)90094-8.

Ministry of Defence © British Crown Copyright 2020/AWE

[21] S. J. Rothman, "The Mechanical Properties of Uranium - A Monograph," Argonne National Laboratory Report - Original Not Found.

[22] H. H. Chiswik, A. E. Dwight, L. T. Lloyd, M. V. Nevitt, and S. T. Zegler, "Advances in the Physical Metallurgy of Uranium and its Alloys," U.S. Atomic Energy Commission, Oct. 1958. DOI: 10.2172/4322509.

[23] J. Sariel, J. Pelleg, and G. Kimmel, "Evaluation of anisotropy in cast and heat treated 'adjusted-uranium,'" *Journal of Nuclear Materials*, vol. 140, no. 3, pp. 288–292, Oct. 1986. DOI: 10.1016/0022-3115(86)90214-X.

[24] D. W. Wheeler and S. T. Morris, "Micro-mechanical characterisation of uranium," *Journal of Nuclear Materials*, vol. 385, no. 1, pp. 122–125, Mar. 2009. DOI: 10.1016/j.jnucmat.2008.09.035.

[25] B. R. T. Frost, *Nuclear Materials - Materials Science and Technology Volume 10A*. 1994 ISBN: 9783527268238.

[26] L. R. Kelman, "Dimensional changes in Uranium Under Thermal Cycling," *Journal of Metallurgy and Ceramics*, vol. 4, 1949. URL: https://www.osti.gov/servlets/purl/1133923.

[27] E. Garlea, R. L. Bridges, V. O. Garlea, D. A. Carpenter, M. A. Hemphill, and J. S. Morrell, "Characterization of a grain size refinement process in cast uranium," *Materials Science and Engineering: A*, vol. 559, pp. 210–216, Jan. 2013. DOI: 10.1016/j.msea.2012.08.082.

[28] G. R. Caskey Jr, "Mechanical Properties of Uranium Plate," Savannah, GA,

Ministry of Defence © British Crown Copyright 2020/AWE

USA, 1959. URL: https://www.osti.gov/servlets/purl/4217393.

[29] D. M. R. Taplin and J. W. Martin, "The effect of grain size and cold work on the tensile properties of alpha-uranium," *Journal of the Less Common Metals*, vol. 7, no. 2, pp. 89–97, Aug. 1964. DOI: 10.1016/0022-5088(64)90048-7.

[30] R. J. McCabe, L. Capolungo, P. E. Marshall, C. M. Cady, and C. N. Tomé, "Deformation of wrought uranium: Experiments and modeling," *Acta Materialia*, vol. 58, no. 16, pp. 5447–5459, Sep. 2010. DOI: 10.1016/j.actamat.2010.06.021.

[31] J. E. Sutcliffe, J. R. Petherbridge, T. Cartwright, R. Springell, and T. B. Scott, "Preparation and analysis of strain-free uranium surfaces for electron and x-ray diffraction analysis," *ArXiv: 1803.05712*, pp. 1–19, 2017.

[32] B. W. Chung, R. G. Erler, and N. E. Teslich, "Three-dimensional microstructural characterization of bulk plutonium and uranium metals using focused ion beam technique," *Journal of Nuclear Materials*, vol. 473, pp. 264–271, May 2016. DOI: 10.1016/j.jnucmat.2016.01.041.

[33] M. W. Mallett, A. F. Gerds, and D. A. Vaughan, "Uranium Sesquicarbide," *Journal of The Electrochemical Society*, vol. 98, no. 12, p. 505, 1951. DOI: 10.1149/1.2778032.

[34] A. M. Kelly, D. J. Thoma, R. D. Field, P. S. Dunn, and D. F. Teter, "Metallographic preparation techniques for uranium," *Journal of Nuclear Materials*, vol. 353, no. 3, pp. 158–166, 2006. DOI: 10.1016/j.jnucmat.2005.12.008.

Ministry of Defence © British Crown Copyright 2020/AWE

[35] R. E. Rundle, N. C. Baenziger, A. S. Wilson, and R. A. McDonald, "The Structures of the Carbides, Nitrides and Oxides of Uranium 1," *Journal of the American Chemical Society*, vol. 70, no. 1, pp. 99–105, Jan. 1948. DOI: 10.1021/ja01181a029.

[36] A. I. Snow, Thesis: , "The uranium-carbon system: the structure of dimethylberyllium and its bearing on chemical valence," Iowa State University, Digital Repository, Ames, 1950. DOI: 10.31274/rtd-180813-16314.

[37] C. S. Choi and M. Staker, "Neutron diffraction texture study of deformed uranium plates," *Journal of Materials Science*, vol. 31, no. 13, pp. 3397–3402, Jul. 1996. DOI: 10.1007/BF00360740.

[38] M. Zecevic, M. Knezevic, I. J. Beyerlein, and R. J. McCabe, "Origin of texture development in orthorhombic uranium," *Materials Science and Engineering: A*, vol. 665, pp. 108–124, May 2016. DOI: 10.1016/j.msea.2016.04.018.

[39] M. Zecevic, M. Knezevic, I. J. Beyerlein, and R. J. McCabe, "Texture formation in orthorhombic alpha-uranium under simple compression and rolling to high strains," *Journal of Nuclear Materials*, vol. 473, pp. 143–156, May 2016. DOI: 10.1016/j.jnucmat.2016.02.021.

[40] J. Sariel, G. Kiminel, and J. Pelleg, "Texture in Low Alloyed Uranium Alloys," in *Second Israel materials engineering conference*, 1984, pp. 104–107. URL: https://inis.iaea.org/collection/NCLCollectionStore/_Public/17/008/17008828.pdf?r=1&r=1.

Ministry of Defence © British Crown Copyright 2020/AWE

[41] E. Schmid and W. Boas, *Plasticity of Crystals, with special Reference to Metals*. London: Springer US, 1950 ISBN: 978-1-5041-1927-6.

[42] R. W. Cahn, "Twinning and slip in αuranium," *Acta Crystallographica*, vol. 4, no. 5, pp. 470–470, Sep. 1951. DOI: 10.1107/S0365110X51001483.

[43] L. T. Lloyd and H. H. Chiswik, "Deformation Mechanisms of Alpha-Uranium Single Crystals," *JOM*, vol. 7, no. 11, pp. 1206–1214, Nov. 1955. DOI: 10.1007/BF03379029.

[44] M. H. Yoo, "Slip modes of alpha uranium," *Journal of Nuclear Materials*, vol. 26, no. 3, pp. 307–318, Jun. 1968. DOI: 10.1016/0022-3115(68)90104-9.

[45] C. A. Calhoun, E. Garlea, R. P. Mulay, T. A. Sisneros, and S. R. Agnew, "Investigation of the effect of thermal residual stresses on deformation of α uranium through neutron diffraction measurements and crystal plasticity modeling," *Acta Materialia*, vol. 85, pp. 168–179, Feb. 2015. DOI: 10.1016/j.actamat.2014.11.007.

[46] J. P. Hirth, J. Lothe, and T. Mura, "Theory of Dislocations (2nd ed.)," *Journal of Applied Mechanics*, vol. 50, no. 2, pp. 476–477, Jun. 1983. DOI: 10.1115/1.3167075.

[47] B. A. Bilby and A. G. Crocker, "The theory of the crystallography of deformation twinning," *Proceedings of the Royal Society of London. Series A. Mathematical and Physical Sciences*, vol. 288, no. 1413, pp. 240–255, Oct. 1965. DOI: 10.1098/rspa.1965.0216.

Ministry of Defence © British Crown Copyright 2020/AWE

[48] A. G. Crocker, "The crystallography of deformation twinning in alpha-uranium," *Journal of Nuclear Materials*, vol. 16, no. 3, pp. 306–326, Jul. 1965. DOI: 10.1016/0022-3115(65)90119-4.

[49] C. A. Calhoun, E. Garlea, T. A. Sisneros, and S. R. Agnew, "In-situ neutron diffraction characterization of temperature dependence deformation in α uranium," *Journal of Nuclear Materials*, vol. 502, pp. 60–67, Apr. 2018. DOI: 10.1016/j.jnucmat.2018.01.036.

[50] S. Mahajan and D. F. Williams, "Deformation Twinning in Metals and Alloys," *International Metallurgical Reviews*, vol. 18, no. 2, pp. 43–61, Jun. 1973. DOI: 10.1179/imtlr.1973.18.2.43.

[51] G. A. Frank, R. Z. Shneck, A. Landau, and A. Venkert, "Subgrains analysis in α uranium using combined TEM and single crystal plasticity theory," *Interface Science*, vol. 10, no. 1, pp. 67–73, 2002. DOI: 10.1023/A:1015189214046.

[52] Y. N. Zuev, I. G. Kabanova, V. V. Sagaradze, N. L. Pecherkina, I. V. Podgornova, and M. L. Mukhin, "Types of Twins and the Dislocation Structure of a Uranium in the Initial and Explosion-Deformed States," *The Physics of Metals and Metallography*, vol. 106, no. 1, pp. 97–109, Jul. 2008. DOI: 10.1134/S0031918X08070132.

[53] M. Bevis, "On the crystallography of deformation twinning in alpha-uranium," *Journal of Nuclear Materials*, vol. 26, no. 2, pp. 235–237, May 1968. DOI: 10.1016/0022-3115(68)90078-0.

Ministry of Defence © British Crown Copyright 2020/AWE

[54] P. E. Marshall, G. Proust, J. T. Rogers, and R. J. McCabe, "Automatic twin statistics from electron backscattered diffraction data," *Journal of Microscopy*, vol. 238, no. 3, pp. 218–229, Oct. 2009. DOI: 10.1111/j.1365-2818.2009.03343.x.

[55] P. Zhou *et al.*, "Twinning behavior of polycrystalline alpha-uranium under quasi static compression," *Journal of Nuclear Materials*, vol. 478, pp. 83–90, Sep. 2016. DOI: 10.1016/j.jnucmat.2016.05.041.

[56] R. McCabe, R. Field, D. Brown, D. Alexander, and C. Cady, "Electron Backscatter Diffraction (EBSD) Characterization of Twinning Related Deformation and Fracture in αUranium," *Microscopy and Microanalysis*, vol. 14, no. S2, pp. 638–639, Aug. 2008. DOI: 10.1017/S1431927608083554.

[57] J. W. Christian and S. Mahajan, "Deformation twinning," *Progress in Materials Science*, vol. 39, no. 1–2, pp. 1–157, 1995. DOI: 10.1016/0079-6425(94)00007-7.

[58] C. D. Barrett, H. El Kadiri, and M. A. Tschopp, "Breakdown of the Schmid law in homogeneous and heterogeneous nucleation events of slip and twinning in magnesium," *Journal of the Mechanics and Physics of Solids*, vol. 60, no. 12, pp. 2084–2099, Dec. 2012. DOI: 10.1016/j.jmps.2012.06.015.

[59] W. . Biggs and P. . Pratt, "The deformation and fracture of alpha-iron at low temperatures," *Acta Metallurgica*, vol. 6, no. 11, pp. 694–703, Nov. 1958. DOI: 10.1016/0001-6160(58)90060-9.

[60] D. M. R. Taplin, Thesis: , "The Mechanical Properties and Fracture of Uranium," University of Oxford, 1964. URL:

Ministry of Defence © British Crown Copyright 2020/AWE

https://ora.ox.ac.uk/objects/uuid:5da5ff68-a787-4f6f-b246-98b55bbd2e25.

[61] A. F. Rocens, "Polysynthetic Twinning in Dolomite," *Journal of the Mineralogical Society of America*, vol. 14, no. 7, pp. 245–250, 1929. URL: https://pubs.geoscienceworld.org/msa/ammin/article-abstract/14/7/245/535518/Polysynthetic-twinning-in-dolomite1?redirectedFrom=fulltext.

[62] R. D. Field, R. J. McCabe, D. J. Alexander, and D. F. Teter, "Deformation twinning and twinning related fracture in coarse-grained αuranium," *Journal of Nuclear Materials*, vol. 392, no. 1, pp. 105–113, Jul. 2009. DOI: 10.1016/j.jnucmat.2009.03.054.

[63] D. M. R. Taplin and J. W. Martin, "The effect of small additions of iron and aluminium on the tensile properties of alpha uranium," *Journal of Nuclear Materials*, vol. 12, no. 1, pp. 50–55, May 1964. DOI: 10.1016/0022-3115(64)90106-0.

[64] A. L. W. Collins and D. M. R. Taplin, "An experimental fracture map for uranium," *Journal of Materials Science*, vol. 13, no. 10, pp. 2249–2256, Oct. 1978. DOI: 10.1007/BF00541681.

[65] R. J. McCabe, A. M. Kelly, A. J. Clarke, and R. Wenk, "Electron Backscatter Diffraction (EBSD) Characterization of Uranium and Uranium Alloys," *Microscopy and Microanalysis*, vol. 18, no. S2, pp. 432–433, Jul. 2012. DOI: 10.1017/S1431927612004011.

Ministry of Defence © British Crown Copyright 2020/AWE

[66] C. F. S. John and E. Teghtsoonian, “Grain size dependence of fracture in α uranium,” *Journal of Nuclear Materials*, vol. 17, no. 2, pp. 111–115, Oct. 1965. DOI: 10.1016/0022-3115(65)90027-9.

[67] D. M. Davies and J. W. Martin, “The effect of inclusions on the fracture of uranium,” *Journal of Nuclear Materials*, vol. 3, no. 2, pp. 156–161, Feb. 1961. DOI: 10.1016/0022-3115(61)90003-4.

[68] C. J. Beevers and G. T. Newman, “Hydrogen embrittlement in uranium,” *Journal of Nuclear Materials*, vol. 23, no. 1, pp. 10–18, Jul. 1967. DOI: 10.1016/0022-3115(67)90125-0.

[69] H. Inouye and A. C. Schaffhauser, “Low-Temperature Ductility and Hydrogen Embrittlement of Uranium - A Literature Review.,” Oak Ridge, TN (United States), Jan. 1969. DOI: 10.2172/4755192.

[70] D. M. R. Taplin and J. W. Martin, “An Effect of Thermal Cycling upon the Ductility Transition in Alpha-Uranium,” *Journal of the Institute of Metals*, vol. 93, pp. 230–232, 1965.

[71] D. M. R. Taplin and J. W. Martin, “The effect of annealing temperature on the ductility and fracture of uranium,” *Journal of the Less Common Metals*, vol. 6, no. 6, pp. 430–433, Jun. 1964. DOI: 10.1016/0022-5088(64)90087-6.

[72] J. Huddart, J. Harding, and P. A. Bleasdale, “The effect of strain rate on the tensile flow and fracture of αuranium,” *Journal of Nuclear Materials*, vol. 89, no. 2–3, pp. 316–330, Apr. 1980. DOI: 10.1016/0022-3115(80)90063-X.

Ministry of Defence © British Crown Copyright 2020/AWE

[73] J. H. Underwood and M. A. Scavullo, "Fracture behaviour of a uranium and a tungsten alloy in a notched component with inertia loading," US Army Armament Research and Development Center, 1983. URL: https://archive.org/details/DTIC_ADA139649.

[74] D. M. R. Taplin and J. W. Martin, "The effect of grain shape on the tensile properties of αuranium," *Journal of Nuclear Materials*, vol. 10, no. 2, pp. 134–139, Oct. 1963. DOI: 10.1016/0022-3115(63)90078-3.

[75] D. M. R. Taplin, "On the question of the grain size dependence of the flow and fracture stress in alpha uranium," *Journal of Nuclear Materials*, vol. 19, no. 2, pp. 208–209, May 1966. DOI: 10.1016/0022-3115(66)90117-6.

[76] G. T. Newman and C. J. Beevers, "On the grain size-fracture stress relationship of uranium," *Journal of Nuclear Materials*, vol. 23, no. 1, pp. 95–97, Jul. 1967. DOI: 10.1016/0022-3115(67)90136-5.

[77] D. M. R. Taplin and G. J. Cocks, "A note on creep-rupture mechanisms in reactor grade uranium," *Journal of Nuclear Materials*, vol. 23, no. 2, pp. 245–248, Aug. 1967. DOI: 10.1016/0022-3115(67)90073-6.

[78] H. Abdolvand and A. J. Wilkinson, "Assessment of residual stress fields at deformation twin tips and the surrounding environments," *Acta Materialia*, vol. 105, pp. 219–231, Feb. 2016. DOI: 10.1016/j.actamat.2015.11.036.

[79] M. Sauzay and M. O. Moussa, "Prediction of grain boundary stress fields and microcrack initiation induced by slip band impingement," *International Journal*

Ministry of Defence © British Crown Copyright 2020/AWE

of Fracture, vol. 184, no. 1–2, pp. 215–240, Nov. 2013. DOI: 10.1007/s10704-013-9878-4.

[80] M. Koyama, E. Akiyama, K. Tsuzaki, and D. Raabe, "Hydrogen-assisted failure in a twinning-induced plasticity steel studied under in situ hydrogen charging by electron channeling contrast imaging," *Acta Materialia*, vol. 61, no. 12, pp. 4607–4618, Jul. 2013. DOI: 10.1016/j.actamat.2013.04.030.

[81] A. . Sleeswyk, "Emissary dislocations: Theory and experiments on the propagation of deformation twins in αiron," *Acta Metallurgica*, vol. 10, no. 8, pp. 705–725, Aug. 1962. DOI: 10.1016/0001-6160(62)90040-8.

[82] A. N. Stroh, "A theory of the fracture of metals," *Advances in Physics*, vol. 6, no. 24, pp. 418–465, Oct. 1957. DOI: 10.1080/00018735700101406.

[83] T. R. Bieler *et al.*, "Fracture initiation/propagation parameters for duplex TiAl grain boundaries based on twinning, slip, crystal orientation, and boundary misorientation," *Intermetallics*, vol. 13, no. 9, pp. 979–984, Sep. 2005. DOI: 10.1016/j.intermet.2004.12.013.

[84] M. J. Marcinkowski and H. A. Lipsitt, "The plastic deformation of chromium at low temperatures," *Acta Metallurgica*, vol. 10, no. 2, pp. 95–111, Feb. 1962. DOI: 10.1016/0001-6160(62)90055-X.

[85] A. Gilbert, G. T. Hahn, C. N. Reid, and B. A. Wilcox, "Twin-induced grain boundary cracking in b.c.c. metals," *Acta Metallurgica*, vol. 12, no. 6, pp. 754–755, Jun. 1964. DOI: 10.1016/0001-6160(64)90230-5.

Ministry of Defence © British Crown Copyright 2020/AWE

[86] C. N. Reid, A. Gilbert, and G. T. Hahn, "[Title Unknown - Original not found]," *Transactions of the Metallurgical Society of the AIME*, vol. 236, p. 1024, 1966.

[87] D. . Williams and G. . Reid, "A dynamic study of twin-induced brittle fracture," *Acta Metallurgica*, vol. 19, no. 9, pp. 931–937, Sep. 1971. DOI: 10.1016/0001-6160(71)90086-1.

[88] N. Grilli, A. C. F. Cocks, and E. Tarleton, "Crystal Plasticity Finite Element Simulations of Cast αUranium," in *XV International Conference on Computational Plasticity. Fundamentals and Applications COMPLAS 2019*, 2019, pp. 1–12.

[89] S. R. Kalidindi, "Incorporation of deformation twinning in crystal plasticity models," *Journal of the Mechanics and Physics of Solids*, vol. 46, no. 2, pp. 267–290, Feb. 1998. DOI: 10.1016/S0022-5096(97)00051-3.

[90] J. W. Hutchinson, "Elastic-Plastic Behaviour of Polycrystalline Metals and Composites," *Proceedings of the Royal Society A: Mathematical, Physical and Engineering Sciences*, vol. 319, no. 1537, pp. 247–272, Oct. 1970. DOI: 10.1098/rspa.1970.0177.

[91] T. O. Erinosho, A. C. F. Cocks, and F. P. E. Dunne, "Texture, hardening and non-proportionality of strain in BCC polycrystal deformation," *International Journal of Plasticity*, vol. 50, pp. 170–192, Nov. 2013. DOI: 10.1016/j.ijplas.2013.04.008.

[92] F. Roters *et al.*, "DAMASK – The Düsseldorf Advanced Material Simulation Kit

Ministry of Defence © British Crown Copyright 2020/AWE

for modeling multi-physics crystal plasticity, thermal, and damage phenomena from the single crystal up to the component scale," *Computational Materials Science*, vol. 158, no. December 2018, pp. 420–478, Feb. 2019. DOI: 10.1016/j.commatsci.2018.04.030.

[93] F. D. Fischer, T. Schaden, F. Appel, and H. Clemens, "Mechanical twins, their development and growth," *European Journal of Mechanics - A/Solids*, vol. 22, no. 5, pp. 709–726, Sep. 2003. DOI: 10.1016/S0997-7538(03)00081-0.

[94] J. Cheng, J. Shen, R. K. Mishra, and S. Ghosh, "Discrete twin evolution in Mg alloys using a novel crystal plasticity finite element model," *Acta Materialia*, vol. 149, pp. 142–153, May 2018. DOI: 10.1016/j.actamat.2018.02.032.

[95] F. Roters, P. Eisenlohr, L. Hantcherli, D. D. Tjahjanto, T. R. Bieler, and D. Raabe, "Overview of constitutive laws, kinematics, homogenization and multiscale methods in crystal plasticity finite-element modeling: Theory, experiments, applications," *Acta Materialia*, vol. 58, no. 4, pp. 1152–1211, Feb. 2010. DOI: 10.1016/j.actamat.2009.10.058.

[96] T. L. Anderson, *Fracture Mechanics*. CRC Press, 2005. DOI: 10.1201/9781420058215 ISBN: 9781420058215.

[97] M. Knezevic and I. J. Beyerlein, "Multiscale Modeling of Microstructure-Property Relationships of Polycrystalline Metals during Thermo-Mechanical Deformation," *Advanced Engineering Materials*, vol. 20, no. 4, p. 1700956, Apr. 2018. DOI: 10.1002/adem.201700956.

Ministry of Defence © British Crown Copyright 2020/AWE

[98] C. A. Calhoun, E. Garlea, T. Sisneros, and S. R. Agnew, "Effects of hydrogen on the mechanical response of αuranium," *Journal of Nuclear Materials*, vol. 465, pp. 737–745, Oct. 2015. DOI: 10.1016/j.jnucmat.2015.07.008.

[99] W. H. Peters and W. F. Ranson, "Digital Imaging Techniques In Experimental Stress Analysis," *Optical Engineering*, vol. 21, no. 3, pp. 427–431, Jun. 1982. DOI: 10.1117/12.7972925.

[100] B. Pan, K. Qian, H. Xie, and A. Asundi, "Two-dimensional digital image correlation for in-plane displacement and strain measurement: a review," *Measurement Science and Technology*, vol. 20, no. 6, p. 062001, Jun. 2009. DOI: 10.1088/0957-0233/20/6/062001.

[101] H. Haddadi and S. Belhabib, "Use of rigid-body motion for the investigation and estimation of the measurement errors related to digital image correlation technique," *Optics and Lasers in Engineering*, vol. 46, no. 2, pp. 185–196, Feb. 2008. DOI: 10.1016/j.optlaseng.2007.05.008.

[102] C. Nonis, C. Niezrecki, T.-Y. Yu, S. Ahmed, C.-F. Su, and T. Schmidt, "Structural health monitoring of bridges using digital image correlation," in *Maintenance, Monitoring, Safety, Risk and Resilience of Bridges and Bridge Networks - Proceedings of the 8th International Conference on Bridge Maintenance, Safety and Management, IABMAS 2016*, 2013, no. April, p. 869507. DOI: 10.1117/12.2009647.

[103] A. D. Kammers and S. Daly, "Digital Image Correlation under Scanning

Ministry of Defence © British Crown Copyright 2020/AWE

Electron Microscopy: Methodology and Validation," *Experimental Mechanics*, vol. 53, no. 9, pp. 1743–1761, Nov. 2013. DOI: 10.1007/s11340-013-9782-x.

[104] S. R. McNeill, W. H. Peters, and M. A. Sutton, "Estimation of stress intensity factor by digital image correlation," *Engineering Fracture Mechanics*, vol. 28, no. 1, pp. 101–112, Jan. 1987. DOI: 10.1016/0013-7944(87)90124-X.

[105] T. H. Becker, M. Mostafavi, R. B. Tait, and T. J. Marrow, "An approach to calculate the J -integral by digital image correlation displacement field measurement," *Fatigue & Fracture of Engineering Materials & Structures*, vol. 35, no. 10, pp. 971–984, Oct. 2012. DOI: 10.1111/j.1460-2695.2012.01685.x.

[106] J. D. Helm, "Improved three-dimensional image correlation for surface displacement measurement," *Optical Engineering*, vol. 35, no. 7, p. 1911, Jul. 1996. DOI: 10.1117/1.600624.

[107] D. W. Brown *et al.*, "Temperature and direction dependence of internal strain and texture evolution during deformation of uranium," *Materials Science and Engineering: A*, vol. 512, no. 1–2, pp. 67–75, Jun. 2009. DOI: 10.1016/j.msea.2009.02.004.

[108] C. A. Calhoun, J. A. Wollmershauser, D. W. Brown, R. P. Mulay, E. Garlea, and S. R. Agnew, "Thermal residual strains in depleted αU," *Scripta Materialia*, vol. 69, no. 8, pp. 566–569, Oct. 2013. DOI: 10.1016/j.scriptamat.2013.06.004.

[109] S. R. Agnew, R. P. Mulay, F. J. Polesak, C. A. Calhoun, J. J. Bhattacharyya, and B. Clausen, "In situ neutron diffraction and polycrystal plasticity modeling

Ministry of Defence © British Crown Copyright 2020/AWE

of a Mg–Y–Nd–Zr alloy: Effects of precipitation on individual deformation mechanisms," *Acta Materialia*, vol. 61, no. 10, pp. 3769–3780, Jun. 2013. DOI: 10.1016/j.actamat.2013.03.010.

[110] E. M. Francis *et al.*, "High-temperature deformation mechanisms in a polycrystalline nickel-base superalloy studied by neutron diffraction and electron microscopy," *Acta Materialia*, vol. 74, pp. 18–29, Aug. 2014. DOI: 10.1016/j.actamat.2014.04.028.

[111] J. Hu and A. C. F. Cocks, "A multi-scale self-consistent model describing the lattice deformation in austenitic stainless steels," *International Journal of Solids and Structures*, vol. 78–79, pp. 21–37, Jan. 2016. DOI: 10.1016/j.ijsolstr.2015.09.021.

[112] K. V. Mani Krishna *et al.*, "The effect of loading direction and Sn alloying on the deformation modes of Zr: An in-situ neutron diffraction study," *Materials Science and Engineering: A*, vol. 650, pp. 497–509, Jan. 2016. DOI: 10.1016/j.msea.2015.10.047.

[113] B. Clausen, D. W. Brown, and I. C. Noyan, "Engineering Applications of Time-of-Flight Neutron Diffraction," *JOM*, vol. 64, no. 1, pp. 117–126, Jan. 2012. DOI: 10.1007/s11837-011-0119-x.

[114] J. R. Santisteban, M. R. Daymond, J. A. James, and L. Edwards, "ENGIN-X: a third-generation neutron strain scanner," *Journal of Applied Crystallography*, vol. 39, no. 6, pp. 812–825, Dec. 2006. DOI: 10.1107/S0021889806042245.

Ministry of Defence © British Crown Copyright 2020/AWE

[115] R. B. Von Dreele, J. D. Jorgensen, and C. G. Windsor, "Rietveld refinement with spallation neutron powder diffraction data," *Journal of Applied Crystallography*, vol. 15, no. 6, pp. 581–589, Dec. 1982. DOI: 10.1107/S0021889882012722.

[116] W. David and J. Jorgensen, "Rietveld refinement with time-of-flight powder diffraction data from pulsed neutron sources," *Proceedings of the International Workshop on the Rietveld Method*, no. October, pp. 13–15, 1990. URL: https://www.osti.gov/biblio/6196985.

[117] H.-R. Wenk, L. Lutterotti, and S. C. Vogel, "Rietveld texture analysis from TOF neutron diffraction data," *Powder Diffraction*, vol. 25, no. 3, pp. 283–296, Sep. 2010. DOI: 10.1154/1.3479004.

[118] A. C. Larson and R. B. Von Dreele, "General Structure Analysis System (GSAS) Manual," *Los Alamos National Laboratory Report LAUR*. 2004. URL: http://www.ccp14.ac.uk/ccp/ccp14/ftp-mirror/gsas/public/gsas/manual/GSASManual.pdf.

[119] W. . Williams, R. . Ibberson, P. Day, and J. . Enderby, "GEM — General materials diffractometer at ISIS," *Physica B: Condensed Matter*, vol. 241–243, pp. 234–236, Dec. 1997. DOI: 10.1016/S0921-4526(97)00561-9.

[120] D. W. Brown *et al.*, "Critical comparison of two independent measurements of residual stress in an electron-beam welded uranium cylinder: Neutron diffraction and the contour method," *Acta Materialia*, vol. 59, no. 3, pp. 864–873, Feb.

Ministry of Defence © British Crown Copyright 2020/AWE

2011. DOI: 10.1016/j.actamat.2010.09.022.

[121] N. C. Popa *et al.*, "Residual-Strain Determination by Least-Squares Refinement of TOF Neutron-Diffraction Measurements of Deformed Uranium," *Advances in X-ray Analysis*, vol. 47, no. May 2014, pp. 373–378, 2004. URL: https://www.researchgate.net/publication/232715754_Residual-Strain_Determination_by_Least-Squares_Refinement_of_TOF_Neutron-Diffraction_Measurements_of_Deformed_Uranium.

[122] M. A. Gharghouri, G. C. Weatherly, J. D. Embury, and J. Root, "Study of the mechanical properties of Mg-7.7at.% Al by in-situ neutron diffraction," *Philosophical Magazine A*, vol. 79, no. 7, pp. 1671–1695, Jul. 1999. DOI: 10.1080/01418619908210386.

[123] A. Fitzner *et al.*, "The effect of aluminium on twinning in binary alpha-titanium," *Acta Materialia*, vol. 103, pp. 341–351, Jan. 2016. DOI: 10.1016/j.actamat.2015.09.048.

[124] L. Nervo, A. King, A. Fitzner, W. Ludwig, and M. Preuss, "A study of deformation twinning in a titanium alloy by X-ray diffraction contrast tomography," *Acta Materialia*, vol. 105, pp. 417–428, Feb. 2016. DOI: 10.1016/j.actamat.2015.12.032.

[125] A. J. Schwartz, M. Kumar, B. L. Adams, and D. P. Field, *Electron Backscatter Diffraction in Materials Science*. Boston, MA: Springer US, 2009. DOI: 10.1007/978-0-387-88136-2 ISBN: 978-0-387-88135-5.

Ministry of Defence © British Crown Copyright 2020/AWE

[126] A. J. Wilkinson and T. B. Britton, "Strains, planes, and EBSD in materials science," *Materials Today*, vol. 15, no. 9, pp. 366–376, Sep. 2012. DOI: 10.1016/S1369-7021(12)70163-3.

[127] D. J. Dingley, A. J. Wilkinson, G. Meaden, and P. S. Karamched, "Elastic strain tensor measurement using electron backscatter diffraction in the SEM," *Journal of Electron Microscopy*, vol. 59, no. S1, pp. S155–S163, Aug. 2010. DOI: 10.1093/jmicro/dfq043.

[128] M. Knezevic *et al.*, "Modeling mechanical response and texture evolution of α uranium as a function of strain rate and temperature using polycrystal plasticity," *International Journal of Plasticity*, vol. 43, pp. 70–84, Apr. 2013. DOI: 10.1016/j.ijplas.2012.10.011.

[129] M. Knezevic *et al.*, "Anisotropic stress–strain response and microstructure evolution of textured αuranium," *Acta Materialia*, vol. 60, no. 2, pp. 702–715, Jan. 2012. DOI: 10.1016/j.actamat.2011.10.041.

[130] T. B. Scott, J. R. Petherbridge, I. Findlay, J. Glascott, and G. C. Allen, "Recrystallisation of uranium resulting from electron beam welding," *Journal of Alloys and Compounds*, vol. 475, no. 1–2, pp. 766–772, May 2009. DOI: 10.1016/j.jallcom.2008.08.003.

[131] R. J. McCabe and D. F. Teter, "Analysis of recrystallized volume fractions in uranium using electron backscatter diffraction," *Journal of Microscopy*, vol. 223, no. 1, pp. 33–39, Jul. 2006. DOI: 10.1111/j.1365-2818.2006.01595.x.

Ministry of Defence © British Crown Copyright 2020/AWE

[132] R. J. McCabe, A. W. Richards, D. R. Coughlin, K. D. Clarke, I. J. Beyerlein, and M. Knezevic, "Microstructure effects on the recrystallization of low-symmetry alpha-uranium," *Journal of Nuclear Materials*, vol. 465, pp. 189–195, Oct. 2015. DOI: 10.1016/j.jnucmat.2015.04.055.

[133] N. Grilli, A. C. F. Cocks, and E. Tarleton, "Crystal plasticity finite element modelling of coarse-grained α-uranium," *Computational Materials Science*, vol. 171, p. 109276, Jan. 2020. DOI: 10.1016/j.commatsci.2019.109276.

[134] F. Bachmann, R. Hielscher, and H. Schaeben, "Grain detection from 2d and 3d EBSD data-Specification of the MTEX algorithm," *Ultramicroscopy*, vol. 111, no. 12, pp. 1720–1733, 2011. DOI: 10.1016/j.ultramic.2011.08.002.

[135] I. R. Cole, Thesis: , "Modelling CPV," Loughborough University, 2015. URL: https://dspace.lboro.ac.uk/2134/18050.

[136] G. Friedel, "Sur les symétries cristallines que peut révéler la diffraction des rayons X.," *C.R. Acad. Sci. Paris*, vol. 157, pp. 1533–1536, 1913.

[137] M. A. M. Bourke, D. C. Dunand, and E. Ustundag, "SMARTS - a spectrometer for strain measurement in engineering materials," *Applied Physics A: Materials Science & Processing*, vol. 74, pp. s1707–s1709, Dec. 2002. DOI: 10.1007/s003390201747.

[138] J. Schindelin *et al.*, "Fiji: an open-source platform for biological-image analysis," *Nature Methods*, vol. 9, no. 7, pp. 676–682, Jul. 2012. DOI: 10.1038/nmeth.2019.

[139] B. Clausen, "SMARTSware manual," 2003. [Online]. Available:

Ministry of Defence © British Crown Copyright 2020/AWE

ftp://ftp.lanl.gov/public/clausen/SMARTSware/SMARTSware_Manual.pdf. [Accessed: 30-Aug-2019].

[140] F. A. Akeroyd *et al.*, "Open Genie Reference Manual - Version 2.0." [Online]. Available: https://www.isis.stfc.ac.uk/Pages/open-genie-user-manual.pdf. [Accessed: 30-Aug-2019].

[141] C. C. Aydıner, J. V. Bernier, B. Clausen, U. Lienert, C. N. Tomé, and D. W. Brown, "Evolution of stress in individual grains and twins in a magnesium alloy aggregate," *Physical Review B*, vol. 80, no. 2, p. 024113, Jul. 2009. DOI: 10.1103/PhysRevB.80.024113.

[142] S. Gražulis *et al.*, "Crystallography Open Database – an open-access collection of crystal structures," *Journal of Applied Crystallography*, vol. 42, no. 4, pp. 726–729, Aug. 2009. DOI: 10.1107/S0021889809016690.

[143] Mathworks, "projective2d - 2-D projective geometric transformation." [Online]. Available: https://uk.mathworks.com/help/images/ref/projective2d.html.

[144] "Inkscape v0.92." [Online]. Available: https://inkscape.org/.

[145] GOM mbH, "GOM ARAMIS Hardware Manual," 2011. URL: Available with online account at www.gom.com.

[146] GOM mbH, "ARAMIS Sensor Configuration Tables," 2011. URL: Available with online account at www.gom.com.

[147] Mathworks, "Smoothing Spline." 2019. URL: https://uk.mathworks.com/help/curvefit/smoothing-splines.html.

Ministry of Defence © British Crown Copyright 2020/AWE

[148] T. B. Britton and A. J. Wilkinson, "Measurement of residual elastic strain and lattice rotations with high resolution electron backscatter diffraction," *Ultramicroscopy*, vol. 111, no. 8, pp. 1395–1404, Jul. 2011. DOI: 10.1016/j.ultramic.2011.05.007.

[149] Y. Guan, B. Chen, J. Zou, T. Ben Britton, J. Jiang, and F. P. E. Dunne, "Crystal plasticity modelling and HR-DIC measurement of slip activation and strain localization in single and oligo-crystal Ni alloys under fatigue," *International Journal of Plasticity*, vol. 88, pp. 70–88, Jan. 2017. DOI: 10.1016/j.ijplas.2016.10.001.

[150] A. D. Kammers and S. Daly, "Small-scale patterning methods for digital image correlation under scanning electron microscopy," *Measurement Science and Technology*, vol. 22, no. 12, p. 125501, Dec. 2011. DOI: 10.1088/0957-0233/22/12/125501.

[151] S. Kabra, J. Kelleher, W. Kockelmann, M. Gutmann, and A. Tremsin, "Energy-dispersive neutron imaging and diffraction of magnetically driven twins in a Ni 2 MnGa single crystal magnetic shape memory alloy," *Journal of Physics: Conference Series*, vol. 746, no. 1, p. 012056, Sep. 2016. DOI: 10.1088/1742-6596/746/1/012056.

[152] S. Preibisch, S. Saalfeld, and P. Tomancak, "Globally optimal stitching of tiled 3D microscopic image acquisitions," *Bioinformatics*, vol. 25, no. 11, pp. 1463–1465, Jun. 2009. DOI: 10.1093/bioinformatics/btp184.

Ministry of Defence © British Crown Copyright 2020/AWE

[153] G. Steidl, J. Persch, R. Hielscher, R. Chan, and R. Bergmann, "Restoration of manifold-valued images by half-quadratic minimization," *Inverse Problems and Imaging*, vol. 10, no. 2, pp. 281–304, May 2016. DOI: 10.3934/ipi.2016001.

[154] R. Brewster, "paint.net v4.1.5," 2018. [Online]. Available: https://www.getpaint.net/index.html.

[155] ASTM, "Standard Practice for Determining Average Grain Size Using Electron Backscatter Diffraction (EBSD) in Fully Recrystallized Polycrystalline Materials," *ASTM International*, pp. 1–5, 2014. DOI: 10.1520/E2627.

[156] R. Hielscher and H. Schaeben, "MTEX Documentation." [Online]. Available: https://mtex-toolbox.github.io/documentation.html.

[157] D. A. Skoog, F. J. Holler, and S. R. Crouch, *Principles of Instrumental Analysis*. Cengage Learning, 2017. URL: https://books.google.co.uk/books?id=n1zEDQAAQBAJ ISBN: 9781305577213.

[158] "Crystallography Supplementary Subject Lecture 7 : Systematic Absences," *University of Oxford*. pp. 1–8. URL: http://goodwin.chem.ox.ac.uk/goodwin/TEACHING_files/l7_handout.pdf.

[159] S. R. MacEwen, J. Faber, and A. P. L. Turner, "The use of time-of-flight neutron diffraction to study grain interaction stresses," *Acta Metallurgica*, vol. 31, no. 5, pp. 657–676, May 1983. DOI: 10.1016/0001-6160(83)90082-2.

[160] R. B. Von Dreele, "Quantitative texture analysis by Rietveld refinement," *Journal of Applied Crystallography*, vol. 30, no. 4, pp. 517–525, Aug. 1997. DOI:

Ministry of Defence © British Crown Copyright 2020/AWE

10.1107/S0021889897005918.

[161] D. Garcia, "Robust smoothing of gridded data in one and higher dimensions with missing values," *Computational Statistics & Data Analysis*, vol. 54, no. 4, pp. 1167–1178, Apr. 2010. DOI: 10.1016/j.csda.2009.09.020.

[162] A. Savitzky and M. J. E. Golay, "Smoothing and Differentiation of Data by Simplified Least Squares Procedures.," *Analytical Chemistry*, vol. 36, no. 8, pp. 1627–1639, Jul. 1964. DOI: 10.1021/ac60214a047.

[163] P. Day *et al.*, "Scientific Reviews: GEM: The General Materials Diffractometer at ISIS-Multibank Capabilities for Studying Crystalline and Disordered Materials," *Neutron News*, vol. 15, no. 1, pp. 19–23, Jan. 2004. DOI: 10.1080/00323910490970564.

[164] STFC, "GEM Webpage." [Online]. Available: https://www.isis.stfc.ac.uk/Pages/Gem.aspx. [Accessed: 06-Mar-2019].

[165] L. Lutterotti, S. Matthies, H.-R. Wenk, A. S. Schultz, and J. W. Richardson, "Combined texture and structure analysis of deformed limestone from time-of-flight neutron diffraction spectra," *Journal of Applied Physics*, vol. 81, no. 2, pp. 594–600, Jan. 1997. DOI: 10.1063/1.364220.

[166] L. Pardo and J. Ricote, *Multifunctional Polycrystalline Ferroelectric Materials: Processing and Properties*. Springer Netherlands, 2011. URL: https://books.google.co.uk/books?id=zoCbtMc0ZZYC ISBN: 9789048128754.

[167] L. Lutterotti, "Materials Texture Analysis." [Online]. Available:

Ministry of Defence © British Crown Copyright 2020/AWE

http://www.ing.unitn.it/~maud/facts/MaterialsTextureAnalysis.pdf.

[168] J. J. Jonas, S. Mu, T. Al-Samman, G. Gottstein, L. Jiang, and Ė. Martin, "The role of strain accommodation during the variant selection of primary twins in magnesium," *Acta Materialia*, vol. 59, no. 5, pp. 2046–2056, Mar. 2011. DOI: 10.1016/j.actamat.2010.12.005.

[169] D. W. Brown, S. R. Agnew, M. A. M. Bourke, T. M. Holden, S. C. Vogel, and C. N. Tomé, "Internal strain and texture evolution during deformation twinning in magnesium," *Materials Science and Engineering: A*, vol. 399, no. 1–2, pp. 1–12, Jun. 2005. DOI: 10.1016/j.msea.2005.02.016.

[170] Y. T. Zhu, X. Z. Liao, X. L. Wu, and J. Narayan, "Grain size effect on deformation twinning and detwinning," *Journal of Materials Science*, vol. 48, no. 13, pp. 4467–4475, Jul. 2013. DOI: 10.1007/s10853-013-7140-0.

[171] M. Knezevic, J. Crapps, I. J. Beyerlein, D. R. Coughlin, K. D. Clarke, and R. J. McCabe, "Anisotropic modeling of structural components using embedded crystal plasticity constructive laws within finite elements," *International Journal of Mechanical Sciences*, vol. 105, pp. 227–238, Jan. 2016. DOI: 10.1016/j.ijmecsci.2015.11.021.

[172] A. Polkowska, M. Warmuzek, J. Kalarus, W. Polkowski, and N. Sobczak, "A comparison of various imaging modes in scanning electron microscopy during evaluation of selected Si / refractory sessile drop couples after wettability tests at ultra-high temperature," *Prace Instytutu Odlewnictwa Transactions of*

Ministry of Defence © British Crown Copyright 2020/AWE

Foundry Research Institute, no. 4, pp. 337–344, 2017. DOI: 10.7356/iod.2017.35.

[173] J. Lansey, "Beautiful and distinguishable line colors + colormap." [Online]. Available: https://uk.mathworks.com/matlabcentral/fileexchange/42673-beautiful-and-distinguishable-line-colors-colormap. [Accessed: 30-Aug-2019].

[174] C. A. Brewer, "ColorBrewer." [Online]. Available: www.ColorBrewer.org. [Accessed: 27-Mar-2019].

Ministry of Defence © British Crown Copyright 2020/AWE

Chapter 8 Appendices

A1 Glossary of Abbreviations

Notation	Description
3D-DIC	Three Dimensional Digital Image Correlation (a.k.a Stereo DIC)
AWE plc.	Atomic Weapons Establishment
CG	Coarse-Grained (microstructure)
CPFE	Crystal Plasticity Finite Element
DB	Dog-Bone (specimen geometry)
DIC	Digital Image Correlation
DU	Depleted Uranium
EBSD	Electron Backscatter Diffraction
EDM	Electrical Discharge Machining
ENGIN-X	Materials Engineering Diffraction Beamline at ISIS
FEGSEM	Field-Emission Gun Scanning Electron Microscope
FG	Fine-Grained (microstructure)
GEM	General Materials Diffractometer (Beamline at ISIS)
HIPPO	High-Pressure-Preferred Orientation (Beamline at LANSCE)
IGV	Instrumental Gauge Volume
IPF	Inverse Pole Figure
ISIS	ISIS Neutron and Muon Source
LANL	Los Alamos National Laboratory, New Mexico, USA
LANSCE	Los Alamos Neutron Science Center (Facility at LANL)
ND	Neutron Diffraction
ND	Normal Direction (in pole figure or in context of rolled material)
PF	Pole Figure
RD	Rolling Direction (in pole figure or in rolled material)
SEM	Scanning Electron Microscope
SF	Schmid Factor
SMARTS	Spectrometer for Materials Research at Temperature and Stress (Beamline at LANSCE)
TD	Transverse Direction (in pole figure or in rolled material)

Ministry of Defence © British Crown Copyright 2020/AWE

A2 Specimen List

A: Magnitude of maximum stress B: Mean gauge region strain at maximum stress C: Maximum gauge region strain at maximum stress						*: Strain measurement unreliable for ENGIN-X experiment.				
Specimen Name	Gauge Cross-section	Load history				Measurement				CPFE Modelling
		Loading type	A (MPa)	B (%)	C (%)	Neutron Diffraction	Neutron Texture	EBSD	3D-DIC	
831	SEM specimen (6 mm × 6 mm× 1.5 mm)	-	-	-	-	-	-	Yes (twins)	-	-
DB-T1	Rectangular, nominally 6.00 mm × 1.50 mm	Tension with intermediate unloads/reloads	208	1.90	~10	-	-	Yes	Yes	Yes, validated model [2]
DB-T2	Rectangular, nominally 6.00 mm × 1.50 mm	Tension with intermediate unloads/reloads	200	1.10	~12	-	-	Yes	Yes	None
DB-T3	Rectangular, nominally 6.00 mm × 1.50 mm	Tension with intermediate unloads/reloads	179	2.06	~10	-	-	Yes	Yes	Yes, calibrated model [2]
ND-T1	Circular 8.00 mm diameter	Tension	310	*	*	ENGIN-X ISIS, UK	GEM ISIS, UK	-	-	Yes, calibrated model [88][133]
ND-T2	Circular 8.00 mm diameter	Tension with final unload	310	*	*	ENGIN-X ISIS, UK	GEM ISIS, UK	-	-	Yes, calibrated model [88][133]
ND-T3	Circular 8.00 mm diameter	Tension with intermediate unloads/reloads	480 Fracture	5.4	~11	SMARTS, LANL, USA	HIPPO, LANL, USA	-	-	-
ND-T4	Circular 8.00 mm diameter	Tension with intermediate unloads/reloads	395 Fracture	5.7	~12	SMARTS, LANL, USA	HIPPO, LANL, USA	-	-	-

Ministry of Defence © British Crown Copyright 2020/AWE

A: Magnitude of maximum stress B: Mean gauge region strain at maximum stress C: Maximum gauge region strain at maximum stress						*: Strain measurement unreliable for ENGIN-X experiment. **: Specimen ND-C2 not tested on ENGIN-X. Undeformed. ***: No DIC measurement at high compressive strains due to containment box				
Specimen Name	Gauge Cross-section	Load history				Measurement				CPFE Modelling
		Loading type	A (MPa)	B (%)	C (%)	Neutron Diffraction	Neutron Texture	EBSD	3D-DIC	
ND-C1	Circular 14.00 mm diameter	Compression with final unload	-310	*	*	ENGIN-X ISIS, UK	GEM ISIS, UK	-	-	Yes, calibrated model [88][133]
ND-C2	Circular 14.00 mm diameter	Compression – test incomplete	**	*	*	**	GEM ISIS, UK	-	-	-
ND-C3	Circular 14.00 mm diameter	Compression with intermediate unloads/reloads	653	~6.3	***	SMARTS, LANL, USA	HIPPO, LANL, USA	-	-	-
ND-C4	Circular 14.00 mm diameter	Compression with intermediate unloads/reloads	771	~7.5	~-15	SMARTS, LANL, USA	HIPPO, LANL, USA	-	-	-

Ministry of Defence © British Crown Copyright 2020/AWE

Ministry of Defence © British Crown Copyright 2020/AWE

A3 Material Characterisation

A3.1 Introduction

In this short section, I present a microstructural characterisation of the cast depleted uranium material that appears in the subsequent chapters. Firstly I show an EBSD analysis of the microstructure, in which grain size and orientation were measured. Twins are identified by their misorientation from their parent grain.

All specimens used in this project were cut from a single cast plate with dimensions 200 mm × 150 mm × 20 mm, from a batch of 20 sourced by AWE plc. from MSC (Manufacturing Sciences Corporation, Oak Ridge, Tennessee, USA) in the late 2000s.

A3.2 Microstructural Characterisation with EBSD

From our literature review, we are aware that cast uranium typically is coarse-grained, and with a strong texture (section 2.2.5), however no microstructural information existed for the cast plate used in this study. In order to provide a foundation for subsequent work, I characterised the microstructure in the material from the grain scale (microns) to the specimen scale (millimetres).

A3.2.1 Method

Specimens were prepared for EBSD analysis at the Interface Analysis Centre, School of Physics, University of Bristol, with training and guidance provided by Dr Chris Jones. After a number of attempts to achieve a satisfactory surface preparation, good EBSD

Ministry of Defence © British Crown Copyright 2020/AWE

data were acquired on a specimen denoted "831" in the sample inventory. The specimen was cuboid with pre-preparation dimensions of 6.0 mm × 6.0 mm × 1.5 mm. It was manufactured at AWE using electro-discharge machining (EDM), with a 0.5 mm diameter hole drilled near one corner to allow it to be oriented consistently in the microscope (see figure 8.2).

The specimen had all external faces ground with 320-grit silicon carbide paper to remove the oxide layer, and was then mounted on an SEM pin stub with cyanoacrylate adhesive with a square face facing upwards. A small bevel was ground on the four outward facing edges to prevent the specimen digging into the grinding paper. Grinding continued through 600, 1200 and 2500-grit papers, followed by a 3 μm diamond polish. The specimen was removed from the stub with acetone and any excess adhesive removed by agitation of the acetone in an ultrasonic bath.

Electropolishing was performed using an acidic electrolyte commonly used in the literature [131][31] comprising ethanol (CH_3CH_2OH), orthophosphoric acid (H_3PO_4), and ethylene glycol ($(CH_2OH)_2$) in a 10:6:6 ratio by volume. The solution was prepared in a volumetric flask, slowly adding the acid to the ethylene glycol-ethanol mixture whilst swirling the flask under a running tap to cool the exothermic reaction. The electropolishing set-up is shown in figure 8.1. The specimen was wrapped in a 0.5 mm diameter gold wire, and suspended by the anode wire into the electrolyte, taking care that the clip did not touch the liquid. A Stuart Scientific Magnetic Stirrer SM1 was used

Ministry of Defence © British Crown Copyright 2020/AWE

to constantly mix the solution in the stainless steel beaker. The anode and cathode wires were connected to the positive and negative terminals of a Digimess PM6003 DC power supply operating in constant current mode. Specimen 831 was polished at 0.4 A, 12 V for 5 minutes to achieve a visible reaction with oxygen bubbles forming at the anode. The specimen was then rinsed under tap water, rinsed with ethanol to remove the water, before being dried gently with soft paper ('blue paper' roll) and mounted to a clean aluminium SEM pin stub using 'silver dag'. The prepared specimen was then transferred promptly to the SEM for EBSD analysis. The SEM used at Bristol for this analysis was a Zeiss Sigma HD VP Field Emission SEM with an EDAX EBSD camera running EDAX OIM™ data acquisition software.

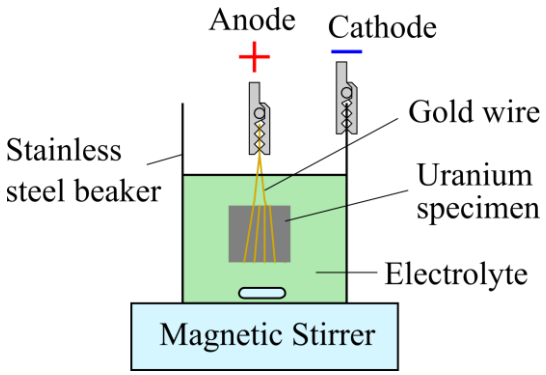


Figure 8.1. Schematic of the electropolishing set-up used to prepare depleted uranium specimens for microstructural examination with EBSD.

A series of six overlapping SEM images covering the entire specimen were captured with the secondary electron detector. A FFT band-pass filter was applied in ImageJ 1.51u (part of the Fiji distribution [138]) to remove spatial frequency components with a wavelength greater than 50 pixels, thereby removing the background intensity gradient

Ministry of Defence © British Crown Copyright 2020/AWE

from each image. The six images were stitched together using the Grid Stitching plugin [152] using the linear blending method. The resulting image is shown in figure 8.2.

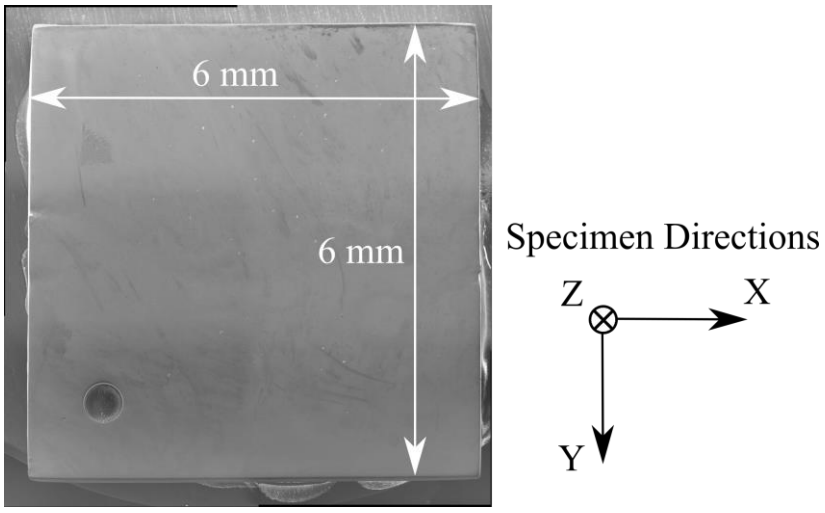


Figure 8.2. Stitched SEM image showing specimen 831 before EBSD analysis.

To prepare for EBSD, the microscope was set to image with an accelerating voltage of 30 kV, 120 μm aperture and 'High Current' mode enabled. EBSD patterns were acquired using 4 × 4 pixel binning, and an exposure time of 25 ms per frame. Image processing was applied to the EBSD patterns during acquisition; background subtraction, dynamic background subtraction, a normalisation of the intensity histogram followed by a median smoothing filter. This process increases the contrast in the image to aid the automated band detection algorithm in indexing each pattern.

A series of eight EBSD scans were taken in order to map the microstructure in a large portion of specimen "831". Scan points were arranged in a hexagonal grid, with 5 μm step size. Each scan was saved into the proprietary `.osc` file format for subsequent analysis.

Ministry of Defence © British Crown Copyright 2020/AWE

A3.2.2 Visualisation of the Microstructure

EBSD data analysis was performed using MTEX [134], a free MATLAB toolbox for EBSD and texture analysis. Firstly, all points with a confidence index less than or equal to 0.05 were removed, as they are the result of poor pattern indexing and have erroneous orientation data. Grains were identified using a 3° misorientation angle threshold, and those smaller than 3 points in area were discarded. A half-quadratic filter [153] was applied to smooth the EBSD data and fill in the non-indexed points. Inverse pole figure maps were generated showing the crystal orientations with respect to the X, Y, and Z specimen directions shown in figure 8.2. The eight images were then stitched together in Paint.net [154] to create the composite maps shown in figure 8.3(b), (c) and (d).The inverse pole figure colour key used is shown in figure 8.3(a). To be consistent throughout this thesis, directions related to the a / (100) / [100] direction in the unit cell will be coloured red, with blue and green used for b / (010) / [010] and c / (001) / [001] directions respectively.

A random selection was made of 2000 points across the entire composite dataset, out of more than 10^6 points in total. The orientations of these points are plotted in figure 8.4 as inverse pole figures with respect to the X, Y and Z specimen directions (sub-figures (a), (b), and (c) and as pole figures with respect to the (100), (010), and (001) plane normal directions in the crystal.

Ministry of Defence © British Crown Copyright 2020/AWE

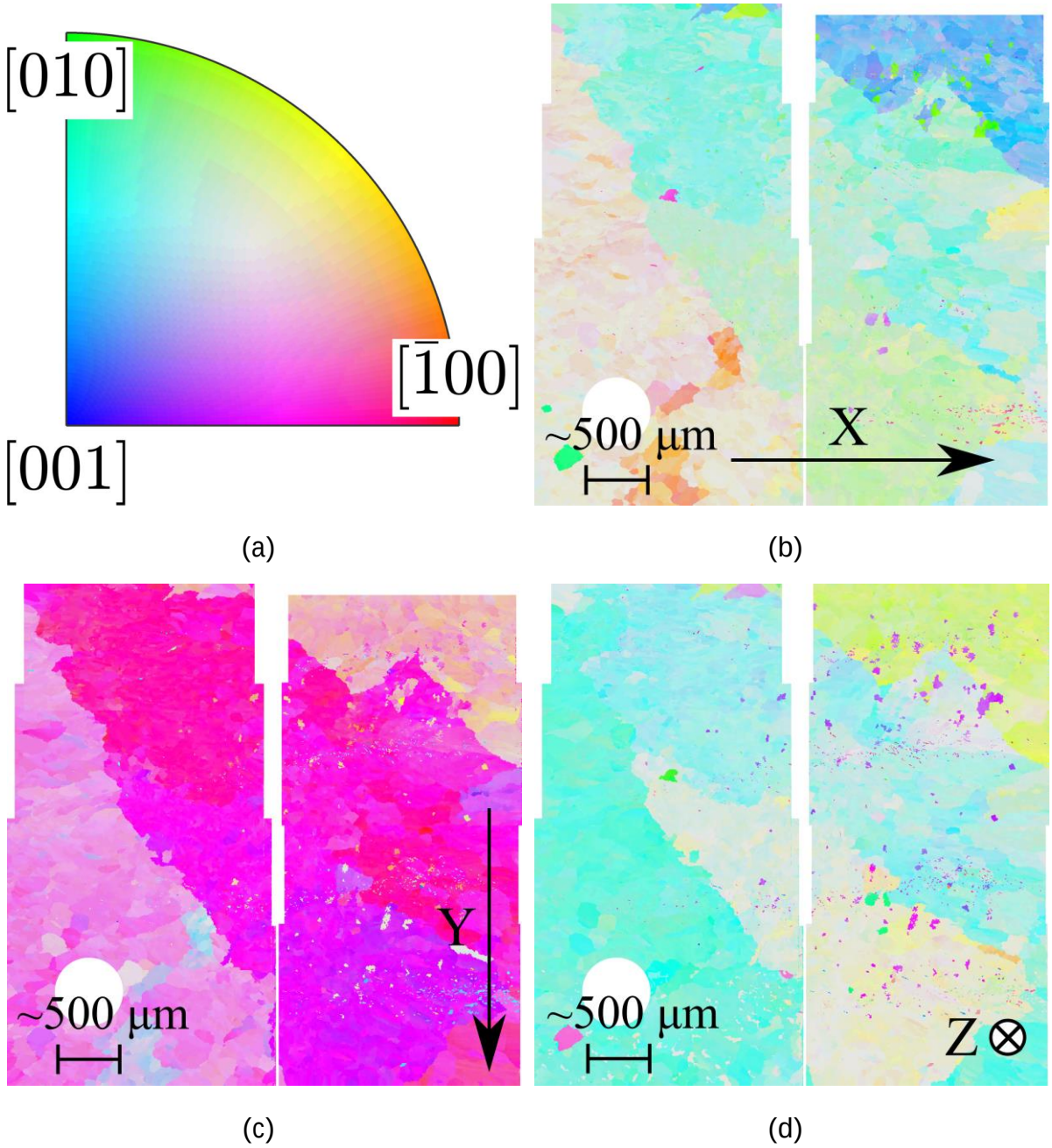


Figure 8.3. Composite orientation maps of the eight EBSD datasets showing grain orientation within specimen "831", with respect to the inverse pole figure colour key shown in sub-figure (a). Step size in each EBSD scan is 5 µm, with points arranged in a hexagonal grid. Sub-figures (b), (c), and (d) show grain orientation with respect to the X, Y and Z (out-of-plane) directions respectively.

Ministry of Defence © British Crown Copyright 2020/AWE

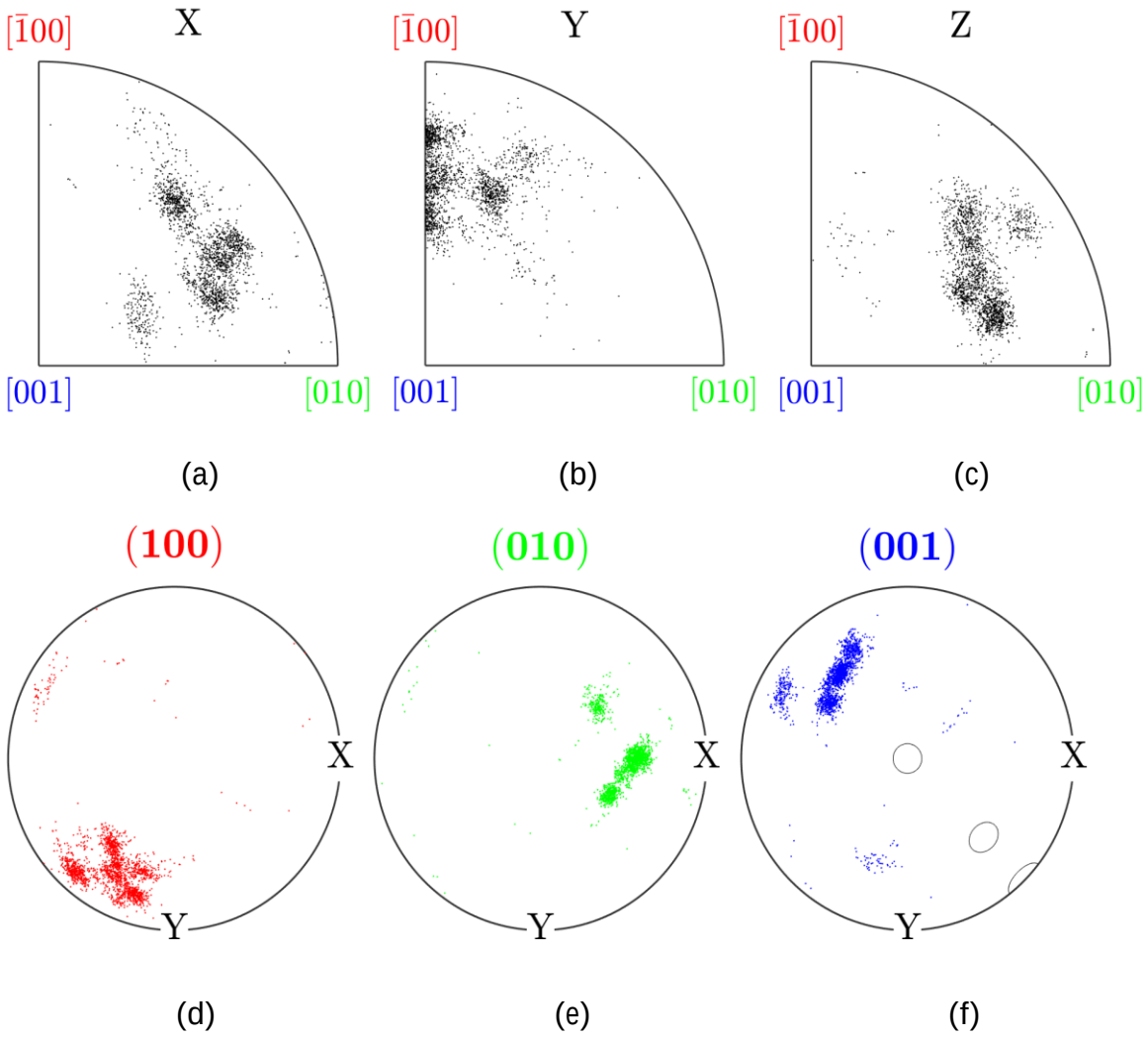


Figure 8.4. Sub-figures (a), (b), and (c) are scatter plots of the orientations of 2000 randomly selected data points from specimen "831", plotted in inverse pole figures with respect to the X, Y and Z specimen directions respectively. Sub-figures (d), (e), and (f) are scatter plots of the orientations of another 2000 points, plotted in pole figures with respect to the (100), (010), and (001) plane normal directions in the crystal. The specimen Z-direction is into the page. The ellipses shown in sub-figure (f) each have an angular radius of 7°, and are comparable in size to the spread of orientations within each cluster.

The microstructure seen in figure 8.3 is coarse, and grain boundaries are not always visible by eye. Across the specimen, there are four clusters of grains, each over 2 mm × 4 mm in cross-sectional area. The presence of these clusters can be seen in the pole figures plotted in sub-figures 8.4(d), (e), and (f), as regions with a high density of points. The spread of orientations within each cluster can be compared with the 7°-radius ellipses drawn on sub-figure 8.4(f); the majority of these lie within a 7° misorientation

Ministry of Defence © British Crown Copyright 2020/AWE

of the apparent cluster centre. A misorientation of between 10° and 25° is present between each cluster.

A3.2.3 Calculation of Grain Size

It is common practice to calculate a representative grain size for a material. This can be compared with the 300 μm to 500 μm grain size given for cast uranium in the literature [23], typically measured with optical microscopy. This process is, however, challenging for this strongly clustered microstructure, as the calculated grain size depends strongly on the parameters used to identify the grain boundaries. Typically, a misorientation threshold is used to group similarly-oriented points together into grains. The ASTM standard "Standard Practice for Determining Average Grain Size Using Electron Backscatter Diffraction (EBSD) in Fully Recrystallized Polycrystalline Materials" [155] suggests the use of a misorientation threshold of 5°, however the cast uranium does not exhibit a recrystallised microstructure with randomly-oriented equiaxed grains. Grain boundary misorientation thresholds of 1° and 3° were applied in MTEX to each of the eight constituent EBSD datasets, and grain statistics were calculated in each case.

The grains identified in one of the EBSD datasets are plotted in figure 8.5. Boundaries with at least a 1° and 3° misorientation are shown in grey and black respectively. As would be expected, the grains identified with the 1° misorientation threshold are smaller than those with the 3° threshold. Large areas of the left-most 'turquoise' grain have no boundaries of 3° misorientation or greater. Whilst the majority of the grains in each case

Ministry of Defence © British Crown Copyright 2020/AWE

are not circular in cross-section, they are equiaxed in the plane of cross-section; no elongation direction is apparent.

The grain diameter is calculated in MTEX as "longest distance between any two vertices of the grain boundary" [156], so that definition is used here. For the 1° and 3° thresholds the arithmetic mean grain diameters are just 43 μm and 59 μm respectively which is clearly not representative of the microstructure seen in figure 8.5. Whilst there are many small grains identified, the majority of the sample area exists as part of the larger grains. A more useful approach is to consider the area contribution of each grain. A histogram of the grain area contribution as a function of grain diameter across the eight EBSD datasets is shown in figure 8.6. It is worth noting here that grains that span the boundary between two adjacent scans are split by the calculation into two smaller grains, and that grains present at the edge of the stitched dataset appear smaller than in reality. Typically, this issue would be avoided by removing grains which impinge on a boundary from each dataset before computing the grain size, but doing so here would result in the removal of the majority of the largest grains in the 3° case, invalidating the grain size distribution.

Ministry of Defence © British Crown Copyright 2020/AWE

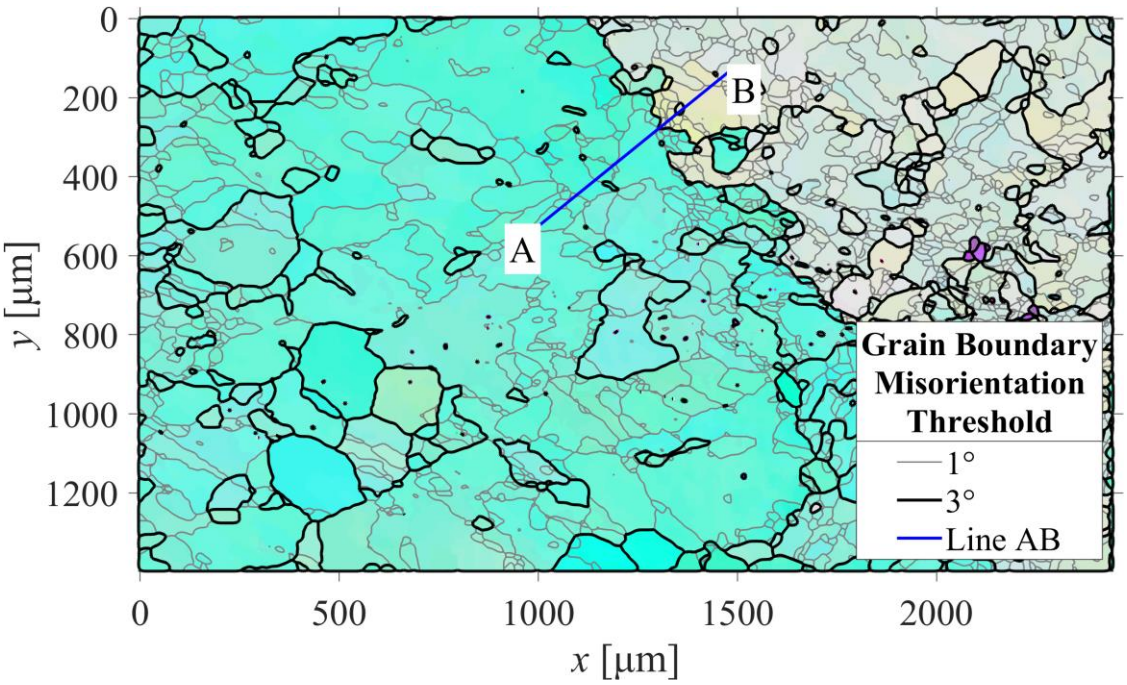


Figure 8.5. EBSD orientation map of one of the EBSD scans from specimen 831, with the crystal direction parallel to the Z-direction in the specimen (into page) coloured according to the inverse pole figure colour key in figure 8.3a. Step size between each data point is 5 µm, with points arranged in a hexagonal grid. Grain boundaries identified using 1° and 3° misorientation thresholds are shown in grey and black respectively. The misorientation along line AB is shown in figure 8.7.

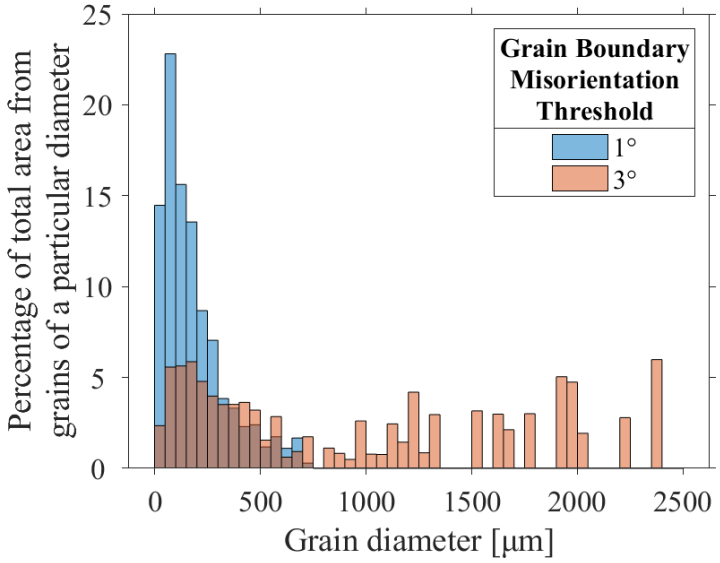


Figure 8.6. Histogram of the grain area contribution as a function of grain diameter, for grains identified with 1° (blue) and 3° (orange) misorientation thresholds. Histogram plotted with a grain diameter bin width of 50 µm. The histogram has been normalised by the total grain area in each case, to allow comparison of the relative area contribution of differently sized grains.

Ministry of Defence © British Crown Copyright 2020/AWE

By inspection of the histogram in figure 8.6, it can be seen that the value of the grain boundary misorientation threshold strongly affects the calculated distribution of grains. A smaller threshold value results in the splitting up of larger regions, thus reducing the area contribution of large grains at the same time as increasing the area contribution from smaller grains. When using a 3° misorientation threshold, there is a significant area fraction from grains larger than 500 μm, and the largest grain is almost 2.5 mm in diameter.

A more representative grain diameter may therefore be calculated by weighting each grain's contribution by its area. This can be achieved by using equation [8.1] , where A_i and d_i are the area and diameter respectively of the i^{th} grain in the dataset.

$$d_w = \frac{\sum_i A_i d_i}{\sum_i A_i} \qquad [8.1]$$

This calculation yields grain diameters of 185 μm and 972 μm for the 1° and 3° misorientation thresholds respectively, which appears sensible for the grain boundaries shown in figure 8.5.

A3.2.4 Grain Boundaries

Two types of grain boundary are present in the material; low-angle boundaries separating the 'grains' within a cluster, and higher-angle boundaries between the clusters. These can be seen by observing the orientation change along a line which crosses these boundaries – line AB in figure 8.5. The misorientation with reference to point A along

Ministry of Defence © British Crown Copyright 2020/AWE

the line AB is plotted in figure 8.7. A large jump in misorientation of approximately 25° is seen 400 μm along the line as the cluster boundary is crossed. Smaller jumps are present either side of the cluster boundary, corresponding to the boundaries between grains in the cluster. The intra-cluster misorientations along line AB are comparable in magnitude to the spread of orientations seen in the pole figures in sub-figures 8.4(d), (e), and (f).

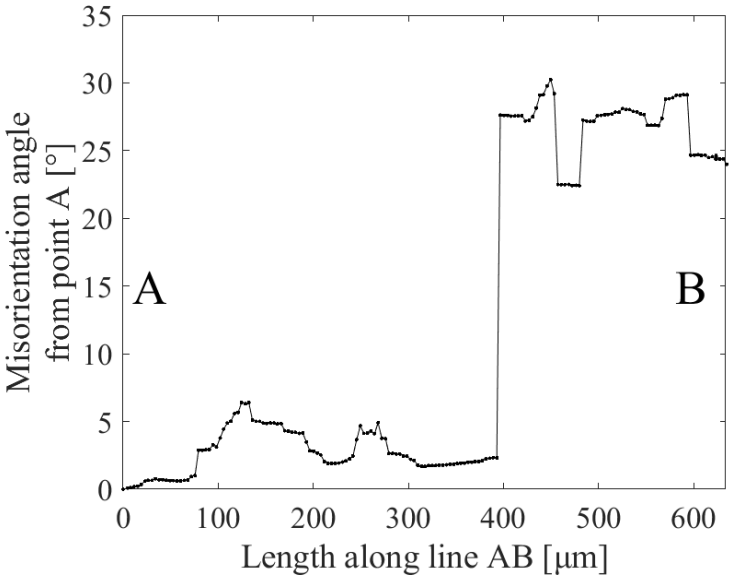


Figure 8.7. The misorientation with respect to point A of points along the line AB shown in figure 8.5. The large jump in misorientation corresponds to the boundary between clusters, whilst the smaller jumps correspond to boundaries between the grains in each cluster.

Since the material is in the as-cast state, it is possible that a solidification texture is present, with a particular grain direction aligned to the solidification direction. Unfortunately no information is available to relate the plate orientation to the solidification direction, and the orientation relationships between the specimens and the plate were lost during specimen manufacture. Although the clusters in specimen 831 have similar orientations, this does not lead to the conclusion of a global texture; just

Ministry of Defence © British Crown Copyright 2020/AWE

four clusters are present here and many more would need to be measured to generate a statistically significant dataset. It is worth stating here that in the subsequent work, a consistent preferential orientation in the material is not observed, even in larger specimens with a known axial alignment between them.

The EBSD scans which comprise figure 8.3 have a coarse step size of 5 μm, and therefore cannot reveal any features on a smaller length scale. In cast uranium, it is expected that deformation twins will be present in the as-cast structure, their formation having relieved the thermal stresses induced during cooling. A single EBSD scan was taken of an area 80 μm × 70 μm, with a hexagonal grid of points and a 0.1 μm step size. The orientation map of this scan is shown in figure 8.8.

The microstructure in the scanned region consists of one dominant grain, coloured light blue in the Z-oriented inverse pole figure in figure 8.8a. To the left hand side of the mapped area, thin, elongated regions of a differing orientation are present, and the majority of these are parallel to one another. From their morphology, they appear to be twins. In the right hand side of the mapped area, there are clusters of round grains of approximately 5 μm in diameter, distributed in two or three main orientations. There are also grains, coloured purple in figure 8.8(a), which exist in both 'streaked' and 'clustered' morphologies. Approximately half-way up the scan, there is a scan drift artefact, in which the scan has suddenly shifted in the y-direction. This is likely due to sample movement during the scan, or specimen charging deflecting the beam.

Ministry of Defence © British Crown Copyright 2020/AWE

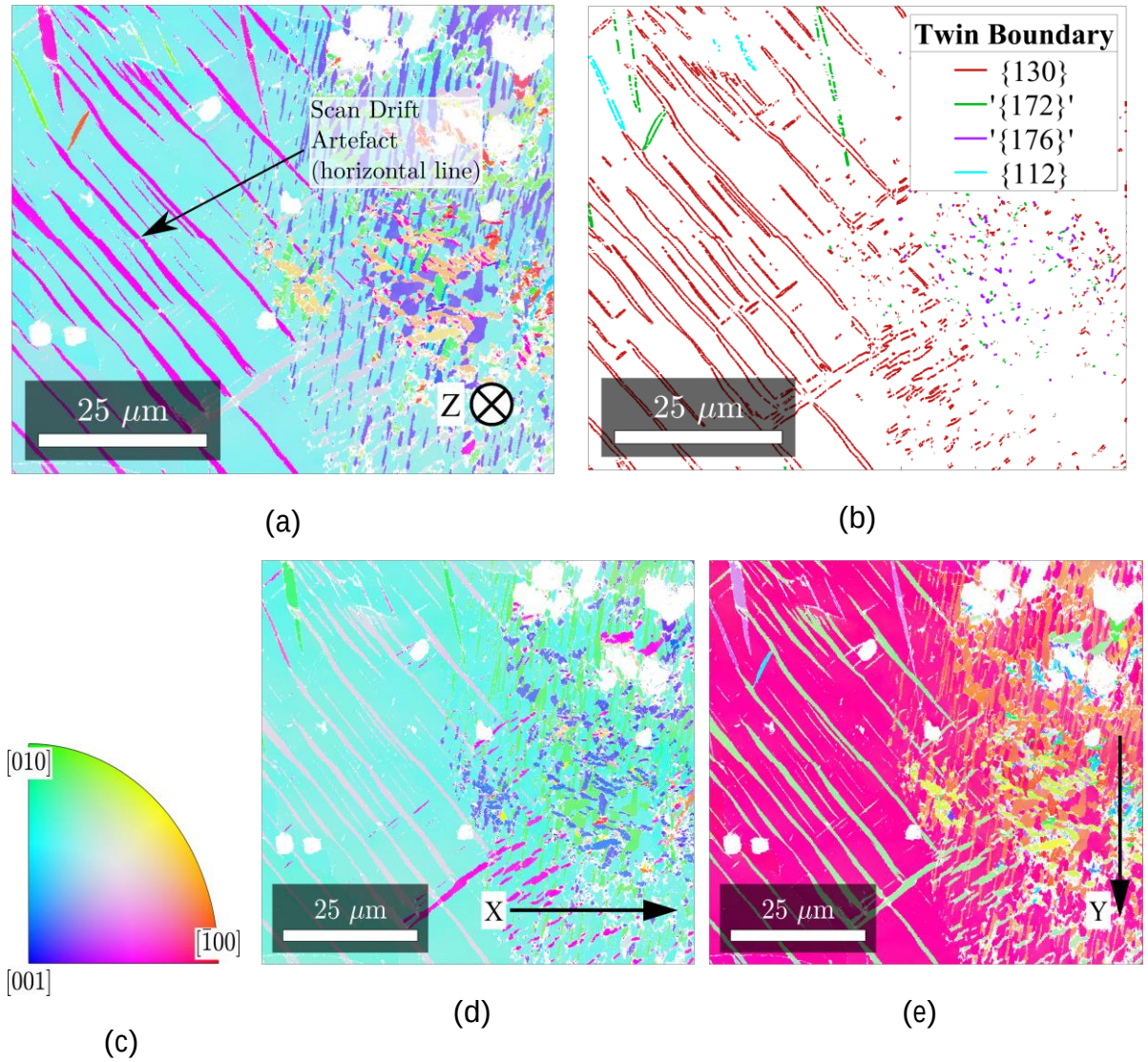


Figure 8.8. EBSD orientation maps of the high-resolution (0.1 μm step size) scan taken on specimen "831". Sub-figures (a), (d) and (e) show the crystal direction parallel to the Z, X and Y specimen axes respectively, according to the inverse pole figure colour key in sub-figure (c). Twins were identified according to their boundary misorientation and their boundaries are coloured in sub-figure (b).

Since each twinning mode results in a unique lattice misorientation between the parent and twinned region, the twins could be identified with an analysis of the EBSD orientation data. Firstly, points with a confidence index of less than 0.05 were removed, as these were observed to exhibit random orientation data. Grains were calculated using a 5° misorientation threshold, and enclosed regions containing fewer than 2 data points

Ministry of Defence © British Crown Copyright 2020/AWE

were removed. For each possible twin, the characteristic misorientation was implemented as an angle-axis pair, with the relevant angles and axes shown in table 8.1. A boundary segment was identified as a twinning boundary if the angle difference between the measured misorientation across the boundary and the twinning misorientation in table 8.1 was less than 5°. The identified twin boundaries are shown in figure 8.8b, and coloured according to their twinning mode; grain boundaries which are not twinning boundaries are not shown.

Table 8.1. Parameters used to define the characteristic twinning misorientation to identify twins in EBSD data.

	Twinning mode			
	{130}	'{172}'	'{176}'	{112}
Misorientation Angle-Axis	69.3°, [001]	93.0°, [$\overline{1}$0 7 0]	78.0°, [0 10 7]	90.0°, [110]

Twins of the {130}, '{172}', and {112} are clearly identified. The most frequently occurring twin is the {130} twin, which exists in two variants. The {130} twins have parallel sides and a nominal width of 3 μm, with a large aspect ratio and lengths of approximately 50 μm. The EBSD scan only measures a cross-section through the microstructure; in reality the twins are three-dimensional, plate-like features. Two variants of the '{172}' twin are present. The single twin of the first variant is trapped between two {130} twins, whilst the twins of the other variant appear to cross over and pass through a number of {130} twins. The largest {112} twin extends from the uppermost tip of a neighbouring {130} twin. Whilst boundaries matching the '{176}'

Ministry of Defence © British Crown Copyright 2020/AWE

twinning orientation were identified in small quantities, they are not sufficiently clear to identify the twins.

Interestingly, the grains coloured purple in figure 8.8(a) are not found to have a twinning orientation with respect to the surrounding material, despite exhibiting a 'streaked' morphology similar to the {130} twins.

The area fraction of {130} twins was calculated by identifying points with a similar orientation. For each variant, a reference point was chosen in the twin and then a misorientation threshold of 20° was used to identify other points of the same twin variant. The threshold value of 20° was chosen empirically as it ensured all points in each twin variant were selected whilst rejecting data from all other features. The combined area fraction across both {130} variants was calculated to be 8.5 %.

The presence of a large number of deformation twins in the as-cast state indicates a high level of deformation induced during the cooling process. As expected from the literature, {130} twins were the most commonly observed twinning mode [56]. The {112} twin is rarely observed, and its presence here suggests a tensile stress parallel to [001] was responsible for its formation [55]. Since α-uranium has a positive thermal expansion coefficient along the c-axis, cooling leads to a reduction in lattice parameter which would be consistent with a tensile stress in this direction if the grain is constrained by its neighbours. However, the presence of such a small area fraction of {112} twins, and the dominance of {130} twins which are not favourable for tension parallel to [001], suggests

Ministry of Defence © British Crown Copyright 2020/AWE

that the formation of {112} twins is due to the local, rather than global stress state. This stress state may have been formed as a result of the growth of the adjacent {130} twins.

A3.2.5 Summary of Microstructure

In summary, the unique microstructure presents challenges to determining conventional microstructural parameters such as grain size. It will be of considerable help for us to keep in mind the typical microstructural features that have been described in this section:

- Grains with diameters in the order of 100 μm are clustered together in regions with similar orientation. These clusters are in the order of 1 mm to 10 mm in diameter.
- The misorientation between these clusters is greater than 25°.
- The misorientation within a cluster is less than 10°.
- The as-cast microstructure contains a large number of deformation twins, predominantly of the {130} type, which occupy an area fraction of up to 10 %.

A3.3 Chemical Composition

A chemical analysis of the cast DU material was provided by AWE plc. at the start of the project. Whilst the method of analysis was not provided, Tom Shaw, an analytical chemist at AWE plc. explained that the carbon determination would be through a combustion-IR absorption technique, and that trace elements are identified via

Ministry of Defence © British Crown Copyright 2020/AWE

Inductively Coupled Plasma – Optical Emission Spectroscopy (ICP-OES) [157]. The averaged chemical composition across this series of plates, in parts per million by weight (ppmw), are shown in table 8.2.

Table 8.2. Averaged chemical composition across the batch of 20 cast DU plates, one of which was used to produce the specimens for this study. Carbon analysis via a combustion-IR absorption technique. Trace element analysis performed by ICP-OES and presented in parts per million by weight (ppmw).

Element	Content (ppmw)
U	Balance
C	608 ± 6
Si	130 ± 10
Ni	130 ± 10
Cr	22 ± 1
Al	39 ± 2
Fe	140 ± 10

A3.4 Summary

In this section, we have performed an investigation of the chemical and microstructural composition of the as-cast depleted uranium tested in this thesis. Now that we have an understanding of the material and its microstructural complexities, we can move on to the main experimental work in this chapter.

Ministry of Defence © British Crown Copyright 2020/AWE

A4 Systematic Absences in Diffraction

The crystallography of the specimen can cause particular peaks to be absent from its diffraction spectrum – these are known as systematic absences. The structure factor for a particular reflection, F_{hkl} describes the total scattering contributions from all atoms in the unit cell. The structure factor is defined in equation [8.2], for *j* atoms in the unit cell at positions (x_j, y_j, z_j). Each type of atom has different atomic scattering factors f_j.

$$F_{hkl} = \sum_j f_j \exp[2\pi \mathrm{i}(hx_j + ky_j + lz_j)] \qquad [8.2]$$

The intensity of a peak in a neutron (or X-ray) diffraction spectrum is proportional to the square of the magnitude of the structure factor, as in equation [8.3].

$$I_{hkl} \propto |F_{hkl}|^2 \qquad [8.3]$$

The condition for a systematic absence is that the structure factor is zero. The symmetry elements of the crystal space group can be used to predict the systematic absences [158]. α-uranium is of space group Cmcm, also known as C 2/m 2/c 2_1/m; it has atoms centred on the C-faces as well as the unit cell vertices, a mirror plane perpendicular to the a-axis, a c-glide perpendicular to the b-axis, and a 2_1 screw axis parallel to the c-axis. The C-centred lattice produces absences where $h + k$ is odd whilst the mirror plane produces none. The c-glide causes absences where $k = 0$ and *l* is odd. Finally, the 2_1 screw axis produces absences where $h = k = 0$ and l is odd. This is a subset of those reflections already made absent by the c-glide, and therefore has no further effect.

Ministry of Defence © British Crown Copyright 2020/AWE

Table 8.3. Systematic absences for the first ten theoretical reflections in alpha-uranium, arranged in descending order by *d*-spacing. The absences introduced by each of the four symmetry elements in the space group are shown, with an absence shown by a filled box. Reflections present in the diffraction pattern are shown in green.

				Systematic Absences				
h	*k*	*l*	*d* (Å)	C	m (2/m)	c (2/c)	m (2_1/c)	Absent
0	1	0	5.869	■				■
0	0	1	4.955			■	■	■
0	1	1	3.786	■				■
0	2	0	2.935					
1	0	0	2.854	■				■
1	1	0	2.567					
0	2	1	2.525					
0	0	2	2.478					
1	0	1	2.473	■		■		■
0	1	2	2.282	■				■
⋮	⋮	⋮	⋮					

Ministry of Defence © British Crown Copyright 2020/AWE

A5 Preliminary Neutron Diffraction Experiments on Cast Uranium

A5.1 Introduction

The first neutron diffraction experiment took place on the ENGIN-X diffractometer at the ISIS Neutron and Muon Source, Rutherford Appleton Laboratory, Didcot, UK, from 4th May 2017 until 7th May 2017. 3 days of beamtime were allocated under experiment number RB1710227, titled "Neutron Diffraction Study of Deformation in Coarse-Grained Cast Alpha-Uranium". A neutron texture measurement was also performed on the GEM beamline at ISIS as part of experiment RB1810071. The proposed aim of the first experiment was to measure the evolution of lattice strain and texture with deformation, in tension and compression, during loading through the yield point. A key goal was to identify the onset of plastic deformation by the deviation of the lattice strain from a linear relationship with applied stress. The suitability of this technique for detecting the formation of deformation twins was investigated.

Specimens were loaded in tension and compression with neutron measurement at each stress level. Analysis of the neutron spectra was performed using single-peak fitting and Rietveld refinement. Lattice strain and peak intensities are investigated, and the asymmetry between tensile and compressive deformation is observed. This is attributed to the tension-compression asymmetry of Schmid factors for twinning. These data are suitable for validation of CPFE simulations.

Ministry of Defence © British Crown Copyright 2020/AWE

Texture changes upon loading were identified in the Rietveld refinement. A novel implementation is presented which verifies that these changes are significant, and not a result of errors in the fitting parameters. The formation of deformation twins is expected to cause a measurable texture change. A method is presented that predicts the texture changes expected upon activation of each possible twin variant, from the relevant crystallographic twinning rotation. This is then applied with the aim of identifying the active twinning modes; however the results are inconclusive.

The experiments at ENGIN-X and GEM were designed and performed before the microstructural characterisation had been performed (sample preparation for EBSD analysis, to investigate the uranium grain size and orientations, is non-trivial). It is deduced that specimen movement during the ENGIN-X tests cause artefacts from texture changes within the measured gauge volume, which overwhelm the deformation-induced texture change. These artefacts occur due to the unusual and very coarse grain clusters in the material. Suggestions are made for improvements in the subsequent in-situ neutron experiments, which are reported in Chapter 4.

A5.2 Experimental Procedure and Data Analysis Methodology

A5.2.1 Neutron Diffraction on ENGIN-X

The ENGIN-X diffractometer is designed for the accurate measurement of changes in peak position in the neutron spectrum, corresponding to lattice strains. A full description of the instrument's capability is given in the literature [114] however the key features

Ministry of Defence © British Crown Copyright 2020/AWE

will be reproduced here for clarity. ISIS is a pulsed neutron source, where bunches of protons are accelerated into a tungsten target at a frequency of 50 pulses per second. The resulting collision generates pulses of neutrons with a range of energies (velocities) and directions, and those which pass through the relevant beam opening in the target station wall can enter the ENGIN-X instrument. A liquid methane moderator slows the neutrons whilst maintaining a high flux in the 1–3 Å wavelength range then a curved supermirror on the 50 m primary flight path to the instrument removes high-energy 'fast' neutrons from the incident spectrum. A beam chopper at the start of the primary flight path defines the detectable wavelength range ($\lambda_{max} - \lambda_{min}$), with increases in wavelength range accompanied by a proportionate decrease in neutron flux.

A schematic of the instrument is shown in figure 8.9. Vertical and horizontal slits define the size of the beam perpendicular to its axis. The two detector banks are centred in the horizontal plane, at ± 90° to the incoming beam. Radial collimators, consisting of parallel sheets coated with neutron-absorbing gadolinium oxide, restrict the neutrons that enter the detector to a defined length parallel to the beam. Together with the slits, the collimators define a nominally cuboid instrumental gauge volume[6] (IGV) from which the detected neutrons must originate. Each detector bank is located 1.53 m from the IGV,

[6] The gauge volume is actually a complex shape, with a Gaussian intensity profile along the beam, and a smoothed cut-off perpendicular to the beam[114]. However, for simplicity, it will be considered as cuboid in this work.

Ministry of Defence © British Crown Copyright 2020/AWE

spans ± 14° in the horizontal plane and ± 21° in the vertical plane, and consists of 5 vertically-stacked banks of vertically aligned ZnS scintillators, which detect the neutrons.

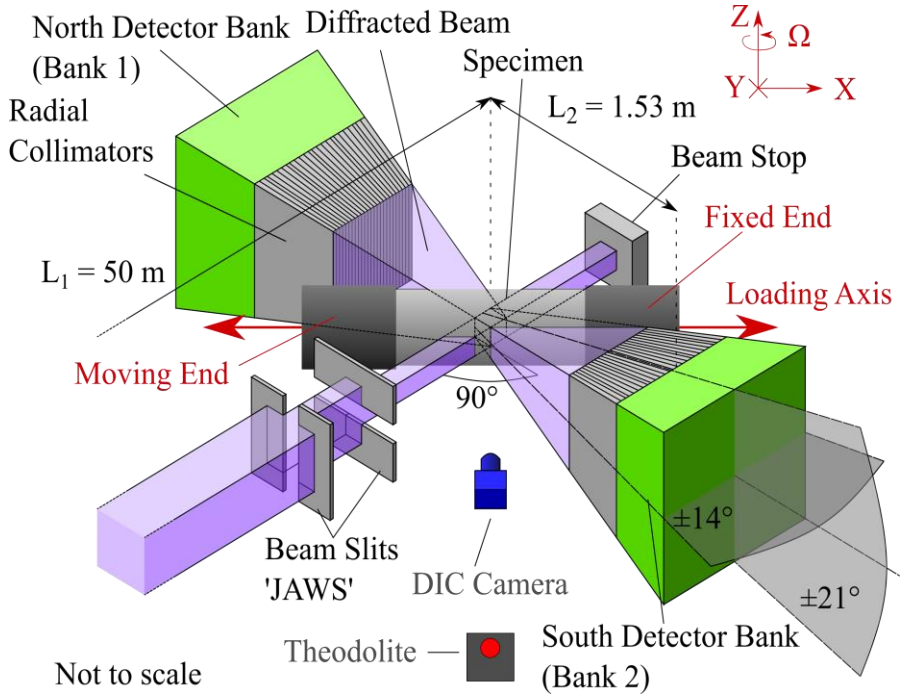


Figure 8.9. Schematic of the ENGIN-X instrument.

An accurate timing system linked to the proton pulse generation records the time-of-flight (TOF), between the neutron leaving the moderator and being detected. Since the experimental geometry is fixed, the time-of-flight can be related to the wavelength of the neutron via equation [8.4], the de Broglie relation,

$$\lambda = \frac{h}{p} = \frac{h}{mv} = \frac{ht}{mL} \qquad [8.4]$$

where *t* is the time-of-flight and *L* is the sum of the primary and secondary path lengths L_1 and L_2 from source to detector.

A crystal of interplanar spacing *d* will diffract neutrons of wavelength λ according to Bragg's law (equation [8.5]),

Ministry of Defence © British Crown Copyright 2020/AWE

$$\lambda = 2d \sin\theta \quad [8.5]$$

Where θ is the diffraction angle.

Equations [8.4] and [8.5] can be combined to form equation [8.6], relating the time-of flight of a peaks in the neutron spectrum with the interplanar spacing in the diffracting crystal. This is the time-of-flight neutron diffraction equation.

$$d = \frac{ht}{2mL \sin\theta} \quad [8.6]$$

The multiple detectors in each detector bank result in more neutron counts, and therefore shorter acquisition times. Each detector, however, has a slightly different scattering angle, so a time-focusing correction is applied to keep the value of $\frac{h}{2mL\sin\theta}$ constant for a particular nominal scattering angle [159].

The specimen is loaded in a horizontally mounted 100 kN Instron servo-hydraulic load frame, mounted on an X-Y-Z-Ω translation stage, with these co-ordinate directions marked in figure 8.9. The Instron load cell is attached to the fixed end of the load frame, and the hydraulic actuator is attached to the moving end. For this experiment, an optical camera (LaVision Imager E-Lite 5M) was mounted on a removable frame such that the specimen in the IGV could be observed. A permanently mounted, calibrated, theodolite was directly behind the camera with its optics aligned with the centre of the IGV. This allowed accurate positioning of each specimen with respect to the IGV.

Ministry of Defence © British Crown Copyright 2020/AWE

A5.2.1.1 Specimen Design

Depleted uranium specimens for tensile and compressive testing were designed in accordance to standard ENGIN-X drawings. Two specimens of each type were produced at AWE plc. with wire EDM and finished manually on a lathe. As shown in figures 8.10(a) and 8.10(b), the tensile specimens had a circular cross-section with a gauge diameter of 8 mm, and a parallel gauge length of 31.4 mm with fillets of 8 mm radius at each end. ISO M12 coarse threads (pitch of 1.75 mm) were added at both ends along the whole length of the shoulder. The two tensile specimens were denoted 'ND-T1' and 'ND-T2' (Neutron Diffraction – Tension 1 & 2).

The compressive specimens were cylindrical, as shown in figures 8.10(c) and 8.10(d), with a diameter of 14 mm and an axial length of 28 mm, giving an aspect ratio of 2. The two compressive specimens were denoted 'ND-C1' and 'ND-C2' (Neutron Diffraction – Compression 1 & 2).

Ministry of Defence © British Crown Copyright 2020/AWE

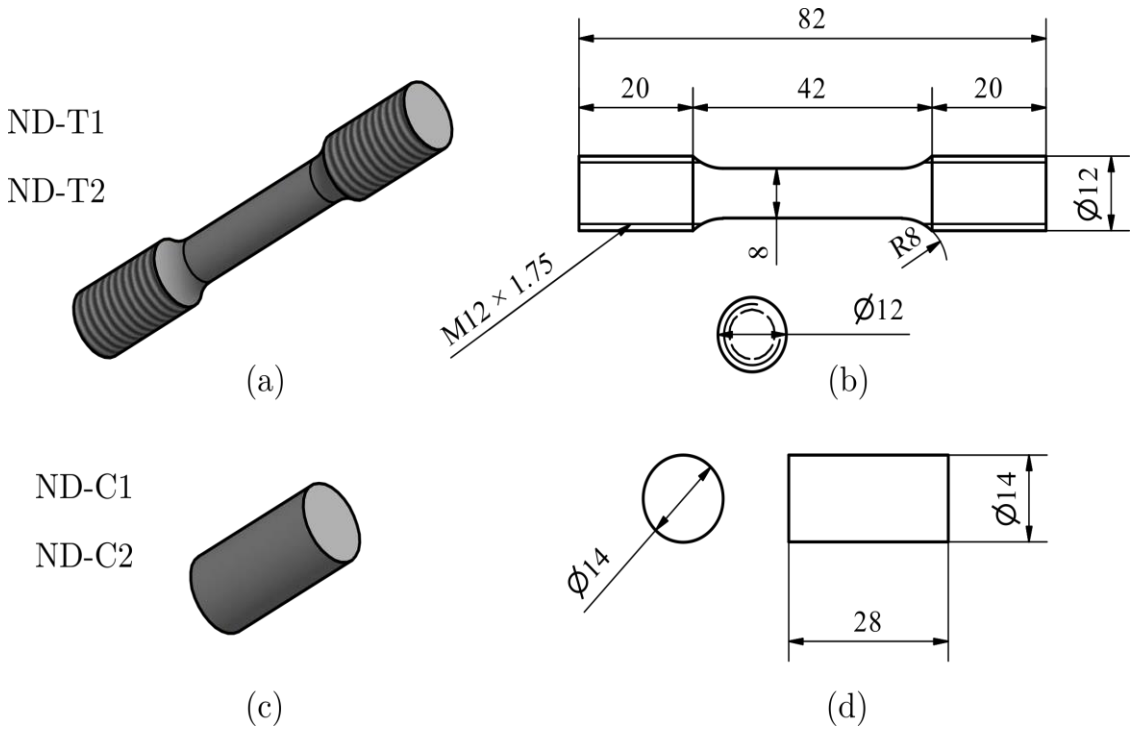


Figure 8.10. 3D rendering and engineering drawing of the tensile specimens, (a) and (b), and compression specimens, (c) and (d), tested at ENGIN-X. All dimensions in mm.

Each specimen was machined to a tolerance of ± 0.05 mm with the gauge region parallel to 0.01 mm. This gives nominal gauge-region cross-sectional areas of 50.27 mm² ± 0.63 mm² and 153.94 mm² ± 1.10 mm² for the tensile and compressive specimens respectively. The 100 kN load capacity of the Instron load frame would allow maximum stresses of 2000 MPa in tension, exceeding the expected fracture stress, and 650 MPa in compression, suitable to impose large strains.

Since the specimens were radioactive, it was necessary to design the experiment to prevent contamination of the ENGIN-X equipment. A set of grip extensions were designed to bridge the gap between the specimens and the load frame. This prevented direct contact between the specimen and the threaded grips, and in the case of the tensile specimen provided the added benefit of allowing the grip extensions to be handled

Ministry of Defence © British Crown Copyright 2020/AWE

instead of handling the specimen directly. The grip extensions were manufactured in the University of Oxford's Department of Engineering Science workshop from HSLA steel, according to the engineering drawings in figure 8.11. In addition to the grip extensions, a plastic tray was placed underneath each compression specimen to catch them in the event that hydraulic power was lost.

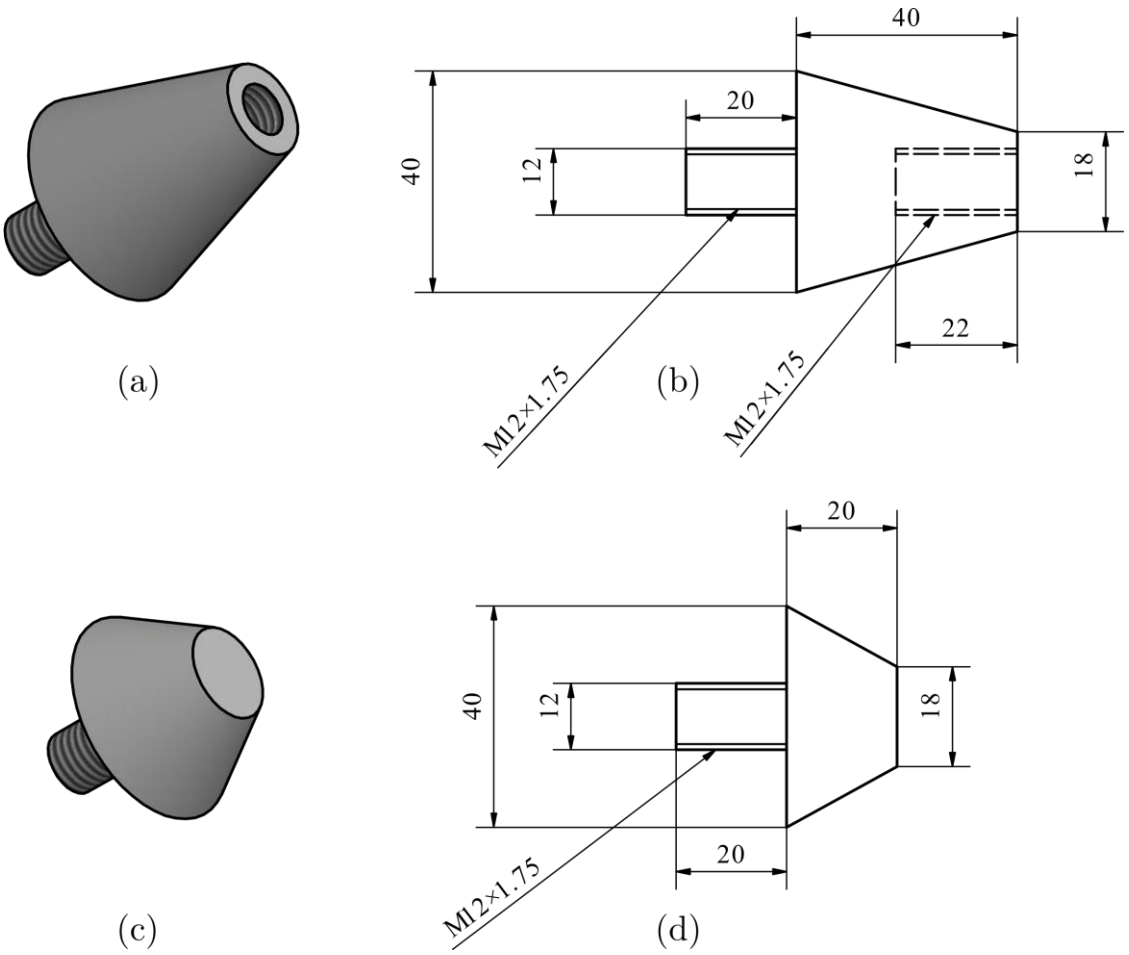


Figure 8.11. 3D rendering and engineering drawing of the tensile (a and b) and compressive (c and d) grip extensions manufactured for the experiment at ENGIN-X. All dimensions in mm.

A5.2.1.2 Experimental Procedure

The experimental procedure detailed in this section was followed for the three specimens tested; ND-T1, ND-T2, and ND-C1. Due to technical issues with the beam at ISIS during

Ministry of Defence © British Crown Copyright 2020/AWE

the experiment, specimen ND-C2 was not plastically deformed before the allocated experimental time ended.

The specimen to be tested was mounted into the load frame using locking pliers, and a small pre-load with a magnitude of 2 MPa (100 N tension, 300 N compression) was applied in load control to hold the specimen in place and to remove any slack in the load frame and grips. The DIC camera was removed to allow direct line of sight from the theodolite to the specimen. The translation table was moved in the X-Z plane to centre the specimen by eye on the theodolite cross-hair, and therefore on the IGV. The aligned specimens ND-T1 and ND-C1, as viewed through the theodolite optics, are shown in figures 8.12(a) and 8.12(b) respectively.

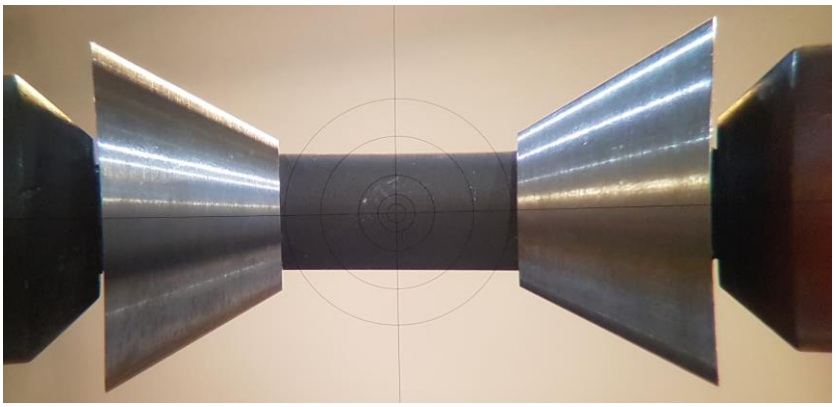
The neutron beam cross-section was defined using the final 'JAWS' slits as (width × height) 4 mm × 8 mm and 4 mm × 12 mm for the tensile and compression specimens respectively. Since the compressive specimens had a larger diameter a larger gauge volume could be used, which allowed a 25 % reduction in the count time for the acquisition of spectra for the compressive specimens, compared to the tensile specimens. 4 mm radial collimators were used throughout the experiment to define the IGV along the beam.

The beam chopper frequency was set to 16.67 Hz, giving a measurable d-spacing range of 0.394 Å to 3.231 Å, which was sufficient to capture the reflections from the main orthogonal {020}, {002} and {200} planes.

Ministry of Defence © British Crown Copyright 2020/AWE



(a)



(b)

Figure 8.12. Aligned specimens (a) ND-T1 and (b) ND-C1, as viewed through the optics of the ENGIN-X theodolite.

The microstructure of our cast uranium is very coarse, with large clusters of similarly oriented grains (section 3.2). If we assume a nominal grain size of 200 μm[7], and cubic grains, we can expect to find on around 16000 grains in the IGV for the tensile specimens, and 24000 grains in the case of the compression specimens. A potential issue with the clustered microstructure was that there may not be enough grains diffracting in each direction, resulting in a 'spotty' diffraction pattern that is not distributed evenly across the detector elements in each detector bank. The diffraction patterns from the individual

[7] A nominal grain size of 200 µm was expected in the proposal and design of the experiment, as the EBSD data were not available at that time.

Ministry of Defence © British Crown Copyright 2020/AWE

detector elements were checked to verify the presence of diffraction peaks across the entire detector bank; good quality diffraction patterns were observed.

The experimental risk assessment dictated that the specimen surface was to be covered in aluminium foil, in order to catch any particles that would be released in the event of specimen fracture. This precluded the use of the conventional clip-gauge extensometer, and optical strain measurement of the specimen with DIC could not be used as the specimen surface was not visible.

It was decided to instead perform DIC on the grip extensions that were applying the load to each specimen, and to use the relative displacements of each end to provide an estimate of the average strain in the specimen. A single 8-bit greyscale image with a resolution of 2448 pixels × 2050 pixels, in landscape orientation, was captured before each neutron measurement was started. Images were captured from the camera over USB using LaVision DaVis v8.

An initial neutron measurement was taken with the sample under pre-load. This would act as the reference, unstrained, state for the specimen, from which any measured strains could be calculated. The scan duration was determined by the time taken for the integrated beam current to reach a threshold value of 20 μAh for tensile specimens and for 15 μAh for compression specimens. The choice of an integrated current criterion allows for the same number of neutrons to be incident on the sample in each measurement, and simply varies the measurement time to account for fluctuations in

Ministry of Defence © British Crown Copyright 2020/AWE

beam current or beam outages during the measurement. Each measurement is automatically assigned a unique run number which was used to identify the measurement during data analysis. After each neutron measurement was completed, the magnitude of the applied load was increased in load-control at a rate of 1 MPa s^{-1}, followed by a DIC image acquisition and subsequent neutron measurement.

The risk assessment required that the specimens would not be fractured, so a stress limit of 310 MPa was applied, as this was expected to correspond to strains less than 2 %, and therefore not be at risk of fracture.

This procedure was repeated for each specimen until a stress magnitude of 310 MPa was reached, after which the specimen was unloaded to a stress magnitude of 10 MPa at a rate of 1 MPa s^{-1} for specimens ND-T1 and ND-T2, and a rate of 0.67 MPa s^{-1} for specimen ND-C1. For specimens ND-T1 and ND-C1, the magnitude of the load was increased by 10 MPa between each scan, whilst in ND-T2 a smaller step size of 5 MPa was chosen between 110 MPa and 190 MPa with a larger 20 MPa step size elsewhere, the aim being to better capture the elastic-plastic transition at yield. A summary of the experimental parameters is given in table 8.4.

Table 8.4. Experimental parameters for neutron diffraction of depleted uranium at experiment RB1710227 at ENGIN-X.

Specimen	Pre-load (MPa)	Load step (MPa)	Peak. stress (MPa)	Scan duration (μAh)	Beam width (mm)	Beam height (mm)	Radial collimation (mm)	Scan at unload?
ND-T1	2	10	310	20	4	8	4	No
ND-T2	2	5 or 20	310	20	4	8	4	−10 MPa
ND-C1	−10	−10	−310	15	4	12	4	−10 MPa

Ministry of Defence © British Crown Copyright 2020/AWE

A5.2.1.3 Data Preparation

Initial processing of the experimental data was performed in the ENGIN-X OpenGenie software [140]. This is a routine analysis method for data from this beamline. Since spotty diffraction did not occur, the spectra from all elements in a detector bank were summed into a single histogram, taking into account the differences in flight path for each element, using the OpenGenie routine 'rfocus'.

A recent calibration measurement performed on a CeO_2 powder sample, was used to determine the diffractometer constants DIFC, DIFA and ZERO which relate the neutron time-of-flight of a reflection to the d-spacing via the quadratic relation shown in equation [8.7]:

$$t = \mathrm{DIFC}\ d + \mathrm{DIFA}\ d^2 + \mathrm{ZERO} \qquad [8.7]$$

A5.2.1.4 Single-peak fitting

Single-peak fits were performed using the `analyse_scan/peaks` routine in OpenGenie. An upper and lower time-of-flight bound were defined for each peak and the profile `Vexp`[140] consisting of a Voigt convoluted with a sharp-edged exponential with a linear background was fitted:

$$y\ t\ = Mt + C + \left(A \times \left(\mathrm{F}_{\mathrm{Voigt}}\ t, t_0, \sigma, \tau\ * \mathrm{F}_{\mathrm{exp}}\ t, \tau\ \right)\right) \qquad [8.8]$$

where

Ministry of Defence © British Crown Copyright 2020/AWE

$$\mathrm{F}_{\mathrm{Voigt}}\ t, t_0, \sigma, \gamma\ = \frac{1}{\sigma\sqrt{2\pi}} \exp\left(\frac{-\ t - t_0\ ^2}{2\sigma^2}\right) * \frac{\gamma}{\pi\ t^2 + \gamma^2} \qquad [8.9]$$

and

$$F_{exp}\ t, \tau\ \begin{cases} 0 & if\ t/\tau < \ 0 \\ \dfrac{1}{|\tau|} \exp \dfrac{-t}{\tau} & if\ t/\tau > \ 0 \end{cases} \qquad [8.10]$$

This results in 7 real-valued parameters being fitted; $\mathrm{M}, \mathrm{C}, \mathrm{A}, \mathrm{t}_{\mathrm{o}}, \sigma, \gamma$ and τ. The integrated intensity of each peak was normalised by the intensity of that peak in the initial pre-load neutron measurement such that peaks with relative intensities greater than 1 have increased in intensity during the experiment, and vice versa. The d-spacing of a peak is found by transforming t_0, the centroid of the Gaussian function, using equation [8.7]. Lattice strains for a reflection {*hkl*}, ε^{hkl}, were calculated from the measured d-spacing using equation [8.11] where the reference lattice spacing for that reflection, ε_0^{hkl}, is the value measured with the sample in the initial unloaded state.

$$\varepsilon^{\mathrm{hkl}} = \frac{d^{hkl} - d_0^{hkl}}{d_0^{hkl}} \qquad [8.11]$$

This choice of reference state means we are measuring the elastic strain changes that are produced as a result of external stress, and does not quantify any initial residual stress state that will be present in the material.

Ministry of Defence © British Crown Copyright 2020/AWE

A5.2.1.5 Rietveld refinement

A Rietveld refinement method in the GSAS software package [118] was used to fit multi-peak profiles to the measured spectra. This fits parameters including the lattice parameters, peak profile (shape), and peak intensity (sample texture) to the entire spectrum at once. Consequently this method cannot detect variations in the position or intensity of individual peaks in isolation, but rather is sensitive to changes affecting the entire spectrum, such as preferred grain orientation changing the intensities of the particular diffraction peaks.

Peak Profile

The peak profile used is 'TOF profile 3' from the GSAS manual [118], discussed here for completeness. This profile, $H\ \Delta T$, assumes Lorentzian peak broadening and consists of a pseudo-Voigt convolved with back-to-back exponentials:

$$H\ \Delta T\ = P\ \Delta T\ * E\ \Delta T \qquad [8.12]$$

which can be equivalently expressed as:

$$H\ \Delta T\ = \int P\ \Delta T - \tau\ \ E\ \tau\ \ d\tau \qquad [8.13]$$

where $\Delta T = t - t_0$ is the difference between the reflection position t_0 and the point on the profile t and τ is a dummy variable of integration.

Ministry of Defence © British Crown Copyright 2020/AWE

The back-to-back exponentials $E\ t\ $ represent the time-of-flight profile of the generated neutrons at the spallation source [115], with a steep increases and shallower decrease in neutron count with increasing time-of-flight:

$$E\ t\ = \begin{cases} 2N\ exp(\alpha t) & if\ t \leq 0 \\ 2N\ exp(-\beta t) & if\ t \geq 0 \end{cases} \quad [8.14]$$

where $\alpha > \beta > 0$ and the normalisation factor *N* is defined as:

$$N = \frac{\alpha\beta}{2(\alpha + \beta)} \quad [8.15]$$

where α and β are d-spacing dependent coefficients:

$$\alpha = \frac{\alpha_1}{d} \ \text{ and } \ \beta = \beta_0 + \frac{\beta_1}{d^4} \quad [8.16]$$

where α_0, β_0, and β_1 are fitting parameters.

The pseudo-Voigt $P(t)$ is a linear combination of a Lorentzian, $L\ t\ ,$ and a Gaussian, $G\ t, \sigma\ ,$ profile with relative proportions determined by a mixing factor η.

$$P\ t\ = \eta L\ t, \gamma\ +\ 1 - \eta\ G\ t, \sigma \quad [8.17]$$

The Lorentzian profile is defined as:

$$L\ t, \gamma\ = \frac{1}{2\pi} \frac{\gamma}{\left(\frac{\gamma}{2}\right)^2 + t^2} \quad [8.18]$$

where the Lorentzian coefficient, γ, is defined as:

$$\gamma = \gamma_0 + \gamma_1 d + \gamma_2 d^2 \quad [8.19]$$

Ministry of Defence © British Crown Copyright 2020/AWE

where γ_0, γ_1, and γ_2 are the fitting parameters. Other parameters defined in GSAS, γ_{1e}, γ_{2e}, γ_{2s}, and those comprising γ_L, were held at zero. The Gaussian profile is defined as:

$$G\ t,\sigma\ \frac{1}{\sqrt{2\pi\sigma^2}} = \exp\left(-\frac{t^2}{2\sigma^2}\right) \quad [8.20]$$

where the variance of the Gaussian, σ^2, is defined as:

$$\sigma^2 = \sigma_0^2 + \sigma_1^2 d^2 + \sigma_2^2 d^4 \quad [8.21]$$

where σ_0^2, σ_1^2, and σ_2^2 are the fitting parameters.

Peak Width Contributions

The overall peak width has contributions from both the Gaussian and Lorentzian coefficients σ and γ. These are experimentally derived from at least three peak-broadening contributions; instrumental broadening, particle size broadening and strain broadening. Instrumental broadening is related to the minimum resolvable peak width by the instrument in the case of a perfect specimen with no other broadening contributions. Peak broadening can be induced by sub-micron crystallites, however it will be seen that this has no effect in this coarse-grained material, so can be ignored. Strain broadening is related to strain-induced defects within the crystalline lattice. Each set of hkl planes within the gauge volume has a range of d-spacings due to local elastic strains, such as those around dislocations. Plastic deformation typically increases the dislocation density, therefore the magnitude of strain broadening is often related to the

Ministry of Defence © British Crown Copyright 2020/AWE

amount of plastic strain. This relation is only qualitative without a tedious calibration procedure.

For the 'TOF profile 3' peak profile used here, the particle size broadening is Lorentzian, and proportional to d^2 [118], so it affects the third term of equation [8.19]. The parameter γ_2 is related to the particle size via equation [8.22], where C is the diffractometer constant DIFC, K is the Scherrer constant, a shape factor with a value of approximately 1, and p is the particle size (in Angstroms).

$$\gamma_2 = \frac{CK}{p} \qquad [8.22]$$

For ENGIN-X, DIFC is on the order of 10^4, so for 200 μm grains (2×10^6 Å), $\gamma_2 < 0.01$ and is considered negligible.

Strain broadening is also Lorentzian, and proportional to d [118], so affects γ_1 in the second term of equation [8.21]. The instrumental broadening is Gaussian in shape, so can be deconvoluted from the Lorentzian broadening, so no corrections are needed.

Refinement Process

The refinement was performed using the GENLES least-squares algorithm in GSAS. The reduced chi-squared statistic, χ_r^2, is calculated after each iteration as a measurement of the goodness of fit. The algorithm was iterated until the change in the values of the parameters between each iteration became small. Specifically, when the parameter $S = \sum_{i=1}^{N_v} \left(\frac{\Delta v_i}{\sigma_i}\right)^2$ became less than a threshold of 0.01, where N_v is the number of variables

Ministry of Defence © British Crown Copyright 2020/AWE

being refined, σ_i is the standard deviation of the i^{th} variable after the latest refinement step, and Δv_i is the change in the value of the i^{th} variable since the previous refinement iteration.

A multi-step approach was necessary to avoid numerical instability, so the number of degrees of freedom available (i.e. the number of fitting parameters) was increased between each fitting step. An initial fit to each spectrum was performed using the crystal structure of alpha-uranium (spage group = Cmcm, *a* = 2.8533 Å, *b* = 5.8625 Å, *c* = 4.9595 Å, $\alpha = \beta = \gamma = 90°$) as a starting condition. Only the part of the spectrum with *d* > 0.68 Å was fitted as the region with smaller d-spacings contain very closely spaced peaks with high a low signal to noise ratio. A total of 91 reflections were included, from {020} at $d = 2.935$ Å to {315} at $d = 0.682$ Å. The orientation of the 91 reflections with respect to the crystal axes are shown on an inverse pole figure in figure 8.13.

Ministry of Defence © British Crown Copyright 2020/AWE

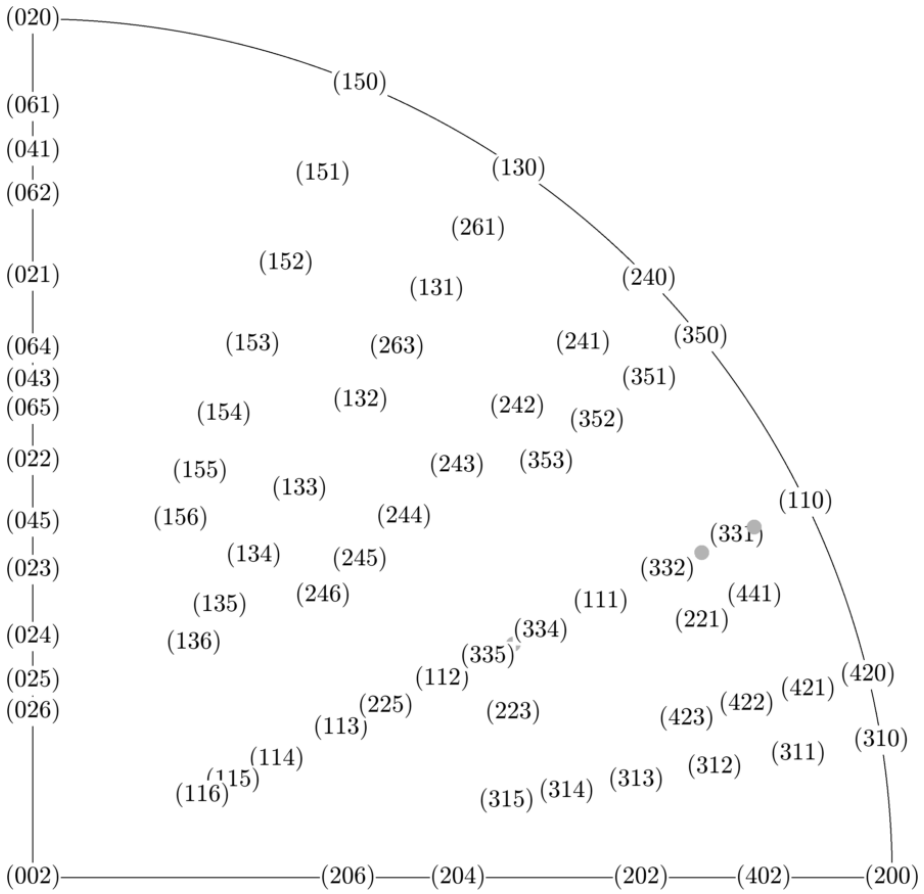


Figure 8.13. Location of the 91 reflections included in the Rietveld refinement, plotted on an inverse pole figure. The reflection position is located at the centre of each label, with the exception of the (223), (221), and (441) reflections, whose location is marked by a grey marker directly above the label. Where a reflection is a multiple of another reflection, for example the (040) and (020) reflections, only the lowest-order reflection is shown.

Optimisation of the three lattice parameters (*a*, *b*, *c*) was performed in the secondary fitting step.

The tertiary step involved refining the shape of the peak profile by varying the parameters σ_1 and γ_1, which capture the effects of peak broadening due to sample straining[107]. A damping factor, which slows down the rate of change of the parameters with each fitting iteration by applying only a fraction of the calculated shift, was necessary to avoid numerical instability. The applied shift is calculated as $\Delta v_i^{\mathrm{app}} = \left(1 - \frac{\mathrm{D}}{10}\Delta \mathrm{v}_\mathrm{i}^{\mathrm{calc}}\right)$ where *D* is the damping factor and $\Delta \mathrm{v}_\mathrm{i}^{\mathrm{app}}$ and $\Delta \mathrm{v}_\mathrm{i}^{\mathrm{calc}}$ are the applied and

Ministry of Defence © British Crown Copyright 2020/AWE

calculated changes in the value of the i^{th} variable. A damping factor of 3, corresponding to the applied shift being 70 % of the calculated shift, was found to be suitable for this dataset.

The final fitting step involved quantifying the preferred orientation, known as texture, within the sample. The previous fitting step assumed scattering was coming from a completely random distribution of grains, and that the integrated intensity of the peak is only related to the structure factor of the crystal and the multiplicity of the reflection – i.e. it should be the same in all directions, and therefore be measured the same in the two opposing detector banks. If the sample contains a texture, with more grains having a particular {*hkl*} plane aligned along the direction of the relevant diffraction vector for a particular detector (the axial direction for the North Bank and the horizontal transverse direction for the South Bank), then the measured intensity of the {*hkl*} reflection in that detector will be larger than for a random texture.

Peak Intensities – Rietveld Texture Measurement

Quantifying the ratio between the measured intensity in a {*hkl*} reflection, and the {*hkl*} peak intensity expected from a random distribution of grains, gives a measure of texture along the diffraction vector, in units of multiples of random distribution (MRD). A measurement is therefore available for each of the 91 reflections in the d-spacing range analysed. These measurements could be plotted as points in spherical co-ordinates in the crystal co-ordinate system where the radius is equal to the texture (in MRD) and the

Ministry of Defence © British Crown Copyright 2020/AWE

direction is parallel to the {*hkl*} plane normal. It is desirable to fit a smoothly varying function to these scattered data points, and the spherical harmonics are used as orthogonal basis functions for this purpose. The implementation of this method in GSAS is described by Von Dreele et al. [160] The general axis equation for the preferred orientation correction factor, O, is shown in equation [8.23], where h is the direction with respect to the crystal axes, and y is the direction with respect to the specimen axes. The correction factor, O, is created from a finite series of spherical harmonics, where L is the order of the harmonics and the C_l^{mn} are the coefficients of the spherical harmonic functions that consist of k_l^m and k_l^m [118].

$$\mathrm{O}\ h, y\ = 1 + \sum_{l=2}^{L} \frac{4\pi}{2l+1} \sum_{m=-l}^{l} \sum_{n=-l}^{l} C_l^{mn} k_l^m\ h\ k_l^n\ y \qquad [8.23]$$

The values of the harmonic factors k_l^m and k_l^m depend on the relative orientation between the reflection direction and the crystal and macroscopic specimen axes respectively. Friedel's law [136] states that the intensities of the (hkl) and the (hkl) are equal, which results in only the 'even' $L = 2, 4, 6 \ldots$ terms contributing to the texture correction factor, as noted by Von Dreele [160].

The value of the preferred orientation correction factor O along a particular direction is a measure of the texture, in MRD, along that direction. The order, L of the harmonics defines the sharpest texture that can be described by the fitting function. If L is too low, any sharp textures will be poorly fitted, but if it is too large, overfitting will occur which can result in certain directions being assigned values which are negative, which is

Ministry of Defence © British Crown Copyright 2020/AWE

unphysical. Refinements were performed with L = 8, 10, 12, and 14, and L = 10 was found to be most suitable for this analysis. A damping factor of 3 was necessary to ensure convergence. The values of the preferred orientation correction factor as a function of crystal direction were converted to inverse pole figures (IPFs) using the SMARTSinvpol script from SMARTSware [139].

A5.2.1.6 Rietveld Texture Measurement Error Analysis

Texture measurement via this method relies on the fitting of multiple parameters, and the fitting uncertainty associated with each of these parameters propagates into the resulting inverse pole figure representation of texture. The least squares fitting in GSAS reports the spherical harmonic coefficients C_l^{mn} and their associated error $\sigma(C_l^{mn})$ in the .LST files that are created during the refinement. Since we were interested in identifying potentially small changes in the sample texture, it was desirable to quantify the uncertainty in each the final inverse pole figures. Unfortunately, the SMARTSinvpol routine used to convert the coefficients C_L^{mn} to the texture IPF did not perform such a calculation, and as it is a 'black box' to the end user, it was not possible to modify the code.

In this section, I present the method I developed to allow the quantification of the effect of the uncertainties in the coefficients C_l^{mn} on the inverse pole figure representation of texture. Whilst the theory underpinning this is simple, it enables a useful quantification

Ministry of Defence © British Crown Copyright 2020/AWE

of the error in measured textures when performing a GSAS/SmartsInvPol analysis of engineering neutron diffraction measurements.

It is necessary to obtain an expression for the texture, implemented in GSAS as the orientation-dependent Preferred Orientation Correction Factor $\mathrm{O}(\mathbf{r})$, as a function of the spherical harmonic coefficients C_l^{mn}. Conventional error analysis formulae can then be applied to relate the uncertainties in these coefficients, $\sigma(C_l^{mn})$, to the uncertainties in the texture, $\sigma\ O(\mathbf{r})$.

We begin with equation [8.23], taken from the GSAS manual. To simplify the notation, I have combined the summations over l, m, and n into the single summation symbol in equation [8.24].

$$\mathrm{O}(\mathbf{r}) = 1 + \sum_{l,m,n} \frac{4\pi}{2l+1} C_l^{mn}\ k_l^m(\mathbf{r})\ k_l^n(\mathbf{r}). \qquad [8.24]$$

IPF Basis Functions

I shall then define the basis functions $B_l^{mn}(\mathbf{r})$, where $B_l^{mn}(\mathbf{r}) = \frac{4\pi}{2l+1} k_l^m(\mathbf{r})\ k_l^n(\mathbf{r})$. In the current case where $L = 10$, there are 20 basis functions defined. The total orientation function $\mathrm{O}(\mathbf{r})$ is a linear combination of the basis functions $B_l^{mn}\ \mathbf{r}$ weighted by their coefficients C_l^{mn}, as shown in equation [8.25].

$$\mathrm{O}(\mathbf{r}) = 1 + \sum_{l,m,n} C_l^{mn}\ \mathrm{B_l^{mn}}(\mathbf{r}) \qquad [8.25]$$

Ministry of Defence © British Crown Copyright 2020/AWE

By introducing the definition $I_l^{mn}(\mathbf{r}) = C_l^{mn}\ \mathrm{B}_1^{\mathrm{mn}}(\mathbf{r})$, the total orientation function can be represented as a sum of single terms, which facilitates error analysis.

$$\mathrm{O}(\mathbf{r}) = 1 + \sum_{l,m,n} I_l^{mn}(\mathbf{r}) \qquad [8.26]$$

$$\mathrm{O}(\mathbf{r}) = 1 + I_2^{00}(\mathbf{r}) + I_2^{02}(\mathbf{r}) + \cdots \qquad [8.27]$$

Applying the conventional error combination formula[8] gives equation [8.28].

$$\sigma^2\ O(\mathbf{r})\ = \sigma^2\ 1\ + \sigma^2\ I_2^{00}(\mathbf{r})\ + \sigma^2\ I_2^{02}(\mathbf{r})\ + \cdots \qquad [8.28]$$

$$\sigma^2\ O(\mathbf{r})\ = \sigma^2\ I_2^{00}(\mathbf{r})\ + \sigma^2\ I_2^{02}(\mathbf{r})\ + \cdots \qquad [8.29]$$

So we must obtain an expression for $\sigma^2\ I_l^{mn}(\mathbf{r})$. Since $I_l^{mn}(\mathbf{r})$is the product of C_l^{mn} and $\mathrm{B}_1^{\mathrm{mn}}(\mathbf{r})$, the relevant error combination formula[9] gives equation [8.30].

$$\left(\frac{\sigma\ I_l^{mn}(\mathbf{r})}{I_l^{mn}(\mathbf{r})}\right)^2 = \left(\frac{\sigma\ C_l^{mn}}{C_l^{mn}}\right)^2 + \left(\frac{\sigma\ \mathrm{B}_1^{\mathrm{mn}}(\mathbf{r})}{\mathrm{B}_1^{\mathrm{mn}}(\mathbf{r})}\right)^2 \qquad [8.30]$$

The basis functions $B_l^{mn}(\mathbf{r})$ are defined exactly, so $\sigma\ B_l^{mn}(\mathbf{r})\ = 0$. We can then obtain the simple expression in equation [8.33] for the error in each harmonic contribution $I_l^{mn}(\mathbf{r})$.

$$\frac{\sigma\ I_l^{mn}(\mathbf{r})}{I_l^{mn}(\mathbf{r})} = \frac{\sigma\ C_l^{mn}}{C_l^{mn}} \qquad [8.31]$$

[8] If $Z = A \pm B \pm C$, the standard error in Z, σ_Z, is calculated as $\sigma_Z{}^2 = \sigma_A{}^2 + \sigma_B{}^2 + \sigma_C{}^2$. The absolute errors are added in quadrature.

[9] If $Z = AB$, the standard error in Z, σ_Z, is calculated as $\frac{\sigma_Z}{Z}{}^2 = \frac{\sigma_A}{A}{}^2 + \frac{\sigma_B}{B}{}^2$. The fractional errors are added in quadrature.

Ministry of Defence © British Crown Copyright 2020/AWE

$$\sigma\ I_l^{mn}(\mathbf{r})\ = \frac{\sigma\ C_l^{mn}}{C_l^{mn}} C_l^{mn}\ \mathrm{B_l^{mn}}(\mathbf{r}) \quad [8.32]$$

$$\sigma\ I_l^{mn}(\mathbf{r})\ = \sigma\ C_l^{mn}\ \ \mathrm{B_l^{mn}}(\mathbf{r}) \quad [8.33]$$

Substituting equation [8.33] into equation [8.29], we can obtain equation [8.34], an expression for the error $\sigma\ O(\mathbf{r})$ in the total orientation distribution as a function of the basis functions and the errors in each of the spherical harmonic coefficients.

$$\sigma^2\ O(\mathbf{r})\ = \sigma^2\ C_2^{00}\ \ \mathrm{B_2^{00}}(\mathbf{r})^2 + \sigma^2\ C_2^{02}\ \ \mathrm{B_2^{02}}(\mathbf{r})^2 + \cdots \quad [8.34]$$

$$\sigma\ O(\mathbf{r})\ = \sqrt{\sigma^2\ C_2^{00}\ \ \mathrm{B_2^{00}}(\mathbf{r})^2 + \sigma^2\ C_2^{02}\ \ \mathrm{B_2^{02}}(\mathbf{r})^2 + \cdots} \quad [8.35]$$

Therefore we must know the basis functions $B(\mathbf{r})$ in order to calculate the error in the measured orientation distribution.

Calculation of the basis functions and the total orientation function is hidden within the GSAS routines. I developed a method to generate IPF visualisations of the basis functions such that these could then be summed, weighted by their coefficients, to produce the overall orientation distribution as an IPF (equation [8.25]). The error in the calculated IPF can then be calculated and visualised using equation [8.35].

Let $O^{l'm'n'}(\mathbf{r})$ be $O(\mathbf{r})$ with $C_{l'}^{m'n'} = 1$, and all other $C_l^{mn} = 0$. Applying this to equation [8.25], we see that only two terms remain.

$$\mathrm{O^{l'm'n'}}\ \mathbf{r}\ = 1 + 1 \bullet B_{l'}^{m'n'}\ \mathbf{r} \quad [8.36]$$

Rearranging for $B_{l'}^{m'n'}(\mathbf{r})$,

Ministry of Defence © British Crown Copyright 2020/AWE

$$B_{l'}^{m'n'}(\mathbf{r}) = \mathrm{O}^{\mathrm{l'm'n'}}(\mathbf{r}) - 1 \qquad [8.37]$$

Therefore each basis function can be obtained using equation [8.38].

$$B_{L'}^{m'n'}(\mathbf{r}) = \mathrm{O}^{\mathrm{l'm'n'}}(\mathbf{r}) - \mathrm{O}^{000}(\mathbf{r}) \qquad [8.38]$$

I found that it was possible to modify the .LST files to set the relevant l, m, and n parameters to 0 and 1. In this way, a separate .LST file was created for each of the 20 basis functions. Figure 8.14 shown the section of the .LST file in the case where the desired *l*, *m*, and *n* are 2, 0, and 0 respectively By using these files as inputs to `SmartsInvPol`, I could generate an IPF representation of $O^{l'm'n'}(\mathbf{r})$ for each basis component. Then, as in equation [8.38], by subtracting from these IPFs the IPF of $O^{000}(\mathbf{r})$ (a value of 1 in all crystal directions), one could retrieve the individual basis functions $B_{l'}^{m'n'}(\mathbf{r})$.

```
⋮

Orientation distribution coefficients for powder data:
 Phase no.:    1 Damping factors:    0    3 Sample symm. 0
 Sample orientation angles om-0, chi-0 & phi-0:    0.00    0.00    0.00 pn:   0   0   0
 Index(lmn):   2  0  0 pn   2  0  2 pn   4  0  0 pn   4  0  2 pn   4  0  4 pn   6  0  0 pn   6  0  2 pn   6  0  4 pn
 Coeff.    :   1.0000   0   0.0000   0   0.0000   0   0.0000   0   0.0000   0   0.0000   0   0.0000   0   0.0000   0
 Index(lmn):   6  0  6 pn   8  0  0 pn   8  0  2 pn   8  0  4 pn   8  0  6 pn   8  0  8 pn  10  0  0 pn  10  0  2 pn
 Coeff.    :   0.0000   0   0.0000   0   0.0000   0   0.0000   0   0.0000   0   0.0000   0   0.0000   0   0.0000   0
 Index(lmn):  10  0  4 pn  10  0  6 pn  10  0  8 pn  10  0 10 pn
 Coeff.    :   0.0000   0   0.0000   0   0.0000   0   0.0000   0

⋮
```

Figure 8.14. The relevant section of the .LST file used to generate the $O^{200}(\mathbf{r})$ texture component from which the first basis function, $B_2^{00}(\mathbf{r})$, was calculated using equation [8.38]. Note that the coefficients (labelled 'Coeff.') have been set to 1 for the desired $l = 2$, $m = n = 0$ component, whilst all other coefficients are set to zero.

The 20 basis functions for the case where $L = 10$ are shown in figure 8.15.

Ministry of Defence © British Crown Copyright 2020/AWE

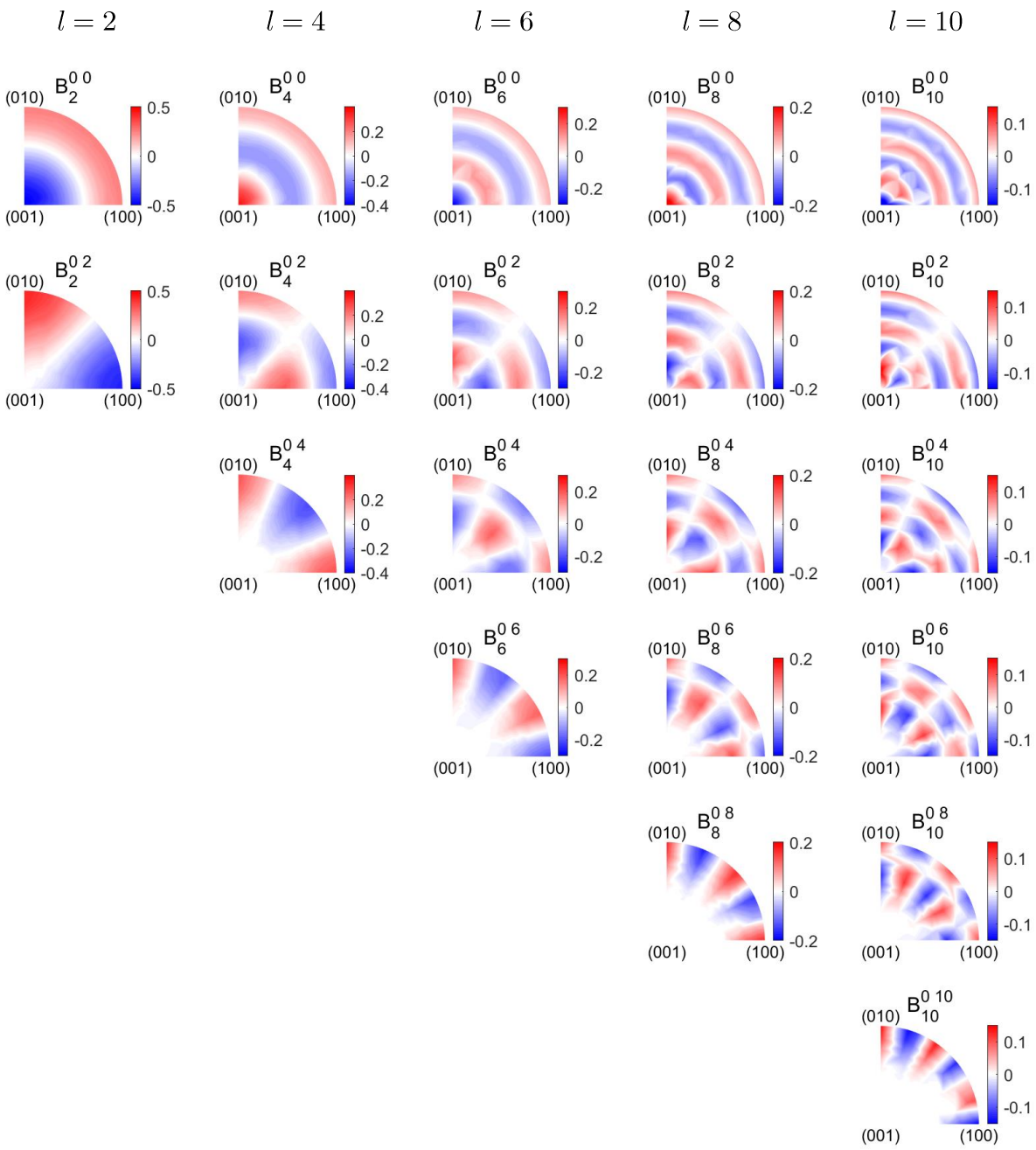


Figure 8.15. Spherical harmonic basis functions $B_L^{mn}(\mathbf{r})$ implemented in GSAS for the ENGIN-X experiment, for the case where $L = 10$, plotted as a function of crystal orientation on the orthorhombic inverse pole figure.

A5.2.1.7 Calculation of lattice parameter strains from Rietveld data

In a similar manner to the lattice strains ε_{hkl} calculated from the single-peak fits using equation [8.11], the variation in lattice parameter can be converted to a *lattice parameter*

Ministry of Defence © British Crown Copyright 2020/AWE

strain as defined in equation [8.39]. The lattice parameters of the unit cell are *a*, *b*, and *c* and their zero-strain reference lattice parameters are a_0, b_0, and c_0 respectively.

$$\varepsilon_a = \frac{a - a_0}{a_0} \qquad \varepsilon_b = \frac{b - b_0}{b_0} \qquad \varepsilon_c = \frac{c - c_0}{c_0} \qquad [8.39]$$

An issue with this calculation from experimental data is that the value of strain depends strongly on the value of the reference lattice parameters (in general denoted d_0). Since these are conventionally taken to be the measured lattice parameter with the specimen under pre-load, any error in this measured *d*-spacing can result in incorrect strains. Figure 8.16 shows the variation of the *a*-parameter in specimen T1 with stress in the initial stages of the test. There is variation in the measured lattice parameter such that the experimental d_0 parameter (red dot) is greater than what would be expected by a simple extrapolation of the best-fit line through the data (dotted line) to the pre-load stress. In fact, a more suitable value for the d_0 parameter would be the intersection of this best-fit line with the zero-stress y-axis. This has two benefits; firstly, the use of a best-fit line reduces the dependence of d_0 on a single measurement point, and secondly it allows a true zero-stress reference d_0 to be used instead of an arbitrary pre-stress value. It is not suitable to just use the literature values for the unit cell parameters[14] as these will differ from the real values due to residual stresses and differences in chemistry.

Ministry of Defence © British Crown Copyright 2020/AWE

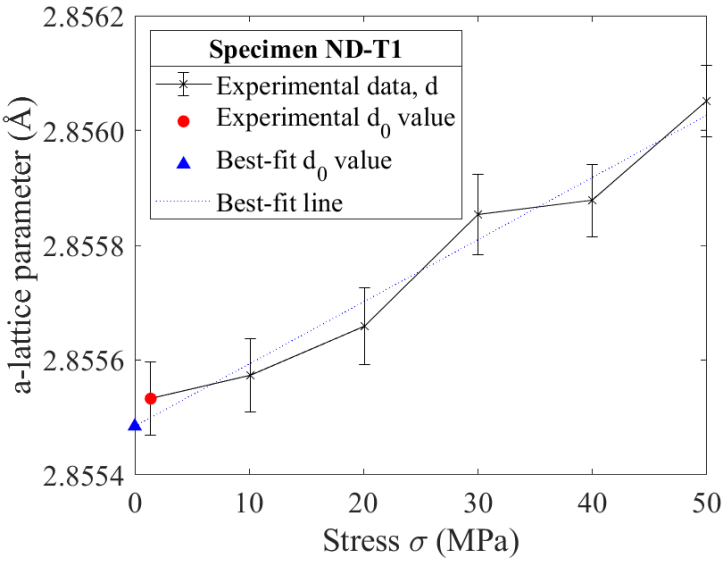


Figure 8.16. Variation in lattice parameter as a function of stress, in specimen T1 with stress in the intital stages of the test on ENGIN-X. The experimental d_0 value at the pre-load of 2 MPa (red circle) is shown alongside the d_0 value extrapolated from the best-fit line (blue triangle).

Fitting through a larger number of data points will give the most accurate measurement of d_0, however care must be taken to only include data points in the elastic region, at stresses below the yield point, where the lattice parameter varies linearly with applied stress. Inclusion of data points after the yield point will change the gradient and intercept of the fitted line and therefore give an incorrect d_0 value. For this data, it can be challenging to identify the yield point as the deviations from linearity are not always clear. For example, in figure 8.17, the a-parameter exhibits a linear response at low stress and a clear deviation from this gradient at higher stresses. Whilst the b-parameter does deviate from linearity, the point of deviation is not easily observable in this figure. In both cases, it is challenging to robustly identify the point of transition away from linearity, and requires an element of human judgement.

Ministry of Defence © British Crown Copyright 2020/AWE

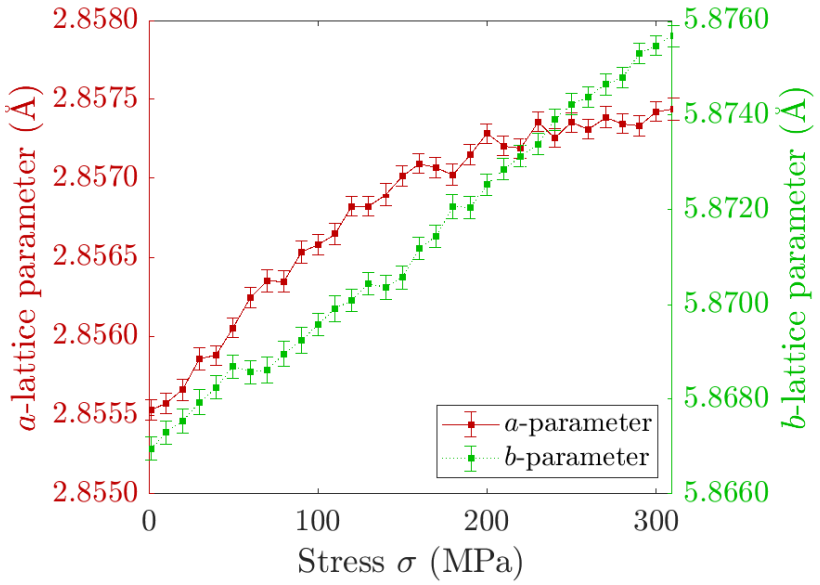


Figure 8.17. Variation of the *a* and *b* lattice parameters as a function of stress for specimen ND-T1. The deviation from linearity is more easily identifiable for the a-parameter than for the b-parameter. Note the y-axes have a different scale for each parameter.

Identification of Crystallographic Yield Point

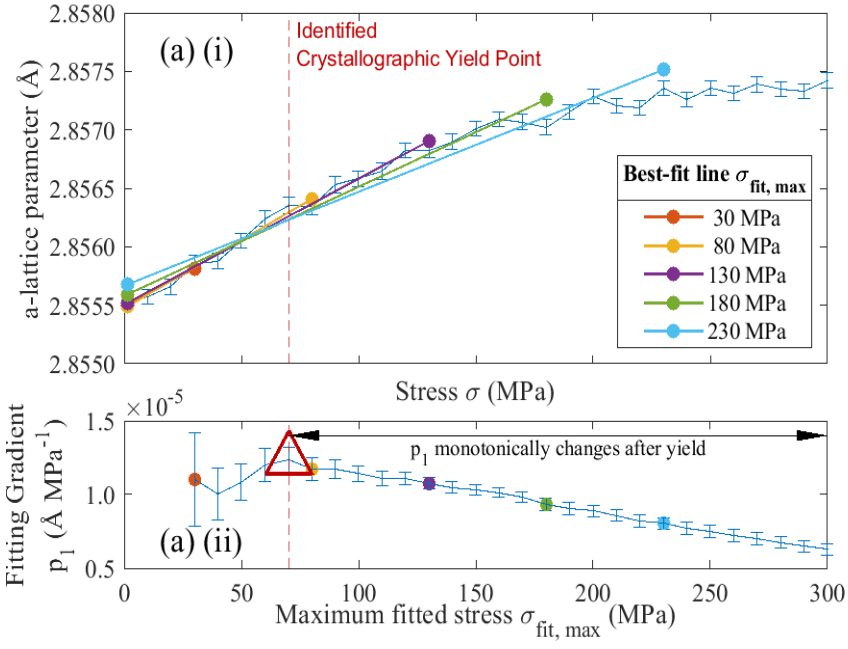
I developed a simple method which allowed a clearer and less subjective identification of the yield point. A series of best-fit lines of the form $d = p_1\sigma + p_2$ were fitted through an increasing number of consecutive data points, starting from the elastic region; the first line was fitted through the first four data points, the next through the first five, and so on. For each line, the two fitting parameters p_1 and p_2 were calculated in MATLAB using the `fit` function (linear least squares) with the 1st order polynomial `poly1`.

The gradients, p_1, of the best-fit lines containing data exclusively from the elastic region should be similar. As soon as data points from the non-linear region start to be included in the fitting dataset, the gradient will deviate from the previous values. It is possible to identify this point by inspection of a plot of the fitted gradient p_1 as a function of the fitting dataset size (figure 8.18 (a)(ii) and (b)(ii)), and therefore calculate the stress at

Ministry of Defence © British Crown Copyright 2020/AWE

which the lattice parameters stop responding linearly. After yield, the gradient p_1 will monotonically decrease or increase, depending on whether the lattice parameter is saturating or becoming more compliant.

Even in the challenging case of figure 8.18 (b), the yield point can be identified by eye as the start of the monotonically increasing gradient p_1.



Ministry of Defence © British Crown Copyright 2020/AWE

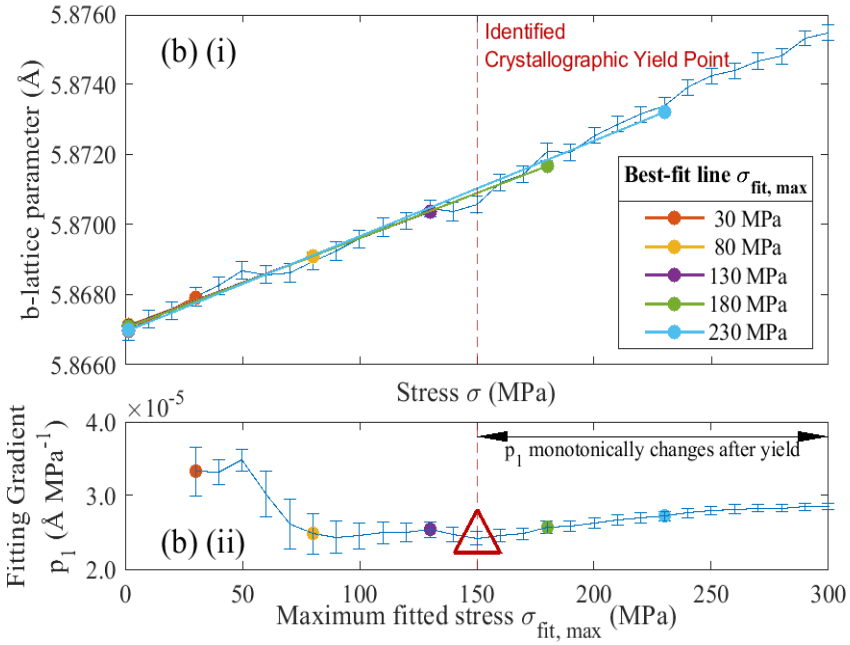


Figure 8.18. Identification of the a- and b- lattice parameter yield point in specimen ND-T1 in which the deviation from linearity is (a) well-defined and (b) challenging to identify by eye. The variation in the best-fit line gradient p_1 as a function of the maximum stress in the fitting dataset $\sigma_{\text{fit, max}}$ is shown in the lower sub-figure (ii). A selection of five best-fit lines are shown in the upper sub-figure (i), with $\sigma_{\text{fit, max}}$ for each line displayed in the legend. The yield point, shown as the dashed vertical line, was identified by eye as the start of the monotonically varying region in the lower graph (ii).

Once the yield point has been identified, the intercept of the best-fit line through the elastic region with the lattice parameter axis (y-axis in figure 8.18 (i)) is the load-free lattice parameter, d_0. The lattice parameter strains were then recalculated using this new reference value using equation [8.39].

Calculation of Intergranular Strains

A parameter of interest in similar studies [107] is the intergranular lattice parameter strain, ε_i^{int}, where i can represent either of the lattice parameters a, b, or c. It is defined as the difference between the measured elastic strain, ε_i, and the strain predicted from the applied stress σ_{app} and a relevant modulus E_i, as in equation [8.40].

Ministry of Defence © British Crown Copyright 2020/AWE

$$\varepsilon_i^{int} = \varepsilon_i - \frac{\sigma_{app}}{E_i} \qquad [8.40]$$

I let the modulus equal the gradient of the best-fit line through the elastic region of the stress-strain curve plotting σ_{app} against ε_i (figure 8.19). An alternative choice would have been to use the directional single-crystal modulus, for example E_{200} for E_a, however since the strain ε_a has contributions from all lattice planes (hkl) with $h \neq 0$, the lattice parameter modulus would be expected to be a complex mix of these E_{hkl} moduli.

To calculate the lattice parameter stiffness, E_i, a line of the form $\sigma_{app} = p_1\varepsilon_i + p_2$ was fitted through the elastic region of the stress - lattice parameter strain data. The intercept p_2 was constrained to equal zero such that the line passed through the origin; therefore the gradient p_1 was equal to the stiffness E_i. An estimation of the standard deviation in E_1 was calculated from the confidence indices returned by the `fit` function.

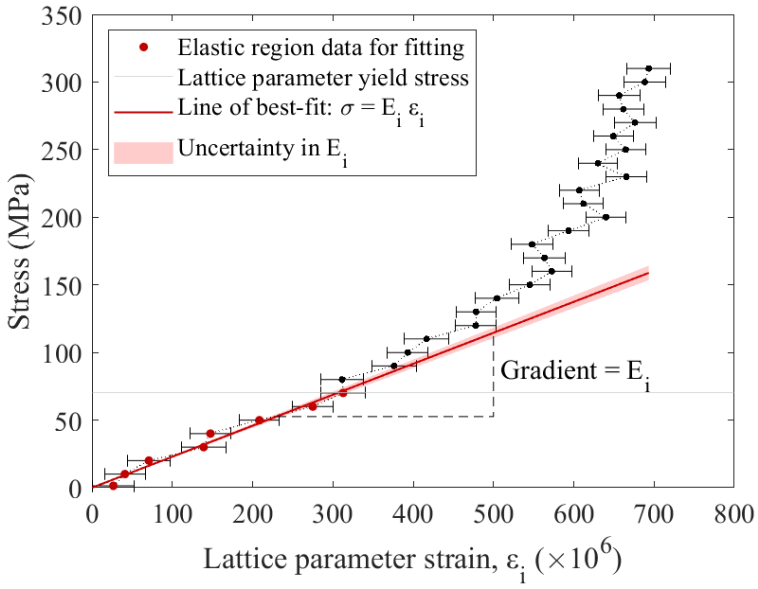


Figure 8.19. Calculation of the lattice parameter modulus E_i as the gradient of the best-fit line through the elastic region of the plot of stress as a function of lattice parameter strain ε_i. Crystallographic yield stress = 70 MPa, Crystallographic yield strain = 320 $\mu\varepsilon$ or 0.032 %

Ministry of Defence © British Crown Copyright 2020/AWE

Calculation of Strain Broadening

The strain broadening of the peaks can be expressed as the dimensionless quantity S from parameters of the Rietveld refinement using equation [8.41], where C is the diffractometer constant DIFC and γ_1 is the linear coefficient of the Lorentzian broadening coefficient in equation [8.19] on page 380.

$$S(\%) = \frac{1}{C}\gamma_1 \times 100\% \qquad [8.41]$$

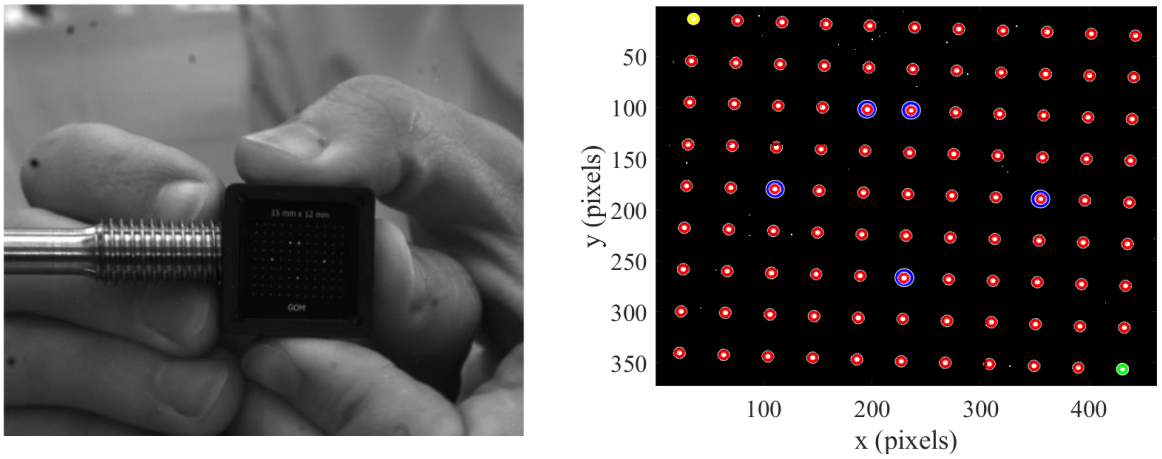
A5.2.1.8 DIC strain analysis

The optical images of the specimen acquired after each load increase were processed with digital image correlation to measure the displacement of each grip extension. From the relative displacement of the grips, it was intended to estimate the strain in the specimen.

Whilst the measurement of strain requires no image calibration, since it is a dimensionless quantity, an image calibration was performed such that the absolute translation of the specimen during the test could be measured. Before the test, an image was taken of a GOM CQG4146 15 mm × 12 mm calibration cube, held such that the front face was in the focal plane of the camera. An image of the front face of the cube is shown in figure 8.20(a). The calibration pattern comprises 99 white dots arranged in a 11 × 9 square array, with a 1.5 mm spacing between the nearest dots. The image was processed in MATLAB to calculate the pixel size. Firstly, it was converted to a binary image, then circles were identified using the `imfindcircles` function in the Image Processing Toolbox. The 'sensitivity' parameter was increased until all of the circles were

Ministry of Defence © British Crown Copyright 2020/AWE

correctly identified in figure 8.20 (b). A pair of dots at opposite corners were identified and the slant distance, in pixels, between the centres of the fitted circles was calculated. Since the cube is designed such that the distance between these points is $\sqrt{(12.00\ \mathrm{mm})^2 + (15.00\ \mathrm{mm})^2} = 19.21\ \mathrm{mm}$, the pixel size was calculated to be 36.70 μm ± 0.07 μm.



(a) (b)

Figure 8.20. (a) The calibration image taken at the start of the experiment of a GOM CQG4146 calibration cube, with 1.5 mm dot spacing. (b) The calibration dots identified in MATLAB. The distance, in pixels, between the yellow and green dots was used to calculate the pixel size.

Digital Image Correlation

Image processing and digital image correlation was performed in LaVision DaVis 8.4.0. The series of optical images for each specimen were imported, with the image taken at pre-load selected as the reference. A user-selected geometric mask was applied to select the grip extensions at each end of the specimen. A separate dataset was created for each one, resulting in 8 datasets across the 4 specimens. For specimens ND-T1, ND-C1 and ND-C2, Digital image correlation was performed using the LSM (least-squares matching) algorithm, with a subset size of 199 pixels × 199 pixels and a step size of 49 pixels ×

Ministry of Defence © British Crown Copyright 2020/AWE

49 pixels. For specimen ND-T2, reflection of light into the camera caused overexposure along the front of the grip extension, and the LSM algorithm could not converge on a solution. A subset size of 49 pixels × 49 pixels and a step size of 25 pixels × 25 pixels was found to be suitable in this case. The seeding point was chosen to be a point which exhibits a good speckle pattern and an intensity which does not change significantly during the test. Figure 8.21(a) shows the displacement field for the 100 MPa tensile loading state of specimen ND-T1. The outline of the geometric mask is shown by the white dotted line. It can be seen that the grip has moved to the left, as expected. The calculated displacement is not uniform across the grip extension. Since the grip extensions are round and tapered, the distance from the camera to the surface varies with both *x* and *y* co-ordinate, so for a given specimen translation, the magnitude of the observed pixel displacement will be greater for the centre region which is closest to the camera. As the load is increased from the pre-load, there is a slight rotation of the grips as they align themselves with the specimen. The combination of these two effects accounts for the variation in measured displacement across the grip extension.

A second geometric mask was applied to the vector displacement field, to select the data points in a small rectangular region, approximately 7 mm × 5 mm in size, close to the specimen. The resulting displacement field is shown in figure 8.21(b).

Ministry of Defence © British Crown Copyright 2020/AWE

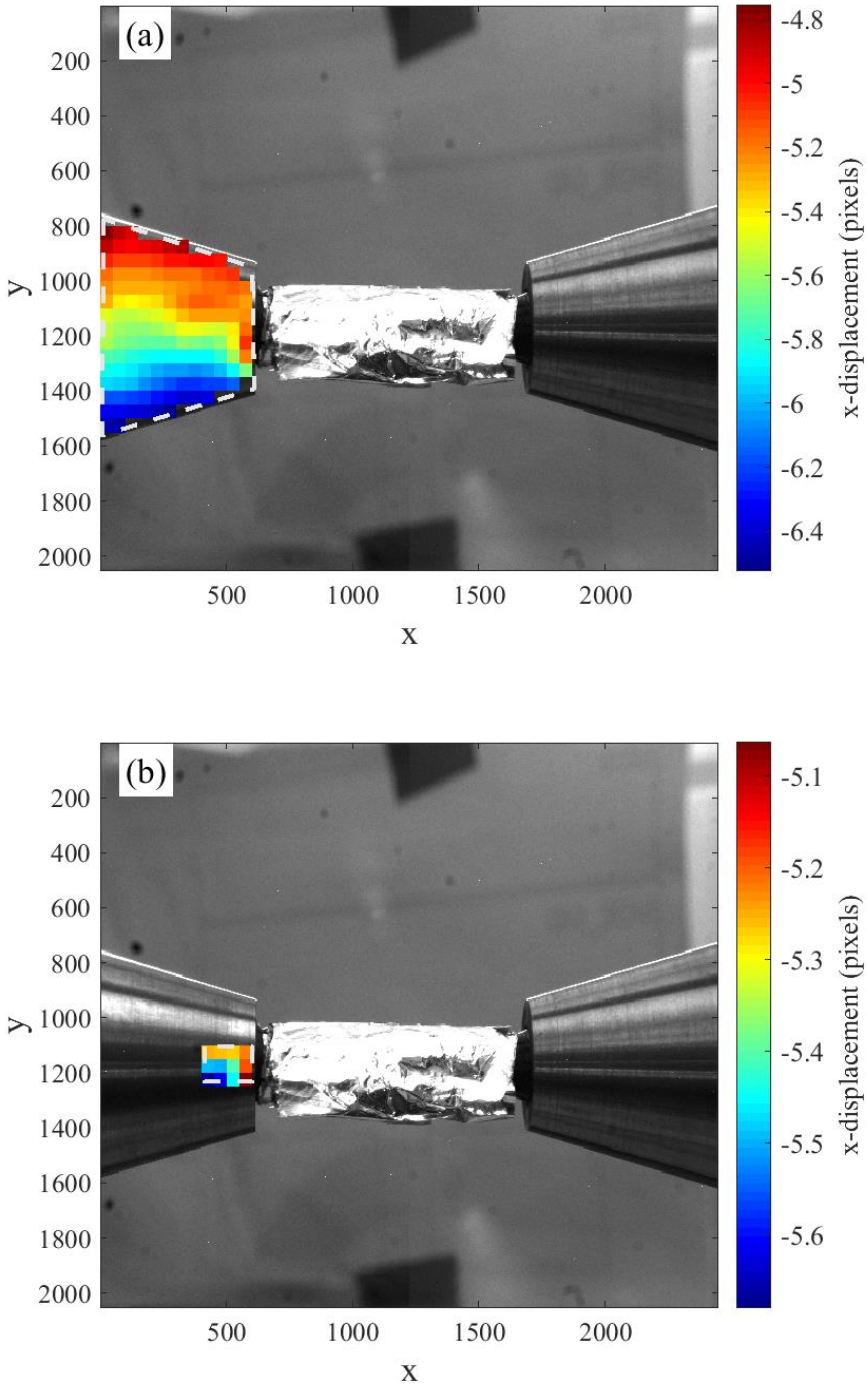


Figure 8.21. DIC displacement data for the 100 MPa tensile load step on the left grip extension for specimen T1. The data squares are coloured according to the magnitude of the x-displacement. The outline of the geometric mask is shown by the white dotted line. The samples were covered in foil, so DIC could not be performed on their surface. Subfigure (a) shows the results from the DIC calculation on the left hand (moving end) grip extension. Subfigure (b) shows the same data after a rectangular mask is applied, to restrict the data to that close to the sample position.

Ministry of Defence © British Crown Copyright 2020/AWE

The displacement fields were processed in MATLAB to obtain the displacements $\boldsymbol{u}^{\mathrm{moving}}$ and $\boldsymbol{u}^{\mathrm{fixed}}$, of the moving and fixed grip extensions respectively. The value of each displacement component u_x and u_y was mean of the x and y components of the vectors in the displacement field, and the error in each component was their standard deviation.

For a few load steps, images were not acquired due to human error. The displacements of these missing points were interpolated using the `inpaintn` function of Garcia[161] which uses an algorithm based on the discrete cosine transform (DCT). Then, outliers were identified as points with a fractional error $\frac{\sigma\, u_x}{u_x}$ greater than 1. These outliers were removed and the missing points interpolated with `inpaintn` . Finally, a Savitsky Golay smoothing filter[162] was applied to the data using the `sgolayfilt` function, with a 3rd order polynomial and a frame length of 15 points. The effect of each processing step is shown in figure 8.22.

An estimation of the total (elastic + plastic) strain in the specimen was calculated via equation [8.42] where u_x^{moving} and u_x^{fixed} are the mean displacements, as measured by DIC, of the moving and fixed grip extensions. L_{gauge} is a representative gauge length for each specimen, set as 42 mm for the tensile specimens ND-T1 and ND-T2 (the distance between the threaded regions of the specimen), and at 28 mm for the compression specimens ND-C1 and ND-C2 (the specimen length).

Ministry of Defence © British Crown Copyright 2020/AWE

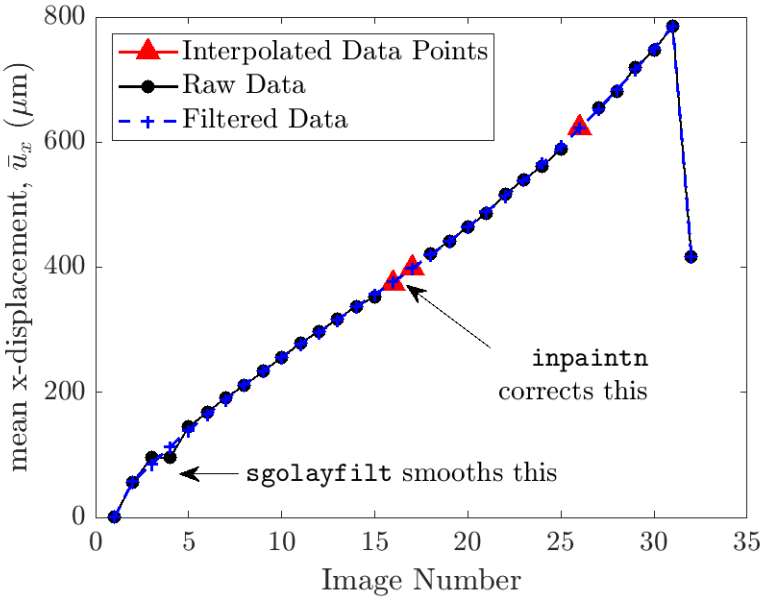


Figure 8.22. Processing of DIC-measured displacements, showing the raw data (black circles), the interpolated data points (red triangles) after the use of `inpaintn[161]`, and the final data after the application of the Savitsky-Golay filter (blue crosses). Displacements shown are from the moving grip extension on specimen C1.

$$\varepsilon_{xx,\mathrm{DIC}} = \frac{u_x^{\mathrm{moving}} - u_x^{\mathrm{fixed}}}{L_{\mathrm{gauge}}} \qquad [8.42]$$

$$\varepsilon_{xx,\mathrm{DIC}} = \frac{\Delta u_x}{L_{\mathrm{gauge}}} \qquad [8.43]$$

$\varepsilon_{x,\mathrm{DIC}}$ is therefore an estimate of the total strain in the specimen.

For both tensile specimens ND-T1 and ND-T2, the threaded grip extensions moved with respect to the specimens as the load was increased. For ND-T1, the measurements suggested the surface of the grip extension on the fixed end initially moved more than the grip extension at the moving end implying a negative sample extension, which is clearly unphysical in tension. I believe that the threaded joints between specimen and grip extension deformed slightly during the test, and the combined rotation and out-of-

Ministry of Defence © British Crown Copyright 2020/AWE

plane motion caused the observed displacements. The DIC measured strain is therefore unreliable, and will not be considered in the analysis.

A5.2.2 Neutron Texture Measurement on GEM

The Reitveld refinement and texture measurement described so far allows the determination of the texture along two perpendicular axes (parallel to the diffraction vectors in each of the two detector banks). This presents a challenge when simulating the microstructure to perform crystal plasticity simulations, as there is a rotational ambiguity in the texture along each axis. A full measurement of the texture, in all directions, would allow a more accurate microstructure to be built in a CPFE model.

The original plan was to perform a pre- and post-test measurement during the ENGIN-X experiment using the Eulerian cradle sample positioner, however this would have been slow, and extra time would have been required to exchange the cradle with the load frame. Since we had limited experimental time on experiment RB1710227, it was decided there to focus on solely measuring the in-situ deformation. It was then thought that a post-test measurement of the texture changes due to deformation could be made by comparing the texture in deformed and undeformed regions of the specimen; between the deformed gauge region and the undeformed grip region in the tensile specimens, and between the deformed and undeformed compression specimens. It was clear, however, that this was not possible once the coarse-grained microstructure had been revealed with EBSD. The texture in a region the size of the neutron IGV varies strongly over a few

Ministry of Defence © British Crown Copyright 2020/AWE

millimetres, so it would not be possible to compare different regions of the same specimen, yet alone different specimens. Unfortunately this means that it is only possible to measure the full sample texture post-deformation, but as it will be apparent from the axial texture measurements, the deformation-induced texture change at the small applied strains is negligible.

To this end, a neutron measurement was performed on the GEM beamline at ISIS to measure the full sample texture in the post-test state of the specimens tested at ENGIN-X; ND-T1, ND-T2, ND-C1 and ND-C2. 24 hours of experimental time were obtained as part of experiment RB1810071, titled "The effect of the onset of plastic deformation on texture in cast alpha-uranium", which took place from 17th-18th September 2018. The instrument is described by Day et al. [163] with up-to-date technical details available on the GEM webpage [164]. It is typically used as a powder diffractometer, and has good angular coverage and consequently fast acquisition times. The instrument has a primary flight path from the source of 17 m, giving a much brighter beam than at ENGIN-X. Time-of-flight detectors are arranged in six banks, as shown in figure 8.23, with an angular coverage from 1.1° to 169.3°. The specimen is mounted on an X-Y-Z goniometer, which is lowered into a vacuum vessel inside the instrument which is pumped down during data acquisition. The beam is shaped by horizontal and vertical slits to give it a rectangular cross-section upon incidence with the specimen.

Ministry of Defence © British Crown Copyright 2020/AWE

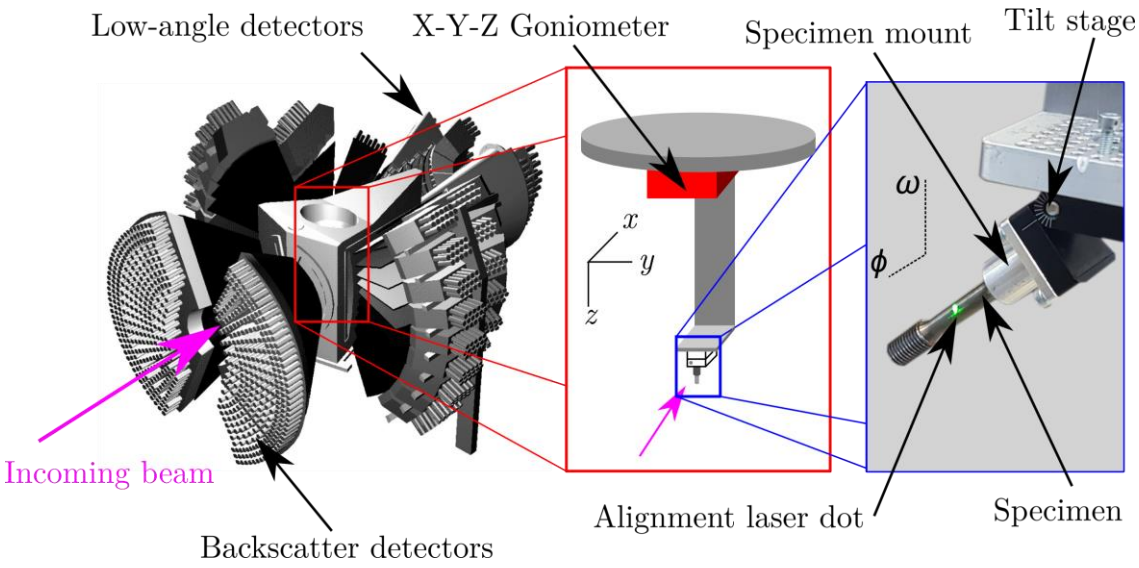


Figure 8.23. Diagram showing the detector arrangement in GEM, ISIS, as well as the specimen location on the X-Y-Z goniometer, which sits in the beam. The goniometer axes X, Y and Z are shown, as well as the instrument rotation axes ω and ϕ. The neutron beam is incident from the left hand side. 3D schematic of GEM reproduced from Hannon et al. [163]

Since the detectors do not have coverage above and below the specimen, it was necessary to perform two scans for each specimen, with a rotation angle of 45° about the ϕ axis between them. The combined data provided enough information to calculate a full texture.

Before testing the uranium, a texture measurement was performed on a calcite ($CaCO_3$) specimen with a known texture. The measured data were inspected to check for swapped cables on the detectors; GEM is often used as a powder diffractometer where the signals from detectors in each of the 7 banks are summed, so swapped cables would not usually be noticed. For texture measurement, however, the wiring is crucial.

Each specimen was mounted on a Thorlabs FP90/M Adjustable Flip Platform via an aluminium sample holder. The tensile specimens used a threaded connection to the sample holder whilst the compression specimens were mounted with UHU® All Purpose

Ministry of Defence © British Crown Copyright 2020/AWE

Adhesive. The flip platform had tick marks from which a 45° tilt about the ϕ-axis could be achieved. Figure 8.24 shows a CAD drawing of the tensile and compression

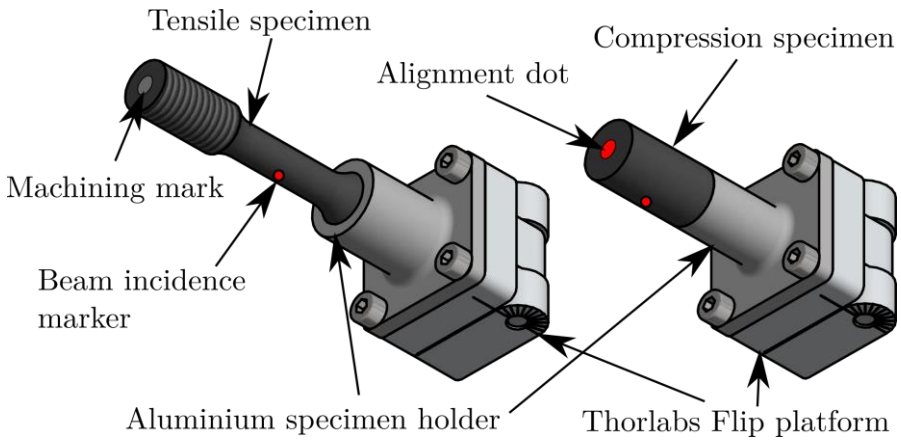


Figure 8.24. Specimens were mounted on a tilt stage with an aluminium sample holder. Each specimen was marked and aligned such that its orientation relative to the instrument was known. The tensile specimens had a machining mark on one end; this was aligned such that it was visible when mounted, therefore pointing 'downwards' in the instrument when the tilt stage was at 0° ϕ-rotation. The compression specimens had no obvious surface features, so a red dot was applied with a marker pen to one of the cylinder ends; this was mounted in a similar manner.

The alignment process was performed with the goniometer sitting in a cradle outside of the instrument. 3 alignment lasers were attached to the cradle; their beams converging at the centre of the beam-specimen interaction volume when the goniometer is inside the instrument. One laser pointed along the beam direction, and one pointed vertically up from beneath the specimen. The *x* and *y* co-ordinates of the goniometer were adjusted until the vertical laser aligned with the centre of the specimen end face. The z co-ordinate was then adjusted to position the beam-incidence laser dot at the longitudinal centre. The desired *z* co-ordinate was calculated as the mean of the *z* co-ordinates required to position the laser dot at two points equidistant from the centre; the specimen ends, for the compression specimens, and the ends of the parallel gauge region, for the tensile

Ministry of Defence © British Crown Copyright 2020/AWE

specimens. The beam incidence position was then marked on the specimen with a marker pen.

The beam width was increased fully to its maximum of 20 mm, and the beam height set to 5 mm. The region of the specimen inside the neutron beam for each tilt angle is shown in figure 8.25.

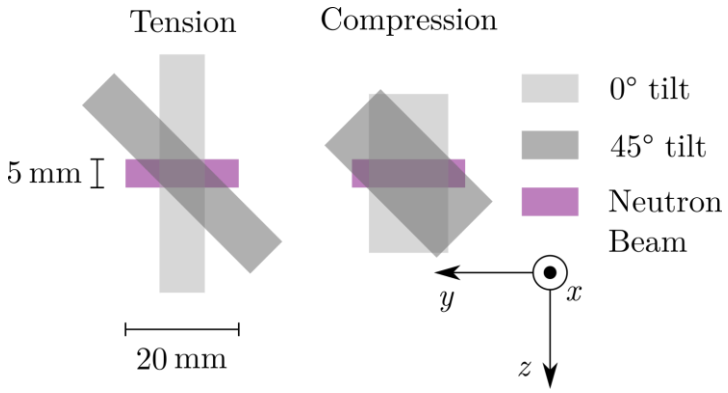


Figure 8.25. GEM scanning geometry for specimens at 0° and 45° ϕ-tilt angle. The beam cross-section is shown in purple.

Scan times of 5 minutes, corresponding to an integrated target current density of 15 μAh, were found to give spectra of sufficient quality for texture analysis.

A5.2.2.1 GEM data processing

The raw data from GEM were processed at ISIS to produce three data files per scan. Two .gda files contained the spectra for each of the 160 detector regions, with a separate file being generated for the 0° and 45° ϕ-tilt angle scans. A `.maud` file contained the instrumental configuration; the DIFA, DIFC and ZERO parameters for each detector region, allowing for the conversion from time-of-flight to d-spacing (equation [8.7]) whilst accounting for the differing secondary flight path lengths for each detector.

Ministry of Defence © British Crown Copyright 2020/AWE

Texture analysis was performed using MAUD – Materials Analysis Using Diffraction, a Java-based Rietveld program for diffraction data written by Luca Lutterotti based on his earlier work [165]. The theory behind the texture analysis process is described in detail by Wenk et al. [117]; a summary of the relevant steps will be presented here. MAUD performs a Rietveld refinement on multiple spectra and fits texture using the E-WIMV algorithm, before generating pole figures (PFs) and inverse pole figures (IPFs) to represent the texture.

The E-WIMV (Extended Williams-Imhof-Matthies-Vinel) method is an iterative method to calculate the orientation distribution function (ODF) from experimental data [166]. The ODF space is discretised into cells in which the value of the ODF is calculated. The WIMV is favourable to the spherical harmonics method used in GSAS to fit the axial textures on ENGIN-X as it always returns a positive ODF, and can easily fit sharp textures in low-symmetry materials [167].

The initial peak positions were taken from the relevant Crystal Information File, `9008584 (Alpha Uranium).cif` from the Crystallography Open Database (COD) [142]. The dataset from the $\phi = 45°$ tilt scan were imported with a 45° ϕ-offset which rotates the data into alignment with the $\phi = 0°$ dataset. From this point onwards, both datasets are combined and can be treated as one in the analysis. The low-angle detectors collect data over a large d-spacing range, up to 10 Å, however since the higher angle detectors can only measure to smaller d-spacings, the data at larger d-spacings suffer from poor

Ministry of Defence © British Crown Copyright 2020/AWE

counting statistics. At small d-spacings, multiple peaks are overlapping and each peak is captured by only one or two data points, so the Rietveld refinement cannot fit accurately in this region. Since the largest d-spacing of interest is the (020) peak at 2.935 Å, only data in the range 0.8 Å – 3.2 Å were included in the analysis. An example of the average of the spectra from the 160 detector regions is shown in figure 8.26 as the black dotted line.

The Rietveld refinement was performed in four stages, with an increasing number of parameters freed for refinement in each iteration. The Marqardt Least Squares algorithm was selected to minimise the linear weighted sum of squares of the deviation of the model fit from the experimental data (WSSq). Firstly, all parameters were fixed at their default values apart from a scale factor which was refined to match the integrated peak intensity across the whole spectrum. The background was manually refined with a second order polynomial, shown in green in figure 8.26. This was then held constant throughout the subsequent refinement steps. If the specimen was not centred perfectly in the beam, the difference in TOF between opposing detector banks can shift the d-spacings slightly. The specimen *x*, *y*, and *z* co-ordinates in the Rietveld refinement were refined to correct for this. An example of this initial fit is shown as the red line in figure 8.26.

The lattice parameters *a*, *b* and *c*, were refined to correct the peak positions. The initial and refine peaks are shown as the red and blue tick marks respectively in figure 8.26. Peak-broadening parameters were then refined, including crystallite size and microstrain

Ministry of Defence © British Crown Copyright 2020/AWE

terms. Texture refinement was then activated, using the E-WIMV method with an 10° × 10° ODF cell size. Refinement iterations were performed until the WSSq was no longer seen to change. Applying a texture sharpening factor of 2 reduced the WSSq by approximately a factor of 2 after a subsequent refinement. The average of the fitted spectra is shown as the blue line in figure 8.26.

Axial Orientation Alignment

The orientation of the specimens on the instrument were not recorded during the ENGIN-X diffraction experiment. There is therefore an ambiguity in the axial orientation of the specimens, i.e. an uncertainty in the ω-rotation necessary to generate correct pole figures. However, it was possible to identify the ω-rotation by generating IPFs for a series of ω-values and comparing them with the IPFs produced in GSAS from the ENGIN-X data. In MAUD, the three specimen directions are denoted ND, TD and RD (for Normal Direction, Transverse Direction and Rolling Direction, a convention relating to textures in rolled plates).

An example of the orientation alignment process is shown in figure 8.28, which shows representative data from specimen ND-T1. The IPFs from the North and South banks on ENGIN-X are shown at the top of the figure. Beneath, are shown the IPFs along the ND, RD and TD directions for ω-rotations of $0°$, $30°$, $60°$, and $90°$. The TD IPF does not change with ω-rotation, so corresponds to a diffraction vector along the specimen axis; and qualitatively matches the North bank ENGIN-X IPF.

Ministry of Defence © British Crown Copyright 2020/AWE

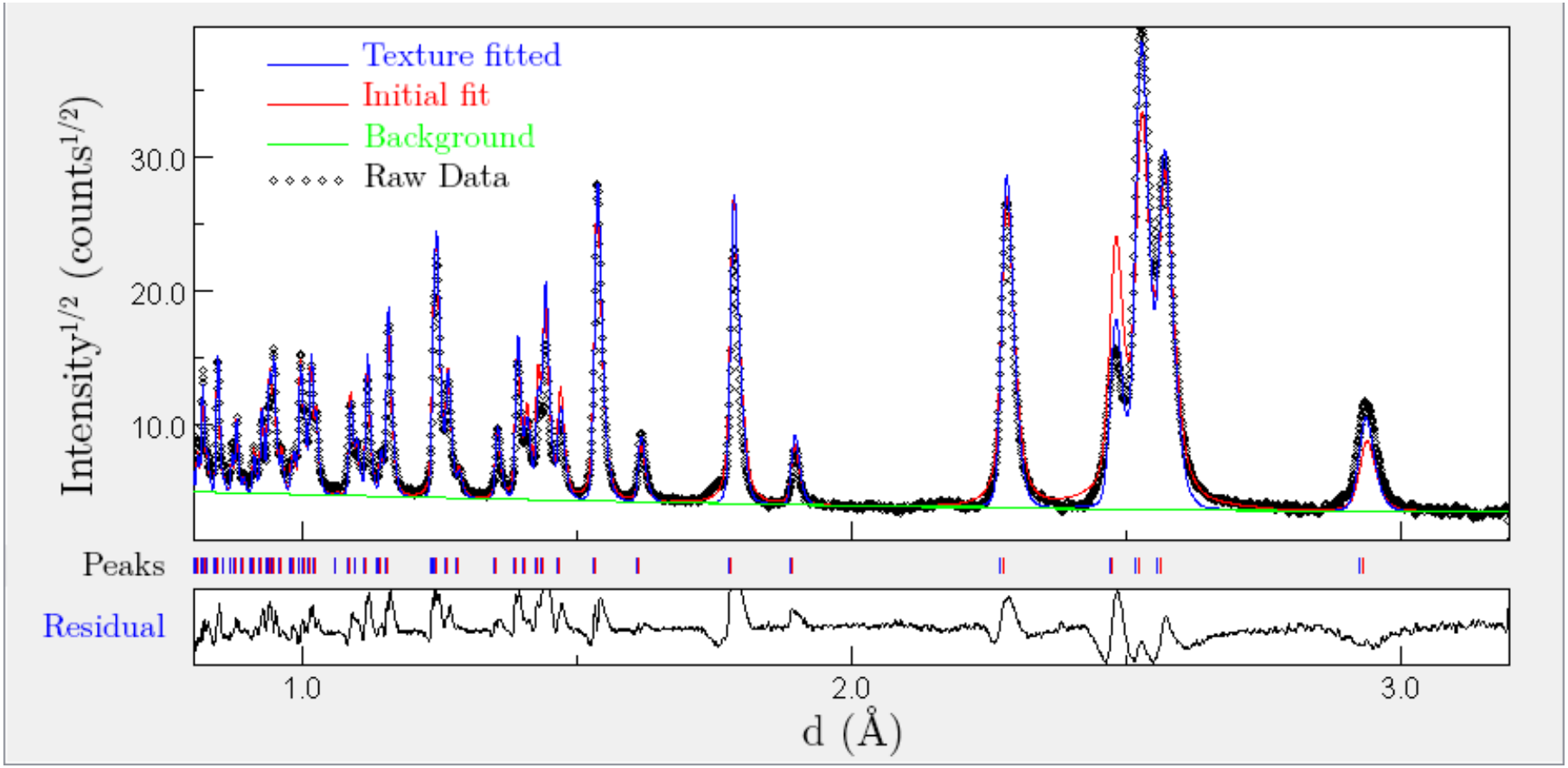


Figure 8.26. Rietveld fitting of the GEM data using MAUD. The initial fit (red) to the measured spectra (black) is refined using the E-WIMV algorithm to measure texture (blue). A second order polynomial is used to fit the background (green).

Ministry of Defence © British Crown Copyright 2020/AWE

At a particular value of ω, denoted ω_{aligned}, the ND IPF will appear qualitatively similar to the IPF from the ENGIN-X South bank (diffraction vector perpendicular to the specimen axis). At a value of $\omega_{\text{aligned}} + 90°$, the RD IPF will match. Due to way the E-WIMV cells are located in orientation space, the texture calculation produces higher angular resolution IPFs along the RD than the ND, so I selected the RD at $\omega = \omega_{\text{aligned}}$ to be equivalent to the ENGIN-X South bank. In the example in figure 8.28, the RD IPF is qualitatively similar to the South bank IPF at $\omega = \omega_{\text{aligned}} = 15°$; the IPFs for this orientation are shown in the black box.

The relationship between the ENGIN-X experiment co-ordinates and those used in MAUD is summarised in figure 8.27. The directions RD, TD, and ND make a right-handed set, with the TD direction parallel to the $q_{//}$ diffraction vector (North bank) and the RD direction antiparallel to the $q_{\perp}$ diffraction vector (South bank). The orientation of pole figures generated by MAUD is shown in figure 8.27(iii).

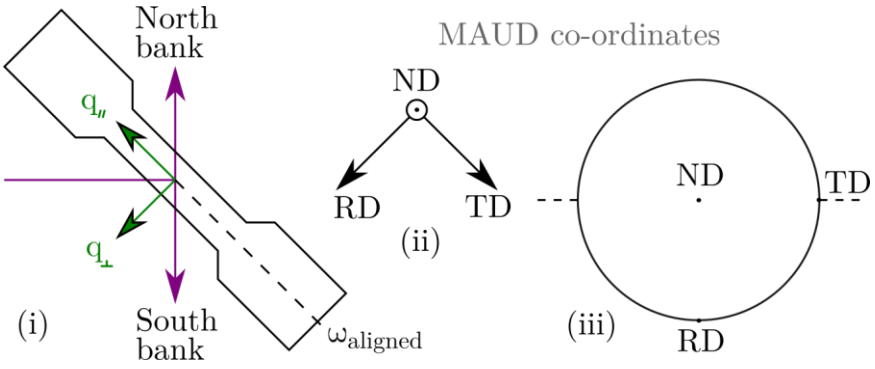


Figure 8.27. Relationship between MAUD co-ordinate system (ii) and ENGIN-X specimen (i). Pole figures generated in MAUD are oriented as shown (iii).

Ministry of Defence © British Crown Copyright 2020/AWE

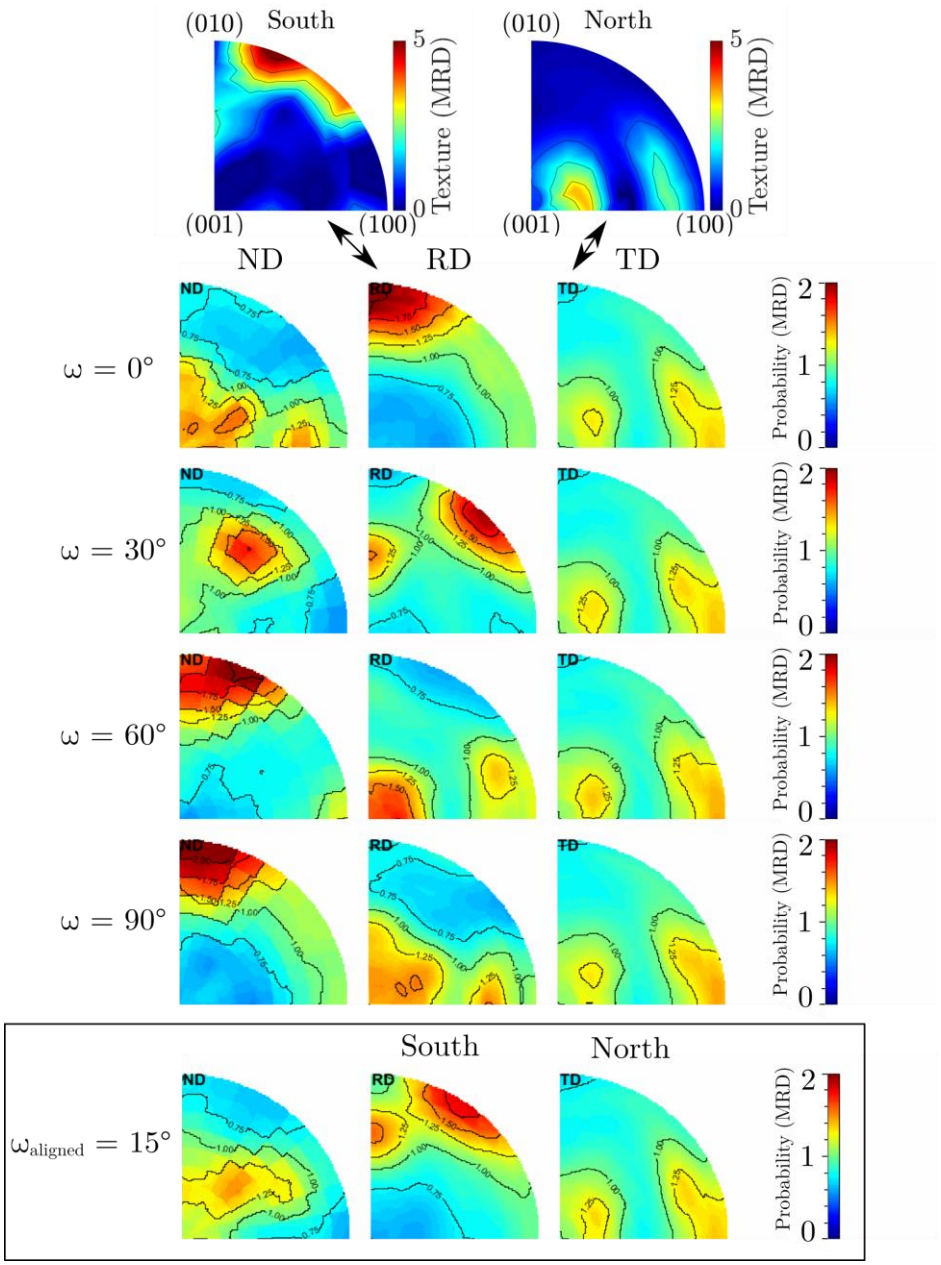


Figure 8.28. Selection of ω value that brings MAUD co-ordinates into alignment with ENGIN-X experiment. IPFs for North and South banks of ENGIN-X from specimen ND-T1 are shown at the top of the figure. Below are IPFs along the ND, RD and TD for a range of ω-rotation angles. It can be seen that the TD in MAUD corresponds to the North bank. The RD in MAUD was chosen to correspond to the South bank; an ω-rotation of 15° gives good agreement between them.

Ministry of Defence © British Crown Copyright 2020/AWE

A5.3 Results

A5.3.1 Neutron Spectra

The neutron spectra acquired on ENGIN-X and GEM were of good quality, with the majority of peaks well-resolved. Example spectra, taken from the specimens held under pre-load on ENGIN-X, are shown in figure 8.29 and figure 8.30 with the spectra from North and South banks coloured in black and red respectively. The refined peak positions are shown; the first 25 peaks have their indices labelled. For each specimen, there is a significant difference between the spectra from each of the two detector banks. This suggests a strong texture, with only certain grain families oriented well for diffraction in a particular bank.

As expected, the peak with the largest d-spacing is the (020) reflection at 2.935 Å. The peaks get closer together at smaller d-spacings. Single-peak fitting in OpenGenie is only possible for non-overlapping peaks; for approximately 20 reflections in each case. Some peaks have a very low intensity and are not distinguishable from the background – these peaks cannot be fitted.

Ministry of Defence © British Crown Copyright 2020/AWE

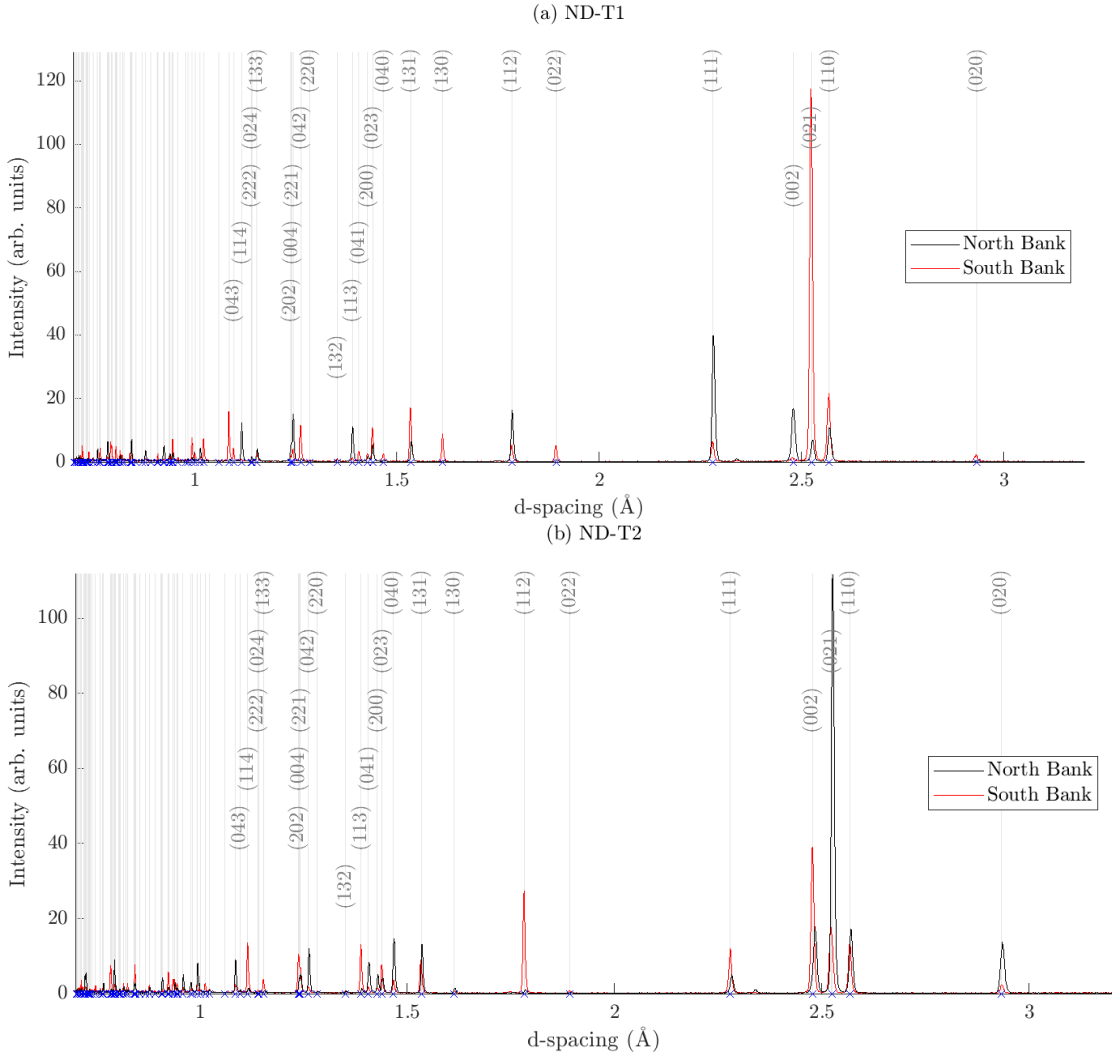


Figure 8.29. Time-of-flight neutron diffraction spectra from the North bank (black) and South bank (red) detectors on ENGIN-X for each of the tensile specimens tested. Spectra are from specimens held at pre-load. Intensities are in arbitrary units. Only spectra in the range 0.7 Å < 3.2 Å are shown.

Ministry of Defence © British Crown Copyright 2020/AWE

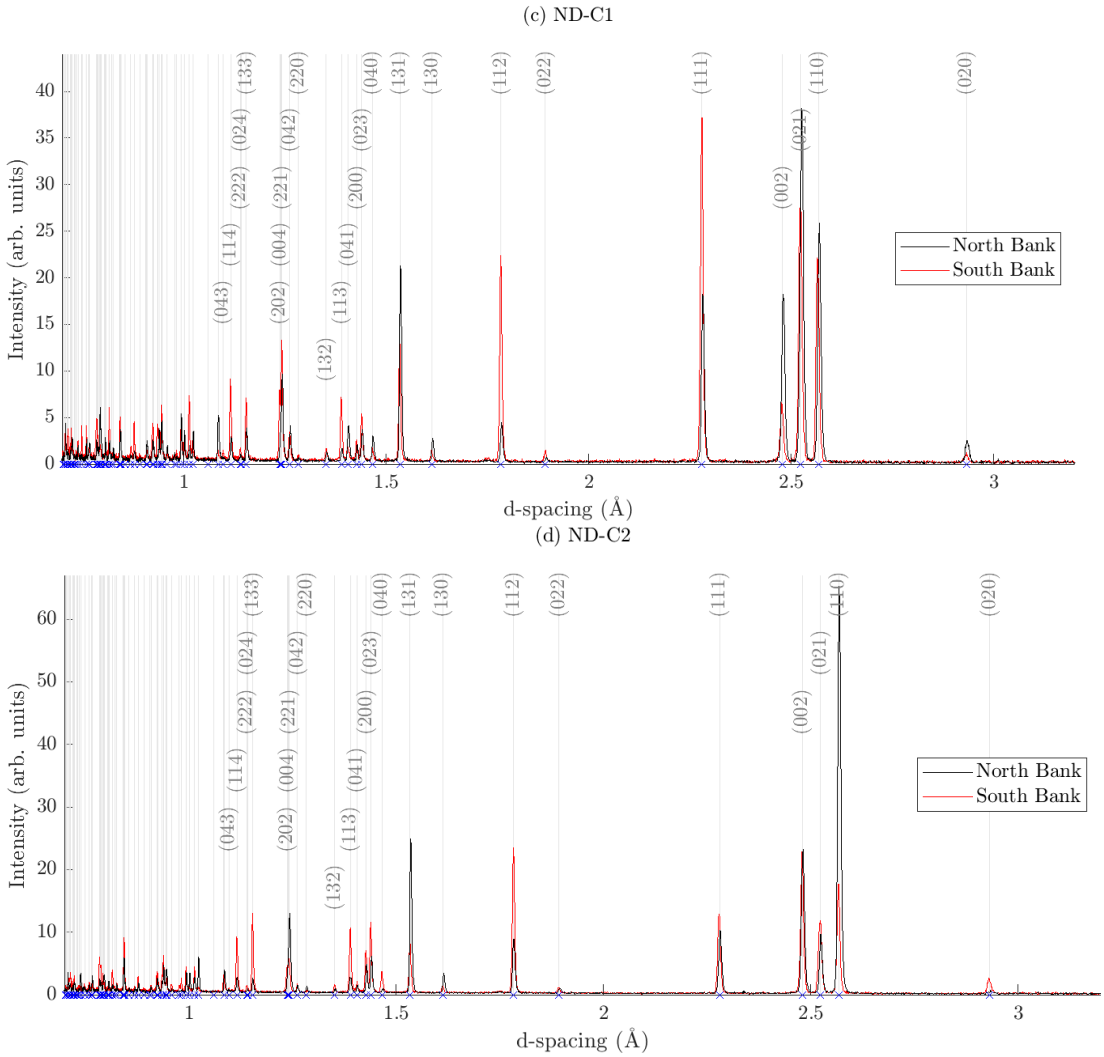


Figure 8.30. Time-of-flight neutron diffraction spectra from the North bank (black) and South bank (red) detectors on ENGIN-X for each of the compression specimens tested. Spectra are from specimens held at pre-load. Intensities are in arbitrary units. Only spectra in the range 0.7 Å < 3.2 Å are shown.

A5.3.2 Texture in the Gauge Region

Figure 8.31, figure 8.32, and figure 8.33 on pages 421, 422, and 423 show the measured textures in the centre of the gauge region in specimens ND-T1, ND-T2 and ND-C1 respectively. In each case, sub-figure (i) contains the inverse pole figures of the axial texture in the gauge volume on ENGIN-X, along axes parallel (North bank) and perpendicular (South bank) to the loading axis.

Ministry of Defence © British Crown Copyright 2020/AWE

Sub-figures (ii), (iii) and (iv) visualise the full[10] textures measured on GEM. In sub-figures labelled (ii), the inverse pole figures of texture along the ND, RD and TD directions defined in MAUD for GEM are shown (see figure 8.27). The TD and RD are equivalent to the North and South bank directions on ENGIN-X, at the selected values of $\omega_{\mathrm{aligned}}$ of 15°, 90° and 0° for specimens ND-T1, ND-T2 and ND-C1 respectively. Sub-figures labelled (iii) show pole figures of the full texture.

The intensity (MRD) of the pole figures is proportional to the volume fraction of the gauge volume oriented in that particular direction. The pole figures from each specimen have local maxima which correspond to dominant grain orientations. Since the microstructure of these specimens has large clusters of a similar orientation it can be assumed that the peaks in the pole figures correspond to the orientations of the grain clusters in the gauge volume.

Each specimen has two or three discrete grain orientations. It was possible to infer the orientation of these grains from the position of the local maxima in the orthogonal (200), (020) and (002) pole figures, and converting from the stereographic co-ordinates to the laboratory frame. On each pole figure, the approximate orientation of the dominant grain clusters are shown. These orientations are also shown with the same symbols on the IPFs in sub-figures (i) and (ii).

[10] In this context, 'full' texture refers to the fact that the texture is measured along multiple axes spanning the majority of possible directions. This is unlike the axial textures measured on ENGIN-X, which only quantified the pole densities along two perpendicular directions.

Ministry of Defence © British Crown Copyright 2020/AWE

Sub-figures labelled (iv) present a 3D visualisation of the orientations of these dominant grain clusters. A unit cell is plotted with its orientation defined with respect to the RD, TD and ND directions. The (200), (020) and (002) plane normals are shown as red, green and blue lines respectively.

From the measured orientations, I calculated the crystal plane normal (hkl) parallel to the loading direction. The indices have been rounded to those low-order reflections present in the spectrum, accounting for the systematic absences caused by the uranium crystal structure (Appendix A4). For example, the axis (1 41 11) is close to (061), a uranium reflection.

Specimen ND-T1 contains two grain clusters in the gauge volume. The (020) axes of both grains are near to the RD, with a misorientation of approximately 90° about the (020) axis between them. Grain cluster 1 has its (115) axis parallel to the tensile direction; this is parallel to (422) in the second cluster. In the ENGIN-X IPFs, the cluster parallel to (115) has a higher intensity, whilst in the GEM data the intensities are similar.

Ministry of Defence © British Crown Copyright 2020/AWE

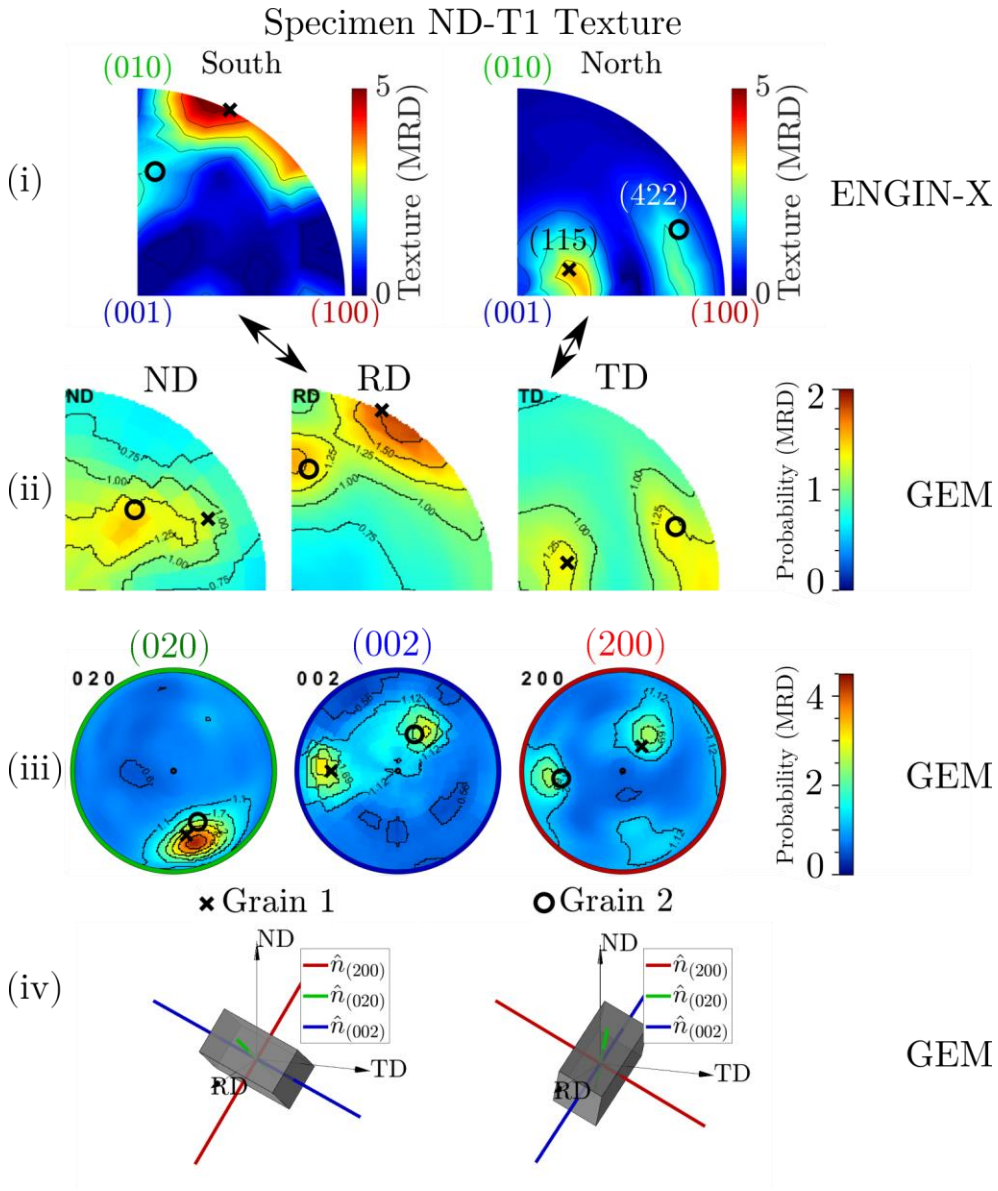


Figure 8.31. Neutron-measured texture in specimen ND-T1. The approximate orientation of the two dominant grain clusters is shown with circles and crosses. (i) Inverse pole figures of axial texture parallel (North bank) and perpendicular (South bank) to the loading axis, inside the 4 mm × 4 mm × 8 mm gauge volume on ENGIN-X. (ii) Inverse pole figures of texture along the ND, RD and TD directions defined in MAUD for GEM (see figure 8.27). The TD and RD are equivalent to the North and South bank directions on ENGIN-X, at the selected value of $\omega_{aligned} = 15°$. (iii) (020), (002) and (200) pole figures. (iv) Graphical representation of the orientation of the uranium unit cell in each of the two grain clusters. Axes normal to (200), (020) and (002) are shown in red, green and blue respectively.

Ministry of Defence © British Crown Copyright 2020/AWE

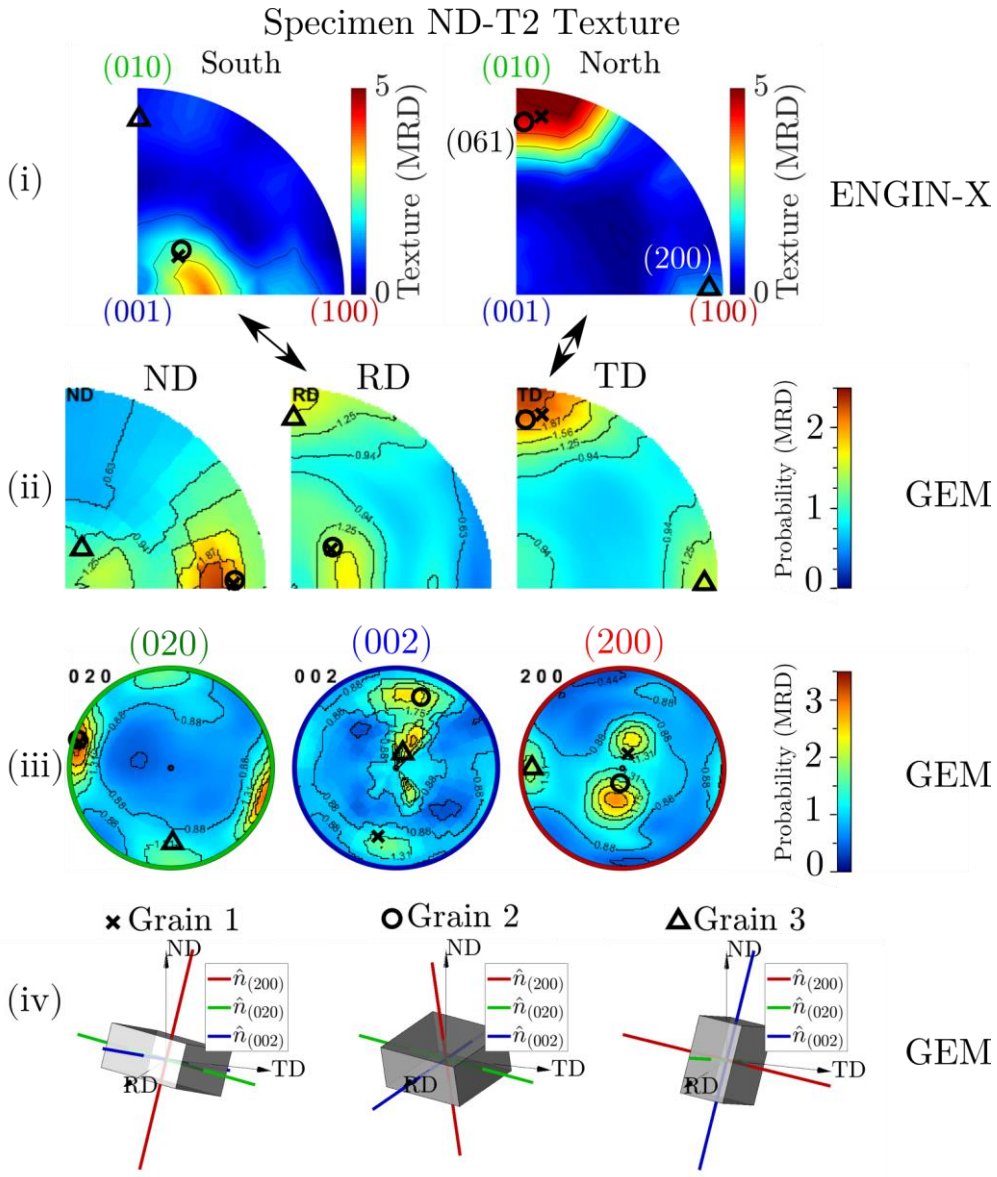


Figure 8.32. Neutron-measured texture in specimen ND-T2. The approximate orientation of the three dominant grain clusters is shown with circles, crosses, and triangles respectively. (i) Inverse pole figures of axial texture parallel (North bank) and perpendicular (South bank) to the loading axis, inside the 4 mm × 4 mm × 8 mm gauge volume on ENGIN-X. (ii) Inverse pole figures of texture along the ND, RD and TD directions defined in MAUD for GEM (see figure 8.27). The TD and RD are equivalent to the North and South bank directions on ENGIN-X, at the selected value of $\omega_{aligned} = 90°$. (iii) (020), (002) and (200) pole figures. (iv) Graphical representation of the orientation of the uranium unit cell in each of the two grain clusters. Axes normal to (200), (020) and (002) are shown in red, green and blue respectively.

Ministry of Defence © British Crown Copyright 2020/AWE

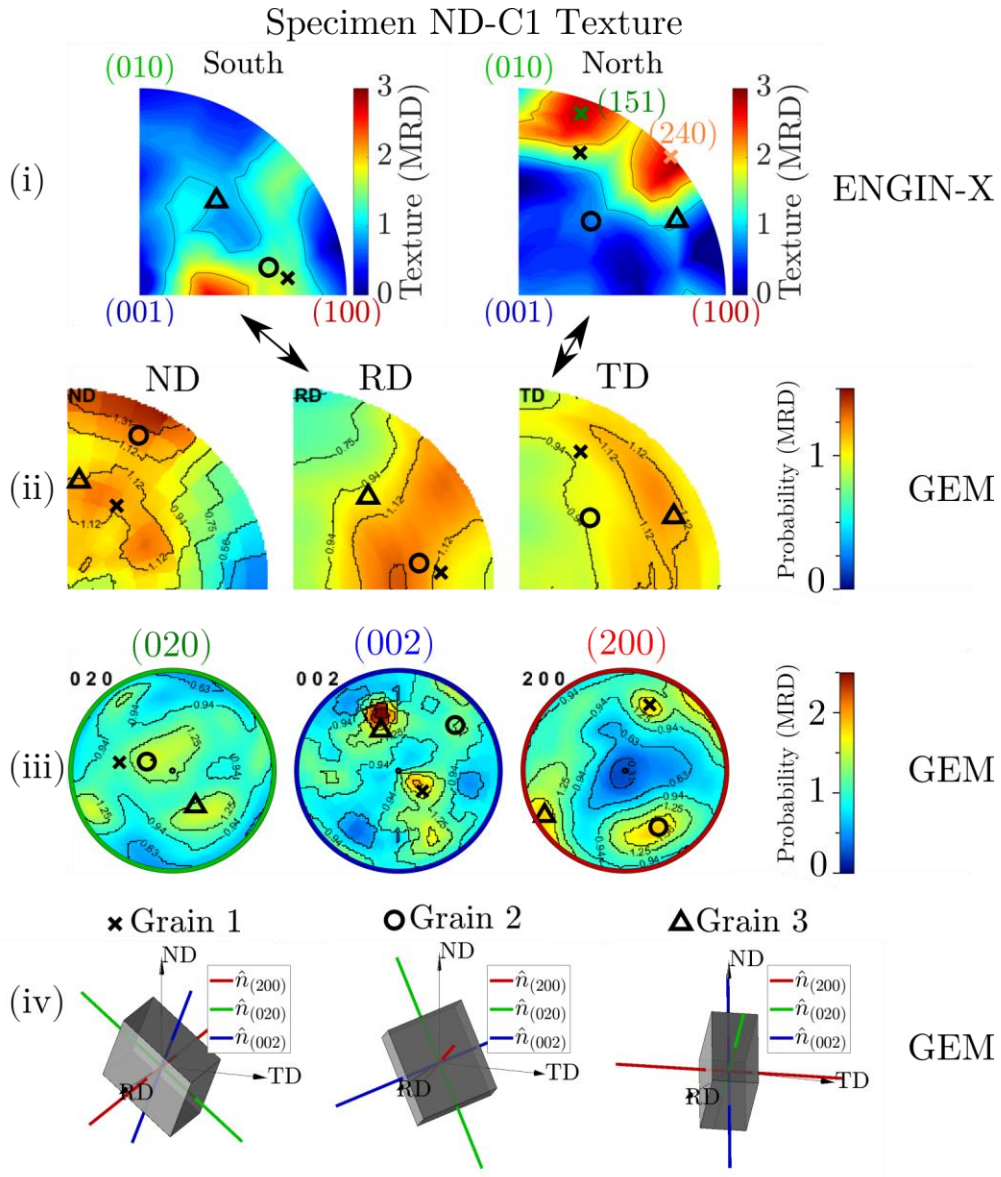


Figure 8.33. Neutron-measured texture in specimen ND-C1. The approximate orientation of the three dominant grain is shown clusters with circles, crosses, and triangles respectively. (i) Inverse pole figures of axial texture parallel (North bank) and perpendicular (South bank) to the loading axis, inside the 4 mm × 4 mm × 12 mm gauge volume on ENGIN-X. (ii) Inverse pole figures of texture along the ND, RD and TD directions defined in MAUD for GEM (see figure 8.27). The TD and RD are equivalent to the North and South bank directions on ENGIN-X, at the selected value of $\omega_{aligned} = 0°$. (iii) (020), (002) and (200) pole figures. (iv) Graphical representation of the orientation of the uranium unit cell in each of the two grain clusters. Axes normal to (200), (020) and (002) are shown in red, green and blue respectively.

The gauge volume of specimen ND-T2 contains three clusters. The (020) axes of grains 1 and 2 are parallel and close to the tensile direction (TD // (061)). The axes of grains 1 and 3 are parallel to one another such that $200\ _1 // \ 002\ _3$, $020\ _1 // \ 200\ _3$ and

Ministry of Defence © British Crown Copyright 2020/AWE

$002_1 // 020_3$. Grains 1 and 2 have similar intensities whilst grain 3 must be smaller, giving a lower intensity.

Specimen ND-C1 shows no alignment between the grain clusters. At least three grain clusters are seen in the GEM PFs, with axes (152), (146) and (221) parallel to the compression direction. The three grain clusters identifiable from the GEM full texture measurement do not match as well with the ENGIN-X data. The TD IPF in figure 8.33(ii) shows a weaker texture than is seen in the North bank IPF in figure 8.33(i). The compression specimens have a larger cross-sectional area than the tensile specimens, therefore the uncollimated GEM beam samples a proportionally higher number of grains than the collimated (and therefore sample-size-independent) ENGIN-X beam. This would result in the GEM experiment sampling a larger number of grain clusters, leading to a weaker measured texture. For the purposes of interpreting the deformation, specimen ND-C1 is thought of as comprising two grain clusters, oriented with (151) and (240) plane normals parallel to the loading direction.

A5.3.3 Predicting Deformation using the Schmid Factor

A criterion based on a critical resolved shear stress is commonly used for slip. For twinning, which undergoes lattice rotation and shear, this is not necessarily the correct criterion, and other parameters such as the normal stress on the twinning plane or the presence of neighbouring grains [168] are sometimes relevant. However, the Schmid

Ministry of Defence © British Crown Copyright 2020/AWE

factor is still suggested to at least partially control the initiation of twinning[169]. This is commonly applied in literature [49][55] due to its simplicity.

The orientation of each cluster affects the ability for each deformation mode to activate. The Schmid Factor (SF) for each grain was calculated for each of the known deformation mechanisms; Wall, Floor, Chimney and Roof slip and $\{130\}$, '$\{172\}$', '$\{176\}$' and $\{112\}$ twinning. These are shown in the left half of table 8.5. A high SF for a particular deformation mode indicates that the grain is well-orientated for deformation in that mode. Slip is possible for positive and negative SFs – slip just proceeds in an antiparallel directions – so the absolute value of the SF is shown in the case of slip. Twinning is not possible for a negative SF. Values of SF ≤ 0, where deformation could not occur at any stress, are coloured in red. The maximum SF for each grain is shown in bold.

A high SF does not necessarily result in deformation if the critical resolved shear stress for deformation on that mode is high. The applied stress that would initiate deformation on a single mode (excluding the presence of all other modes) was calculated using equation [8.44].

$$\sigma_{\mathrm{crit}} = \frac{\tau_{\mathrm{crit}}}{\mathrm{SF}} \qquad [8.44]$$

The critical resolved shear stresses τ_{crit} for slip were taken from Calhoun's 2013 paper [108]. The critical stress for twinning is thought to vary strongly with grain size [170], and no data are available for coarse-grained cast uranium. Our clustered material is closer to being a single crystal than to the fine-grained microstructures investigated by

Ministry of Defence © British Crown Copyright 2020/AWE

Calhoun [108], Knezevic [171] or McCabe [30]. The τ_{crit} for {130} twinning was taken from Daniel's 1971 paper [18] on single crystal deformation. The ratio between the τ_{crit} of the $\{130\}$ and of the '$\{172\}$' twins was assumed to be 1:1.75, as in Calhoun's work [108]. Since $\{112\}$ twinning is the reciprocal twinning mode of '$\{172\}$' twinning, I made the assumption that $\tau_{\mathrm{crit}}^{\{112\}} = \tau_{\mathrm{crit}}^{\{172\}}$. I could not find a value for $\tau_{\mathrm{crit}}^{\{176\}}$ in the literature. The estimated stress magnitude required to initiate deformation on each system is shown on the right hand side of table 8.5.

Ministry of Defence © British Crown Copyright 2020/AWE

Table 8.5. The Schmid Factor (SF) and critical stress magnitude for deformation (σ_{crit}) for each grain cluster in specimens ND-T1, ND-T2 and ND-C1. τ_{crit} values of 7 MPa, 10 MPa, 35 MPa and 235 MPa were used for Wall, Floor, Chimney and Roof slip respectively, taken from Calhoun's 2013 paper[108]. τ_{crit} values of 25 MPa[18], 44 MPa and 44 MPa were used for $\{130\}$, '$\{172\}$' and $\{112\}$ twinning respectively. Values of SF ≤ 0, where deformation could not occur at any stress, are coloured in red. The maximum SF for each grain is shown in bold.

			Specimen						
			ND-T1		ND-T2			ND-C1	
		Grain Cluster	1	2	1	2	3	1	2
		Symbol	✖	○	✖	○	△	✖	✖
		Loading Axis	115 T	422 T	061 T	061 T	200 T	151 C	240 C
Schmid Factor (SF)	Slip	Wall	0.05	0.21	0.00	0.00	0.00	0.34	0.50
		Floor	0.30	0.25	0.00	0.00	0.00	0.08	0.00
		Chimney	0.06	0.46	0.38	0.38	0.39	0.47	0.32
		Roof	0.48	0.11	0.48	0.48	0.00	0.48	0.31
	Twin	$\{130\}$	0.06	0.46	-0.45	-0.45	0.47	0.44	0.17
		'$\{172\}$'	0.40	0.35	-0.26	-0.26	0.16	0.49	0.32
		'$\{176\}$'	-0.17	0.35	0.23	0.23	0.16	0.08	0.11
		{112}	0.35	0.33	-0.16	-0.16	0.12	0.49	0.34
Estimated σ_{crit} (MPa)	Slip	Wall	137	33	-	-	-	21	14
		Floor	33	40	-	-	-	126	-
		Chimney	555	77	92	92	89	74	110
		Roof	494	2090	487	487	-	492	757
	Twin	$\{130\}$	448	54	-	-	54	57	149
		'$\{172\}$'	109	124	-	-	274	90	138
		'$\{176\}$'	----------No τ_{crit} data for '$\{176\}$' twins----------						
		{112}	124	133	-	-	353	90	127

Due to its high CRSS, Roof slip is not expected to occur in any of the specimens at the applied stresses up to 310 MPa.

A5.3.3.1 Expected Deformation in ND-T1

The first grain cluster in specimen ND-T1 has a low SF for Wall slip and {130} twinning. It is however suitably oriented for floor slip. The second cluster is well-oriented for Wall slip, Floor slip and {130} twinning in tension. It would be expected that the gauge volume first deforms via a combination of floor slip in grain cluster 1, and wall slip in grain cluster 2, at a low stress of approximately 40 MPa. This would then be

Ministry of Defence © British Crown Copyright 2020/AWE

accompanied by {130} twinning in grain cluster 2, oriented near (422), at approximately 55 MPa applied tensile stress.

A5.3.3.2 Expected Deformation in ND-T2

None of the grains in specimen ND-T2 are well-oriented for Wall or Floor slip. Grain clusters 1 and 2 have similar orientations, and all twinning systems except '{176}' have negative Schmid Factors, so cannot activate. Grain cluster 3 is well-oriented for {130} twinning only, so deformation in the gauge volume of specimen ND-T2 should occur in this cluster from 55 MPa.

A5.3.3.3 Expected Deformation in ND-C1

Both clusters are well-oriented for deformation via Wall slip, with this expected to occur almost immediately during loading. The low critical resolved shear stress of the {130} twin suggests this twin will be the first to activate in the gauge volume – in grain cluster 1 at approximately 60 MPa.

In summary, specimens ND-T1 and ND-C1 are expected to initiate deformation by Wall slip at low applied stresses. All specimens are expected to undergo {130} twinning in the grain cluster with the highest Schmid Factor for this twin type.

A5.3.4 Lattice Strain Development

The (hkl) lattice strain measures the average elastic strain on the (hkl)-planes of the family of grains with their (hkl)-plane normals parallel to the diffraction vector. In this section, data from the North detector bank are presented, where the diffraction vector

Ministry of Defence © British Crown Copyright 2020/AWE

is parallel to the loading direction and therefore the measured strains are most easily related to the applied load. The strain data from the South detector bank do not easily contribute towards understanding of the deformation process, as they measure Poisson's ratio effects which are complicated by the strong texture. Lattice parameter strains are calculated from the Rietveld refinement (page 393) and show the relative distortion of the average unit cell due to the applied stress state. The '*a*' lattice parameter strain contains contributions from all of the (hkl) lattice strains where $h \neq 0$, as noted by Brown et al. [107]. High elastic strain corresponds to a high stress being supported through these grains. Grains which can support a high stress without this stress being relieved via deformation are plastically hard, whilst those whose elastic strains saturate (i.e. can no longer support any increase in stress) are plastically soft.

The development of lattice strains on the orthogonally-oriented (200), (020) and (002) families of grains is plotted in figure 8.34 as a function of applied stress using open markers. The strains of the three lattice parameters *a*, *b*, and *c* are plotted using filled markers. The errors in the lattice strains are larger as they are calculated from a single-peak fit, rather than a Rietveld refinement which fits over all peaks in the spectrum. Data from the literature are shown for comparison, with Brown et al. performing tension along the rolling direction (RD) and transverse direction (TD) of rolled uranium plate [107]. Calhoun et al. performed tension and compression along the RD and compression along the TD [45].

Ministry of Defence © British Crown Copyright 2020/AWE

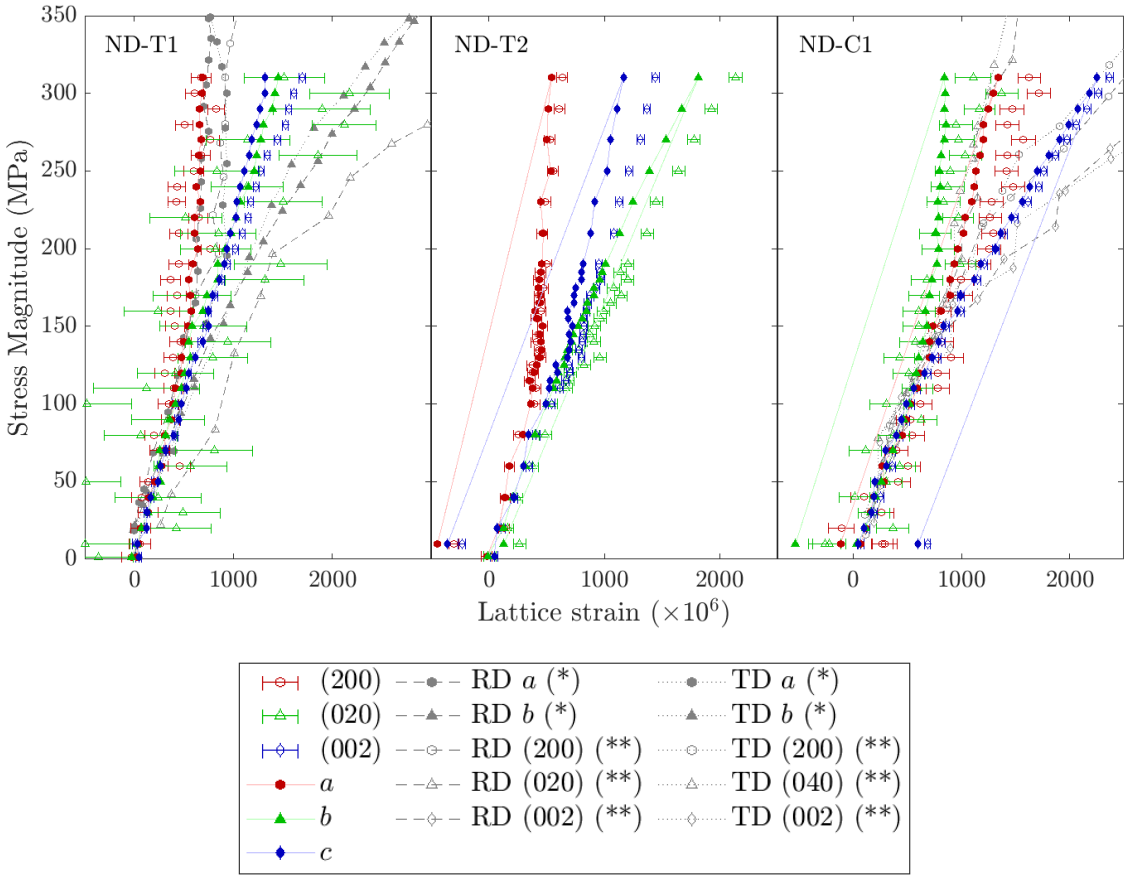


Figure 8.34. Development of lattice strain as a function of the magnitude of the applied stress for specimens ND-T1, ND-T2 and ND-C1. Lattice strains for the (200), (020) and (002) reflections were measured from single-peak fitting. Lattice parameter strains for the *a*, *b* and *c* lattice parameters were calculated from the Rietveld refinement. Specimens ND-T2 and ND-C1 were unloaded to a stress magnitude of 10 MPa after reaching maximum load. Stress and lattice strain data from specimen ND-C1, tested in compression, were multiplied by -1 such that the data appears visually similar to the tensile data. Data from the literature are shown for comparison, with Brown et al. [107] (*) performing tension along the rolling direction (RD) and transverse direction (TD) of rolled uranium plate. Calhoun et al. [45] (**) performed tension and compression along the RD and compression along the TD.

The strain expected from a grain family deforming elastically (with no plasticity) is simply the extrapolation of the linear elastic response in the low-stress region. The stress at which deviation of a (hkl) strain occurs from the elastic response, calculated using the method on page 395, corresponds to the stress at which plastic deformation occurs - of any mode that can relieve stresses along the (hkl) direction. The gradient of the lattice

Ministry of Defence © British Crown Copyright 2020/AWE

parameter strains in the linear elastic region is shown in table 8.6 along with the stress at which the lattice parameter strains begin to deviate from linearity.

Table 8.6. Elastic lattice parameter gradient and crystallographic yield point

	Elastic Gradient (GPa)			Crystallographic Yield Point – Magnitude of stress at point of deviation from initial elastic gradient (MPa)		
	a	b	c	a	b	c
ND-T1	229 ± 8	241 ± 5	207 ± 3	70	150	150
ND-T2	299 ± 5	196 ± 1	203 ± 4	140	145	140
ND-C1	187 ± 4	198 ± 2	207 ± 5	110	100	100
RD Tension[107] (Fine-grained)	196	169	141	Approximately 200 MPa		

The lattice strain response in the two tensile specimens is qualitatively similar. After a linear elastic response at low stresses, the strains on the (200) planes and *a* lattice parameter saturate, with less stress being held across grains of this orientation[11].

The deviation from linearity is not the same in specimens ND-T1 and ND-T2. The former exhibits a deviation of its *a*-parameter from linearity at 70 MPa, which does not fully saturate until 150 MPa. The latter saturates immediately at the point of deviation from linearity at 140 MPa. Whilst the a-parameter saturates in both tensile specimens, the responses of the *b*- and *c*- parameters are different. In specimen ND-T1, the *b*- and *c*- parameter strains are close to being equal, and deviate very little from the linear

[11] To be clear, 'this orientation' refers to the family of grains whose (200) planes are parallel to the tensile direction. More generally in this work, grains 'in the (*hkl*) orientation' are those grains whose (*hkl*) planes are parallel to the loading direction.

Ministry of Defence © British Crown Copyright 2020/AWE

elastic behaviour. The c-parameter of specimen ND-T2 relaxes slightly, whilst its b-parameter takes up more of the strain.

The lattice strains (200), (020) and (002) qualitatively follow the lattice parameter strains *a*, *b*, and *c* respectively. The equivalent single-peak response of the most highly-strained lattice parameter is always greater. This was similarly observed by Brown et al.[107], where it was explained by the fact that the lattice parameter strains are moderated by contributions from multiple diffracting planes.

In compression, the response is markedly different, with the b-parameter deviating from linearity at 100 MPa and saturating at approximately 200 MPa. In this case, the *c*-parameter takes up most of the strain, with the *a*-parameter slightly relaxing. The *a*-parameter and (200) strains in our material relax slightly however in Calhoun's work[45] the (200)-oriented grains took up a larger proportion of the applied strain.

Since only one specimen was tested in compression in this experiment, it was not possible to identify any consistent features of the lattice strain response in the same way as in tension.

By inspection of table 8.6, the elastic gradients of the c lattice parameter are consistent between the three specimens, whilst there is little correlation between the gradients of the a and b lattice parameters. The single-crystal moduli E_{hkl} along the (200), (020) and (002) plane normals are 204 GPa, 149 GPa and 209 GPa respectively. It might be expected that therefore the b-lattice parameter would have the smallest gradient. By

Ministry of Defence © British Crown Copyright 2020/AWE

inspection of figure 2.3 in section 2.2.2 however, it can be seen that the real response will be much more complicated, as the b-parameter includes contributions from all planes with $k \neq 0$, which have stiffnesses from 148 GPa to 288 GPa (figure 2.3(a)).

The fact that the elastic gradient of the *a* parameter of 299 GPa is greater than the maximum possible elastic stiffness in uranium of 288 GPa suggests that the *a* parameter is not behaving perfectly elastically in this low-stress region, and that relaxation is starting to occur at lower stresses than we observed from the deviation from linearity.

Despite significant microstructural and texture differences, there is qualitative agreement between the lattice strain response of our coarse-grained cast uranium and the fine-grained rolled uranium tested in the literature – *a*-parameter strains saturate in tension whilst *b*-parameter strains saturate in compression.

A5.3.4.1 Intergranular Strain

Plastic deformation introduces heterogeneity into the elastic strains, above and beyond the heterogeneity induced by the material's anisotropic stiffness tensor. Plastic deformation is also anisotropic, with different yield stresses in different directions, with different deformation modes being favoured in tension and compression. Initiation of plasticity in a particular family of grains relaxes the strains, and therefore the stresses, in those grains. However, the rest of the material still has to accommodate the stress, so elastic strains in non-yielding grains must increase to a level to balance the applied stress. In the analogy of a composite material comprising plastically-soft and plastically-

Ministry of Defence © British Crown Copyright 2020/AWE

hard grains, the stress would be transferred to the plastically-hard grains as the plastically-soft grains yield.

The intergranular lattice parameter strains, as defined in equation [8.40] on page 398, quantify this anisotropy as the deviation of the lattice parameter strains from what would be expected in purely elastic loading (linear). Since we have *d*-spacings at zero applied load as a reference, we are measuring the intergranular strains related to plastic anisotropy, rather than those related to thermal stresses.

Figure 8.35 shows the development of intergranular strains as a function of applied stress. Positive intergranular strains correspond to a greater proportion of the stress being carried by these grains (the plastically-hard grains) whilst negative intergranular strains are associated with the stress relaxation caused by plastic deformation (the plastically-soft grains).

There are no intergranular strains during elastic loading (as is implied by our definition of elastic loading being the linear region of the lattice strain, and intergranular strains being simply the deviation from this response). From the relevant yield point (see table 8.6), the intergranular strains develop linearly with applied stress up to the maximum applied stress of 310 MPa.

Ministry of Defence © British Crown Copyright 2020/AWE

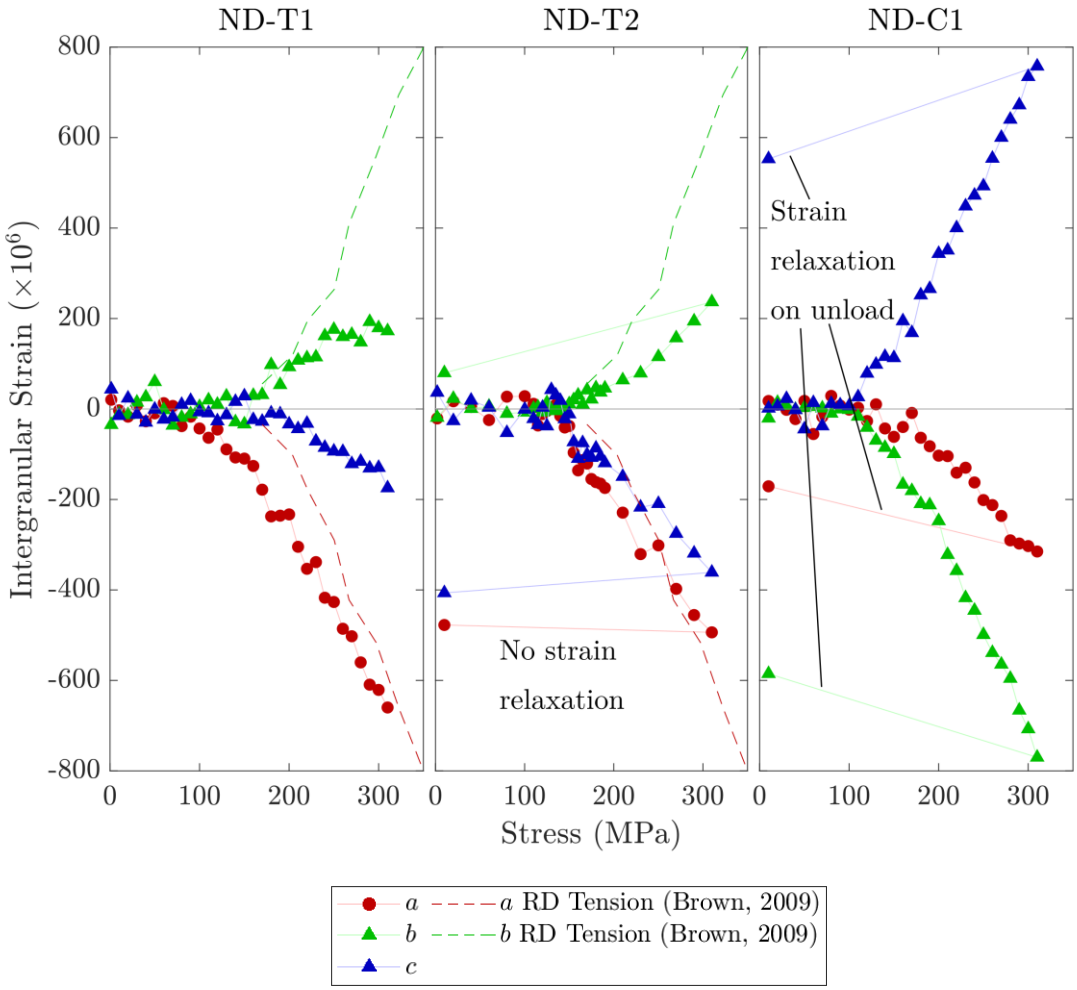


Figure 8.35. Development of intergranular strains as a function of applied stress. Positive intergranular strains correspond to a greater proportion of the stress being carried by these grains. Negative intergranular strains are associated with the stress relaxation caused by plastic deformation. N.B. the compression data have had the sign of the stress and intergranular strain changed to make the data visually comparable to the tensile data. Data from fine-grained specimens tested by Brown et al. [107] are included for comparison with the data from the tensile specimens.

In tension, the magnitude of the a-parameter intergranular strains is larger than for the b- or c-parameter. In compression, the magnitudes are the same. Data from the tensile specimens can be compared with equivalent data from fine-grained uranium, from Brown et al. [107]. They exhibit a similar a-parameter response whilst at a given stress the b-parameter intergranular strains are smaller in the coarse-grained material than in the fine-grained material.

Ministry of Defence © British Crown Copyright 2020/AWE

Specimens ND-T2 and ND-C1 had a neutron measurement taken after unloading from the maximum stress. If the unloading was purely elastic, it would be expected that each lattice strain would follow a path with a gradient equal to that during their elastic loading. ND-T2 behaves mostly in this manner, with only slight strain relaxation detectable. ND-C1 behaves in a more complex manner, with a reduction in intergranular strain detectable in all three lattice parameters. Since only one measurement was taken during unload, it is not possible to determine where this non-linearity was introduced.

A5.3.4.2 Strain Broadening

It would be expected that at high stresses, the induced plastic deformation leads to a broadening of the peaks, due to the introduction of dislocations and inhomogeneities in the strain on a particular family of grains. This is captured by the strain broadening parameter (equation [8.41] on page 399). Note that the absolute value is less relevant here, we are only interested in the trend as a function of stress. Figure 8.36 shows the development of strain broadening as a function of the magnitude of the applied stress, for each of the three samples tested on ENGIN-X.

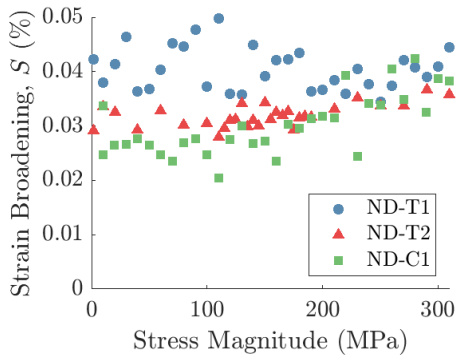


Figure 8.36. Development of strain broadening in the Rietveld refinement as a function of the magnitude of applied stress.

Ministry of Defence © British Crown Copyright 2020/AWE

The strain broadening from specimen ND-T1 exhibits a lot of scatter with no discernible trend. Specimens ND-T2 and ND-C1 show no change in broadening at stresses below approximately 200 MPa, then the broadening increases by approximately 30 % by 310 MPa. This is in agreement with the detection of plastic deformation in the development of intergranular strains, and suggests that little plastic deformation is occurring at low stresses. It could be argued that since the strain broadening parameter *S* is non-zero in the supposedly elastic region at low stress, then there must be some intrinsic plasticity here. This may be as a result of the plasticity that is in the material as a result of thermal stresses during cooling after casting. However, the ENGIN-X spectrometer is not particularly sensitive to peak width, so it would not be wise to read too much into the absolute values of the data, and instead focus on the trends. It was not possible to compare these data with those from the literature since the latter were presented as a function of *plastic* strain, which we cannot calculate in the absence of accurate DIC measurements. The relatively low applied stress of 310 MPa only corresponded to a plastic strain of less than 0.2 % in Brown et al.'s [107] work, only one or two data points.

A5.3.5 Axial Texture Changes

Plastic deformation will produce a reorientation of the crystal lattice that may be detectable in the measured textures. Slip would induce a steady rotation, seen as a 'peak' in the texture moving steadily from one location to another. Deformation twins have a fixed orientation relationship with respect to the parent grain, which would cause a

Ministry of Defence © British Crown Copyright 2020/AWE

decrease in intensity in the 'parent' orientation and an increase in texture in the 'twin' orientation. We cannot identify the twins present in the initial pre-load state, as contributions from twins and the parent grains cannot be separated. We can however aim to identify the twins induced via deformation from the changes in the measured texture.

All of specimens had sharp textures, with peaks of up to 6 MRD with other orientations contributing < 0.5 MRD. At the relatively low applied strains, the expected volume fraction of twins induced would be small [38]. The texture changes may be difficult to identify by inspection of the texture IPFs alone. Therefore, the texture difference, $\Delta \mathrm{O}(\mathbf{r})$, was calculated by subtracting the IPF values measured at pre-load from each IPF at load (equation [8.45]). The error in these texture differences was calculated using standard error analysis formulae, shown in equation [8.46]:

$$\Delta \mathrm{O}(\mathbf{r}) = \mathrm{O}(\mathbf{r}) - \mathrm{O}_{\text{pre-load}}(\mathbf{r}) \qquad [8.45]$$

$$\sigma\ \Delta \mathrm{O}(\mathbf{r})\ = \sqrt{\sigma\ O(\mathbf{r})\ ^2 + \sigma(\mathrm{O}_{\text{pre-load}}(\mathbf{r}))^2} \qquad [8.46]$$

Figure 8.37 shows the measured texture changes as IPFs at a few selected stress levels. The first row (a-d) shows the axial texture in the North bank, along the loading axis. The second (e-g), third (h-j), fourth (k-m) and fifth rows (n-p) show the change in texture, relative to the pre-load state, at applied stress magnitudes of 20, 110, 210 and 310 MPa respectively. The first IPF on the final row (q) shows the quantification of the error in the texture change IPF for ND-T1 shown in sub-figure (e). The magnitude and

Ministry of Defence © British Crown Copyright 2020/AWE

distribution of the error is similar for all of the texture change IPFs. The final two IPFs show the texture change, relative to the initial pre-load, retained after unloading to 10 MPa at the end of the experiment. It shows any residual texture change, which would be expected to be that induced by plastic deformation. It will be seen later, however, that movement of the specimen during the test complicates this interpretation.

As would be expected in the initial stages of elastic loading, no specimens exhibit a texture change by 20 MPa. All specimens then show a texture change at higher stresses, especially those over 210 MPa. The magnitude of the error shown in figure 8.37(q) is much smaller than any of the measured texture changes. This tells us that the changes are due to real changes in the spectra, not just errors associated with the fitting.

Despite this, there still seems to be a variation in the textures measured between subsequent scans. It is only practical to present texture difference IPFs for a few load steps, but this raises the question whether the observed changes are part of an overall trend, or just an anomaly in the particular IPF plotted. The value of the texture change is plotted for a few key directions as a function of stress in figure 8.38 (a)(ii), (b)(ii) and (c)(ii). The directions of interest are either reflections for which good single-peak-fits were obtained, or directions for which a texture change was observed in the Rietveld refinement. The plotted directions are shown on the IPFs to the right of each figure.

The single-peak intensities should follow the same trend as the equivalent direction in the Rietveld refinement, and are plotted in figure 8.38 (a)(i), (b)(i) and (c)(i).

Ministry of Defence © British Crown Copyright 2020/AWE

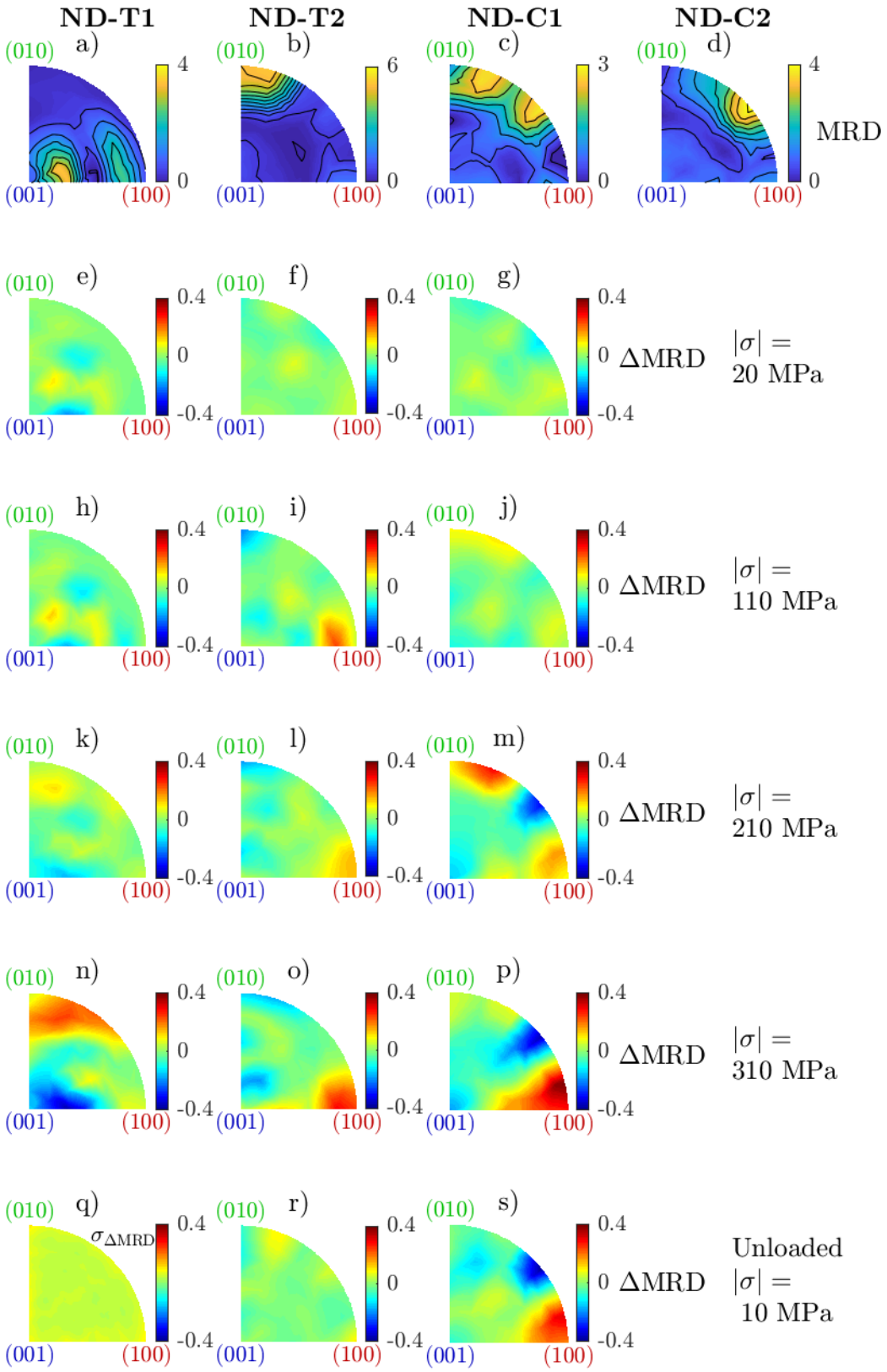


Figure 8.37. Changes in sample texture observed as a function of stress. Sub-figures (a-d) show the texture at pre-load in MRD. The IPFs in the subsequent rows show the texture change with respect to these pre-load textures at increasing stress levels (rows) for each specimen (columns). The last row shows the texture change remaining after unload (r & s), and a visualisation of the fitting error (q).

Ministry of Defence © British Crown Copyright 2020/AWE

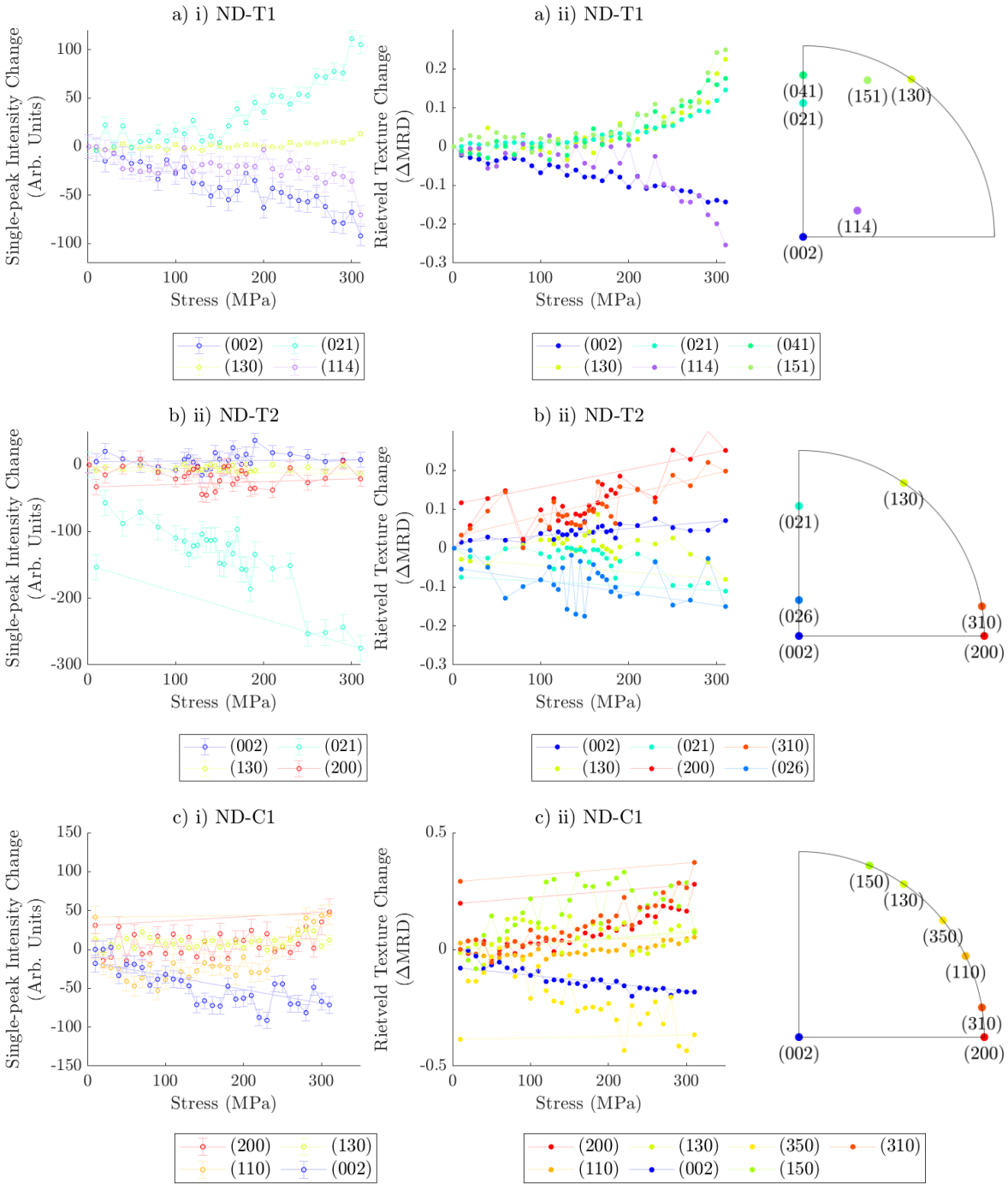


Figure 8.38. Development of single-peak intensity (i) and texture (ii) as a function of stress for key directions in the inverse pole figure (iii) identified in figure 8.37, for each of the three specimens ND-T1 (a), ND-T2 (b) and ND-C1 (c).

Ministry of Defence © British Crown Copyright 2020/AWE

A5.3.5.1 Specimen ND-T1

For specimen ND-T1, no significant texture change is observed up to 110 MPa, followed by a slight decrease in texture between (001) and (100) by 210 MPa. By 310 MPa, in figure 8.37(n), this change strengthens, with an increase of 0.4 MRD in the upper section of the IPF near (130) and a decrease near (114). The single-peak fits, in figure 8.38(a)(i), follow similar trends to their equivalent direction in the pole figures; (002) and (114) decrease, whilst (021) and (130) increase.

For both single-peak fits and the Rietveld refinement, the (002) intensity steadily decreases as the stress is increased. Similar agreement is seen for the (021) reflection, with no change until approximately 150 MPa, then the intensity increases with an increasing gradient. The single-peak intensity for the (130) reflection does not significantly increase, whilst in the Rietveld refinement it increases at the same rate as (151), which is located in the region of maximum texture increase in the IPF. This may be a result of the finite order of spherical harmonics used to fit the textures (10^{th} order in this case). The real texture change may have been sharper than what is possible to fit with the linear combination of the basis functions shown in figure 8.15. However, the good agreement between the (002) and (021) single-peak and Rietveld fits suggests that the observed texture changes are not just artefacts of fitting.

Ministry of Defence © British Crown Copyright 2020/AWE

A5.3.5.2 Specimen ND-T2

In ND-T2, the texture changes were less distinct. By 110 MPa (figure 8.37(i)), we see an increase in texture in the IPF near (100), which increases up to a maximum texture change of approximately 0.3 MRD at 310 MPa. The strong texture in this specimen makes interpretation of the single-peak intensities challenging; the majority of intensity is near (010) resulting in small peaks and poor fitting statistics in other locations. Out of the peaks whose intensity change was larger than the fitting error, only the (021) peak was seen to change with stress. It decreased linearly with stress, and upon unload, retained a change of approximately 50 % of its maximum value. The (200) single-peak intensity, which the Rietveld refinement predicts to increase significantly, does not change.

The Rietveld data, in figure 8.38(b)(ii), show the texture near (100) does indeed increase by approximately 0.25 MRD, whilst the (021) and (026) intensities decrease. All texture changes are approximately linear with stress and upon unload retain a texture change between 20 and 50 percent of the change at maximum stress.

A5.3.5.3 Specimen ND-C1

For the specimen loaded in compression, there is qualitative agreement between the Rietveld texture changes and single-peak intensities. Any decreases in intensity, such as those in the (002) and (350) directions, occur linearly with stress. The associated increase

Ministry of Defence © British Crown Copyright 2020/AWE

near (310) is not seen until stresses over 100 MPa. An increase in texture near (150) at 210 MPa disappears by 310 MPa.

The increase in texture in one direction with a concomitant decrease in another suggests the formation of deformation twins. Upon unloading, over half of the texture change seen at maximum stress is retained, as would be expected after plastic deformation.

A5.4 Discussion

The deformation shows a clear asymmetry between tension and compression. In tension, the (200)-oriented grains are deforming, whilst in compression, those oriented with the load direction near (020) deform. This suggests a strong influence of {130} or '{172}' twinning, which both have positive Schmid Factors for tension near (200) and compression near (020) (see figure 2.12)

That the (002)-oriented grains slightly deform in tension suggests that '{172}' twins are active to some extent. In tension, the Schmid Factors for Wall, Floor, Chimney slip and {130} and '$\{17\bar{6}\}$' twinning are zero or negative, so these deformation mechanisms cannot be responsible for the deformation on the (002) planes. Roof slip does have a positive SF, but the high CRSS would likely preclude deformation. This suggests some '{172}' or {112} twinning is occurring in the (002)-oriented grains as these have positive SFs in this orientation.

Ministry of Defence © British Crown Copyright 2020/AWE

A5.4.1 Initiation Stresses – comparison with prediction

We can compare the initiation stresses predicted in section A5.3.3 with that observed by looking at the lattice strain in the grain clusters most closely aligned to the texture peaks. For example, in specimen ND-T1, there are grain clusters near (115) and (422) so deformation in these clusters would lead to the saturation of elastic strain on these planes.

The fact that only a limited number of single-peak fits are available complicates the analysis. Single-peak fitting was not possible on (115) and (422), so we selected the nearby reflections in the inverse pole figure for which single-peak fits were obtained. This is the (114) peak in the case of the (115)-oriented cluster and the (110) and (111) peaks in the case of (422)-oriented grains. The (114) plane normal is misoriented from (115) by only 4.6°, whilst the (110) and (111) are misoriented from (422) by 19.7° and 16.3° respectively. The latter misorientations are large, and the resolved shear stress will be significantly different on the (110) and (111) planes compared to the (422) plane for which the Schmid factors were calculated.

To allow comparison of the experiment with the predictions, the activation stresses were recalculated using the Schmid factors at the reflection orientation.

Ministry of Defence © British Crown Copyright 2020/AWE

In a stress vs lattice strain plot, an increase in gradient would be expected for each reflection, corresponding to plasticity in these 'soft' grains and inelastic loading in a 'hard' orientation. The curves are plotted in figure 8.39.

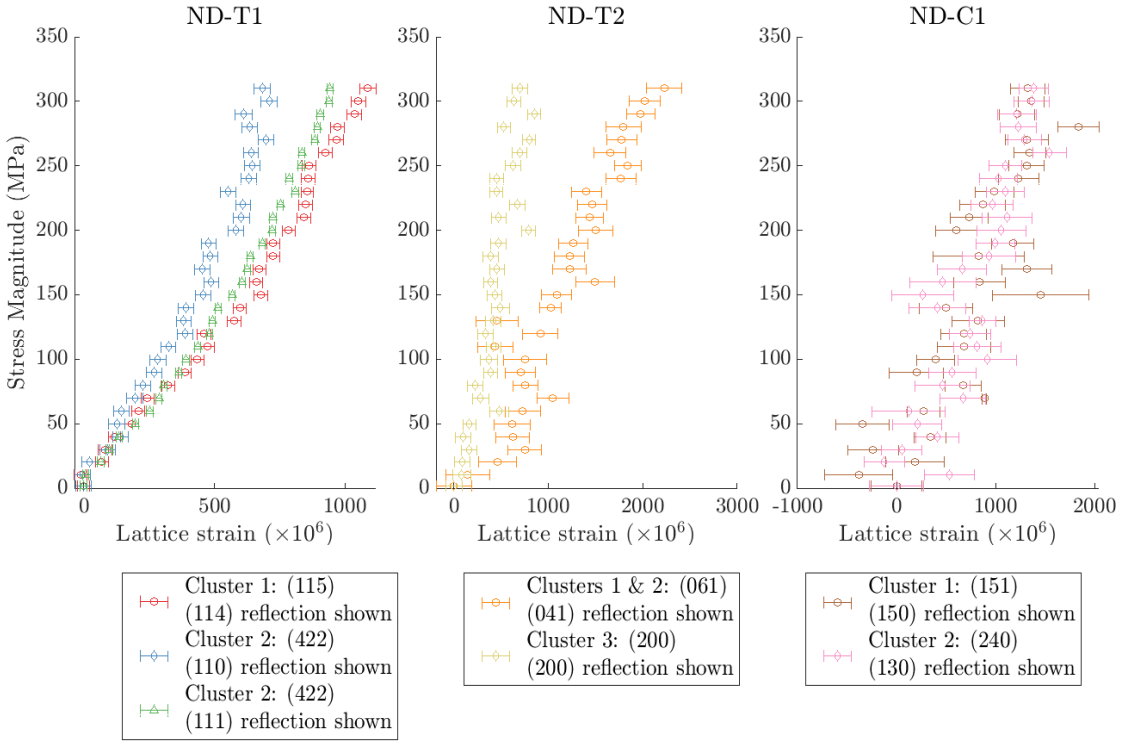


Figure 8.39. Development of elastic lattice strain as a function of stress in the families of grains aligned closest to the grain clusters in each specimen. Plastically deforming grains will have a saturation of their elastic strain (increase in gradient).

The expected deformation is compared with the experimentally observed data in table 8.7. Plasticity is detected in each grain cluster that is predicted to deform, and as expected, no plastic deformation was observed in clusters 1 and 2 in specimen ND-T2. It is not possible to identify the active deformation mode solely from the saturation of elastic lattice strain.

Ministry of Defence © British Crown Copyright 2020/AWE

Table 8.7. Comparison of predicted deformation modes with experimentally observed initiation of plasticity. The misorientation between the grain cluster and the selected reflection is shown. Large misorientations correspond to significant differences in the stress states in the grain cluster and the reflection, so the observed activation stresses cannot be reliably compared to those predicted.

Specimen	Grain Cluster hkl_{GC}	Closest Reflection hkl_{ref} & misorientation from hkl_{GC}	Expected deformation modes			Observed response	
			Main deformation modes	Activation Stress on hkl_{GC} (MPa)	Activation Stress on hkl_{ref} (MPa)	Plasticity?	Plasticity Initiation Stress on hkl_{ref} (MPa)
ND-T1	1 (115)	(114) – 4.6°	Floor slip	33	28	Yes	60
	2 (422)	(110) – 19.7° & (111) – 16.3°	Wall slip {130} twins	33 54	18-23 58-73	Yes	100
ND-T2	1 (061)	(041) – 5.3°	No deformation expected		------	No	N/A
	2 (061)	(041) – 5.3°	No deformation expected		------	No	N/A
	3 (200)	(200) – 0°	{130} twins	54	54	Yes	50 - 100
ND-C1	1 (151)	(150) – 12.4°	Wall slip {130} twins	21 57	20 54	Yes	200
	2 (240)	(130) – 11.4°	Wall slip	14	15	Yes	130

In the two tensile specimens, plasticity was initiated in the grain cluster with the lowest activation stress at a stress comparable to that predicted. However the plasticity in the second grain cluster in specimen ND-T1 occurred at a higher stress than predicted. It could also be possible that the initiation of plasticity in the first grain modified the local stress state in such a way that the stress in the second grain did not reach such a high level. This would be possible if both grain clusters were arranged in 'series' with respect to the loading axis. Alternatively, and more likely, the CRSS parameters in the literature may not be applicable to this microstructure.

The majority of the gauge volume of specimen ND-T2 was aligned with its (020) axis along the loading direction, which was not expected to deform by any mode except the

Ministry of Defence © British Crown Copyright 2020/AWE

rare '{176}' mode, for which an estimation of the CRSS was not available. The (020) reflection behaves plastically hard, as seen by inspection of figure 8.34.

A5.4.2 Identifying Twinning Mode from Texture Changes

The measured texture changes were compared with the predicted texture changes from twinning in an attempt to identify the active twinning modes. The calculation of the predicted texture changes is discussed in section 3.5 on page 76 in the main body of the thesis. The reader should refer to figure 3.9 (p.87) and figure 3.10 (p.88) for the possible texture changes due to twinning in tension and compression respectively.

A5.4.2.1 Specimen ND-T1

The tensile twinning deformation predicted on page 427 for specimen ND-T1 was the formation of {130} twins in grain cluster 2 oriented near (422). By comparison of the observed texture change in figure 8.37 with the twinning reorientations in figure 3.9, it can be seen that {130} twins could not be solely responsible for the observed texture changes of a decrease near (115) and an increase near (010). The first variant of '{172}' twinning, shown in figure 3.9(b), could be responsible for the observed change, however '{172}' twinning in cluster 1 was predicted to occur at a much higher stress than the {130} twinning in cluster 2. No decrease in texture was observed in cluster 2, suggesting that this cluster was not deforming by twinning.

Ministry of Defence © British Crown Copyright 2020/AWE

The magnitude of the observed texture change is small, with increases and decrease of approximately 0.25 MRD seen at the maximum stress of 310 MPa (figure 8.38). This is small compared to the textures which have maxima of almost 4 MRD corresponding to just a 7 % decrease in texture along (115).

A5.4.2.2 Specimen ND-T2

The only twinning deformation predicted in specimen ND-T2 was '{176}' twinning in clusters 1 and 2 near (061). There is no evidence for this; in figure 8.37 no decrease in texture was seen near (061) in ND-T2, and figure 3.9 shows '{176}' twinning of this orientation cannot be responsible for the increase near (200).

{130} twinning was predicted in cluster 3 near (200), however the texture increase here is not consistent with the decrease expected if twinning was occurring.

A5.4.2.3 Specimen ND-C1

In the compression specimen, the predicted deformation was {130} twinning at 60 MPa in the cluster near (151), near the top-left of the IPF in figure 8.37, however no texture decrease was seen in this orientation. Figure 8.38 shows an increase in texture near (200), that by inspection of figure 3.10 would be consistent with the general activation of {130} and '{172}' twins. Specific deformation modes cannot be identified, and none satisfactorily explain the observed texture change.

Ministry of Defence © British Crown Copyright 2020/AWE

A5.4.2.4 Discussion of observations

In general, the texture changes could not be explained by formation of a single twin variant. The texture changes were not very distinct and therefore do not provide strong evidence for the formation of the twins that were predicted by the Schmid factor analysis.

Factors which could contribute to the observations were identified:

1. Multiple twins were activating simultaneously in such a way that the texture changes from each twin add to give the observed texture change.
2. A significant part deformation is actually slip, and the deforming crystal is therefore slowly rotating. In the case of specimen ND-C1, the texture increases and decreases are adjacent to one another in the IPF, which could be evidence for slip in this specimen.
3. The observed texture change is partially or wholly an artefact of the movement of the specimen during the test. This effect is actually quite significant and is discussed in the following section.

A5.4.3 Texture Movement Artefacts

The measured texture depends on the distribution of crystal orientations within the gauge volume, which is fixed with respect to the instrument. During loading, it is possible that the specimen moves due to the compliance of the load frame. Specimen movement could cause a texture change to be measured if the gauge volume moves into a region of the specimen with a different texture. This effect is discussed in detail in section 3.6 in

Ministry of Defence © British Crown Copyright 2020/AWE

the main body of the thesis, where a derivation of the magnitude of a potential texture change artefact is presented.

For our experiment on ENGIN-X, the gauge volume had dimensions of either 4 mm × 4 mm × 8 mm (tension) or 4 mm × 4 mm × 12 mm (compression) so $l = 4$ mm in both cases. Using equation [3.23], the fractional change in gauge volume as a function of specimen movement is shown in figure 8.40.

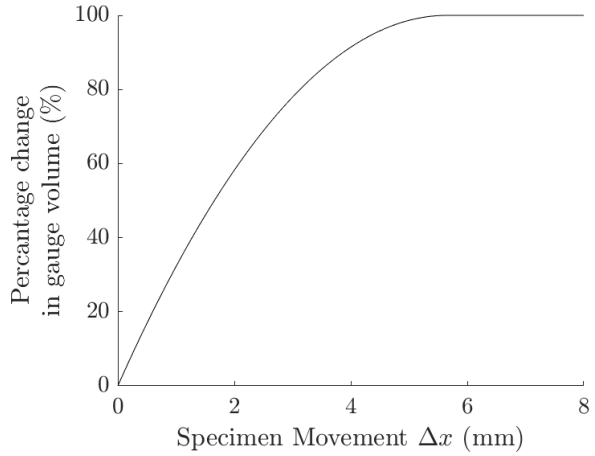


Figure 8.40. Fractional change in texture as a function of specimen movement for the experiment on ENGIN-X, calculated using equations [3.23] and [3.26] with $l = 4$ mm.

The change in texture would therefore be expected to be close-to-linear with the specimen displacement up to displacements of approximately 2 mm.

A5.4.3.1 Observed Specimen Movement

The axial displacement of the specimens from that during the scan at pre-load was calculated from the DIC displacement data as the average of the *x*-displacements of the specimen grips at the 'fixed' and 'moving' ends. The gauge volume movement for

Ministry of Defence © British Crown Copyright 2020/AWE

specimens ND-T1, ND-T2 and ND-C1 is shown in figure 8.41(a) as a function of applied stress.

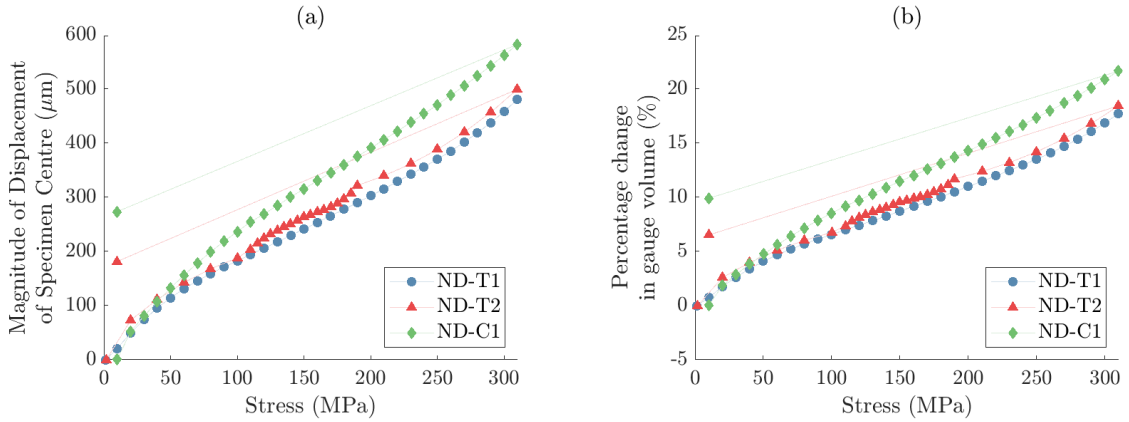


Figure 8.41. (a) Specimen movement as a function of applied stress. (b) Maximum possible texture change artefact; the percentage change in GV as a function of stress.

Using equation [3.23], this was converted into a percentage change in the gauge volume, which gives an upper bound to the texture change artefact. At maximum load, all specimens experience displacements that could introduce texture changes up to 15-20 % in the case where the specimen texture changes abruptly in the vicinity of the gauge volume.

A5.4.3.2 Significance of Specimen Movement

For all specimens tested, the texture change artefact is approximately linear with applied stress. At maximum load, a change in texture of up to 15-20 % could be expected from this effect. With the texture in a grain cluster on the order of 3 MRD, this would correspond to changes of 0.45-0.6 MRD, which is only slightly larger than the observed changes of 0.4 MRD.

Ministry of Defence © British Crown Copyright 2020/AWE

Specimen ND-T1 exhibits a linear decrease of single-peak intensity of the (002) and (114) reflections with stress (figure 8.38(a)(i)), which suggests that specimen movement is at least partially responsible for the observed texture change. That there is a non-linear increase in (021) intensity rules out this artefact as the sole contribution to the texture change.

In specimen ND-T2, a linear decrease in (021) peak intensity is observed. At unload, the specimen displacement is the same as at 100 MPa applied load so, if the texture change is solely an artefact of specimen movement, we would expect the texture change at unload to be the same as at 100 MPa. This is seen to be true by inspection of figure 8.38(b)(i) and (b)(ii) on page 441.

The magnitude of displacement is largest for the compression specimen. Its larger cross-sectional area requires a larger force for a given stress, and therefore a larger deflection in the load frame. A linear decrease is seen in the (350) and (002) Rietveld intensities with applied stress (figure 8.38(c)(ii)). At unload, the displacement is the same as at 120 MPa, but the texture change is larger than what could be explained by specimen movement alone. This supports the hypothesis that the texture change is due to plastic deformation. There is a significant difference between the behaviour seen in the Rietveld refinement, which at unload retains the majority of the texture change seen at maximum load, and the SPF intensities, which do not.

Ministry of Defence © British Crown Copyright 2020/AWE

On page 449 it was seen that the observed texture change for ND-C1 was not easily identifiable as twinning. Since no sudden texture increase was observed (which would distinguish it from any specimen movement artefact), we can conclude that twinning did not occur to a detectable level in the gauge volume of specimen ND-C1. Deformation could therefore have been via Wall slip; grain cluster 2, in which the texture decrease was observed, is in the perfect orientation for this mode with a SF of 0.5. Slip deformation rotates the crystal such that the loading axis moves towards the slip direction. For Wall slip, the slip direction is [100], which would fit the observed texture change, so we can conclude that the dominant deformation mode in the gauge volume of specimen ND-C1 was Wall slip.

A5.5 Summary

This appendix presented an experiment on the ENGIN-X instrument at ISIS to measure the deformation of coarse-grained uranium. Two specimens were tested in tension, and one in compression.

Single-peak fitting and Rietveld refinement were used to fit the measured diffraction spectra. Axial texture measurement was successfully performed using spherical harmonics in the Rietveld refinement. A novel implementation was used to quantify the error in the measured axial textures; this verified that any changes were not due to fitting error in the harmonic parameters, which may have been an issue for the sharp textures in our coarse-grained material. Between two and three grain clusters were

Ministry of Defence © British Crown Copyright 2020/AWE

present in the gauge volume of each specimen. By performing a measurement on GEM at ISIS, the full texture can be measured – this matches well with those measured on ENGIN-X, and provides a more complete orientation measurement for use in subsequent CPFE modelling in a supporting project.

The Schmid factor was used to predict the primary deformation mode and yield stress for each grain cluster.

The lattice parameter strain, calculated from the Rietveld refinement, was less noisy than the equivalent lattice strain calculated from single-peak fitting. The tension / compression asymmetry of deformation twinning is apparent in the lattice parameter strains. In tension, (200)-oriented grains are plastically soft whilst (020)-oriented grains are seen to be plastically hard. The opposite is seen in compression.

By inspection of the lattice strain for reflections from the dominant grain clusters, it was possible to measure the stress at which plasticity activates in each of these grains. Activation was seen in certain families of grains from approximately 50 MPa in the tensile specimens and at significantly higher stresses in the compression specimen. The deformation mode cannot be identified from the lattice strains alone. This qualitatively agreed with the predictions using CRSS values from the literature, in that all grains which were predicted to deform did deform, and vice versa. The initiation stresses did not match which suggests the CRSS parameters were not applicable for this

Ministry of Defence © British Crown Copyright 2020/AWE

microstructure. Subsequent CPFE modelling work should identify an optimised set of deformation parameters.

Calculation and inspection of the 'texture differences' with respect to the texture measured at pre-load allowed small texture changes to be identified in the presence of strong textures. A novel method was developed to predict the texture changes expected in the North bank detector upon activation of each variant of the $\{130\}$, '$\{172\}$', '$\{176\}$', and $\{112\}$ twinning modes. These were presented on inverse pole figures with pairs of parent and twin orientations plotted. Different texture changes are expected in tension and compression due to the asymmetric Schmid factors for twinning.

It was not possible however to positively identify, from the observed texture changes, the operational twinning modes in any of the specimens. In materials with coarse or clustered grains, where the similarly-oriented regions are a similar size to the instrumental gauge volume, specimen movement can introduce significant artefacts into the measured texture changes. The magnitude of this artefact is large enough to have caused some or all of the observed gauge volume deformation. This is likely to have been responsible for the texture changes observed in specimen ND-T2.

Some deformation was however observed in the other specimens. The non-linear texture change in specimen ND-T1 is the combination of deformation-induced texture change and artefacts of specimen movement. The texture change in the compression specimen,

Ministry of Defence © British Crown Copyright 2020/AWE

ND-C1, is much larger than the movement artefact, and was formed by Wall slip in the gauge volume.

Ministry of Defence © British Crown Copyright 2020/AWE

Ministry of Defence © British Crown Copyright 2020/AWE

A6 Deformation and Fracture in Chapter 4

A6.1 Heterogeneity of Deformation

DIC captures the development of the strain field at the specimen surface adjacent to the neutron gauge volume. In general, heterogeneities developed at a very low strain, and then increased in magnitude as the stress level was increased.

The specimens have a circular cross-section, so the top and bottom parts of the specimen are further away from the camera. Consequently, a uniform displacement will appear slightly smaller in the regions that are further away, as the motion subtends a smaller angle in the camera's field of view. However, the application of the DIC mask restricts the data to the central section of each specimen where this effect is minimised. The magnitude of the measured strains is much larger than any potential artefact.

The uncertainty in the DIC-measured axial strains was estimated as the standard deviation in the strain measurement at the first load above pre-load, where the deformation was small, elastic, and uniform across the specimen surface. The axial strain uncertainty in each DIC dataset is shown in table 8.8.

Table 8.8. DIC axial strain error

Specimen	$\sigma(\varepsilon_{xx})$ (%)
ND-T3	0.08
ND-T4	0.05
ND-C3	0.02
ND-C4	0.02

Ministry of Defence © British Crown Copyright 2020/AWE

In each case, the DIC error is several orders of magnitude less than the measured strains, so can be ignored.

In this section, I will present the axial, tangential, and shear strains (ε_{xx}, ε_{yy}, and ε_{xy}) on the surface of each specimen at a post-straining unload of 10 MPa stress magnitude. For the tensile specimens, the last unload before fracture (unload C) was chosen, and for the compression specimens, the last unload for which DIC data was available was selected (ND-T3: unload D, ND-T4: unload E).

Positive strains (tensile in the case of the normal strains ε_{xx} and ε_{yy}) are coloured in red, and regions of negative strain in blue. A grid of vector arrows is overlaid on each image to show the form of the displacement field. The displayed field is the measured displacement field after the subtraction of the mean displacement to remove the rigid body translation. This highlights the relative motion of each part of the specimen.

Finally, histograms are plotted showing the distribution of strain at the surface of the gauge volume in each specimen. In each case, the 95th percentile axial strain is labelled; this is the magnitude of axial strain at which 5 % of the data points have a greater magnitude of axial strain. Comparing this to the mean strain allows a simple evaluation of the high-strain 'tail' of the distribution, associated with stress concentrations.

Ministry of Defence © British Crown Copyright 2020/AWE

A6.1.1 Specimen ND-T3

In specimen ND-T3, the strain concentration that initiated fracture was located outside the field of view of the camera, to the right-hand side of the images. A smaller field of view was used to image this specimen compared to subsequent specimens. Consequently, the images have a smaller pixel size and more details can be seen in the strain distribution.

By inspection of the displacement vectors in figure 8.42, it can be seen that the gauge region shears, with the right-hand side moving upwards compared to the left-hand side of the image.

The axial strain appears to be completely positive, as expected for deformation in tension. It is, however, not uniform, with large regions at low strains of around 2%, and regions of high strain (> 5%) aligned at 45 degrees to the loading axis. Regions of negative tangential strain are coincident with regions of high axial strain, as expected for a material with a positive Poisson's ratio. There is no clear pattern in the regions of positive and negative shear.

The histogram in figure 8.43 shows a smooth distribution of axial strain (blue) with the shear strain (green) evenly distributed about zero. This is expected as no strain concentration is present in the DIC images. 5% of the axial strains are greater than 6.5% in magnitude.

Ministry of Defence © British Crown Copyright 2020/AWE

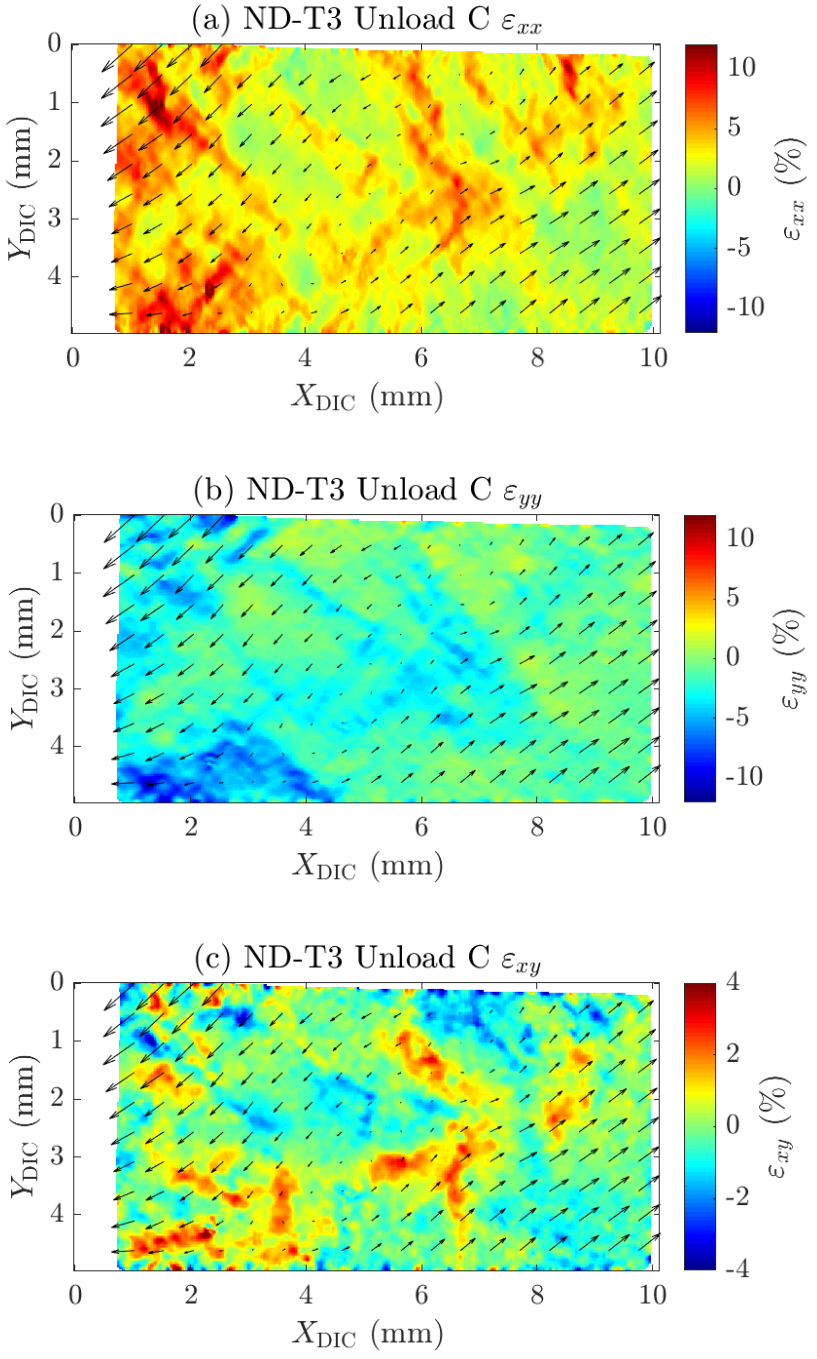


Figure 8.42. DIC strain fields (a) ε_{xx} (axial), (b) ε_{yy} (tangential), and (c) ε_{xy} (shear) from specimen ND-T3 at unload C, corresponding to a mean axial strain of 3.0 %. Positive strains are coloured in red, negative strains in blue. Arrows show the displacement of the specimen surface relative to the average motion (i.e. ignoring translational rigid body movement). Vector lengths are scaled to ensure visibility.

Ministry of Defence © British Crown Copyright 2020/AWE

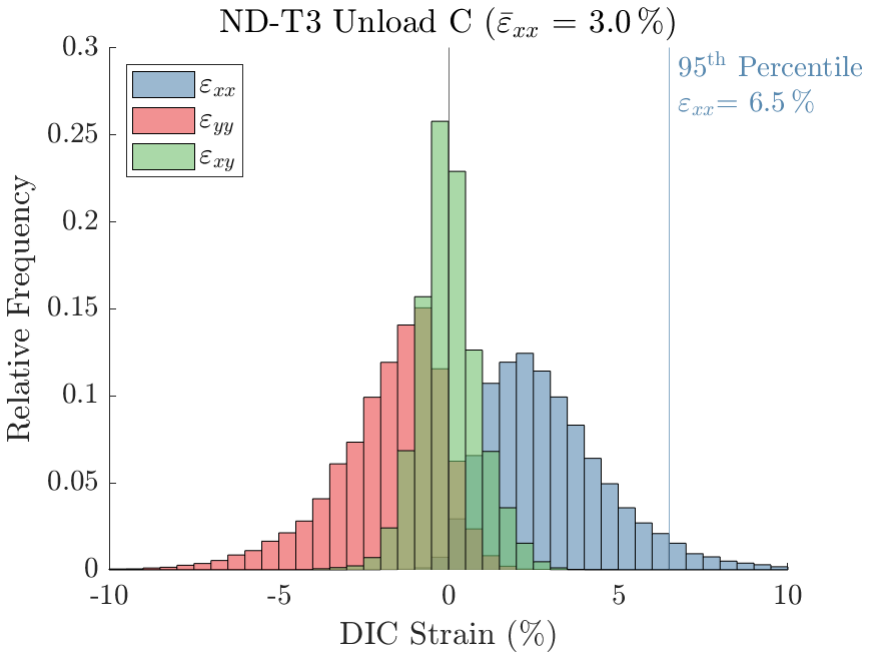


Figure 8.43. Histogram showing the distribution of the ε_{xx} (axial, blue), ε_{yy} (tangential, red), and ε_{xy} (shear, green) strains in specimen ND-T3 at unload C. Bars are plotted with a 0.5 % bin width. The 95th percentile axial strain is marked as a vertical blue line.

A6.1.2 Specimen ND-T4

Specimen ND-T4 has a strain concentration in the left hand side of its gauge region, aligned at 45 degrees to the loading axis. The maximum tensile and shear strain is at the bottom left of the image, consistent with the location of fracture initiation.

The displacement field clearly shows localised shearing along a line running from the strain concentration at the bottom-left to the top-centre of the image. Close to this line, the right-hand side is moving towards the top-right of the image, and the left-hand is moving in the opposite direction. Away from this line, there is fairly uniform movement of the specimen along its axis, away from the strain concentration. This shows that the majority of the deformation is localised near this shear line.

Ministry of Defence © British Crown Copyright 2020/AWE

At unload C, approximately 50% of the gauge volume has an axial strain greater than 5%. The region to the right of the shear line strains to a lesser extent, with axial strains between 1% and 3%. The maximum axial strain of 12% is at the bottom left of the image. The shear strain is concentrated in this region, as expected for localised shear deformation.

A peak in the axial strain distribution occurs between 1% and 2% strain. This is predominantly the contributions from the low-strain right hand side of the DIC image. There is a broad distribution of larger strains with a near-constant frequency until 10% strain. The 95th percentile strain is 10.2%.

Ministry of Defence © British Crown Copyright 2020/AWE

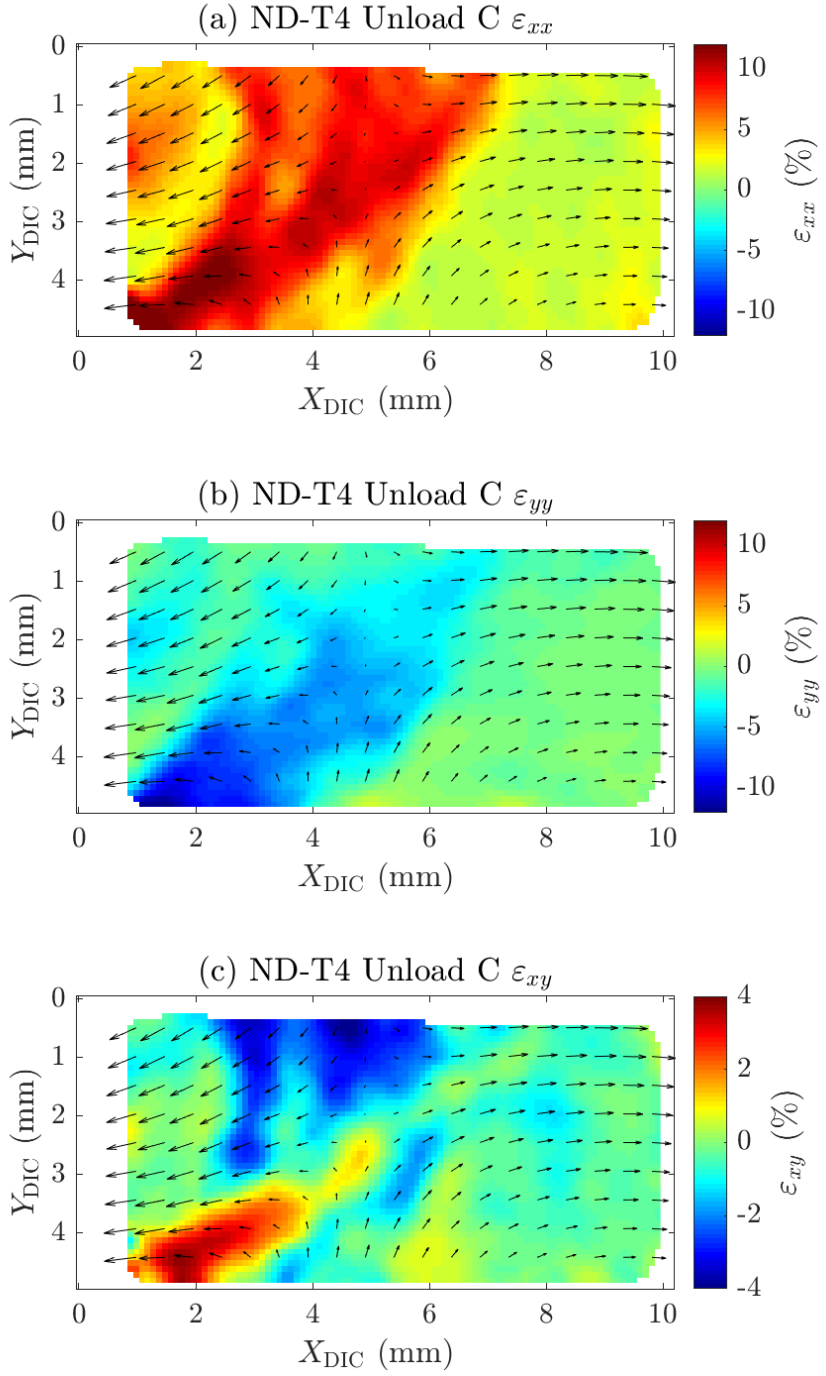


Figure 8.44. DIC strain fields (a) ε_{xx} (axial), (b) ε_{yy} (tangential), and (c) ε_{xy} (shear) from specimen ND-T4 at unload C, corresponding to a mean axial strain of 4.8 %. Positive strains are coloured in red, negative strains in blue. Arrows show the displacement of the specimen surface relative to the average motion (i.e. ignoring translational rigid body movement). Vector lengths are scaled to ensure visibility.

Ministry of Defence © British Crown Copyright 2020/AWE

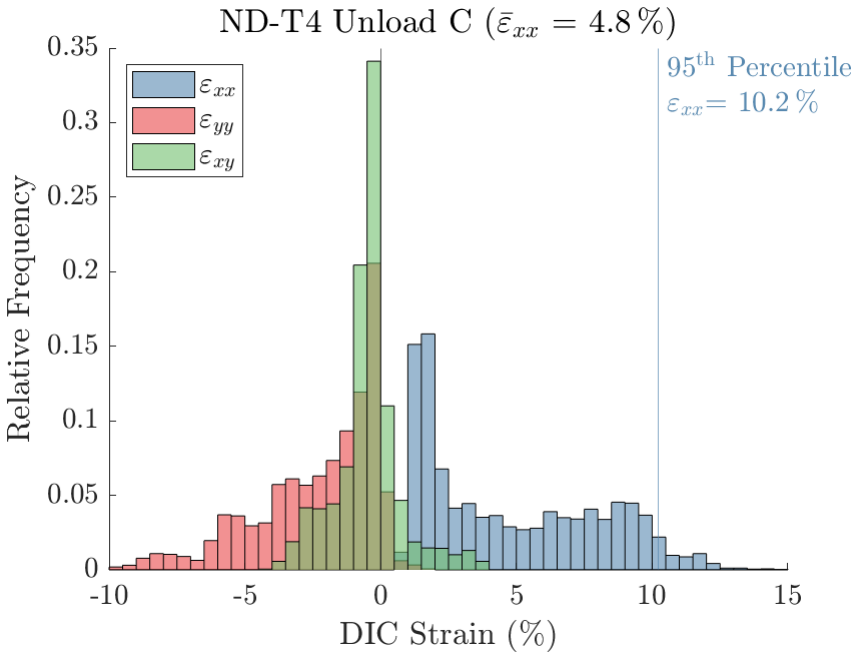


Figure 8.45. Histogram showing the distribution of the ε_{xx} (axial, blue), ε_{yy} (tangential, red), and ε_{xy} (shear, green) strains in specimen ND-T4 at unload C. Bars are plotted with a 0.5 % bin width. The 95th percentile axial strain is marked as a vertical blue line.

A6.1.3 Specimen ND-C3

The strain field in specimen ND-C3 is fairly uniform, with a mean strain of $-4\,\%$. Overall, the specimen shears such that the top-right part of the specimen moves up and over the bottom left.

A small region of strong shear is seen in the top right of figure 8.46(c), at 45 degrees to the loading axis. There is an associated tensile tangential strain (ε_{yy}) but no detectable change in axial strain (ε_{xx}); it is therefore a tangential bulging of the specimen in this region.

Ministry of Defence © British Crown Copyright 2020/AWE

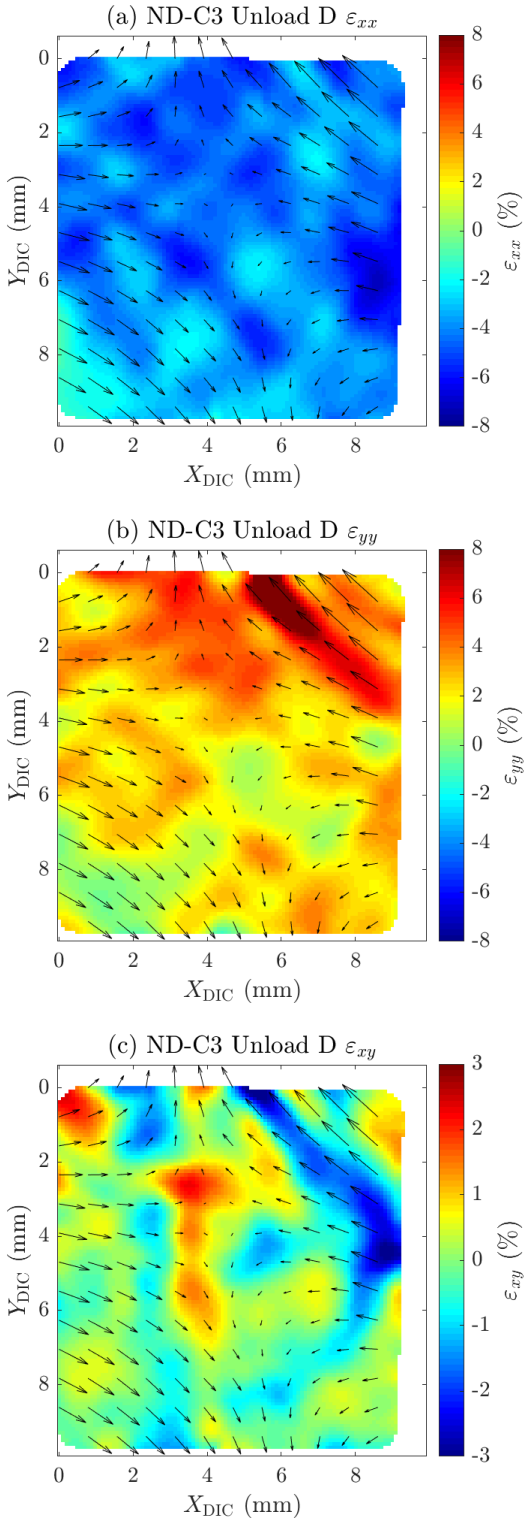


Figure 8.46. DIC strain fields (a) ε_{xx} (axial), (b) ε_{yy} (tangential), and (c) ε_{xy} (shear) from specimen ND-C3 at unload D, corresponding to a mean compressive axial strain of 4.0 %. Note that this is before the final loading cycle is performed. Positive strains are coloured in red, negative strains in blue. Arrows show the displacement of the specimen surface relative to the average motion (i.e. ignoring translational rigid body movement). Vector lengths are scaled to ensure visibility.

Ministry of Defence © British Crown Copyright 2020/AWE

In the absence of a large strain concentration, the distribution of strain is close to a normal distribution. The 95th percentile of compressive axial strain magnitude is 5.7 %, which is less than 1.5 times the magnitude of the mean strain.

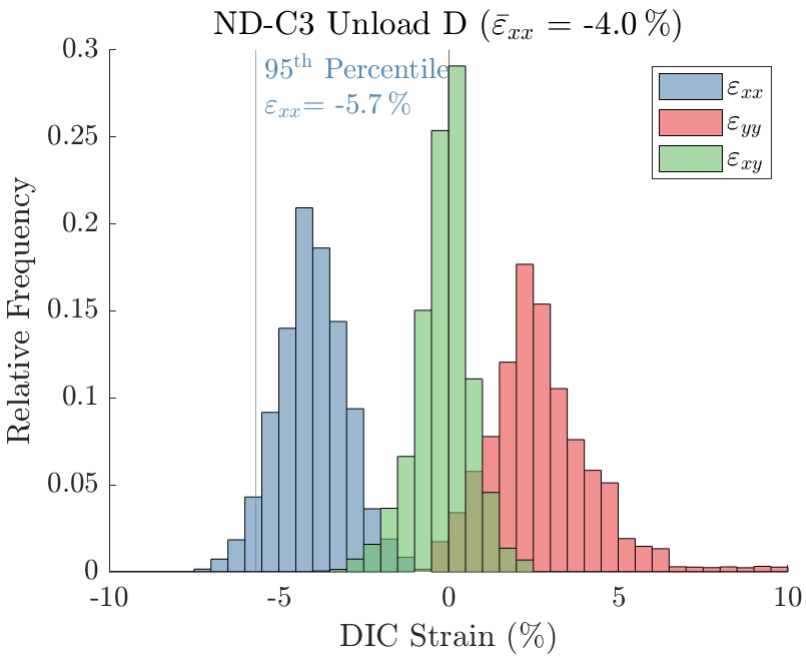


Figure 8.47. Histogram showing the distribution of the ε_{xx} (axial, blue), ε_{yy} (tangential, red), and ε_{xy} (shear, green) strains in specimen ND-C3 at unload D. Bars are plotted with a 0.5 % bin width. The 95th percentile axial strain is marked as a vertical blue line, defining more compressive strains as larger.

Ministry of Defence © British Crown Copyright 2020/AWE

A6.1.4 Specimen ND-C4

The lower-left region of specimen ND-C4, shown in figure 8.48, undergoes very limited deformation. The upper-right of the gauge volume moves up and left with respect to the left-hand side. This corresponds to a negative shear strain and an anticlockwise rotation of the displacement vectors.

There are regions towards the right-hand side showing a strong localisation of deformation, with shear strain in excess of 6 %. In some regions approximately 1 mm × 1 mm in size, the tangential tensile strain is in excess of 10 % with an axial compressive strain up to 20 %.

Unlike in the other specimens, where the mean shear strain was between -1.5 % and 1.5 %, the mean shear strain is -4 %.

The distribution of axial strains has a tail which extends to very large compressive strains, with 5 % of the data points having ε_{xx} values great in magnitude than 15.1 %.

Ministry of Defence © British Crown Copyright 2020/AWE

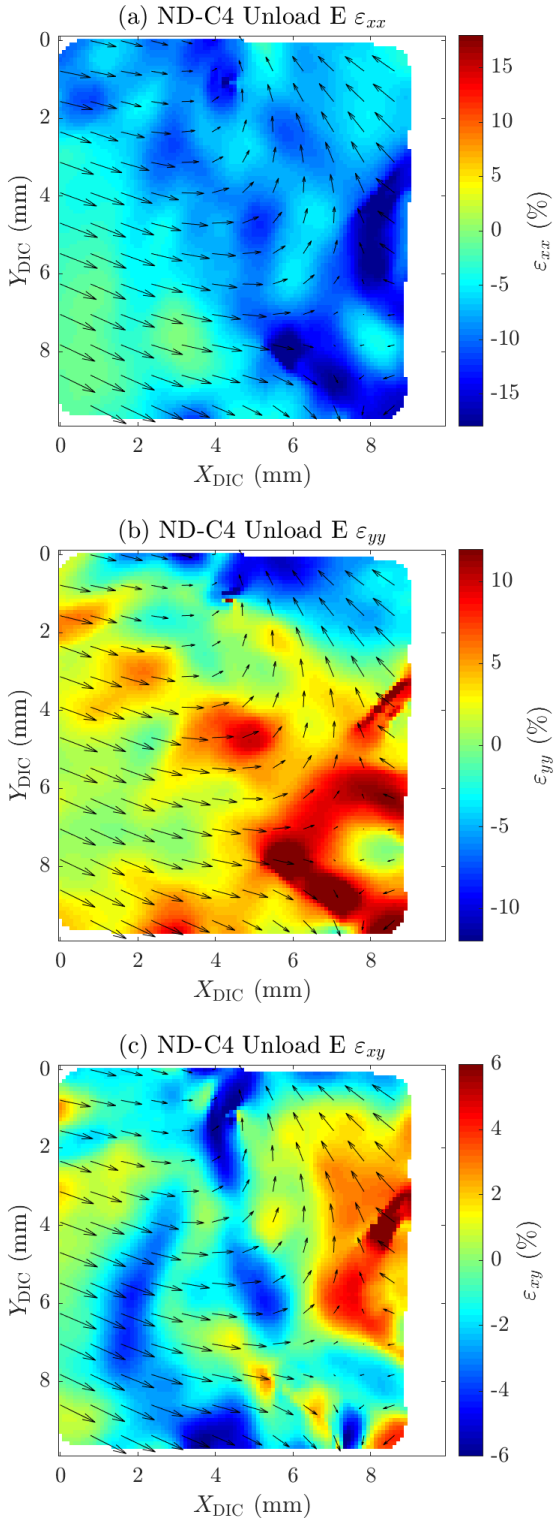


Figure 8.48. DIC strain fields (a) ε_{xx} (axial), (b) ε_{yy} (tangential), and (c) ε_{xy} (shear) from specimen ND-C4 at unload E, after the final loading cycle, corresponding to a mean compressive axial strain of 7.4 %. Positive strains are coloured in red, negative strains in blue. Arrows show the displacement of the specimen surface relative to the average motion (i.e. ignoring translational rigid body movement). Vector lengths are scaled to ensure visibility.

Ministry of Defence © British Crown Copyright 2020/AWE

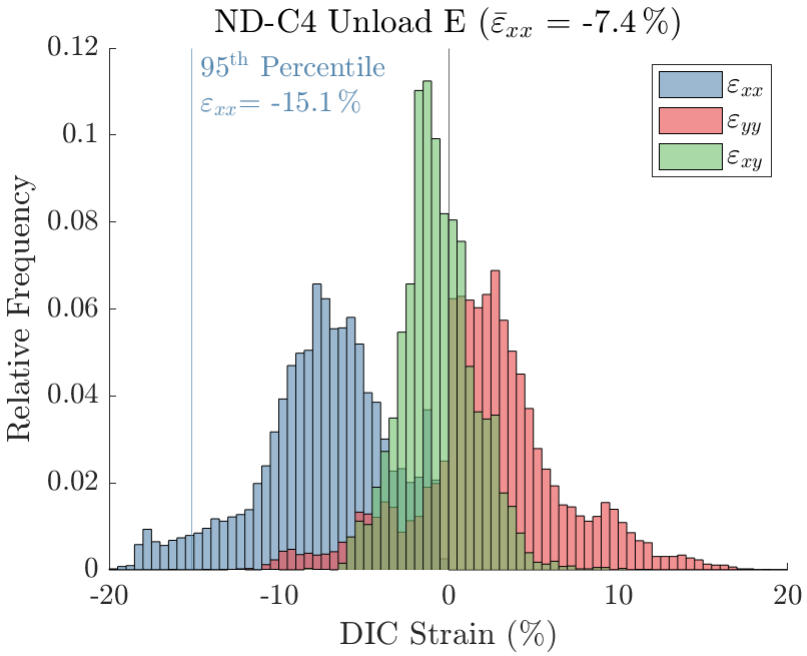


Figure 8.49. Histogram showing the distribution of the ε_{xx} (axial, blue), ε_{yy} (tangential, red), and ε_{xy} (shear, green) strains in specimen ND-C3 at unload D. Bars are plotted with a 0.5 % bin width. The 95th percentile axial strain is marked as a vertical blue line, defining more compressive strains as larger.

A6.2 Fracture and Fractography

Both tensile specimens failed via fast fracture, with a crack propagating approximately perpendicular to the loading direction. SEM fractography was kindly performed on the fracture surfaces of specimens ND-T3 and ND-T4 by Dr Rod McCabe at Los Alamos National Laboratory. Images were taken with the T1, T2 and Everhardt-Thornley Detector (ETD) at a working distance of ~8.0 mm and an accelerating voltage of 5.00 kV. The T1 detector was operating in the (A+B) mode which maximised atomic number contrast. The T2 detector is an 'in-lens' detector which receives an almost-pure secondary electron (SE) signal[172] and therefore showed excellent topographic contrast, in particular of edge features. The ETD was operated in the SE mode and therefore showed good overall topographic contrast.

Ministry of Defence © British Crown Copyright 2020/AWE

The fractography looked at 9 regions across the fracture surfaces of the two specimens. For each region, up to 5 images were taken, with magnifications between 100× and 5000× giving fields-of-view of approximately 2 mm to 40 μm. For each magnification, 3 images were taken – one with each detector. In this section, micrographs are shown of two regions in specimen ND-T3 (regions A and B) and also specimen ND-T4 (regions C and D). Detector T2 images are presented as they show good topographical contrast, with the exception of region C in specimen ND-T4, for which images from the ETD are most useful.

The location of each region within the specimen was not recorded.

A6.2.1 Specimen ND-T3

Specimen ND-T3 fractured at a stress of 480 MPa. Just before fracture, the mean DIC strain ε_{xx} in the gauge volume was 5.4 % with local strains in excess of 15 %. Fracture occurred at the edge of the parallel gauge region, to the right-hand side of the specimen as viewed by the DIC camera (but outside its field of view). The specimen completely broke apart, with the fracture surface being perpendicular to the specimen axis. By eye, the surface was rough, but with some 'shiny' reflections visible indicating the presence of smaller flatter regions. It will be seen that these are cleavage planes, and a high density of twins are visible intersecting these planes. Figure 8.50 is a photograph of the specimen after fracture, viewed along the axis of the incoming beam towards the source.

Ministry of Defence © British Crown Copyright 2020/AWE



Figure 8.50. Fracture of specimen ND-T3. The DIC camera is located at the top-right of the image, so the fracture occurred at the right hand end of the parallel gauge region of the specimen, as viewed by the camera.

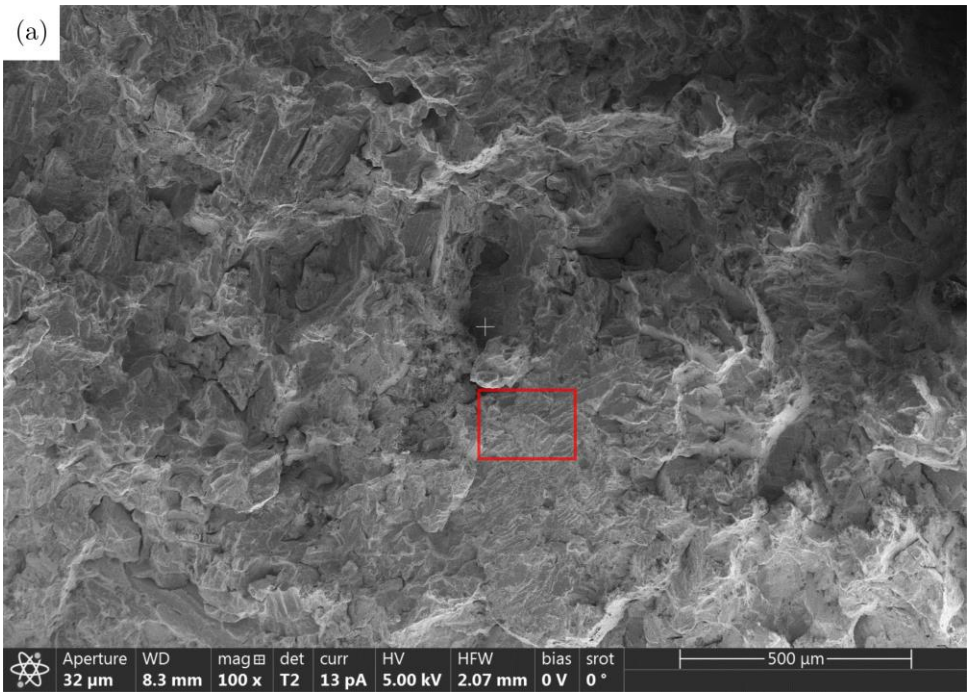
A6.2.1.1 Region A (ND-T3)

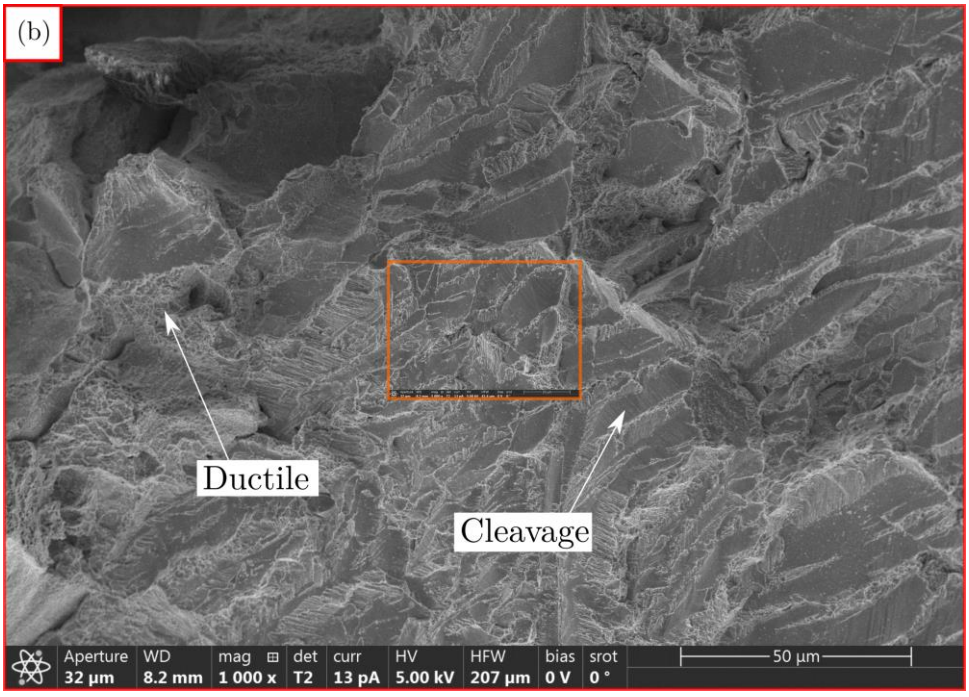
Region A in specimen ND-T3, shown in figure 8.51(a), shows that the microscopic topography is not flat, with significant protrusions with widths of 200 μm to 500 μm. The features are angular, suggesting intercrystalline (grain boundary) fracture. In figure 8.51(b), the left-hand side has regions of rough surface indicative of ductile fracture, whilst the right-hand side shows flat regions with widths ~20 μm and lengths >50 μm, with rougher lines of ~5 μm width between them. These features are aligned from the bottom-left to the top-right of the images.

At a higher magnification, in subfigure (c), the flat areas are smooth, with twins visible across the image. The majority of these twins appear as darker regions, and run from top-left to bottom-right, suggesting a similar crystallographic orientation for the

Ministry of Defence © British Crown Copyright 2020/AWE

underlying grain across the whole image. The twins are between 0.5 μm and 1 μm in width, and in some places are tapered and show the classic lenticular morphology.





Ministry of Defence © British Crown Copyright 2020/AWE

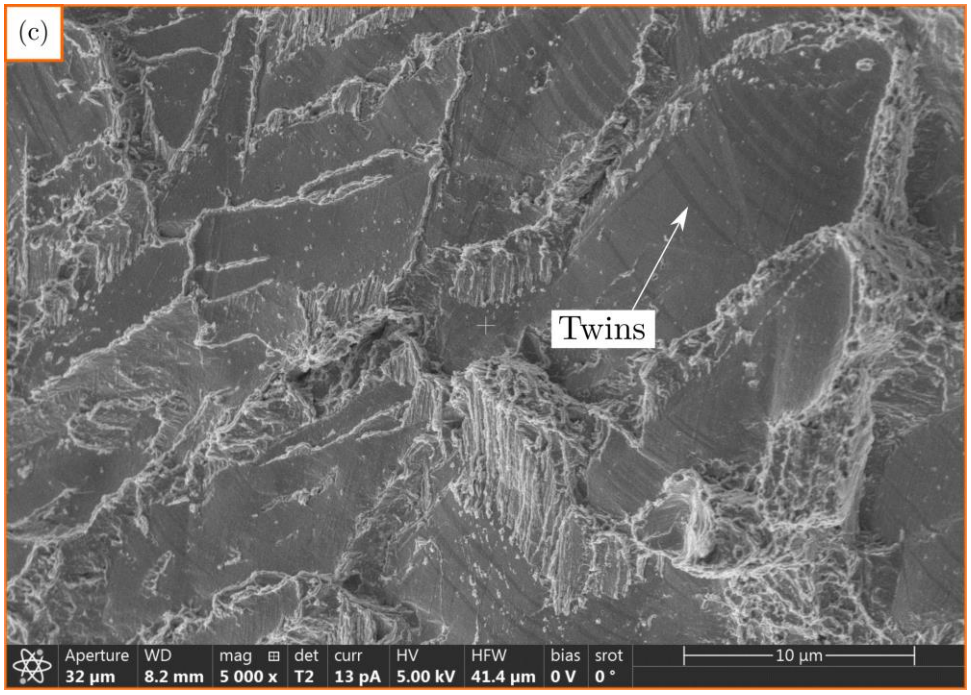


Figure 8.51. SEM fractography image showing a region A of the fracture surface of specimen ND-T3. Images acquired using the T2 detector at magnifications of (a) 100×, (b) 1000×, and (c) 5000×. Deformation twins are visible intersecting the cleavage planes in the top-right corner of subfigure (c).

A6.2.1.2 Region B (ND-T3)

Region B shows an angular fracture surface, with a flat region in the centre of figure 8.52(a) that is much larger than those seen in region A. Figure 8.52(b) shows this region is in excess of $200\,\mu\mathrm{m}$ in size with steps separating it from regions of a similar morphology. At this magnification, twins are not visible.

Ministry of Defence © British Crown Copyright 2020/AWE

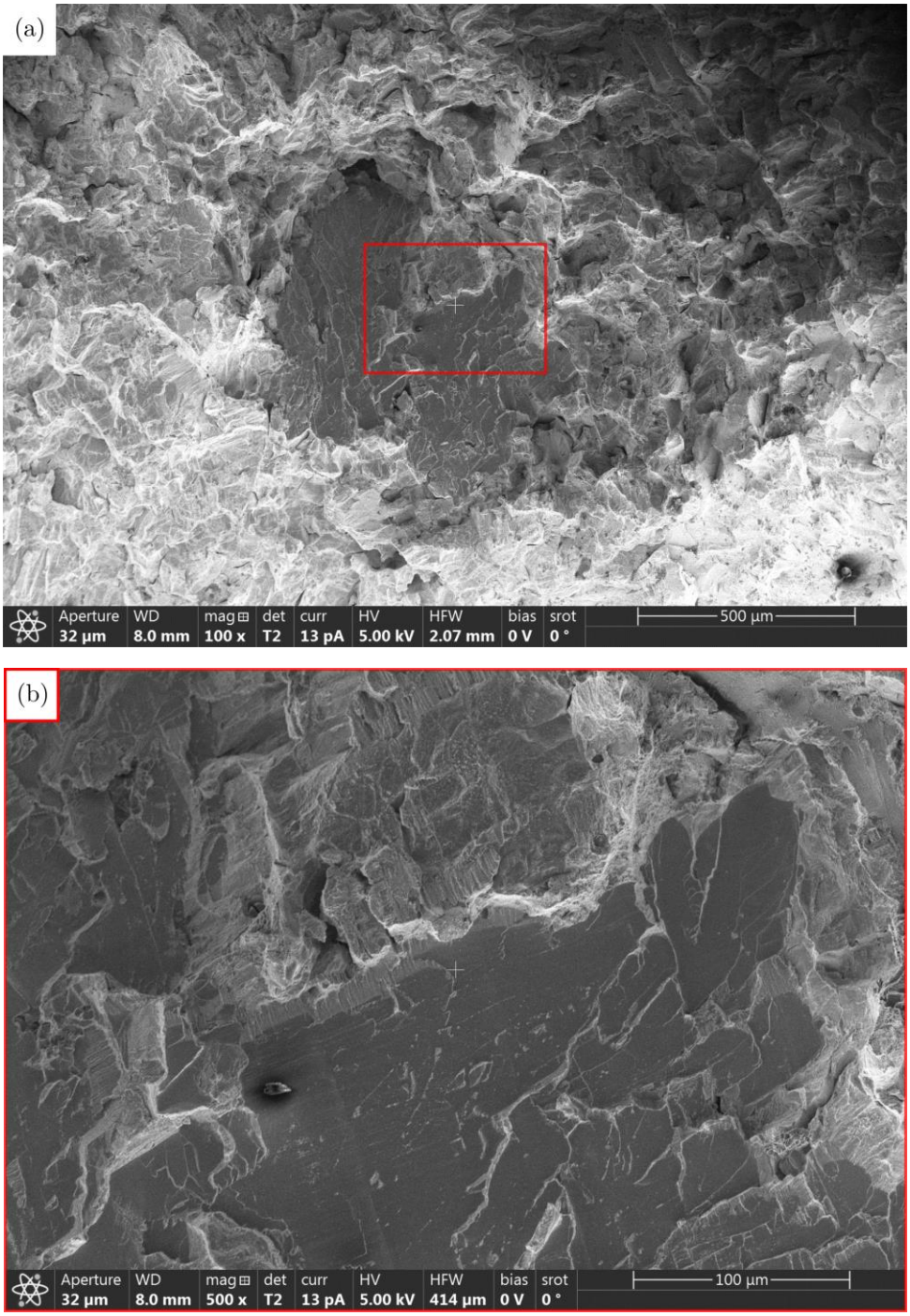


Figure 8.52. SEM fractography image showing a region B of the fracture surface of specimen ND-T3. Images acquired using the T2 detector at magnifications of (a) 100× and (b) 500×. Large cleavage planes are visible at the centre of the images.

A6.2.2 Specimen ND-T4

The second specimen fractured at 395 MPa, 5.7 % strain, near the centre of the gauge volume; slightly left of the centre, as viewed from the DIC camera. The fracture did not

Ministry of Defence © British Crown Copyright 2020/AWE

completely separate the specimen at the uppermost surface, suggesting the crack initiated on the lower surface and propagated upwards. From the DIC measurement taken just before fracture, a large concentration of normal strain ($\varepsilon_{xx}^{\max} = 15.7\,\%$) and shear strain ($\varepsilon_{xy}^{\max} = 5.9\,\%$) was seen towards the bottom-left of the image, (figure 8.44). This is coincident to the position of crack initiation on the lower surface of the specimen.

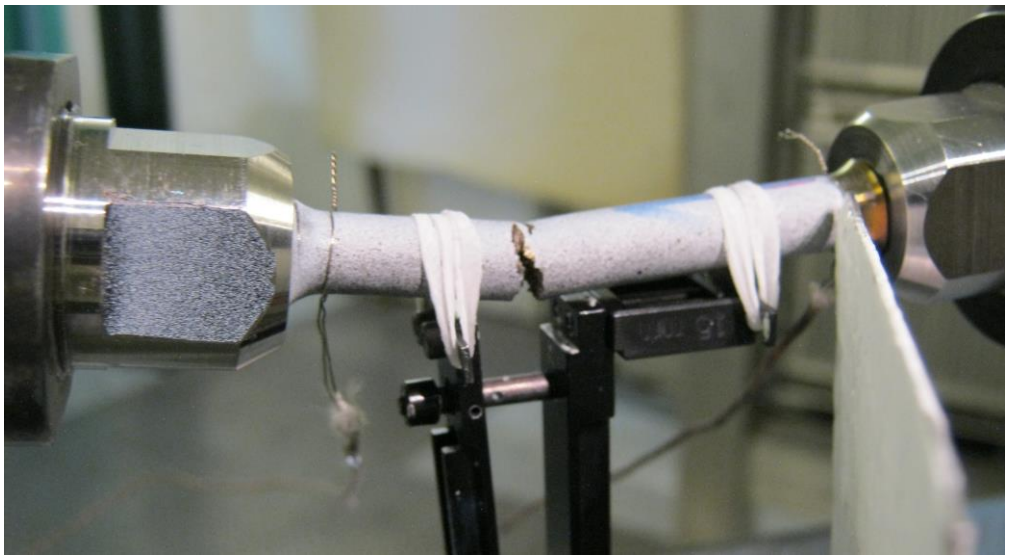


Figure 8.53. Fracture of specimen ND-T4, viewed from the position of the DIC camera. Fracture occurred in the gauge region, with the crack initiating at the lower surface and propagating upwards.

Ministry of Defence © British Crown Copyright 2020/AWE

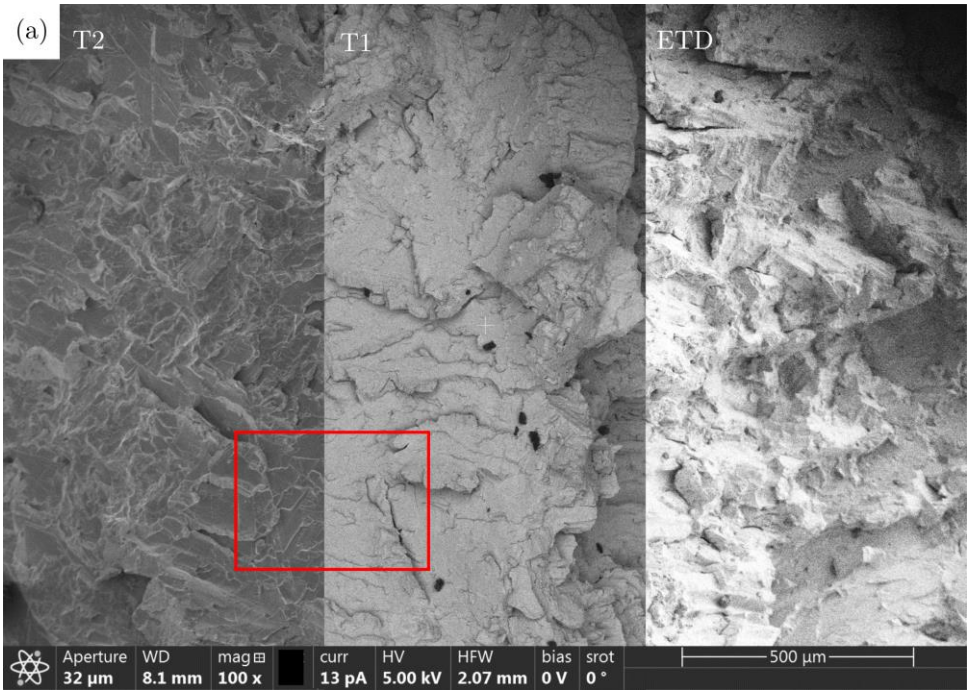
A6.2.2.1 Region C (ND-T4)

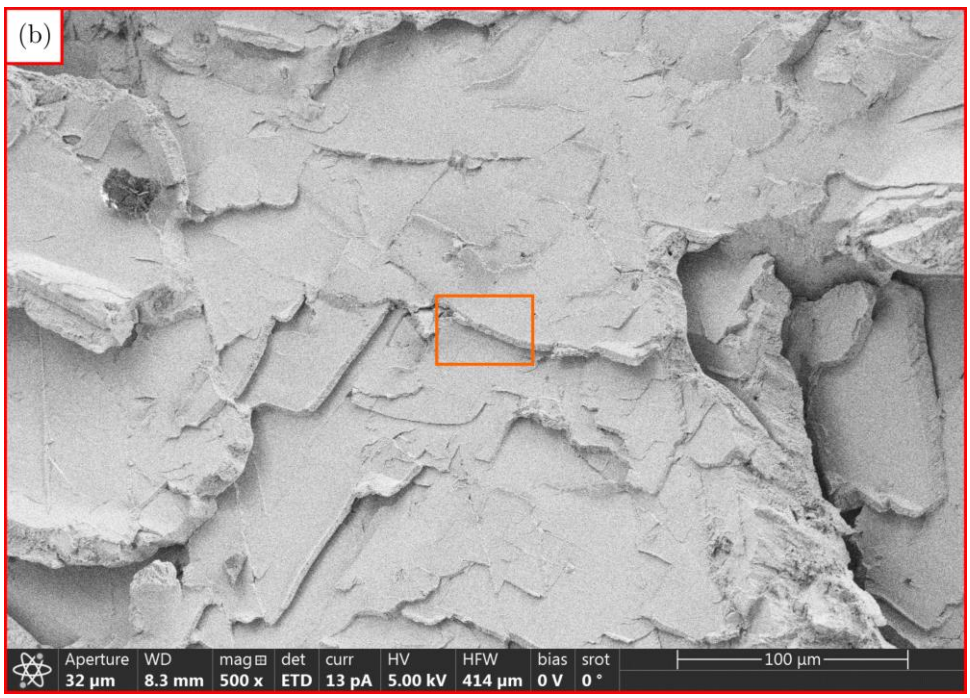
Figure 8.54(a) is a composite image of region C in specimen ND-T4, with sections taken with the T2, T1 and ETD detectors. The T1 detector is sensitive to atomic number contrast, with higher atomic numbers (higher electron density) backscattering more electrons and appearing lighter. Carbides are visible on the fracture surface as dark features approximately 30 μm in diameter.

Subfigure (b) shows chevron-like features which suggest a transgranular mode of fast fracture. At the highest magnification of 5000×, a single edge of a chevron feature is shown in subfigure (c). The protruding layer is comprised of two layers, with a total thickness of approximately 3 μm. Thin lightly-coloured streaks are visible on the top surface, originating at the point of fracture of the protruding layer.

This layer could be a '{172}' twin, which are known propagation paths for fracture and typically have similar thicknesses to the observed feature[62].

Ministry of Defence © British Crown Copyright 2020/AWE





Ministry of Defence © British Crown Copyright 2020/AWE

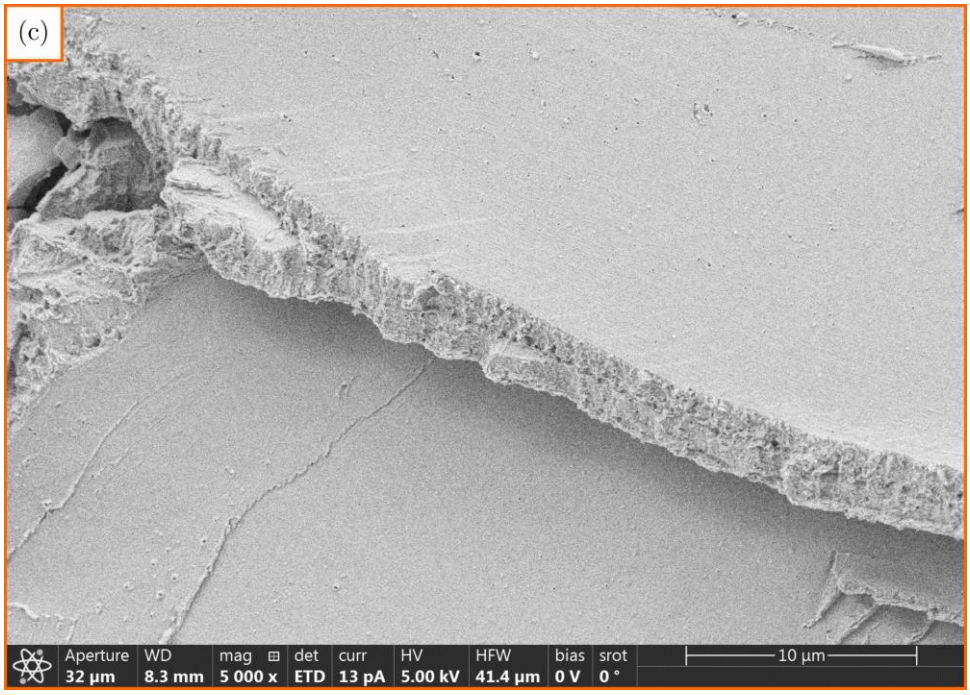


Figure 8.54. SEM fractography image showing a region C, part of the fracture surface of specimen ND-T4. (a) Composite low-magnification image showing images from the T1, T2 and ETD detectors. For (b) and (c), the ETD produced images in which the three-dimensional topography was clearest. Images acquired at magnifications of (a) 100×, (b) 500×, and (c) 5000×.

Ministry of Defence © British Crown Copyright 2020/AWE

A6.2.2.2 Region D (ND-T4)

The high-resolution micrograph in figure 8.55 shows two different fracture surface morphologies close to one another – cleavage on the left-hand side and ductile fracture with evidence of void nucleation and coalescence on the right.

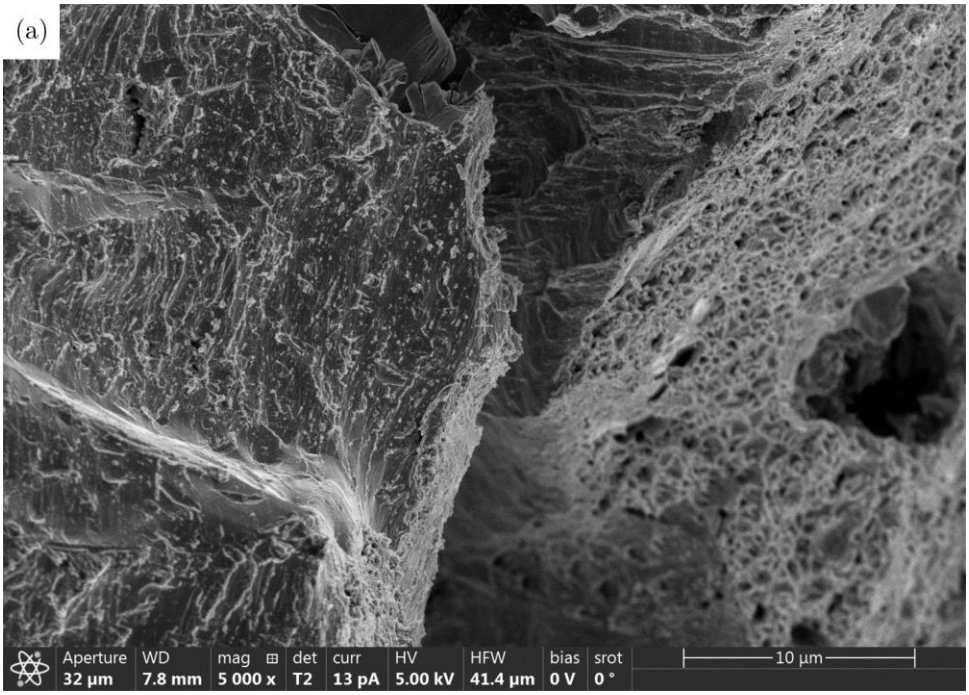


Figure 8.55. SEM fractography image showing a region D in specimen ND-T4. T2 images acquired at 5000× magnification. Both cleavage and ductile fracture are visible within this very small region.

Ministry of Defence © British Crown Copyright 2020/AWE

Ministry of Defence © British Crown Copyright 2020/AWE

A7 CPFE Modelling of Uranium

A7.1 Method

A crystal plasticity model was implemented by Nicolò Grilli as a user material subroutine (UMAT) in the ABAQUS finite element software package. This was used to simulate the ENGIN-X experiment from Chapter 3. The model included all variants of Wall, Floor, Chimney and Roof slip, and the 2 variants of {130} twinning. 8000 grains were included in the simulation, with the central 1000 grains representing the gauge volume during diffraction. The grain orientations in the central region were generated using the experimentally measured texture distribution (figure 8.56); the remaining 7000 grains were oriented randomly. To assess the effect of the spatial clustering of grains, an extra simulation was run with the grains in the (115) and (312) texture components in ND-T1 distributed as a bicrystal rather than randomly distributed in the gauge volume.

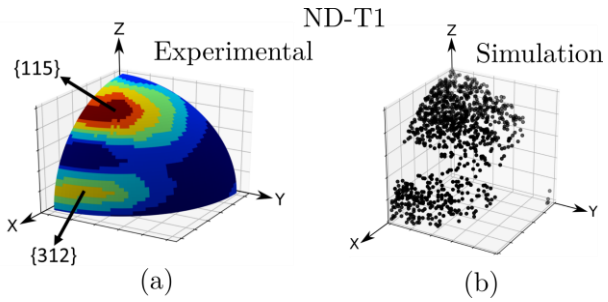


Figure 8.56. (a) 3D representation of axial texture in specimen ND-T1 (see figure 8.31) with respect to the crystal axes: $x \equiv (100)$, $y \equiv (010)$, and $z \equiv (001)$. (b) Orientations of grains generated from the orientation distribution in (a). Modified from Grilli et al.[88].

Residual stresses are present in the specimens in their as-machined state which would affect the subsequent deformation. Thermal residual stresses would build upon cooling and would be partially relaxed by the machining process. These stresses and strains were

Ministry of Defence © British Crown Copyright 2020/AWE

simulated by quenching all 8000 grains from 400 ℃ to 20 ℃ followed by a cutting of the specimen; removal of the 7000 randomly-oriented grains.

The uniaxial tension or compression in the mechanical test was simulated by applying a velocity boundary condition to one face (A) of the specimen, with the opposing face (B) fixed, such that the deformation was aligned with the simulated axial texture. The stress was calculated as the average of the stresses on face A. Flow curves could therefore be generated by plotting this calculated stress against the applied strain at each simulation strain increment.

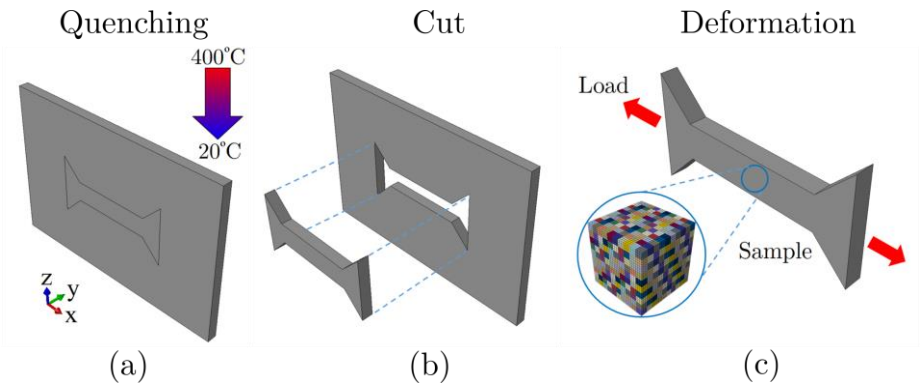


Figure 8.57. The processing steps prior to deformation are simulated in the CPFE model. (a) Quenching specimen from $400℃$ to $20℃$ to simulate the build-up of thermal residual stresses. (b) Cutting specimen from larger material to partially relax these stresses. (c) Deforming the specimen in uniaxial tension or compression. Modified from Grilli et al.[133].

The diffraction process was simulated by selecting grains in the diffraction condition to contribute to the measured lattice strains. A grain is in the diffraction condition for the (*hkl*) reflection if the beam reflected from the (*hkl*) plane, q_r, is within a particular angular range (θ_D, Ψ_D) from q_d, the vector from the specimen to the centre of the detector (see figure 8.58). Letting the projection of q_r onto the *x*-*y* plane be $q_{r//}$, the angle θ_D was defined as the angle between q_d and $q_{r//}$, and the angle Ψ_d was defined as

Ministry of Defence © British Crown Copyright 2020/AWE

the angle between q_r and $q_{r//}$. The detection condition was therefore given by equations [8.47] and [8.48], with the angular values chosen to match the geometry of the ENGIN-X detectors (figure 8.9)

$$-14° < \theta_D < 14° \quad [8.47]$$

$$-21° < \Psi_D < 21° \quad [8.48]$$

The (*hkl*) lattice strain was calculated as the average of the strains on the grains whose (*hkl*) plane normals were parallel to diffraction vectors that cause the reflected beam to satisfy the detection condition. This enabled plotting of lattice strain vs. stress curves for comparison with the experimental data.

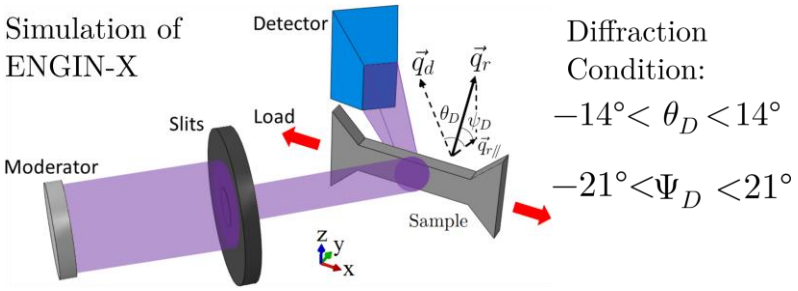


Figure 8.58. The diffraction process is simulated by selecting grains in the diffraction condition to contribute to the measured lattice strains. A grain is said to be in the diffraction condition for the (*hkl*) reflection if the beam reflected from the (*hkl*) plane, q_r, is within an angular range (θ_D, Ψ_D) from q_d, the vector from the specimen to the centre of the detector. Modified from Grilli et al.[133].

Parameters including the constant friction stress for each slip system, and the CRSS for {130} twinning, were optimised to obtain the best fit between experiment and simulation for both specimens ND-T1 and ND-C1.

Ministry of Defence © British Crown Copyright 2020/AWE

Ministry of Defence © British Crown Copyright 2020/AWE

A8 Calculations

A8.1 Schmid Factor Calculations

A MATLAB script was written to calculate the Schmid factor as a function of direction for the deformation systems in uranium. The procedure follows the flowchart in figure 8.59. Firstly, each deformation system is defined in the form $\{hkl\}\langle uvw\rangle$ where $\{\mathrm{hkl}\}$ refers to the slip plane or twinning plane $\boldsymbol{K_1}$, and $\langle uvw\rangle$ refers to the slip direction or the twinning direction $\boldsymbol{\eta_1}$. A set of possible symmetrically equivalent variants of the deformation system are calculated (step A in the flowchart); for completeness, these are shown in table 8.9.

Table 8.9. Deformation system variants used in MATLAB code.

Deformation system	Variants			
Wall slip	010 [100]			
Floor slip	001 [100]			
Chimney slip	(110)[110]	110 [110]		
Roof slip	021 [112]	021 [112]	(021)[112]	(021)[112]
{130} twins	130 [310]	(130)[310]		
'{172}' twins	' 172 '[312]	'(172)'[312]	'(172)'[312]	'(172)'[312]
'{176}' twins	'(176)'[512]	'(176)'[512]	'(176)'[512]	' 176 '[512]
{112} twins	112 [372]	(112)[372]	(112)[372]	(112)[372]

Lattice vectors $\boldsymbol{a}$, $\boldsymbol{b}$, and $\boldsymbol{c}$ are defined in a general right-handed Cartesian co-ordinate system as $[a,0,0]$, $[0,b,0]$, and $[0,0,c]$. Reciprocal lattice vectors $\boldsymbol{a}^*$, $\boldsymbol{b}^*$, and $\boldsymbol{c}^*$ are calculated via equation [8.49].

Ministry of Defence © British Crown Copyright 2020/AWE

$$\boldsymbol{a}^* = \frac{\boldsymbol{b} \times \boldsymbol{c}}{\boldsymbol{a} \bullet (\boldsymbol{b} \times \boldsymbol{c})} \qquad \boldsymbol{b}^* = \frac{\boldsymbol{c} \times \boldsymbol{a}}{\boldsymbol{b} \bullet (\boldsymbol{c} \times \boldsymbol{a})} \qquad \boldsymbol{a}^* = \frac{\boldsymbol{a} \times \boldsymbol{b}}{\boldsymbol{c} \bullet (\boldsymbol{a} \times \boldsymbol{b})} \qquad [8.49]$$

The $[uvw]$ plane normal is converted into the Cartesian crystal co-ordinate system via equation [8.50], and the hkl plane normal is converted via equation [8.51] (step B in the flowchart)

$$\boldsymbol{d} = ha + kb + lc \qquad [8.50]$$

$$\boldsymbol{n} = h\boldsymbol{a}^* + k\boldsymbol{b}^* + l\boldsymbol{c}^* \qquad [8.51]$$

In order to plot the Schmid factor as a function of loading direction in the inverse pole figure, an array of loading vectors $\boldsymbol{r}$ with even angular spacing in spherical polar co-ordinates is created (step C in the flowchart). The code also accepts a single loading direction in the form (hkl) or $[uvw]$ (or a list of such directions), which are then converted into the Cartesian basis using the equations above. In this case, no figures are plotted, and the script can be used to calculate the Schmid factor for a known experimental loading direction, for example. The Schmid factor is then calculated (step D) as:

$$\mathrm{SF} = \cos\lambda \cos\phi \qquad [8.52]$$

where λ is the angle between the loading direction and the slip/twinning direction,

$$\cos\lambda = \frac{\boldsymbol{r} \bullet \boldsymbol{d}}{|\boldsymbol{r}||\boldsymbol{d}|} \qquad [8.53]$$

and ϕ is the angle between the loading direction and the slip/twinning plane normal.

Ministry of Defence © British Crown Copyright 2020/AWE

$$\cos\phi = \frac{\boldsymbol{r} \bullet \boldsymbol{n}}{|\boldsymbol{r}||\boldsymbol{n}|} \quad [8.54]$$

In each case $0 < \lambda < 180°$ and $0 < \phi < 180°$ so $-0.5 < \mathrm{SF} < 0.5$.

In the case of slip, a negative Schmid factor will induce slip in a direction antiparallel to the defined slip direction $[uvw]$. The direction of slip is irrelevant when identifying if a slip system will activate, so in step E of the flowchart, the absolute value of the Schmid factor is taken if the deformation mechanism is slip:

$$\mathrm{SF}_{\mathrm{slip}} = |\mathrm{SF}| \quad [8.55]$$

The Schmid factor therefore varies from $0 < \mathrm{SF} < 0.5$ for slip. Deformation twinning is polar [57], so a twin will not activate if the Schmid factor is negative. By default, the SF is calculated for tensile deformation. Compression changes the sign, but not the magnitude, of the SF:

$$\mathrm{SF}_{\mathrm{twin}}^{\mathrm{compression}} = -\mathrm{SF}_{\mathrm{twin}}^{\mathrm{tension}} \quad [8.56]$$

For a particular loading direction, the variant with the highest SF will be the most likely to operate. Therefore the overall SF for a deformation mode, $\mathrm{SF}_{\mathrm{max}}$, is calculated as the maximum (most positive) SF out of all the symmetrically equivalent variants (step F). The calculated Schmid factors for each variant, and the overall $\mathrm{SF}_{\mathrm{max}}$ are displayed in table 8.10 - table 8.17.

In all cases of twinning and slip, deformation along $[uvw]$ will produce an equal SF to deformation along $[uv\overline{w}]$. The plots of $\mathrm{SF}_{\mathrm{max}}$ always exhibit orthorhombic symmetry whilst the individual SFs for each variant do not.

Ministry of Defence © British Crown Copyright 2020/AWE

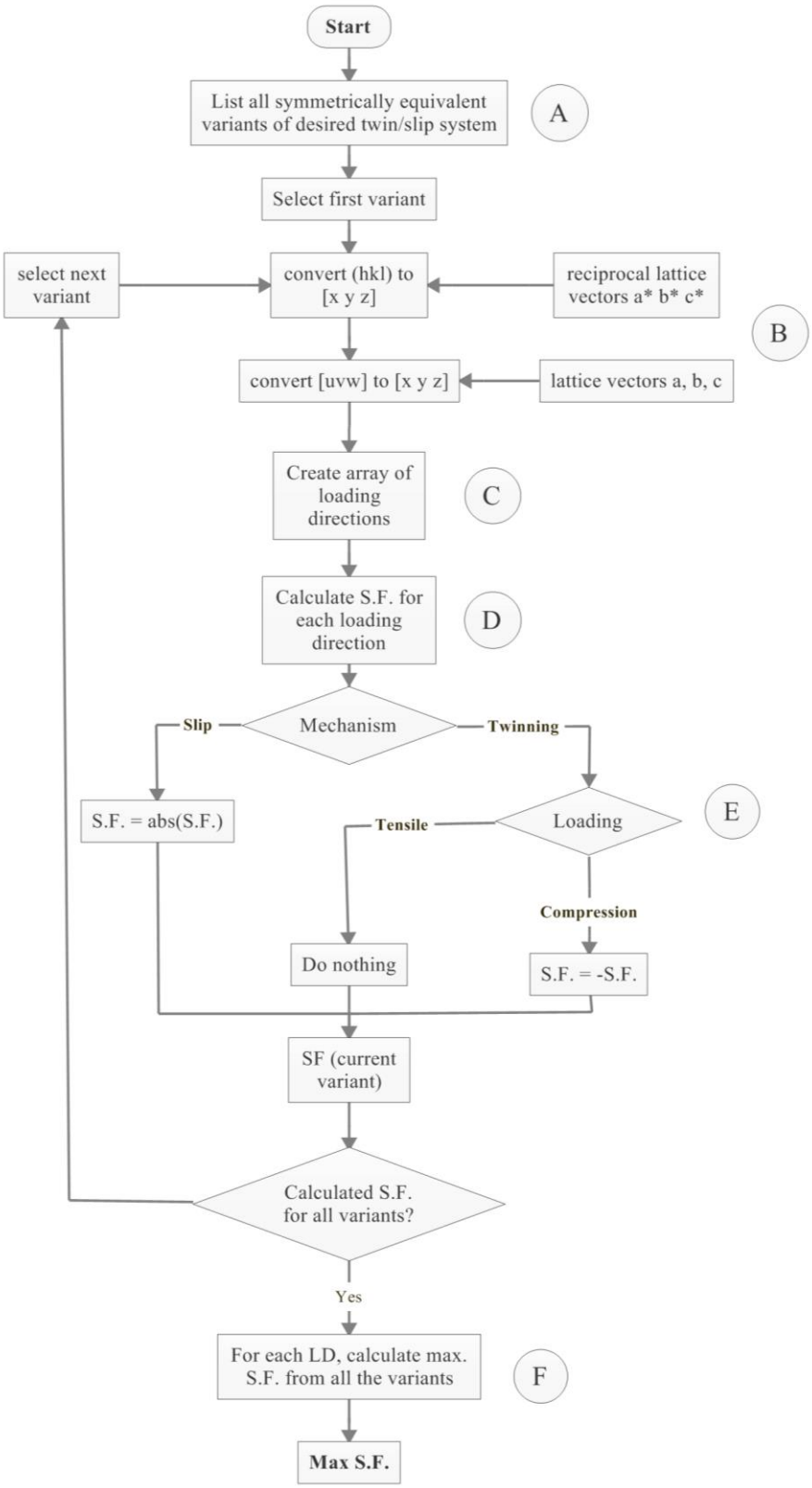


Figure 8.59. Flowchart detailing the process from which the Schmid Factors (SFs) as were calculated as a function of crystal direction, as seen in the figures in section 2.3.

Ministry of Defence © British Crown Copyright 2020/AWE

Table 8.10. Inverse pole figure plots of the Schmid factor (SF) for each symmetry variant of the Wall slip deformation mode. Positive SFs are shown in red, negative SFs in blue.

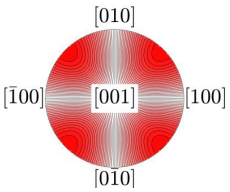
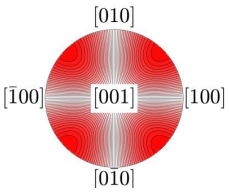
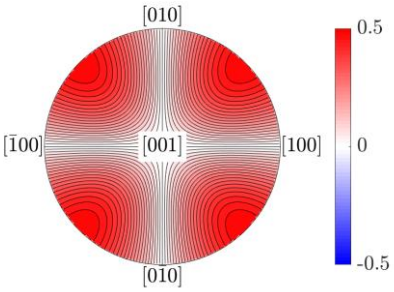
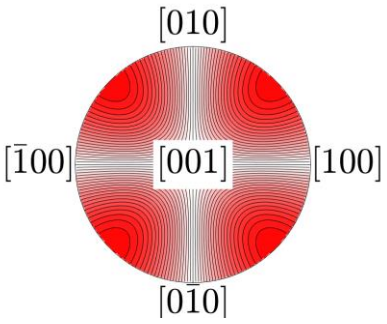
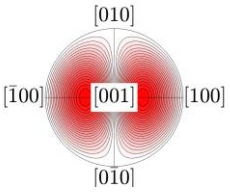
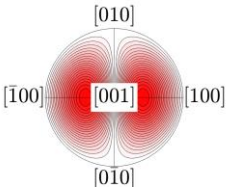
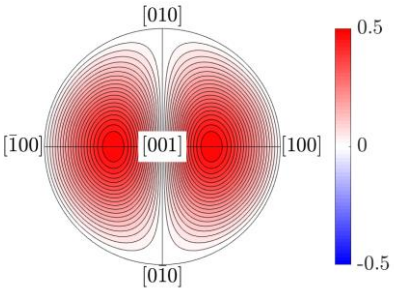
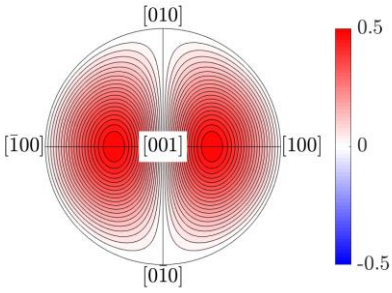
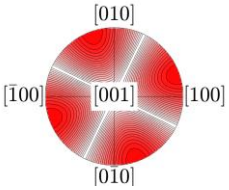
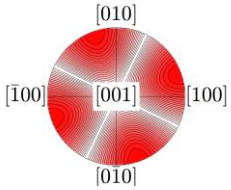
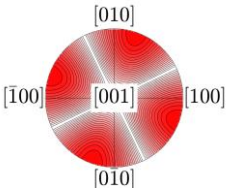
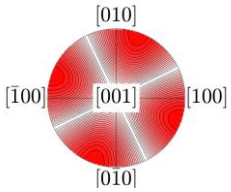
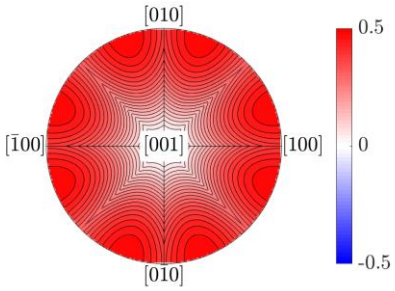
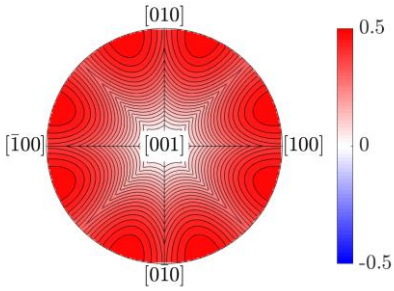
	Wall Slip $\{010\}\langle100\rangle$	
	Tension	Compression
Variant 1 $010\ [100]$		
SF_{max}		

Table 8.11. Inverse pole figure plots of the Schmid factor (SF) for each symmetry variant of the Floor slip deformation mode. Positive SFs are shown in red, negative SFs in blue.

	Floor Slip $\{001\}\langle100\rangle$	
Mode	Tension	Compression
Variant 1 $001\ [100]$		
SF_{max}		

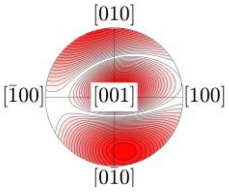
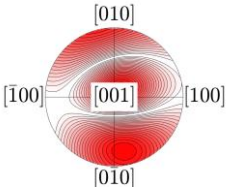
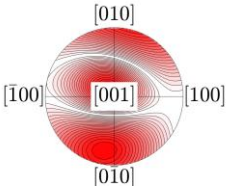
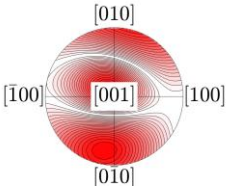
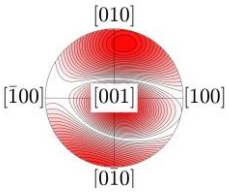
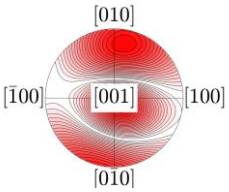
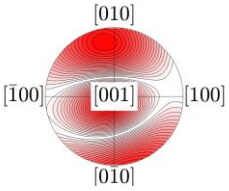
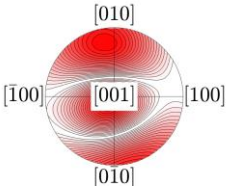
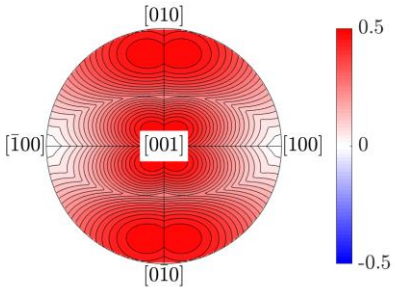
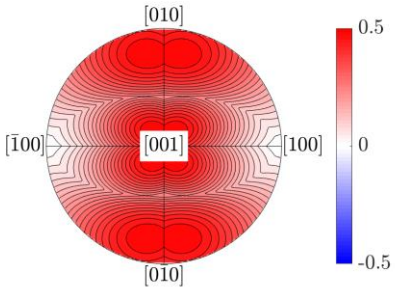
Ministry of Defence © British Crown Copyright 2020/AWE

Table 8.12. Inverse pole figure plots of the Schmid factor (SF) for each symmetry variant of the Chimney slip deformation mode. Positive SFs are shown in red, negative SFs in blue.

Chimney Slip $\{\mathbf{110}\}\langle\mathbf{110}\rangle$		
Mode	Tension	Compression
Variant 1 $(110)[110]$		
Variant 2 $110\ [110]$		
$\mathrm{SF}_{\max}$		

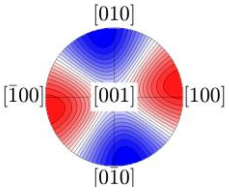
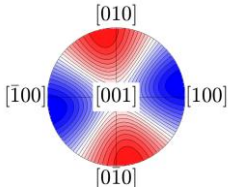
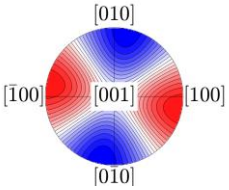
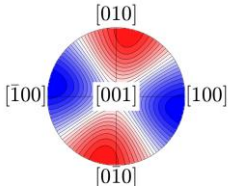
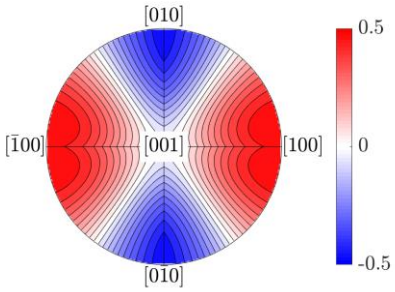
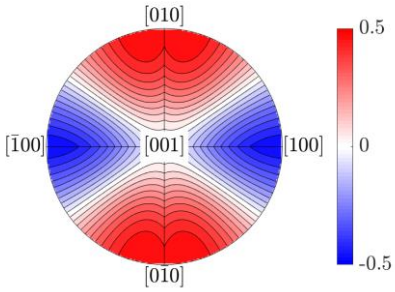
Ministry of Defence © British Crown Copyright 2020/AWE

Table 8.13. Inverse pole figure plots of the Schmid factor (SF) for each symmetry variant of the Roof slip deformation mode. Positive SFs are shown in red, negative SFs in blue.

Roof Slip $\{\mathbf{021}\}\langle\mathbf{112}\rangle$		
Mode	Tension	Compression
Variant 1 $\{021\}[112]$		
Variant 2 $\{021\}[112]$		
Variant 3 $\{021\}[112]$		
Variant 4 $\{021\}[112]$		
$\mathrm{SF}_{\max}$		

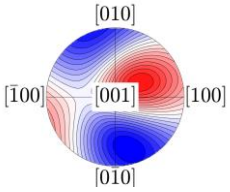
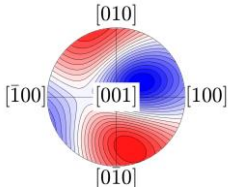
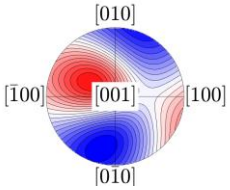
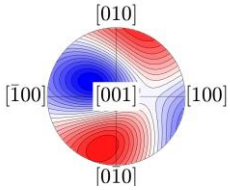
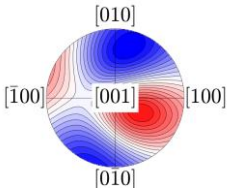
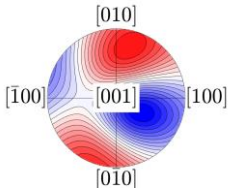
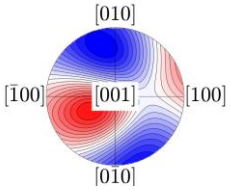
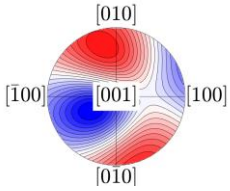
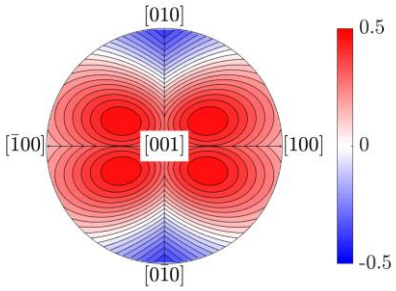
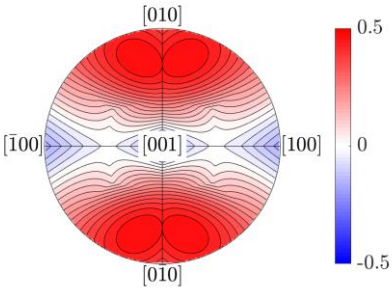
Ministry of Defence © British Crown Copyright 2020/AWE

Table 8.14. Inverse pole figure plots of the Schmid factor (SF) for each symmetry variant of the {130} twinning deformation mode. Positive SFs are shown in red, negative SFs in blue.

{130} Twinning $\{\mathbf{130}\}\langle\mathbf{310}\rangle$		
Mode	Tension	Compression
Variant 1 $130\ [310]$		
Variant 2 $(130)[310]$		
$\mathrm{SF}_{\max}$		

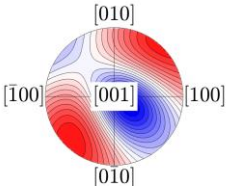
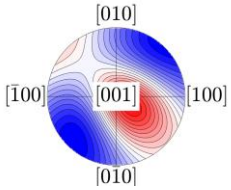
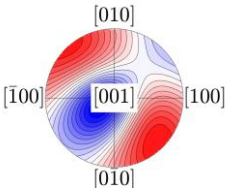
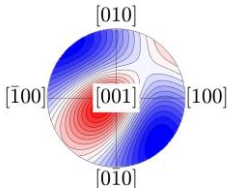
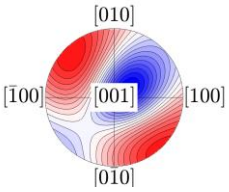
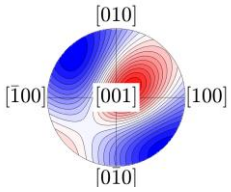
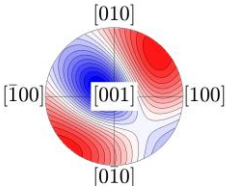
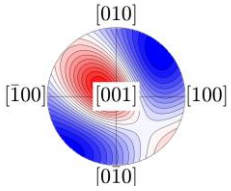
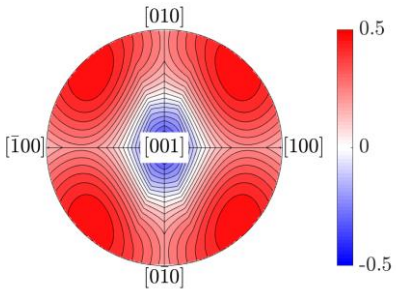
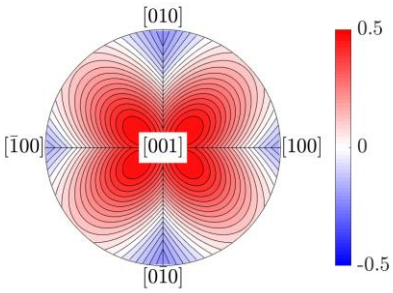
Ministry of Defence © British Crown Copyright 2020/AWE

Table 8.15. Inverse pole figure plots of the Schmid factor (SF) for each symmetry variant of the '{172}' twinning deformation mode. Positive SFs are shown in red, negative SFs in blue.

'{172}' Twinning '{172}'⟨312⟩		
Mode	Tension	Compression
Variant 1 '172'[312]		
Variant 2 '(172)'[312]		
Variant 3 '(172)'[312]		
Variant 4 '(172)'[312]		
SF_{max}		

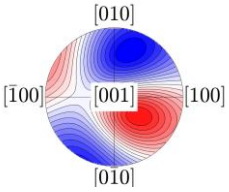
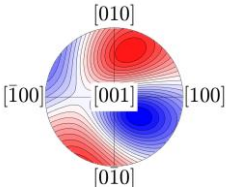
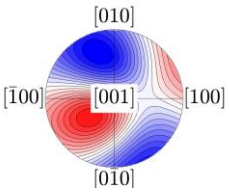
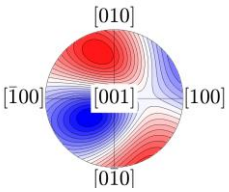
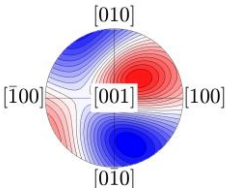
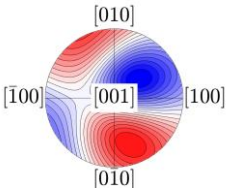
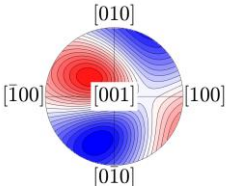
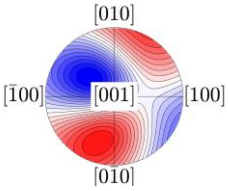
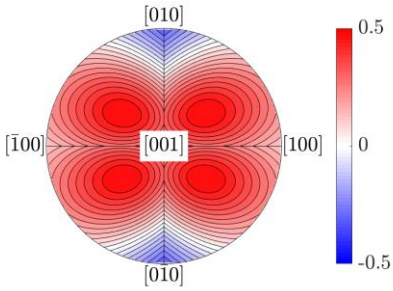
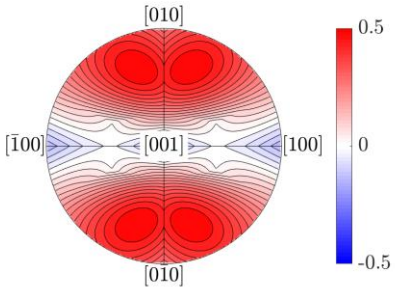
Ministry of Defence © British Crown Copyright 2020/AWE

Table 8.16. Inverse pole figure plots of the Schmid factor (SF) for each symmetry variant of the '{176}' twinning deformation mode. Positive SFs are shown in red, negative SFs in blue.

'{176}' Twinning $'\{176\}'\langle 512\rangle$		
Mode	Tension	Compression
Variant 1 $'(176)'[512]$		
Variant 2 $'(176)'[512]$		
Variant 3 $'(176)'[512]$		
Variant 4 $'(176)'[512]$		
$\mathrm{SF}_{\max}$		

Ministry of Defence © British Crown Copyright 2020/AWE

Table 8.17. Inverse pole figure plots of the Schmid factor (SF) for each symmetry variant of the {112} twinning deformation mode. Positive SFs are shown in red, negative SFs in blue.

{112} Twinning $\{\mathbf{112}\}\langle\mathbf{372}\rangle$		
Mode	Tension	Compression
Variant 1 $112\ [372]$		
Variant 2 $(112)[372]$		
Variant 3 $(112)[372]$		
Variant 4 $(112)[372]$		
$\mathrm{SF}_{\max}$		

Ministry of Defence © British Crown Copyright 2020/AWE

A8.2 Extensometer Calculations for Chapter 4

A8.2.1 Offsetting the extensometer

For the compression specimens, a positive strain offset was applied by pre-straining the extensometer. This allowed a larger compressive strain to be measured. It was necessary to calculate the strain in the specimen, $\varepsilon_{\text{sample}}$, from the indicated extensometer strain, $\varepsilon_{\text{displayed}}$. Equation [8.57] relates the actual sample strain to l, the actual extensometer spacing, and l_1 the offset gauge length.

$$\varepsilon_{\text{sample}} = \frac{l - l_1}{l_1} \qquad [8.57]$$

The offset gauge length is the result of adding an offset extension of Δl_{offset} to the standard (25 mm) gauge length of the extensometer, l_0:

$$l_1 = l_0 + \Delta l_{\text{offset}}. \qquad [8.58]$$

During loading, the extensometer will record the strain:

$$\varepsilon_{\text{displayed}} = \frac{l - l_0}{l_0} \qquad [8.59]$$

which can be rearranged to show

$$l = l_0(1 + \varepsilon_{\text{displayed}}). \qquad [8.60]$$

After the offset is applied, and before loading begins, the extensometer will be at the offset length and therefore will record the 'offset' strain:

$$\varepsilon_{\text{exchange}} = \frac{l_1 - l_0}{l_0} \qquad [8.61]$$

which can be rearranged to show

Ministry of Defence © British Crown Copyright 2020/AWE

$$l_1 = l_0(1 + \varepsilon_{\text{offset}}). \qquad [8.62]$$

Substituting equations [8.60] and [8.62] into equation [8.57], we find

$$\varepsilon_{\text{sample}} = \frac{l_0(1 + \varepsilon_{\text{displayed}}) - l_0(1 + \varepsilon_{\text{offset}})}{l_0(1 + \varepsilon_{\text{offset}})} \qquad [8.63]$$

which simplifies to

$$\varepsilon_{\text{sample}} = \frac{(1 + \varepsilon_{\text{displayed}})}{(1 + \varepsilon_{\text{offset}})} - 1 \qquad [8.64]$$

This results in a linear relationship between the displayed extensometer strain and the sample strain, as shown in figure 8.60.

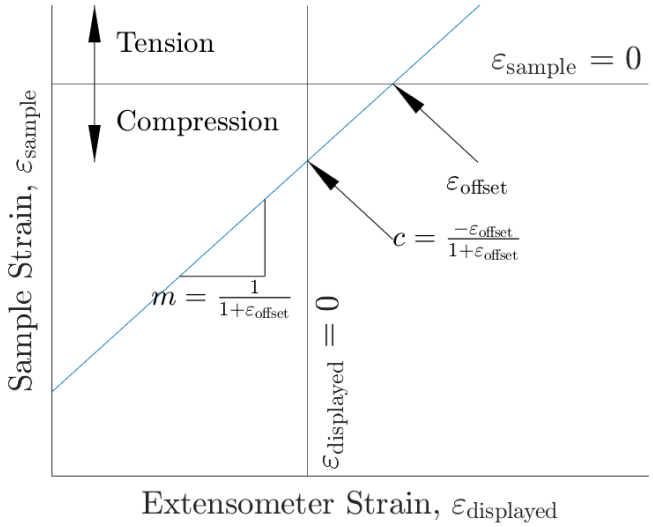


Figure 8.60. There is a linear relationship between the displayed extensometer strain and the sample strain. The gradient is inversely proportional to the offset strain.

Ministry of Defence © British Crown Copyright 2020/AWE

A8.2.2 In-situ exchange of extensometers

During testing of specimen ND-C3 on SMARTS, the 25 mm extensometer was exchanged for a 10 mm extensometer at a nominal sample strain, $\varepsilon_{\text{exchange}}$, of 4.5 %. It was therefore required to convert the displayed strain, $\varepsilon_{\text{displayed}}$, to the correct sample strain, $\varepsilon_{\text{sample}}$.

During subsequent loading after exchange, the displayed strain will be

$$\varepsilon_{\text{displayed}} = \frac{l_2 - l_1}{l_1} \quad [8.65]$$

Where l_2 is the length of the 10 mm extensometer after loading and l_1 is the new reference gauge length in the Instron controller (10 mm). Therefore,

$$l_2 = l_1(1 + \varepsilon_{\text{displayed}}). \quad [8.66]$$

The actual sample strain after this subsequent loading is

$$\varepsilon_{\text{sample}} = \frac{l_2 - l_0}{l_0} \quad [8.67]$$

where l_0 is the original (unstrained) length of the section of the sample that had a length l_1 at the exchange point. Substituting equation [8.66] into equation [8.67],

$$\varepsilon_{\text{sample}} = \frac{l_1(1 + \varepsilon_{\text{displayed}}) - l_0}{l_0}. \quad [8.68]$$

All this is now required is to find an expression for l_0. At exchange,

$$\varepsilon_{\text{offset}} = \frac{l_1 - l_0}{l_0} \quad [8.69]$$

therefore

Ministry of Defence © British Crown Copyright 2020/AWE

$$l_0 = \frac{l_1}{1 + \varepsilon_{\text{exchange}}} \qquad [8.70]$$

Substituting equation [8.70] into equation [8.68],

$$\varepsilon_{\text{sample}} = \frac{l_1(1 + \varepsilon_{\text{displayed}}) - \dfrac{l_1}{1 + \varepsilon_{\text{exchange}}}}{\dfrac{l_1}{1 + \varepsilon_{\text{exchange}}}}. \qquad [8.71]$$

Therefore, by rearranging,

$$\varepsilon_{\text{sample}} = (1 + \varepsilon_{\text{displayed}})(1 + \varepsilon_{\text{exchange}}) - 1. \qquad [8.72]$$

Ministry of Defence © British Crown Copyright 2020/AWE

A8.3 Texture Change Correction Errors for Chapter 4

From the equations in section 4.2.7, we know the reference texture, $O_{\mathrm{ref}}(\boldsymbol{r})$, is linearly interpolated from the two neighbouring pre-load textures $O_{\mathrm{A}}(\boldsymbol{r})$ and $O_{\mathrm{B}}(\boldsymbol{r})$ using equation [4.10],

$$O_{\mathrm{ref}}\ \boldsymbol{r}\ = f_{\mathrm{AB}} O_{\mathrm{B}}\ \boldsymbol{r}\ + (1 - f_{\mathrm{AB}}) O_{\mathrm{A}}\ \boldsymbol{r} \qquad [8.73]$$

where $y_{\mathrm{A}} < y_{\mathrm{ref}} < y_{\mathrm{B}}$ and f_{AB} is the fractional displacement of the specimen between positions A and B:

$$f_{\mathrm{AB}} = \frac{y_{ref} - y_{\mathrm{A}}}{y_{\mathrm{B}} - y_{\mathrm{A}}} \qquad [8.74]$$

Letting $P = f_{\mathrm{AB}} O_{\mathrm{B}}\ \boldsymbol{r}$ and $Q = (1 - f_{\mathrm{AB}}) O_{\mathrm{A}}\ \boldsymbol{r}$,

$$O_{\mathrm{ref}}\ \boldsymbol{r}\ = P + Q \qquad [8.75]$$

Therefore, since addition requires adding the absolute errors in quadrature:

$$\sigma(O_{\mathrm{ref}}\ \boldsymbol{r}\ ) = \sqrt{\sigma\ P\ ^2 + \sigma\ Q\ ^2} \qquad [8.76]$$

Expressions for $\sigma(P)$ and $\sigma(Q)$ can then be found. To perform this simple error estimation we had to assume that the errors in *P* and *Q* are independent. Since textures $O_{\mathrm{A}}\ \boldsymbol{r}$ and $O_{\mathrm{B}}\ \boldsymbol{r}$ are likely to be similar, there may be some correlation between the errors, although there is no systematic correlation between the two measurements in the texture calculations. The assumption is however useful as it allows a simple estimation of the uncertainty in the measured texture changes.

Ministry of Defence © British Crown Copyright 2020/AWE

P is the product of f_{AB} and $O_{\mathrm{B}}\ r$ therefore the fractional errors add in quadrature:

$$\left(\frac{\sigma\ P}{P}\right)^2 = \left(\frac{\sigma\ f_{\mathrm{AB}}}{f_{\mathrm{AB}}}\right)^2 + \left(\frac{\sigma(O_{\mathrm{B}}\ r\ )}{O_{\mathrm{B}}\ r}\right)^2 \quad [8.77]$$

The error in f_{AB} can be calculated from the standard deviation of the DIC-measured y_{ref}. Letting $f_{\mathrm{AB}} = \alpha/\beta$, where $\alpha = y_{\mathrm{ref}} - y_{\mathrm{A}}$ and $\beta = y_{\mathrm{B}} - y_{\mathrm{A}}$,

$$\left(\frac{\sigma\ f_{\mathrm{AB}}}{f_{\mathrm{AB}}}\right)^2 = \left(\frac{\sigma\ \alpha}{\alpha}\right)^2 + \left(\frac{\sigma\ \beta}{\beta}\right)^2. \quad [8.78]$$

The errors $\sigma(\alpha)$ and $\sigma\ \beta$ can are given by:

$$\sigma\ \alpha\ ^2 = \sigma\ y_{\mathrm{ref}}\ ^2 + \sigma\ y_{\mathrm{A}}\ ^2 \quad [8.79]$$

$$\sigma\ \beta\ ^2 = \sigma\ y_{\mathrm{B}}\ ^2 + \sigma\ y_{\mathrm{A}}\ ^2 \quad [8.80]$$

Q is the product of $(1 - f_{\mathrm{AB}})$ and $O_{\mathrm{A}}\ r$ therefore the fractional errors add in quadrature:

$$\left(\frac{\sigma\ Q}{Q}\right)^2 = \left(\frac{\sigma\ 1 - f_{\mathrm{AB}}}{1 - f_{\mathrm{AB}}}\right)^2 + \left(\frac{\sigma(O_{\mathrm{A}}\ r\ )}{O_{\mathrm{A}}\ r}\right)^2 \quad [8.81]$$

Since

$$\sigma\ 1 - f_{\mathrm{AB}}\ ^2 = \sigma\ 1\ ^2 + \sigma\ f_{AB}\ ^2 \quad [8.82]$$

$$\sigma\ 1 - f_{\mathrm{AB}}\ ^2 = \sigma\ f_{AB}\ ^2 \quad [8.83]$$

Then, by substituting equation [8.83] into [8.81],

Ministry of Defence © British Crown Copyright 2020/AWE

$$\left(\frac{\sigma\ Q}{Q}\right)^2 = \left(\frac{\sigma\ f_{\mathrm{AB}}}{1-f_{\mathrm{AB}}}\right)^2 + \left(\frac{\sigma(O_{\mathrm{A}}\ r\ )}{O_{\mathrm{A}}\ r}\right)^2. \qquad [8.84]$$

Where $\sigma\ f_{\mathrm{AB}}$ can be found by rearranging equation [8.78]

Equations [8.77] and [8.84] can be re-arranged to get expressions for $\sigma\ P$ and $\sigma\ Q$.

The error in $O_{\mathrm{ref}}\ \boldsymbol{r}$ can be found by substituting these expressions into equation [8.76].

Ministry of Defence © British Crown Copyright 2020/AWE

A8.4 Estimation of stress-error in tensile tests in Chapter 5

In chapter Chapter 5, the stress in the uranium, σ_{U}, was calculated as a function of the displacement, *x*, was calculated from equation [8.85], where $F_{\mathrm{tot}}(x)$ is the force in the load cell, $F_{\mathrm{Cu}}(x)$ is the estimated force in the copper, and A_{U} is the measured gauge cross-sectional area of the specimen

$$\sigma_{\mathrm{U}}(x) = \frac{F_{\mathrm{tot}}(x) - F_{\mathrm{Cu}}(x)}{A_{\mathrm{U}}} \qquad [8.85]$$

In this section I will present an estimation of the error in the stress measurement, by estimating the errors in each variable.

The cross-sectional area A_{U} was calculated as the product of the gauge region width w and thickness t. The area was calculated for three evenly spaced points along the gauge region from measurements with digital calipers with precision 0.01 mm. For a typical specimen, the mean thickness was around 1.10 mm with a scatter between measurements of up to $\pm\ 0.03$ mm. The widths were identical at each point within the precision of the measurement.

Taking $w = 6.00$ mm $\pm\ 0.01$ mm and $t = 1.10$ mm $\pm\ 0.03$ mm, the fractional error in the area can be estimated via equation [8.86]

$$\frac{\sigma(A_{\mathrm{U}})}{A_{\mathrm{U}}} = \sqrt{\left(\frac{\sigma(w)}{w}\right)^2 + \left(\frac{\sigma(t)}{t}\right)^2} \qquad [8.86]$$

Ministry of Defence © British Crown Copyright 2020/AWE

$$= 0.0273$$

There is therefore up to a 2.7 % error in the area measurement.

The force in the uranium is calculated from the load-cell measurement and the estimated copper force using equation [8.87].

$$F_{\mathrm{U}}(x) = F_{\mathrm{tot}}(x) - F_{\mathrm{Cu}}(x) \qquad [8.87]$$

The error in the force in the uranium can therefore be calculated as

$$\sigma\big(F_{\mathrm{U}}\ x\ \big) = \sqrt{\ \sigma(F_{\mathrm{tot}}\ x\ )^{\ 2} + \ \sigma(F_{\mathrm{Cu}}\ x\ )^{\ 2}}. \qquad [8.88]$$

The load cell is specified to have an accuracy of $\pm\ 1\,\%$ within the range 10 N – 5000 N. The largest absolute error will therefore occur at the maximum load of approximately 1800 N – so $\sigma\ F_{tot}\ \approx \pm\ 18\,\mathrm{N}$. The error in the extrapolated copper load was estimated to be $\pm\ 10\,\mathrm{N}$, corresponding to a fractional error of 2 % at a load of 500 N. The absolute error in the uranium measurement was therefore estimated to be between 10 N (due to the copper load extrapolation) and the maximum of 21 N calculated from equation [8.88].

The fractional error in the stress $\sigma_{\mathrm{U}} = F_{\mathrm{U}}/A_{\mathrm{U}}$ is given by equation [8.89]

$$\frac{\sigma(\sigma_{\mathrm{U}})}{\sigma_{\mathrm{U}}} = \sqrt{\left(\frac{\sigma\ F_{\mathrm{U}}}{F_{\mathrm{U}}}\right)^{2} + \left(\frac{\sigma\ A_{\mathrm{U}}}{A_{\mathrm{U}}}\right)^{2}} \qquad [8.89]$$

$$= \sqrt{\left(\frac{21}{1800}\right)^{2} + \ 0.0273\ ^{2}}$$

$$= \sqrt{\ 0.0117\ ^{2} + \ 0.0273\ ^{2}}$$

Ministry of Defence © British Crown Copyright 2020/AWE

$$= 0.0297$$

There is therefore, at worst, a 3% error in the stress measurements. The largest contribution to this error is from the variation in the specimen thickness within the gauge region, caused by differences in mechanical polishing pressure and differing electropolishing rates.

Ministry of Defence © British Crown Copyright 2020/AWE

A8.5 Estimation of Compressive Buckling Stress on SMARTS

The compression specimens typically tested on SMARTS are cylinders with a length of 24 mm and a diameter of 10 mm; an aspect ratio of 2.4. Our specimens are wider, at 14 mm diameter, and have an aspect ratio of 2.0. The buckling stress was estimated by the Euler buckling equation [8.90], where *E* is the Young's Modulus, *I* is the second moment of area of the axial cross section, *L* is the specimen length and *K* is a factor related to the constraint at the end of the specimen.

$$F^{\text{buckling}} = \frac{\pi^2 EI}{(KL)^2} \qquad [8.90]$$

For the cylindrical cross-section of these specimens,

$$I = \frac{\pi}{2} r^4 \qquad [8.91]$$

where *r* is the cylinder radius. Therefore,

$$F^{\text{buckling}} = \frac{\pi^3 E r^4}{2(KL)^2}. \qquad [8.92]$$

The Young's modulus, *E*, and constraint factor, *K*, are the same for the two specimen types. Letting the default SMARTS specimen have dimensions r_A and L_A, and a buckling stress F_A^{buckling}, and our specimen have dimensions r_B and L_B, and a buckling stress F_B^{buckling}:

$$F_A^{\text{buckling}} = \frac{\pi^3 E r_A^4}{2(KL_A)^2}. \qquad F_B^{\text{buckling}} = \frac{\pi^3 E r_B^4}{2(KL_B)^2}. \qquad [8.93]$$

Ministry of Defence © British Crown Copyright 2020/AWE

The ratio of the buckling stress of our specimen to that of the default specimen is given by equation [8.94].

$$\frac{F_B^{\text{buckling}}}{F_A^{\text{buckling}}} = \frac{r_B^4}{L_B^2}\frac{L_A^2}{r_A^4} \qquad [8.94]$$

For $r_A = 5\,\text{mm}$, $L_A = 24\,\text{mm}$, $r_B = 7\,\text{mm}$, and $L_B = 28\,\text{mm}$, this evaluates to

$$\frac{F_B^{\text{buckling}}}{F_A^{\text{buckling}}} = 2.8 \qquad [8.95]$$

Ministry of Defence © British Crown Copyright 2020/AWE

Ministry of Defence © British Crown Copyright 2020/AWE

A9 Additional Data - Chapter 5

A9.1 Tensile Rig Initial Design

The initial design for the tensile rig focused on satisfying requirements C and D in section 5.3.1on page 213 - dissipating energy in the event of a specimen fracture and transferring load to the specimen without direct contact from the tensile grips. The plan was to then encase the entire rig in a transparent Perspex box to satisfy the other requirements.

Instead of applying force to the specimen by clamping down on the shoulders of the specimen, load could be applied by contact to the fillets between the gauge region and the shoulders. The material applying the load could be gripped by the tensile grips and increasing grip displacement would transmit a tensile load to the specimen.

A ductile material was loaded in parallel to the uranium specimen to absorb the released elastic strain energy in the event of specimen fracture. It bridged the gap between the two tensile grips, maintaining the integrity of the grip-specimen-grip fixture, preventing rapid motion of the specimen.

The initial design is shown in figure 8.61. The rig consists of a single machined piece of aluminium, with 4 mm thick material transferring load from the grips to the specimen and 1 mm material in parallel to the specimen. The tensile grips would clamp on to the regions shaded in red.

Ministry of Defence © British Crown Copyright 2020/AWE

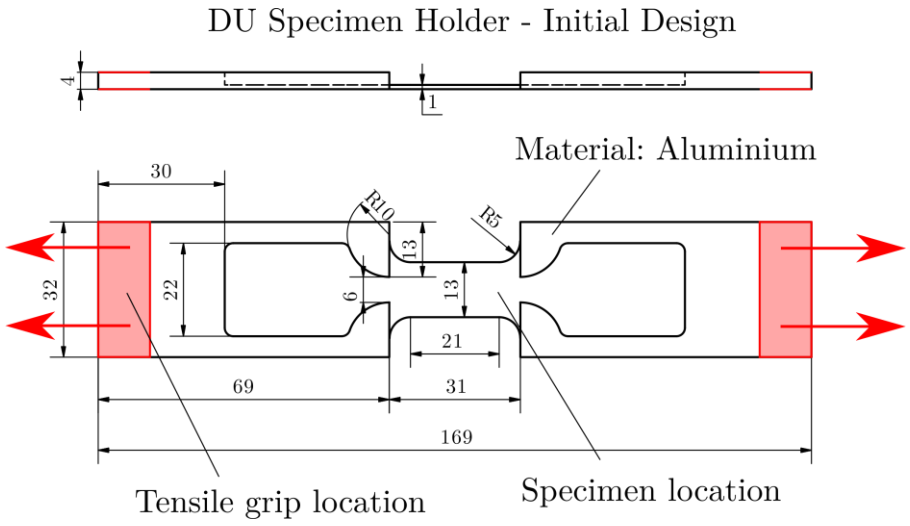


Figure 8.61. Drawing of initial design for tensile rig for uranium testing in Oxford. Tensile load would be applied by the Shimadzu wedge grips on the regions shaded in red.

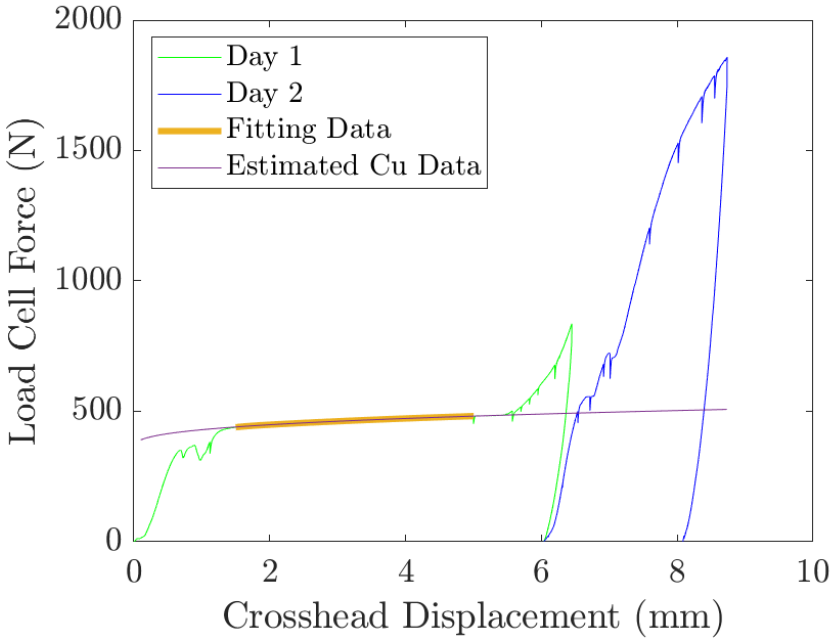
A number of issues were found with this design which prevented its use. Firstly, the component is sacrificial, and an entirely new rig would have to be machined for each test. The geometry is complex, and would require a considerable time of expensive CNC machining in the workshop to produce sufficient components for validation and testing.

In addition, it was found that the DIC camera system cannot be calibrated successfully if the specimen is enclosed with Perspex as the higher refractive index of Perspex distorts the image from each camera, and the distortion is strongly dependent on the alignment of the cameras, Perspex shield and specimen surface. These parameters would be hard to control during a test – for example the shield and specimen may move or rotate slightly as load is applied.

Ministry of Defence © British Crown Copyright 2020/AWE

A9.2 Loading Curves

(a) DB-T1 Load-Displacement Data



(b) DB-T1 Calculated Stress-Displacement Data

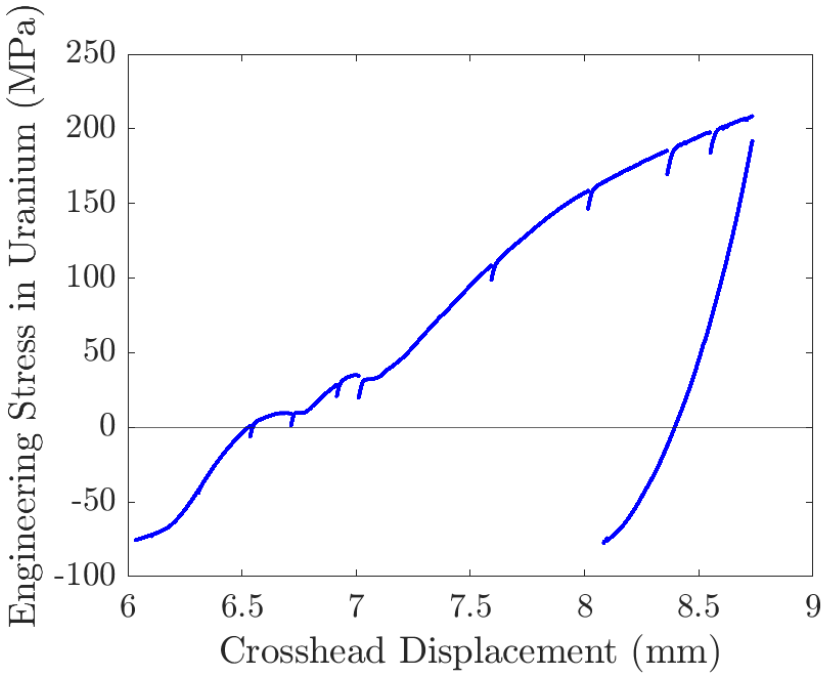
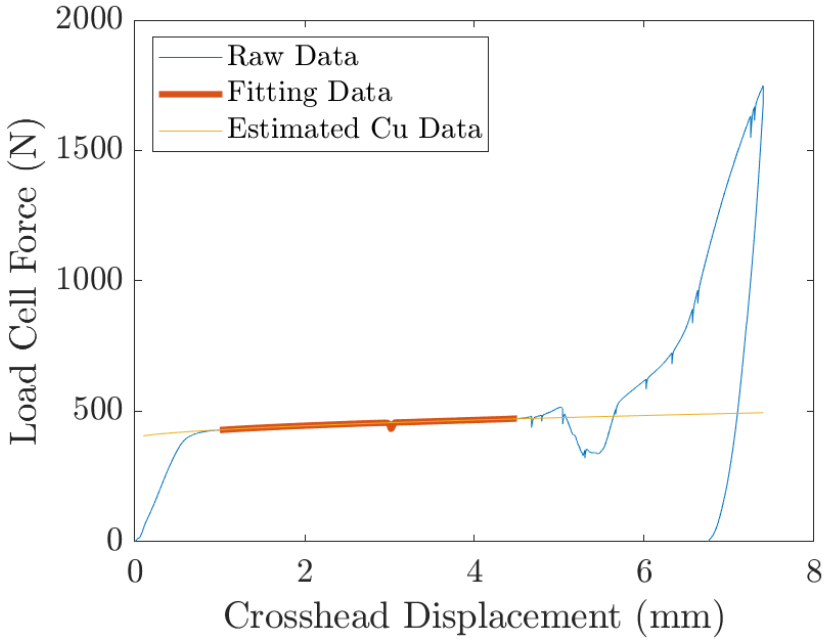


Figure 8.62. Tensile test data for specimen DB-T1. (a) Load-Displacement data from the Shimadzu load frame. (b) Stress-displacement data calculated by subtraction of the estimated copper load from the total load, and converting to stress via the measured specimen cross-sectional area. Only data from the second day of testing was analysed and it was assumed that no plastic deformation had occurred on day 1.

Ministry of Defence © British Crown Copyright 2020/AWE

(a) DB-T2 Load-Displacement Data



(b) DB-T2 Calculated Stress-Displacement Data

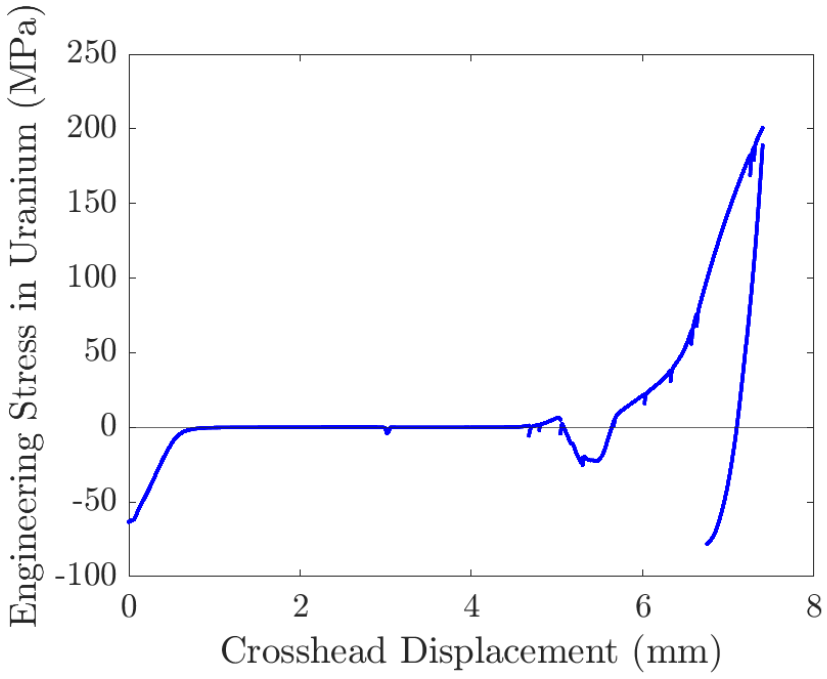
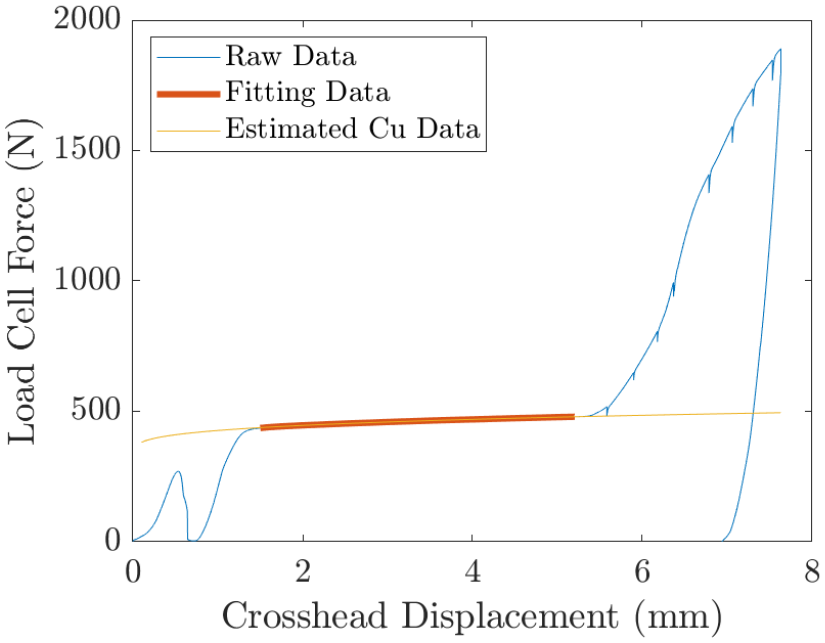


Figure 8.63. Tensile test data for specimen DB-T2. (a) Load-Displacement data from the Shimadzu load frame. (b) Stress-displacement data calculated by subtraction of the estimated copper load from the total load, and converting to stress via the measured specimen cross-sectional area.

Ministry of Defence © British Crown Copyright 2020/AWE

(a) DB-T3 Load-Displacement Data



(b) DB-T3 Calculated Stress-Displacement Data

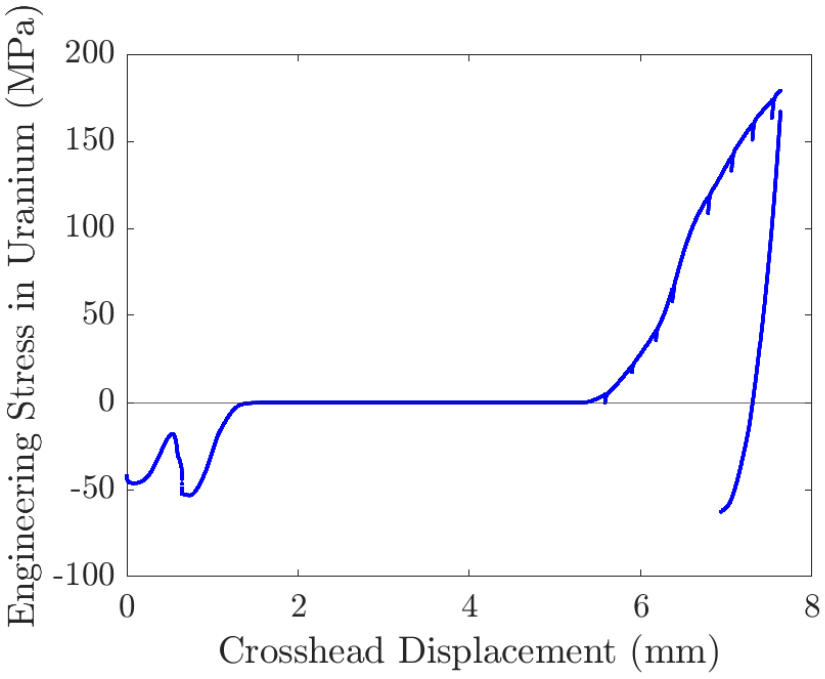


Figure 8.64. Tensile test data for specimen DB-T3. (a) Load-Displacement data from the Shimadzu load frame. (b) Stress-displacement data calculated by subtraction of the estimated copper load from the total load, and converting to stress via the measured specimen cross-sectional area.

Ministry of Defence © British Crown Copyright 2020/AWE